Finite deformation of particulate geomaterials: frictional and anisotropic Critical State elasto-plasticity

WILLIAM MICHAEL COOMBS

Durham University

Finite deformation of particulate geomaterials: frictional and anisotropic Critical State elasto-plasticity

Thesis by

William Michael Coombs

Submitted as partial consideration towards
the degree of Doctor of Philosophy

Computational Mechanics Group
School of Engineering & Computing Sciences
Durham University
United Kingdom

June 2011

Finite deformation of particulate geomaterials: frictional and anisotropic Critical State elasto-plasticity

William Michael Coombs

Abstract

This thesis is concerned with the theoretical development and numerical implementation of efficient constitutive models for the analysis of particulate media (specifically clays) in structures undergoing geometrically non-linear behaviour. The Mohr-Coulomb and modified Cam-clay constitutive models have both been examined and extended to provide greater realism. Findings from this thesis will interest engineers working in numerical methods in solid mechanics, along with those investigating continuum mechanics, inelastic constitutive modelling and large strain plasticity. Although focused on soil plasticity, this research has relevance to other areas, such as metal forming and bio-engineering.

Initially the concepts of material and geometric non-linearity are reviewed. A general implicit backward Euler stress integration algorithm is detailed, including the derivation of the algorithmic consistent tangent. A framework for the analysis of anisotropic finite deformation elasto-plasticity is presented and a full incremental finite-element formulation provided. The first constitutive model developed in this thesis is a non-associated frictional perfect plasticity model based on a *modified Reuleaux* triangle. It is shown, through comparison with experimental data, that this model has advantages over the classical Mohr-Coulomb and Drucker-Prager models whilst still allowing for analytical implicit stress integration. An isotropic hyperplastic family of models which embraces the concept of a Critical State is then developed. This family is extended to include inelastic behaviour within the conventional yield surface and a Lode angle dependency on the anisotropic yield function which maintains convexity of both the surface and uniqueness of the Critical State cone. A calibration procedure is described and the integration and linearisation of the constitutive relations are detailed. All of the developed models are compared with established experimental data. Finally the models are verified for use within finite deformation finite-element analyses. The importance of deriving the algorithmic consistent tangent is demonstrated and the influence of varying levels of model sophistication assessed in terms of both global behaviour and simulation run-time.

Declaration

The work in this thesis is based on research carried out in the Computational Mechanics Group, School of Engineering and Computing Sciences, Durham University. No part of this report has been submitted elsewhere for any other degree or qualification and it is all my own work unless referenced to the contrary in the text.

Acknowledgements

The following research would not have been possible without generous funding from both the Engineering and Physical Sciences Research Council[1] and the School of Engineering and Computing Sciences, Durham University. This support is gratefully acknowledged.

Numerous people from the School of Engineering and Computing Sciences have help me during my time at Durham University. First I would like to thank my supervisor Roger Crouch who has inspired me throughout my research to always *"ask why?"*. He was never too busy to make time to listen and help rationalise my thoughts, particularly at beginning of my PhD. His depth and breadth of knowledge has been invaluable. It was Charles Augarde who first suggested I start my PhD and throughout my studies his knowledge in numerical geomechanics has been very useful and his general advice gratefully received. I must also mention Claire Heaney, whose mathematical background and rigour was a great help during the first two years of my PhD. Additional thanks should go to David Toll, who made Antonio Gens' PhD thesis available to me. This has been an invaluable resource of soil testing experimental data. I am also grateful to all those members of the Computational Mechanics Group that provided useful discussions and contrasts to my research and who, through light relief during the working day, kept my sanity in check.

Thanks must go to Ian Collins at The University of Auckland, New Zealand. The two weeks of June 2010 spent visiting and working with Ian in Auckland helped to shape the final year of my PhD. Our conversations during this time clarified and enhanced my knowledge and understanding of hyperplasticity.

I believe that having some distraction from research is essential to consolidate ideas and thoughts. Thank you to everyone that has encouraged and inspired me during my cycling, kayaking and climbing activities.

Finally I would like to thank Jo. Throughout my PhD, and particularly during the writing of this thesis, she has been extremely supportive and understanding, always knowing when I need to be dragged away from, or left alone with, my research.

Will Coombs
Durham, June 2011

[1] EPSRC grant number EP/D077117/1.

Contents

List of Figures

List of Tables

Nomenclature & abbreviations

For convenience the nomenclature, in addition to a list of abbreviations, has been split into six sections. The *identifiers* and *operators* can be combined with or operate on any of the *scalars* (*material constants* or *others*), *tensors*, *vectors* or *matrices*, respectively.

Abbreviations

AC	anisotropic consolidation [hollow cylinder test series]
ALE	arbitrary Lagrangian-Eulerian
B-L	Bhowmik-Long
bE	backward Euler
CAS	critical anisotropic state
CPP	closest point projection
CPPM	closest point projection method
CS	Critical State
CSL	Critical State line
CSS	Critical State surface
CSSM	Critical State soil mechanics
D-P	Drucker-Prager
DTC	drained triaxial compression
DTE	drained triaxial extension
EMSS	energy mapped stress space
FE	finite-element
FEM	finite-element method
GNL	geometric non-linearity
GPM	governing parameter method
Gud	Gudehus
HCA	hollow cylinder apparatus
HCL	hydrostatic consolidation line
IC	isotropic consolidation [hollow cylinder test series]
K	Kaolin
KTK	Kuhn-Tucker-Karush
LAD	Lode angle dependency
LC	London clay
LCT	Lower Cromer till
M-C	Mohr-Coulomb
M-N	Matsuoka-Nakai
MCC	modified Cam-clay
mR	modified Reuleaux
MS	Monterey Sand
N-R	Newton-Raphson
NAF	Non-associated [plastic] flow
NCL	normal consolidation line
OCR	overconsolidation ratio
P-R	Prandtl-Reuss
SFBM	San Francisco Bay mud
SMBS	Santa Monica Beach sand
UTC	undrained triaxial compression
UTE	undrained triaxial extension
vM	von Mises
W-W	Willam-Warnke
$\alpha\gamma$	isotropic single-surface two-parameter model
$\beta\alpha\gamma$	anisotropic single-surface two-parameter model
2s$\alpha\gamma$	isotropic two-surface two-parameter model
2s$\beta\alpha\gamma$	anisotropic two-surface two-parameter model

Identifiers

${}^{0}(\cdot)$	initial condition of $(\cdot)$ for the Newton-Rahpson procedure
${}^{\varsigma}(\cdot)$	energy-mapped version of $(\cdot)$
$(\cdot)^{\mathrm{ep}}$	elasto-plastic quantity of $(\cdot)$
$(\cdot)^{\mathrm{e}}$	elastic component of $(\cdot)$
$(\cdot)^{\mathrm{p}}$	plastic component of $(\cdot)$
$(\cdot)^{\varphi}$	dissipative stress quantity
$(\cdot)_{\gamma}$	deviatoric invariant of $(\cdot)$
$(\cdot)_{cp}$	quantities associated with the closest point stress return
$(\cdot)_{cs}$	value of $(\cdot)$ at the Critical State
$(\cdot)_{K_0}$	measure of $(\cdot)$ under K_0 loading
$(\cdot)_{mp}$	material point quantity of $(\cdot)$
$(\cdot)_{n+1}$	value of $(\cdot)$ in the current configuration
$(\cdot)_{n}$	value of $(\cdot)$ in the previous configuration
$(\cdot)_{r}$	backward Euler return value of $(\cdot)$
$(\cdot)_{sym}$	symmetric component of $(\cdot)$
$(\cdot)_{t}$	trial value of $(\cdot)$
$(\cdot)_{v}$	volumetric component of $(\cdot)$
$(\cdot)_{\mathrm{fd}}$	finite deformation version of $(\cdot)$
$\hat{(\cdot)}$	principal components of $(\cdot)$

Scalars (material constants)

α, γ	material constants controlling the shape and direction of plastic flow of the two-parameter yield surfaces
α_f, α_g	opening angles of the modified Reuleaux yield surface and plastic potential cones
$\varepsilon^{\mathrm{e}}_{v0}$	reference elastic volumetric strain

κ, λ	bi-logarithmic elastic and plastic compressibility indicae
ϕ	friction angle
ϕ_g	dilation angle
$\bar{\rho}_e$	relative size of the deviatoric radius under triaxial extension with respect to that under triaxial compression
σ_c	Mohr-Coulomb yield stress (Pa)
σ_y	yield stress (Pa)
υ	Poisson's ratio
ξ_c	hydrostatic yield stress (Pa)
$\bar{a}$, $\bar{r}$	constants for the modified Reuleaux deviatoric function
a_β, b_β, x_β	constants controlling the volumetric target, deviatoric target and relative contributions for the evolution of anisotropy
c	apparent cohesion (Pa)
C_β	constant controlling the rate of evolution of anisotropy
C_χ	constant controlling the rate of translation of the inner yield surface
E	Young's modulus (Pa)
k	constant of passive earth pressure
M	classical gradient of the Critical State line in the p versus q plane
N	Critical State line gradient in the p versus q_{txl} plane
p_r	reference pressure (Pa)
R	constant ratio of the size of the inner yield surface to that of the outer yield surface
a_1, a_2	constants for the Willam-Warnke deviatoric function
G	shear modulus (Pa)

Scalars (other)

$\alpha_{d\sigma}$	incremental stress path direction
β	measure of the inclination of the yield surface off the hydrostatic axis in triaxial stress space
η	stress ratio
ε	scalar strain measure
$\varepsilon_{\theta z}$	shear strain the in axial-circumferential plane
ε_z, ε_r, ε_θ	axial, radial and circumferential strain
$\dot{\gamma}$, $\Delta\gamma$	rate and increment of the plastic consistency parameter
$\dot{\Phi}$	dissipation rate function
$\dot{\Phi}_1$, $\dot{\Phi}_2$	rate of dissipation on the outer and inner yield surfaces (W/m^3)
Ψ	free-energy function (J/m^3)
Ψ_1, Ψ_2	elastic and plastic components of the free-energy function (J/m^3)
φ	arc angle for the modified Reuleaux deviatoric function
ψ	effective friction angle
$\bar{\rho}$	normalised deviatoric radius
ρ	deviatoric stress invariant (Pa)
ρ_g	density (N/m^3)
σ_z, σ_r, σ_θ	axial, radial and circumferential stress (Pa)
$\sigma_{z\theta}$	shear stress in the axial-circumferential plane (Pa)
θ	Lode angle
θ_c	angular circumferential displacement
θ_{hp}, ϕ_{hp}	angular measures for the unit direction vector
ξ	hydrostatic stress invariant (Pa)
ξ_g	intersection of the plastic potential with the hydrostatic axis (Pa)
A, B	parameters controlling the two-parameter yield surface shape (Pa)
A_f, B_f	parameters controlling the inner yield surface shape (Pa)
b	intermediate principal stress ratio
b_m	parameter controlling the Lode angle dependent two-parameter yield surface shape (Pa)
d_β	parameter controlling the evolution of anisotropy
e, v	void ratio and specific volume
e_{A} to e_{D}	instability indicators
f, F	yield functions
H	scalar measure of the plastic tangent stiffness
I_1, J_2, J_3	first, second and third invariants of stress (Pa)
J	volume ratio (determinant of the deformation gradient)
J_2^β, J_3^β	second and third local deviatoric stress invariants (Pa)
K	bulk modulus (Pa)
(l/l_0)	contraction/dilation ratio
l	length or height (m)
M_T	torque (Nm)
n_1, n_2, n_3	directional components of a unit vector
n_p	number of particles
n_u	number of unknowns in the backward Euler stress integration algorithm
n_{gp}	number of element Gauss points
n_{mc}	number of material constants
n_{pgp}	number of elasto-plastic Gauss points
p	hydrostatic pressure (Pa)
p_a	ratio of the size of the Critical State yield surface, p_c, to the current hydrostatic pressure

p_c	hydrostatic size of the yield surface for the Critical State models (Pa)
p_o, p_i	external and internal pressures (Pa)
p_t	total pressure (Pa)
p_0	projection centre hydrostatic pressure (Pa)
p_β	local hydrostatic pressure measure from the inner surface apex (Pa)
p_A	apex hydrostatic pressure (Pa)
q	deviatoric stress invariant (Pa)
q_{txl}	stress deviator, the difference between the major and minor principal stresses ($\sigma_3 - \sigma_1$) (Pa)
r_o, r_i	external and internal radii (m)
t	time
t_1, t_2, t_3	energy-mapped stress space transformation constants
u	pore water pressure (Pa)
u_i, u_o	internal and external displacements (m)
V, V_0	volume in the current and reference configurations (m^3)
$\dot{W}^{\text{p}}$	plastic work rate (W/m^3)
W	axial load (N)
w	weight function (m^3)
tol	tolerance

Tensors

β_{ij}	tensorial measure of the inclination of the yield surface
χ_{ij}	shift stress (Pa)
δ_{ij}	Kronecker delta tensor
ε_{ij}	strain tensor
φ_{ij}	dissipative stress (Pa)
φ_i	motion
σ_{ij}	Cauchy stress (Pa)
σ_i	principal stresses (Pa)
τ_{ij}	Kirchhoff stress (Pa)
b_{ij}, C_{ij}	left and right Cauchy-Green strain tensors
E_{ij}	Green-Lagrangian strain
F_{ij}	deformation gradient
n_i	normal direction unit tensor
$(Q^{(\cdot)}_{at})_{jk}$	acoustic tensor of $D^{(\cdot)}_{ijkl}$
R_{ij}	rotational component of the deformation gradient
u_i	deformation (or displacement)
v_{ij}, U_{ij}	left and right stretch tensors
x_i, x_i^{p} X_i	current, fictitious and original configurations

Vectors

$\{\beta\}$	internal material parameters
$\{\chi\}$	shift stress vector (Pa)
$\{\eta\}$	imposed displacement field (m)
$\{\varepsilon\}$	strain vector
$\{\gamma\}$	deviatoric strain vector
$\{\varphi\}$	dissipative stress vector (Pa)
$\{r\}$	local stress ratio vector
$\{\breve{\sigma}\}$	image point stress vector (Pa)
$\{\sigma\}$	Cauchy stress vector (Pa)
$\{\sigma_0\}$	projection centre stress vector (Pa)
$\{\sigma_e\}$	*exact* stress return corresponding to a sub-incremented solution (Pa)
$\{\varsigma\}$	energy-mapped stress vector (Pa)
$\{\xi\}$	instability characteristic vector
$\{b\}$	backward Euler residuals
$\{f^b\}$	body forces per unit volume (N/m^3)
$\{f^{\text{ext}}\}$	external force vector (N)
$\{f^{\text{int}}\}$	internal force vector (N)
$\{f^{\text{oobf}}\}$	out-of-balance force vector (N)
$\{f^e\}$	element force vector (N)
$\{g_{,\sigma}\}$	direction of plastic flow
$\{H_\beta\}$	evolution of the internal variables
$\{n\}$	unit normal direction vector
$\{n_f\}$, $\{n_g\}$	orientation of the modified Reuleaux yield surface and plastic potential edges
$\{s\}$	deviatoric stresses (Pa)
$\{s^\beta\}$, $\{s^r\}$	local measures of deviatoric stress (Pa)
$\{t\}$	surface traction per unit area (N/m^2)
$\{x\}$	backward Euler unknowns
$\{v_i\}$	the ith eigenvector of a matrix
$\{1\}$	$\{1 \quad 1 \quad 1 \quad 0 \quad 0 \quad 0\}^T$

Matrices

$[\beta]$	backstress matrix
$[\gamma]$	deviatoric strain matrix
$[\Lambda^{\text{e}}]$	elastic spin matrix
$[A^{alg}]$	consistent tangent Hessian matrix
$[A]$	backward Euler Hessian matrix
$[B]$, $[G]$	spatial six- and nine-component strain-displacement matrices (m^{-1})
$[B^D]$	derivative of $(b^{\text{e}}_t)_{ij}$ with respect to the deformation gradient, mutliplied by the deformation gradient
$[C^{\text{ep}}]$	infinitesimal elasto-plastic compliance matrix (Pa^{-1})
$[C^{\text{e}}]$	elastic compliance matrix (Pa^{-1})
$[D^\beta]$	derivative of the return stress with respect to the trial anisotropy (Pa)
$[D^\chi]$	derivative of the return stress with respect to the trial centre of the inner yield surface
$[D^{\text{ep}}]$	infinitesimal elasto-plastic tangent stiffness matrix (Pa)
$[D^{\text{e}}]$	elastic stiffness matrix (Pa)

$[D^{cst}]$	anisotropic spatial consistent tangent stiffness matrix (Pa)
$[D^{cst}_{\beta}]$	backstress contribution to the anisotropic spatial consistent tangent stiffness matrix (Pa)
$[D^{cst}_{\sigma}]$	isotropic spatial consistent tangent stiffness matrix (Pa)
$\left[D^{alg}\right]$	small strain algorithmic consistent tangent stiffness matrix (Pa)
$[\bar{F}]$	F-bar deformation gradient
$[F]$	deformation gradient matrix
$[F_p]$	particle orientation-based fabric matrix
$[F_{iso}]$	isochoric component of the deformation gradient
$[J]$	Jacobian matrix
$[K]$	global stiffness matrix (N/m)
$[k^e]$	element stiffness matrix (N/m)
$[L]$	derivative of $\ln(b^{\mathrm{e}}_t)_{ij}$ with respect to $(b^{\mathrm{e}}_t)_{ij}$
$[L_{\beta}]$	partial derivative of the inverse square root of the symmetric b^{e}_{ij} tensor with respect to its argument
$\left[L^{\mathrm{p}}\right]$	plastic velocity gradient
$[N]$	nodal shape functions
$[Q]$	orthogonal rotation matrix
$[Q^{(\cdot)}_{at}]$	acoustic matrix of $D^{(\cdot)}_{ijkl}$
$\left[R\right]$	rotational component of the deformation gradient matrix
$[s^{\beta}]$	local deviatoric stress matrix (Pa)
$[S^D]$	nine by nine stress component matrix $\sigma_{il}\delta_{jk}$ (Pa)
$[s]$	deviatoric stress matrix (Pa)
$[T]$	transformation matrix
$[U_{\beta}]$, $[V_{\beta}]$	matrix contributions to $[D^{cst}_{\beta}]$
$[0]$	three by three null matrix
$[1]$, $[I]$	three by three and six by six identity matrices

Operators

$(\cdot)_{,xx}$	the second partial derivative of $(\cdot)$ with respect to x
$(\cdot)_{,x}$	partial derivative of $(\cdot)$ with respect to x
$(\cdot)^T$	transpose of $(\cdot)$
$\hat{(\cdot)}$	principal quantity of $(\cdot)$
$\delta(\cdot)$	iterative increment in $(\cdot)$
$\Delta(\cdot)$	increment of $(\cdot)$
$\dot{(\cdot)}$	rate of $(\cdot)$
$\langle(\cdot)\rangle$	ramp function of $(\cdot)$
$\mathring{(\cdot)}$	Green-McInnis-Naghdi rate of $(\cdot)$
$\mid(\cdot)\mid$	absolute value of $(\cdot)$
$\parallel(\cdot)\parallel$	L2 norm of $(\cdot)$
$\det(\cdot)$	determinant of $(\cdot)$
$\mathrm{tr}(\cdot)$	trace of $(\cdot)$
$\tilde{(\cdot)}$	incremental hardening law of $(\cdot)$ for use within the bE stress integration method
$d(\cdot)$	differential of $(\cdot)$

Chapter 1

Introduction

> *"Geomaterials are very complex... in order to analyse it is always necessary to idealise."*
>
> JB Burland, foreword to *Plasticity and Geotechnics*, H-S Yu (2006).

In-situ geotechnical materials often exhibit significant anisotropy in their stiffness due to the deposition process and the particulate nature of their fabric. Even at very low strains (<0.01%), geomaterials display non-linear, energy-dissipating behaviour, with slip (inelasticity) developing early in the deformation response. Under loading the interaction and movement of soil particles results in rearrangement of the contact networks between the constituent fabric, potentially leading to significant volume changes, force-transfer instabilities and localisation.

Designing efficient foundations for large terrestrial structures on (towers, dams, offshore platforms) or within (tunnels, caverns) soft sediments can pose significant challenges for geotechnical engineers. Careful site investigations can enable the stratification of the subsoil to be detected. Knowledge of the heterogeneity and characterisation of the soil through field or laboratory testing can then allow finite-element analyses to make valuable predictions of the foundation behaviour. The quality of such simulations depends largely on the level of geometric detail captured, the appropriateness of the assumed boundary conditions, the physics embraced and the degree of realism provided by the chosen, properly calibrated, constitutive models. Theoretical issues surrounding the behaviour when large deformations and strains (10% or more) occur can further complicate the analysis.

Requirement from industry

The largest element of technical and financial risk in any civil engineering project normally lies in the ground [15]. Most geotechnical construction activities are on, or close to, a project's critical path, therefore any delays in the ground can cause a project overrun, in both schedule and budget [11]. 37% of projects surveyed by the Institution of Civil Engineers overran due to geotechnical problems [15]. Despite this, on average, only 0.2–2% of a project's total budget will be spent on site investigation [29]; providing a challenging task for geotechnical engineers as they try to assess correctly the appropriate ground solution.

With the increasing need to develop construction projects in highly congested urban land, such as city centres, the proximity of existing buildings and infrastructure poses further challenges. The incorrect assessment of ground conditions, or not appropriately accounting for material behaviour, can have serious consequences. The collapse of a tunnel during the construction of Heathrow airport terminal 4 in October 1994 was partially due to *"the lack of appreciation of the differences between hard rock* [for which the tunnelling method was originally designed] *and soft clay behaviour"* [13]. Several factors contributed to the collapse but the *"design was not considered sufficiently robust"* [13]. No one was injured, however, a

Health and Safety Executive prosecution followed involving costs of $250 million [13].

Previous examples have shown that significant savings can be made by accounting for a material's anisotropy and small strain non-linearity (rather than just the post-yielding response), leading to a dramatic change in the appropriate foundation or construction solution. One such example was the King's Place project in central London, where it was possible to move from a piled to a shallow foundation solution; giving rise to a considerable cost saving [31].

New projects, such as London's £15.9 billion Crossrail link, will involve intricate tunnelling paths which must avoid underground train stations, sewers, power lines and other obstacles, whilst causing the minimum disruption to existing services [35]. In order to (i) assess accurately the impact of such construction on existing buildings and services and (ii) arrive at the most appropriate design solution, fast and accurate three-dimensional engineering analyses are essential.

Evidence from academia

Stallebrass and Taylor [30] demonstrated that *"conventional* [isotropic] *constitutive models of soil behaviour show very poor predictions"* when used to model a circular footing loaded in a centrifuge test. The analysis was improved by the inclusion of a model that (i) accounted for the recent stress history on the material response and (ii) introduced small strain dissipative (inelastic) material behaviour.

Whittle and Hashash [32] commented that the inaccuracies in numerical predictions of ground deformations arise from two sources (i) *"inadequate laboratory and field characterisation of relevant engineering properties"* and (ii) *"approximate representations of constitutive behaviour used in the finite element model"*. Their study used both classical isotropic and advanced anisotropic constitutive models to predict the deformation of a braced excavation in a deep layer of normally consolidated clay. They showed that in order to predict a realistic failure mechanism, the soil's small strain stiffness and anisotropic stress-strain behaviour must be accounted for. In 2009, Kung *et al.* [19] presented the back-analysis of a braced excavation in Taipei clay. The paper concluded that simple isotropic models are unable to capture satisfactorily the observed surface settlement response, due to an inability to account for the *overconsolidated* soil's small strain non-linearity.

Through comparisons with *in-situ* measurements, Zdravković *et al.* [37] showed that failing to account for the strength anisotropy inherent in soft clays resulted in the incorrect prediction of an embankment's failure height. More recently, in 2008 Möller and Vermeer [21] compared numerical predictions of surface settlements during tunnel installation with *in-situ* measurements. They concluded that in order to capture the observed surface settlement the analysis required *"an advanced constitutive soil model"* that could account for the the small strain stiffness of soils, *"otherwise computed settlement troughs will be flat and shallow rather than steep and deep"* [21].

1.1 Behaviour of particulate media

One of the major differences between particulate media and other engineering materials, such as metals, is that a large proportion of their volume is composed of voids (typically around 40–60% by volume). Therefore, the deformation of soils typically involves permanent changes in volume as the relative positions of the material particles change. Soil particle sizes and shapes can range from less than 2μm for *plate-like* clays up to 60mm for *rotund* coarse gravels [34], often with significant size variation within a given soil sample. A soil's mechanical properties and permeability will depend on the proportion, interconnectivity, shape and orientation of its constituent fabric and voids, as a result of its previous geological and stress history.

This thesis is restricted to the behaviour of saturated[1] soils. The majority of complex geotechnical

[1] That is the voids are fully filled with either water or air.

analysis undertaken in the UK, such as tunnelling, deep excavations and foundations of offshore structures, are dominated by the saturated behaviour of soils. Concepts such as partially saturated soil mechanics[2] or coupled fluid flow analysis fall outside the scope of this thesis.

Clay fabric

Clay minerals comprise hydrous aluminium phyllosilicates (weathered feldspars) lying within one of four major groups: kaolin, smectite, illite or chlorite. The particles are fine-grained (typically less than 2μm in diameter), with a sheet-like morphology. As a consequence of the tetrahedral or octahedral atomic lattice, the *platelets* generally carry a negative electric charge on their faces (attracting cations present in the pore fluid to form a double-layer cloud around the silicate layers) and a positive charge on their edges. The surfaces provides an active site for chemical interaction. Multiple platelets form domains; attached in edge-to-edge, edge-to-face or stacked face-to-face configurations. For mineral sheets ranging from 0.05 to 1μm in size, the ionic strength of the fluid medium is seen as the controlling factor for the domain size. For larger platelet sizes (but less than 20μm) face-to-face interactions dominate the local forces between the structural units. Domains may group together to form flocculated clusters as a consequence of van der Waals attraction and edge-to-face double-layer repulsion. Clusters will continue to grow until their weight, due to gravitational forces, becomes significantly larger than the inter-particle surface forces. On a larger scale, clusters can group together to form peds. On the granular scale of clusters and peds, frictional forces control the mechanics rather than electrostatic or van der Waals forces. Therefore, these clusters can behave in similar way to sands. Similarly to the crushing of granular materials, at some level of stress these clusters break-down. When this occurs the subsequent behaviour of the material will be influenced by the rearrangement and alignment of the individual clay particles. Large scale shearing in clays can eventually cause the particles to become highly oriented, producing polished surfaces (slickensides) within the rupture zone. This residual state is not generally considered to be the same as Casagrande's [5] *Critical State*. The distinction between the residual state and the Critical State is not entirely clear. Furthermore, exactly when the mechanical behaviour of clay is controlled by clusters or platelets remains uncertain. Finally, there is no conclusive evidence as to whether the packing of clay platelets is anisotropic or effectively isotropic at the Critical State.

Discrete element modelling

Since the pioneering work of Cundall and Strack [7], *discrete element modelling* has provided valuable insights into the mechanical behaviour of granular media. This method was developed as a research tool for informing the development of physically sound continuum models by investigating the micro-mechanics of granular materials [36]. Within each time step, two calculations are undertaken. Firstly the computationally expensive task of contact detection and calculation of the associated frictional and acceleration forces is performed. Secondly, momentum balance is applied to each particle to determine the new location at the end of the time step [7].

Modelling soils as vast assemblies of individual particles (rather than an averaged macroscopic continuum) suggests that the physics could be addressed more faithfully; providing more fundamental origins for the material constants of continuum models. Yet the computational burden of handling the three-dimensional contact between irregularly shaped grains is by no means small for large numbers of particles. Determining realistic local traction-slip relationships for clays is even more troublesome. To give some idea of the scale of the problem, a 38mm diameter cylindrical triaxial sample could contain 10^{15} platelets. The region beneath a large engineering structure might comprise 10^{26} such particles. Discrete element method simulations running on multi-core computers currently allow at most 10^7 particles [24]. Even

[2] See Lu and Liko [20], amongst others, for more information on unsaturated soil mechanics.

assuming dramatic improvements in processing power, it is most unlikely that we will be able to routinely handle tera-scale (10^{12}) simulations within the next decade.

The majority of discrete element studies have focused on granular materials. Anandarajah [1] reported on the first use of a discrete element model for clays, using line elements where the chemo-electrical interactions between clay platelets were used to form the contact laws between particles. In that work, just 250 elements were used; each particle measuring 0.1μm in length. Reasonable qualitative agreement was reached between the simulations and observations of real clay behaviour under uniaxial compressive straining. That work was later extended to allow the clay platelets to flex [2]. The two-dimensional simulations were still restricted to a small (18μm square) region using 431 particles. The key finding was that anisotropic behaviour was governed by the orientation of the force chains running through clusters of clay particles. This argument was used to explain the anisotropic mechanical behaviour of some clays with no obvious directional preference in their platelet orientation.

Recent two-dimensional discrete element analyses of elongated particles by Fu and Dafalias [9, 10] reveal that internal force chains are progressively organised to approach co-alignment under continuous shearing. These observations have suggested that, irrespective of prior anisotropy, the same mean orientation of non-spherical grains is attained within localised shear bands when approaching the Critical State.

Despite scale limitations, the information obtained from discrete element studies should be used, where appropriate, to guide the development of continuum models and potentially challenge some of the ideas embedded in classical continuum mechanics. Such a multi-scale strategy, where in discrete element simulations inform the construction of macroscopic continuum models, is very attractive.

Observed soil behaviour

The majority of experimental soil testing is conducted using a triaxial cell. The axi-symmetric apparatus allows independent control over two principal stresses: through the axial load and the cell pressure. In undrained soil testing, fluid is not allowed to leave (or enter) the soil sample; resulting in an isochoric response. During triaxial compression, the axial load is increased whilst maintaining a constant cell pressure.

Other common experimental rigs developed for the study of soil include the oedometer, used to evaluate the one-dimensional straining of soil and the direct shear box (for granular material). More sophisticated experimental equipment, such as the *true triaxial* rig and the *hollow cylinder apparatus*[3], allows greater control so that a larger proportion of stress space can be explored.

The stress deviator versus strain deviator[4] response of Spestone Kaoline under undrained triaxial loading (compression), unloading and re-loading is reproduced (after Roscoe and Burland [26]) in Figure 1.1. The unloading and re-loading behaviour of the clay showed little hysteresis in the initial part of the test. The stiffness of the material reduced when approaching the previous unloading stress level. This reduction in stiffness was a consequence of material *yielding*, where the unloading point served as the current yield point of the soil. This non-linearity is a result of the sliding, rotation, re-alignment and general re-arrangement of clay particles, clusters or peds. As the magnitude of the unload-reload cycles increase, significant hysteresis is observed in re-loading response of the clay following unloading. This hysteresis is a consequence of the dissipative re-arrangement of the soil fabric on unloading. The single experimental test (Figure 1.1) serves to demonstrate many of the key features of clay behaviour, namely:

[3]The true triaxial rig allows control over the three principal stresses applied on the surface of a cube. The hollow cylinder apparatus allows control over the three normal stresses in addition to one shear stress via the independent control over the internal and external pressure, axial load and torque. See Wood [33], amongst others, for more details on these experimental apparatus.

[4]Here, the stress deviator is the difference between the axial and radial stresses, similarly the strain deviator is the different between the axial and radial strains.

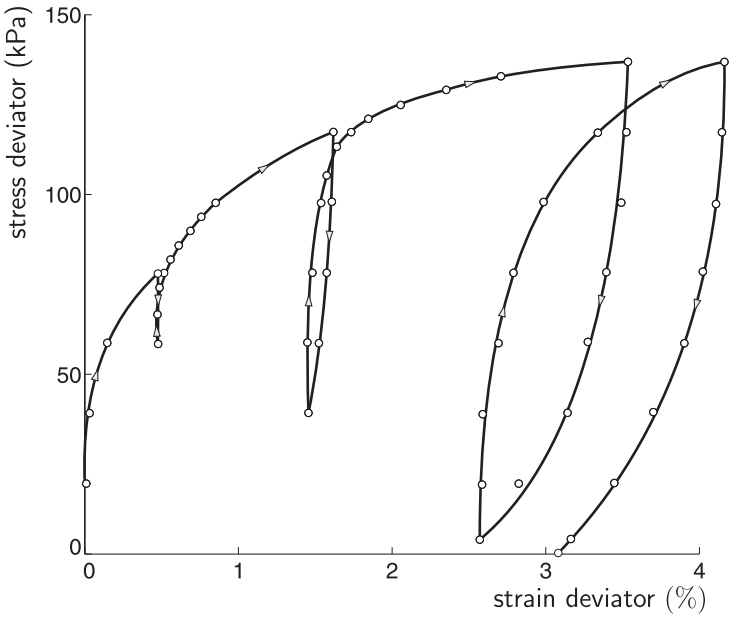

Figure 1.1: Experimental response of cycles of undrained triaxial compression and unloading on Spestone Kaolin (after Roscoe and Burland [26]).

(i) *non-linearity*: throughout the stress-strain response;

(ii) *stiffness reduction*: gradual yielding of the soil fabric on loading and unloading when experiencing large stress cycles;

(iii) *memory*: recent unloading points serve as current yield points for the soil; and

(iv) *hysteresis*: increasing in magnitude with increasing stress cycles (although the response under many repeated stress cycles is not shown in Figure 1.1).

Particulate material, by definition, is comprised of many separate grains, platelets or clusters of particles which can give rise to a complex fabric. As mentioned, even if a complete classification of the particles, in terms of their shape, size, packing and arrangement within a soil body was attempted, predicting the mechanical response of such an assembly would be at very least cumbersome. Here, the idealisation of a continua is adopted where the behaviour of this discrete system of particles is represented using the methods of *continuum mechanics*.

1.2 Constitutive modelling

Analysis of engineering structures requires the specification of a relationship between stress and strain for the materials under consideration. These *constitutive models* play a central role in any boundary value simulation and are required for almost every method in soil mechanics, from analytical predictions of foundation settlements to planning field investigations and laboratory testing. In 1990, Wood [34] opened the introduction of his *Soil Behaviour and Critical State Soil Mechanics* text with a quote from Baran and Sweezy [3]. Here, one sentence has been extracted about the use of models in engineering:

> *"The purpose of these models is not to give a mirror image of reality, not to include all its elements in their exact sizes and proportions, but rather to single out and make available for intensive investigation those elements which are decisive."*

In other words, models are required to bring out the important features of a problem and disregard those that are irrelevant.

Early constitutive relations were based on a linear *elastic* relationship between stress and strain. Such relations were subsequently extended to include *non-linear elastic* behaviour and *perfect plasticity*. Simple *frictional perfect plasticity* models, such as Mohr-Coulomb and, later, Drucker-Prager [8] constitutive formulations, are the most widely used material models able to capture the idealised basic behaviour of soils. Despite their popularity, these simple plasticity models fail to capture two fundamental yield dependencies: (i) on the Lode angle, in the case of the Drucker-Prager model and (ii) on the intermediate principal stress, in the case of the Mohr-Coulomb model. These omissions in the shear strength are overcome, whilst maintaining the basic features of these two classical models, by the frictional model presented in Chapter 4. However, it is not possible to reproduce the volumetric response of clays under hydrostatic (or one-dimensional) consolidation with many of the cone-type models.

It was not until the 1960s, motivated by the desire to reproduce experimental behaviour with greater realism and aided by the increase in computational power, that more sophisticated constitutive models first appeared. Critical State soil mechanics (CSSM), developed in the 1950s and 60s at Cambridge University by Roscoe and co-workers [25–27], is arguably the most successful framework for modelling the behaviour of soils. The foundations of CSSM were laid far earlier by the work of Casagrande [5], in 1936, on dense and loose sand samples. It was Casagrande who proposed the powerful idea that:

> *"Every cohesionless soil has a certain critical density, in which state it can undergo any amount of deformation or actual flow without volume change."*

This *critical void ratio* is the key assumption behind CSSM. Many of the most successful constitutive models for particulate media can trace their roots to the work of Roscoe and co-workers [25–27] on Critical State theory. The modified Cam-clay model (following on from the original Cam-clay model [27]) was the first hardening plasticity model to become generally accepted for the analysis of clays [33].

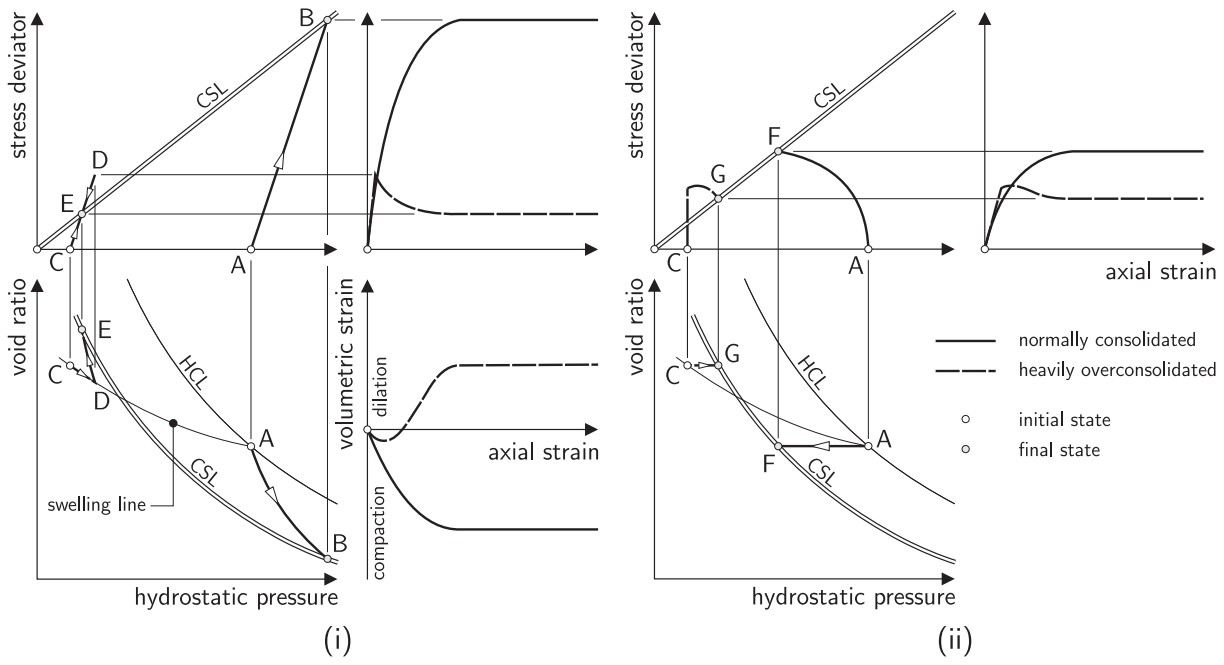

Figure 1.2: Concepts of Critical State soil mechanics: (i) drained and (ii) undrained triaxial compression tests on normally consolidated and heavily overconsolidated samples.

Figure 1.2 presents the key concepts of CSSM using drained and undrained triaxial compression tests on normally consolidated and heavily overconsolidated samples[5]. The drained response is shown in Figure 1.2 (i) in terms of: hydrostatic pressure versus stress deviator, axial strain versus stress deviator, hydrostatic pressure versus void ratio[6] and axial strain versus volumetric strain. The normally consolidated sample starts at A (on the hydrostatic consolidation line, HCL) and under drained compression moves to B. During this load path the soil undergoes volumetric compaction, reducing the void ratio, until reaching the unique Critical State line (CSL) where the soil displays isochoric behaviour with unbounded distortion but no change in state. The heavily overconsolidated sample starts at C, following swelling from a normally consolidated state at A. Under drained compression, the material initially compacts until reaching D, where the sample begins to dilate. The soil continues to dilate, with increasing void ratio, until reaching the Critical State at E. The undrained (isochoric) response under the same loading is shown in Figure 1.2 (ii). There is zero volume change for both of the tests as fluid is not allowed to enter or leave the samples, resulting in a constant void ratio. The normally consolidated sample starts at A and attains the Critical State at F, whereas the overconsolidated sample begins at C and finishes at G. The axial strain-stress deviator response is quite different for the two samples, with the overconsolidated sample reaching a peak load prior to arrival at the Critical State. The CSSM framework is able to account qualitatively for all of these experimentally observed aspects of soil behaviour.

Although many soil models have treated the medium as isotropic, sheet-like platelets within soft sediments inevitably give rise to a preferred orientation of the fabric, which can have a pronounced influence on physical properties. Thus a number of extensions to the widely-used (isotropic) modified Cam-clay plasticity model have been proposed to capture this directional bias, along with small strain inelastic behaviour. Often these additions are nothing more than elaborate curve-fitting exercises designed to reproduce a material's experimental behaviour, without properly accounting for thermodynamics [38] or the implications on the original CSSM framework. Unlike models developed for other engineering materials, a direct link has yet to be made between (i) the degree of anisotropy in these models and (ii) the evolving material fabric, for example, the orientational distribution of contacts.

In 1985, motivated by what he saw as the shortcomings of then current constitutive models, Gudehus [12] established the following *requirements* of a model. He claimed that such a model should: (G.i) cover frequently occurring processes, (G.ii) reflect repeatedly observed properties and (G.iii) be manageable. These three requirements are equally applicable today as they were over 30 years ago. However, the first requirement should perhaps be extended to require that the model is able to cover *all processes* rather than those that frequently occur in geotechnical analyses. The second requirement is that the material model should, qualitatively if not quantitatively, reproduce the general trends observed in experimental behaviour. The final request relates to the complexity and clarity of the model (and its supporting documentation) together with the ease and feasibility (both technically and economically) of determination of the material constants. Gudehus' *manageable* requirement deserves to be further split into:

(a) *tractability*: clear derivation and presentation of the constitutive algorithm;

(b) *material constants*: a complete determination procedure should be given, including the specification and evaluation of experimental tests. Typical ranges and default values should be specified; and

(c) *well-posed*, both numerically and analytically: the model should be able to produce physically realistic solutions, demonstrate solution uniqueness and be stable, when appropriate, to small changes

[5] A soil is said to be normally consolidated if it is at the highest stress in its history; having an overconsolidation ratio (OCR) of one. An overconsolidated soil has been unloaded from some previous maximum stress level; with an OCR greater than one (where the OCR is the ratio of the current to previous maximum stress level).

[6] The void ratio is the volume of voids normalised with respect to the volume of solids in a soil sample.

in material constants.

If these three conditions are achieved, the model should be *user invariant*, that is, different users will obtain the same, or very similar, results from the same calibration data [12]. The manageability requirement echoes Chen's [6] warning about the academic development of models for particulate media:

> *"This advanced development may produce the danger of a possible separation between the practical soil engineer and the theoretical academic engineer".*

Indeed some believe that this has already happened. Bolton has declared that *"a gulf has arisen between research and practice in geotechnical engineering"* [4].

Since the 1960s there has been a dramatic growth in the number of constitutive models available in academic literature. In 1985, in order to aid evaluation of the vast array of available models, Chen [6] proposed the following three *basic criteria for model evaluation*:

(C.i) *theoretical evaluation* with respect to continuum mechanics: continuity, stability and uniqueness;

(C.ii) *experimental evaluation*: ability to reproduce experimental results and ease of calibration with standard laboratory tests; and

(C.iii) *numerical and computational evaluation*: ease of implementation with non-linear boundary value codes.

These criteria should be balanced to achieve rigour in terms of respecting fundamental continuum mechanics principles, realistic material behaviour and relative simplicity in terms of implementation [6].

In 1987 Prévost and Wolf [23] placed further restrictions on several of the above conditions, with the following three constitutive algorithm requirements:

(P.i) *"complete... able to make statements about the material behaviour for all stress and strain paths"*;

(P.ii) *"identify the model parameters by means of a small number of standard, or simple material tests"*; and

(P.iii) *"founded on some physical interpretation of the ways in which the material is responding to changes in applied stress or strain".*

The first point goes further than Gudehus' [12] point (G.i), requiring *"all stress and strain paths"* rather than just those that frequently occur. The second point, similar to Gudehus [12] and Chen [6], places importance on the ease of calibration. In light of points (P.i) and (P.ii), throughout this thesis, particular attention was paid to the robustness and calibration procedure of the developed constitutive models. The third point places a requirement on understanding the physical processes behind a material's response, rather than treating constitutive modelling as an elaborate curve-fitting exercise [23].

In the context of geomechanics, the term "constitutive model" is something of a misnomer. Models typically demand little or no information on mineralogy, grain geometry or packing. Instead they request parameters obtained largely from axi-symmetric tests, which make no direct investigation of the fabric. Despite this, if constructed in a thermodynamically consistent manner, spatially averaged representations can satisfactorily simulate the distortion, dilation and compaction of aggregated clusters of mineral platelets; which individually slip and flex to alter the void space morphology, reorganising the network of force-transfer pathways under macroscopic deformation.

The intention of this thesis was not to develop a new constitutive model from scratch, but rather to identify weaknesses in existing models and remove these limitations using a *consistent* framework, drawing on ideas founded in thermodynamic principles [38] and introducing representations of plastic anisotropy.

1.3 Numerical analysis

Early geotechnical modelling was based on empirical or semi-empirical methods and dependent on the experience of the geotechnical engineer [33]. However, these preliminary theoretical methods were limited to simple engineering problems, such as the long-term settlement or ultimate failure strength prediction of a strip footing. Numerical analysis (or modelling) is an essential tool for cases where these simple methods are no longer applicable. This inapplicability often results from the problem's geometry or the departure of material behaviour from the idealisations necessary in theoretical methods. Potts' 2003 Rankine Lecture [22] posed the following question:

> *"Is numerical analysis just an advanced toy for academics and the privileged few, or is it in a position to provide a genuine tool for routine geotechnical analysis?"*

Potts used examples, from the simple analysis of a rigid strip footing to the complex multi-stage analysis of the Pisa Tower and the Jubilee line extension in central London, to demonstrate the potential (and pitfalls) of numerical analysis over conventional methods. The key benefits of numerical analysis were summarised as:

(i) *"Numerical analyses can do everything conventional analysis can do, plus much more."*;

(ii) *"Their ability to predict mechanisms of behaviour is a major advantage."*; and

(iii) *"Numerical analysis can deal with both simple and complex problems."*

However Potts [22] also warned that: there *"are uncertainties in the numerical algorithms"*, there *"are limitations with current constitutive models"* and the *"results from numerical analysis are user dependent."* His paper demonstrated that with the correct information (on ground conditions, material properties and geometry) and tools (constitutive models and the displacement-based finite-element method), that numerical modelling [22]

> *"... is by far the best analysis tool that geotechnical engineers have at their disposal."*

Finite-element method

The finite-element method has been widely and successfully used in the analysis of engineering problems over the last 50 years. This method allows many aspects of soil behaviour to be taken into account, such as time dependent deformations, non-linear elasto-plasticity and soil-structure interaction. However, the use of advanced constitutive models within the finite-element method is still largely restricted to academia. Displacement-based non-linear finite-element analyses solve problems by applying the imposed loads (or displacements) in increments. Within each increment, equilibrium is sought between applied external forces and internal resisting forces within the material body. This represents a minimisation process which requires an iterative solution strategy that continues until the out-of-balance (residual) force falls below a specified tolerance. The solution scheme adopted throughout this thesis is the Newton-Raphson method (see Kreyszig [18] p. 841 for more details). The Newton-Raphson approach requires the stiffness matrix (relating force and displacement) to be updated at each iteration along with a re-calculation of the material stresses associated with the current strains using the constitutive relations.

Stress integration

The use of constitutive models within the finite-element method (or similar displacement-based analysis code) requires an incremental relationship between stress and strain. However, inelastic constitutive relations are typically developed in rate form which must be integrated for use in practical boundary

value simulations. Stress integration methods can be broadly split into: exact, implicit and explicit methods. Exact stress integration is currently only possible for a small number of simple constitutive models, therefore an approximate method must be used for more complicated material models. Here a general fully implicit backward Euler stress integration method is adopted, as described in Chapter 2. The backward Euler method has advantages over explicit methods, in terms of (i) enforcement of the yield (and consistency) condition, (ii) smaller errors, particularly when experiencing large strain increments and (iii) derivation of an algorithmic consistent tangent. The drawback of implicit methods is that they are more complicated than explicit routines.

The rate of convergence of the global equilibrium Newton-Raphson iterative solution algorithm is highly sensitive to the form of the stiffness matrix relating forces to displacements. Implicit methods allow the derivation of a tangent consistent with the stress integration routine. Simo and Taylor [28] showed that this algorithmic *consistent tangent* leads to optimum asymptotic quadratic convergence of the global equilibrium equations. The consistent tangent stiffness matrices have been provided for all of the models developed in this thesis.

Geometric non-linearity

The majority of geotechnical boundary value simulations are analysed using the the assumption of infinitesimal strains, based on a linear relationship between strains and displacements. However, as commented by Hinton [14]:

> *"..linear analysis is wrong, the world essentially exhibits nonlinear behaviour and it is entirely fortuitous that the assumption of linear behaviour enables accurate response to be predicted."*

It is important to detect during an analysis, when the changing structural geometry will play a significant role on its subsequent displacement response. Geometrically non-linear (or finite deformation) formulations account for this effect during the loading process, making the linear relationship between strain and displacement redundant. Unlike infinitesimal small strain analysis, the field of finite deformation analysis has yet to be fully unified. Several approaches to geometric non-linear analysis have been proposed. These use different measures of stress and strain, together with different methods that account for changing geometry.

Certain choices for stress and strain measures can be advantageous, particularly when recalling Gudehus' [12] *manageability* requirement and Chen's [6] *ease of implementation* criterion. This thesis uses an *updated Lagrangian* logarithmic strain-Kirchhoff stress formulation (as described in Chapter 3). The use of a logarithmic strain-Kirchhoff stress relationship, in conjunction with an implicit exponential map for the plastic flow equation, allows for the implementation of standard small strain constitutive algorithms within the finite deformation framework without modification. These stress and strain measures provide the basis of the most successful, straightforward ways of implementing large strain elasto-plasticity [17].

1.4 Scope and outline

This thesis is concerned with the theoretical and numerical development and subsequent implementation of efficient, accurate constitutive models for the analysis of particulate media (specifically clays) undergoing geometrically non-linear behaviour. In particular, the Mohr-Coulomb and modified Cam-clay constitutive models, as the most widely used models in practical numerical analysis, have been critically examined and extended to provide greater richness and realism. The work is cast within the framework of *conventional continuum mechanics*, without the use of *enriched (or non-local) continua* (see Jirásek [16], amongst others). Findings from this thesis will interest engineers working in numerical methods in solid mechanics, along with those working in continuum mechanics, inelastic constitutive modelling and

large strain plasticity. Although focused on soil plasticity, this research has relevance to other areas such as metal forming and bio-engineering.

Research in this thesis can be split into three distinct sections:

I. This introduction provides the background for the research.

II. The second and third chapters distill the essential tools which are used throughout the later chapters. These reviews cover the effects of material and geometric non-linearity.

- Chapter 2 on *material non-linearity*, introduces the basic principles of constitutive modelling. Starting with three main approaches to elasticity, this chapter presents the three classes of inelasticity. Stress integration approaches are then reviewed, including explicit, implicit and exact integration methods in addition to some recent alternative techniques. A general implicit backward Euler stress integration algorithm is described in detail. The chapter closes with the derivation of a tangent which is consistent with the implicit stress integration method.
- Chapter 3 is concerned with the numerical modelling of structures exhibiting *geometric non-linearity*. Initially the basic kinematics of finite deformation are given, leading to an investigation into some common simple deformation fields. A framework for the analysis of isotropic finite deformation elasto-plasticity is presented and extended for the case of plastic anisotropy. The full incremental finite-element formulation is provided and the framework is verified using six numerical examples.

III. The main part of this thesis is concerned with the development and implementation of several classes of constitutive model for geotechnical analysis. Theoretical derivation, integration, linearisation, numerical implementation and calibration are fully described for each of the developed models.

- Chapter 4 develops a novel non-associated *simple frictional plasticity* model based on a *modified Reuleaux* triangle. It is shown through comparison with experimental data that the model has significant advantages over the classical Mohr-Coulomb and Drucker-Prager models, whilst still allowing for analytical implicit stress integration. The errors associated with the three models are quantified and the run-time advantage of analytical backward Euler stress integration, over an iterative method, is demonstrated.
- Chapter 5 presents the theoretical development and numerical implementation of a family of *isotropic α-γ hyperplasticity* models that embrace the concept of a Critical State. It is shown that non-associated flow is a natural development of hyperplasticity and that a Lode angle dependency can be incorporated in a straightforward manner. The model is integrated using an iterative implicit backward Euler scheme and the influence of the form of the yield function is demonstrated. Errors are quantified for the backward Euler scheme. Particular attention is paid to the robustness of the algorithm and its linearisation when deriving the algorithmic consistent tangent. The model is fully calibrated and its performance compared with established experimental data.
- Chapter 6 develops a family of two-surface *anisotropic β-α-γ hyperplasticity* models that overcome many of the inadequacies of the isotropic model presented in Chapter 5. This new model combines a Lode angle dependency with an anisotropic yield function, yet maintains both surface convexity and uniqueness of the Critical State cone within a hyperplastic framework. Inelastic behaviour is introduced within the conventional yield surface through the specification of an additional term in the dissipation function. A complete calibration procedure is described

and the integration and linearisation of the constitutive relations are discussed. Similarly to the previous section, the importance of selecting an appropriate yield function is stressed, the errors associated with the integration scheme quantified and the robustness of the stress return verified. Finally the chapter compares the two-surface anisotropic model predictions with experimental data designed to reveal the anisotropic behaviour of geomaterials.

- Chapter 7 presents *numerical analyses* using the constitutive models developed in the preceding three chapters, cast within the finite deformation framework developed in Chapter 3. The influence of varying levels of sophistication of the different models is assessed in terms of (i) their influence on the global behaviour and (ii) in terms of the run-times associated with the simulations. A sensitivity analysis is conducted with the two-surface anisotropic model developed in Chapter 6 and the importance of deriving the algorithmic consistent tangent demonstrated. The final section in this chapter presents a detailed analysis of recent experimental data from a hollow cylinder apparatus including (i) material point simulations, (ii) finite-element discretisation of the hollow cylinder and (iii) an instability investigation designed to detect loss of a continuum response during loading.

Conclusions and recommendations for future work are given in Chapter 8.

1.4.1 Notation

For compactness and clarity, this thesis uses both index and matrix/vector notation where appropriate. Stress and strain are nine-component quantities, however due to symmetry in the shear quantities, six-component vector notation is used in this thesis. Chapters 2, 3 and 4 use a tension positive notation, whereas Chapters 5 and 6 use a compression positive notation. The reason for this is two-fold. The general convention within solid mechanics is to treat tension positive, therefore the general theoretical development of the numerical framework is presented using that convention. However, the majority of the geotechnical community work with a compression positive notation as, in general, the constitutive behaviour for geotechnical particulate media falls within the compressive region of stress space.

The numerical algorithms used in this thesis were developed using MATLAB m-script and later implemented in Fortran90. Unless stated otherwise the numerical simulations were run in MATLAB. Those which have been written in Fortran90 are identified within the text.

Chapter 1 references

[1] A Anandarajah, *Discrete element method for simulating behavior of cohesive soils*, J. Geotech. Eng.-ASCE 120 (1994), 1593–1615.

[2] A Anandarajah, *On the influence of fabric anisotropy on the stress-strain behaviour of clays*, Comput. Geotech. 27 (2000), 1–17.

[3] PA Baran & PM Sweezy, *Monopoly capital: an essay on the American economic and social order*, Penguin Books, 1968.

[4] MD Bolton & YP Chen, *Micro-geomechanics*. In: S Springman (ed.), International Workshop on Constitutive and Centrifuge Modelling: Two Extremes, Monte Verita, Switzerland, 2001.

[5] A Casagrande, *Characteristics of cohesionless soils affecting the stability of slopes and earth fills*, Contributions to soil mechanics, Boston Socitey of Civil Engineers (1936), 257–276

[6] WF Chen, *Constitutive Relations for Concrete Rock and Soils: Discusser's Report*. In: Z Baẑant (ed.), Mechanics of Geomaterials, 65–86, John Wiley & Sons Ltd., 1985.

[7] PA Cundall & ODL Strack, *A discrete numerical model for granular assemblies*, Géotechnique 29 (1979), 47–65.

[8] DC Drucker & W Prager, *Soil mechanics and plastic analysis or limit design*, Quart. Appl. Math. 10 (1952), 157–164.

[9] P Fu & YF Dafalias, *Fabric evolution within shear bands of granular materials and its relation to critical state theory*, Int. J. Numer. Anal. Meth. Geomech. (2010).

[10] P Fu & YF Dafalias, *Study of anisotropic shear strength of granular materials using DEM simulation*, Int. J. Numer. Anal. Meth. Geomech. 35 (2011), 1098–1126.

[11] JS Goldsworthy, MB Jaksa, WS Kaggwa, GA Fenton, DV Griffiths & HG Poulos, *Cost of foundation failures due to limited site investigations*, International conference on Structural and Foundation Failures, 2004.

[12] G Gudehus, *Requirements for Constitutive Relations for Soils*. In: Z Baẑant (ed.), Mechanics of Geomaterials, 47–63, John Wiley & Sons Ltd., 1985.

[13] JE Hellings, *Geotechnical failure: the cause is not always obvious and may be complex* http://reliability.geoengineer.org/TC40/13ARC_Hellings.pdf, 2007, accessed 6th June 2009.

[14] E Hinton, *NAFEMS introduction to nonlinear finite element analysis*, NAFEMS, 1992.

[15] *Inadequate site investigation*, Institution of Civil Engineers, 1991.

[16] M Jirásek, *Nonlocal theories in continuum mechanics*, Acta Polytech. 44 (2004), 16–34.

[17] D-N Kim, FJ Montáns, and K-J Bathe, *Insight into a model for large strain anisotropic elasto-plasticity*, Comput. Mech. 44 (2009), 651–668.

[18] E Kreyszig, *Advanced engineering mathematics*, John Wiley & Sons, 1999.

[19] GT-C Kung, C-Y, Ou & CH Juang, *Modeling small-strain behavior of Taipei clays for finite element analysis of braced excavations*, Comput. Geotech. 36 (2009), 304–319.

[20] N Lu & WJ Likos, *Unsaturated soil mechanics*, John Wiley & Sons, 2004.

[21] SC Möller & PA Vermeer, *On numerical simulation of tunnel installation*, Tunn. Undergr. Sp. Tech., 23 (2008), 461–475.

[22] DM Potts, *Numerical analysis: a virtual dream or peactical reality?*, Géotechnique 53 (2003), 535–573.

[23] JH Prévost & JP Wolf, *Nonlinear soil mechanics and dynamic soil-structure interaction*, Lausanne, Switzerland, 1987.

[24] CA Radeke, BJ Glasser & JG Kinast, *Large-scale powder mixer simulations using massively parallel GPU architectures*, Chem. Eng. Sci. 65 (2010), 6435–6442.

[25] KH Roscoe, AN Schofield & CP Wroth, *On the yielding of soils*, Géotechnique 8 (1958), 22–53.

[26] KH Roscoe & JB Burland, *On the generalised stress-strain behaviour of 'wet' clay*. In: J Heyman & FA Leckie (eds.), Engineering Plasticity (1968), Cambridge University Press, 535–609.

[27] AN Schofield & CP Wroth, *Critical State Soil Mechanics*, McGraw-Hill Publishing Company Limited, 1968.

[28] JC Simo & RL Taylor, *Consistent tangent operators for rate-independent elastoplasticity*, Comput. Meth. Appl. Mech. Engrg. 48 (1985), 101–118.

[29] *Site Investigation & Engineering Practice*, Allied Exploration & Geotechnics Limited, 2007.

[30] SE Stallebrass, & RN Taylor, *The development and evaluation of a constitutive model for the prediction of ground movements in overconsolidated clay*, Géotechnique 47 (1997), 235–253.

[31] P Stephenson & M Skinner, *Application of numerical analysis to the Kings Place Project*, Workshop on numerical modelling in geomechanics, Newcastle-upon-Tyne, April 2009.

[32] AJ Whittle & YMA Hashash, *Soil modeling and prediction of deep excavation behavior*, in Shibuya, Mitachi & Miura (ed.), Pre-faliure deformation of geomaterials (1994), 589–594.

[33] DM Wood, *Geotechnical modelling*, Spon Press, 2004.

[34] DM Wood, *Soil Behaviour and Critical State Soil Mechanics*, Cambridge Univeristy Press, 1990.

[35] A Wynne, *Getting to the core*, http://www.nce.co.uk/getting-to-the-core/1949566.article, 2008, accessed 7th June 2009.

[36] H-S Yu, *Plasticity and geotechnics*, Springer, 2006.

[37] L Zdravkoić, DM Potts & DW Hight, *The effect of strength anisotropy on the behaviour of embankments on soft ground*, Géotechnique 52 (2002), 447–457.

[38] H Ziegler, *An introduction to thermomechanics*, 2nd edn. North Holland Pub. Co, Amsterdam, 1983.

Chapter 2

Material non-linearity

All materials exhibit some *material non-linearity* (that is, a non-linear relation between stress and strain) under certain multiaxial stress paths. While a linear response may be seen under uniaxial tension for some materials, the behaviour under hydrostatic compression is typically non-linear. Soils can exhibit highly inelastic material behaviour, with different stress-strain paths under loading and unloading. Inelastic constitutive formulations using plasticity theory first appeared following the study of metals in the 1950s (see Hill [16] for more information on the early history of plasticity theory). However, the use of such methods for particulate media was not immediate. Indeed, Wroth and Palmer [53] commented that:

> *"Plasticity theory was developed by people who thought in terms of metals, and for about twenty years workers in soil mechanics have been looking at the theory, rather as outsiders, and asking whether it had anything to offer them."*

The application of these theories to geomaterials was initiated by the work of Drucker and Prager [14] who included a pressure dependence into the constitutive equations. Since that time much work has been done to develop sophisticated (some might say, over-complicated) plasticity models for soil and rock.

This chapter begins by briefly reviewing the concepts of elasticity in Section 2.1. Material inelasticity is considered in Section 2.2, presenting the classical rate formulation of plasticity and outlining the theories of hyperplasticity and incrementally non-linear hypoplasticity. Section 2.3 is concerned with stress integration. It discusses the three main methods of explicit, implicit and exact integration in addition to some recently proposed alternative methods. A general algorithm for the adopted implicit backward Euler (bE) stress integration method is then presented. Section 2.4 provides a general description of the linearisation of the constitutive relations in order to derive an algorithmic tangent consistent with the bE stress integration procedure. Finally, observations are drawn in Section 2.5.

2.1 Elasticity

Elasticity can be defined as the ability of a material to return to its original state once an applied load, causing deformation, is removed. There are three classes of elasticity theory: elasticity, hyperelasticity and hypoelasticity. Elastic formulations (also known as *Cauchy elastic models* [6]), according to the description as used by Fung [15], allow the Cauchy stress to be expressed as a single-valued function of the elastic strain $\{\sigma(\varepsilon^{\mathrm{e}})\}$, where $\{\varepsilon^{\mathrm{e}}\}$ is the elastic strain vector. For linear elasticity the following relation holds

$$\{\sigma\} = [D^{\mathrm{e}}]\{\varepsilon^{\mathrm{e}}\}. \tag{2.1}$$

In the case of isotropic linear elasticity, the stiffness matrix[1] $[D^{\mathrm{e}}]$ is given by

$$[D^{\mathrm{e}}] = \frac{E}{(1+\upsilon)(1-2\upsilon)}\Big[(1-2\upsilon)[I] + \upsilon\{1\}\{1\}^T\Big], \qquad \text{where} \qquad \{1\} = \{1 \quad 1 \quad 1 \quad 0 \quad 0 \quad 0\}^T \tag{2.2}$$

E is Young's modulus, υ is Poisson's ratio and $[I]$ is the six by six identity matrix. Elasticity laws are *path-independent* and *reversible*. That is, for a given strain level, the stress is uniquely defined. Despite its limitations in simulating the behaviour of real materials, an isotropic linear elasticity provides the description for the elastic response many widely-used constitutive models for soils in engineering practice, such as the frictional Mohr-Coulomb (M-C) and Drucker-Prager (D-P) models.

Hyperelasticity formulations (also known as *secant* formulations or *Green elastic* models [6]) derive the stress-elastic strain relationship from a scalar free-energy function, Ψ, by taking the derivative of this function with respect to elastic strain

$$\{\sigma\} = \{\Psi_{,\varepsilon^{\mathrm{e}}}\}. \tag{2.3}$$

The elastic stiffness matrix is obtained from the second derivative of Ψ

$$[D^{\mathrm{e}}] = [\Psi_{,\varepsilon^{\mathrm{e}}\varepsilon^{\mathrm{e}}}]. \tag{2.4}$$

If Ψ is a quadratic function of elastic strain, then it is possible to recover a linear elastic material obeying (2.1). Hyperelastic laws are path independent, reversible, easy to implement numerically[2] and are able to reproduce several characteristics associated with the behaviour of soils, such as: non-linearity, dilation, stress-induced anisotropy and strain-softening [6]. However, higher-order hyperelastic laws require the specification of a considerable number of material constants[3] (which can be hard to determine experimentally).

Hypoelastic formulations are based on a non-unique rate relationship between stress and elastic strain, of the form

$$\{\dot{\sigma}\} = [D^{\mathrm{e}}]\{\dot{\varepsilon}^{\mathrm{e}}\}, \tag{2.5}$$

where an over-dot denotes a rate quantity. If $[D^{\mathrm{e}}]$ is constant, then the hypoelastic relationship obeys (2.1), making it equivalent to specifying linear-elastic relationship. However, $[D^{\mathrm{e}}]$ is generally not constant; typically being dependent on the current level of stress. These models are able to provide material behaviour that is dependent on the past stress history, being both path-dependent and irreversible. However, hypoplastic models can introduce unwanted stress-induced anisotropy and under general stress states the distinction between unloading and loading is not clear (requiring additional assumptions) [6].

It is important to note that some hypoelastic material formulations are non-conservative, effectively creating energy and thereby violating the first law of thermodynamics [6]. Also hypoelastic models can produce non-closed cycles of strain for closed cycles of stress, in direct contradiction of the notion of elasticity [19]. In contrast to hypoelasticity, hyperelasticity formulations restrict the elastic material behaviour to thermodynamically reasonable results. Such hyperelastic forms will be used throughout the remainder of this thesis.

[1] Note, (2.2) relates engineering (rather than tensorial) strains to Cauchy stress. There is a factor of two on the shear strains when moving between engineering and tensorial descriptions of strain. Engineering strains are used throughout this thesis unless stated otherwise.

[2] The elastic law is formed through Ψ as a path independent relation between stress and strain, for a given value of strain the stress can be trivially calculated as can the appropriate elastic stiffness tangent.

[3] For example, an isotropic third-order relation between stress and strain requires nine constants, whereas a fifth-order requires 14 [6].

2.1.1 Principal stress space

Stress and strain are nine-dimensional quantities, with six independent values. In all that follows, the following vector ordering of stress (and strain) is used

$$\{\sigma\} = \{\sigma_{xx} \quad \sigma_{yy} \quad \sigma_{zz} \quad \sigma_{xy} \quad \sigma_{yz} \quad \sigma_{zx}\}^T, \tag{2.6}$$

alternatively, in matrix notation

$$[\sigma] = \begin{bmatrix} \sigma_{xx} & \sigma_{xy} & \sigma_{zx} \\ \sigma_{xy} & \sigma_{yy} & \sigma_{yz} \\ \sigma_{zx} & \sigma_{yz} & \sigma_{zz} \end{bmatrix} = \sum_{i=1}^{3} \sigma_i \{v_i\}\{v_i\}^T \tag{2.7}$$

The eigenvalues of $(2.7)_1$ are the principal stresses σ_i with eigenvectors $\{v_i\}$. Isotropic constitutive relations can be formulated in principal stress space, as the principal directions of stress and strain are coincident. Also, using principal components allows any stress state to be visualised in three-dimensional space.

2.1.2 Stress and strain invariants

Stress and strain invariants are often used as an alternative representation of a material's state. They are invariant to Euclidian transformations (rotations and translations). The most commonly used invariants of stress are

$$I_1 = \mathrm{tr}([\sigma]), \qquad J_2 = \frac{1}{2}\mathrm{tr}([s][s]) \qquad \text{and} \qquad J_3 = \frac{1}{3}\mathrm{tr}([s][s][s]). \tag{2.8}$$

where the deviatoric (traceless) stress is $[s] = [\sigma] - I_1[1]/3$ and $[1]$ is the three by three identity matrix. These invariants are related to the useful Haigh-Westergaard cylindrical stress measures

$$\xi = \frac{I_1}{\sqrt{3}}, \qquad \rho = \sqrt{2J_2}, \qquad \text{and} \qquad \theta = \frac{1}{3}\arcsin\left(\frac{-3\sqrt{3}}{2}\frac{J_3}{J_2^{3/2}}\right) \quad \in [-\pi/6, \pi/6], \tag{2.9}$$

where ξ is the hydrostatic stress, ρ is a measure of the deviatoric stress and θ is the Lode angle. The principal stresses can be obtained from

$$\{\hat{\sigma}\} = \frac{\xi}{\sqrt{3}}\{1\} + \sqrt{\frac{2}{3}}\rho\left\{\sin(\theta - 2\pi/3) \qquad \sin(\theta) \qquad \sin(\theta + 2\pi/3)\right\}^T, \tag{2.10}$$

where $\hat{(\cdot)}$ denotes a principal quantity in vector/matrix format. The volumetric, ε_v, and deviatoric, ε_γ, strain invariants can be defined as

$$\varepsilon_v = \mathrm{tr}([\varepsilon]), \qquad \varepsilon_\gamma = \sqrt{\mathrm{tr}([\gamma][\gamma])}, \qquad \text{where} \qquad [\gamma] = [\varepsilon] - \varepsilon_v[1]/3. \tag{2.11}$$

2.2 Inelasticity

The term *inelasticity* broadly covers: *plasticity*, time dependent *viscosity* and material *damage*. However, only the former is considered here.

The theory of plasticity is concerned with solid materials that undergo permanent *plastic* deformations when stressed. In this work we restrict our attention to inviscid materials (that is, those materials where the material response is independent of the rate of load application). For a review of the early history

and development of plasticity the reader is referred to the classical text by Hill [16]. As with elasticity, there are several approaches to inelastic material behaviour, the main three are: *classical plasticity*, *hyperplasticity* and *hypoplasticity*. These three classes are now briefly examined.

2.2.1 Classical plasticity

Conventional *classical plasticity* theories are based on the specification of scalar yield (f) and plastic potential (g) functions that, combined with an elasticity relationship and laws governing the evolution of an internal material parameters, allow formulation of the constitutive equations.

The yield function

The yield function (or yield criterion), f, is a central idea in classical plasticity theory. It was first used for soils in 1773 by Coloumb and later for metals in 1864 by Tresca [16]. In stress space the yield function defines the boundary ($f = 0$) between an admissible elastic region inside the yield surface ($f < 0$) and an inadmissible region outside the yield surface ($f > 0$). Any stress state must lie either inside (elastic) or on (elasto-plastic) the yield surface, that is $f \leq 0$.

Classical rate formulation

The four key components of elasto-plasticity are now listed.

(i) The additive decomposition of the strain into elastic and plastic components is expressed as

$$\{\varepsilon\} = \{\varepsilon^{\mathrm{e}}\} + \{\varepsilon^{\mathrm{p}}\}, \tag{2.12}$$

where $\{\varepsilon^{\mathrm{p}}\}$ is the plastic strain.

(ii) A rate relationship is assumed to exist between the elastic strains and the Cauchy stresses

$$\{\dot{\sigma}\} = \big[D^{\mathrm{e}}\big]\{\dot{\varepsilon}^{\mathrm{e}}\}. \tag{2.13}$$

(iii) A plastic flow rule is prescribed

$$\{\dot{\varepsilon}^{\mathrm{p}}\} = \dot{\gamma}\{g_{,\sigma}\}, \tag{2.14}$$

where $\{g_{,\sigma}\}$ is the direction of plastic flow (the derivative of the plastic potential with respect to stress) and $\dot{\gamma}$ the plastic consistency parameter that controls the magnitude of the plastic strains.

(iv) The Kuhn-Tucker-Karush (KTK) consistency conditions are enforced

$$\dot{\gamma} \geq 0, \qquad f\big(\{\sigma\},\{\beta\}\big) \leq 0 \qquad \text{and} \qquad \dot{\gamma} f\big(\{\sigma\},\{\beta\}\big) = 0, \tag{2.15}$$

where f is a function of stress $\{\sigma\}$ and the internal material parameters $\{\beta\}$ specify the size, location, orientation and shape of the surface.

Rearranging and substituting the rate form of (2.12) into (2.13), we obtain the stress rate as

$$\{\dot{\sigma}\} = \big[D^{\mathrm{e}}\big]\big\{\{\dot{\varepsilon}\} - \{\dot{\varepsilon}^{\mathrm{p}}\}\big\}. \tag{2.16}$$

Replacing the plastic strain in (2.16) with (2.14), gives

$$\{\dot{\sigma}\} = \big[D^{\mathrm{e}}\big]\big\{\{\dot{\varepsilon}\} - \dot{\gamma}\{g_{,\sigma}\}\big\}. \tag{2.17}$$

Introducing the consistency condition for hardening elasto-plasticity

$$\dot{f} = \{f_{,\sigma}\}^T\{\dot{\sigma}\} + \{f_{,\beta}\}^T\{\dot{\beta}\} = 0 \tag{2.18}$$

and substituting (2.17) for the stress rate, we obtain

$$\dot{f} = \{f_{,\sigma}\}^T\left[D^{\mathrm{e}}\right]\left\{\{\dot{\varepsilon}\} - \dot{\gamma}\{g_{,\sigma}\}\right\} + \{f_{,\beta}\}^T\{\dot{\beta}\} = 0. \tag{2.19}$$

Assuming that, similarly to the evolution of plastic strains, the internal variable rate is given by

$$\{\dot{\beta}\} = -\dot{\gamma}\{H_\beta\}, \tag{2.20}$$

where $\{H_\beta\}$ defines the instantaneous evolution of the internal variables. Substituting (2.20) into (2.19) and rearranging, the consistency parameter follows as

$$\dot{\gamma} = \frac{\{f_{,\sigma}\}^T\left[D^{\mathrm{e}}\right]\{\dot{\varepsilon}\}}{\{f_{,\sigma}\}^T\left[D^{\mathrm{e}}\right]\{g_{,\sigma}\} + H}. \tag{2.21}$$

where $H = \{f_{,\beta}\}^T\{H_\beta\}$ is a scalar measure of the plastic tangent stiffness. Substituting (2.21) into (2.17)

$$\{\dot{\sigma}\} = \left[D^{\mathrm{e}}\right]\left\{\{\dot{\varepsilon}\} - \left(\frac{\{f_{,\sigma}\}^T\left[D^{\mathrm{e}}\right]\{\dot{\varepsilon}\}}{\{f_{,\sigma}\}^T\left[D^{\mathrm{e}}\right]\{g_{,\sigma}\} + H}\right)\{g_{,\sigma}\}\right\} \tag{2.22}$$

and rearranging to obtain the infinitesimal elasto-plastic tangent, $[D^{\mathrm{ep}}]$, as

$$\{\dot{\sigma}\} = \underbrace{\left[D^{\mathrm{e}}\right]\overbrace{\left[[I] - \left[\frac{\{g_{,\sigma}\}\{f_{,\sigma}\}^T\left[D^{\mathrm{e}}\right]}{\{f_{,\sigma}\}^T\left[D^{\mathrm{e}}\right]\{g_{,\sigma}\} + H}\right]\right]}^{\text{rank-one update of } [D^{\mathrm{e}}]}}_{[D^{\mathrm{ep}}]}\{\dot{\varepsilon}\}. \tag{2.23}$$

The infinitesimal elasto-plastic tangent provides a relationship between the instantaneous rate of the change of stress in terms of strain. For the case of associated plastic flow (that is, when the yield and plastic potential functions are equal), $[D^{\mathrm{ep}}]$ will be symmetric[4]. However, in the case of non-associated plastic flow, where $g \neq f$, the major symmetry of $[D^{\mathrm{ep}}]$ is lost.

2.2.2 Hyperplasticity

Hyperplastic formulations, arising from the pioneering works of Ziegler [55] and Houlsby [18], allow the constitutive equations to be derived from a free-energy function and a dissipation rate function [19]. Once these functions have been specified, the stress-elastic strain law, yield function and flow rule can all be obtained without the requirement for any additional assumptions. Textbook accounts of the thermomechanics of materials can be found in volumes by Ziegler [55] and Maugin [32], amongst others. The following equations use tensorial notation to avoid any possible confusion arising from the shear components of stress and strain when using vector notation. The rate of work done by a hyperplastic material is given by

$$\sigma_{ij}\dot{\varepsilon}_{ij} = \dot{\Psi} + \dot{\Phi}, \qquad \text{where} \qquad \dot{\Phi} \geq 0. \tag{2.24}$$

Ψ denotes the free-energy function and $\dot{\Phi}$ identifies the dissipation rate, both defined per unit volume. The later must be strictly positive when plastic deformation occurs. σ_{ij} represents the stress tensor and $\dot{\varepsilon}_{ij}$

[4]Provided the elastic stiffness matrix $[D^{\mathrm{e}}]$ is also symmetric.

the total strain rate tensor. The inequality ($\dot{\Phi} \geq 0$) is the statement of the second law of thermodynamics for isothermal deformations.

The free energy function is typically defined in terms of the total, ε_{ij}, and plastic, $\varepsilon^{\mathrm{p}}_{ij}$, strains [7]. However, here we limit ourselves to the case of *de-coupled materials* where Ψ (and its associated rate) can be split into two components: one in terms of the elastic strains and the other in terms of the plastic strains

$$\Psi = \Psi_1(\varepsilon^{\mathrm{e}}_{ij}) + \Psi_2(\varepsilon^{\mathrm{p}}_{ij}) \qquad \text{and} \qquad \dot{\Psi} = \left(\frac{\partial \Psi_1}{\partial \varepsilon^{\mathrm{e}}_{ij}}\right)\dot{\varepsilon}^{\mathrm{e}}_{ij} + \left(\frac{\partial \Psi_2}{\partial \varepsilon^{\mathrm{p}}_{ij}}\right)\dot{\varepsilon}^{\mathrm{p}}_{ij}. \tag{2.25}$$

The first term gives the stress-elastic strain relation

$$\sigma_{ij} = \frac{\partial \Psi_1}{\partial \varepsilon^{\mathrm{e}}_{ij}}, \tag{2.26}$$

and the second term in $(2.25)_2$ provides the *shift stress*

$$\chi_{ij} = \frac{\partial \Psi_2}{\partial \varepsilon^{\mathrm{p}}_{ij}}, \tag{2.27}$$

which identifies the centre of the yield surface in true stress space. Through these shift stresses, the second part of the free-energy function defines the kinematic hardening of the yield surface, whereas any isotropic hardening is controlled by the dissipation rate, $\dot{\Phi}$.

The dissipation rate itself depends on the plastic strain rate in addition to the total strains, $\dot{\Phi}(\varepsilon_{ij}, \varepsilon^{\mathrm{p}}_{ij}, \dot{\varepsilon}^{\mathrm{p}}_{ij})$, however it cannot depend on the total strain rate otherwise purely elastic deformation could result in dissipation. For inviscid elasto-plasticity models, the dissipation rate is homogeneous of degree one in the plastic strain rates [8], giving

$$\dot{\Phi} = \frac{\partial(\dot{\Phi})}{\partial(\dot{\varepsilon}^{\mathrm{p}}_{ij})}\dot{\varepsilon}^{\mathrm{p}}_{ij}. \tag{2.28}$$

Using the dissipation rate we can define a *dissipative stress*

$$\varphi_{ij} = \frac{\partial(\dot{\Phi})}{\partial(\dot{\varepsilon}^{\mathrm{p}}_{ij})}, \tag{2.29}$$

thus (2.28) becomes

$$\dot{\Phi} = \varphi_{ij}\dot{\varepsilon}^{\mathrm{p}}_{ij}. \tag{2.30}$$

The dissipative stress is linked to true stress space through the shift stress, χ_{ij}. Substituting (2.25) and (2.30) into (2.24), we obtain

$$\sigma_{ij}\dot{\varepsilon}_{ij} = \left(\frac{\partial \Psi_1}{\partial \varepsilon^{\mathrm{e}}_{ij}}\dot{\varepsilon}^{\mathrm{e}}_{ij} + \frac{\partial \Psi_2}{\partial \varepsilon^{\mathrm{p}}_{ij}}\dot{\varepsilon}^{\mathrm{p}}_{ij}\right) + \varphi_{ij}\dot{\varepsilon}^{\mathrm{p}}_{ij}. \tag{2.31}$$

Using (2.26) and (2.27), (2.31) becomes

$$\sigma_{ij}\dot{\varepsilon}_{ij} = \sigma_{ij}\dot{\varepsilon}^{\mathrm{e}}_{ij} + \Big(\chi_{ij} + \varphi_{ij}\Big)\dot{\varepsilon}^{\mathrm{p}}_{ij}, \tag{2.32}$$

providing the following relationship between total, shift and dissipative stresses

$$\sigma_{ij} = \chi_{ij} + \varphi_{ij}. \tag{2.33}$$

The dissipation rate is not equal to the plastic work rate. The later is given by the product of the true

stress with plastic strain rate

$$\dot{W}^{\mathrm{p}} = \sigma_{ij}\dot{\varepsilon}^{\mathrm{p}}_{ij} = \dot{\Phi} + \chi_{ij}\dot{\varepsilon}^{\mathrm{p}}_{ij}. \tag{2.34}$$

Due to the constraints imposed by the second law of thermodynamics, $\dot{\Phi}$ must always be greater or equal to zero but there is no restriction on the sign of $\dot{W}^{\mathrm{p}}$. The last term in (2.34) indicates the plastic work associated with the recoverable elastic deformations arising from plastic strains when soil grains are *locked* in the soil fabric [9]. The concepts of dissipated and stored plastic work can be demonstrated using the one-dimensional kinematic hardening rheological model in Figure 2.1 (i), comprising of a spring (a) which is in parallel with a second spring and slider (b). The system is subjected to an increasing total stress, σ, followed by unloading until $\sigma_b = 0$, as shown in Figure 2.1 (ii). The components of stored and dissipated plastic work can be seen in Figure 2.1 (iii). Plastic dissipation occurs in the slider. Stored plastic work is a consequence of the frozen elastic energy in spring a which is restrained by the plastic slider.

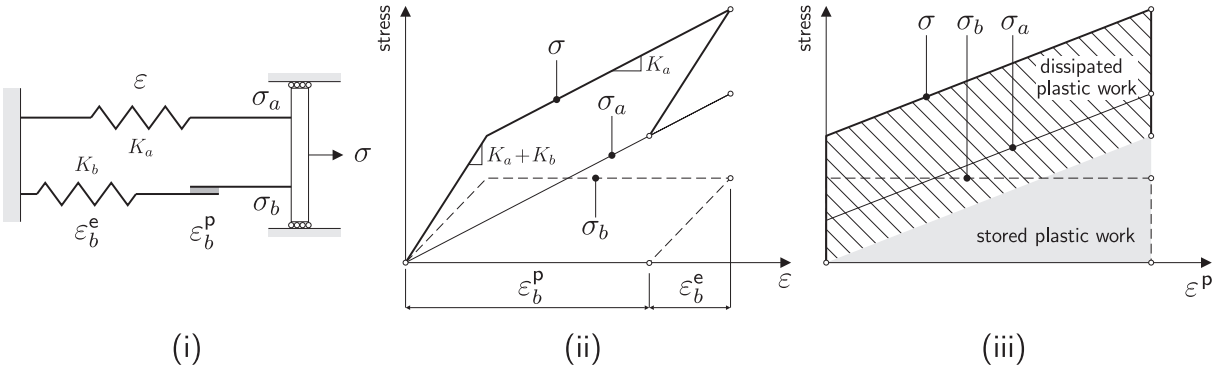

Figure 2.1: (i) Rheological model of a one-dimensional kinematic hardening elasto-plastic system (ii) stress-total strain response (iii) stress-plastic strain response.

It can be shown that the plastic strain increment is given by a normal flow rule in dissipative stress space [7]. This only implies an associated model in true stress space under the condition that the dissipation rate is independent of the true stress, σ_{ij}. For the case when the free-energy function only depends on the elastic strains, the shift stresses are zero and the true and dissipative stress space are identical.

2.2.3 Incrementally non-linear hypoplasticity

Hypoplastic formulations describe the mathematical equations of plasticity using an *incrementally non-linear*[5] approach [24], understood as a "*generalization of hypoelasticity*" [25]. It was motivated by the inability of classical plasticity theories to describe experimentally observed incremental non-linearity [24]. In line with hypoelasticity, the constitutive equations are formulated through the specification of the stress rates in terms of the strain rates, typically of the form [25]

$$\{\dot{\sigma}\} = \underbrace{\{h(\{\sigma\},\{\dot{\varepsilon}\})\}}_{\text{rate-independent}} + \underbrace{\{g(\{\sigma\},\{\dot{\varepsilon}\},\{\ddot{\varepsilon}\})\}}_{\text{rate-dependent}}. \tag{2.35}$$

The first term is used to describe the rate independent response, with the requirement that $\{h\}$ is (i) isotropic, positive homogeneous of degree one in $\{\dot{\varepsilon}\}$ and (ii) non-linear in the strain rate to exhibit dissipative behaviour [25]. For the case where $\{h\}$ is linear in the strain rate we recover a hypoelastic

[5]Incremental linearity was defined by Kolymbas as *"the ostensibly self-evident assumption that the application of two small stress- (or strain-) increments has the same effect as the application of their vector sum, when these increments tend to zero"* [24].

response. The second term in (2.35) describes the rate dependence (including viscosity) of the hypoplastic material, such that under a constant strain rate ($\{\ddot{\varepsilon}\} = \{0\}$) the contribution of this term vanishes [24].

The concept of yielding in hypoplastic formulations is different to that under classical plasticity. Hypoplastic yielding was described by Kolymbas [25] as *"the condition of vanishing stiffness"*, that is when

$$\{\dot{\sigma}\} = \big\{h(\{\sigma\}, \{\dot{\varepsilon}\})\big\} = \{0\}, \tag{2.36}$$

at particular values of $\{\sigma\}$ and $\{\dot{\varepsilon}\}$. This condition can be used to describe a *hypoplastic yield surface* in both stress space, through $f(\{\sigma\}) = 0$, and strain-rate space[6], through $h(\{\dot{\varepsilon}\}) = 0$. The shape of these surfaces will depend on the form of the hypoplastic constitutive relations. However, $f(\{\sigma\}) = 0$ does not define a bound between the admissible and inadmissible stress states, as with classical plasticity, but rather the point of vanishing stiffness. An additional surface, known as the *bound surface*, envelopes all feasible stress paths.

The constitutive model described by (2.35) is *amorphous* (that is, without memory of internal structure) such that under a cyclic straining, the response of the n^{th} cycle is the same as the first [25]. To include the effect the material's past history on the incremental stress response, the first term in (2.35) must be modified to

$$\{\dot{\sigma}\} = \big\{h(\{\sigma\}, \{\dot{\varepsilon}\}, \{\beta\})\big\}, \tag{2.37}$$

where $\{\beta\}$ is a set of internal material parameters known as the *structure tensor* which contains information about the material history. The initial condition (and subsequent evolution) of this structure tensor is difficult to specify as it cannot be determined directly through experiments.

The main shortcoming of hypoplastic formulations is that, unlike hyperplasticity models, they do not explicitly satisfy the laws of thermodynamics, being able to generate or consume energy [19]. In addition, they can be unnecessarily complex, the models are difficult to validate and the formulations can contain internal contradictions [5].

2.2.4 Inelastic constitutive relations

The field of constitutive modelling is continually expanding and the library of available models is overwhelming. It is not feasible (or appropriate) here to review the full suite of material models published in the academic literature. A useful review of constitutive models was provided by Yu [54] in 2002. This covered materials from rocks, soils and concrete to metals, polymers and ceramics. For details on classical metal plasticity models (such as those using the von Mises and Tresca yield functions) see Hill [16], amongst many others, and for their numerical implementation see Simo and Hughes [43]. The recent book by de Souza Neto *et al.* [46] provides information (including numerical implementation) on the classical Mohr-Coulomb and Drucker-Prager [14] models. Wood [52] gives information on constitutive models for geotechnical modelling including the widely used modified Cam-clay model [40, 42] and discusses some of its many extensions. Throughout the following chapters reference is made, when appropriate, to existing constitutive models (including their advantages, disadvantages and implementation) when introducing the proposed related methods and models.

2.3 Stress integration

Constitutive models are invariably developed in rate form. However, for a model to be used, in practical boundary value simulations or even at a material point level, it is necessary to integrate the constitutive equations (2.13), (2.14) and (2.20) subjected to the KTK constraints (2.15). For a displacement based

[6]Note, that de to the rate independence of h on $\{\dot{\varepsilon}\}$, $h(\{\dot{\varepsilon}\}) = 0$ is a cone in strain-rate space.

finite-element (FE) program (or other boundary value simulation method), we are faced with the question:

> *Starting from a initial state with a known elastic strain* $\{\varepsilon^e_n\}$ *and internal variables* $\{\beta_n\}$*, when subjected to a strain increment* $\{\Delta\varepsilon\}$*, what is the updated elastic strain* $\{\varepsilon^e_{n+1}\}$ *(or the equivalently the stress,* $\{\sigma_{n+1}\}$*) and internal variables* $\{\beta_{n+1}\}$*?*

For the case where the trial stress, $\{\sigma_t\}$, corresponding to the trial elastic strain state, $\{\varepsilon^{\mathrm{e}}_t\} = \{\varepsilon^{\mathrm{e}}_n\}+\{\Delta\varepsilon\}$, lies within the yield surface, their is no need to integrate the rate equations (provided a linear or secant elasticity law is adopted). However, if the trial stress state lies outside the yield surface ($f > 0$), an integration procedure is required to update the elastic strain and internal variables. This integration is the central problem in computational plasticity and has received significant research interest since the 1960s.

The paper by Kojić [22] provides a review of the integration procedures for use in the finite-element method (FEM). The paper identified four essential properties for any practical stress integration algorithm:

(i) *robustness*; applicable to all physical conditions and the ability to handle large strain increments;

(ii) *accuracy*; accurate stress integration for a range of strain increments (both small and large);

(iii) *efficiency*; computational efficiency is essential as the stress integration algorithm lies at the heart of any numerical stress analysis code; and

(iv) *stability*; numerically stable, both to changes in the strain increment and material constants.

Stress integration procedures can be broadly split into three categories:

(i) *explicit* methods, where the stress integration is formulated based on the conditions at the start of the strain increment;

(ii) *implicit* methods, formulated based on the conditions at the end of the strain increment; and

(iii) closed-form *exact stress integration*.

These three integration methods are now briefly reviewed, in addition to some recent alternative approaches.

Explicit methods

Explicit methods have their routes in the pioneering work of Ilyushin in 1943 [20]. This paper (published in Russian) proposed an iterative elastic method, for the elasto-plastic analysis of a thin shell, where the solution is obtained by a sequence of elastic steps with each successive step taking the previous step as the starting state [31]. Ilyushin's *method of successive elastic solutions*[7] was subsequently used by Mendelson [33] to integrate a Prandtl-Reuss (P-R)[8] constitutive model. Nayak and Zienkiewicz [35] were the first to propose a general explicit stress integration procedure for use within the FEM. The paper presented a series of FE simulations using the perfect plasticity Tresca and P-R constitutive models in addition to strain hardening and softening plasticity models. Subsequently several models have been integrated using the technique established by Nayak and Zienkiewicz [35]. This explicit *forward Euler* method can be summarised by the following steps:

[7] See Chapter 9 of Mendelson [33] pp. 164-212 for details on the *method of successive elastic solutions*.

[8] The Prandtl-Reuss constitutive model combines linear isotropic elasticity with a non-hardening von Mises yield criterion with associated isochoric radial plastic flow (as explained by Simo and Hughes [43], p. 89).

(i) subjected to a strain increment, $\{\Delta\varepsilon\}$, calculate the trial stress state, $\{\sigma_t\}$ outside the yield surface ($f > 0$);

(ii) the contact stress is obtained through finding the intersection of the ray between the initial stress state, $\{\sigma_n\}$, and the trial stress state with the yield surface. This intersection point is

$$\{\sigma_i\} = a \times [D^{\mathrm{e}}]\{\Delta\varepsilon\}, \tag{2.38}$$

where a is the proportion of the strain increment responsible for purely elastic behaviour and $(\cdot)_i$ denotes a quantity associated with the intersection state;

(iii) the intersection stress is then modified to account for the remainder of the strain path

$$\{\sigma_{n+1}\} = \{\sigma_i\} + (1-a)[D_i^{\mathrm{ep}}]\{\Delta\varepsilon\}, \tag{2.39}$$

where $[D_i^{\mathrm{ep}}]$ is calculated at the intersection stress from (2.23). However, generally this updated stress state will be at an inadmissible stress location ($f > 0$);

(iv) finally a corrector can then be used to return the stress state back onto the yield surface. Multiple corrections maybe required to converge to within a specified tolerance.

Several methods have been proposed for this final correction step (see [35]). Sub-incrementation can be used to reduce the errors associated with the procedure. However, the greatest disadvantage of this explicit method is that it does not enforce the consistency condition (2.15) at the end of the applied strain increment [49].

In addition to not satisfying the consistency condition, explicit methods suffer from two other shortcomings [22], namely:

(i) relatively low accuracy (for example see Krieg and Krieg [29]); and

(ii) the use of $[D^{\mathrm{ep}}]$ to construct the global stiffness matrix does not result in asymptotic quadratic convergence of the global equilibrium equations.

Recently Rezaiee-Pajand *et al.* [39] have proposed new explicit integration methods based on exponential maps for a mixed linear-hardening associated flow D-P model. Integrating plasticity relations using exponential maps was initiated by the work of Hong and Liu [17] based on the internal symmetries inherent in bi-linear plasticity models[9]. Although Rezaiee-Pajand *et al.* [39] showed that the run-time (for a given error) for their proposed method was advantageous over that of other traditional implicit and explicit methods, and that the errors were comparable to that of the bE method, their method is restricted to models that contain particular *internal symmetries*. The generalisation of this method, if indeed possible, to incorporate any arbitrary constitutive model has yet to be presented. Also, the derivation (or in fact the existence) of an algorithmic tangent consistent with the stress integration procedure is not currently available.

Implicit methods

In implicit methods the stresses are integrated at the updated (or returned, final) stress state, at the end of the strain increment. The use of implicit integration for inelasticity was initiated in 1964 by Wilkins [51] for a P-R model. That paper used the *radial return algorithm* which was later extended by Krieg and Key [28] for the case of von Mises plasticity with mixed hardening.

[9] That is, models that combine linear elasticity with linear kinematic hardening.

Central to many implicit methods is the idea of splitting[10] the stress integration problem into:

(i) an elastic predictor, given (for linear-elastic materials) by

$$\{\sigma_t\} = [D^{\mathrm{e}}] \underbrace{\big\{\{\varepsilon_n^{\mathrm{e}}\} + \{\Delta\varepsilon_{n+1}\}\big\}}_{\{\varepsilon_t^{\mathrm{e}}\}}; \qquad \text{and} \tag{2.40}$$

(ii) a plastic corrector

$$\{\sigma_{n+1}\} = [D^{\mathrm{e}}]\big\{\{\varepsilon_t^{\mathrm{e}}\} - \{\Delta\varepsilon^{\mathrm{p}}\}\big\}, \tag{2.41}$$

where $\{\Delta\varepsilon^{\mathrm{p}}\}$ are the incremental plastic strains over the return path and $\{\varepsilon_{n+1}^{\mathrm{e}}\} = \big\{\{\varepsilon_t^{\mathrm{e}}\} - \{\Delta\varepsilon^{\mathrm{p}}\}\big\}$ are the updated elastic strains.

The texts by Crisfield [13] and Simo and Hughes [43] provide a detailed review of these implicit return algorithms and the latter gives a general return mapping procedure for rate-independent plasticity. The plastic corrector stage is typically performed iteratively until the residuals associated with the unknowns fall within a specified tolerance.

The main advantage of implicit (over explicit) methods is the fact that the consistency conditions are enforced at the end of the strain increment. One drawback of the iterative bE *closest point projection method* (CPPM) is the requirement to calculate the derivatives of the flow rule and hardening laws with respect to the unknowns at each iteration. These derivatives can become quite involved for complicated constitutive models. Also, unless the appropriate form of the yield function and plastic flow direction are specified, the method can suffer from convergence difficulties[11]. Other problems can arise if discontinues, such as corners of apexes, are not correctly dealt with (see Chapter 4).

Several other implicit methods have been proposed such as the *generalised trapezoidal rule* [37], *generalised midpoint rule* [37], *cutting plane algorithm* [44] and *governing parameter method*[12] [21–23]. Details of these algorithms are not included here. For more information on these approaches see Kojić [22] or Simo and Hughes [43], amongst others.

Some simple plasticity models allow for analytical integration[13] based on the implicit bE method. Currently, models that can be integrated analytically include the classical P-R, Tresca, M-C and D-P models, in addition to a hyperbolic, circular deviatoric section, cone model [12] and the *modified Reuleaux* [10, 11] model (as detailed in Chapter 4 of this thesis). The integration algorithm for the latter two models were formulated using energy-mapped stress space (EMSS) (initially proposed by Crouch *et al.* [12] for associated flow perfect plasticity models and later extended to the more general case of non-associated plastic flow by Coombs and Crouch [11]). This space allows the stress integration to be reduced down to the problem of finding the geometric closest point on the yield surface to the trial stress state in EMSS (as discussed in Section 4.3.1). However, the analytical integration based on geometric considerations is only available for polynomials of fourth order or less (unless higher order equations may be easily factorised). The full family of models that allow analytical bE integration has yet to be determined [12]. In addition to these perfect plasticity models, Simo and Hughes [43] provided a number of closed-form solutions for J_2 plasticity models which include isotropic and kinematic hardening. The main advantages of analytical integration, over that of iterative methods, is its robustness and speed. Analytical bE stress integration is discussed in more detail in Chapter 4.

[10] Known as the *operator splitting* method [38].

[11] The issue of selecting an appropriate yield function is discussed in more detail in Chapter 5.

[12] Initially named the *effective-stress-function algorithm* [23].

[13] Note, it is important to distinguish between analytical integration based on implicit methods and exact integration. Analytical integration will not (except in some special cases, such as when the direction of plastic flow is constant throughout the return path) be error free.

Implicit methods have significant advantages in accuracy over the earlier, simpler, explicit methods [29] and allow for the determination of a tangent stiffness matrix consistent with the stress integration procedure which can significantly enhance the convergence rate of the global equilibrium equations. Indeed, recently Anandarajah [1] suggested that

> *"It appears that the optimal method available at present for implementing elasto-plastic constitutive models is to use CPPM to integrate the rate equations at the Gauss points in finding the stress increment for a given strain increment, and to use consistent tangent operator in the global Newton's iterations."*

He further remarked that

> *"The main advantage is that the method for the most part is stable and provides optimal accuracy."*

Anandarajah's claims are perhaps over-stated. However, the general implicit bE stress integration method (as presented in Section 2.3.1) can be applied to many constitutive algorithms and it is now used as the benchmark with which to assess other integration methods [2, 49].

Exact stress integration

Currently, exact stress integration is only available for a few select simple plasticity models, such as the widely used P-R and D-P [14] formulations. The P-R updating procedure for perfect plasticity was initially proposed by Krieg and Krieg [29] and later, also including the algorithmic consistent tangent, by Wei *et al.* [50][14]. This was subsequently extended to the case linear isotropic hardening by Szabó [47] and mixed linear hardening by Kossa and Szabó [26]. Loret and Prévost [30] provided the exact stress integration procedure for the pressure sensitive D-P constitutive model with linear hardening and non-associated plastic flow. Although these semi-analytical methods provide a robust error-free stress return, their computational overheads exceed that of other stress integration procedures for these simple plasticity models [27]. Indeed, Loret and Prévost commented that their method was *"computationally too slow to be used routinely in actual calculations"* [30]. However, their solution provided a means of comparison for other approximate methods, from which they concluded that the implicit bE method is indeed attractive.

Alternative methods

Recently several alternative methods have been proposed for the integration of the constitutive relations. Brannon and Leelavanichkul [3] proposed a *nested multi-stage return algorithm* for a single-surface three-invariant dependent rock constitutive model. Initially the trial state outside the yield surface is returned analytically onto a D-P cone (that encloses the true yield surface). An implicit iterative *steepest-descent* algorithm is then used to return this intermediate point onto the correct yield surface. The approach was proposed to eliminate the potential problems of converging to an inappropriate state outside the true yield surface. However, this initial step is superfluous if the appropriate form of yield function is adopted[15].

Becker [2] proposed an alternative method where the direction of plastic flow is recast as a function of both the current stress state and the strain increment (that is, $\{g_{,\sigma}(\sigma, \Delta\varepsilon)\}$). This numerically *"very robust"* [2] method was motivated by the potential instability of implicit methods when large strain

[14] Note that no reference to this exact integration procedure was made in the recent book on "computational methods for plasticity" by de Souza Neto, Perić and Owen [46]. This omission was scrutinised by a recent final year research project at Durham University by Turnbull [48] that verified the stress return and consistent tangent of Wei *et al.* [50].

[15] This point is discussed in more detail in Section 5.3.2.

increments are applied. The authors found that the method was less accurate than the more traditional methods for small strain increments but more accurate when large strain increments were applied.

Vrh *et al.* [49] proposed the *next increment corrects error* explicit integration scheme that claims to combine the simplicity of the forward Euler scheme with the accuracy of bE integration. The method is based on the idea that the error from one strain increment should be considered in the next integration step, *"thus enabling the error from the previous increment to be adequately reduced in the very next increment"* [49]. For the examples presented, the errors were shown to be comparable to (although, not an improvement on) those of the bE method, but with considerable run-time advantages over the latter method. However, both Becker [2] and Vh *et al.* [49] used an explicit FE code where the advantage (in terms of convergence to the global equilibrium) of implicit methods, in allowing derivation of an algorithmic consistent tangent, could not be realised.

2.3.1 Implicit backward Euler stress integration

Throughout this thesis a fully implicit bE stress integration scheme is used. As discussed in the previous sections, the popularity of such a procedure over explicit schemes is due to its relatively high accuracy for a given numerical effort, particularly when large strain increments are applied [4]. Simo and Hughes [43] showed that the bE integration corresponds to the minimisation of

$$\big\{\{\sigma_r\}-\{\sigma_t\}\big\}^T\big[C^{\mathrm{e}}\big]\big\{\{\sigma_r\}-\{\sigma_t\}\big\}, \tag{2.42}$$

with respect to the return stress $\{\sigma_r\}$ (where $\big[C^{\mathrm{e}}\big]=\big[D^{\mathrm{e}}\big]^{-1}$ is the elastic compliance matrix). This minimisation is subject to the KTK consistency conditions (2.15). $(\cdot)_t$ and $(\cdot)_r$ denote quantities associated with the trial state and the return state respectively. Starting with the following unknowns

$$\{x\}=\big\{\{\varepsilon^{\mathrm{e}}\}\qquad\{\beta\}\qquad\Delta\gamma\big\}^T, \tag{2.43}$$

where $\Delta\gamma$ is the increment in the consistency parameter consistent with the direction of plastic flow at the final (converged) stress state for the integrated plastic strain path. Combined with the residuals

$$\{b\}=\left\{\begin{array}{c}\{\varepsilon^{\mathrm{e}}\}-\{\varepsilon^{\mathrm{e}}_t\}+\Delta\gamma\{g_{,\sigma}\}\\ \{\beta\}-\{\beta_t\}-\{\Delta\tilde{\beta}\}\\ f\end{array}\right\}=\left\{\begin{array}{c}\{b_1\}\\ \{b_2\}\\ b_3\end{array}\right\}, \tag{2.44}$$

where $\{\Delta\tilde{\beta}\}$ and $\{\beta_t\}$ are the incremental hardening law for and trial values of the internal variables. We define the Hessian matrix from the derivatives of the residuals with respect to the unknowns

$$[A]=\left[\begin{array}{ccc}[b_{1,\varepsilon^{\mathrm{e}}}] & [b_{1,\beta}] & \{b_{1,\Delta\gamma}\}\\ [b_{2,\varepsilon^{\mathrm{e}}}] & [b_{2,\beta}] & \{b_{2,\Delta\gamma}\}\\ \{b_{3,\varepsilon^{\mathrm{e}}}\}^T & \{b_{3,\beta}\}^T & b_{3,\Delta\gamma}\end{array}\right]. \tag{2.45}$$

Forming this matrix, from (2.44) and (2.43), we obtain

$$[A]=\left[\begin{array}{ccc}[I]+\Delta\gamma[g_{,\sigma\sigma}][D^{\mathrm{e}}] & \Delta\gamma[g_{,\sigma\beta}] & \{g_{,\sigma}\}\\ -[\Delta\tilde{\beta}_{,\sigma}][D^{\mathrm{e}}] & [I]-[\Delta\tilde{\beta}_{,\beta}] & -\{\Delta\tilde{\beta}_{,\Delta\gamma}\}\\ \{f_{,\sigma}\}^T[D^{\mathrm{e}}] & \{f_{,\beta}\}^T & 0\end{array}\right]. \tag{2.46}$$

The iterative increment[16] in the unknowns is given by

$$\{\delta x\} = -[A]^{-1}\{b\}, \tag{2.47}$$

with the starting conditions

$$\{{}^0\varepsilon^{\mathrm{e}}\} = \{\varepsilon_t^{\mathrm{e}}\}, \qquad {}^0\Delta\gamma = 0 \qquad \text{and} \qquad \{{}^0\beta\} = \{\beta_t\}, \qquad \therefore \qquad \{{}^0b\} = \Big\{\{0\} \quad \{0\} \quad {}^0f\Big\}^T, \tag{2.48}$$

where the pre-superscript denotes the iteration number. Figure 2.2 illustrates the numerical sequence for the bE stress return. The Newton-Raphson iterative process continues until the residuals converge to within a specified tolerance. Throughout the stress return, all of the derivatives are evaluated at the current state. This requires the repeated evaluation of the derivatives at each iteration in addition to the inversion of the Hessian matrix (2.46).

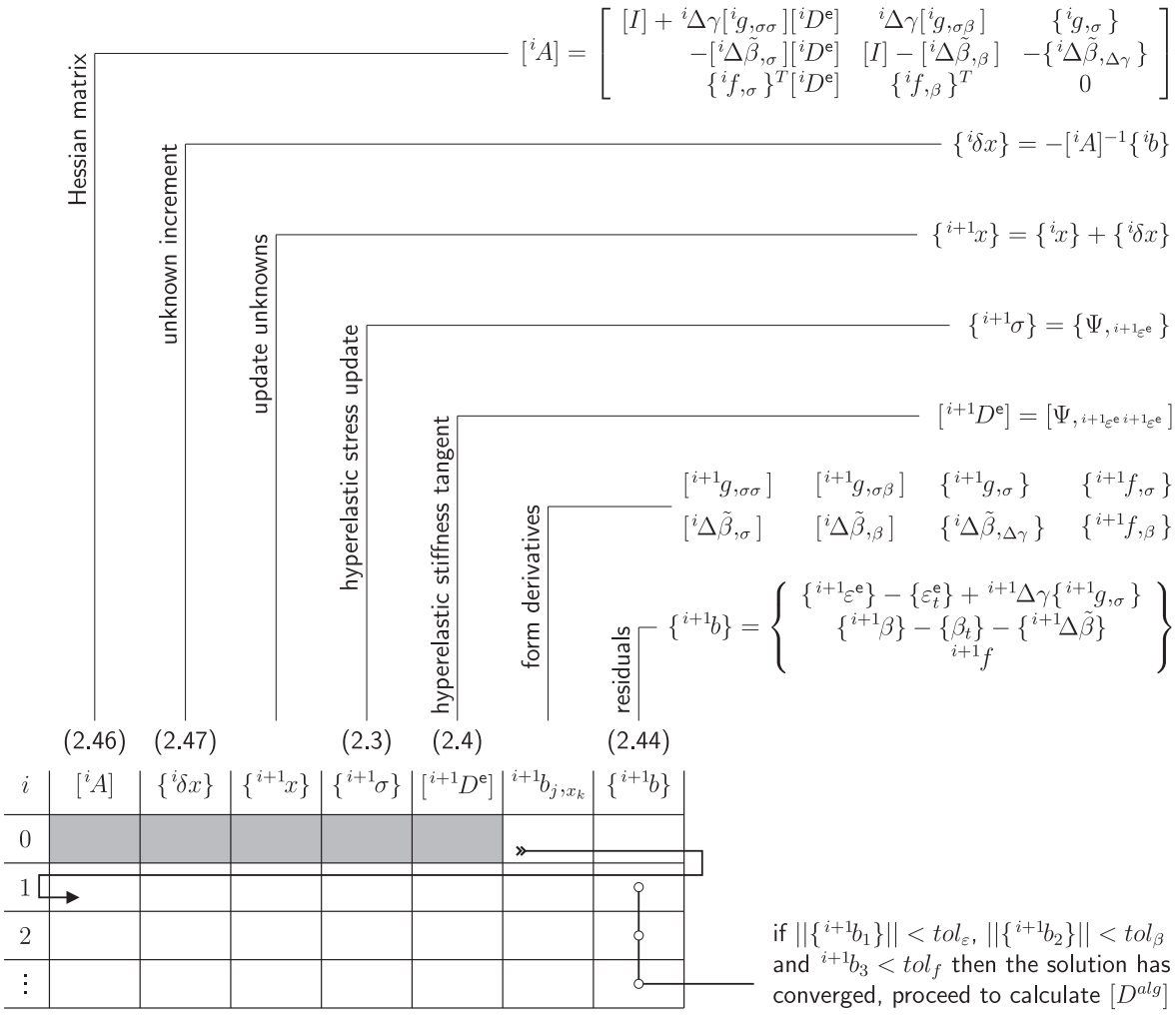

Figure 2.2: Backward Euler stress return sequence.

[16]The iterative increment of $(\cdot)$ is denoted by $\delta(\cdot)$ using a lower-case delta to denote that this increment is the contribution to the unknowns for a given iteration. The total increment in the unknowns, $\{\Delta x\}$, is given by the summation of the iterative increments (from (2.47)) over the number of iterations required to converge within a specified tolerance.

2.4 Consistent linearisation

Stress integration methods, such as the bE procedure described in the previous section, provide an algorithmic incremental constitutive law for stress calculation given a level of strain. For inelastic materials the *algorithmic consistent tangent* [45] is the tangent that is consistent with the stress updating procedure. This tangent describes how the return stress changes as a function of the trial elastic strain. Nagtegaal [34] was the first to propose a consistent tangent for the implicit radial return algorithm. It was later shown, for a general implicit bE stress integration algorithm, that the use of the consistent tangent within the global equilibrium iterations (for example, within the FEM) allows for asymptotic quadratic convergence of the residual out-of-balance force, leading to optimum efficiency of the Newton-Raphson solver [45]. The consistent tangent can be defined as

$$\left[D^{alg}\right] = \left[\sigma_{,\varepsilon_t^{\mathrm{e}}}\right] \tag{2.49}$$

and obtained through linearising the residuals (2.44) with respect to the trial elastic strain, $\{\varepsilon_t^{\mathrm{e}}\}$. The first row of (2.44) becomes

$$[C^{\mathrm{e}}]\{d\sigma\} + \Delta\gamma\Big([g_{,\sigma\sigma}]\{d\sigma\} + [g_{,\sigma\beta}]\{d\beta\}\Big) + d\Delta\gamma\{g_{,\sigma}\} = \{d\varepsilon_t^{\mathrm{e}}\}, \tag{2.50}$$

where $d(\cdot)$ denotes the differential[17] of $(\cdot)$. Considering the second row, we obtain

$$\{d\beta\} - [\Delta\tilde{\beta}_{,\beta}]\{d\beta\} - [\Delta\tilde{\beta}_{,\sigma}]\{d\sigma\} - \{\Delta\tilde{\beta}_{,\Delta\gamma}\}d\Delta\gamma = 0. \tag{2.51}$$

Finally the third row, from the consistent condition, gives

$$\{f_{,\sigma}\}^T\{d\sigma\} + \{f_{,\beta}\}^T\{d\beta\} = 0. \tag{2.52}$$

Combining (2.50)-(2.52), we obtain

$$\underbrace{\begin{bmatrix} [C^{\mathrm{e}}] + \Delta\gamma[g_{,\sigma\sigma}] & \Delta\gamma[g_{,\sigma\beta}] & \{g_{,\sigma}\} \\ -[\Delta\tilde{\beta}_{,\sigma}] & [I] - [\Delta\tilde{\beta}_{,\beta}] & -\{\Delta\tilde{\beta}_{,\Delta\gamma}\} \\ \{f_{,\sigma}\}^T & \{f_{,\beta}\}^T & 0 \end{bmatrix}}_{[A^{alg}]^{-1}} \begin{Bmatrix} \{d\sigma\} \\ \{d\beta\} \\ d\Delta\gamma \end{Bmatrix} = \begin{Bmatrix} \{d\varepsilon_t^{\mathrm{e}}\} \\ \{0\} \\ 0 \end{Bmatrix}. \tag{2.53}$$

Multiplying both sides of (2.53) by $[A^{alg}]$, gives rise to the consistent tangent

$$\begin{Bmatrix} \{d\sigma\} \\ \{d\beta\} \\ d\Delta\gamma \end{Bmatrix} = \begin{bmatrix} [D^{alg}] & [A_{12}^{alg}] & \{A_{13}^{alg}\} \\ [A_{21}^{alg}] & [A_{22}^{alg}] & \{A_{23}^{alg}\} \\ \{A_{31}^{alg}\}^T & A_{32}^{alg} & A_{33}^{alg} \end{bmatrix} \begin{Bmatrix} \{d\varepsilon_t^{\mathrm{e}}\} \\ \{0\} \\ 0 \end{Bmatrix}. \tag{2.54}$$

Calculation of the consistent tangent requires the derivatives of the unknowns with respect to the residuals at the final return state. Unlike the infinitesimal elasto-plastic tangent, $[D^{\mathrm{ep}}]$, the algorithmic tangent is dependent on the return path rather than just the final stress state. In the limit where $\{\varepsilon_t^{\mathrm{e}}\} \to \{\varepsilon_n^{\mathrm{e}}\}$ the infinitesimal and consistent tangents become coincident.

For general plasticity, where the yield function and plastic potential are not equal, both $[D^{\mathrm{ep}}]$ and $[D^{alg}]$ will be non-symmetric. Ortiz and Martin [36] provide an interesting discussion on the form of the

[17] A differential is defined as the product between the derivative of a function, with respect to its argument, multiplied by the infinitesimal increment in the same argument [41].

fully implicit stress integration algorithms that preserve symmetry of the consistent tangent.

2.5 Observations

The following observations can be drawn from this chapter:

(i) hyperplastic constitutive models can be derived from two scalar functions, namely the free-energy function (providing the elasticity law) and the dissipation function (providing the yield function and direction of plastic flow);

(ii) implicit integration, unlike explicit methods, enforces the consistency condition precisely and sets the current standard in terms of accuracy, when integrating constitutive relations; and

(iii) the implicit bE integration scheme facilitates the derivation of the algorithmic consistent tangent which allows for optimum asymptotic quadratic convergence when solving the global equilibrium equations.

Chapter 2 references

[1] A Anandarajah, *Computational Methods in Elasticity and Plasticity: Solids and Porous Media*, Springer, 2010.

[2] R Becker, *An alternative approach to integrating plasticity relations*, Int. J. Plasticity 27 (2011), 1224–1238.

[3] RM Brannon & S Leelavanichkul, *A multi-stage return algorithm for solving the classical damage component of constitutive models for rocks, ceramics, and other rock-like media*, Int. J. Fract. 163 (2010), 133–149.

[4] JL Chaboche & G Cailletaud, *Integration methods for complex plastic constitutive equations*, Comput. Meth. Appl. Mech. Engrg. 133 (1996), 125–155.

[5] R Chambon, J Desrues & W Hammad, *CLoE, a new rate-type constitutive model for geomaterials theoretical basis and implementation*, Int. J. Numer. Anal. Meth. Geomech. 18 (1994), 253–278.

[6] WF Chen & E Mizuno, *Nonlinear analysis in soil mechanics: theory and implementation*, Elsevier, 1990.

[7] IF Collins & GT Houlsby, *Application of thermomechanical principles to the modelling of geoetchnical materials*, Proc. R. Soc. Lond. A. 453 (1997), 1975–2001.

[8] IF Collins & PA Kelly, *A thermomechanical analysis of a family of soil models*, Géotechnique 52 (2002), 507–518.

[9] IF Collins, *The concept of stored plastic work or frozen elastic energy in soil mechanics*, Géotechnique 55 (2005), 373–382.

[10] WM Coombs & RS Crouch, *Non-associated Reuleaux plasticity: Analytical stress integration and consistent tangent for finite deformation mechanics*, Comput. Meth. Appl. Mech. Engrg. 200 (2011), 1021–1037.

[11] WM Coombs, RS Crouch & CE Augarde, *Reuleaux plasticity: Analytical backward Euler stress integration and consistent tangent*, Comput. Meth. Appl. Mech. Engrg. 199 (2010), 1733–1743.

[12] RS Crouch, H Askes & T Li, *Analytical CPP in energy-mapped stress space: application to a modified Drucker-Prager yield surface*, Comput. Meth. Appl. Mech. Engrg. 198 (2009), 853–859.

[13] MA Crisfield, *Non-linear Finite Element Analysis of Solids and Structures. Volume 1: Essentials*, John Wiley & Sons Ltd, 1991.

[14] DC Drucker & W Prager, *Soil mechanics and plastic analysis or limit design*, Quart. Appl. Math. 10 (1952), 157–164.

[15] YC Fung, *Foundations of solid mechanics*, Prentice-Hall Inc., 1965.

[16] R Hill, *The mathematical theory of plasticity*, Oxford University Press, London, 1950.

[17] H-K Hong & C-S Liu, *Internal symmetry in bilinear elastoplasticity* Int. J. Nonlin. Mech. 34 (1999), 279–288.

[18] GT Houlsby, *A Study of Plasticity Theories and Their Applicability to Soils*, PhD. Thesis, University of Cambridge, 1981.

[19] GT Houlsby & AM Puzrin, *Principles of hyperplasticity*, Springer-Verlag London Limited, 2006.

[20] AA Ilyushin, *Some problems in the theory of plastic deformation*, Prikl. Mat. Mekh. 7 (1943), 245–272.

[21] M Kojić, *The Governing Parameter Method for implicit integration of viscoplastic constitutive relations for isotropic and orthotropic metals*, Compt. Mech. 19 (1996), 49–57.

[22] M Kojić, *Stress integration procedures for inelastic material models within the Finite Element Method*, Appl. Mech. Rev. 55 (2002), 389–414.

[23] M Kojić & KJ Bathe, *Inelastic analysis of solids and structures*, Springer, 2005.

[24] D Kolymbas, *A rate-dependent constitutive equation for soils* Mech. Res. Comm. 4 (1977), 367–372.

[25] D Kolymbas, *An outline of hypoplasticity*, Arch. Appl. Mech. 61 (1991), 143–151.

[26] A Kossa & L Szabó, *Exact integration of the von Mises elastoplasticity model with combined linear isotropic-kinematic hardening*, Int. J. Plasticity 25 (2009), 1083–1106.

[27] A Kossa & L Szabó, *Numerical implementation of a novel accurate stress integration scheme of the von Mises elastoplasticity model with combined linear hardening*, Finite Elem. Anal. Des. 46 (2010), 391–400.

[28] RD Krieg & SM Key, *Implementation of a time dependent plasticity theory and structural computer programs*. In: JA Stricklin & KJ Saczalski (eds.), Constituive Equations in Viscoplasticity: Computational and Engineering Aspects, ASME, New York, 20 (1976), 125–137.

[29] RD Krieg & DB Krieg, *Accuracies of numerical solution methods for the elastic-perfactly plastic model*, J. Press. Vess.-T. ASME 99 (1977), 510–515.

[30] B Loret & JH Prévost, *Accurate numerical solutions for drucker-prager elastic-plastic models*, Comput. Meth. Appl. Mech. Engrg. 54 (1986), 259–277.

[31] GA Maugin, *A.A. Ilyushin's works: an appraisal from Paris*, J. Eng. Math. (2011), doi: 10.1007/s10665-010-9450-4.

[32] GA Maugin, *The thermomechanics of plasticity and fracture*, Cambridge University Press, 1992.

[33] A Mendelson, *Plasticity: theory and application*, The Macmillan Co., NY, 1968.

[34] JC Nagtegaal, *On the implementation of inelastic constitutive equations with special reference to large deformation problems*, Comput. Meth. Appl. Mech. Engrg. 33 (1982), 469–484.

[35] GC Nayak & OC Zienkiewicz, *Elasto-plastic stress analysis. A generalization for various constiutive relations including strain softening*, Int. J. Numer. Meth. Eng. 5 (1972), 113–135.

[36] M Ortiz & JB Martin, *Symmetry-preserving return ampping algorithms and incrementally extremal paths: a unification of concepts*, Int. J. Numer. Meth. Eng. 28 (1989), 1839–1853.

[37] M Ortiz & EP Popov, *Accuracy and stability of integration algorithms for elastoplastic constitutive relations*, Int. J. Numer. Meth. Eng. 21 (1985), 1561–1576.

[38] M Ortiz & JC Simo, *An analysis of a new class of integration algorithms for elastoplastic constitutive relations*, Int. J. Numer. Meth. Eng. 23 (1986), 353–366.

[39] M Rezaiee-Pajand, M Sharifian & M Sharifian, *Accurate and approximate integrations of Drucker-Prager plasticity with linear isotropic and kinematic hardening*, Eur. J. Mech. A-Solid 30 (2011), 345–361.

[40] KH Roscoe & JB Burland, *On the generalised stress-strain behaviour of 'wet' clay*. In: J Heyman & FA Leckie (eds.), Engineering Plasticity (1968), Cambridge University Press, 535–609.

[41] SL Salas, E Hille & G Etgen, *Calculus*, 9th ed., John Wiley & Sons Inc., 2003.

[42] AN Schofield & CP Wroth, *Critical State Soil Mechanics*, McGraw-Hill Publishing Company Limited, 1968.

[43] JC Simo & TJR Hughes, *Computational inelasticity*, Springer, New York, 1998.

[44] JC Simo & M Ortiz, *A unified approach to finite deformation elastoplastic analysis based on the use of hyperelastic constitutive equations*, Comput. Meth. Appl. Mech. Engrg. 49 (1985), 221–245.

[45] JC Simo & RL Taylor, *Consistent tangent operators for rate-independent elastoplasticity*, Comput. Meth. Appl. Mech. Engrg. 48 (1985), 101–118.

[46] EA de Souza Neto, D Perić & DRJ Owen, *Computational methods for plasticity: Theory and applications*, John Wiley & Sons Ltd, 2008.

[47] L Szabó, *A semi-analytical integration method for J2 flow theory of plasticity with linear isotropic hardening*, Comput. Meth. Appl. Mech. Engrg. 198 (2009), 2151-2166.

[48] C Turnbull, *The exact stress integration of elasto-plasticity models*, MEng. Final Year Research Report, Durham Univeristy, 2010.

[49] M Vrh, M Halilovič & B Štok, *Improved explicit integration in plasticity*, Int. J. Numer. Meth. Eng. 81 (2010), 910–938.

[50] Z Wei, D Perić & DRJ Owen, *Consistent linearization for the exact stress update of Prandtl-Reuss non-hardening elastoplastic models*, Int. J. Num. Meth. Eng. 39 (1996), 1219–1235.

[51] M Wilkins, *Calculation of elastic-plastic flow*, in S Fernback & M Rotenberg (eds.), Methods of Computational Physics, Vol 3, Academic Press, N.Y., 1964.

[52] DM Wood, *Geotechnical modelling*, Spon Press, 2004.

[53] CP Wroth & A Palmer, *Preface to the Proceedings of the symposium on Plasticity and Soil Mechanics*, Cambridge, (1973), 13–15.

[54] M-H Yu, *Advances in strength theories for materials under complex stress state in the 20th Century*, Appl. Mech. Rev. 55 (2002), 169–218.

[55] H Ziegler, *An introduction to thermomechanics*, 2nd edn. North Holland Pub. Co, Amsterdam, 1983.

Chapter 3

Geometric non-linearity

The majority of engineering stress analyses are performed using the assumption of infinitesimal strains and small displacements where a linear relationship links strains to displacements. However, such an assumption might lead to a poor estimate of the true structural response. Finite deformation (or geometrically non-linear, GNL) analysis takes account of the structure's evolving geometry, giving rise to a non-linear relationship between strains and displacements. GNL analysis provides a more physically realistic result. It is important to note that GNL analysis does not necessarily predict larger displacements than infinitesimal analysis. One simple example is a linear elastic cylindrical triaxial specimen under undrained triaxial compression or extension[1]. Infinitesimal analysis will predict the same linear response under compression and extension. GNL analysis will predict progressive stiffening of the sample under compressive loading but softening under tensile loads. GNL deformation analyses can be split into four categories; combinations of infinitesimal or finite strains and small or large rotations, all with large displacements. This chapter deals with the most general of the four divisions; that of large displacements and rotations with finite strains.

There are three main approaches to GNL analysis:

(i) *Lagrangian* formulations follow the motion of all particles in a body from the original to the final configuration [13].

(ii) *Eulerian* formulations track the motion of a material through a stationary control volume [13].

(iii) *Co-rotational* formulations adopt a set of coordinate axes that rotate with the body [5, 6].

The mechanical analysis of solids tends to be based on a Lagrangian description of motion, as it provides a more natural and effective approach compared to Eulerian techniques; which are largely used for the study of fluid motion. Using an Eulerian approach for stuctural problems would require control volumes to be continually re-calculated due to changes in the geometry. This requirement stems from the need (in Eulerian formulations) to keep track of the matter moving in-to and out-of a control volume.

Lagrangian formulations are further split into *total* and *updated* approaches where the static and kinematic variables are referred to either the initial or the previously calculated configurations respectively. The two methods should give identical results, although there can be considerable differences in numerical efficiency [1].

Co-rotational formulations were originally developed for the analysis of trusses, beams and shells (rather than continuum elements) motivated by the desire to make use of existing small strain linear

[1]Undrained triaxial compression and extension tests maintain a constant volume. The displacement in the vertical direction indicates the test type (compressive or tensile) and the perpendicular displacements are such that a constant volume is maintained.

finite-elements. Such formulations have subsequently been extended to three-dimensional continuum elements [6]. The approach splits the deformation field into local element straining and global element transformation/rotation. The majority of the formulations are limited to small strains, although they do allow for finite deformations/rotations.

Arbitrary Lagrangian-Eulerian (ALE) methods attempt to combine the advantages of the Lagrangian and Eulerian formulations whilst removing a number of their limitations [8]. The ALE approach allows nodes within an analysis to move with the continuum (as with Lagrangian analyses), remain stationary (as with the Eulerian formulation) or move arbitrarily (through some specified way to give a continuous re-zoning capability) within the domain. ALE can handle greater mesh distortions than a purely Lagrangian method, with more resolution than a purely Eulerian approach, but it requires an additional mapping space to be defined. ALE also requires an appropriate time step to be chosen for the particular analysis under consideration [8]. Thus far, it has seen little attention in the analysis of geomechanical problems, mainly due to its complexity [24].

This chapter describes an *updated Lagrangian*[2] logarithmic strain-Kirchhoff stress formulation which can be used for anisotropic inelastic constitutive models. The use of a logarithmic strain-Kirchhoff stress relationship, in conjunction with an implicit exponential map for the plastic flow equation, allows for the implementation of standard small strain constitutive algorithms within the finite deformation framework without modification. These stress and strain measures provide the basis of the most successful, straightforward ways of implementing large strain elasto-plasticity [16].

Section 3.1 reviews the basic kinematics of finite deformations. The concept of isotropic finite deformation elasto-plasticity, using a logarithmic strain-Kirchhoff stress approach, is introduced and the incremental formulation provided in Section 3.2. Section 3.3 extends the work of the preceding sections to cover the case of anisotropic elasto-plasticity. The finite-element implementation and numerical validation are provided in Sections 3.4 and 3.5 respectively. Observations are drawn in Section 3.6.

This chapter uses both indicae and matrix/vector notation in order to provide a compact description of the governing equations. Section 3.1 and the first half of Section 3.2 use indicae notation to introduce the basic components of finite deformation inelasticity. Section 3.2.1 onwards mainly uses matrix/vector notation to facilitate the numerical implementation of the finite deformation framework. Unfortunately, those working in finite deformation mechanics have yet to agree on a common nomenclature. Here, as far as possible, symbols have been used that have been adopted within the majority of the publications in the field.

3.1 Kinematics of deformation

Consider a material body in space defined using a stationary Cartesian co-ordinate system. At time $t = 0$ the position of a material point is denoted by X_i, where i denotes one of the three possible indices 1, 2 or 3 (that is, x, y and z if the local coordinates coincide with the cartesian references system, as shown in Figure 3.1). This is the reference (or material) configuration of the body. The current position of the body at time t is given by

$$x_i = \varphi_i(X_i, t), \tag{3.1}$$

[2]There is possible confusion with the term *updated Lagrangian*. A number of the earlier updated formulations were approximate in that they are restricted to small (or even constant) elastic strains [2]. This restriction does not hold here. In this work, the term *updated Lagrangian* refers to the strategy used by Holzapfel [13] and Bathe [1], where the linearisation of the internal virtual work is performed in the current configuration using the spatial derivatives. For more details see [1, 35], amongst others. As noted (and demonstrated through numerical examples) by Bathe *et al.* [2] *"provided that the appropriate constitutive relations are used, the* [total and updated Lagrangian] *equations yield identical solutions"*. Another possible confusion is through the use of the term "total formulations" by some authors (such as Gabriel and Bathe [10]) to indicate those constitutive relations where the total stresses are obtained from the total strains using a hyperelastic relationship.

where $\varphi_i(X_i, t)$ defines the motion of the body over time, referenced to its initial state. This motion is known as the *Lagrangian description of motion*. The displacement of a material point within this body is

$$u_i(X_i, t) = x_i(X_i, t) - X_i \qquad \text{or alternatively as} \qquad u_i(x_i, t) = x_i - X_i(x_i, t), \tag{3.2}$$

in terms of the material (or reference) and spatial (or current) configurations. It is important to distinguish between the descriptions of motion:

(i) a material description of motion is based on where the material *was* at $t = 0$; whereas

(ii) a spatial description is formulated in terms of where the material *is*.

If the same material body is loaded from its reference configuration X_i, to a current deformed configuration x_i, it may undergo some stretching and rigid body translation and/or rotation. By considering the infinitesimal vectors dX_i and dx_i embedded in the reference and current configurations (see Figure 3.1), we introduce the *deformation gradient* , F_{ij}, as

$$dx_i = F_{ij} dX_j. \tag{3.3}$$

This deformation gradient provides the fundamental link between current and reference configurations

$$F_{ij} = \frac{\partial x_i}{\partial X_j} = \delta_{ij} + \frac{\partial u_i}{\partial X_j}, \tag{3.4}$$

where δ_{ij} is the Kronecker delta tensor ($\delta_{ii} = 1$ and $\delta_{ij} = 0$ when $i \neq j$). F_{ij} provides a description of rigid body rotation and stretch, but contains incomplete information on the translation of a material point. For a purely rigid body translation $F_{ij} = \delta_{ij}$, that is, the deformation gradient contains no indication of the magnitude of the translation. Through polar decomposition[3] of the deformation gradient

$$F_{ij} = R_{ik} U_{kj} = v_{ik} R_{kj}, \tag{3.5}$$

we obtain the rotational tensor R_{ij} and the right (material), U_{ij}, and left (spatial), v_{ij}, symmetric stretch tensors respectively (as shown in Figure 3.1). These stretch tensors can be obtained directly from the deformation gradient via

$$U_{ij} = \sqrt{C_{ij}} = \sqrt{F_{ki} F_{kj}}, \qquad \text{and} \qquad v_{ij} = \sqrt{b_{ij}} = \sqrt{F_{ik} F_{jk}}, \tag{3.6}$$

where C_{ij} and b_{ij} are known as the right and left *Cauchy-Green* strain tensors[4] (note the position of the non-transposed deformation gradient in (3.6)). The rotation tensors can subsequently be obtained via the inversion of their compatible stretch tensor ($R_{ij} = F_{ik} U^{-1}_{kj}$ or $R_{ij} = v^{-1}_{ik} F_{kj}$). However, C_{ij}, b_{ij}, U_{ij} and v_{ij}, are not suitable measures of strain for a stress-strain relationship because they contain non-zero components during rigid body motion. The polar decomposition of the deformation gradient (3.5) allows the deformation to be split into a sequence of two deformations; from the initial state to a fictitious configuration via a stretch U_{ij} (or a rotation R_{ij}), followed by a rotation R_{ij} (or a stretch v_{ij})

[3]The polar decomposition theorem states that any non-singular second order tensor can be decomposed uniquely into the product of an otherogonal tensor (associated with the rotation of the material point) and a symmetric tensor (associated with the material stretch) [36]. Cauchy noted that *"any motion of a body in the vicinity of a material particle can be written as a pure rotation of three orthogonal directions followed by a pure stretch along those directions"*.

[4]The fractional power of a second order tensor is calculated by first finding the principal values of the tensor, applying the fractional power to the principal values and then reforming the nine-component second order tensor through spectral decomposition using the directions associated with the original tensor.

to arrive at the current configuration. The left and right Cauchy-Green strain tensors are linked through the rotational tensor via

$$U_{ij} = R_{ki} v_{kl} R_{kj}. \tag{3.7}$$

The deformation gradient allows us to define the *volume ratio*, J, derived through consideration of the change of an infinitesimal volume between the reference and current configurations [35], as

$$J = \frac{dV}{dV_0} = \det(F_{ij}) > 0. \tag{3.8}$$

$\det(\cdot)$ is the determinant of $(\cdot)$. dV and dV_0 are the infinitesimal volumes in the current (deformed) and reference (initial) configurations respectively (see Figure 3.1). For *isochoric* deformations, J is equal to unity. Whereas for volumetric deformations, consisting of pure contraction or dilation, the deformation is uniform in all directions and the deformation gradient is $F_{ij} = (l/l_0)\delta_{ij}$, where (l/l_0) is the contraction (or dilation) ratio.

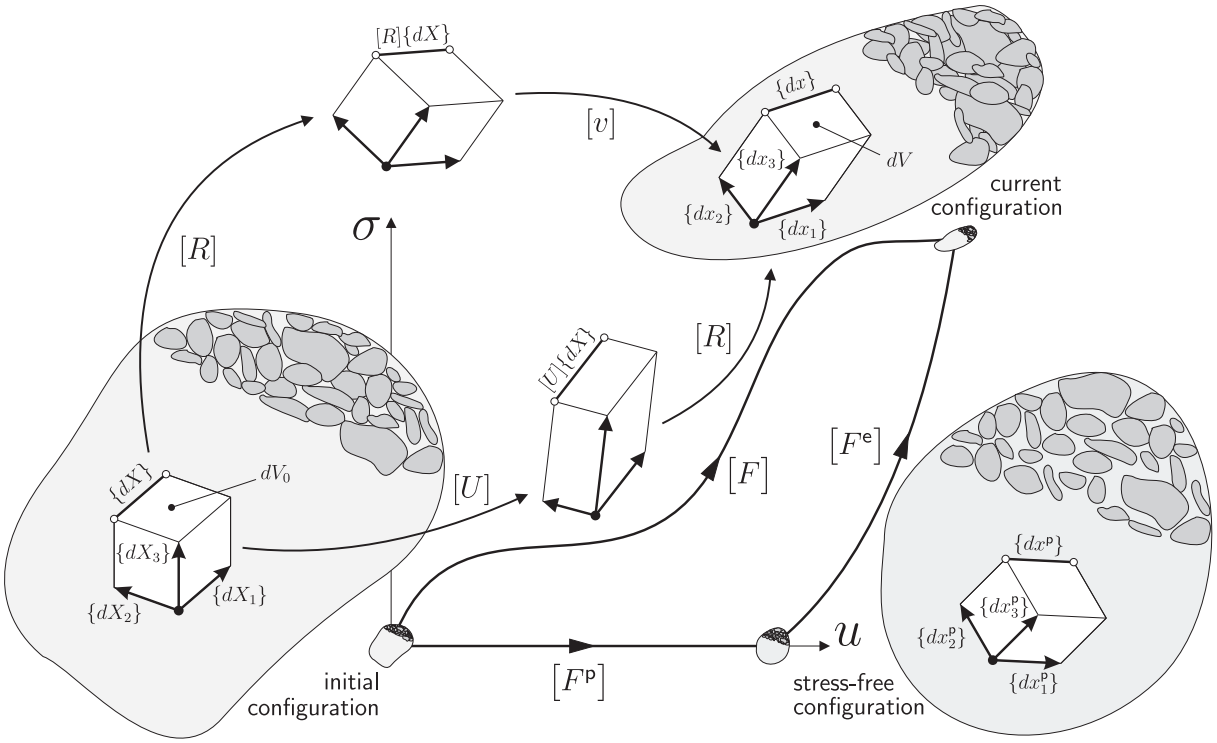

Figure 3.1: Kinematic link between the initial (X_i), current (x_i) and stress free (x_i^{p}) configurations for a schematic stress-displacement path. The deformation gradient ($[F]$) links the initial (or reference) and current configurations using a rotation ($[R]$) and a stretch ($[v]$ or $[U]$). Similarly, the plastic ($[F^{\mathrm{p}}]$) and elastic ($[F^{\mathrm{e}}]$) deformation gradients link the initial to stress-free and stress-free to current configurations respectively.

Finite deformation analysis allows multiple measures of strain to be defined. With small displacements these reduce to the standard infinitesimal strain quantity [9]. One such measure is the Green-Lagrangian strain, defined as

$$E_{ij} = \frac{1}{2}\left(\frac{\partial u_i}{\partial X_j} + \frac{\partial u_j}{\partial X_i} + \frac{\partial u_k}{\partial X_i}\frac{\partial u_k}{\partial X_j}\right) = C_{ij} - \delta_{ij}. \tag{3.9}$$

This strain tensor is invariant to rigid body motion. It should be noted that the higher-order third term in $(3.9)_1$ is missing in infinitesimal strain theories. When u_i is sufficiently small, the contribution of this

high-order term is negligible. Henceforth we make use of the spatial logarithmic strain measure

$$\varepsilon_{ij} = \ln(v_{ij}), \tag{3.10}$$

where the natural logarithm of a tensor is calculated in a way that is analogous to a fractional power[4]. The advantages of using this measure of strain are listed in Section 3.2.

Similarly to measures of strain, there are a number of alternative measures of stress used in finite deformation analysis (refer to Holzapfel's text [13], amongst others, for a description of candidate stress measures). Here we make use of the symmetric Kirchhoff stress, defined as

$$\tau_{ij} = J\sigma_{ij}, \tag{3.11}$$

where σ_{ij} is the Cauchy, or true stress, tensor. We see that the Kirchhoff and Cauchy stress tensors are related by the change in volume between the current (deformed) and original configurations.

3.1.1 Simple deformation field investigations

Before continuing with the development of the finite deformation framework, it is useful to investigate some simple material point deformation fields. Here the material responses, subjected to the displacement fields shown in Figure 3.2 of (i) one-dimensional compression, (ii) hydrostatic compression, (iii) isochoric axial extension and (iv) simple shear, are examined. We restrict the investigation to the case of linear isotropic elasticity, with the material elastic stiffness matrix given by (2.2). Using small strain theory the four displacement fields shown in Figure 3.2 would have a linear deformation-strain-stress response.

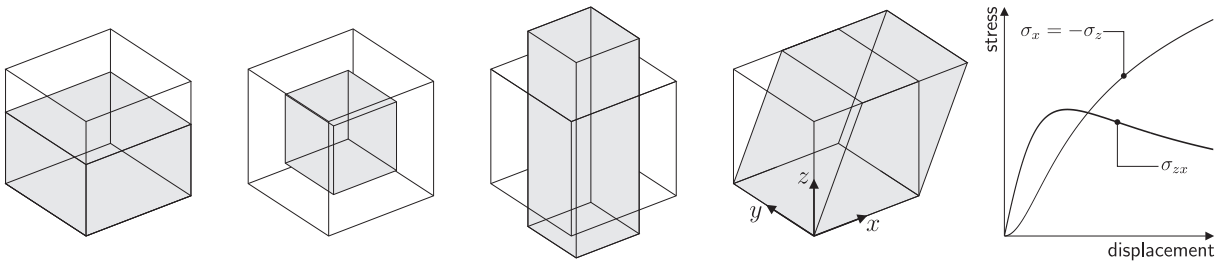

Figure 3.2: Conceptual material point investigations for simple deformation fields (i) uniaxial straining, (ii) hydrostatic compression, (iii) isochoric axial extension, (iv) simple shear and (v) stress response for simple shear.

One-dimensional compression

The deformation gradient, left Cauchy-Green strain and logarithmic strain for uniaxial straining, as shown in Figure 3.2 (i), are

$$[F] = \begin{bmatrix} 1 & 0 & 0 \\ 0 & 1 & 0 \\ 0 & 0 & h/h_0 \end{bmatrix}, \qquad [b] = \begin{bmatrix} 1 & 0 & 0 \\ 0 & 1 & 0 \\ 0 & 0 & (h/h_0)^2 \end{bmatrix} \qquad \text{and} \qquad [\varepsilon] = \begin{bmatrix} 0 & 0 & 0 \\ 0 & 0 & 0 \\ 0 & 0 & \ln(h/h_0) \end{bmatrix},$$

where h_0 and h are the original and current cube heights. The volume ratio is $J = h/h_0$, which combined with (2.2) yields the Cauchy stress as

$$\{\sigma\} = \frac{h_0\Big(\ln(h) - \ln(h_0)\Big)}{h}\left(\frac{E}{(1+\upsilon)(1-2\upsilon)}\right)\Big\{\upsilon \quad \upsilon \quad (1-\upsilon) \quad 0 \quad 0 \quad 0\Big\}^T.$$

Assuming that $h_0 = 1$, the Cauchy stress is linearly dependent on $\ln(h)/h$. For $h < 1$ and $h > 1$ the stress in the z direction will be negative and positive respectively. As h reduces, a physically reasonable stiffening response is observed in the Cauchy stress. That is, displacement increments, Δh, yield a progressively increasing stress increment $\{\Delta\sigma\}$.

Hydrostatic compression

As shown in Figure 3.2 (ii), the deformation gradient, left Cauchy-Green strain and logarithmic strain for hydrostatic compression are

$$\big[F\big] = l/l_0\big[1\big], \qquad \big[b\big] = (l/l_0)^2\big[1\big] \qquad \text{and} \qquad \big[\varepsilon\big] = \ln(l/l_0)\big[1\big],$$

where l_0 and l are the original and current lengths of the cube. The volume ratio and Cauchy stress are $J = (l/l_0)^3$ and

$$\{\sigma\} = \frac{l_0^3\Big(\ln(l) - \ln(l_0)\Big)}{l^3}\left(\frac{E}{(1-2\upsilon)}\right)\Big\{1 \quad 1 \quad 1 \quad 0 \quad 0 \quad 0\Big\}^T,$$

respectively. Once again assuming that $l_0 = 1$, the Cauchy stress is linearly dependent on $\ln(l)/l^3$, and a stiffening response is observed in the resultant stress as l reduces under hydrostatic compression.

Undrained extension or compression

Isochoric extension (and compression) is an important material point state for soils as the majority of available experimental data on particulate materials are gathered from triaxial cells. If no fluid is allowed to leave or enter the cell (i.e. an undrained test), then the volume change is zero; $J = 1$. The deformation gradient and logarithmic strain for isochoric compression, as shown in Figure 3.2 (iii), are

$$[F] = \begin{bmatrix} \sqrt{l_0/l} & 0 & 0 \\ 0 & \sqrt{l_0/l} & 0 \\ 0 & 0 & l/l_0 \end{bmatrix} \qquad \text{and} \qquad [\varepsilon] = \begin{bmatrix} \ln(l_0/l)/2 & 0 & 0 \\ 0 & \ln(l_0/l)/2 & 0 \\ 0 & 0 & \ln(l/l_0) \end{bmatrix}.$$

If $l_0 = 1$, the normal components of the Cauchy stress are

$$\{\hat{\sigma}\} = \left(\frac{E}{(1+\upsilon)(1-2\upsilon)}\right)\Big\{\ln(1/l)/2 + \upsilon\ln(l) \qquad \ln(1/l)/2 + \upsilon\ln(l) \qquad \upsilon\ln(1/l) + (1-\upsilon)\ln(l)\Big\}^T.$$

The axial and lateral stresses will be opposite in sign. Under triaxial extension, where $l > l_0$ and $\Delta l > 0$, the stress response will display softening with increasing axial deformation. The converse is true for triaxial compression, where $l < l_0$ and $\Delta l < 0$, where both stress responses will hardening as the axial length reduces.

Simple shear

The isochoric deformation gradient ($J = 1$) and the left Cauchy-Green strain for simple shear, as shown in Figure 3.2 (iv), are

$$[F] = \begin{bmatrix} 1 & 0 & \Delta l \\ 0 & 1 & 0 \\ 0 & 0 & 1 \end{bmatrix} \quad \text{and} \quad [b] = \begin{bmatrix} 1+(\Delta l)^2 & 0 & \Delta l \\ 0 & 1 & 0 \\ \Delta l & 0 & 1 \end{bmatrix},$$

where Δl is the top face sheared distance. The principal logarithmic strains are

$$\{\hat{\varepsilon}\} = \frac{1}{2}\Big\{\ln\big(1+\Delta l^2/2+\Delta l\sqrt{\Delta l^2/4+1}\big) \qquad 0 \qquad \ln\big(1+\Delta l^2/2-\Delta l\sqrt{\Delta l^2/4+1}\big)\Big\}^T.$$

As the top face sheared distance Δl increases, initially the shear stress increases before reaching maximum and then softening (as shown in Figure 3.2 (v)). The normal stresses σ_x and σ_z are equal in magnitude and opposite in sign with the stress response shown in Figure 3.2 (v). Throughout the deformation process $\sigma_y = 0$.

3.2 Finite elasto-plasticity

Unlike infinitesimal strain analysis, the decomposition of deformation into elastic and plastic components is not so straightforward and remains an area of ongoing research. The pioneering work of Green and Naghdi [11] made use of an additive formulation employing generalised strain measures, thereby retaining the structure of the classical infinitesimal theory of plasticity. However, it was shown by Itskov [15] that this formulation exhibits a spurious non-constant shear stress response for the case of simple shear using a Prandtl-Reuss perfect plasticity model, thereby restricting the model to situations where only moderate plastic strains occur.

In all that follows use is made of the more successful approach (supported by micromechanical observations [16, 22]) of multiplicative decomposition of the deformation gradient into elastic and plastic components. Simo and Ortiz [30] were the first to propose the use of a computational framework for the implementation of finite deformation analysis based entirely on the multiplicative decomposition of the deformation gradient. This *Lee decomposition* [17, 18] of (3.4) is given as follows

$$F_{ij} = F^{\mathrm{e}}_{ik} F^{\mathrm{p}}_{kj} \tag{3.12}$$

where F^{e}_{ij} and F^{p}_{ij} are the elastic and plastic components of the deformation gradient respectively. Lee [17, 18] introduced the concept of a theoretical *fictitious stress-free* state, x^{p}_i, where a material body is unloaded and dissected into infinitesimally small elements to eliminate any internal residual stress (see Figure 3.1). The elastic and plastic components of the deformation gradient are given by

$$F^{\mathrm{e}}_{ij} = \frac{\partial x_i}{\partial x^{\mathrm{p}}_j} = v^{\mathrm{e}}_{ik} R^{\mathrm{e}}_{kj} \qquad \text{and} \qquad F^{\mathrm{p}}_{ij} = \frac{\partial x^{\mathrm{p}}_i}{\partial X_j} = v^{\mathrm{p}}_{ik} R^{\mathrm{p}}_{kj}. \tag{3.13}$$

(3.12) is recovered through (3.4) using the chain rule. Here the elastic and plastic deformation gradients have been split using the polar decomposition into the (elastic or plastic) left stretch tensor, v^{e}_{ik} and v^{p}_{ik}, and a rotation tensor, R^{e}_{kj} and R^{p}_{kj}. Figure 3.1 shows how the elastic and plastic deformation gradients contribute to the current configuration. v^{p}_{ik} describes a plastic stretching between the reference and stress-free configurations, whereas v^{e}_{ik} is the elastic stretch between the stress-free and current configurations. R^{e}_{kj} and R^{p}_{kj} provide the rotations between the stress-free to current configurations and reference to

stress-free configurations respectively. The elastic logarithmic strain tensor follows as

$$\varepsilon^{\mathrm{e}}_{ij} = \ln(v^{\mathrm{e}}_{ij}) = \frac{1}{2}\ln(b^{\mathrm{e}}_{ij}), \qquad \text{where} \qquad v^{\mathrm{e}}_{ij} = \sqrt{b^{\mathrm{e}}_{ij}} = \sqrt{F^{\mathrm{e}}_{ik}F^{\mathrm{e}}_{jk}} \tag{3.14}$$

and b^{e}_{ij} is the elastic left Cauchy-Green strain tensor.

The majority of the early finite deformation elasto-plasticity formulations developed in the 1970s and 80s were based on hypoelastic constitutive models. These models relied on the derivation of objective[5] stress rates. It is possible to specify any number of stress rates that satisfy objectivity. Yet many of these formulations exhibit oscillatory stress responses under constant load paths. They may also fail to satisfy the laws of thermodynamics; erroneously dissipating or creating energy within an elastic response.

Instead of adopting hypoelasticity, we define a hyperelastic relation between the elastic logarithmic strain and Kirchhoff stress as

$$\tau_{ij} = \frac{\partial \Psi}{\partial \varepsilon^{\mathrm{e}}_{ij}}, \tag{3.15}$$

where Ψ is the free energy function defined per unit volume (see Chapter 2). Through the use of a hyperelastic constitutive relationship, Simo and Ortiz [30] demonstrated that *incremental objectivity*[6] is trivially satisfied.

3.2.1 Incremental formulation

The deformation gradient acts as the driving variable for finite deformation analysis. Given a displacement increment, the associated increment in the deformation gradient is obtained as

$$\left[\Delta F_{n+1}\right] = \left[\left[1\right] - \left[\frac{\partial(\Delta u)_{n+1}}{\partial x_{n+1}}\right]\right]^{-1} = \left[1\right] + \left[\frac{\partial(\Delta u)_{n+1}}{\partial x_{n}}\right] \tag{3.16}$$

where Δu is the incremental displacement and the subscripts $_{n+1}$ and $_{n}$ denote the current and previously converged configurations. The increment in the deformation gradient $\left[\Delta F_{n+1}\right]$ is calculated using the non-linear strain-displacement matrix, as detailed in Appendix B.1.1, (B.2)-(B.5). The updated deformation gradient is obtained, using a spatial description, as

$$\left[F_{n+1}\right] = \left[\Delta F_{n+1}\right]\left[F_{n}\right]. \tag{3.17}$$

Alternatively the current deformation gradient can be calculated, using a material formulation (that is using displacements referenced from, and nodal positions in, the original configuration) as follows

$$\left[F_{n+1}\right] = \left[1\right] + \left[\frac{\partial u_{n+1}}{\partial X}\right]. \tag{3.18}$$

The increment in the deformation gradient may be subsequently calculated from

$$\left[\Delta F_{n+1}\right] = \left[F_{n+1}\right]\left[F_{n}\right]^{-1} \tag{3.19}$$

[5] Truesdell and Noll stated the *principle of material frame-indifference* (or objectivity) as that *"constitutive equations must be invariant under changes of frame of reference"* [39]. Holzapfel added that *"constitutive equations must be frame indifferent with respect to Euclidean transformations"* (translations and rotations) and that if this condition is violate then 'the results are meaningless' [13]. The origins of the principle of material frame-indifference, lie within the works of Hooke, Poisson and Cauchy, between 1675 and 1829, generalised by the work of Zaremba in 1903. For a more detailed discussion on objectivity and objective rates see [13, 36, 39], amongst others.

[6] Incremental objectivity was concisely defined by Pinsky *et al.*[25] as *"a physical requirement expressing the fact that the algorithm has to be invariant with respect to superimposed rigid body motions occurring over the time step"*. The hyperelasticity law used here does not contain any stress rates thus the need to integrate elastic rate equations in a way that ensures incremental objectivity is removed.

The trial left elastic Cauchy-Green strain matrix follows as

$$\left[b_t^{\mathrm{e}}\right] = \left[\Delta F_{n+1}\right]\left[b_n^{\mathrm{e}}\right]\left[\Delta F_{n+1}\right]^T, \tag{3.20}$$

where $\left[b_n^{\mathrm{e}}\right]$ from the previously converged solution is obtained from

$$\left[b_n^{\mathrm{e}}\right] = \exp\left(2\left[\varepsilon_n^{\mathrm{e}}\right]\right) \tag{3.21}$$

and $[\varepsilon_n^{\mathrm{e}}]$ is the elastic logarithmic strain from the previously converged configuration. The trial elastic logarithmic strain is then given by

$$\left[\varepsilon_t^{\mathrm{e}}\right] = \frac{1}{2}\ln\left(\left[b_t^{\mathrm{e}}\right]\right). \tag{3.22}$$

This is used as the input for the constitutive model[7].

Plastic flow update

An important consideration when implementing a finite deformation elasto-plastic constitutive model is the numerical approximation to the plastic flow equations and the associated update of the plastic deformation gradient. This is achieved through the following procedure.

(i) First we transform the *plastic velocity gradient*[8], given by the standard definition in the stress-free configuration [13] as

$$\left[L^{\mathrm{p}}\right] = \left[\dot{F}^{\mathrm{p}}\right]\left[F^{\mathrm{p}}\right]^{-1}, \tag{3.23}$$

into the current configuration, where $\left[F^{\mathrm{p}}\right]$ and $\left[\dot{F}^{\mathrm{p}}\right]$ are the current value and instantaneous rate of the plastic deformation gradient respectively. This is achieved using the rotational component of the elastic deformation gradient $[R^{\mathrm{e}}]$

$$\left[\tilde{L}^{\mathrm{p}}\right] = \left[R^{\mathrm{e}}\right]\left[\left[\dot{F}^{\mathrm{p}}\right]\left[F^{\mathrm{p}}\right]^{-1}\right]\left[R^{\mathrm{e}}\right]^T, \tag{3.24}$$

where $\left[\tilde{L}^{\mathrm{p}}\right]$ is the rate of plastic deformation (or stretching) in the current configuration.

(ii) With the assumption of zero *plastic spin*[9], the symmetric component of the *spatial* plastic velocity gradient (the rate of plastic stretching in the current configuration) is given by

$$\left[\tilde{L}^{\mathrm{p}}\right] = \dot{\gamma}\left[g_{,\tau}\right]. \tag{3.25}$$

(iii) Combining equations (3.24) and (3.25), the plastic velocity gradient (in the intermediate configuration) becomes

$$\left[L^{\mathrm{p}}\right] = \dot{\gamma}\left[R^{\mathrm{e}}\right]^T\left[\frac{\partial g}{\partial \tau}\right]\left[R^{\mathrm{e}}\right]. \tag{3.26}$$

[7]Note that the exponential and logarithm of the matrices in (3.21) and (3.22), respectively, are obtained by finding the eigenvalues associated with the matrix, taking the exponential or logarithm of the principal values and then reforming the general nine-component matrix using the eigenvectors associated with the original matrix.

[8]The plastic velocity gradient defines the instantaneous rate of plastic deformation in the fictitious stress-free configuration.

[9]That is, the plastic velocity gradient is symmetric. This plastic spin represents an instantaneous rate of rigid spinning of the intermediate configuration. The assumption of zero plastic spin is appropriate for the case of plastic isotropy and can be applied without limitations. The case of zero plastic spin with kinematically hardening plastic anisotropy results in an error of second order in the elastic strains [35] (discussed in more detail in Section 3.3). See Dafalias for a detailed discussion on plastic spin [7].

Webber and Anand [40] and Eterovic and Bathe [9] showed that, through the use of an implicit exponential integration map, the updated plastic deformation gradient can be given by[10]

$$\left[F^{\mathrm{p}}_{n+1}\right] = \left[R^{\mathrm{e}}_{n+1}\right]^T \exp\left[\Delta\gamma \left.\frac{\partial g}{\partial[\tau]}\right|_{n+1}\right] \left[R^{\mathrm{e}}_{n+1}\right]\left[F^{\mathrm{p}}_{n}\right]. \tag{3.27}$$

The updated elastic deformation gradient is given by

$$\left[F^{\mathrm{e}}_{n+1}\right] = \left[F_{n+1}\right]\left[F^{\mathrm{p}}_{n+1}\right]^{-1} = \left[\Delta F\right]\left[F_n\right]\left[F^{\mathrm{p}}_{n+1}\right]^{-1} = \left[\Delta F\right]\left[F^{\mathrm{e}}_{n}\right]\left[F^{\mathrm{p}}_{n}\right]\left[F^{\mathrm{p}}_{n+1}\right]^{-1}, \tag{3.28}$$

where $[\Delta F]$ is the increment in the deformation gradient. Substituting (3.27) into (3.28), we obtain

$$\left[F^{\mathrm{e}}_{n+1}\right] = \left[\Delta F\right]\left[F^{\mathrm{e}}_{n}\right]\left[R^{\mathrm{e}}_{n+1}\right]^T \exp\left[-\Delta\gamma \frac{\partial g}{\partial[\tau]}\right] \left[R^{\mathrm{e}}_{n+1}\right]. \tag{3.29}$$

Post multiplying both sides of (3.29) by $[R^{\mathrm{e}}_{n+1}]^T$

$$\left[v^{\mathrm{e}}_{n+1}\right] = \left[F^{\mathrm{e}}_{t}\right]\left[R^{\mathrm{e}}_{n+1}\right]^T \exp\left[-\Delta\gamma \left.\frac{\partial g}{\partial[\tau]}\right|_{n+1}\right]. \tag{3.30}$$

Rearranging (3.30) and multiplying by the transpose of each side, we obtain

$$\left[v^{\mathrm{e}}_{n+1}\right] \exp\left[2\Delta\gamma \left.\frac{\partial g}{\partial[\tau]}\right|_{n+1}\right] \left[v^{\mathrm{e}}_{n+1}\right] = \left(\left[v^{\mathrm{e\ trial}}_{n+1}\right]\right)^2. \tag{3.31}$$

Further rearrangement and square rooting of both sides, gives

$$\left[v^{\mathrm{e}}_{n+1}\right] = \left[v^{\mathrm{e}}_{t}\right] \exp\left[-\Delta\gamma \left.\frac{\partial g}{\partial[\tau]}\right|_{n+1}\right]. \tag{3.32}$$

Taking the logarithm of both sides (and presenting the strains in the conventional vector notation), we recover the infinitesimal format of the elastic strain update formula with Hencky logarithmic strains and Kirchhoff stresses

$$\left\{\varepsilon^{\mathrm{e}}_{n+1}\right\} = \left\{\varepsilon^{\mathrm{e}}_{t}\right\} - \Delta\gamma \left\{ \left.\frac{\partial g}{\partial \tau}\right|_{n+1} \right\}. \tag{3.33}$$

Subjected to a trial logarithmic elastic strain, an isotropic small strain constitutive model will return the updated elastic logarithmic strain $\{\varepsilon^{\mathrm{e}}_{n+1}\}$, Kirchhoff stress $\{\tau_{n+1}\}$, algorithmic consistent tangent $[D^{alg}]$ and any required internal variables. The updated Cauchy stress is subsequently obtained by rearranging (3.11) as

$$\left[\sigma_{n+1}\right] = \frac{1}{J_{n+1}}\left[\tau_{n+1}\right], \tag{3.34}$$

where J_{n+1} is the volume ratio obtained from the current deformation gradient (3.8).

Force integration

When implementing this finite deformation framework within a discretised numerical scheme, such as the finite-element method (FEM), we employ an equilibrium equation to balance the material stresses with the externally applied loads. The spatial principle of virtual work for the equilibrium of a body [1] can

[10] Note that (3.27) uses the isotropy of the tensor exponential function $\exp([Q][\cdot][Q]^T) = [Q]\exp[\cdot][Q]^T$, for any orthogonal tensor $[Q]$ [35].

be written as

$$\int \Big(\{\sigma\}[\eta_{,x}] - \big\{ \{f^b\} - \rho_g \{u_{,tt}\} \big\}^T \{\eta\} \Big) \mathrm{d}V - \int \Big(\{t\}^T \{\eta\} \Big) \mathrm{d}A = 0, \tag{3.35}$$

where $\{\eta\}$ is the imposed displacement field, $\{f^b\}$ and $\{t\}$ are the body forces per unit deformed volume and surface traction per unit deformed area respectively. $[\eta_{,x}]$ is the spatial gradient of the displacement field and ρ_g and $\{u_{,tt}\}$ are the density and acceleration of the deformed unit volume. It is assumed that (3.35) is satisfied for any arbitrary displacement field within the material body. Discretisation of (3.35) results in the following expression that must be satisfied for the imposed nodal displacements $\{u\}$

$$\{f^{\mathrm{int}}(\{u\})\} - \{f^{\mathrm{ext}}\} = \{0\}, \tag{3.36}$$

where the internal $\{f^{\mathrm{int}}\}$ and external forces $\{f^{\mathrm{ext}}\}$ are obtained from

$$\{f^{\mathrm{int}}\} = \int \Big([B]^T \{\sigma\} \Big) \mathrm{d}V, \qquad \{f^{\mathrm{ext}}\} = \int \Big([N]^T \{f^b\} \Big) \mathrm{d}V + \int \Big([N]^T \{t\} \Big) \mathrm{d}A. \tag{3.37}$$

$[B]$ is the six-component non-linear strain-displacement matrix containing the derivatives of the nodal shape functions $[N]$ with respect to the updated (current) nodal coordinates.

Newton-Raphson algorithm

The solution of (3.36) (that is, find $\{u\}$ for a given $\{f^{\mathrm{ext}}\}$) requires a robust, efficient numerical algorithm. Here, the Newton-Raphson (N-R) scheme is used as it is able to achieve asymptotic quadratic rates of convergence, provided that the appropriate tangent is used and the initial solution lies within the bowl of convergence. The problem reduces to finding the solution to a linear system of equations

$$[K]\{\delta u_{m+1}\} = \{f_m^{\mathrm{oobf}}\}, \tag{3.38}$$

where $m+1$ is the current iteration within the N-R procedure and $\{f^{\mathrm{oobf}}\} = \{f^{\mathrm{ext}}\} - \{f^{\mathrm{int}}\}$ is the residual out-of-balance-force for the unknown increment in the displacements $\{\delta u_{m+1}\}$. The total increment in the displacements within a loadstep is given by the summation of the incremental displacements from all of the N-R iterations within that loadstep, that is

$$\{u_{n+1}\} = \{u_n\} + \sum_{m=1}^{n_{NRit}} \{\delta u_{m+1}\}, \tag{3.39}$$

where n_{NRit} is the total number of N-R iterations to find convergence in the $n+1$th loadstep. The global stiffness matrix $[K]$ is given by

$$[K] = \left[\frac{\partial \{f^{\mathrm{oobf}}\}}{\partial \{u_{n+1}\}} \right] = \int \Big([G]^T [D_\sigma^{cst}] [G] \Big) \mathrm{d}V, \tag{3.40}$$

where $[G]$ is the nine-component spatial strain-displacement matrix and $[D_\sigma^{cst}]$ is the isotropic spatial consistent tangent stiffness matrix. For infinitesimal theory, this tangent is the small strain algorithmic consistent stiffness matrix, $[D^{alg}]$, introduced previously in Chapter 2. For finite deformation analysis, $[D_\sigma^{cst}]$ is given by

$$\left(D_\sigma^{cst}\right)_{ijkl} = \frac{1}{J} \left. \frac{\partial \tau}{\partial F} \right|_{ijkm} F_{lm} - \sigma_{il} \delta_{jk}. \tag{3.41}$$

The derivation of this tangent is given in Appendix A. The N-R procedure continues until the convergence criteria is satisfied, such that

$$\frac{|\{f^{\text{oobf}}\}|}{|\{f^{\text{ext}}\}|} \leq tol, \tag{3.42}$$

where *tol* is the specified tolerance. The initial starting conditions for the solution scheme are taken as the previously converged (or initial for the first loadstep) displacements and associated internal forces.

Numerical implementation

The integrals for the element force and stiffness matrix are approximated through Gaussian quadrature. Using this approach, the element internal force vector is given by

$$\{f^e\} = \sum_{i=1}^{n_{gp}} \big[B_{n+1}\big]_i \{\sigma_{n+1}\}_i \det\Big(\big[J\big]_i\Big) w_i, \tag{3.43}$$

where n_{gp} is the number of Gauss points[11] associated with the element and w is the weight function (see Bathe p. 462 [1], amongst others, for the weights and sampling points of standard Gaussian quadrature). The Jacobian matrix, $[J]$, contains the derivatives of the updated global coordinates with respect to the element local coordinate system[12]. It provides the link between the local element and the global structural coordinate systems. The element stiffness matrix is determined using

$$\big[k^e\big] = \sum_{i=1}^{n_{gp}} \big[G_{n+1}\big]_i \big[D_\sigma^{cst}\big]_i \big[G_{n+1}\big]_i^T \det\Big(\big[J\big]_i\Big) w_i. \tag{3.44}$$

The consistent isotropic spatial tangent stiffness matrix, $[D_\sigma^{cst}]_i$, is given by

$$\big[D_\sigma^{cst}\big] = \frac{1}{2J_{n+1}} \big[D^{alg}\big]\big[L\big]\big[B^D\big] - \big[S^D\big]. \tag{3.45}$$

$[D^{alg}]$ is the small strain algorithmic tangent stiffness matrix (which is consistent with the stress integration scheme used at the material point) obtained from the constitutive model. The other matrices in (3.45) are given by

$$L_{ijkl} = \frac{\partial \ln(b_t^{\text{e}})_{ij}}{\partial (b_t^{\text{e}})_{kl}}, \qquad B^D_{ijkl} = \delta_{ik}(b_t^{\text{e}})_{jl} + \delta_{jk}(b_t^{\text{e}})_{il} \qquad \text{and} \qquad S^D_{ijkl} = \sigma_{il}\delta_{jk}. \tag{3.46}$$

$[L]$ is determined as a particular case of the derivative of a general symmetric second order tensor function with respect to its argument[13]. This framework was first described by de Souza Neto and Perić [33], who demonstrated the importance of using the exact derivatives of the tensor quantities by making comparisons with the approximate derivatives through convergence analysis. $[S^D]$ is the non-symmetric stress corrector term. The presence of $[S^D]$ in the isotropic spatial consistent tangent (3.45) means that it is not possible to write $\big[D_\sigma^{cst}\big]$ in six by six matrix notation; the element stiffness matrix $\big[k^e\big]$ must be calculated using the nine-component quantities.

[11] Gaussian integration uses grids of material points to sample the stress (and strain) field through an element to provide the internal forces at the nodes. Typically a standard three-dimensional eight-noded hexahedral element uses 8 Gauss points whereas a 20-noded element would use 27 points (for full integration).

[12] $[J]$ is obtained from the product of the derivatives of the nodal shapefunctions (with respect to the element local coordinates) with the global element nodal coordinates (see Appendix B.1.2).

[13] Traditionally the derivative of a tensor function with respect to its argument has been solved by considering the spectral decomposition of the tensor function and using the product rule to obtain the derivative. However, calculation of the derivative in the case of repeated eigenvalues requires the use of eigen–projections to overcome the non-uniqueness of the eigenvalues, a result originally obtained by Carlson and Hoger [3]. Miehe [19] subsequently presented two methods for the calculation of the derivative of a symmetric second order tensor with respect to is argument.

3.3 Finite plastic anisotropy

In this section, anisotropy is introduced through the plasticity relationships whilst maintaining the assumption of isotropic hyperelasticity. If an anisotropic elasticity relation is used, then in general the stresses and elastic strains do not commute. This introduces additional complications into the plastic return mapping equations and the ability to reduce the effects of finite deformations into simple pre and post processing operations on the conventional small strain constitutive model is lost [16]. The use of anisotropic elasticity (in addition to anisotorpic plasticity) remains an area of ongoing research. Some researches have returned to the use of additive relationships [20]. Alternative formulations have been proposed that maintain the multiplicative Lee decomposition of the deformation gradient, logarithmic strains and exponential map of stress return equation, but include the plastic spin [7] as an internal variable [16, 22]. In finite deformation analysis where strains are large, a material's response is dominated by its inelastic behaviour [16]. For this reason, all that follows is restricted to the case of elastic isotropy.

When introducing anisotropic plasticity, the equations from the preceding sections need to be modified to account for an evolving backstress tensor, which represents the anisotropy inherent (or induced) in the material. This backstress provides a measure of the *centre*, or orientation, of the yield surface. The evolution of this backstress is controlled by the particular form of the constitutive model. The implementation follows the pioneering work of Eterovic and Bathe [9] who provided the first hyperelastic, kinematically hardening multiplicative plastic, finite deformation formulation, which was later adopted by de Souza Neto and co-workers [32, 33, 35]. One of the major advantages of this framework is that the constitutive model's stress integration procedure maintains the same small strain format. However, there is an error associated with this update. This error stems from the fact that the recovery of the small strain integration format (3.33) assumes that the direction of plastic flow $\{g_{,\tau}\}$ and the elastic measures of deformation commute. Obviously, the introduction of plastic anisotropy can invalidate this assumption. However, de Souza Neto *et al.* [35] showed that the error is second order in the elastic strains. This limits the algorithm to the case of small elastic strains (but arbitrarily large plastic deformation)[14].

The evolution of the backstress tensor must be frame-invariant. The Green-McInnis-Naghdi rate (as a special case of the Oldroyd rate [13]) is obtained by rotating $\big[\beta\big]$ to the reference configuration, taking the material derivative and subsequently rotating back to the deformed configuration. The rate of this backstress matrix with respect to the elastic rotation is given by

$$\big[\mathring{\beta}\big] = \big[R^{\mathrm{e}}_t\big]\left[\frac{d}{dt}\left(\big[R^{\mathrm{e}}_t\big]^T\big[\beta\big]\big[R^{\mathrm{e}}_t\big]\right)\right]\big[R^{\mathrm{e}}_t\big]^T = \big[\dot{\beta}\big] - \big[\Lambda^{\mathrm{e}}\big]\big[\beta\big] + \big[\beta\big]\big[\Lambda^{\mathrm{e}}\big], \tag{3.47}$$

where $\big[\Lambda^{\mathrm{e}}\big] = \big[\dot{R}^{\mathrm{e}}\big]\big[R^{\mathrm{e}}\big]^T$ is the elastic spin and $\big[R^{\mathrm{e}}_t\big]$ is the trial elastic rotation. The deformation gradient transforms[15] under an arbitrary rotation $[Q]$ according to

$$[F] \longrightarrow [Q][F]. \tag{3.48}$$

Using the multiplicative decomposition of the deformation gradient (3.12), we obtain

$$[F^{\mathrm{e}}][F^{\mathrm{p}}] \longrightarrow [Q][F^{\mathrm{e}}][F^{\mathrm{p}}]. \tag{3.49}$$

[14] This limitation is reasonable for the analysis of soils where the behaviour is dominated by the plastic sliding, crushing and rearrangement between grains. Note, that for the case of isotropic elasto-plasticity there is no limit on the magnitude of the elastic strains.

[15] The deformation gradient is a two-point tensor as only one of its two indices is in the spatial frame, this means that the deformation gradient transforms as a vector rather than a matrix.

From (3.49), the elastic and plastic components of the deformation gradient transform as

$$[F^{\mathrm{e}}] \longrightarrow [Q][F^{\mathrm{e}}] \qquad \text{and} \qquad [F^{\mathrm{p}}] \longrightarrow [F^{\mathrm{p}}]. \tag{3.50}$$

Using the polar decomposition $[F^{\mathrm{e}}] = [R^{\mathrm{e}}][U^{\mathrm{e}}]$, we obtain the transformation of $[R^{\mathrm{e}}]$ as

$$[R^{\mathrm{e}}][U^{\mathrm{e}}] \longrightarrow [Q][R^{\mathrm{e}}][U^{\mathrm{e}}] \qquad \therefore \qquad [R^{\mathrm{e}}] \longrightarrow [Q][R^{\mathrm{e}}]. \tag{3.51}$$

From $(3.51)_2$, and noting that the backstress matrix (and rate thereof) transform according to

$$[\beta] \longrightarrow [Q][\beta][Q]^T \qquad \text{and} \qquad [\dot{\beta}] \longrightarrow [Q][\dot{\beta}][Q]^T + [\dot{Q}][\beta][Q]^T + [Q][\beta][\dot{Q}]^T, \tag{3.52}$$

we find that (3.47) transforms according to

$$\begin{aligned} \big[\mathring{\beta}\big] \quad \longrightarrow \quad & [Q][\dot{\beta}][Q]^T + [\dot{Q}][\beta][Q]^T + [Q][\beta][\dot{Q}]^T - [Q][\dot{R}^{\mathrm{e}}][R^{\mathrm{e}}]^T[\beta][Q]^T - [\dot{Q}][\beta][Q]^T \\ & + [Q][\beta][\dot{R}^{\mathrm{e}}][R^{\mathrm{e}}]^T[Q]^T + [Q][\beta][Q]^T[\dot{Q}][Q]^T. \end{aligned} \tag{3.53}$$

Using the fact that skew tensor $[\dot{Q}][Q]^T$ obeys the following [13]

$$[\dot{Q}][Q]^T = -\Big[[\dot{Q}][Q]^T\Big]^T = -[Q][\dot{Q}]^T, \tag{3.54}$$

(3.53) reduces to

$$\big[\mathring{\beta}\big] \longrightarrow [Q][\dot{\beta}][Q]^T - [Q]\big[\Lambda^{\mathrm{e}}\big][\beta][Q]^T + [Q][\beta]\big[\Lambda^{\mathrm{e}}\big][Q]^T. \tag{3.55}$$

(3.55) demonstrates that (3.47) is objective with respect to rotation as it transforms according to

$$\big[\mathring{\beta}\big] \longrightarrow [Q]\big[\mathring{\beta}\big][Q]^T. \tag{3.56}$$

The objective finite-strain extension of the evolution of the backstress tensor is obtained from

$$\big[\mathring{\beta}\big] = \dot{\gamma}\big[\tilde{\beta}\big], \tag{3.57}$$

where $\big[\tilde{\beta}\big]$ is the evolution equation for the backstress matrix with the same format as that of the equivalent small strain plasticity model, except that it is formulated in terms of Kirchhoff (rather than Cauchy) stresses.

3.3.1 Incremental formulation

We require an *incrementally objective algorithm* (a term introduced by Hughes and Winget [14]) for the updating of (3.57). Or rather, we require an integration algorithm in the local configuration that remains unaltered by imposed rigid body motions. Using an implicit integration scheme and following the approach outlined by Simo and Hughes [26] for the Green-McInnis-Naghdi rate (see boxes 8.1 and 8.2 on pp. 293–4 of Simo and Hughes for more information), we obtain

$$\big[\beta_{n+1}\big] = \big[\Delta\Lambda^{\mathrm{e}}\big]\big[\beta_n\big]\big[\Delta\Lambda^{\mathrm{e}}\big]^T + \Delta\gamma\big[\tilde{\beta}\big], \tag{3.58}$$

where the orthogonal incremental elastic spin is given by

$$\big[\Delta\Lambda^{\mathrm{e}}\big] = \big[R^{\mathrm{e}}_t\big]\big[R^{\mathrm{e}}_n\big]^T. \tag{3.59}$$

Here $\left[R_t^{\mathrm{e}}\right]$ and $\left[R_n^{\mathrm{e}}\right]$ are the elastic rotation matrices associated with the trial and previously converged state respectively. The trial elastic rotation $\left[R_t^{\mathrm{e}}\right]$ is obtained from the polar decomposition of the trial elastic deformation gradient

$$\left[F_t^{\mathrm{e}}\right] = \left[\Delta F_{n+1}\right]\left[F_n^{\mathrm{e}}\right], \tag{3.60}$$

through

$$\left[R_t^{\mathrm{e}}\right] = \left[v_t^{\mathrm{e}}\right]^{-1}\left[F_t^{\mathrm{e}}\right], \qquad \text{where} \qquad \left[v_t^{\mathrm{e}}\right] = \sqrt{\left[F_t^{\mathrm{e}}\right]\left[F_t^{\mathrm{e}}\right]^T} = \sqrt{\left[b_t^{\mathrm{e}}\right]} = \exp\Big(\left[\varepsilon_t^{\mathrm{e}}\right]\Big). \tag{3.61}$$

Equivalently, the trial elastic deformation gradient can be calculated using

$$\left[F_t^{\mathrm{e}}\right] = \left[F_{n+1}\right]\left[F_n^{\mathrm{p}}\right]^{-1}, \tag{3.62}$$

where $[F_n^{\mathrm{p}}]$ is the plastic deformation gradient from the previously converged state. The deformation gradient and the elastic strain tensor no longer provide sufficient information to track the kinematics of finite deformation anisotropy; we must also track the evolution of the elastic deformation gradient. $[F^{\mathrm{e}}]$ is updated according to

$$\left[F_{n+1}^{\mathrm{e}}\right] = \left[v_{n+1}^{\mathrm{e}}\right]\left[R_{n+1}^{\mathrm{e}}\right], \qquad \text{where} \qquad \left[R_{n+1}^{\mathrm{e}}\right] = \left[R_t^{\mathrm{e}}\right] \tag{3.63}$$

and $\left[v_{n+1}^{\mathrm{e}}\right]$ is calculated from

$$\left[v_{n+1}^{\mathrm{e}}\right] = \sqrt{\left[b_{n+1}^{\mathrm{e}}\right]} = \exp\Big(\left[\varepsilon_{n+1}^{\mathrm{e}}\right]\Big). \tag{3.64}$$

Therefore elastic deformation gradient replaces the elastic logarithmic strain as the stored elastic kinematic variable. From $[F^{\mathrm{e}}]$, the elastic stretch, rotational and strain matrices can all be calculated. Using the following trial backstress matrix as an input to the small strain constitutive algorithm

$$\left[\beta_t\right] = \left[\Delta\Lambda^{\mathrm{e}}\right]\left[\beta_n\right]\left[\Delta\Lambda^{\mathrm{e}}\right]^T, \tag{3.65}$$

the constitutive model will return the updated backstress tensor $\left[\beta_{n+1}\right]$ through (3.58). The incremental evolution equation $\Delta\gamma\left[\tilde{\beta}\right]$ provides this update, maintaining the format of the conventional small strain algorithm.

The introduction of anisotropy, in the form of a backstress tensor, modifies the spatial consistent tangent as the trial backstress is not fixed; it is dependent on the deformation gradient. $\{\beta_t\}$ is now obtained by rotating $\{\beta_n\}$ into the current configuration through (3.65). The elastic rotation increment is a function of the trial elastic deformation gradient $[F_t^{\mathrm{e}}]$, see (3.59), which in turn is a function of the previous plastic deformation gradient $[F_n^{\mathrm{p}}]$ and the current deformation gradient $[F_{n+1}]$. The derivative of the updated Kirchhoff stress with respect to the deformation gradient becomes

$$\left[\tau_{,F}\right] = \left[\tau_{,\varepsilon_t^{\mathrm{e}}}\right]\left[\varepsilon_t^{\mathrm{e}}{}_{,b_t^{\mathrm{e}}}\right]\left[b_t^{\mathrm{e}}{}_{,F_{n+1}}\right] + \left[\tau_{,\beta_t}\right]\left[\beta_{t,R_t^{\mathrm{e}}}\right]\left[R_t^{\mathrm{e}}{}_{,F_{n+1}}\right], \tag{3.66}$$

where $\left[\tau_{,\varepsilon_t^{\mathrm{e}}}\right]$ is the small strain algorithmic tangent $\left[D^{alg}\right]$. $\left[\tau_{,\beta_t}\right] = \left[D^{\beta}\right]$, called here the small strain consistent backstress tangent, describes how the updated Kirchhoff stress changes as a function of the trial backstress with frozen internal variables and $\{\varepsilon_t^{\mathrm{e}}\}$. This matrix is obtained in a manner analogous to the formulation of the small strain consistent tangent. (3.66) can be written as

$$\left[D^{cst}\right] = \left[D_{\sigma}^{cst}\right] + \left[D_{\beta}^{cst}\right], \tag{3.67}$$

where $\left[D^{cst}_{\sigma}\right]$ is given by (3.45) and $\left[D^{cst}_{\beta}\right]$ by

$$\left[D^{cst}_{\beta}\right] = \frac{2}{J_{n+1}} \left(\sum_{i=1}^{n_\beta} \left[U^i_\beta\right] \right) \left[V_\beta\right]. \tag{3.68}$$

The lengthy derivation of $\left[D^{cst}_{\beta}\right]$ is not included in this chapter for sake of brevity (see Appendix A.2 for the full derivation). The summation term in (3.68) is included to account for the possibility of constitutive models with more than one representation of backstress, such as multiple surface kinematically hardening plasticity models, where n_β is the number of backstress quantities. $\left[U^i_\beta\right]$ contains the quantities associated with the backstress that contribute to the spatial stiffness

$$\left(U^i_\beta\right)_{ijkl} = D^{\beta_i}_{ijkn} (\beta^i_t)_{ln}. \tag{3.69}$$

$\left[V_\beta\right]$ contains purely geometric effects

$$\left(V_\beta\right)_{ijkl} = 2(L_\beta)_{inkm} (b^{\mathrm{e}}_t)_{lm} (v^{\mathrm{e}}_{tr})_{nj} + (v^{\mathrm{e}}_{tr})^{-1}_{ik} (v^{\mathrm{e}}_{tr})_{lj}, \qquad \text{with} \qquad \left(L_\beta\right)_{inkm} = \left. \frac{\partial (b^{\mathrm{e}}_t)^{-1/2}}{\partial b^{\mathrm{e}}_t} \right|_{inkm}. \tag{3.70}$$

$\left[L_\beta\right]$ is calculated in an analogous way to $\left[L\right]$, introduced in $(3.46)_1$. The element stiffness matrix is calculated using (3.44), but with (3.67) replacing $\left[D^{cst}_{\sigma}\right]$. Calculation of the element force vector using (3.43) remains unchanged. The algorithmic material point calculation sequence for the anisotropic finite deformation formulation is given in Figure 3.3, where i denotes the material point. Note, that this material point sequence sits within the inner most loop of a numerical analysis code (Figure 3.4) and will be followed for every material point within every element for each iteration within all of the analysis' loadsteps.

3.4 Finite-element implementation

The anisotropic finite deformation framework described in this chapter was initially implemented in MATLAB m-script and later in Fortran90 for finite-element (FE) analyses. This chapter has focused on the derivation of a concise, consistent framework for finite deformations. Appendix B describes the implemented FE code in more detail, giving the matrix algebra required for the three-dimensional and two-dimensional plane strain and axi-symmetric implementations.

The following points summarise the modifications required for an infinitesimal linear elastic finite-element code in order to implement the updated Lagrangian large strain formulation.

(i) The primary internal variable is the deformation gradient, $[F]$.

(ii) The elastic deformation gradient, $[F^{\mathrm{e}}]$, replaces the elastic strain as the stored kinematic variable tracking the state of the material points.

(iii) The trial backstress $\{\beta_t\}$ is modified to account for the elastic rotations.

(iv) The derivatives of the shape functions are calculated with respect to the updated nodal coordinates.

(v) The non–symmetric material spatial (nine by nine, 81 component) tangent modulus, $[D^{cst}]$, and the full strain-displacement matrix, $[G]$, are used to form the element stiffness matrix.

(vi) The global equilibrium equation is solved using the N-R scheme.

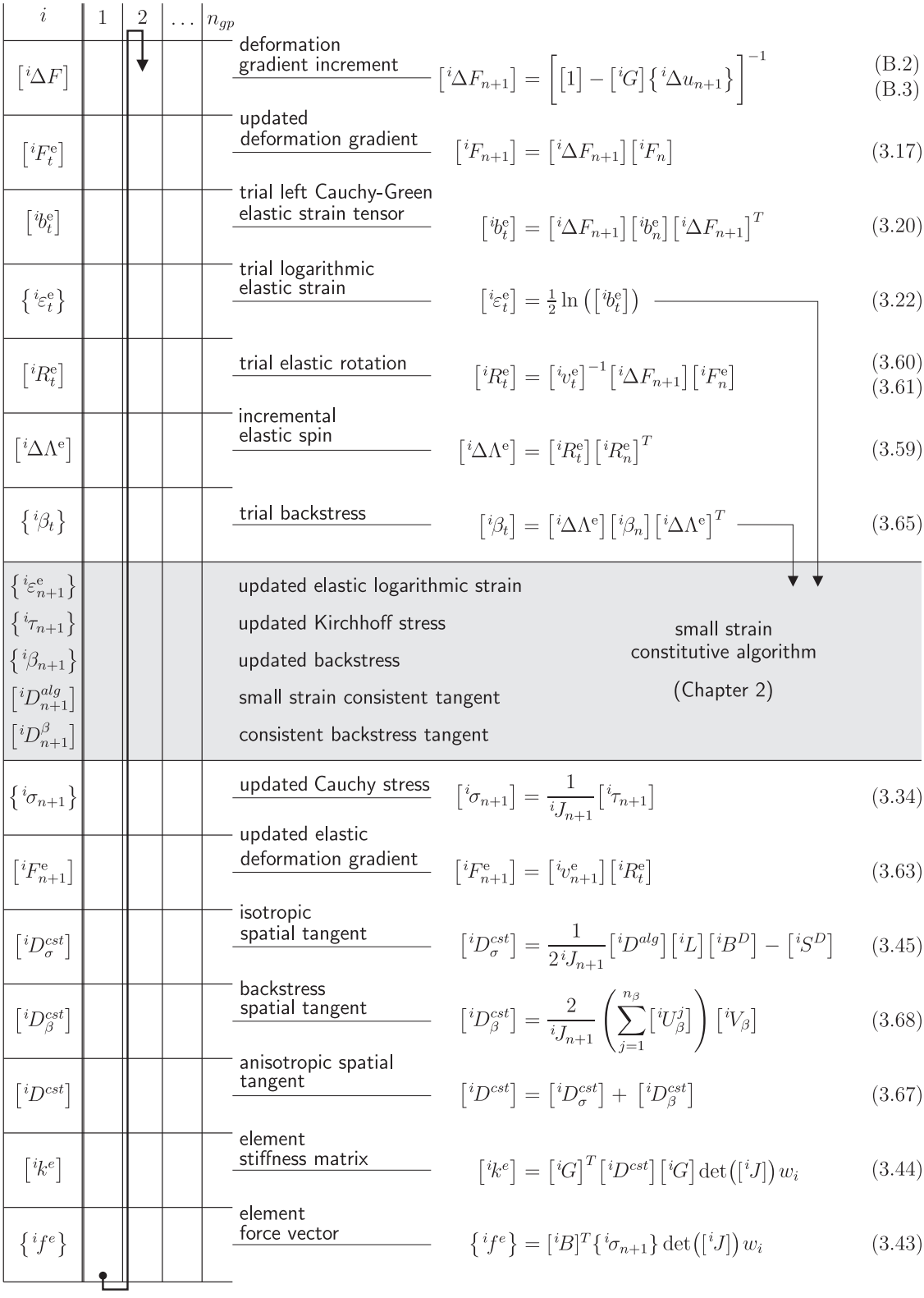

Figure 3.3: Anisotropic finite deformation material point algorithm sequence where i denotes the material point number and n_{gp} is the total number of Gauss points.

Figure 3.4 illustrates the non-linear FE algorithm sequence and locates the GNL material point sequence, as given in Figure 3.3, within the global FE code. Prior to beginning this sequence, the FE code

must set up the initial global stiffness matrix ($[^0K]$) based on the nodal coordinates, element topology and elastic stiffness of the Gauss points. This $[^0K]$ provides the initial estimate for the nodal displacements at the start of each loadstep through solving (3.38) for $\{\delta u\}$. For subsequence iterations within a loadstep, the global stiffness matrix is obtained using the spatial consistent tangent $[D^{cst}]$ at each material point. The N-R algorithm will iterate until (3.42) is satisfied. Once this tolerance has been achieved, the analysis proceeds with the next loadstep.

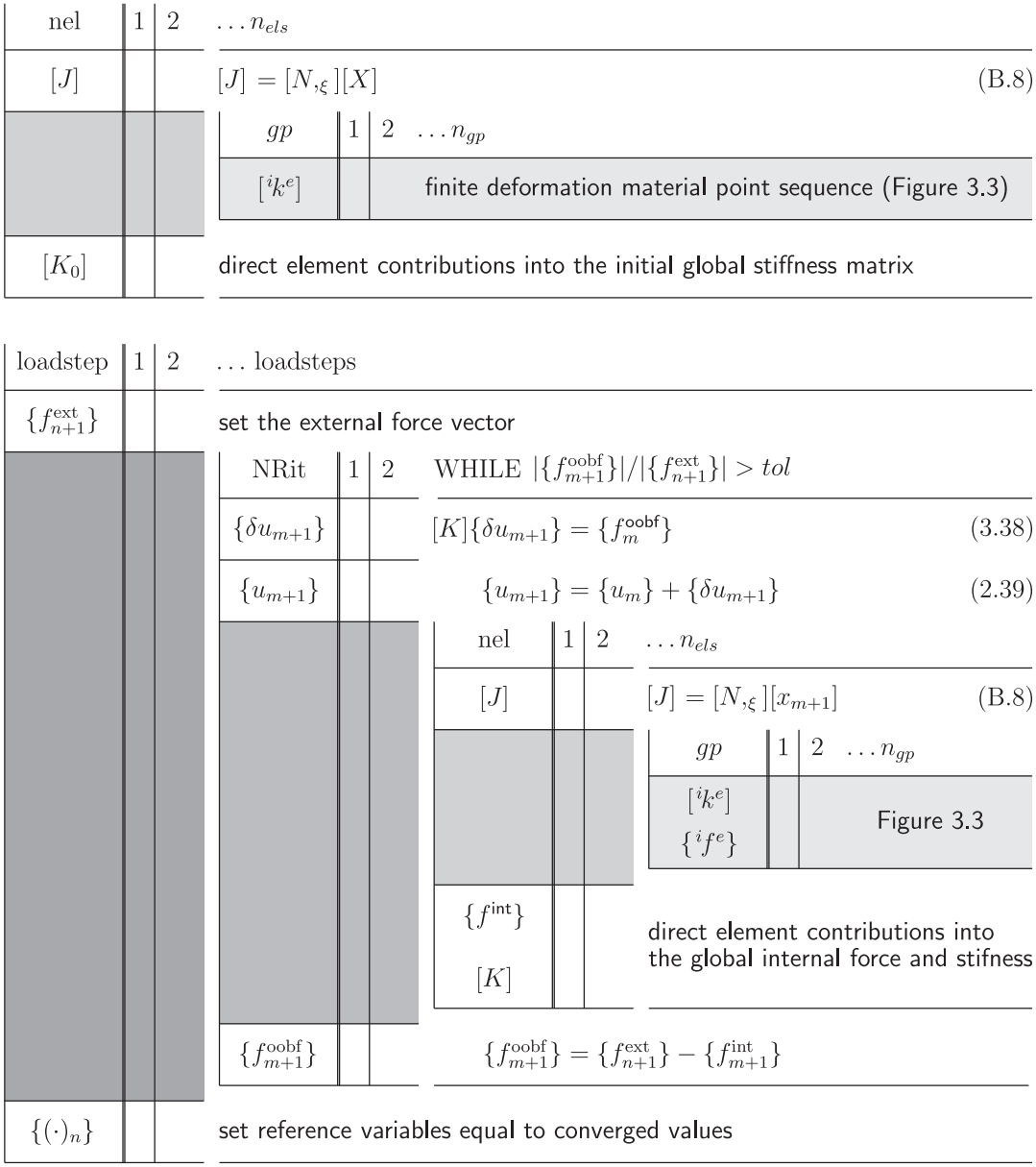

Figure 3.4: Finite-element algorithm sequence.

3.4.1 Algorithmic considerations

The FEM has transformed geomechanical analysis. A number of open source codes now encourage researchers to extend or modify the basic algorithms, yet most three-dimensional codes are expressed in tens of thousands of lines of C, C++ or Fortran, requiring significant time investment from researchers who wish to develop the codes further. Few freeware FE programs offer the capability to include three-

dimensional inelastic finite deformation analysis. Researchers are faced with having to write their own algorithms from scratch or mastering very lengthy codes, which are largely understandable only by those close to the original development. However, high level computational environments, such as MATLAB, allow engineers, scientists and mathematicians to produce powerful numerical analysis scripts rapidly. By using lean, efficient algorithms and subfunctions, it is possible to write the main routine of the elasto-plastic finite deformation FE program within a single page [4]. Once a program spills onto multiple pages the ability to easily visualise its structure is lost and the opportunity for error detection is reduced. Transparent programs facilitate re-analysis, adjustment, improvement and experimentation, resulting in polished, robust algorithms. These programming 'gems' should be clear, easy to read, check, edit and modify. The motivation for compact algorithms is inspired by Trefethen's cry for cleaner, shorter code, within the philosophy of *"one page, ten digit, five second"* algorithms [38]. This philosophy has been adopted in all of the research undertaken by the author.

3.4.2 Element incompressibility

It is widely appreciated that near-incompressible constitutive models combined with low order elements when used in FE analysis, can lead to over-stiff, unrealistic predictions which exhibit volumetric locking. Material models with isochoric plastic flow, such as the widely used Prandtl-Reuss and Tresca constitutive models, or isotropic elastic models with a high Poisson's ratio, are particularly susceptible. Low order elements, such as four-noded quadrilaterals (4-NQ) or eight-noded hexahedrons, are unable to represent general volume-preserving displacements due to their low polynomial basis [35]. One solution is to adopt higher order elements with reduced integration, such as eight-noded quadrilaterals (8-NQ) or twenty-noded hexahedrons with four and eight-point Gaussian quadrature respectively. However, for large simulations the use of lower order elements is computationally advantageous. For a typical two dimension analysis using one millon elements (arranged in a $1,000$ by $1,000$ grid) using 4-NQs, the total number of degrees of freedom is $2,004,002$. This increases two-fold to $6,008,002$ for 8-NQs. It is worth noting that although the use of lower order elements reduces the overall size of an analysis, higher order elements may be preferred, especially if high strain gradients are expected [42]. In a finite-element code, the solution of the global system of equations (3.38) consumes a considerable computational overhead.

Several formulations have been proposed to facilitate the use of low order elements for near isochoric problems [23, 28, 31, 34, 35]. One such formulation, presented by de Souza Neto and co-authors [34, 35], is the F-bar method. Here the equations for the three-dimensional implementation are briefly presented. For a more detailed discussion see de Souza Neto *et al.* [35]. It is assumed that the deformation gradient can be split into volumetric, $[F_v]$, and isochoric, $[F_{\text{iso}}]$, components

$$\big[F\big] = \big[F_{\text{iso}}\big]\big[F_v\big], \qquad \text{where} \qquad \big[F_{iso}\big] = J^{-1/3}\big[F\big] \qquad \text{and} \qquad \big[F_v\big] = J^{1/3}\big[1\big]. \tag{3.71}$$

The F-bar method calculates the volumetric component of the deformation gradient at the centre of the element, denoted $\big[F_{v_0}\big]$. The modified F-bar deformation gradient is given by

$$\big[\bar{F}\big] = \big[F_{\text{iso}}\big]\big[F_{v_0}\big] = \left(\frac{J_v}{J}\right)^{1/3}\big[F\big], \tag{3.72}$$

where J_v is the determinant of the volumetric component of the deformation gradient evaluated at the element centroid. The F-bar element is obtained by replacing $[F]$ with $[\bar{F}]$ when calculating the stresses and element stiffness. The internal force calculation (3.43) remains unchanged apart from the use of $\{\sigma\}$ based on $[\bar{F}]$. However, the element tangent stiffness is modified to include an additional term, as described by de Souza Neto *et al.* [35] (see p. 652 for details).

3.5 Numerical verification

Verification: Is the program doing what it claims to be doing? Wood, D.M. (2004).

This section presents six finite deformation boundary value problems ranging from plane-strain elastic beams to three-dimensional anisotropic inelastic unit cube simulations. These analyses provide verification that the finite deformation finite-element framework described in this chapter accurately captures the kinematics of large deformations.

3.5.1 Elastic beams

The first problem considered involves the analysis of a simply-supported slender small beam of length 254mm and depth 5.08mm subjected to a uniform transverse pressure of 276kPa applied in 20 equal loadsteps. The beam had a Young's modulus[16] of 68.95GPa and Poisson's ratio of 0.25. Due to symmetry, only half of the beam was discretised using 80 two-dimensional plane strain eight-noded fully integrated (nine-point Gaussian quadrature) quadrilateral elements, as shown in Figure 3.5 (i). The analytical solution for this problem was provided by Timoshenko and Woinowsky-Krieger [37]. The numerical simulation and the analytical solution (shown by discrete points) pressure versus displacement responses are compared in Figure 3.5 (i). The finite-element result shows good agreement with the analytical solution.

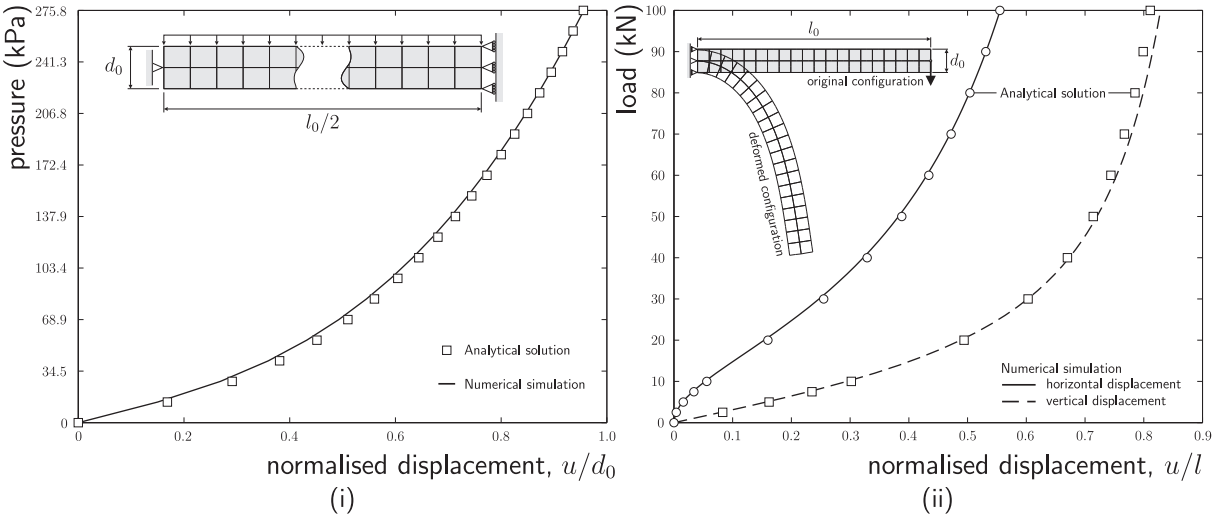

Figure 3.5: Finite deformation analysis of (i) a simply supported beam subjected to a uniform pressure and (ii) a cantilever subjected to a vertical mid-side load.

The second analysis is of an elastic cantilever beam subjected to a vertical mid-height point load on its free end. The large, moderately soft, deep beam (of length 10m and depth 1m) was discretised using 40 full integrated eight-noded plane strain elements, as shown in Figure 3.5 (ii). The cantilever material had a Young's modulus of 12MPa and Poisson's ratio of 0.2. The vertical load of 100kN was applied in 50 loadsteps. The load-displacement response for the loaded node is given in Figure 3.5 (ii) for both horizontal and vertical displacements. The final (unexaggerated) deformed configuration is shown in Figure 3.5 (ii), demonstrating the analysis' large displacements. Close agreement is seen between the numerical simulation and the analytical solution provided by Molstad [21] for both horizontal and vertical displacements.

[16]Note that the pressure and Young's modulus have been selected to agree with the original imperial values, the same is true for the pressure axis in Figure 3.5 (i).

3.5.2 Rigid plasticity

Thick walled cylinder expansion

The expansion of a thick walled cylinder was analysed with both the three-dimensional (with inclined boundary conditions) and two-dimensional axi-symmetric FE codes. A cylinder with internal and external radii $a_0 = 10$ and $b_0 = 20$mm respectively was expanded to an internal radius of 85mm in 75 equal displacement-controlled loadsteps. The cylinder had a Young's modulus of 11.05GPa and a Poisson's ratio of 0.454 (corresponding to a bulk and shear moduli of $K = 40$GPa and $G = 3.8$GPa, as used by Simo and Hughes [26]). A perfect plasticity Prandtl-Reuss constitutive model with a low yield stress of just $\sigma_y = 0.5$MPa modeled the material behaviour[17]. These particular material constants (and structural dimensions) were chosen by Simo and co-workers [26, 29, 30] to devise a problem dominated by the plastic response. The plane strain axi-symmetric analysis was discretised into 20 equally spaced eight-noded quadrilateral elements with reduced four-point Gaussian quadrature. The three-dimensional analysis modelled a three degree ($\pi/60$ radians) slice of the cylinder with inclined boundary conditions using 20 equally space eight-noded hexahedral F-bar elements.

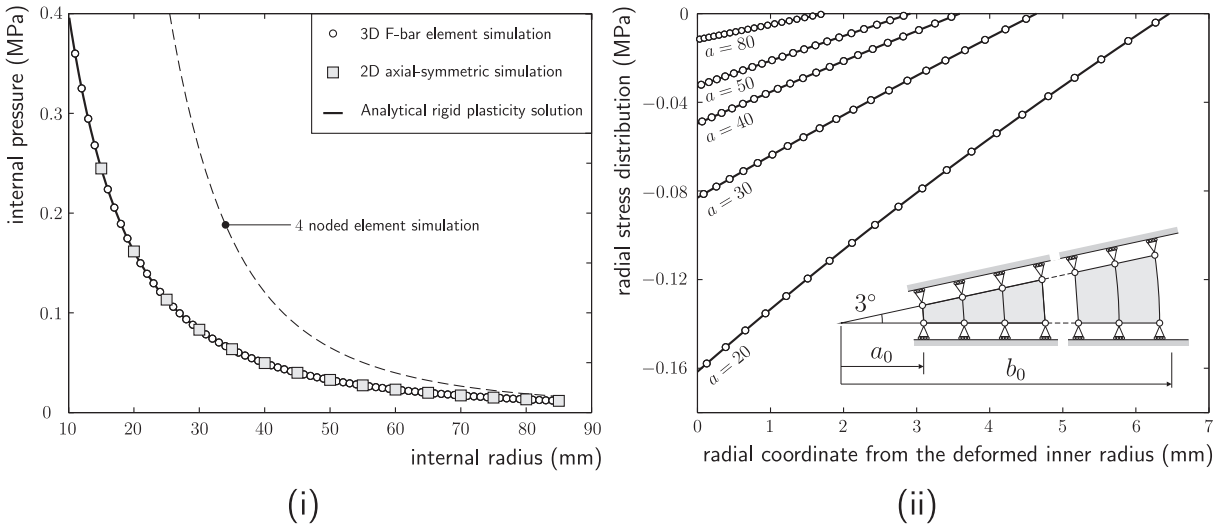

Figure 3.6: Rigid plastic expansion of a thick walled cylinder: (i) pressure-displacement response (ii) radial stress distribution.

Figure 3.6 (i) presents the pressure versus internal radius response and shows a comparison with the analytical isochoric rigid plastic solution[18] [12], given by

$$p = \frac{2\sigma_y}{\sqrt{3}} \ln\left(\frac{\sqrt{b_0^2 - a_0^2 + a^2}}{a}\right), \tag{3.73}$$

where σ_y is the yield stress, a is the current internal radius and p is the internal pressure. The axi-symmetric analysis using only 15 equal displacement-controlled increments is also shown. As the internal radius increases, the internal pressure drops due to a reduction in the cylinder's wall thickness. A load-controlled analysis would not be able to follow the load-deformation response of the cylinder unless an arc-length method was employed.

[17]The exactly integrated Prandtl-Reuss constitutive model, originally presented with the associated consistent tangent by Wei, Peric and Owen [41], was used to eliminate any possible errors associated with the material model.

[18]The rigid plastic solution is obtained by assuming that the elastic strains are negligible and that there is no change in volume due to an isochoric plastic flow rule. This allows the external radius to be calculated for a given internal radius, the ratio of these radii along with the yield stress, provides the analytical solution.

The radial stress distribution through the wall of the cylinder is given in Figure 3.6 (ii). The results from the axi-symmetric and three-dimensional analyses overlay and provide excellent agreement with the analytical solution. An analysis of the same problem, but discretised using 20 four-noded fully integrated axi-symmetric elements, is shown in Figure 3.6 (i). It significantly over-estimates the peak pressure by around 300% due to volumetric locking. Increasing the number of four-noded elements to 200 improves the simulation, although it is still inferior to that of the other elements, and at a greatly increased computational cost.

Thick walled sphere expansion

Here we analyse the expansion of a thick-walled sphere using the three-dimensional FE code. The large sphere had inner and outer radii of $a_0 = 12.5$ and $b_0 = 20$ metres respectively. The material was modelled with a Young's modulus of 1GPa and a Poisson's ratio of $v = 0.45$. Again, a three-degree slice of the problem was discretised using 20 equally spaced eight-noded isoparametric hexahedral F-bar elements and also with 20, twenty-noded hexahedral elements with reduced eight-point Gaussian quadrature. The inner radius was expanded by 15 metres in 30 loadsteps. Figure 3.7 (i) compares the pressure-displacement response with the analytical rigid plastic solution [12], given by

$$p = 2\sigma_y \ln\left(\frac{\sqrt[3]{b_0^3 - a_0^3 + a^3}}{a}\right). \tag{3.74}$$

The results from the two numerical simulations agree such that they are indistinguishable in Figure 3.7. The numerical simulation has excellent agreement with the analytical solution for both the pressure-displacement response and the radial stress distribution through the wall of the sphere.

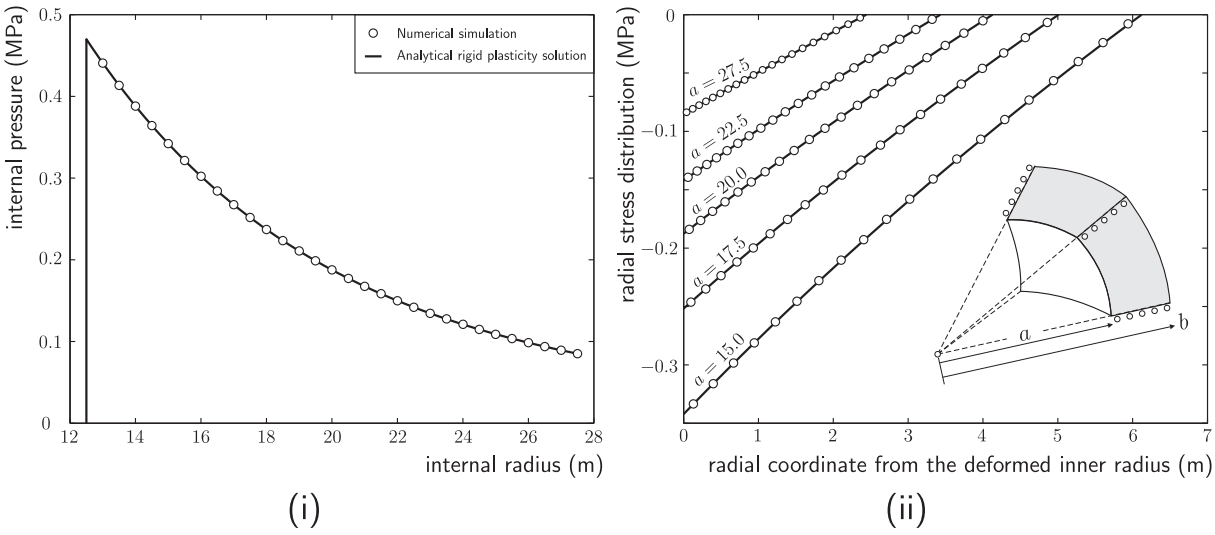

Figure 3.7: Rigid plastic expansion of a thick walled sphere: (i) pressure-displacement response (ii) radial stress distribution.

3.5.3 Double-notched plate

Here we present the analysis of the plane strain stretching of a double-notched plate. The problem was initially presented by Nagtegaal *et al.* [23] for small strain plasticity to demonstrate the spurious response of standard finite-elements and was subsequently re-analysed in a number of papers [27, 28, 34]. The plate had a Young's modulus of 206.9GPa, Poisson's ratio of 0.29 and was modelled using an elastic-perfectly plastic Prandtl-Reuss constitutive model with yield stress of $\sigma_y = 0.45$GPa. Nagtegaal *et al.* [23] provided

the small strain analytical limit load, controlled by the stress at the notch $\sigma_{\text{lim}} \approx 2.97\sigma_y$. The specimen had a total height and width of 30mm and 10mm respectively, with a 2mm unit linking ligament at mid height. For this geometry the small strain limit load is $F_{\text{lim}} \approx 2.673$kN. Due to symmetry, only one quarter of the specimen was discretised using 75 elements, as shown in Figure 3.8. A displacement of 0.3mm was applied in 100 equal displacement-controlled increments.

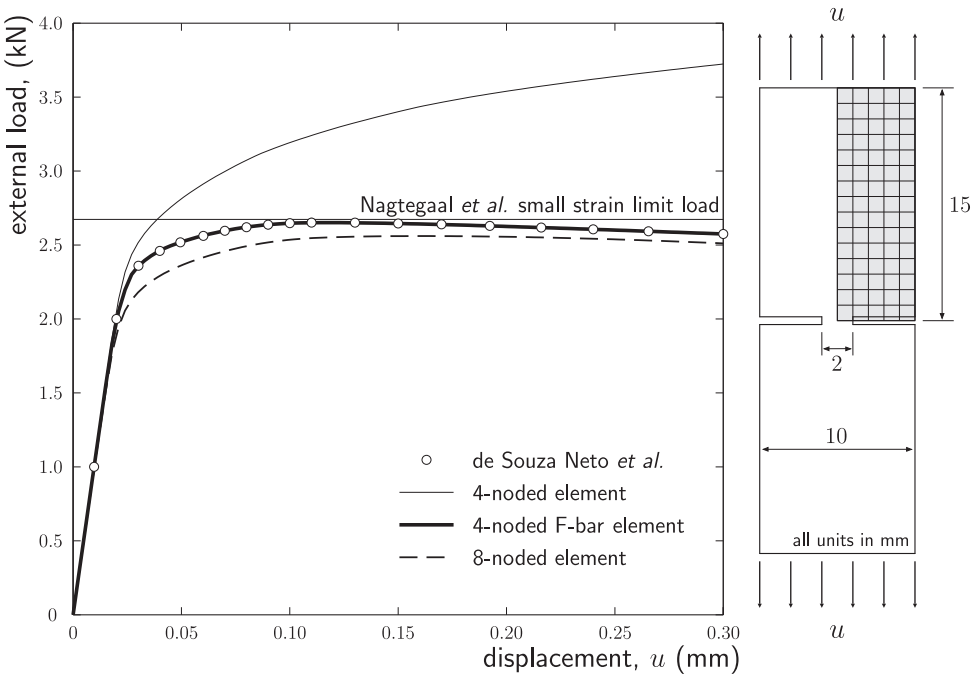

Figure 3.8: Finite deformation analysis of a double notched plate.

The external load (total edge reaction) versus displacement response is shown in Figure 3.8 using standard four and eight-noded quadrilateral elements in addition to a four-noded F-bar element. The F-bar simulation shows excellent agreement with the solution provided by de Souza Neto *et al.* [34]. The standard four-noded element produces an over-stiff response and fails to capture the presence of a limit load. The eight-noded element is able to capture this limit load better, but at an increased computational cost. The limit load predicted by both the four-noded F-bar and the eight-noded reduced integration elements are lower than that of the analytical small strain solution. This is due to the thickness of the ligament reducing as the deformation proceeds. This reduction in width concentrates the stress in the ligament, resulting in a lower peak force and a post-peak softening response not predicted by the small strain analysis.

3.5.4 Three-dimensional unit cube

Corner load

The final analysis is of a 1m unit cube constrained on three faces subjected to a vertical compressive load at its unrestrained corner. The model was discretised (equally in each direction) using 125 twenty-noded hexahedral elements with reduced eight-point Gaussian quadrature. The material behaviour was provided by a linear kinematically-hardening von Mises plasticity model (as described by Simo and Hughes [26]) with a yield stress of $\sigma_y = 100$Pa and a hardening modulus of $H = 10$kPa. A Young's modulus of 100kPa and a Poisson's ratio of 0.2 were used for the material's elastic properties. A compressive vertical load of 15N was applied in 10 equal loadsteps. The force versus normalised displacement (as a percentage of the size of the unit cube) response is shown in Figure 3.9 (i) together with the final loadstep convergence

result in Figure 3.9 (ii). A tolerance of 1×10^{-9} was used in (3.42) on the global normalised out-of-balance force. The vertical displacement of the corner node at the end of the analysis was -0.145.

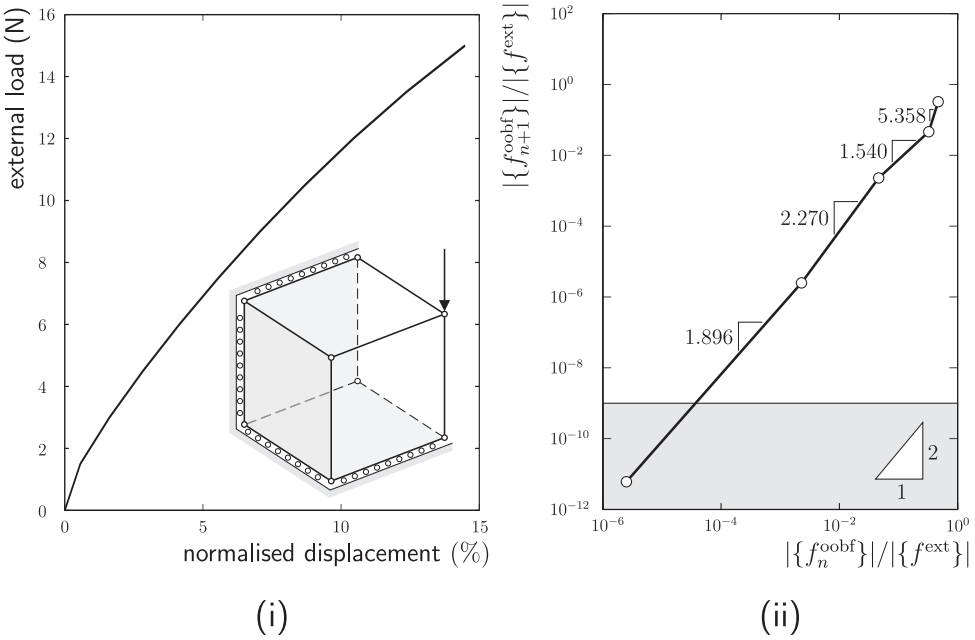

Figure 3.9: Three-dimensional unit cube investigations with a kinematically hardening von Mises plasticity model: corner load (i) force versus displacement response and (ii) final loadstep bi-logarithmic convergence rate.

Figure 3.9 (ii) plots the nomalised residual out-of-balance force for the current iteration against that of the previous iteration. The gradient of this line plotted on a bi-logarithmic scale indicates the rate of convergence between iterations, given by the following expression

$$\lim_{n\to\infty} \frac{|\{f_{n+1}^{\text{oobf}}\}|}{|\{f_n^{\text{oobf}}\}|} = \lim_{n\to\infty} {}^{k}r_{n+1}, \tag{3.75}$$

where k is the order of convergence. Figure 3.9 (ii) shows that the analysis approaches a quadratic rate of convergence. The final loadstep shows a reduction in the convergence rate due to the finite precision available in MATLAB.

3.6 Observations

This chapter has presented a framework for the analysis of problems involving anisotropic finite deformations. The framework has been verified using six numerical examples, making comparisons with established analytical and numerical solutions. The key conclusions drawn from this chapter are listed below.

(i) Isotropic elasto-plasticity constitutive algorithms can be implemented within a finite deformation framework without modification.

(ii) Anisotropic inelastic constitutive relations can be implemented (to within a second order error in the elastic strains) without modification to their stress integration algorithm, provided that an additional stiffness tangent describing the rate of change of the backstress with the trial elastic strains $[D_\beta]$, is made available.

(iii) The effects of finite deformation within a FE code may be seen as pre- and post-processors on the constitutive algorithm.

(iv) Three-dimensional FE codes need not be lengthy; it is possible to express the overall program within one page of m-script [4].

(v) The use of the appropriate spatial consistent tangent allows the FE code to achieve asymptotic quadratic rates of convergence.

The following three chapters:

4. derive a new, simple, non-associated flow frictional plasticity model based on a *modified Reuleaux* triangle;

5. provide the full algorithmic treatment of a family of isotropic hyperplastic two-parameter Critical State models; and

6. introduce a new two-surface anisotropic hyperplastic Critical State plasticity model.

Chapter 7 presents several boundary value simulations using the constitutive models developed in Chapters 4 through 6, implemented within the finite deformation framework presented in this chapter.

Chapter 3 references

[1] KJ Bathe, *Finite Element Procedures*, Praentice-Hall, New Jersey, 1996.

[2] KJ Bathe, E Ramm & EL Wilson, *Finite element formulations for large deformation dynamic analysis*, Int. J. Numer. Meth. Eng. 9 (1975), 353–386.

[3] DE Carlson & A Hoger, *The derivative of a tensor-valued function of a tensor*, Quart. Appl. Math 44 (1986), 409–423.

[4] WM Coombs, RS Crouch & CE Augarde, *70-line 3D finite deformation elastoplastic finite-element code*. In: T Benz and S Nordal (eds.), 7th European Conference on Numerical Methods in Geoetchnical Engineering (2010), 151–156.

[5] MA Crisfield, *Non-lienaer finite element analysis of solids and structures. Volume 1: Essentials*, John Wiley & Sons Ltd., 1991.

[6] MA Crisfield & GF Moita, *A unified co-rotational framework for solids, shells and beams*, Int. J. Solids Struct. 33 (1996), 2969–2992.

[7] YF Dafalias, *Plastic spin: necessity or redundancy?*, Int. J. Plas. 14 (1998), 909–931.

[8] J Donea, A Huerta, J-Ph Ponthot & A Rodríguez-Ferran, *Arbitrary Lagrangian-Eulerian Methods*. In: Encyclopedia of Computational Mechanics 14 (2004), 413–437.

[9] AL Eterovic & KJ Bathe, *A hyperplastic-based large strain elasto-plastic constitutive formulation with combined isotropic-kinematic hardening using the logarithmic stress and strain measures*, Int. J. Numer. Meth. Engng. 30 (1990), 1099–1114.

[10] G Garbiel & KJ Bathe, *Some computational issues in large strain elasto-plastic analysis*, Comput. Struct. 56 (1995), 249–267.

[11] AE Green & PM Naghdi, *A general theory of of an elastic-plastic continuum*, Arch. Ration. Mech. An. 18 (1965), 251–281.

[12] R Hill, *The mathematical theory of plasticity*, Oxford University Press, London, 1950.

[13] GA Holzapfel, *Nonlinear solid mechanics*, John Wiley & Sons Ltd. 2000.

[14] TJR Hughes & J Winget, *Finite rotation effects in numerical integration of rate constitutive equations arising in large-deformation analysis*, Int. J. Numer. Meth. Eng. 15 (1980), 1862–1867.

[15] M Itskov, *On the application of the additive decomposition of generalised strain measures in large strain plasticity*, Mech. Res. Commun. 31 (2004), 507–517.

[16] D-N Kim, FJ Montáns, and KJ Bathe, *Insight into a model for large strain anisotropic elasto-plasticity*, Comput. Mech. 44 (2009), 651–668.

[17] EH Lee, *Elastic-plastic deformation at finite strains*, J. App. Mech. 36 (1969), 1–6.

[18] EH Lee and DT Lu, *Finite-strain elastic-plastic theory with application to plane-wave analysis*, J. App. Phys. 38 (1967), 19–27.

[19] C Miehe, *Comparison of two algorithms for the computation of fourth-order isotropic tensor functions*, Comput. Struct. 66 (1998), 37–43.

[20] C Miehe, M Apel, & M Lambrecht, *Anisotropic additive plasticity in the logarithmic strain space: modular kinematic formulation and implementation based on incremental minimization principles for standard materials*, Comput. Meth. Appl. Mech. Engrg. 191 (2002), 5383–5425.

[21] TK Molstad, *Finite deformation analysis using the finite element method*, PhD. Thesis, Univeristy of British Columbia, 1977.

[22] FJ Montáns & KJ Bathe, *Towards a model for large strain anisotropic elasto-plasticity*. In: Oate E, Owen R (eds.) Computational plasticity. Springer, Berlin, 2007, 13-36.

[23] JC Nagtegaal, DM Parks & JR Rice, *On numerically accurate finite element solutions in the fully plastic range*, Comput. Meth. Appl. Mech. Engrg. 4 (1974), 153–177.

[24] M Nazem, D Sheng, JP Carter & SW Sloan, *Arbitrary Lagrangian-Eulerian method for large-strain consolidation problems* Int. J. Numer. Anal. Meth. Geomech. 32 (2008), 1023–1050.

[25] PM Pinsky, M Ortiz & KS Pister, *Numerical integration of rate constitutive equations in finite deformation analysis*, Comput. Meth. Appl. Mech. Engrg. 40 (1983), 137–158.

[26] JC Simo & TJR Hughes, *Computational inelasticity*, Springer, New York, 1998.

[27] JC Simo & F Armero, *Geometrically non-linear enhanced strain mixed methods and the method of incompatible modes*, Int. J. Numer. Meth. Eng. 33 (1992), 1413–1449.

[28] JC Simo & MS Rifai, *A class of mixed assumed strain methods and the method of incompatible modes*, Int. J. Numer. Meth. Eng. 29 (1990), 1595–1638.

[29] JC Simo, *A framework for finite strain elastoplasticity based on maximum plastic dissipation and the multiplicative decomposition. Part II: computational aspects*, Comput. Meth. Appl. Mech. Engrg. 68 (1988), 1–31.

[30] JC Simo & M Ortiz, *A unified approach to finite deformation elastoplastic analysis based on the use of hyperelastic constitutive equations*, Comput. Meth. Appl. Mech. Engrg. 49 (1985), 221–245.

[31] JC Simo, RL Taylor & KS Pister, *Variational and projection methods for the volume constraint in finite deformation elasto-plasticity*, Comput. Meth. Appl. Mech. Engrg. 51 (1985), 177–208.

[32] EA de Souza Neto, D Perić & DRJ Owen, *A model for elastoplastic damage at finite strains: algorithmic issues and applications*, Eng. Comput. 11 (1994), 257–281.

[33] EA de Souza Neto & D Perić, *A computational framework for a class of fully coupled models for elastoplastic damage at finite strains with reference to the linearization aspects*, Comput. Meth. Appl. Mech. Eng. 130 (1996), 179–193.

[34] EA de Souza Neto, D Perić, M Dutko & DRJ Owen, *Design of simple low order finite elements for large strain analysis of nearly incompressible solids*, Int. J. Solids Structs 33 (1996), 3277–3296.

[35] EA de Souza Neto, D Perić & DRJ Owen, *Computational methods for plasticity: Theory and applications*, John Wiley & Sons Ltd, 2008.

[36] A Spencer, *Continuum Mechanics*, Dover Publications, 1980.

[37] SP Timoshenko & S Woinowsky-Krieger, *Theory of Plates and Shells*, McGraw-Hill, 1959.

[38] LN Trefethen, *Ten digit algorithms*, Conference on Numerical Analysis, Dundee, 2005.

[39] C Truesdell & W Noll, *The non-linear field theories of mechanics*, Springer-Verlag, 1965.

[40] G Weber & L Anand, *Finite deformation constitutive equations and a time integration procedure for isotropic, hyperelastic-viscoplastic solids*, Comput. Meth. Appl. Mech. Engrg. 79 (1990), 173–202.

[41] Z Wei, D Perić & DRJ Owen, *Consistent linearization for the exact stress update of Prandtl-Reuss non-hardening elastoplastic models*, Int. J. Num. Meth. Engng. 39 (1996), 1219–1235.

[42] DM Wood, *Geotechnical modelling*, Spon Press, 2004.

Chapter 4

Simple frictional plasticity

The compressive strength and inelastic deformation of particulate materials, such as soils, fractured rocks, grains and powders, are dependent on the effective hydrostatic pressure. This behaviour is characteristic of media where the mechanics is dominated by frictional forces. Mohr-Coulomb (M-C) and Drucker-Prager (D-P) [14] are two of the most widely used pressure-sensitive constitutive models in the literature which can capture this behaviour in an idealised way. Indeed, it was commented by Wood [35] that:

> *"Any program that is seriously intended for geotechnical application should certainly permit the use of the elastic-perfect plastic Mohr-Coulomb model. Whether such a model will permit the rather necessary luxury of nonassociated flow is less certain though rather crucial..."*

The M-C[1] criterion assumes that plastic frictional sliding will occur once the minor principal stress falls below some proportion of the major principal stress. The D-P [14] criterion provides a smooth approximation to the six-faceted M-C yield function (as shown in Figure 4.1). However, these two simple frictional perfect plasticity models have inherent inadequacies, namely:

(i) the D-P yield surface exhibits no Lode angle dependency (LAD); and

(ii) the M-C surface has no sensitivity to the intermediate principal stress, σ_2.

Multiaxial experiments show that both factors influence yielding and peak stresses. Inclusion of these dependencies in constitutive models is necessary in order to capture properly the deformation of geotechnical structures [4]. The *modified Reuleaux* (mR) [9–12] deviatoric section presented in this chapter was investigated as it arguably gives the greatest realism to the constitutive modelling of soil (has a sensitivity to both θ and σ_2) whilst still allowing for an analytical backward Euler (bE) stress integration procedure[2].

Numerous other deviatoric yielding criteria have been proposed in literature for particulate media, for example [3, 5, 20, 23, 34], that include both a dependency on the intermediate principal stress and the Lode angle. However, currently none of these deviatoric functions, when applied to fricitional plasticity[3], allow analytical bE stress integration.

This chapter draws on the published papers of Coombs and co-workers [9–12] on Reuleaux plasticity. Section 4.1 introduces the mR deviatoric yielding criterion. The criterion is compared with experimental data in Section 4.2, showing its advantages over M-C and D-P. The single-step analytical bE stress return

[1] Shield [30] was the first to formalise the M-C failure criterion in three-dimensions, although it was separately established by Prager and Bishop in unpublished work.

[2] The mR model was originally presented at the Association for Computational Mechanics in Engineering UK conference in 2010 [12] (achieving the best PhD presentation award) and in 2011 named one of the three finalists of the prestigious Cooling Prize [10].

[3] Note, it would be possible to construct an analytical stress integration procedure for a rigid plasticity model (a model with isochoric plastic flow and without a dependence on the hydrostatic stress) for some of these deviatoric yielding criteria.

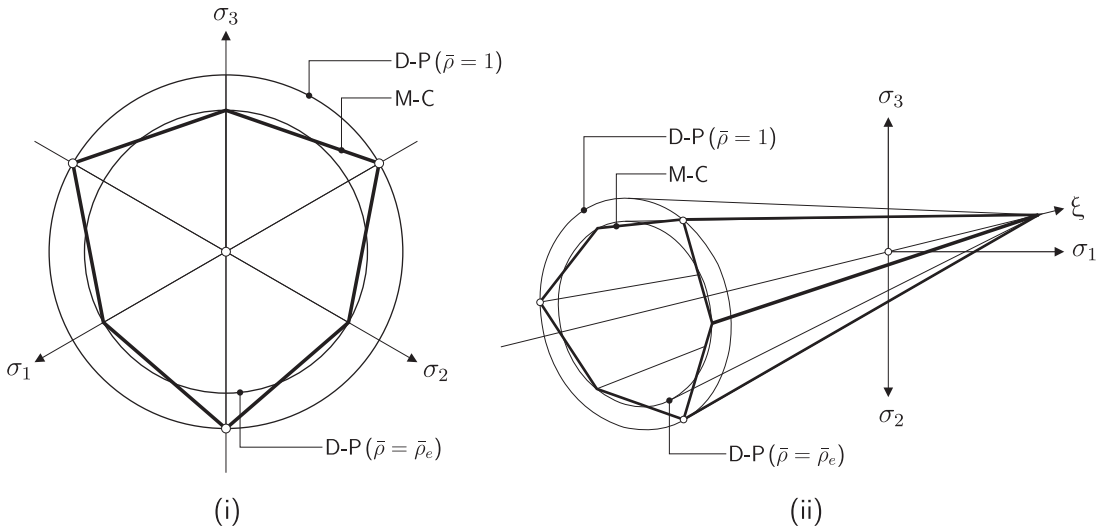

Figure 4.1: Mohr-Coulomb (M-C) and Drucker-Prager (D-P) constitutive models: (i) deviatoric sections and (ii) in principal stress space.

for non-associated plastic flow (NAF) is described in Section 4.3. The robustness, associated errors and run time of the stress integration procedure is analysed in Section 4.4. Section 5.5 gives the consistent linearisation of the integration scheme and observations are draw in Section 4.6. In all that follows, $[\dot{\cdot}]$ and $[\bar{\cdot}]$ identify terms associated with principal and shear components of generalised stiffness matrices. We adopt a tension positive convention and order the principal stresses such that σ_1 is the most compressive, while σ_3 is the most tensile (that is $\sigma_1 \leq \sigma_2 \leq \sigma_3$). The constitutive models examined in this chapter are defined using Haigh-Westergaard cylindrical coordinates, see (2.10) in Section 2.1.1.

4.1 Reuleaux plasticity

The Reuleaux triangle can trace its origins back to the 1830s where the shape was used in cam-actuated steam engine regulators. It was not until 1876 that the first written discussion of the geometry appears to have been provided by Franz Reuleaux [24, 28]. The shape was originally described by Reuleaux [28] as:

> *"...from the corners of an equilateral triangle, arcs be drawn with radii equal to the length of one of the sides, we obtain figure which we may call an equilateral curve-triangle."*

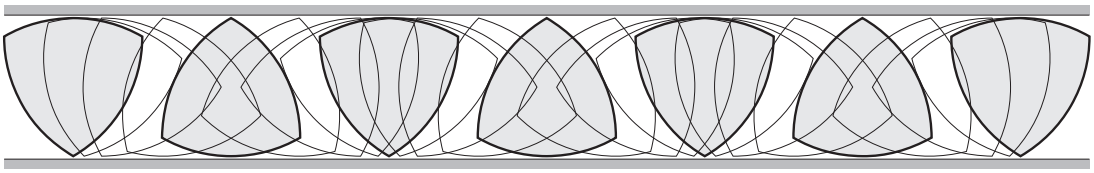

This Reuleaux *curve-triangle* belongs to a family of curved shapes of constant breadth (that is, rolling polygons which maintain a constant height)[4]. The shape with six-fold symmetry is formed through three equal circular arcs projected from the triangle's corners, as shown in Figure 4.2 (i).

Coombs *et al.* [11] extended the Reuleaux triangle such that the arc centres are allowed to translate along the extension meridians, creating the *modified Reuleaux triangle* as shown in Figure 4.2 (ii). This shape was investigated as, due to its geometric form, it offered the potential for analytical bE stress

[4]Other examples of these polygons that roll with a constant height are the sterling twenty and fifty pence coins.

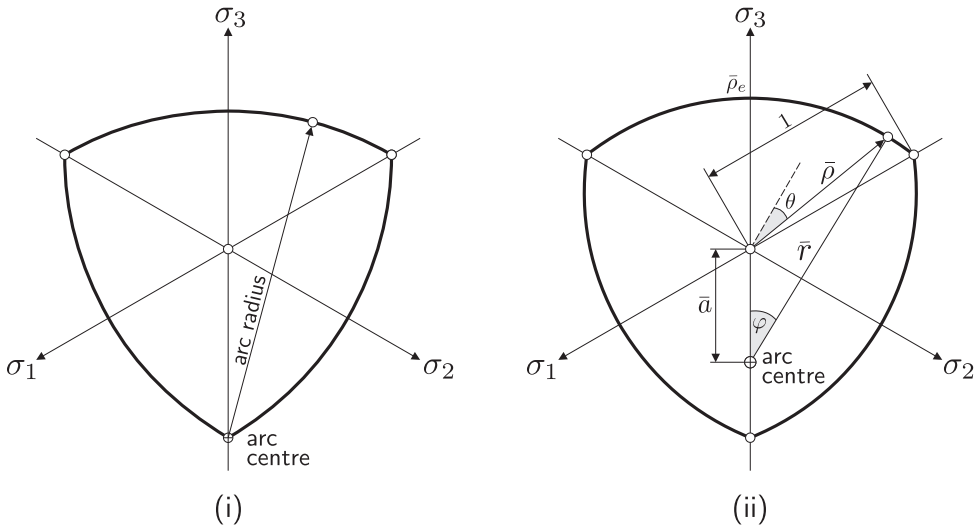

Figure 4.2: (i) Reuleaux triangle ($\bar{\rho}_e = 0.732$). (ii) modified Reuleaux triangle ($\bar{\rho}_e = 0.8$).

integration whilst providing advantages (in terms of experimental data reproduction) over the classical M-C and D-P plasticity models. From Figure 4.2 (ii), we find that the mR LAD is

$$\bar{\rho}(\theta) = \sqrt{\bar{a}^2 + \bar{r}^2 - 2\bar{a}\,\bar{r}\cos(\varphi)}, \qquad \text{where} \qquad \bar{r} = \frac{\bar{\rho}_e^2 - \bar{\rho}_e + 1}{2\bar{\rho}_e - 1} \qquad \text{and} \qquad \bar{a} = \bar{r} - \bar{\rho}_e. \tag{4.1}$$

$\bar{\rho}$ is the deviatoric yield stress (for a given θ) normalised with respect to the deviatoric yield stress on the compression meridian ($\sigma_1 < \sigma_2 = \sigma_3$). The arc angle, φ, is defined as

$$\varphi = \frac{\pi}{6} + \theta - \arcsin\left(\frac{\bar{a}\sin(5\pi/6 - \theta)}{\bar{r}}\right). \tag{4.2}$$

$\bar{\rho}_e \in [0.5, 1]$ is the normalised size of the radius under triaxial extension ($\sigma_1 = \sigma_2 < \sigma_3$). Note, that $\bar{a}$ and $\bar{r}$ are constant for a given $\bar{\rho}_e$. As $\bar{\rho}_e \to 0.5$ both $\bar{r}$ and $\bar{a}$ tend to ∞ and the deviatoric section becomes an equilateral triangle. If $\bar{\rho}_e = 1$ then $\bar{\rho} = 1$ and we recover a circular deviatoric section centred on the hydrostatic axis (as found in the D-P model). If the arc centres are located on the yield surface compression meridians (that is, if $\bar{r} = 1 + \bar{\rho}_e$ so that $\bar{a} = 1$ and $\bar{\rho}_e = 0.732$) then the shape reduces to that of the original Reuleaux triangle. In the absence of multiaxial data, $\bar{\rho}_e$ can be defined such that the mR triangle coincides with M-C at the extension meridians

$$\bar{\rho}_e = \frac{2 + k}{2k + 1}, \qquad \text{where} \qquad k = \frac{1 + \sin(\phi)}{1 - \sin(\phi)} \tag{4.3}$$

and ϕ is the friction angle of the material under triaxial compression. This means that the mR deviatoric function can be used instead of the M-C function with no additional material parameters.

The mR cone can be defined as

$$f = \rho - \alpha_f \bar{\rho}\Big(\xi - \xi_c\Big) = 0, \tag{4.4}$$

where $\xi_c = c\sqrt{3}\cot(\phi)$ is the hydrostatic tensile yield strength (the intersection of the yield surface with the hydrostatic axis), c is the *apparent cohesion*[5] and α_f is the opening angle of the cone, $\alpha_f = -\tan(\phi)$.

[5]We use the term "apparent cohesion" as c is a manifestation of the interlocking material fabric rather than a tensile strength from a cohesive bond.

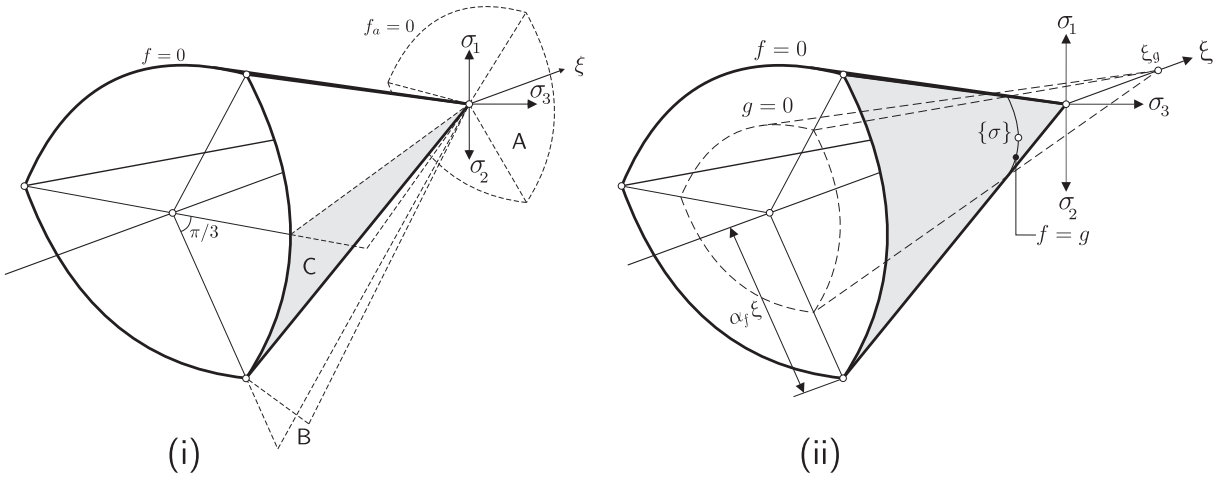

Figure 4.3: Modified Reuleaux cone in principal stress space: (i) A apex, B edge and C surface return regions. (ii) Yield surface-plastic potential interaction.

Thus (4.4) defines a cone with a mR deviatoric section and linear meridians, pinned on the hydrostatic axis at ξ_c, see Figure 4.3.

It is widely accepted that frictional plasticity models employing a volumetric associated flow rule overestimate the dilation seen in particulate media. To overcome this shortfall, Coombs and Crouch [9] proposed the following plastic potential

$$g = \rho - \alpha_g \bar{\rho}\Big(\xi - \xi_g\Big) = 0, \tag{4.5}$$

where ξ_g is the intersection of the plastic potential with the hydrostatic axis and $\alpha_g = -\tan(\phi_g)$ is the opening angle of the plastic potential surface. ϕ_g gives the dilation angle under triaxial compression, $\phi_g \in [0, \phi]$. Combining (4.4) and (4.5) with a linear hyperelastic relationship (as given by (2.2)), leads to a perfect plasticity model with non-associated volumetric plastic flow but associated deviatoric plasticity. The plastic potential is defined such that it passes through the stress state under consideration, as shown in Figure 4.3 (ii). To achieve this

$$\xi_g = \xi - \frac{\alpha_f}{\alpha_g}(\xi - \xi_c), \tag{4.6}$$

where ξ is the hydrostatic stress of the point on the yield surface.

4.2 Comparisons with established pressure-sensitive criteria

M-C and D-P [14] are two of the most widely used pressure-sensitive constitutive models in the literature. Their descriptions are now given. The M-C criterion can be defined using the following yield function

$$f = k\sigma_3 - \sigma_1 - \sigma_c = 0, \qquad \text{where} \qquad \sigma_c = 2c\sqrt{k}. \tag{4.7}$$

The M-C normalised deviatoric radius (or LAD), as shown in Figure 4.1 (i), can be expressed as

$$\bar{\rho}(\theta) = \frac{\sqrt{3}\bar{\rho}_e}{2a_1 \sin(5\pi/6 - a_2 - \theta)} \qquad \text{where} \qquad a_2 = \arcsin\left(\frac{\sqrt{3}\bar{\rho}_e}{2a_1}\right) \qquad \text{and} \quad a_1 = \sqrt{1 + (\bar{\rho}_e)^2 - \bar{\rho}_e}. \tag{4.8}$$

Combining (4.8) with (4.4) provides an alternative description of the M-C yield function (4.7).

The D-P [14] criterion provides a smooth approximation to the six-faceted M-C yield function. It is de-

fined such that plastic yielding will occur once ρ reaches some ratio of the hydrostatic stress (independent of θ)

$$f = \rho - \alpha_f \bar{\rho}(\xi - \xi_c) = 0. \tag{4.9}$$

Here $\bar{\rho}$ is a constant, as shown in Figure 4.1, defining a circular cone with its axis centered on the hydrostatic axis. Setting $\bar{\rho} = 1$ or $\bar{\rho} = \bar{\rho}_e$ allows (4.9) to coincide with the M-C criterion at the extension or compression meridians. When intersecting at the extension meridians, $\bar{\rho}_e$ is obtained from (4.3).

It can be seen from (4.7) and (4.9) that the M-C and D-P models have no dependency on the intermediate principal stress, σ_2, and the Lode angle, θ, respectively. Real materials exhibit dependencies on both [6, 29]. In rocks, the influence of θ is most clearly seen in the biaxial plane where yield surfaces which neglect this measure provide poor fits to experimental data. Intermediate principal stress values close to the most compressive principal stress confine microfractures to develop mainly in the plane formed by the direction of those two stresses [15]. The formulation of compaction bands [19] and fault slip patterns in complex fracture fields [25] have also recently been shown to be controlled by σ_2. Thus its inclusion in a geomechanics model is now considered essential.

The M-C, D-P and mR deviatoric functions are compared with experimental data from (i) Monterey sand [20], (ii) Kaolin [2], (iii) San Francisco Bay mud [21] and (iv) Santa Monica Beach sand [22] in Figure 4.4. The left of Figure 4.4 compares experimental data in terms of θ-$\bar{\rho}(\theta)$. D-P has no dependence on θ, (that is, constant $\bar{\rho}$ for all θ) and therefore provides a poor fit to the experimental data.

Table 4.1 provides a quantitative measure of the error between $\bar{\rho}$ and the experimental data for the four models. The error was calculated as

$$\text{error} = \frac{1}{n}\sum_{i=1}^{n} |\bar{\rho}_i - \bar{\rho}(\theta_i)|, \tag{4.10}$$

where i denotes the experimental data point (out of a total of n) with $\bar{\rho}_i$ and θ_i being the experimental normalised deviatoric radius and Lode angle, respectively. mR provides an improved fit over M-C and D-P for all of the materials. Note that, in Figures 4.4 (ii) and (iii) $\bar{\rho}_e$ for the mR was not set equal to $\bar{\rho}_e$ for M-C.

model		M-C	D-P ($\bar{\rho} = 1$)	D-P ($\bar{\rho} = \bar{\rho}_e$)	mR
material	MS	0.0343	0.2154	0.1286	0.0154
	K	0.0505	0.1404	0.0966	0.0136
	SFBM	0.0697	0.1187	0.1713	0.0229
	SMBS	0.0418	0.1004	0.0307	0.0275

Table 4.1: $\bar{\rho}$ errors between M-C, D-P and mR and experimental data from Monterey sand (MS), Kaolin (K), San Francisco Bay mud (SFBM), Santa Monica Beach sand (SMBS).

The right of Figure 4.4 compares experimental data in terms of the ratio of the intermediate principal stress $b = (\sigma_2 - \sigma_3)/(\sigma_1 - \sigma_3)$ versus the effective friction angle ψ, where the latter is calculated from the expression given by Griffiths [17]

$$\psi = \arcsin\left(\frac{\sqrt{3}\eta\cos(\theta)}{\sqrt{2} + \eta\sin(\theta)}\right), \qquad \text{with} \qquad \eta = \frac{\rho}{\xi}. \tag{4.11}$$

The experimental data show a dependence on the intermediate principal stress σ_2. The D-P model can be fixed such that it coincides with M-C at a specified b. If this occurs at $b = 0$, then the deviatoric

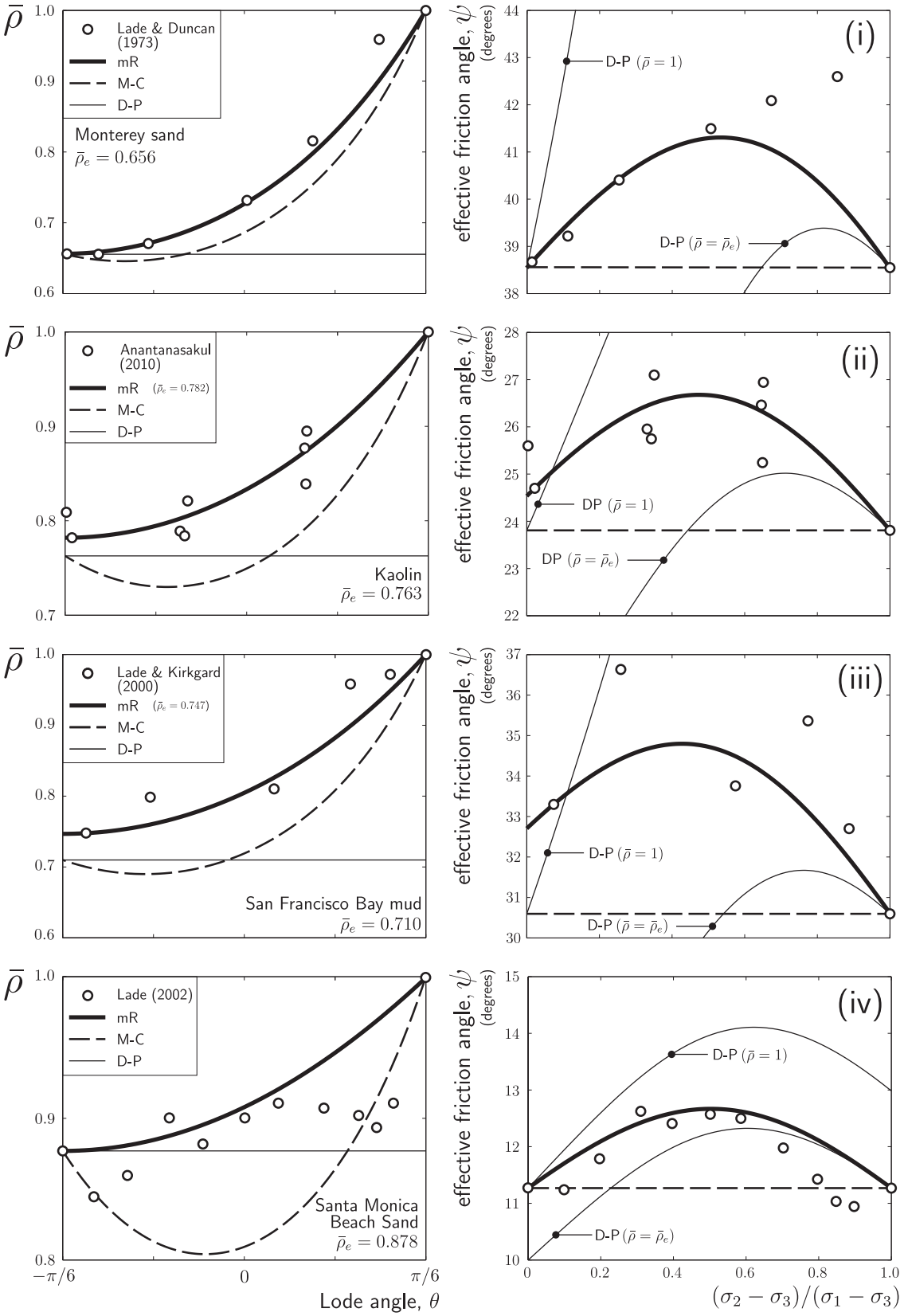

Figure 4.4: Comparison of Mohr-Coulomb (M-C), Drucker-Prager (D-P) and modified Reuleaux (mR) with experimental data: (i) Monterey sand [20], (ii) Kaolin [2], (iii) San Francisco Bay mud [21] and (iv) Santa Monica Beach sand [22].

radius significantly over-estimates the effective friction angle, whereas if this occurs at $b = 1$, then it under estimates ψ. Of the three formulations considered here, only the mR model, having a dependency on both θ and σ_2, is able to qualitatively reproduce the experimentally observed material behaviour. mR provides significantly reduced quantitative errors compared to the D-P and M-C deviatoric functions (see Table 4.1). For example the mR LAD reduces the M-C deviatoric error by 44.9%, 26.9%, 32.9%, and 65.8% for Monterey sand, Kaolin, San Francisco Bay mud and Santa Monica Beach sand respectively.

4.3 Analytical stress integration

The advantages of the mR LAD over the D-P and M-C models have be demonstrated. In order to progress further, the algorithmic aspects of the mR model are now detailed. A model defined by an isotropic linear hyperelastic law (stiffness matrix given by (2.2)) together with a mR cone yield surface described by (4.4) and direction of plastic flow defined by (4.5) is now examined. Consider the trial elastic stress $\{\sigma_t\}$ (given by a trial elastic strain $\{\varepsilon_t^{\mathrm{e}}\}$) lying outside the yield surface ($f > 0$). For this state, there are three distinct stress return regions associated with the mR cone, as shown in Figure 4.3 (i), namely:

A. return to the stress origin (point): Apex return;

B. return to the compression meridian (line): Edge return; and

C. return to the surface: Non-planar surface return.

The closest point projection (CPP) solution is examined for each of the above regions in Sections 4.3.2-4.3.4. The pseudo-code for the mR constitutive model is given in Figure 4.5, detailing the algorithmic steps for each of the three stress return regions. However, first the concept of energy-mapped stress space (EMSS) is introduced.

4.3.1 Energy-mapped stress space

Simo and Hughes [32] noted that the bE integration method corresponds to the *"closest projection of the* [trial elastic stress] *onto the yield surface in the energy norm"* obtained from the minimisation of (2.42) with respect to the return stress $\{\sigma_r\}$ [31]. In the more recent paper by Crouch *et al.* [13] the concept of working in an EMSS was clarified. The technique was later extended to the case of non-associated plastic flow by Coombs and Crouch [9]. This space facilitates visualisation of any CPP stress return and permits an analytical bE stress return for certain yield surfaces based on purely geometric methods. The return stress is not generally the closest point geometrically in standard stress space, but rather the stress that minimises the energy square norm (2.42), as shown in Figure 4.6. Energy-mapped $\{\varsigma\}$ space [13] is linked to true stress space through

$$\frac{1}{E}\{\varsigma\}^T\{\varsigma\} = \{\sigma\}^T\big[C^{\mathrm{e}}\big]\{\sigma\}, \tag{4.12}$$

where E is the Young's modulus of the material. This allows us to find the geometric closest point (in $\{\varsigma\}$ space) through use of the following transformation

$$\{\varsigma\} = \big[T\big]\{\sigma\}. \tag{4.13}$$

For isotropic linear elasticity, $[T]$ is solely a function of Poisson's ratio υ. Given the elastic compliance matrix

$$\big[C^{\mathrm{e}}\big] = \big[D^{\mathrm{e}}\big]^{-1} = \frac{1}{E}\begin{bmatrix} [1] - \upsilon\big[\{\hat{1}\}\{\hat{1}\}^T - [1]\big] & [0] \\ [0] & 2(1+\upsilon)[1] \end{bmatrix}, \tag{4.14}$$

1. INPUT: $\{\varepsilon_t^{\mathrm{e}}\}$, v, E, α, β, ξ_c and $\bar{\rho}_e$
   (a) Transform the trial elastic strain $\{\varepsilon_t^{\mathrm{e}}\}$ into its principal components and store the associated eigenvectors.
   (b) Calculate the principal (elastic) trial stress $\{\sigma_t\} = [\hat{C}^{\mathrm{e}}]^{-1}\{\varepsilon_t^{\mathrm{e}}\}$.
   (c) Determine the value of the yield function f at the trial state (4.4).
   (d) IF $f < tol$
      i. Elastic response, $\{\sigma_{cp}\} = \{\sigma_t\}$, $\{\varepsilon_{cp}^{\mathrm{e}}\} = \{\varepsilon_t^{\mathrm{e}}\}$.
      ii. $[D^{alg}] = [C^{\mathrm{e}}]^{-1}$
   (e) ELSE
      i. Transform ξ_t and ρ_t into energy-mapped stress space and form $\{\varsigma_t\}$ using the Haigh-Westergaard expression (2.10), where ξ_t, ρ_t and $\{\varsigma_t\}$ replace ξ, ρ and $\{\sigma\}$.
      ii. Determine the value of the apex boundary function ${}^{\varsigma}f_a$ from (4.20).
      iii. IF ${}^{\varsigma}f_a < tol$
         - Apex return, $\{\sigma_{cp}\} = \xi_c/\sqrt{3}\{1\}$ and $\{\varepsilon_{cp}^{\mathrm{e}}\} = [\hat{C}^{\mathrm{e}}]\{\sigma_{cp}\}$.
         - $[D^{alg}] = [0]$ (4.33).
      iv. ELSE
         - Hydrostatically translate the trial stress point by ${}^{\varsigma}\xi_c$ so that the yield surface intersects with the stress origin.
         - Solve for ${}^{\varsigma}\xi_{cp}$ using (4.29).
         - Calculate θ_{cp} using (4.31).
         - IF $\theta_{cp} < \pi/6$
            – Surface return, calculate ${}^{\varsigma}\rho_{cp} = {}^{\varsigma}\alpha\bar{\rho}(\theta)\,{}^{\varsigma}\xi_{cp}$ using $\bar{\rho}(\theta)$ from (4.1).
            – Transform ${}^{\varsigma}\xi_{cp}$ and ${}^{\varsigma}\rho_{cp}$, in energy-mapped stress space, back to ξ_{cp} and ρ_{cp} in conventional stress space.
            – Calculate $\{\sigma_{cp}\}$ from the Haigh-Westergaard expression (2.10).
            – Determine the derivatives required in order to calculate $[D^{alg}]$ from (4.43).
         - ELSE
            – Line return, calculate ${}^{\varsigma}\xi_{cp}$ from (4.19).
            – Determine θ_{cp} and ${}^{\varsigma}\rho_{cp}$ from (4.21).
            – Transform ${}^{\varsigma}\xi_{cp}$ and ${}^{\varsigma}\rho_{cp}$, in energy-mapped stress space, back to ξ_{cp} and ρ_{cp} in conventional stress space.
            – Calculate $\{\sigma_{cp}\}$ from the Haigh-Westergaard expression (2.10).
            – Determine $[D^{alg}]$ from (4.40).
         - END IF
         - Hydrostatically translate $\{\sigma_{cp}\}$ by ξ_c to return the yield surface to its original position.
      v. END IF
   (f) END IF
   (g) Transform the principal components back to generalised space using the eigenvectors from the trial elastic strain stored at 1.(a).
2. OUTPUT: $\{\sigma_{cp}\}$, $\{\varepsilon_{cp}^{\mathrm{e}}\}$ and $[D^{alg}]$

Figure 4.5: Pseudo-code for the NAF modified Reuleaux constitutive model.

where $\{\hat{1}\} = \{1 \quad 1 \quad 1\}^T$, $[T]$ becomes

$$[T] = \begin{bmatrix} t_1[1] + t_2[\{\hat{1}\}\{\hat{1}\}^T - [1]] & [0] \\ [0] & t_3[1] \end{bmatrix}, \tag{4.15}$$

where

$$t_1 = \frac{\sqrt{1-2\upsilon} + 2\sqrt{1+\upsilon}}{3}, \qquad t_2 = \frac{\sqrt{1-2\upsilon} - \sqrt{1+\upsilon}}{3} \qquad \text{and} \qquad t_3 = \sqrt{2(1+\upsilon)}. \tag{4.16}$$

This mapping leads to a squashing and a stretching of the yield surface in the hydrostatic and deviatoric directions respectively

$${}^{\varsigma}\xi = \xi\sqrt{1-2\upsilon}, \qquad {}^{\varsigma}\rho = \rho\sqrt{1+\upsilon} \qquad \text{and} \qquad {}^{\varsigma}\theta = \theta, \tag{4.17}$$

where ${}^{\varsigma}(\cdot)$ denotes a quantity associated with energy-mapped space . Once the closest point solution in energy-mapped stress space has been found, the solution can be transformed back to conventional stress space. For non-associated flow plasticity, the return stress is the stress state on the yield surface where the normal to the plastic potential passes through the trial stress state, as shown in Figure 4.6 (ii).

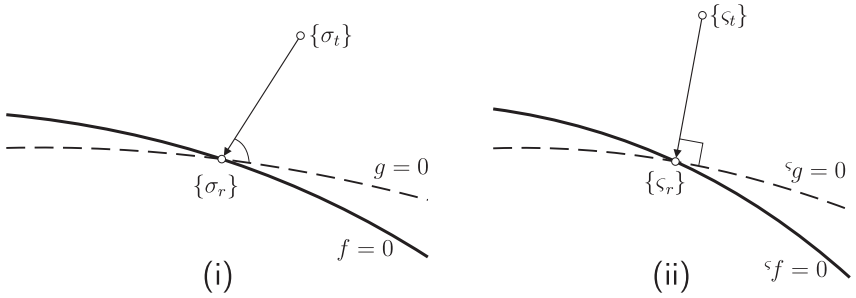

Figure 4.6: CPP stress return in (i) conventional stress space and (ii) in EMSS.

In the case of non-linear elasticity, the energy-mapped surface takes on additional curvature. For example, if a linear variation in bulk modulus with pressure and a constant shear modulus were adopted, then a D-P [14] cone would transform into a convex quadratic cone for which an analytical bE solution would be possible. For more complex forms (that is, non-linear meridians and non-circular deviatoric cross-section) the solution would require a polynomial of 5^{th} order (or higher) to be solved numerically[6].

The EMSS also provides a valuable framework with which to view hardening/softening plasticity since the return point will remain closest to the trial point (for the case of associated flow) with respect to the evolving yield surface. The full range of plasticity models which retain analytic bE solutions has not yet been identified.

The energy-mapped opening angles of the yield surface and plastic potential, ${}^{\varsigma}\alpha_f$ and ${}^{\varsigma}\alpha_g$, are given by

$${}^{\varsigma}\alpha_f = \frac{\alpha_f\sqrt{1+\upsilon}}{\sqrt{1-2\upsilon}} \qquad \text{and} \qquad {}^{\varsigma}\alpha_g = \frac{\alpha_g\sqrt{1+\upsilon}}{\sqrt{1-2\upsilon}}. \tag{4.18}$$

Increasing υ widens the opening angle of the mR yield and plastic potential surfaces. Throughout the following, and without loss of generality, the yield surface is assumed to be pinned at the stress origin, $\xi_c = 0$. For cases where $\xi_c \neq 0$, the trial stress state can be hydrostatically translated by ξ_c in order to accommodate a tensile apex.

[6]It is widely known that, in general, it is only possible to find the analytical solution to a polynomial of fourth order or less.

4.3.2 Apex return

If ${}^{\varsigma}f_a \leq 0$, then the trial stress point $\{\varsigma_t\}$ will be returned onto the apex of the mR cone, with

$$\{\sigma_{cp}\} = (\xi_c/\sqrt{3})\{1\}, \tag{4.19}$$

where $(\cdot)_{cp}$ denotes quantities associated with the closest point (the analytical stress return point) and $\{1\} = \{1 \quad 1 \quad 1\}^T$. The mR EMSS apex boundary function is given by

$${}^{\varsigma}f_a = {}^{\varsigma}\rho + \frac{1}{{}^{\varsigma}\alpha_g \bar{\rho}}\left({}^{\varsigma}\xi - {}^{\varsigma}\xi_c\right) = 0. \tag{4.20}$$

This boundary function defines an inverted mR cone pinned at the apex of the yield surface, as shown in Figure 4.3 (i). Points lying on or inside this surface (${}^{\varsigma}f_a \leq 0$) must return to the apex of the yield surface.

4.3.3 Edge return

For trial stresses outside the yield surface returning onto the compression meridian

$$\theta_{cp} = \pi/6 \qquad \text{and} \qquad {}^{\varsigma}\rho_{cp} = {}^{\varsigma}\alpha_f \, {}^{\varsigma}\xi_{cp}. \tag{4.21}$$

One obtains the solution for ${}^{\varsigma}\rho_{cp}$ in this case by recognising that the return vector from the trial point will be orthogonal to the direction of the plastic potential compression meridian line in EMSS. Therefore we may write

$$\{{}^{\varsigma}n_g\}^T\left\{\{\varsigma_{cp}\} - \{\varsigma_t\}\right\} = 0, \tag{4.22}$$

where $\{{}^{\varsigma}n_g\}$ is the direction of the plastic potential compression merdian, given by

$$\{{}^{\varsigma}n_g\} = \left\{1 - \sqrt{2}\,{}^{\varsigma}\alpha_g \qquad 1 + {}^{\varsigma}\alpha_g/\sqrt{2} \qquad 1 + {}^{\varsigma}\alpha_g/\sqrt{2}\right\}^T. \tag{4.23}$$

A point on the compression meridian of the energy-mapped yield surface is given by

$$\{\varsigma\} = \frac{{}^{\varsigma}\xi}{\sqrt{3}}\left\{1 - \sqrt{2}\,{}^{\varsigma}\alpha_f \qquad 1 + {}^{\varsigma}\alpha_f/\sqrt{2} \qquad 1 + {}^{\varsigma}\alpha_f/\sqrt{2}\right\}^T. \tag{4.24}$$

Substituting (4.23) and (4.24), for $\{{}^{\varsigma}n\}$ and $\{\varsigma_{cp}\}$, into (4.22), we obtain an equation which can be solved for ${}^{\varsigma}\xi_{cp}$

$${}^{\varsigma}\xi_{cp} = \frac{\left(\varsigma_{t_2} + \varsigma_{t_3}\right)\left(1 + {}^{\varsigma}\alpha_g/\sqrt{2}\right) + \varsigma_{t_1}\left(1 - \sqrt{2}\,{}^{\varsigma}\alpha_g\right)}{\sqrt{3}(1 + {}^{\varsigma}\alpha_f \, {}^{\varsigma}\alpha_g)}. \tag{4.25}$$

Subsequently ${}^{\varsigma}\xi_{cp}$ and ${}^{\varsigma}\rho_{cp}$ can be transformed back into conventional principal stress space (recall that θ remains unchange moving between conventional and EMSS) to calculate the final return stress $\{\sigma_{cp}\}$ using the Haigh-Westergaard expression (2.10). These stresses are then transformed back to generalised stress space through use of the eigenvectors associated with the generalised trial stress state (C.17).

4.3.4 Non-planar surface return

Assuming that a trial elastic stress $\{\varsigma_t\}$ outside the yield will return onto the non-singular portion of the yield surface, we can define the square of the distance between that trial point and a point on the surface

at the same φ_t in any deviatoric plane[7] at a given ${}^{\varsigma}\xi_t$ (see Figure 4.7) as

$$l^2 = (r_t - r)^2 + ({}^{\varsigma}\xi - {}^{\varsigma}\xi_t)^2. \tag{4.26}$$

Substituting $r = \bar{r}\,{}^{\varsigma}\alpha_g({}^{\varsigma}\xi - {}^{\varsigma}\xi_g)$ and

$$r_t^2 = a^2 + {}^{\varsigma}\rho_t^2 - 2a\,{}^{\varsigma}\rho_t C \qquad \Big(\text{where} \quad C = \cos(5\pi/6 - \theta_t) \quad \text{and} \quad a = \bar{a}\,{}^{\varsigma}\alpha_g({}^{\varsigma}\xi - {}^{\varsigma}\xi_g)\Big) \tag{4.27}$$

into (4.26), taking the partial derivative of l^2 with respect to ${}^{\varsigma}\xi$ and setting that derivative equal to zero, we obtain

$$\begin{aligned} \frac{\partial l^2}{\partial\,{}^{\varsigma}\xi} &= \bar{a}^2\,{}^{\varsigma}\alpha_g{}^2\,{}^{\varsigma}\xi r_t - \bar{a}^2\,{}^{\varsigma}\alpha_g{}^2\,{}^{\varsigma}\xi_g r_t - \bar{a}\,{}^{\varsigma}\alpha_g\,{}^{\varsigma}\rho_t C r_t - r_t^2\bar{r}\,{}^{\varsigma}\alpha_g - \ldots \\ &\quad -\bar{r}\,{}^{\varsigma}\alpha_g({}^{\varsigma}\xi - {}^{\varsigma}\xi_g)(\bar{a}^2\,{}^{\varsigma}\alpha_g{}^2\,{}^{\varsigma}\xi - \bar{a}^2\,{}^{\varsigma}\alpha_g{}^2\,{}^{\varsigma}\xi_g - \bar{a}\,{}^{\varsigma}\alpha_g\,{}^{\varsigma}\rho_t C) + ({}^{\varsigma}\xi\bar{r}^2\,{}^{\varsigma}\alpha_g{}^2 - {}^{\varsigma}\xi_g\bar{r}^2\,{}^{\varsigma}\alpha_g{}^2 + {}^{\varsigma}\xi - {}^{\varsigma}\xi_t)r_t = 0. \end{aligned} \tag{4.28}$$

Note that throughout the partial differentiation we ignore the dependance of ${}^{\varsigma}\xi_g$ on ${}^{\varsigma}\xi$. Through manipulation and substituting ${}^{\varsigma}\xi_g$ from (4.6) (with $\xi_c = 0$) into (4.28), we obtain the following quartic in ${}^{\varsigma}\xi_{cp}$

$$\left({}^{\varsigma}\xi_{cp}\right)^4 A_1 + \left({}^{\varsigma}\xi_{cp}\right)^3 A_2 + \left({}^{\varsigma}\xi_{cp}\right)^2 A_3 + {}^{\varsigma}\xi_{cp} A_4 + A_5 = 0, \tag{4.29}$$

where

$$\begin{aligned} A_1 &= \bar{a}^2\,{}^{\varsigma}\alpha_f{}^2 B_1^2 - 4\bar{a}^4\bar{r}^2\,{}^{\varsigma}\alpha_f{}^4\,{}^{\varsigma}\alpha_g{}^2, \\ A_2 &= 12\bar{a}^3\bar{r}^2\,{}^{\varsigma}\alpha_f{}^3\,{}^{\varsigma}\alpha_g{}^2\rho_t C - 2\bar{a}^2\,{}^{\varsigma}\alpha_f{}^2 B_1 B_2 - 2\bar{a}\,{}^{\varsigma}\alpha_f\,{}^{\varsigma}\rho_t C B_1^2, \\ A_3 &= \bar{a}^2\,{}^{\varsigma}\alpha_f{}^2 B_2^2 + {}^{\varsigma}\rho_t^2 B_1^2 + 4\bar{a}\,{}^{\varsigma}\alpha_f\,{}^{\varsigma}\rho_t C B_1 B_2 - 9\bar{a}^2\bar{r}^2\,{}^{\varsigma}\alpha_f{}^2\,{}^{\varsigma}\alpha_g{}^2\,{}^{\varsigma}\rho_t^2 C^2 - 4\bar{a}^2\bar{r}^2\,{}^{\varsigma}\alpha_f{}^2\,{}^{\varsigma}\alpha_g{}^2\,{}^{\varsigma}\rho_t^2, \\ A_4 &= 6\bar{a}\bar{r}^2\,{}^{\varsigma}\alpha_f\,{}^{\varsigma}\alpha_g{}^2\,{}^{\varsigma}\rho_t^3 C - 2\,{}^{\varsigma}\rho_t^2 B_1 B_2 - 2\bar{a}\,{}^{\varsigma}\alpha_f\,{}^{\varsigma}\rho_t C B_2^2, \\ A_5 &= {}^{\varsigma}\rho_t^2 B_2^2 - {}^{\varsigma}\rho_t^4\bar{r}^2\,{}^{\varsigma}\alpha_g{}^2, \end{aligned}$$

$$B_1 = \bar{a}^2\,{}^{\varsigma}\alpha_f\,{}^{\varsigma}\alpha_g + \bar{r}^2\,{}^{\varsigma}\alpha_f\,{}^{\varsigma}\alpha_g + 1 \qquad \text{and} \qquad B_2 = \bar{a}\,{}^{\varsigma}\alpha_g\,{}^{\varsigma}\rho_t C + \xi_t.$$

This quartic can be solved for ${}^{\varsigma}\xi_{cp}$ (see Simo and Hughes [31] p. 138, amongst others, for the solution of a quartic). Once ${}^{\varsigma}\xi_{cp}$ is known, then the other quantities identifying the position of the closest point on the mR surface can be calculated. φ_{cp} is given by the sine rule

$$\varphi_{cp} = \arcsin\left(\frac{{}^{\varsigma}\rho_t \sin(5\pi/6 - \theta_t)}{r_t}\right), \tag{4.30}$$

where r_t is calculated at the solution ${}^{\varsigma}\xi_{cp}$ using (4.27). ${}^{\varsigma}\rho_{cp} = {}^{\varsigma}\alpha_f\bar{\rho}(\theta)\,{}^{\varsigma}\xi_{cp}$ with $\bar{\rho}(\theta)$ given by (4.1) and θ_{cp} determined from the cosine rule

$$\theta_{cp} = \frac{5\pi}{6} - \arccos\left(\frac{a_{cp}^2 + {}^{\varsigma}\rho_{cp}^2 - r_{cp}^2}{2a_{cp}\,{}^{\varsigma}\rho_{cp}}\right), \tag{4.31}$$

r_{cp} and a_{cp} are values associated with ${}^{\varsigma}\xi_{cp}$. The stress return for the non-associated mR cone is equivalent to the closest point to the plastic potential in energy-mapped space. The yield and plastic potential

[7] Note that the trial point will return along a constant φ_t towards the arc centre of the plastic potential. This allows a ray of potential return points on the yield surface to be identified.

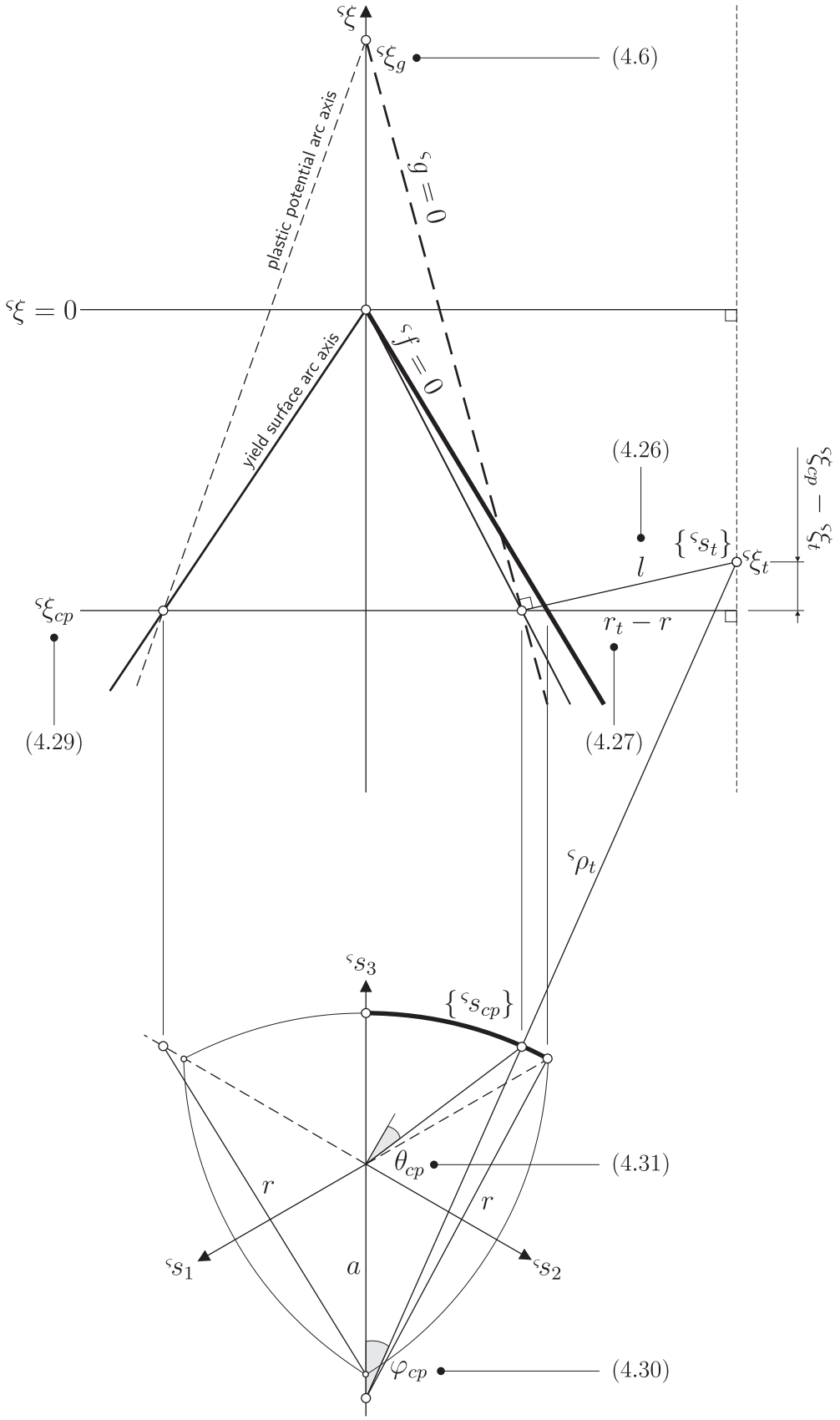

Figure 4.7: Geometric illustration of the mR non-planar surface return solution in EMSS.

surfaces coincide at the return stress state. For the special case of isochoric plastic flow ($\psi_g = 0$), trial points outside the yield surface return in their deviatoric ξ plane, $\xi_{cp} = \xi_t$, removing the need to find the solution to the quartic (4.29).

4.3.5 Tension cut-off

Coombs and Crouch [9] extended the realism of the mR constitutive model by including an additional NAF mR cone, with a high friction angle, to provide a tension cut-off. The addition of this cut-off increased the number of return regions to seven. All of these regions allowed for an analytical stress return based on an EMSS approach. The non-planner surface, edge and apex return for the additional surface were handled in the same way as presented in Sections 4.3.1 to 4.3.3. However, returning to the intersection between the two surfaces required special attention. The full algorithmic and numerical procedure was provided in [9]. It has been omitted here for the sake of brevity.

4.4 Numerical investigations

The analytical bE stress integration procedure (as described in the preceding section) is now examined. The robustness of the algorithm is first verified, errors are then quantified and the algorithm run-times compared with a conventional iterative integration procedure. All of the analyses in this section used a Young's modulus of 100MPa and a Poisson's ratio of 0.2.

4.4.1 Robustness

The robustness of the analytical stress integration procedure described in the preceding section (with the pseudo-code given in Figure 4.5) was tested using three-dimensional Gudehus [18] stress plots. The friction and dilation angles were set to $\pi/9$ and $\pi/18$, respectively, with an apparent cohesion of 100kPa and a normalised deviatoric radius under triaxial extension of $\bar{\rho}_e = 0.8$.

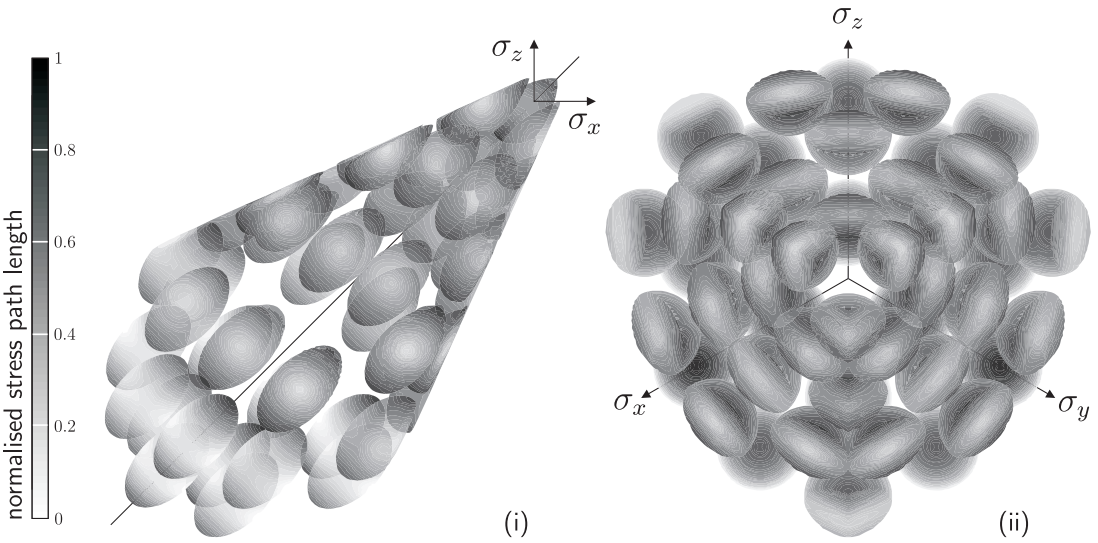

Figure 4.8: Gudehus stress surface plots in (i) σ_x versus σ_z plane and (ii) deviatoric section (looking in a negative hydrostatic direction).

Starting from an initial principal stress state of $\{\sigma\} = \{-1 \quad -1 \quad -1\}^T$MPa, the mR constituitve model was subjected to 64 strain probes of length $10,000\mu$ (that is, 1×10^{-2}). At the updated stress state (from those initial strain probes), the constitutive model was subjected to 832 strain probes for the 64 starting stress states. Each *sphere* had a strain radius of $2,000\mu$ (that is, 2×10^{-3}). The directions of the individual strain probes (for both the starting state and the subsequent strain probe *sphere*) were

obtained using the HEALPix software [16], dividing the surface of the sphere into equal area patches. The stress surfaces corresponding to these strain *spheres* are shown in Figure 4.8. The surfaces are shaded according to the distance from the starting stress state, with the black and white regions corresponding to the largest and smallest radii respectively.

If the 832 strain probes cause a purely elastic response, then the corresponding stress surfaces will be ellipsoids with their major axis aligned with the space diagonal (hydrostatic axis) and circular deviatoric sections. In the special case of a zero Poisson's ratio (or when visualising the surfaces in EMSS), the Gudehus stress surface will be spherical. For the case of perfect plasticity, when the strain probes experience an inelastic stress response, the stress surfaces are bounded by the yield surface. This effect can be seen in Figure 4.8 when the influence of the mR yield surface is clearly visible. The smoothness of the stress surfaces demonstrates the robustness of the stress integration algorithm. Points which fail to converge, or converge to an inappropriate stress state, would appear as spikes or discontinuities in the stress surfaces. One of the major advantages of the analytical bE stress integration procedure is that will provide an appropriate solution for any trial strain state, thereby eliminating the potential convergence problems associated with iterative schemes.

4.4.2 Error analysis

The errors associated with the implicit stress return procedure for the M-C, D-P and mR cone models are now analysed. The accuracy of the return algorithms were assessed for normalised trial deviatoric radii of $\rho_t/(\alpha_f\bar{\rho}(\theta_t)\xi_t) \in [1,6]$ and trial Lode angles $\theta_t \in [-\pi/6, \pi/6]$, in three sextants of stress space. The friction and dilation angles were set to $\pi/6$ and $\pi/12$, respectively, with the normalised deviatoric radius under triaxial extension for mR coinciding with that of M-C ($\bar{\rho}_e = 0.714$). The apparent cohesion was set to zero. A hydrostatic pressure of $\xi = -1$MPa was used for all of the initial and elastic trial stress states. In this material point analysis, the starting stress state was located on the yield surface at the shear meridian ($\theta = 0$) in the sextant where $\sigma_x \leq \sigma_y \leq \sigma_z$. The models were then subjected to a strain increment corresponding to the trial stress state under consideration, see Figure 4.9 (i). The return stress from this single strain increment was compared (using a Fortran90 script) with the *exact* solution deemed to be obtained by splitting the strain increment into 1,000 sub-increments.

The following error measure was used to assess the accuracy of the return algorithms

$$\text{error} = \frac{\sqrt{\Big\{\{\sigma_{cp}\} - \{\sigma_e\}\Big\}^T \Big\{\{\sigma_{cp}\} - \{\sigma_e\}\Big\}}}{\sqrt{\{\sigma_e\}^T\{\sigma_e\}}}, \tag{4.32}$$

where $\{\sigma_e\}$ is the *exact* solution and $\{\sigma_{cp}\}$ is the analytical single increment *closest point* return. Stress iso-error maps are shown in Figure 4.9. The maximum errors in each of the three sextants are given in Table 4.2. Due to symmetry, Figure 4.9 (ii) displays only half of the iso-error map for D-P. The maximum errors for the three models are 11.81%, 8.09% and 8.86% for M-C, D-P and mR, all located in the trial stress sextant $\sigma_x \leq \sigma_z \leq \sigma_y$. In regions $\sigma_y \leq \sigma_x \leq \sigma_z$ and $\sigma_x \leq \sigma_y \leq \sigma_z$, the mR model has the lowest maximum error.

Large regions of stress space lead to mR model errors of less than 1%. In the sextant where $\sigma_x \leq \sigma_y \leq \sigma_z$, zero error appears along the locus $\theta_t = 0$, $\rho_t/(\alpha_f\bar{\rho}\xi_t) = 1$ to $\theta_t \to -0.3128$, $\rho_t/(\alpha_f\bar{\rho}\xi_t) \to \infty$. Here the trial stress returns back to the original stress state on the shear meridian in a radial direction towards the arc centre. Larger errors are associated with trial stresses near the extension meridian and in the vicinity of the compression meridian return region. These are due to the increased tangential component of the trial stress increment (that is, moving further over the curved surface). The errors follow the same

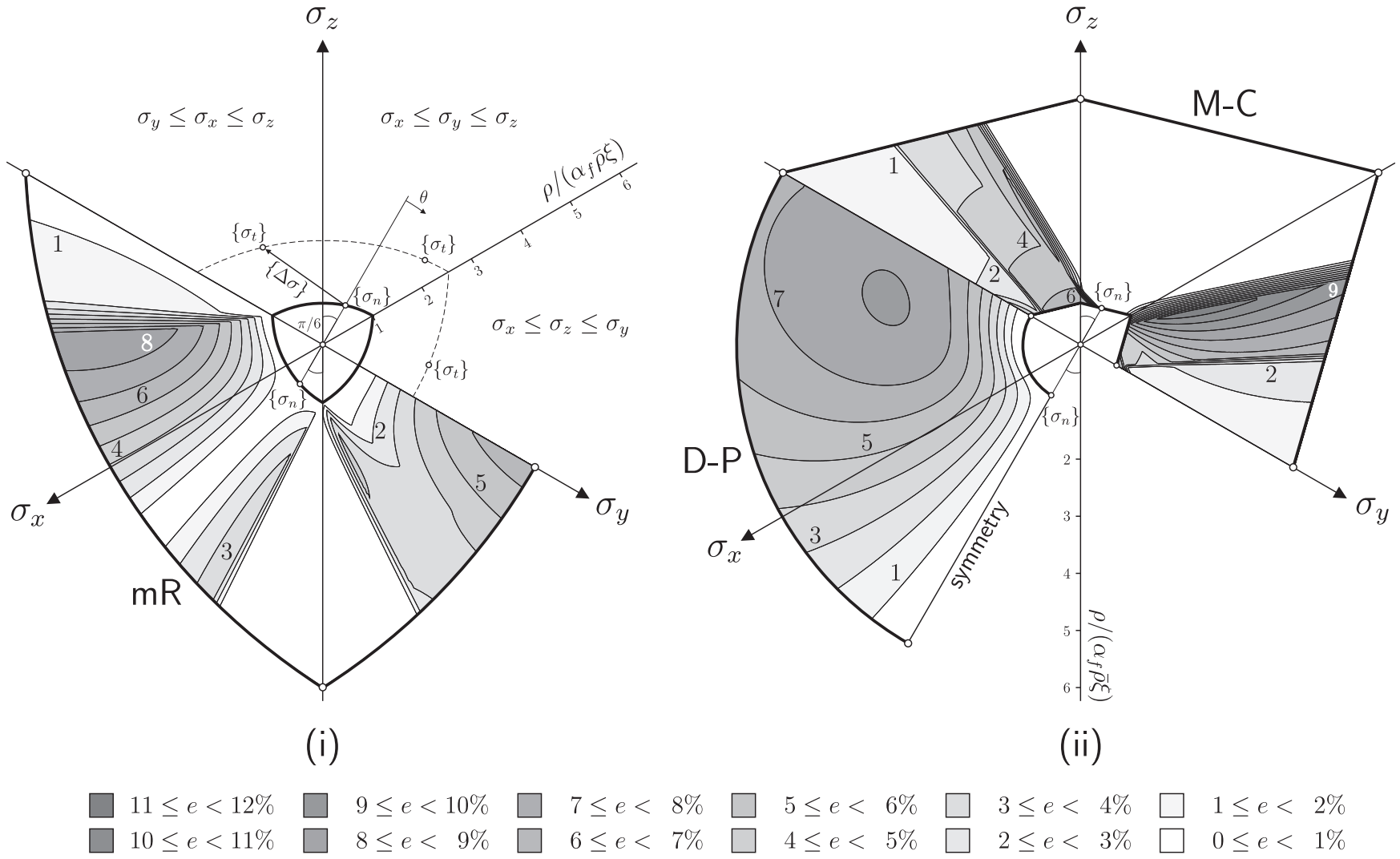

Figure 4.9: Single step analytical stress return error analysis for (i) modified Reuleaux (mR) cone and (ii) Mohr-Coulomb (M-C) and Drucker-Prager (D-P).

general pattern as reported for the associated Reuleaux plasticity model by Coombs *et al.* [11]. The maximum error is higher under NAF, compared with associated plasticity. This is due to the NAF rule increasing the length of the integrated stress return [9]. However, the previously published error analysis on mR plasticity concentrated on stress returns starting and returning in the same sextant [9, 11].

model	trial stress sextant		
	$\sigma_y \leq \sigma_x \leq \sigma_z$	$\sigma_x \leq \sigma_y \leq \sigma_z$	$\sigma_x \leq \sigma_z \leq \sigma_y$
M-C	6.81%	6.86%	11.81%
D-P	8.09%	4.94%	8.09%
mR	6.50%	3.79%	8.86%

Table 4.2: Maximum errors for M-C, D-P and mR constitutive models for trial stresses in three sextants of stress space.

For a large portion of the region where $\sigma_x \leq \sigma_y \leq \sigma_z$, the M-C model has zero error. However, when crossing corner regions there is an error which can introduce significant inaccuracy when using a single step return. It appears that some authors [7, 8] are unaware of this feature, as they suggest that the bE integration for M-C is exact. Implicit stress return algorithms only require information about the trial stress (or elastic strain) state. For isotropic formulations, on receiving a trial stress state, the constitutive model calculates the principal stresses and orders them such that $\sigma_1 \leq \sigma_2 \leq \sigma_3$ (or using some other preferential ordering). The return principal stresses are subsequently calculated and then converted back into six-component generalised stresses. When an applied strain increment changes the ordering of the principal stresses and the stress path moves through a corner return region, there will be an error associated with the stress return. This type of error is present for any yield surface with corners.

Figure 4.10 demonstrates the stress return algorithm (for the mR model) when the applied strain increment changes the ordering of the principal stress between the original (or previously converged) and trial stress states, crossing a corner region. This analysis was conducted with the same material parameters as above except that $\phi = \pi/9$, $\phi_g = 0$, $\bar{\rho}_e = 0.8$ and the cohesion $c = 100$kPa, allowing the stress return to be visualised in the π-plane. The initial stress state $\{\sigma_n\}$ was located at the intersection of the shear meridian with the yield surface. An unordered principal strain increment of $\{\Delta\varepsilon\} = \{-1.6131 \quad 1.8065 \quad -0.1934\}^T \times 10^{-3}$ was applied in a single step and also in two carefully selected steps, where the strain increment was split such that (i) the first increment locates the trial stress $\{\sigma_{t_1}\}$ on the boundary of the region that will result in a corner return and (ii) the second increment supplies the remainder of the total strain increment. Figure 4.10 (i) demonstrates the stress return in principal stress space where the components $(\sigma_x, \sigma_y, \sigma_z)$ are not associated with any particular ordering. That is, σ_x (and σ_y or σ_z) may be the major, intermediate or minor principal stress. In this way, stress points can exist in all six sextants of the π-plane. Hereafter we refer to this as true stress space. Figure 4.10 (ii) illustrates the processes in principal stress space where the ordering $\sigma_1 \leq \sigma_2 \leq \sigma_2$ holds. In true stress space, applying the strain increment in a single step results in a trial stress state $\{\sigma_t\}$ in the sextant where $\sigma_x \leq \sigma_z \leq \sigma_y$. This trial state will return onto the yield surface at $\{\sigma_{cp}\}$. In the ordered principal stress space, the trial point is again located at $\{\sigma_t\}$. This principal trial stress will return to $\{\sigma_{cp}\}$ which (for this case) coincides with the same return stress in true stress space. When the strain increment is split into two components, the first trial $\{\sigma_{t_1}\}$ returns one of the yield surface's compression meridians at $\{\sigma_{cp}\}$. The remainder of the increment results in the trial $\{\sigma_{t_2}\}$ which returns to $\{\sigma_{cp_2}\}$. Viewing this two-step process in principal stress space, the initial increment is identical to that in true stress space. The second increment is mirrored about the $\sigma_z = \sigma_y$ axis so that it remains

in the $\sigma_1 \leq \sigma_2 \leq \sigma_2$ sextant. Once the return is formed in principal stress space, it is then transformed back into true stress space. For the case demonstrated, the relative error (using (4.32) with $\{\sigma_e\}$ taken as $\{\sigma_{cp_2}\}$) between the single step and the two step return was 10.27%. An *absolute* error of 12.5% was recorded against the result when splitting the strain increment into 10,000 subincrements.

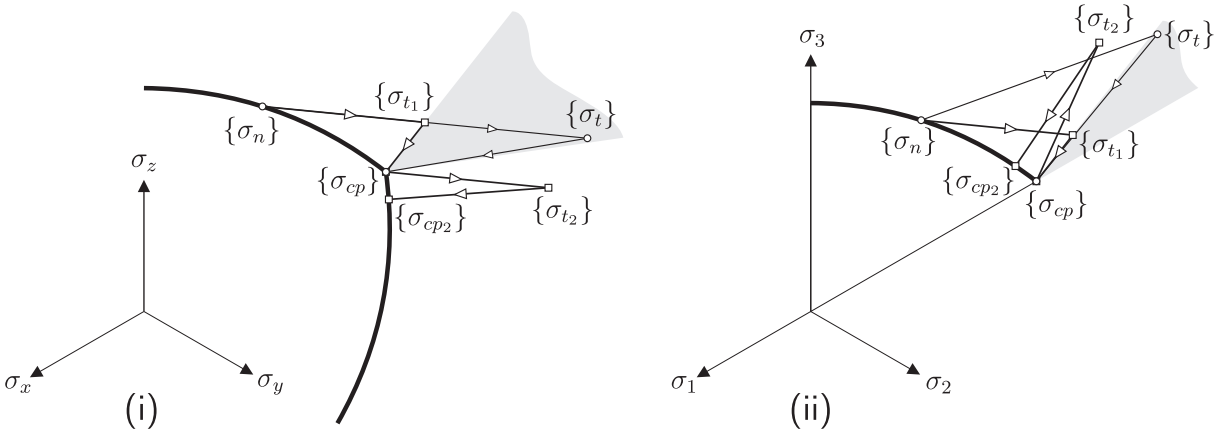

Figure 4.10: mR stress return crossing a corner. The figures illustrate a comparison between a single step and two specifically selected increments in (i) true stress space (ii) ordered principal stress space.

The mR plasticity model contains an edge (at the compression meridians) and an apex which, by using the approach of Clausen *et al.* [7, 8], are dealt with exactly[8]. Surprisingly, the unnecessary process of rounding corners is still used by some researchers, for example for the M-C constitutive model [1]. This rounding introduces an additional numerical approximation, increasing the error associated with the stress integration procedure.

4.4.3 Material run-time analysis

Here the run time for the mR model using the single-step analytical bE return is compared with a conventional iterative bE stress return. The analysis considered trial stresses $\rho_t/(\alpha_f \bar{\rho} \xi_t) \in [1, 6]$ and $\theta_t \in [-\pi/6, \pi/6]$. $\phi = \pi/9$, $\phi_g = \pi/18$ and $\bar{\rho}_e = 0.8$ define the mR cone and a hydrostatic pressure of $\xi_t = -1$MPa was used for all of the elastic trial stresses. The constitutive model was subjected to a strain increment corresponding to the elastic trial stress state under consideration, see the right of Figure 4.11. When returning to the corner (or the tensile apex), both the approaches (analytical and numerical bE) use the same single-step return discussed in the preceding sections. However, when returning onto the non-planar surface, the conventional (numerical) bE method requires multiple local iterations to obtain convergence. The number of iterations and the ratio of the numerical to analytical bE run times are presented in Figure 4.11. The analytical return demonstrates a 2-4 times speed-up over the iterative numerical method (for the considered trial stress states). The increase in time required for the iterative approach is due, in part, to repeatedly calculating the first and second derivatives of the yield function with respect to stress. The non-smooth (stepped) region close to $\theta_t = \pi/12$ is a consequence of the finite grid size either side of the return region B-C boundary (that is the boundary between edge and surface returns, as shown in Figure 4.3).

Note that although the same general trends are observed as for the associated case reported by Coombs *et al.* [11], a different form of the yield function, f, was used in this chapter (in agreement with that used in later work by Coombs and Crouch [9]). Both yield functions describe the same yield surface, but they

[8]That is, without some numerically approximation or local rounding. Note that de Souza Neto *et al.* [33] also provide a method for dealing with the corner regions without local rounding.

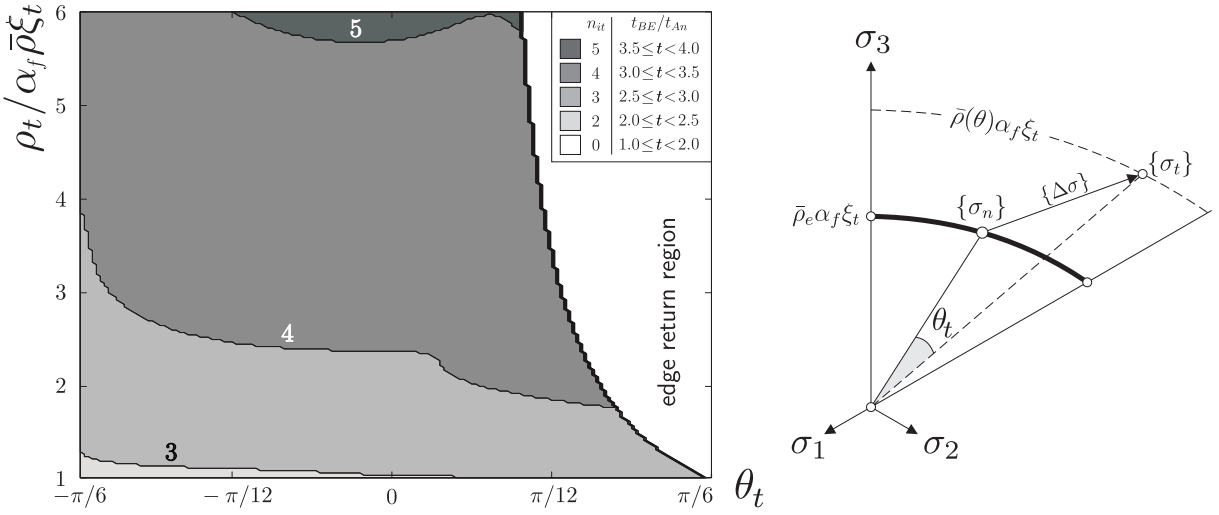

Figure 4.11: Run time comparisons between conventional iterative backward Euler and the single-step analytical backward Euler stress returns.

have different f fields outside the yield surface, which can significantly affect the rate of converegence of an iterative backward Euler stress return[9]. As a result, the maximum number of iterations for the iterative NAF model to converge (to the same tolerance) was reduced from 7 (for the case of associated flow in [11]) to 5.

4.5 Consistent linearisation

Section 2.4 highlighted the importance of forming the algorithmic tangent through consistent linearisation of the bE stress return procedure. Here, that tangent is given for each of the three return regions.

4.5.1 Apex consistent tangent

As Clausen *et al.* have shown [7], the elasto-plastic consistent tangent for a hydrostatic apex return is simply

$$\left[D^{alg}\right] = [0]. \tag{4.33}$$

Due to this null stiffness matrix, the use of a non-zero apparent cohesion is imperative. If all of the material points in a boundary value analysis started at the yield surface apex, then the global stiffness matrix would also null (that is, it would give a system with zero stiffness).

4.5.2 Edge consistent tangent

The consistent tangent for an edge return is obtained following the NAF approach given by Clausen *et al.* [8]. By considering the vector orientation of the yield surface compressive meridian (edge)

$$\{n_f\} = \left\{1 - \sqrt{2}\alpha_f \qquad 1 + \alpha_f/\sqrt{2} \qquad 1 + \alpha_f/\sqrt{2}\right\}^T, \tag{4.34}$$

and that of the plastic potential

$$\{n_g\} = \left\{1 - \sqrt{2}\alpha_g \qquad 1 + \alpha_g/\sqrt{2} \qquad 1 + \alpha_g/\sqrt{2}\right\}^T, \tag{4.35}$$

[9]The influence of f on an iterative bE stress integration routine is discussed in more detail in Chapter 5.

we obtain the 3×3 (that is, in principal form) infinitesimal elasto-plastic tangent matrix as

$$\left[\hat{D}^{ep}\right] = \frac{\{n_f\}\{n_g\}^T}{\{n_f\}^T\left[\hat{C}^{\mathrm{e}}\right]\{n_g\}}, \tag{4.36}$$

where $\left[\hat{C}^{\mathrm{e}}\right]$ is the 3×3 (principal) elastic compliance matrix. The 6×6 elasto-plastic tangent matrix is then given by

$$\left[D^{ep}\right] = \begin{bmatrix} \left[\hat{D}^{ep}\right] & [0] \\ [0] & (E/2(1+v))\,[1] \end{bmatrix}. \tag{4.37}$$

The consistent tangent follows as

$$\left[D^{alg}\right] = \left[Q\right]\left[D^{ep}\right], \qquad \text{where} \qquad [Q] = \begin{bmatrix} [1] & [0] \\ [0] & [\bar{Q}] \end{bmatrix}. \tag{4.38}$$

Using the fact that $\sigma_2 = \sigma_3$ for a return onto the edge, $[\bar{Q}]$ was shown in [11] to be equal to

$$[\bar{Q}] = \begin{bmatrix} \frac{\sigma_1-\sigma_2}{\sigma_{t_1}-\sigma_{t_2}} & 0 & 0 \\ 0 & 0 & 0 \\ 0 & 0 & \frac{\sigma_1-\sigma_3}{\sigma_{t_1}-\sigma_{t_3}} \end{bmatrix}, \tag{4.39}$$

where σ_{t_i} are the principal trial stresses and σ_i are the principal return stresses. From (4.38) and (4.39) the consistent tangent, for the edge return, can be written as

$$\left[D^{alg}\right] = \begin{bmatrix} \left[\hat{D}^{ep}\right] & [0] \\ [0] & (E/2(1+v))\,[\bar{Q}] \end{bmatrix}. \tag{4.40}$$

Once the consistent tangent has been formed in principal stress space (4.40) it must be transformed back to generalised stress space, see Appendix C.3 for details on this transformation.

4.5.3 Non-planar consistent tangent

The consistent tangent for the non-associated non-planar surface return is calculated following the procedure given in Section 2.4, thereby obtaining

$$\underbrace{\begin{bmatrix} \left[\hat{C}^{\mathrm{e}}\right] + \Delta\gamma[g_{,\hat{\sigma}\hat{\sigma}}\,] & \{g_{,\hat{\sigma}}\,\} \\ \{f_{,\hat{\sigma}}\,\}^T & 0 \end{bmatrix}}_{[A^{alg}]^{-1}} \begin{Bmatrix} \{d\hat{\sigma}\} \\ d\Delta\gamma \end{Bmatrix} = \begin{Bmatrix} \{d\hat{\varepsilon}^{\mathrm{e}}_t\} \\ 0 \end{Bmatrix}. \tag{4.41}$$

The principal consistent tangent $[\hat{D}^{alg}]$ is obtained by pre-multiplying both side by $[A^{alg}]$, as shown by (2.54) in Section 2.4 of Chapter 2. We assume that (and without loss of generality) the yield surface apex lies at the stress origin ($\xi_c = 0$) when taking derivatives with respect to $\{\hat{\sigma}\}$. The derivatives required for (4.41) are given by

$$\begin{aligned} \{g_{,\hat{\sigma}}\,\} &= \{\rho_{,\hat{\sigma}}\,\} - \alpha_f\xi\{\bar{\rho}_{,\hat{\sigma}}\,\} - \alpha_g\bar{\rho}\{\xi_{,\hat{\sigma}}\,\}, \\ [g_{,\hat{\sigma}\hat{\sigma}}\,] &= [\rho_{,\hat{\sigma}\hat{\sigma}}\,] - (\alpha_f+\alpha_g)\{\xi_{,\hat{\sigma}}\,\}\{\bar{\rho}_{,\hat{\sigma}}\,\}^T - \alpha_f\xi[\bar{\rho}_{,\hat{\sigma}\hat{\sigma}}\,] \qquad \text{and} \\ \{f_{,\hat{\sigma}}\,\} &= \{\rho_{,\hat{\sigma}}\,\} - \alpha_f\xi\{\bar{\rho}_{,\hat{\sigma}}\,\} - \alpha_f\bar{\rho}\{\xi_{,\hat{\sigma}}\,\}. \end{aligned} \tag{4.42}$$

The derivatives of the stress invariants and the mR LAD are provided in Appendix C.1 and Appendix C.2 respectively. The full 6×6 consistent tangent is given by

$$\left[D^{alg}\right] = \begin{bmatrix} \left[\hat{D}^{alg}\right] & [0] \\ [0] & \big(E/2(1+v)\big)[\bar{Q}] \end{bmatrix}, \tag{4.43}$$

where $\left[\hat{D}^{alg}\right]$ is the consistent tangent in principal form, from (4.41), and $[\bar{Q}]$ given by [7], was shown in [11] to be

$$[\bar{Q}] = \begin{bmatrix} \frac{\sigma_1-\sigma_2}{\sigma_{t_1}-\sigma_{t_2}} & 0 & 0 \\ 0 & \frac{\sigma_2-\sigma_3}{\sigma_{t_2}-\sigma_{t_3}} & 0 \\ 0 & 0 & \frac{\sigma_1-\sigma_3}{\sigma_{t_1}-\sigma_{t_3}} \end{bmatrix}. \tag{4.44}$$

4.6 Observations

A NAF mR cone perfect plasticity model has been investigated in some detail. Although simple, it provides a valuable extension to the existing family of pressure-dependent soil models whilst still allowing for an analytical bE stress integration procedure. The following conclusions summarise the key findings from this chapter:

(i) the analytical bE stress integration procedure guaranties material point convergence for any trial elastic strain and requires no local iterations;

(ii) this single step stress return provides a 2-4 times speed gain over the conventional iterative bE approach;

(iii) corners can be simply dealt with using analytical procedures for perfect plasticity models;

(iv) when moving between stress sextants across a corner there can be an additional error associated with the implicit stress return procedure. This error can be removed by using a two-part sub-stepping algorithm (as shown in Figure 4.10);

(v) the mR deviatoric yield criterion provides a significantly improved fit to the deviatoric yielding behaviour of particulate materials over M-C and D-P (see Figure 4.4) by containing a dependency on both the Lode angle and the intermediate principal stress; and

(vi) the mR cone model overcomes the inadequacies inherent in, and provides a suitable replacement for, both the M-C and D-P models, and yet requires no additional material constants ($\bar{\rho}_e$ can be obtained from the friction angle, ϕ).

This chapter has been limited to the case of perfect-plasticity constitutive models. It would be possible to extend the mR constitutive model to include hardening effects, such as isotropic hardening/softening and/or rotation. However, the forms of hardening that would allow for an analytical stress integration are yet to be determined. Also, purely frictional (cone-type) models fail to capture the volumetric response of clays under hydrostatic (or one-dimensional) consolidation. For example, isotropic compaction of the mR constitutive model produces a fully recoverable (linear) elastic response, failing to reproduce the inelastic behaviour of clays under this loading. To include this feature, a yield surface with compressive closure on the hydrostatic axis is required. The following chapter develops such a model within the framework of hyperplasticity and embracing the concepts of Critical State soil mechanics.

Chapter 4 references

[1] AJ Abbo & SW Sloan, *A smooth hyperbolic approximation to the MohrCoulomb yield criterion*, Comput. Struct. 54 (1995), 427-441.

[2] P Anantanasakul, *Three-dimensional experiments and modelling of anisotropic clay*, PhD. Thesis, Oregon State University (2010).

[3] JP Bardet, *Lode dependences for isotropic pressure-sensitive elastoplastic materials*, ASME J. Appl. Mech. 57 (1990), 498–506.

[4] T Benz, M Wehnert & PA Vermeer, *A Lode angle dependent formulation of the Hardening Soil model*, 12th IACMAG (2008), 653–660.

[5] SK Bhowmik & JH Long, *A general formulation for the cross sections of yield surfaces in octahedral planes*. In: GN Pande and J Middleton (eds.) NUMENTA 90 (1990), 795–803.

[6] M Cai, *Influence of intermediate principal stress on rock fracturing and strength near excavation boundaries-Insight from numerical modeling*, Int. J. of Rock Mech. Min. 45 (2008), 763–772.

[7] J Clausen, L Damkilde & L Andersen, *Efficient return algorithms for associated plasticity with multiple yield planes*, Int. J. Numer. Meth. Eng. 66 (2006), 1036–1059.

[8] J Clausen, L Damkilde & L Andersen, *An efficient return algorithm for non-associated plasticity with linear yield criteria in principal stress space*, Comput. Struct. 85 (2007), 1795–1807.

[9] WM Coombs & RS Crouch, *Non-associated Reuleaux plasticity: Analytical stress integration and consistent tangent for finite deformation mechanics*, Comput. Meth. Appl. Mech. Engrg. 200 (2011), 1021–1037.

[10] WM Coombs, *Reuleaux plasticity: overcoming Mohr-Coulomb and Drucker-Prager limitations*, presented at the BGA 42nd Cooling prize competition, Loughborough, 2011.

[11] WM Coombs, RS Crouch & CE Augarde, *Reuleaux plasticity: Analytical backward Euler stress integration and consistent tangent*, Comput. Meth. Appl. Mech. Engrg. 199 (2010), 1733–1743.

[12] WM Coombs, RS Crouch & CE Augarde, *On the use of Reuleaux plasticity for geometric non-linear analysis*. In: 18th UK Conference on Computational Mechanics (ACME-UK), 2010, 113–116.

[13] RS Crouch, H Askes & T Li, *Analytical CPP in energy-mapped stress space: application to a modified Drucker-Prager yield surface*, Comput. Meth. Appl. Mech. Engrg. 198 (2009), 853–859.

[14] DC Drucker & W Prager, *Soil mechanics and plastic analysis or limit design*, Quart. Appl. Math. 10 (1952), 157–164.

[15] E Fjær & H Ruistuen, *Impact of the intermediate principal stress on the strength of heterogeneous rock*, J. Geophys. Res. 107 (2002).

[16] KM Górski, E Hivon, AJ Banday, BD Wandelt, FK Hansen, M Reinecke & M Bartelmann, *HEALPix: a framework for high-resolution discretization and fast analysis of data distributed on the sphere*, Astrophys. J. 622 (2005), 759–771.

[17] DV Griffiths, *Failure criteria interpretation based on Mohr-Coulomb friction*, ASCE J. Geotech. Eng. 116 (1990), 986–999.

[18] G Gudehus, *Comparison of some constitutive laws for soils under radially symmetric loading and unloading*. In: Proceedings of the 3rd International Conference on Numerical Methods in Geomechanics, Aachen, 1979, 1309–1323.

[19] K Issen & V Challa, *Influence of the Intermediate Principal Stress on Compaction Localization Conditions*, The 41st U.S. Symposium on Rock Mechanics (USRMS), June 17–21, 2006.

[20] PV Lade & JM Duncan, *Cubical triaxial tests on conhesionless soil*, J. Soil Mech. Found. Div. ASCE 99 (1973), 793–812.

[21] PV Lade & MM Kirkgard, *Effects of stress rotation and changes of b-values on cross-anisotropic behavior of natural K_0-consolidated soft clay*, Soils Found. 40 (2000), 93–105.

[22] PV Lade, *Instability, shear banding and failure in granular materials*, Int. J. Solids Struct. 39 (2002), 3337–3357.

[23] H Matsuoka & T Nakai, *Stress-deformation and strength characteristics of soil under three different principal stresses*, Proc. JSCE 232 (1974), 59–70.

[24] FC Moon, *Franz Reuleaux: Contributions to 19th C. kinematics and theory of machines*, Tech. report, Cornell Library Technical Reports and Papers, 2002.

[25] AP Morris & DA Ferrill, *The importance of the effective intermediate principal stress (σ'_2) to fault slip patterns*, J. Struct. Geol. 31 (2009), 950–959.

[26] DM Potts & L Zdravković, *Finite element analysis in geotechnical engineering: application*, Thomas Telford Publishing, London, 2001.

[27] JH Prévost, *A Simple Plasticity Theory for Cohesionless Frictional Soils*, Soil Dyn. Earthq. Eng. 4 (1985), 9–17.

[28] F Reuleaux, *The kinematics of machinery: Outlines of a theory of machines*, Macmillan and Co., London, 1876.

[29] A Säyao & YP Vaid, *Effect of intermediate principal stress on the deformation response of sand*, Can. Geotech. J. 33 (1996), 822–828.

[30] RT Shield, *On Coulomb's law of failure in soils*, J. Mech. Phys. Solids 4 (1955), 10–16.

[31] JC Simo & TJR Hughes, *Computational inelasticity*, Springer, New York, 1998.

[32] JC Simo & TJR Hughes, *General return mapping algorithims for rate-independent plasticity*, Constitutive Laws for Engineering Materials: Theory and Applications, Cambridge University Press, 1987.

[33] EA de Souza Neto, D Perić & DRJ Owen, *Computational methods for plasticity: Theory and applications*, John Wiley & Sons Ltd, 2008.

[34] KJ Willam & EP Warnke, *Constitutive model for the triaxial behaviour of concrete*, Proceedings of the May 17-19 1974, International Association of Bridge and Structural Engineers Seminar on Concrete Structures Subjected to Triaxial Stresses, held at Bergamo Italy, 1974.

[35] DM Wood, *Geotechnical modelling*, Spon Press, 2004.

Chapter 5

Isotropic hyperplasticity

Frictional perfect-plasticity models provide a valuable but oversimplified idealisation of the inelastic behaviour of geomaterials. Drucker *et al.* [21] commented on the limitations of these elementary plasticity models:

> *"Soils having cohesion and internal friction are often considered to be perfectly plastic solids... However, such idealized treatment will often result in a marked difference between prediction and experimental fact. In particular, the strong dependence of the volume change under shearing action on the prior history of the soil cannot be properly taken into account."*

Purely frictional, perfect plasticity models, such as those presented in the preceding chapter, fail to capture the compactive volumetric response of clays under hydrostatic (or one-dimensional) drained loading. For example, simulating hydrostatic compression using a modified Reuleaux (mR) constitutive model produces a purely linear elastic response, which fails to reproduce the permanent compaction of clays under this loading. Such models are also unable to reproduce the differing volumetric responses of dense and loose soils when sheared, where dense samples dilate but loose samples compact. Through undertaking shear box tests on dense and loose sands, Casagrande [7] proposed the concept of a Critical State (CS), concluding that:

> *"Every cohesionless soil has a certain critical density, in which state it can undergo any amount of deformation or actual flow without volume change."*

Casagrande coined the term *critical void ratio* and found that it was influenced by the effective pressure, with higher pressures resulting in lower critical void ratios. This relationship between pressure and void ratio is known as the Critical State Line (CSL). The CS was succinctly defined by Roscoe *et al.* [42] as the ultimate state at which soil *"continues to deform at constant stress and void ratio"*. The key concepts of CS soil mechanics were explained using the drained and undrained response of a normally and a heavily overconsolidaed soil in Figure 1.2 of Section 1.2.

Many of the most successful constitutive models for particulate media can trace their roots to the works of Roscoe and co-researchers [42, 43] and, independently, Parry [37] on CS theory. Within this theory, the modified Cam-clay (MCC) constitutive model (following on from the original Cam-clay model [44]) was the first hardening plasticity model to become generally accepted for the analysis of soils [47]. Indeed, it was commented by Potts [38] in 2003 that every geotechnical analysis package should include *"a simple critical-state model such as modified Cam clay"*. This formulation, with associated plastic flow and ellipsoidal yield surface is able to conceptually capture several aspects of real soil behaviour [24]. These features include a volumetric response dependent on the stress history of the material, a unique state boundary surface, for which soils states outside are inadmissible, and a unique void ratio versus

CS stress line [24]. Despite these attractions, Yu [49] (amongst many others) commented that the MCC constitutive formulations significantly overestimate the peak stress on the *dry* side of the CSL (the heavily overconsolidated region) and, due to their associated flow rule, are unable to capture post-peak softening towards the CS in normally consolidated clays.

Building on the pioneering work from Ziegler [50], Houlsby [28] and Collins and Houlsby [8], several hyperplastic (see Section 2.2.2) models have been constructed for geomaterials [9–16, 30, 31, 40, 41]. These offer improvements over the conventional plasticity formulations which, in a number of cases, fail to satisfy fundamental thermodynamic principles. The hyperplastic formulations of Collins and co-workers embrace the CS as an asymptotic state, with the concept of non-associated flow arising naturally.

This chapter draws heavily on the paper by Coombs and Crouch [18]. Section 5.1 is concerned with the formulation of a two-parameter family of CS models using the principles of hyperplasticity introduced in Chapter 2. This family of models is extended to include a dependency on the third invariant of stress (via the Lode angle) in Section 5.2. Section 5.3 presents the backward Euler (bE) stress integration for the two-parameter family of models. The influence of the form of the yield function on the integration procedure is revealed, the errors associated with this implicit return are quantified and the robustness of the algorithm is investigated through Gudehus plots [26]. The section closes by presenting the consistent linearisation of the family of models. Section 5.4 describes the calibration procedure for the two-parameter model. This includes the four classical MCC constants and the additional α and γ material constants. The simulation capability of the two-parameter model is then compared with drained and undrained triaxial experimental data on Lower Cromer till (LCT) from Gens [23] in Section 5.5. Observations on the two-parameter model are made in Section 5.6.

The majority of the relations given in this chapter are expressed using principal stresses (again denoted by $(\hat{\cdot})$). In line with geotechnical convention, compressive stresses are positively valued. Here the principal stresses are ordered so that σ_1 is the most tensile, while σ_3 is the most compressive (that is $\sigma_1 \leq \sigma_2 \leq \sigma_3$). All stresses are treated as effective stresses, although the prime notation is omitted.

5.1 Formulation

5.1.1 Hyperelastic relationship

Particulate media typically demonstrate a dependence of the elastic bulk modulus on the effective pressure, or equivalently on the elastic volumetric strain. One common approach when defining the shear modulus is to calculate it directly from the bulk modulus, assuming a constant Poisson's ratio [24]. However, this leads to a non-linear elasticity model in which energy can be generated from certain loading cycles [4, 29, 51]. Here we use a variable bulk modulus with a constant shear modulus [29]. This can be achieved by adopting an elastic free-energy function of the form

$$\Psi_1 = \kappa p_r \exp\left(\frac{\varepsilon_v^{\mathrm{e}} - \varepsilon_{v0}^{\mathrm{e}}}{\kappa}\right) + G\Big(\{\gamma^{\mathrm{e}}\}^T\{\gamma^{\mathrm{e}}\}\Big) \qquad \left(\text{with} \quad \varepsilon_v^{\mathrm{e}} = \mathrm{tr}[\varepsilon^{\mathrm{e}}] \quad \text{and} \quad \{\gamma^{\mathrm{e}}\} = \{\varepsilon^{\mathrm{e}}\} - \frac{\varepsilon_v^{\mathrm{e}}}{3}\{1\}\right), \tag{5.1}$$

where κ is the bi-logarithmic elastic compressibility index[1], G is the shear modulus, p_r is the reference pressure and $\varepsilon_{v0}^{\mathrm{e}}$ is the elastic volumetric strain at that reference pressure[2]. The true stress is given by

[1] That is, the gradient of the swelling (drained unloading) line in the bi-logarithmic void ratio (or equivalently specific volume) versus hydrostatic pressure plane.

[2] The reference pressure can be considered as the starting pressure for a particular test (with $\varepsilon_{v0}^{\mathrm{e}} = 0$). In order to fix the swelling, normal consolidation and CS lines in the void ratio (or specific volume) versus hydrostatic pressure plane it is necessary to specify an initial void ratio. However, this void ratio is not required for displacement-based finite-element simulations.

the first derivative of (5.1) with respect to elastic strain

$$\{\sigma\} = \{\Psi_{1,\varepsilon^{\mathrm{e}}}\} = p_r \exp\left(\frac{\varepsilon_v^{\mathrm{e}} - \varepsilon_{v0}^{\mathrm{e}}}{\kappa}\right)\{1\} + 2G\{\gamma^{\mathrm{e}}\}. \tag{5.2}$$

The non-linear elastic stiffness matrix is obtained from the second derivative of (5.1) with respect to elastic strain

$$[\hat{D}^{\mathrm{e}}] = [\Psi_{1,\varepsilon^{\mathrm{e}}\varepsilon^{\mathrm{e}}}] = \left(K - \frac{2G}{3}\right)\{\hat{1}\}\{\hat{1}\}^T + 2G[1] \qquad \text{where} \qquad K = \frac{p_r}{\kappa}\exp\left(\frac{\varepsilon_v^{\mathrm{e}} - \varepsilon_{v0}^{\mathrm{e}}}{\kappa}\right), \tag{5.3}$$

where $\{\hat{1}\} = \{1 \quad 1 \quad 1\}^T$. The six-component stiffness and compliance matrices follow as

$$[D^{\mathrm{e}}] = \begin{bmatrix} [\hat{D}^{\mathrm{e}}] & [0] \\ [0] & G[1] \end{bmatrix} \qquad \text{and} \qquad \left[C^{\mathrm{e}}\right] = \left[D^{\mathrm{e}}\right]^{-1} = \begin{bmatrix} \left[\hat{C}^{\mathrm{e}}\right] & [0] \\ [0] & G^{-1}[1] \end{bmatrix} \tag{5.4}$$

where the principal compliance matrix is

$$\left[\hat{C}^{\mathrm{e}}\right] = \frac{1}{9}\left(\frac{1}{K} - \frac{3G}{2}\right)\{\hat{1}\}\{\hat{1}\}^T + \frac{1}{2G}[1] \tag{5.5}$$

and [0] is the 3 by 3 null matrix.

5.1.2 Plasticity relations

As proposed by Collins and Hilder [9], a *two-parameter* family of CS models can be defined using the following dissipation function

$$\dot{\Phi} = \sqrt{(\dot{\varepsilon}_v^{\mathrm{p}}A)^2 + (\dot{\varepsilon}_\gamma^{\mathrm{p}}B)^2}, \qquad \text{where} \quad A = (1-\gamma)p + \frac{\gamma}{2}p_c \quad \text{and} \quad B = M\Big((1-\alpha)p + \frac{\alpha\gamma}{2}p_c\Big). \tag{5.6}$$

The parameters α, $\gamma \in [0,1]$ influence the shape of the yield surface (as shown in Figure 5.1) and the degree of non-association of the plastic flow direction. $p = \mathrm{tr}([\sigma])/3$ is the mean pressure and p_c defines the size of the yield surface. M is the stress ratio at which constant volume plastic shearing occurs (geometrically, this is the gradient of the CSL in $p-q$ space, see Figure 5.2 (i)). The plastic strain invariants, similarly to (2.11), are defined as follows

$$\varepsilon_v^{\mathrm{p}} = \mathrm{tr}[\varepsilon^{\mathrm{p}}] \qquad \text{and} \qquad \varepsilon_\gamma^{\mathrm{p}} = \sqrt{\{\gamma^{\mathrm{p}}\}^T\{\gamma^{\mathrm{p}}\}}, \qquad \text{with} \qquad \{\gamma^{\mathrm{p}}\} = \{\varepsilon^{\mathrm{p}}\} - \frac{\varepsilon_v^{\mathrm{p}}}{3}\{1\}. \tag{5.7}$$

The deviatoric stress invariant, q, is given by

$$q = \sqrt{\{s\}^T\{s\}}, \qquad \text{with} \qquad \{s\} = \{\sigma\} - p\{1\}. \tag{5.8}$$

Note that this q $(5.8)_1$ differs from that often used when describing the triaxial tests of soils (there $q_{\mathrm{txl}} = (\sigma_3 - \sigma_1)$). Assuming a free-energy function of the form [8]

$$\Psi = \Psi_1\big(\{\varepsilon^{\mathrm{e}}\}\big) + \Psi_2\big(\{\varepsilon^{\mathrm{p}}\}\big), \qquad \Psi_2\big(\{\varepsilon^{\mathrm{p}}\}\big) = \frac{\gamma(\lambda-\kappa)}{2}p_r\exp\left(\frac{\varepsilon_v^{\mathrm{p}}}{\lambda-\kappa}\right), \tag{5.9}$$

where λ is the bi-logarithmic plastic compressibility index defining the gradient of the *virgin consolidation* line in bi-logarithmic void ratio (or specific volume) versus hydrostatic pressure space. With Ψ_1 given by

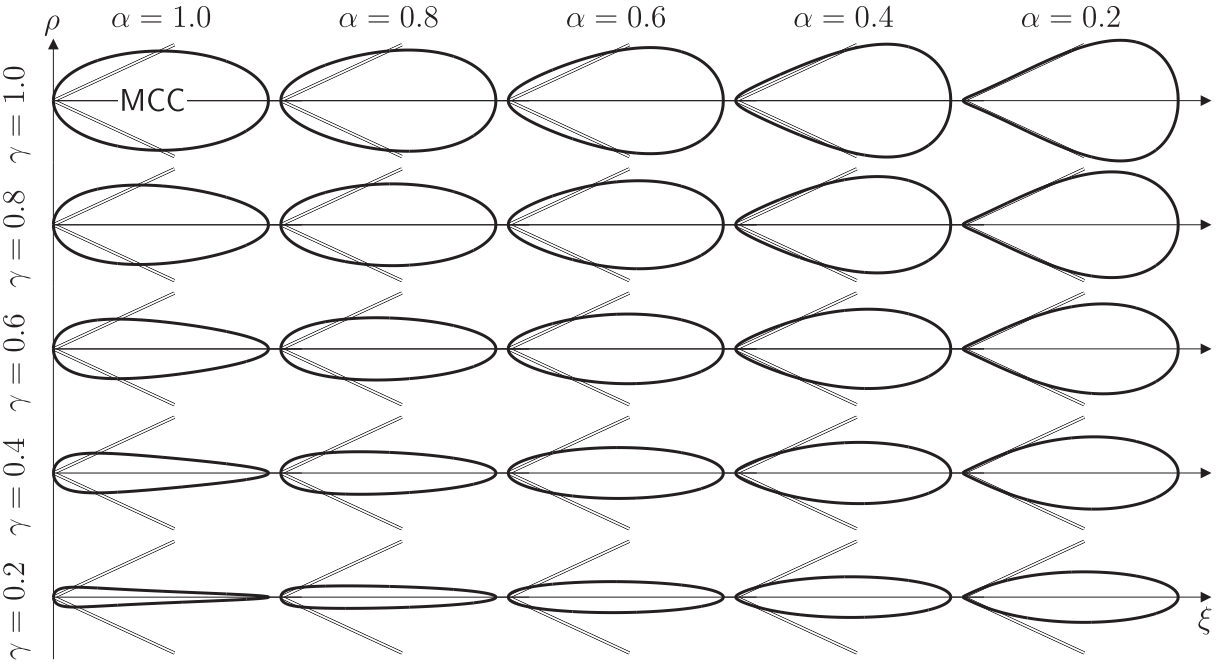

Figure 5.1: Family of yield surfaces in ξ, ρ stress space for the two-parameter CS hyperplastic model with α and γ varying over the range 0.2 to 1.0.

(5.1), the shift stress is defined as

$$\{\chi\} = \frac{\gamma p_c}{2}\{1\}, \qquad \text{with} \qquad p_c = p_r \exp\left(\frac{\varepsilon_v^{\mathrm{p}}}{\lambda - \kappa}\right). \tag{5.10}$$

Moving between dissipative and true stress space corresponds to a (pressure dependent) hydrostatic shifting of the yield surface. The form of hardening implied by (5.9) and (5.10) gives rise to an isotropic expansion/contraction of the surface coupled with a (kinematic) translation along the hydrostatic axis, as shown in Figure 5.2 (i). We can now define the dissipative stress invariants as

$$p^{\varphi} = \frac{\partial \dot{\Phi}}{\partial \dot{\varepsilon}_v^{\mathrm{p}}} = \frac{A^2 \dot{\varepsilon}_v^{\mathrm{p}}}{\dot{\Phi}} \qquad \text{and} \qquad q^{\varphi} = \frac{\partial \dot{\Phi}}{\partial \dot{\varepsilon}_\gamma^{\mathrm{p}}} = \frac{B^2 \dot{\varepsilon}_\gamma^{\mathrm{p}}}{\dot{\Phi}}. \tag{5.11}$$

Rearranging, we obtain the plastic strain rates as

$$\dot{\varepsilon}_v^{\mathrm{p}} = \frac{p^{\varphi}\dot{\Phi}}{A^2} \qquad \text{and} \qquad \dot{\varepsilon}_\gamma^{\mathrm{p}} = \frac{q^{\varphi}\dot{\Phi}}{B^2}. \tag{5.12}$$

Substituting (5.12) into (5.6) and eliminating $\dot{\Phi}$, we obtain the dissipative yield condition[3]

$$f^{\varphi} = (p^{\varphi})^2 B^2 + (q^{\varphi})^2 A^2 - A^2 B^2 = 0. \tag{5.13}$$

This defines an ellipse in dissipative (p^{φ}, q^{φ}) stress space. The dissipative stress invariants p^{φ} and q^{φ} are

[3]Note that the dissipative yield surface f^{φ} should be considered as an instantaneous surface for the stress state under consideration (with A and B treated as constants) and not a bound on the admissible stress states, as with the conventional yield surface f. As the stress state evolves, the major to minor axis ratio of the dissipative yield surface will change through being dependent on the hydrostatic pressure and p_c.

given by

$$p^{\varphi} = \frac{1}{3}\mathrm{tr}[\varphi] \qquad \text{and} \qquad q^{\varphi} = \sqrt{\{s^{\varphi}\}^T\{s^{\varphi}\}}, \qquad \text{where} \qquad \{s^{\varphi}\} = \{\varphi\} - p^{\varphi}\{1\}. \tag{5.14}$$

By substituting $(p - p^{\chi})$ for p^{φ} and q for q^{φ}, we arrive at the following expression for the yield function in true stress space

$$f = (p - \gamma p_c/2)^2 B^2 + q^2 A^2 - A^2 B^2 = 0. \tag{5.15}$$

For this f, the Critical State Surface (CSS) takes the form of a Drucker-Prager circular cone. If $\alpha = \gamma = 1$, then $A = B = p_c/2$ and the conventional MCC yield function with associated plastic flow [43] is recovered. In this case, moving between dissipative and true stress space involves a constant hydrostatic translation of the yield surface, as A and B are given by

$$A = p_c/2 \qquad \text{and} \qquad B = Mp_c/2,$$

independent of the hydrostatic pressure p. For values of $\gamma \in [0, 1]$, the intersection of the CSS and the yield surface occurs at $p = p_c\gamma/2$. The value of α has no influence on the location of that intersection. As γ reduces, so the yield surface becomes narrower deviatorically (see Figure 5.1). When $\gamma = 0$ the yield surface radius disappears. As α reduces, so the yield surface becomes more tear-drop shaped (with the tail at the stress origin, as seen in Figure 5.1). For $\alpha < 0.172$ the yield surface becomes concave near the stress origin [11]. When $\alpha = 0$, the yield surface lies entirely within the CSS.

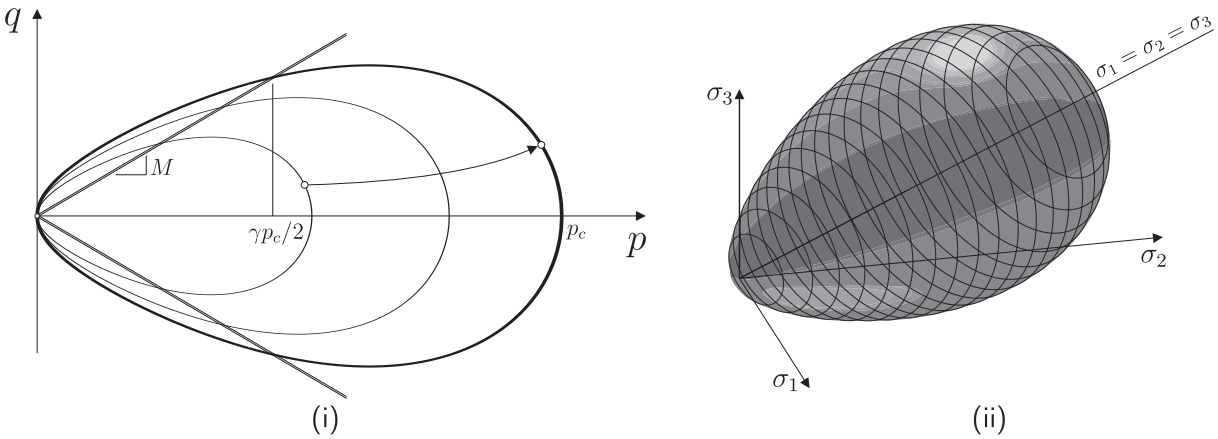

Figure 5.2: Yield surfaces for $\alpha = 0.6$ and $\gamma = 0.9$ with no Lode angle dependency (i) $p - q$ stress space showing isotropic hardening (ii) view of the surface in principal stress space.

By manipulating (5.15), the yield function can be written as

$$\begin{aligned} f &= \Big((p - \gamma p_c/2)^2 - A^2\Big)B^2 + A^2q^2, \\ &= \Big(p^2 - \gamma p_c p + \gamma^2(p_c)^2/4 - (1-\gamma)^2p^2 - \gamma(1-\gamma)p_c p - \gamma^2(p_c)^2/4\Big)B^2 + A^2q^2, \\ &= \Big(\gamma p(2-\gamma)(p - p_c)\Big)B^2 + A^2q^2 = 0. \end{aligned} \tag{5.16}$$

For this family of hyperplastic models, the direction of plastic flow is normal to the yield surface in dissipative stress space. Thus, the dissipative plastic flow direction is formed by taking the derivative of (5.13) with respect to the dissipative stress

$$\{f^{\varphi},_{\varphi}\} = \big(f^{\varphi},_{p^{\varphi}}\big)\{p^{\varphi},_{\varphi}\} + \big(f^{\varphi},_{q^{\varphi}}\big)\{q^{\varphi},_{\varphi}\}. \tag{5.17}$$

Using (5.14), (5.17) becomes

$$\{f^{\varphi}{}_{,\varphi}\} = \frac{2}{3}B^2 p^{\varphi}\{1\} + 2A^2\{s^{\varphi}\}. \tag{5.18}$$

Transforming into true stress space we obtain the direction of plastic flow as

$$\{g_{,\sigma}\} = \frac{2}{3}B^2(p - \gamma p_c/2)\{1\} + 2A^2\{s\}, \tag{5.19}$$

where the notation $\{g_{,\sigma}\}$ is used to suggest an equivalence with the derivative of the plastic potential used in conventional non-associated plasticity theory.

Using (5.6) and $(5.9)_2$ we have obtained the yield surface, direction of plastic flow and the isotropic hardening equations, as well as the hyperelastic relationship from (5.1), to fully define the constitutive relationship.

5.2 Lode angle dependency

It has been shown that ignoring the dependence of constitutive relations on the third invariant of stress can lead to significant overestimation of the stiffness in geotechnical analyses [17, 39]. A number of Lode angle dependencies (LAD) have been proposed in the literature, for example [2, 3, 33, 36, 45, 46]. Collins [11] combined the Matsuoka-Nakai (M-N) yield condition with the CS cone by re-defining q in the Spatially Mobilised Plane [36]. However, implementing the M-N deviatoric yield criteria in this manner constrains the admissible principal stress states to be compressive [9]. This can result in implausible or erroneous return stresses when using an implicit stress integration algorithm where the trial points lie in the tensile region.

Here we follow an alternative approach by introducing the LAD into the constitutive equations be redefining B as follows

$$B = \bar{\rho}(\theta)\underbrace{M\Big((1-\alpha)p + \frac{\alpha\gamma}{2}p_c\Big)}_{b_M}. \tag{5.20}$$

$\bar{\rho}(\theta) = \rho(\theta)/\rho_c$ is the normalised deviatoric radius and ρ_c is the deviatoric radius required to reach yield under a triaxial compression stress path where $\sigma_3/2 = -\sigma_2 = -\sigma_1$. Figure 5.3 compares Lode angle functions from Mohr-Coulomb (M-C) [45], mR [17, 19], M-N [36], Gudehus (Gud) [2], Willam-Warnke (W-W) [46] and Bhowmik-Long (B-L) [3] with four experimental data sets [1, 33–35]. It was shown in the preceding chapter (Figure 4.4) that particulate materials have a dependence on both the Lode angle and the intermediate principal stress. The effective friction angle in Figure 5.3 is again calculated from (4.11). In Figure 5.3, the M-C envelope (unlike the other deviatoric functions) exhibits no sensitivity to σ_2. When compared with experimental data, it is revealed that the Gudehus LAD significantly overestimates both the normalised deviatoric radius and the effective friction angle. Table 5.1 gives the error, calculated from (4.10), between the experimental data and the six LADs. The normalised deviatoric radius under triaxial extension for the M-C, M-N and Gudehus LADs was fixed, given by (4.3); whereas $\bar{\rho}_e$ for the mR, W-W and B-L models was allowed to vary. The values of $\bar{\rho}_e$ for these models are given in Figure 5.3, together with the additional material constant (the normalised shear radius, $\bar{\rho}_s$) required by the B-L model.

Although the Bhowmik-Long LAD arguably provides the most satisfactory fit to the experimental data with the lowest errors in Table 5.1, it requires the additional parameter, $\bar{\rho}_s$, which can only be determined using a rather sophisticated multiaxial test apparatus, of which there are few. The W-W LAD provides a balance between offering good agreement with the experimental data yet, requires only one parameter, $\bar{\rho}_e$.

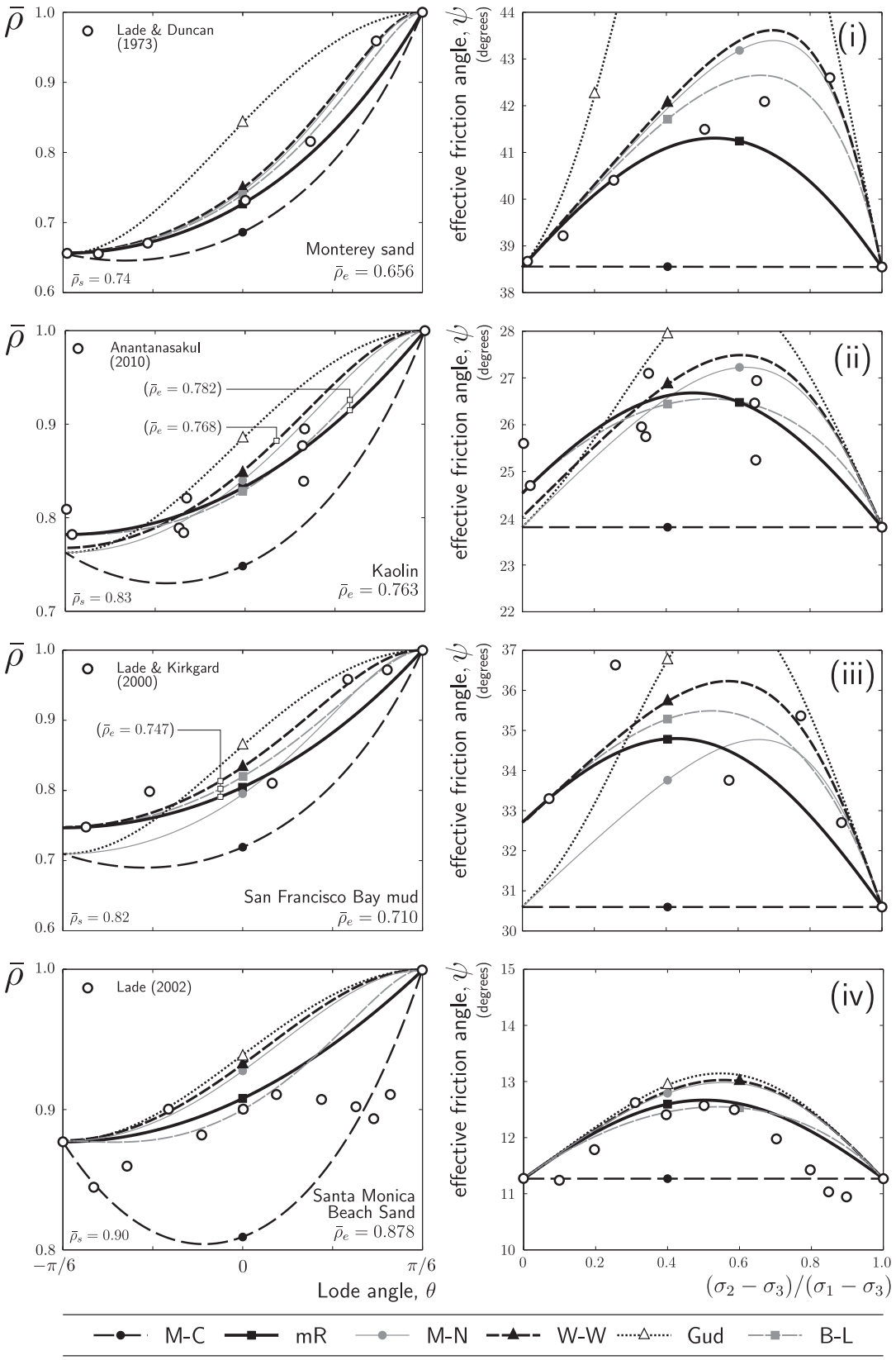

Figure 5.3: Comparison of Lode angle deviatoric functions with experimental data from (i) Monterey sand [33], (ii) Kaolin [1], (iii) San Francisco Bay mud [34] and (iv) Santa Monica Beach sand [35]: deviatoric Lode angle dependency and variation of the effective friction angle with the ratio of the intermediate principal stress.

material	model	M-C	mR	M-N	Gud	W-W	B-L
	MS	0.0343	0.0154	0.0089	0.0453	0.0094	0.0088
	K	0.0505	0.0136	0.0202	0.0375	0.0169	0.0128
	SFBM	0.0697	0.0229	0.0268	0.0344	0.0175	0.0174
	SMBS	0.0418	0.0279	0.0405	0.0447	0.0384	0.0282

Table 5.1: LAD errors between Mohr-Coulomb (M-C), modified Reuleaux [17, 19] (mR), Matsuoka-Makai [36] (M-N), Gudehus [2] (Gud) Willam-Warnke [46] (W-W) and Bhowmik-Long [3] (B-L) and experimental data from Monterey sand (MS) [33], Kaolin (K) [1], San Francisco Bay mud (SFBM) [34], Santa Monica Beach sand (SMBS) [35].

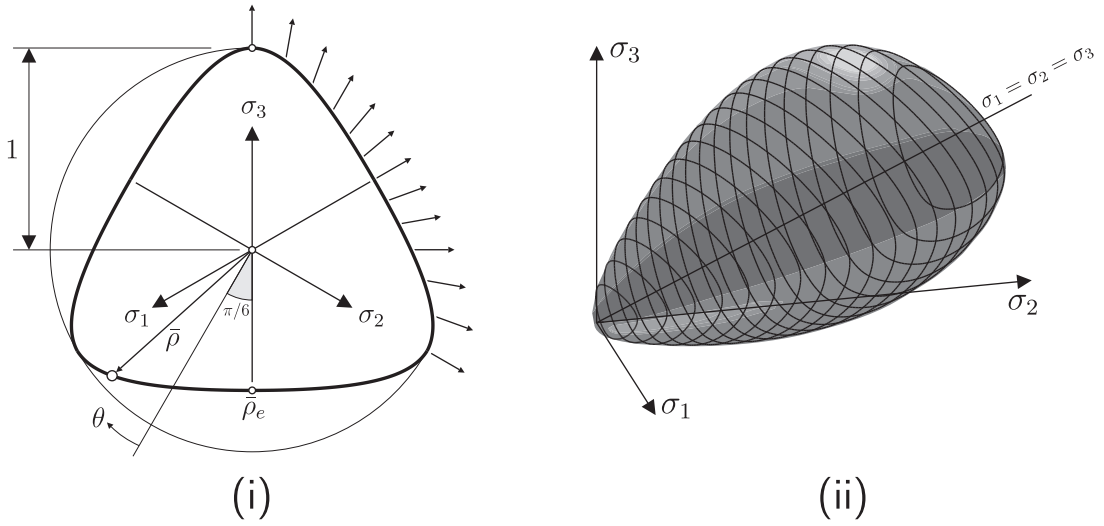

Figure 5.4: (i) Willam-Warnke deviatoric section illustrating the direction of the (non-associated) radial deviatoric plastic flow and (ii) two-parameter ($\alpha = 0.5$, $\gamma = 1$) CS model with a W-W deviatoric section.

The W-W LAD (as seen in Figure 5.4 (i)) can be expressed as

$$\bar{\rho}(\theta) = \frac{a_1 C + \sqrt{2a_1 C^2 + a_2}}{2a_1 C^2 + 1} \quad \in [\bar{\rho}_e, 1] \qquad \text{where} \qquad a_1 = \frac{2(1-\bar{\rho}_e^2)}{(2\bar{\rho}_e - 1)^2}, \qquad a_2 = \frac{5\bar{\rho}_e^2 - 4\bar{\rho}_e}{(2\bar{\rho}_e - 1)^2} \tag{5.21}$$

and $C = \cos(\pi/6 - \theta)$. The Lode angle θ is defined by $(2.9)_3$. $(5.21)_1$ describes a deviatoric section (with six-fold symmetry) formed by a portion of an ellipse. In the absence of triaxial extension data, $\bar{\rho}_e$ can be estimated based on the friction angle (ϕ) through (4.3), so that $\bar{\rho}_e$ coincides with that of M-C. The gradient M, when $\theta = \pi/6$, is obtained (again from the friction angle) through the rearrangement of (4.11) to obtain

$$M = \frac{2\sqrt{6}\sin(\phi)}{3 - \sin(\phi)}. \tag{5.22}$$

For other Lode angles, the gradient is given by $\bar{\rho}(\theta)M$. Note the non-standard definition of M based on the friction angle due to the definition of q from $(5.8)_1$, resulting in a difference of $\sqrt{2/3}$ between (5.22) and the definition used by Schofield and Wroth [44]. The yield equation and the direction of plastic flow are still expressed by (5.16) and (5.19) but with B defined from (5.20). The effect of introducing a W-W LAD on the two-parameter yield surface can be seen in Figure 5.4 (ii). The yield surface has a friction angle of $\phi = \pi/9$ radians and a $\bar{\rho}_e$ value of 0.8.

5.3 Numerical implementation

5.3.1 Backward Euler stress integration

In order to integrate the stress rates over a finite strain increment, once again the bE scheme (as described in Section 2.3) is used. Working with elastic strains as the primary unknown, the return mapping can be expressed as

$$\{\hat{\varepsilon}^{\mathrm{e}}\} = \{\hat{\varepsilon}^{\mathrm{e}}_t\} - \Delta\gamma\{g_{,\hat{\sigma}}\}, \tag{5.23}$$

where $\{\hat{\varepsilon}^{\mathrm{e}}_t\}$ are the principal elastic trial strains. $\Delta\gamma$ is the incremental plastic multiplier for the entire return path and the plastic flow direction $\{g_{,\hat{\sigma}}\}$ is determined at the final return state. The rate of evolution of the size of the yield surface follows from $(5.9)_2$ as

$$\dot{p}_c = \left(\frac{\partial p_c}{\partial \varepsilon^{\mathrm{p}}_v}\right)\dot{\varepsilon}^{\mathrm{p}}_v = \left(\frac{p_c}{\lambda-\kappa}\right)\dot{\varepsilon}^{\mathrm{p}}_v. \tag{5.24}$$

This hardening law is equivalent to specifying a bi-logarithmic linear relationship between the specific volume, v, and the pre-consolidation pressure, p_c [4]. The limitations of the conventional linear relationship between specific volume (or void ratio) and the logarithm of the pre-consolidation pressure were identified by Butterfield [6]. More recently, the appropriateness of the bi-logarithmic law for finite deformation analysis was verified by Hashiguchi [27] and used by Yamakawa *et al.* [48]. Implicit integration of (5.24) yields the following hardening law

$$\tilde{p}_c = \frac{p_{c_n}}{(1 - \Delta\varepsilon^{\mathrm{p}}_v/(\lambda-\kappa))}, \tag{5.25}$$

where p_{c_n} is the size of the yield surface from the previously converged solution associated with the last step (or the initial state at the start of the analysis). We denote the evolution of p_c with $\tilde{(\cdot)}$ to distinguish it from the incremental updating of p_c from the bE method through (2.47). Using (5.23) and (5.25), together with the consistency condition, $f = 0$, we can define the following residuals and unknowns

$$\{b\} = \begin{Bmatrix} \{\hat{\varepsilon}^{\mathrm{e}}\} - \{\hat{\varepsilon}^{\mathrm{e}}_t\} + \Delta\gamma\{g_{,\hat{\sigma}}\} \\ p_c - \tilde{p}_c \\ f \end{Bmatrix} = \begin{Bmatrix} \{0\} \\ 0 \\ 0 \end{Bmatrix} \quad \text{and} \quad \{x\} = \begin{Bmatrix} \{\hat{\varepsilon}^{\mathrm{e}}\} \\ p_c \\ \Delta\gamma \end{Bmatrix}. \tag{5.26}$$

We obtain the (5×5) Hessian matrix (see (2.45) for details on the format of the matrix) from the partial derivatives of the residuals with respect to the unknowns as

$$[A] = \begin{bmatrix} [1] + \Delta\gamma[g_{,\hat{\sigma}\hat{\sigma}}][\hat{D}^{\mathrm{e}}] & \Delta\gamma\{g_{,\hat{\sigma}p_c}\} & \{g_{,\hat{\sigma}}\} \\ -\{\tilde{p}_{c,\hat{\sigma}}\}^T[\hat{D}^{\mathrm{e}}] & 1 - (\tilde{p}_{c,p_c}) & -(\tilde{p}_{c,\Delta\gamma}) \\ \{f_{,\hat{\sigma}}\}^T[\hat{D}^{\mathrm{e}}] & f_{,p_c} & 0 \end{bmatrix}, \tag{5.27}$$

where $[\hat{D}^{\mathrm{e}}]$ is the 3×3 elastic stiffness matrix (5.3). The derivatives of $\tilde{p}_c$ are given by

$$\{\tilde{p}_{c,\hat{\sigma}}\}^T = \Delta\gamma p_n\{\hat{1}\}^T[g_{,\hat{\sigma}\hat{\sigma}}], \qquad (\tilde{p}_{c,p_c}) = \Delta\gamma p_n\{g_{,\hat{\sigma}p_c}\}^T\{\hat{1}\}, \qquad (\tilde{p}_{c,\Delta\gamma}) = p_n\{g_{,\hat{\sigma}}\}^T\{\hat{1}\}, \tag{5.28}$$

with

$$p_n = \frac{\partial\tilde{p}_c}{\partial(\Delta\varepsilon^{\mathrm{p}}_v)} = \frac{p_{c_n}}{(\lambda-\kappa)(1 - \Delta\varepsilon^{\mathrm{p}}_v/(\lambda-\kappa))^2}. \tag{5.29}$$

The derivative of the yield function (5.16) with respect to the principal stresses is given by

$$\{f_{,\hat{\sigma}}\} = \frac{f_{,p}}{3}\{\hat{1}\} + 2A^2\{\hat{s}\} + 2\gamma\bar{\rho}(\theta)b_M^2 p(2-\gamma)(p-p_c)\{\bar{\rho}_{,\hat{\sigma}}\}, \tag{5.30}$$

where b_M is given in (5.20) and

$$f_{,p} \quad = \quad (2-\gamma)\gamma\Big(2\bar{\rho}(\theta)M(1-\alpha)(p-p_c)p + B(2p-p_c)\Big)B + 2A(1-\gamma)q^2. \tag{5.31}$$

The derivative of $\rho(\theta)$ with respect to $\{\hat{\sigma}\}$ is obtained through the chain rule as

$$\{\bar{\rho}_{,\hat{\sigma}}\} = \bar{\rho}_{,\theta}\,\{\theta_{,\hat{\sigma}}\}, \tag{5.32}$$

where the derivative of the Lode angle with respect to stress is given in Appendix C.1. $\bar{\rho}_{,\theta}$ will depend on the particular LAD. The derivative of the W-W LAD (5.21) with respect to stress is given in Appendix C.2.

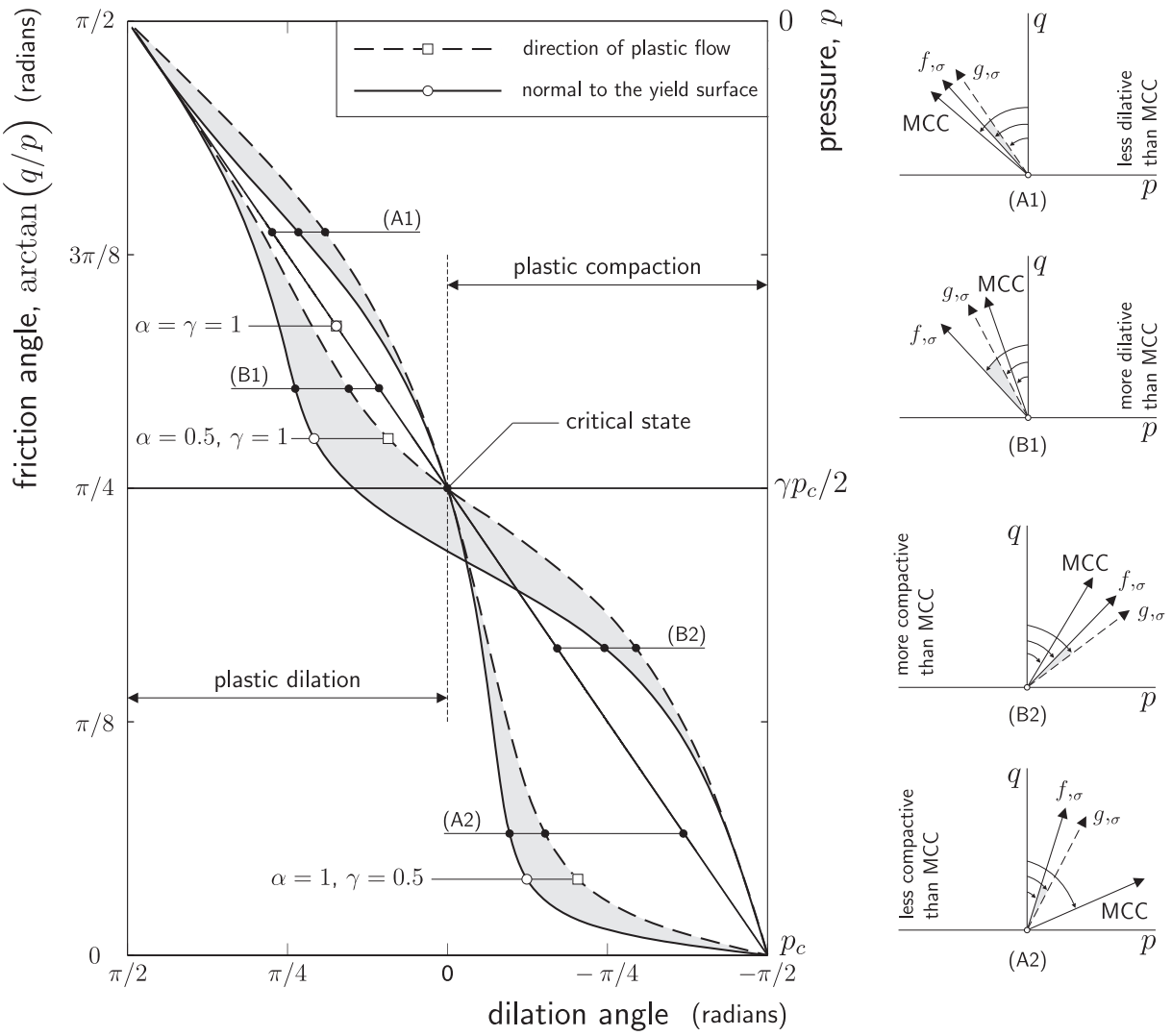

Figure 5.5: Dilation angle for the plastic flow direction and the normal to the yield surface for $\alpha = \gamma = 1$, $\alpha = 0.5$, $\gamma = 1$ (B1-2) and $\alpha = 1$, $\gamma = 0.5$ (A1-2). The width of the shaded region indicates the degree of non-associatedness of the flow.

Comparing (5.30) with (5.19), it is apparent that incorporating a LAD within the constitutive model

results in deviatorically non-associated plastic flow (Figure 5.4 (i)). The model is also volumetrically non-associated, except for the case $\alpha = \gamma = 1$, where the formulation reduces to the classical MCC (albeit with a W-W LAD). Figure 5.5 illustrates the variation of the dilation angle ($-\arctan(\dot{\varepsilon}_v^{\mathrm{p}}/\dot{\varepsilon}_\gamma^{\mathrm{p}})$) with the mobilised friction angle ($\arctan(q/p)$). That figure also shows the direction of the normal to the yield surface for the case where $M = 1$. When $\alpha = 1$, the normals to the yield surface and the direction of plastic flow coincide at $q/p = M$ ($\arctan(q/p) = \pi/4$), whereas for $\alpha \neq 1$ this is no longer the case. For $\alpha \neq 1$ and $\gamma \neq 1$, $\{f_{,\sigma}\}$ and $\{g_{,\sigma}\}$ only coincide at the stress origin and the compressive closure point on the hydrostatic axis (specifically at $p = 0$ and $p = p_c$). When $\alpha \neq 1$ or $\gamma \neq 1$, the normal to the plastic potential is oriented at a lower dilation angle[4] than that given by the normal to the yield surface, for a given stress ratio q/p.

The derivative of (5.16) with respect to p_c is given by

$$f_{,p_c} = \gamma\Big(p(2-\gamma)\big(\gamma\alpha\bar{\rho}(\theta)M(p-p_c) - B\big)B + Aq^2\Big). \tag{5.33}$$

From the direction of plastic flow (5.19), the second derivative of the plastic potential with respect to $\{\hat{\sigma}\}$ follows as

$$[g_{,\hat{\sigma}\hat{\sigma}}] = \frac{1}{3}\{g_{,\hat{\sigma}p}\}\{\hat{1}\}^T + 2A^2[\delta] + \frac{4}{3}\bar{\rho}(\theta)b_M^2(p-\gamma p_c/2)\{\hat{1}\}\{\bar{\rho}_{,\hat{\sigma}}\}^T, \tag{5.34}$$

where $\big[\delta\big] = [1] - \{\hat{1}\}\{\hat{1}\}^T/3$ and

$$\{g_{,\hat{\sigma}p}\} \;=\; \frac{2}{3}\Big(B^2 + 2\bar{\rho}(\theta)MB(1-\alpha)(p-\gamma p_c/2)\Big)\{\hat{1}\} + 4A(1-\gamma)\{\hat{s}\}. \tag{5.35}$$

Finally, the derivative of (5.19) with respect to p_c is obtained as

$$\{g_{,\hat{\sigma}p_c}\} = \frac{\gamma B}{3}\Big(2\alpha\bar{\rho}(\theta)M(p-\gamma p_c/2) - B\Big)\{\hat{1}\} + 2\gamma A\{\hat{s}\}. \tag{5.36}$$

This provides the derivatives necessary to form (5.27).

Note that as a consequence of the magnitude of f (with units of stress raised to the power four) it is necessary to divide f, $\{g_{,\hat{\sigma}}\}$ and their derivatives by a large constant value when implementing the bE return to avoid the Hessian matrix becoming ill-conditioned. Dividing by the yield function value at the trial stress state offers a simple, effective remedy.

The iterative increment in the unknowns, $\{x\}$, is given by (2.47), with the starting conditions given by (2.48). The Newton-Raphson process continues until the residuals converge to within a prescribed tolerance. Throughout the stress return, all of the derivatives are evaluated at the current state. This requires the repeated evaluation of the derivatives at each iteration. The sequence for a general bE stress return was given in Figure 2.2 where i indicates the current iteration number. The pseudo-code for this algorithm is supplied in Figure 5.6.

5.3.2 Influence of the form of f

The form of the yield function, f, significantly affects the robustness and efficiency of the bE stress integration method. The function given by (5.16), with $\bar{\rho}_e = 1$, is quite different to that used by Collins and co-workers [9–11, 13] who adopted the form

$$f = \frac{(p-\gamma p_c/2)^2}{A^2} + \frac{q^2}{B^2} - 1 = 0. \tag{5.37}$$

[4]That is, the dashed lines (plastic flow direction) in Figure 5.5 always lie to the right of the continuous lines (normal to the yield surface).

1. INPUT: $\{\varepsilon_t^e\}$, p_{c_n} and p_r
2. CONSTANTS: κ, λ, G, M, $\bar{\rho}^e$, γ and α
   (a) Transform the trial elastic strain $\{\varepsilon_t^e\}$ into principal strain components (that is, find the eigenvalues and associated eigenvectors)
   (b) Calculate the principal trial elastic stress $\{\hat{\sigma}_t\}$ from (5.2)
   (c) Determine the trial yield function $(5.16)_1$
   (d) IF $f <$ `tol`
      - Elastic response, $\{\hat{\sigma}\} = \{\hat{\sigma}_t\}$ and $\{\varepsilon^e\} = \{\varepsilon_t^e\}$
      - $[\hat{D}^{alg}] = [\hat{D}^e]$ from (5.3)
   (e) ELSE
      - Elastoplastic response, set the initial conditions for the bE stress integration (2.48)
      - Calculate the derivatives required for the Hessian matrix $[A]$ (5.27)
      - WHILE $|\{b\}| >$ `tol` AND `itnum` $<$ `maxIt`
        - `itnum` = `itnum` + 1
        - Form the Hessian matrix $[A]$ (5.27) and calculate the increment in the unknowns (2.47)
        - Update the unknowns $\{\hat{\varepsilon}^e\}$, p_c and $\Delta\gamma$
        - Update $\{\hat{\sigma}\}$ and $[\hat{D}^e]$ from $\{\hat{\varepsilon}^e\}$ using (5.2) and (5.3)
        - Calculate the derivatives required for the Hessian matrix $[A]$ (5.27)
        - Calculate the residuals $\{b\}$ (5.26)
      - Form the six component derivatives required for the consistent tangent from (5.43)
      - Calculate the consistent tangent from (5.44)
   (f) Transform the principal measures back to generalised stress space using the eigenvectors from the trial elastic strain (C.17)
3. OUTPUT: $\{\varepsilon^e\}$, $\{\sigma\}$, $[D^{alg}]$ and p_c

Figure 5.6: Pseudo-code for the two-parameter family of CS models. The tolerance (`tol`) was typically set to 1×10^{-12}, with a maximum of 25 iterations (`maxIt`) to find converegence.

Manipulating (5.13) we can obtain any number of different forms of the yield function in dissipative stress space. Through one such manipulation, we can obtain the following

$$f^{\varphi} = \frac{\left(p^{\varphi}\right)^4}{A^4} - \left(1 - \frac{\left(q^{\varphi}\right)^2}{B^2}\right)^2 = 0 \tag{5.38}$$

which transforms to become

$$f = \frac{\left(p - \gamma p_c/2\right)^4}{A^4} - \left(1 - \frac{q^2}{B^2}\right)^2 = 0 \tag{5.39}$$

in true stress space. (5.16), (5.37) and (5.39) describe the same yield surface. However, the nature of the yield function outside the yield surface ($f > 0$) is very different for the three cases (that is, equations (5.16), (5.37) and (5.39)). Figure 5.7 shows contours of f outside the yield surface for (i) (5.37), (iii) (5.16) and (iv) (5.39) when $\alpha = \gamma = 0.5$ and $\bar{\rho}_e = 1$. Note that these plots have been produced for the case where no LAD is present. Thus the deviatoric stress return is radial in this illustrative example. Where $10 < f$, the contours have been plotted in intervals of 10 up to a maximum of 200. For (5.37) we

see in Figure 5.7 (i) a local minimum around $(p/p_c) = -3$ and very high local curvature plus a maximum around $(p/p_c) = -0.5$ (see detail in Figure 5.7 (ii)). The presence of these minima and maxima could cause significant problems for a bE stress return algorithm. However, they are completely removed by using (5.16); see Figure 5.7 (iii). (5.39) contains negative regions outside the yield surface, as shown in Figure 5.7 (iv). If a trial stress state is located within one of these regions then the constitutive model falsely predicts a purely elastic response despite the stress being outside the yield surface.

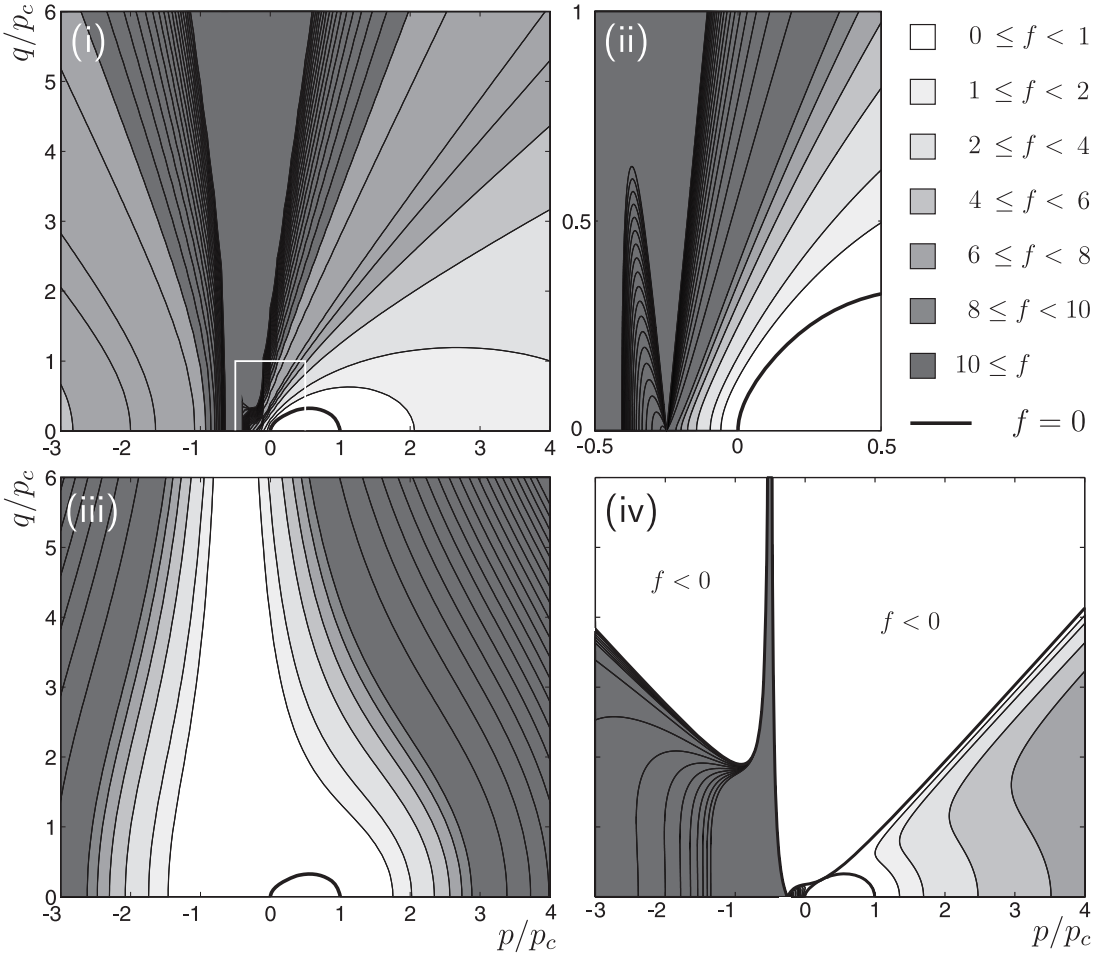

Figure 5.7: Contours of the yield function outside of the yield surface for a two-parameter CS model where $\alpha = \gamma = 0.5$ (i) f given by (5.37) from [9–11, 13], (ii) local detail of f given by (5.37), (iii) f given by (5.16) and (iv) f from (5.39) with negative regions appearing outside the yield surface.

Figure 5.8 shows stress return paths for the three forms of f: (5.16), (5.37) and (5.39). A reference pressure of 100kPa, compressibility index of $\kappa = 0.01$, initial elastic volumetric strain $\varepsilon^{\mathrm{e}}_{v0} = 0$ and a shear modulus of $G = 2$MPa were used for the material's elastic properties. $p_c = 200$kPa, $M = 0.6$, $\lambda = 0.1$, $\alpha = 0.5$, $\gamma = 0.5$ and $\bar{\rho}_e = 1$ define the yield surface. The models were subjected to a trial elastic strain state, as given in Table 5.2, and their return paths observed. The size of the yield surface displayed in Figure 5.8 corresponds to the final $p_{c_{n+1}}$ value from the stress return associated with (5.16).

In Figure 5.8 (i) the different returns associated with the three forms of yield function are compared. The trial state is given a hydrostatic stress of zero (that is, the trial point lies in the π-plane). This provides a particularly challenging state from which to start a bE stress integration. The values of the trial yield function (f_t), trial stress state ($\{\sigma_t\}$), final stress state ($\{\sigma_{n+1}\}$), final size of the yield surface ($p_{c_{n+1}}$) and the number of iterations to find convergence (it_{max}) are given in Table 5.2. The value of the

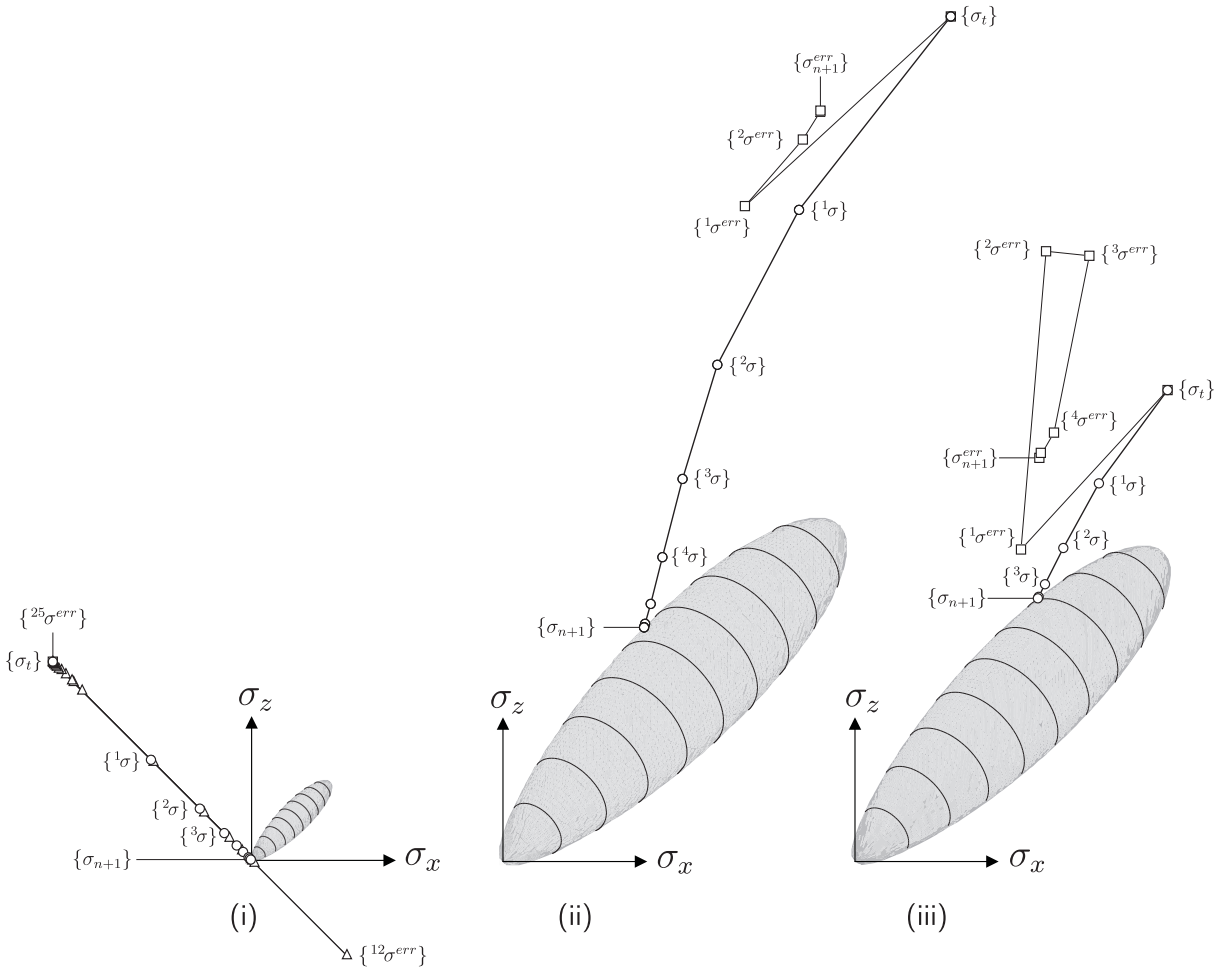

Figure 5.8: Stress returns associated with yield functions (5.16), (5.37) and (5.39) for three different trial states.

yield function (5.39) at the trial state is negative, thus the constitutive model predicts an elastic response, which is not what is intended. (5.37) fails to converge after 24 iterations and the size of the yield surface takes a meaningless negative value. The stress state after the 24^{th} iteration is denoted by $\{^{24}\sigma^{err}\}$. The return path oscillates either side of the stress origin, unable to converge back onto the yield surface. Only the model with the yield function described by (5.16) arrives at the appropriate stress state, although 19 iterations are required to converge within the specified tolerance. In this case the yield surface has contracted (softened) to 27% of its original size due to the significant plastic dilation associated with the stress return.

Figures 5.8 (ii) and (iii) demonstrate the false stress returns produced by (5.39). In addition, this yield function gave rise to incorrect $p_{c_{n+1}}$ values and wrong algorithmic tangent matrices, whereas (5.16) correctly converges back onto the yield surface for both trial stress states in eight and six iterations respectively.

The stress returns shown in Figure 5.8 emphasis the importance of using an appropriate form for f in the bE integration scheme and confirm that (5.16) provides a far more useful expression than (5.37) or (5.39). The stability issues of implicit stress integration algorithms were recently investigated by Brannon and Leelavanichkul [5] who proposed a two stage algorithm to improve the efficiency of such schemes. The first step involved returning to a rigid Drucker-Prager cone, the second stage took this return state as an initial estimate for a steepest-descent return algorithm. Their paper highlighted the importance of

	f	f_t	$\{\varepsilon_t^e\}$	$\{\sigma_t\}$ (kPa)	$\{\sigma_{n+1}\}$ (kPa)	$p_{c_{n+1}}(kPa)$	iterations
(i)	(5.16)	9.492×10^{19}	$\begin{Bmatrix} -0.1444 \\ -0.1100 \\ -0.0756 \end{Bmatrix}$	$\begin{Bmatrix} -137.78 \\ 0 \\ 137.78 \end{Bmatrix}$	$\{-0.156 \quad 0.016 \quad 0.189\}^T$	54.09	19
	(5.37)	1.688×10^2			$\{-137.54 \quad 0 \quad 137.54\}^T$	-6.787×10^6	24+
	(5.39)	-2.814×10^4			$\{-137.78 \quad 0 \quad 137.78\}^T$	200	0
(ii)	(5.16)	4.715×10^{21}	$\begin{Bmatrix} -0.0294 \\ 0.0050 \\ 0.0394 \end{Bmatrix}$	$\begin{Bmatrix} 310.39 \\ 448.17 \\ 585.95 \end{Bmatrix}$	$\{97.75 \quad 130.06 \quad 162.38\}^T$	231.87	8
	(5.39)	3.9639			$\{220.09 \quad 370.40 \quad 520.72\}^T$	204.33	5
(iii)	(5.16)	3.465×10^{20}	$\begin{Bmatrix} -0.0104 \\ 0.033 \\ 0.0171 \end{Bmatrix}$	$\begin{Bmatrix} 216.71 \\ 271.83 \\ 326.94 \end{Bmatrix}$	$\{126.74 \quad 154.62 \quad 182.49\}^T$	213.38	6
	(5.39)	1.905			$\{128.82 \quad 206.09 \quad 283.37\}^T$	206.35	7

Table 5.2: Stress return values for different yield functions (see Figure 5.8).

the form of the yield function, f, identifying the same potential pitfalls of non-uniqueness, inappropriate descent directions and erroneous elastic regions, as addressed in this section.

5.3.3 Error analysis

The accuracy of the stress return algorithm was assessed over the range $1 \leq q_t/q_y \leq 10$ and $-\pi/6 \leq \theta \leq \pi/6$ for $p_t/p_{c_n} = 0.1$, 0.3, 0.5, 0.7 and 0.9 for three of the two-parameter models: $\alpha = \gamma = 1$ (MCC), $\alpha = \gamma = 0.5$ and $\alpha = 0.6$, $\gamma = 0.9$. q_y is the deviatoric yield stress under triaxial compression at a particular pressure, p. A reference pressure of 100kPa, compressibility index of $\kappa = 0.01$, initial elastic volumetric strain $\varepsilon_{v0}^e = 0$ and shear modulus of $G = 2$MPa were used for the material's elastic properties. $p_{c_n} = 200$kPa, $M = 0.6$, $\bar{\rho}_e = 0.8$ and $\lambda = 0.1$ define the yield surface. The starting point for the error analysis was a hydrostatic stress state equal to the pressure under consideration. The constitutive model was then subjected to a deviatoric elastic strain increment corresponding to the trial stress state. The return stress from this single strain increment was compared with the solution obtained by splitting the same strain increment into 1,000 sub-increments and the errors calculated using (4.10).

	p_t/p_{c_n}	(i) $\alpha = \gamma = 1$			(ii) $\alpha = \gamma = 0.5$			(iii) $\alpha = 0.6$, $\gamma = 0.9$		
		$\Delta p_{c_{max}}/p_{c_n}$	it_{max}	e_{max}	$\Delta p_{c_{max}}/p_{c_n}$	it_{max}	e_{max}	$\Delta p_{c_{max}}/p_{c_n}$	it_{max}	e_{max}
(A)	0.1	−11.74%	7	24.08%	−4.48%	7	9.35%	−9.36%	7	20.88%
(B)	0.3	−4.35%	8	8.46%	1.28%	8	3.25%	−3.29%	7	6.75%
(C)	0.5	0.00%	8	0.00%	5.38%	8	13.65%	0.93%	8	1.90%
(D)	0.7	3.09%	7	6.28%	8.18%	9	21.57%	4.05%	8	8.52%
(E)	0.9	5.18%	7	11.62%	9.18%	8	28.02%	6.19%	8	14.23%

Table 5.3: Error and return quantities associated with the iterative bE stress return for the five pressure ratios in Figure 5.9 for $\alpha = \gamma = 1$, $\alpha = \gamma = 0.5$ and $\alpha = 0.6$, $\gamma = 0.9$.

Stress iso-error maps, using the error measure between the single increment and the sub-incremented stress returns defined in the previous chapter by (4.32), are given in Figure 5.9 for (i) $\alpha = \gamma = 1$ (MCC), (ii) $\alpha = \gamma = 0.5$ and (iii) $\alpha = 0.6$, $\gamma = 0.9$. Errors up to 28.0% appear for the $\alpha = \gamma = 0.5$ model at $p_t/p_{c_n} = 0.9$, when q_t/q_y is close to 10; this is not unexpected for such a large strain increment. For

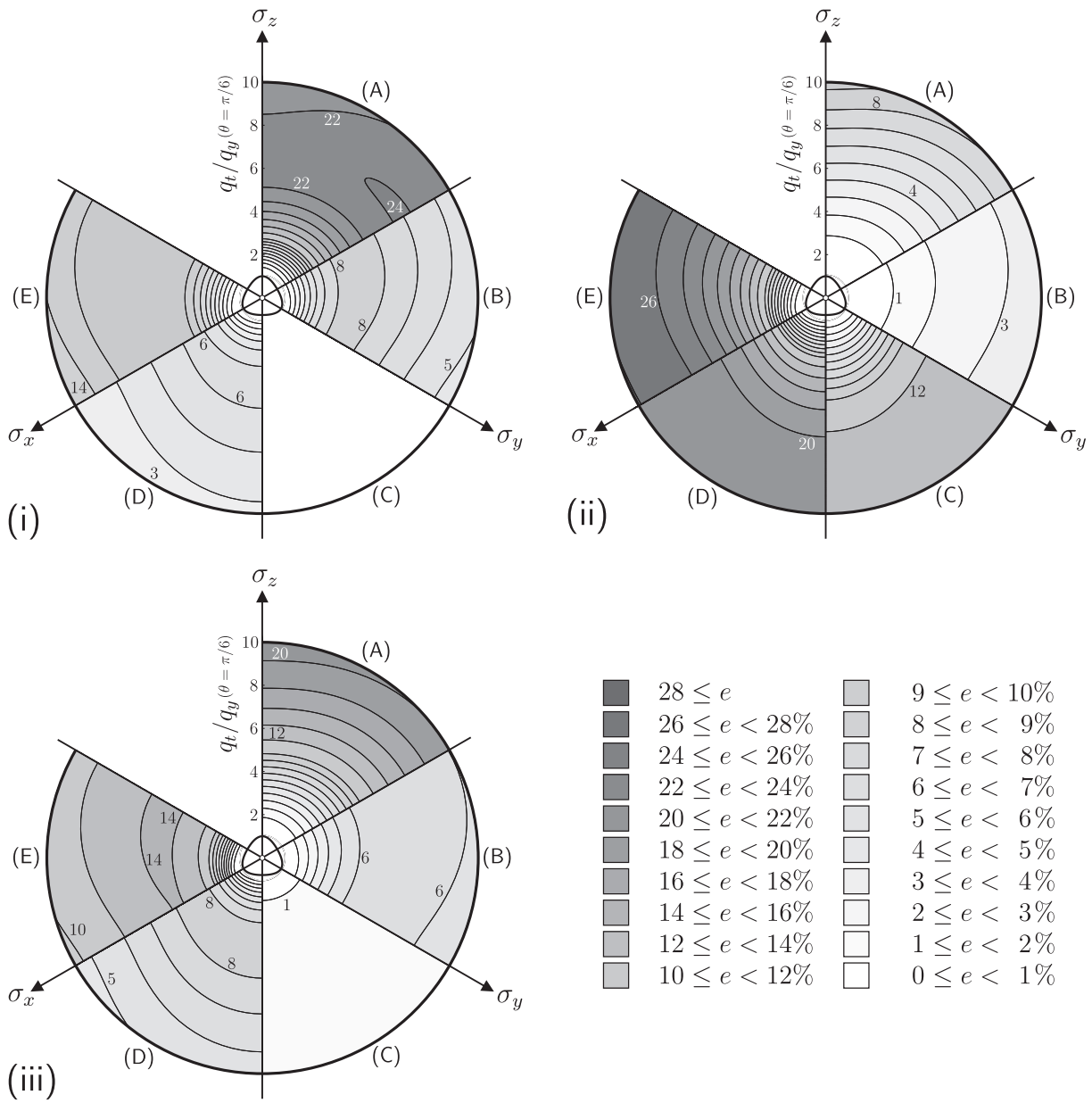

Figure 5.9: Errors associated with the iterative bE stress return for five pressure ratios (A) $p/p_c = 0.1$, (B) $p/p_c = 0.3$, (C) $p/p_c = 0.5$, (D) $p/p_c = 0.7$ and (E) $p/p_c = 0.9$ for (i) $\alpha = \gamma = 1$, (ii) $\alpha = \gamma = 0.5$ and (iii) $\alpha = 0.6$, $\gamma = 0.9$.

the same model at $p_t/p_{c_n} = 0.3$, the maximum error is less than 3.3%. All of the models have stress errors of less than 5% for $q_t/q_y < 2$. For the majority of the pressure ratios (the exception being MCC for $p_t/p_{c_n} = 0.1$), higher errors (within a particular sextant) are seen near the compression meridians due to the higher curvature in the yield surface. The region of the lowest error for all models is near the hydrostatic *centre* of the yield surface ($p/p_c \simeq \gamma/2$), where there is lower meridional curvature in the surface and the direction of plastic flow is near isochoric. For $p_t/p_{c_n} = \gamma/2$ there is no error associated with the bE return, as shown by Figure 5.9 (i) sextant (C). In this case the trial stress will return radially onto the original yield surface at the intersection with the CS cone following constant isochoric plastic flow over its integrated return path. The highest errors are in regions of high curvature and high volumetric plastic flow. The maximum error (e_{max}), maximum number of iterations required to find convergence

(it_{max}) and the largest change in the size of the yield surface ($\Delta p_{c_{max}}$) are given in Table 5.3 for all three models under consideration. For the MCC model, the maximum error of 24.1% occurs at $p_t/p_{c_n} = 0.1$. In the lower pressure ratios, the yield surface of the MCC model softens more than the other models. The opposite is seen for high pressure ratios, with greatest errors and the largest hardening of the yield surface associated with the $\alpha = \gamma = 0.5$ model. Figure 5.9 and Table 5.3 confirm the reasonable behaviour of the integration scheme for the two-parameter family of CS models.

The magnitude of the stress return errors is predominately influenced by the hydrostatic location of the trial stress state in relation to the size of the yield surface (shown in Table 5.3 and Figure 5.9). In regions of greater hydrostatic curvature the error significantly increases. In order to reduce this error a sub-stepping procedure could be used. The rate of change of the derivative of the yield function with respect to hydrostatic pressure coupled with an estimate of the plastic strain path length would provide a suitable measure for assessing the need for splitting the strain increment. However, any sub-stepping procedure would increase the computational cost of the constitutive model. All that follows uses a single increment stress integration procedure.

5.3.4 Integration robustness and energy dissipation

The concepts of stored plastic work and dissipation are illustrated in Figure 5.10, which presents Gudehus plots [26] for $\alpha = 0.6$ and $\gamma = 0.9$. A reference pressure of 100kPa, compressibility index of $\kappa = 0.0073$, initial elastic volumetric strain $\varepsilon^{\mathrm{e}}_{v0} = 0$ and shear modulus of $G = 4$MPa were used for the material's elastic properties. $p_c = 233.3$kPa, $M = 0.964$, $\lambda = 0.0447$ and $\bar{\rho}_e = 0.729$ define the yield surface.

The model was examined by considering 64 different strain spheres, each with 832 strain probes of radius 1000μ (that is 1×10^{-3}) starting at the centre of each sphere. The directions of the individual strain probes were obtained using the HEALPix algorithm [25], which divides the surface of the sphere into equal area patches. Figures 5.10 (i) and (ii) show the stress response (known as Gudehus plots [26]) to these strain increments. The Gudehus surfaces are shaded according to the degree of (i) dissipated and (ii) stored plastic work. The maximum and minimum work for each stress surface are scaled to 1 and 0. These correspond to 164.6 J and −68.8 J, per unit volume respectively.

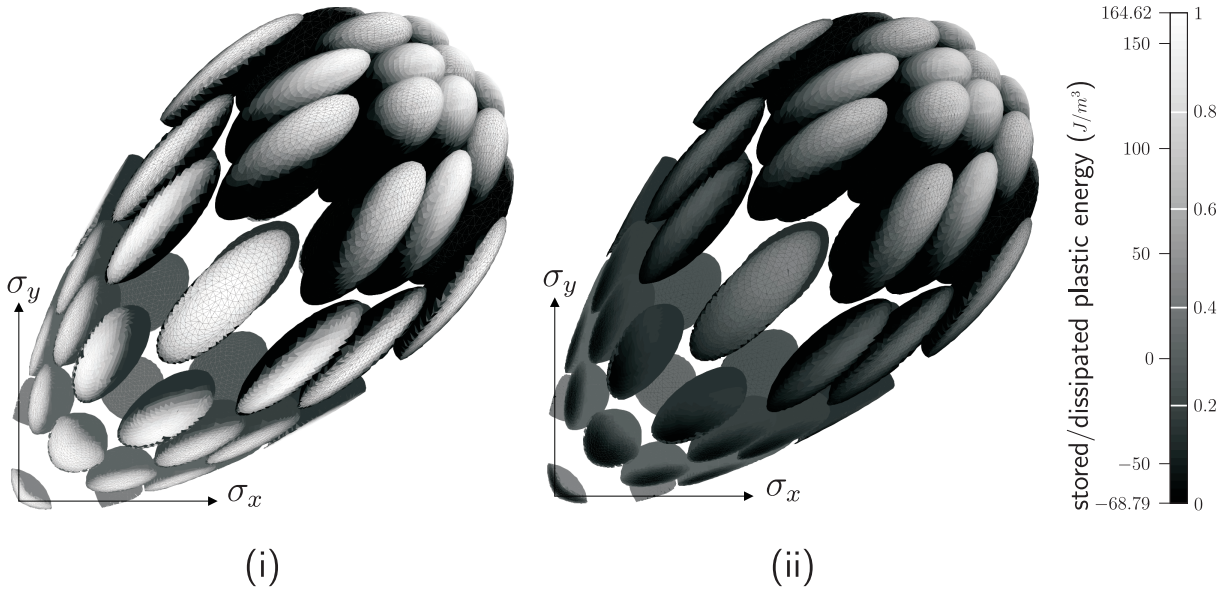

Figure 5.10: Gudehus stress plots with shading according to (i) dissipated plastic energy and (ii) stored plastic energy. The maximum and minimum work for each stress surface is identified by 1 and 0 corresponding to 164.6 J and −68.8 J, per unit volume, respectively.

Figure 5.11 presents a sequence of Gudehus plots for the model with the same material parameters as above but with $p_c = 300$kPa. Figure 5.11 (i) shows results in the $\sigma_x - \sigma_y$ plane. Figure 5.11 (ii) gives the same plots viewed in the deviatoric plane. The model starts at a randomly selected point on the yield surface and is subjected to 1,280 strain probes in directions determined by HEALPix. Once again, the probes are each of length $\sqrt{\{\Delta\varepsilon\}^T\{\Delta\varepsilon\}} = 1\times10^{-3}$. The stress responses and internal material parameters are stored before advancing to the next Gudehus plot. One of the probe responses is randomly chosen as the starting point for the next strain sphere. Five of the 200 stress responses are plotted for strain spheres 1, 50, 100, 150 and 200, where the surfaces are shaded according to the distance between the starting stress and the return stress. The stress path between the strain spheres is also plotted. As the pressure increases, so does the elongation of the stress response. This is due to the pressure-sensitive non-linear elasticity providing an increase in stiffness with pressure. The stress responses, when inside the yield surface, have a circular deviatoric section due to elastic isotropy. The Gudehus plots are flattened in the direction of the yield surface as most of the strain increment is taken up by the plastic response, leaving little for the elastic (and hence stress) response. By means of the stress return surface smoothness, Figure 5.11 serves to demonstrate the well behaved nature and robustness of the implemented constitutive model.

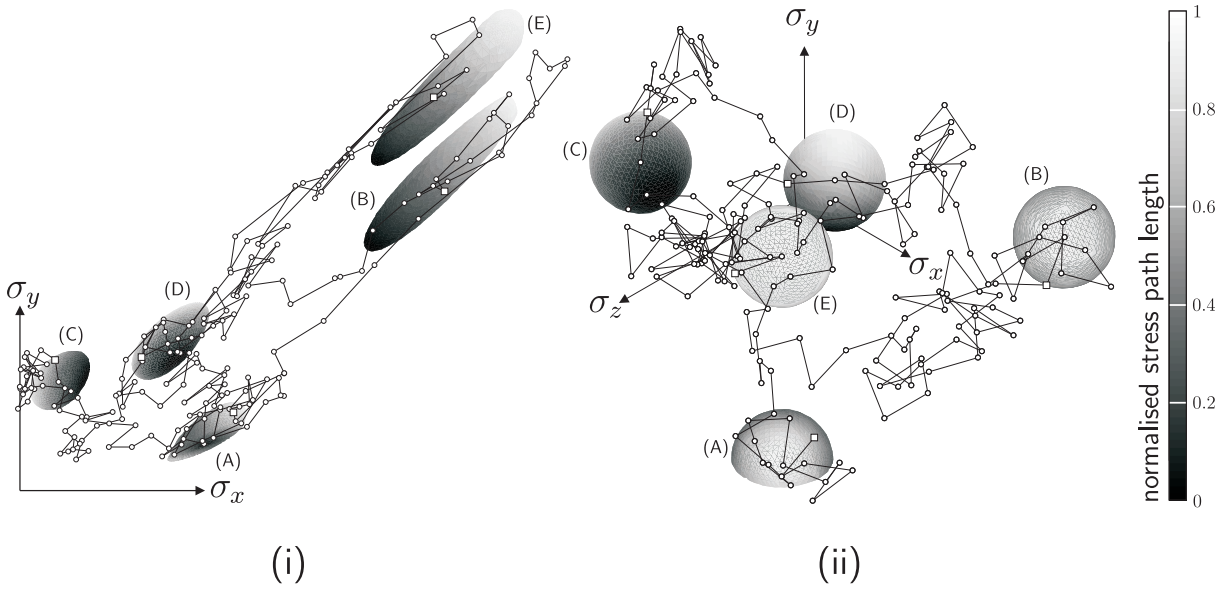

Figure 5.11: Sequence of Gudehus stress plots demonstrating the robustness of the bE stress return algorithm for (i) σ_x-σ_y plane and (ii) deviatoric view. The surfaces are shaded according to the length of the stress path with the maximum and minimum length identified by 1 and 0, respectively. Five of the 200 Gudehus plots are presented for steps 1 (A), 50 (B), 100 (C), 150 (D) and 200 (E).

5.3.5 Linearisation

The consistent tangent (2.49), as introduced in Section 2.4, is obtained through minimising the residuals (5.26) with respect to the trial elastic strain, $\{\varepsilon_t^{\mathrm{e}}\}$. The first row of (5.26) becomes

$$[C^{\mathrm{e}}]\{d\sigma\} + \Delta\gamma\Big([g_{,\sigma\sigma}]\{d\sigma\} + \{g_{,\sigma p_c}\}dp_c\Big) + d\Delta\gamma\{g_{,\sigma}\} = \{d\varepsilon_t^{\mathrm{e}}\}, \tag{5.40}$$

where here six component vectors and matrices are used. Considering the second row, we obtain

$$dp_c - (\tilde{p}_{c,p_c})dp_c - \{\tilde{p}_{c,\sigma}\}^T\{d\sigma\} - (\tilde{p}_{c,\Delta\gamma})d\Delta\gamma = 0. \tag{5.41}$$

Finally the third row, from the consistency condition, yields

$$\{f_{,\sigma}\}^T\{d\sigma\} + f_{,p_c}\, dp_c = 0. \tag{5.42}$$

Combining (5.40)-(5.42), we have

$$\underbrace{\begin{bmatrix} [C^{\mathrm{e}}] + \Delta\gamma[g_{,\sigma\sigma}] & \Delta\gamma\{g_{,\sigma p_c}\} & \{\hat{g}_{,\sigma}\} \\ -\{\tilde{p}_{c,\sigma}\}^T & 1 - (\tilde{p}_{c,p_c}) & -(\tilde{p}_{c,\Delta\gamma}) \\ \{f_{,\sigma}\}^T & f_{,p_c} & 0 \end{bmatrix}}_{[A^{alg}]^{-1}} \begin{Bmatrix} \{d\sigma\} \\ dp_c \\ d\Delta\gamma \end{Bmatrix} = \begin{Bmatrix} \{d\varepsilon_t^{\mathrm{e}}\} \\ 0 \\ 0 \end{Bmatrix}. \tag{5.43}$$

Multiplying both sides of (5.43) by $[A^{alg}]$, we obtain

$$\begin{Bmatrix} \{d\sigma\} \\ dp_c \\ d\Delta\gamma \end{Bmatrix} = \begin{bmatrix} [D^{alg}] & \{A_{12}^{alg}\} & A_{13}^{alg} \\ \{A_{21}^{alg}\}^T & A_{22}^{alg} & A_{23}^{alg} \\ \{A_{31}^{alg}\}^T & A_{32}^{alg} & A_{33}^{alg} \end{bmatrix} \begin{Bmatrix} \{d\varepsilon_t^{\mathrm{e}}\} \\ 0 \\ 0 \end{Bmatrix}, \tag{5.44}$$

where $[D^{alg}]$ is the six-component algorithmic consistent tangent. The six-component vectors and matrices required in (5.43) are given by

$$\{\cdot\} = \begin{Bmatrix} \{\dot{\cdot}\} \\ \{0\} \end{Bmatrix} \qquad \text{and} \qquad [g_{,\sigma\sigma}] = \begin{bmatrix} [g_{,\hat{\sigma}\hat{\sigma}}] & [0] \\ [0] & 2A^2[1] \end{bmatrix}. \tag{5.45}$$

The consistent tangent from (5.44) must be transformed (through (C.17)) using the eigenvectors associated with the trial elastic strain to obtain a stiffness matrix consistent with the six component stresses and strains.

5.4 Calibration

This section presents a calibration procedure for the isotropic family of CS models. The process is demonstrated for LCT using data obtained by Gens [23]. LCT is a low plasticity glacial till with high natural variability, classified as a low-plasticity sandy silty-clay. All of the experimental tests presented by Gens [23] were from reconstituted samples with a specific weight of 2.65. The mineralogy of these samples was comprised of principally quartz with minor proportions of calcite, feldspar and clay minerals. The clay fraction was mainly composed of calcite and illite with smaller components of smectite, kaolinite and chlorite. The material had a liquid limit, plastic limit and plasticity index of 25, 13 and 12 respectively[5]. Approximately 17% of the material was clay (giving an activity of 0.71[6]), the remainder was mainly composed of sand, with very little silt.

5.4.1 Classical constants: κ, λ, M

The classical compressibility constants, κ and λ, can be calibrated from hydrostatic drained loading (consolidation) and unloading (swelling) data. The elastic compressibility index, κ, is obtained as a linear approximation to the swelling line in bi-logarithmic hydrostatic pressure-void ratio (or specific volume) space, as shown in Figure 5.12 (i) for experimental data from Gens [23]. The plastic compressibility

[5]Note, that the plasticity index (the difference between the limit and plastic limits) is a measure of the amount of water that must be added to the soil to reduce its strength by a hundredfold. The plastic limit is defined as the moisture content at which the soil can be rolled out to a rod with diameter of 3mm without crumbling. The liquid limit is the moisture content at which a standard V-groove cut into the soil just closes when shaken using standard equipment.

[6]The activity of a sample is defined as the plasticity index divided by the percentage of clay particles $\leq 2\mu$m present.

index, λ, is calibrated equivalently from virgin compaction data. For LCT [23] the unitless bi-logarithmic compressibility indices are $\kappa = 0.0073$ and $\lambda = 0.0447$. The data is also shown in (ii) semi-logarithmic and (iii) normal space.

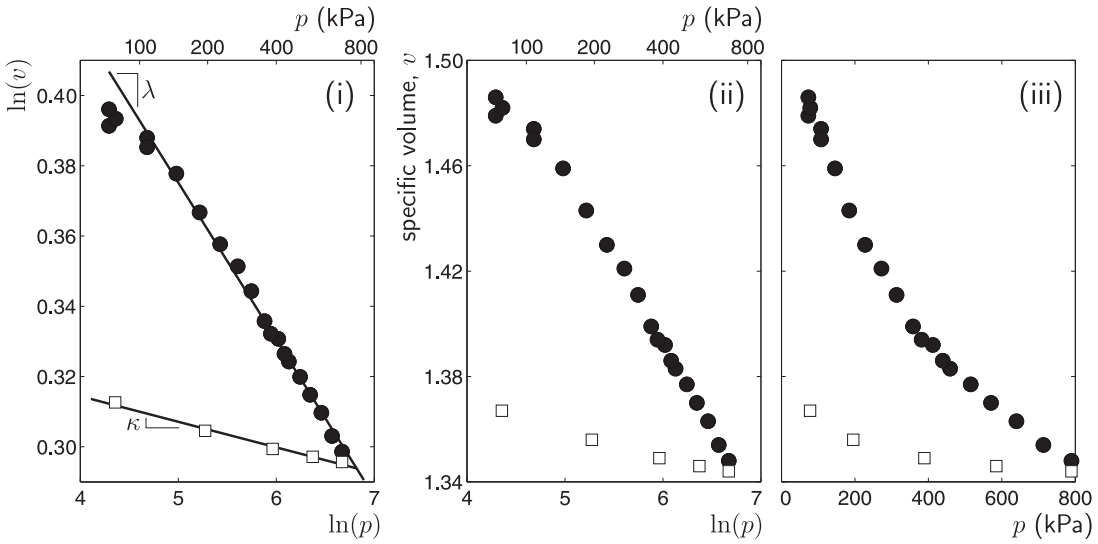

Figure 5.12: Hydrostatic drained loading and unloading experimental data (shown by discrete points) for LCT from Gens [23]: (i) bi-logarithm of pressure-specific volume, (ii) semi-logarithm of pressure-specific volume and (iii) pressure-specific volume.

The gradient of the CSL, M, can be obtained from drained or undrained triaxial compression tests. It is defined as the stress ratio where the material experiences unbounded distortions with no change in volume and no change in stress state. $\bar{\rho}_e$ is obtained as the ratio of this stress gradient under triaxial extension to the equivalent ratio under triaxial compression. For LCT the gradient of the CSL and the normalised deviatoric radius under triaxial extension are $M = 0.964$ and $\bar{\rho}_e = 0.729$.

5.4.2 α and γ specification

The two-parameter family of models presented here extends the classical MCC model by means of the additional dissipation parameters γ and α. These material constants may be determined from undrained triaxial and one-dimensional consolidation test data. In this calibration procedure we assume that under sufficiently large straining during one-dimensional consolidation the elastic strains are negligible. In this case the ratio of the deviatoric to volumetric plastic strains is

$$\frac{\dot{\varepsilon}^{\mathrm{p}}_{\gamma}}{\dot{\varepsilon}^{\mathrm{p}}_{v}} = \frac{A^2(\eta_{K_0})}{B^2\Big(1-\gamma(p_c/p)/2\Big)} = \sqrt{\frac{2}{3}}, \tag{5.46}$$

where $\eta_{K_0} = q/p$ is the stress ratio under one-dimensional (K_0) consolidation. Substituting (5.16) for B^2 and rearranging, we obtain the ratio of the size of the yield surface to the pressure as

$$\left(\frac{p_c}{p}\right) = \frac{\gamma(2-\gamma) + (\eta_{K_0})\sqrt{2/3}}{\gamma(2-\gamma) + \gamma(\eta_{K_0})\sqrt{1/6}}. \tag{5.47}$$

From (5.16), α can then be obtained as

$$\alpha = \frac{(\eta_{K_0})\Big(1+\gamma\big((p_c/p)/2-1\big)\Big)\Big(\gamma(2-\gamma)\big((p_c/p)-1\big)\Big)^{-1/2} - M}{M\Big(\gamma(p_c/p)/2-1\Big)} \tag{5.48}$$

However, (5.48) requires the specification of γ, which can be determined from undrained triaxial compression (UTC) or extension (UTE) data at an overconsolidation ratio (OCR) of two. Figure 5.13 (ii) shows UTC test data from Gens [23]. For OCR = 2, the change of normalised pressure between the starting and final stress states can be used to approximate γ as

$$\gamma \approx \frac{p_f}{p_i} = \frac{2p_f}{p_c}\ , \tag{5.49}$$

where $p_i = p_c/2$ and p_f are the initial and final stress states from the UTC experiment (Figure 5.13 (ii)). The change in the size of the yield surface will be small due to the near isochoric plastic flow (being in close proximity with the CS) so that $2p_f/p_c$ offers a reasonable approximation for γ.

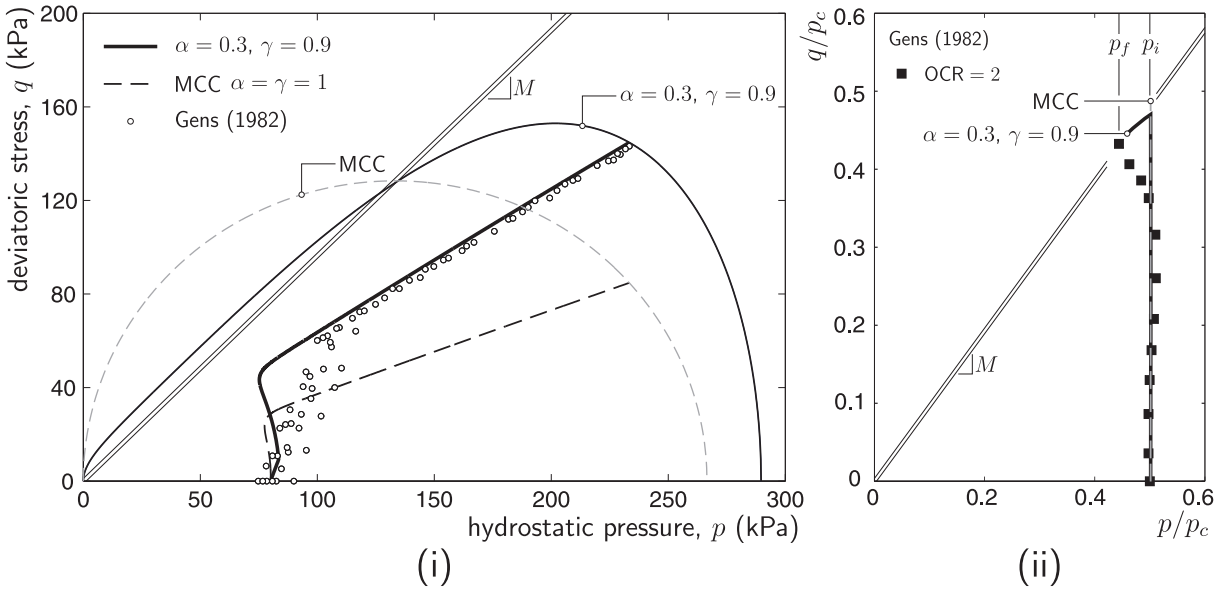

Figure 5.13: Test simulations using the MCC model ($\alpha = \gamma = 1$) and the two-parameter model ($\alpha = 0.3$, $\gamma = 0.9$) compared against experimental data on LCT (shown by discrete points) from Gens [23]: (i) one-dimensional consolidation (ii) UTC with OCR = 2.

Viewed in a different (but equivalent) light, γ controls the distance between the CSL and the hydrostatic consolidation line (HCL). As γ reduces, the position of the CSL moves away from the HCL in the direction of reducing hydrostatic pressure. Figure 5.14 shows experimental data on LCT [23] for hydrostatic consolidation and swelling followed by UTC for OCRs of 1, 1.5, 2, 4 and 10 in (i) specific volume versus hydrostatic pressure and (ii) $\ln(p)$ versus $\ln(v)$ space. The distance between the consolidation and CS lines provides the ratio of the size of the yield surface to the pressure at the CS. From Figure 5.14 (ii) the logarithmic ratio is $\ln(p_c/p)_{cs} = 0.786$ resulting in a ratio of $(p/p_c)_{cs} = 0.45$ between the size of the yield surface and the hydrostatic pressure at the CS. γ is obtained as 0.9, using

$$\gamma = 2\left(\frac{p}{p_c}\right)_{cs}\ , \tag{5.50}$$

which confirms the value obtained by considering the pressure change under UTC at an OCR of 2.

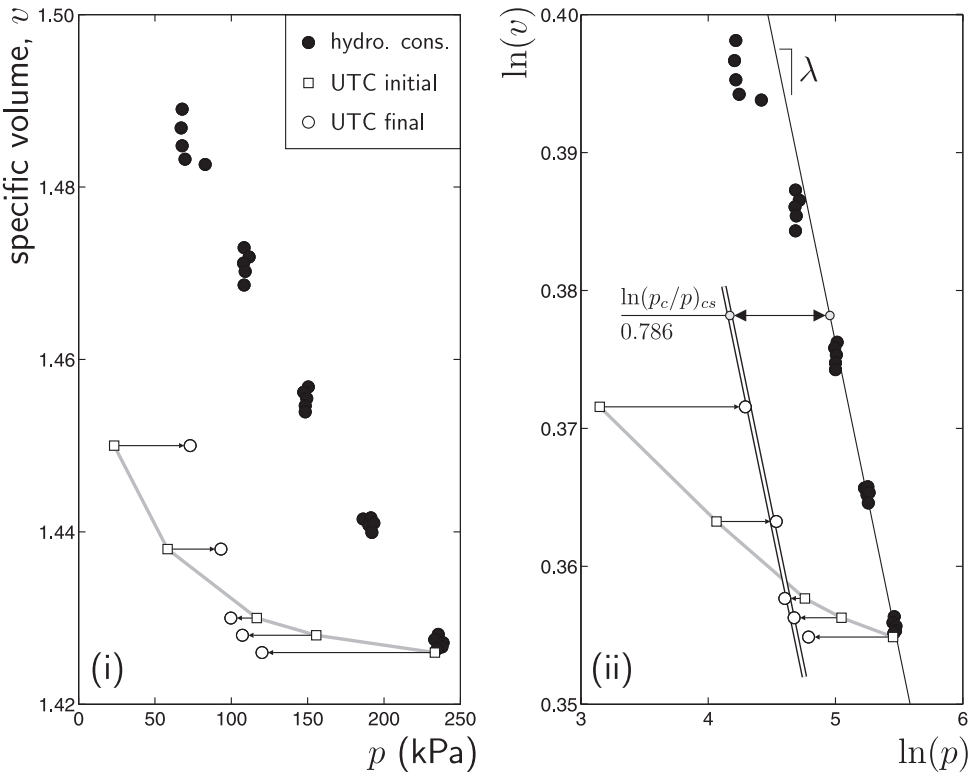

Figure 5.14: Hydrostatic consolidation and swelling following by UTC for OCRs of 1, 1.5, 2, 4 and 10 experimental data on LCT [23]: (i) hydrostatic pressure-specific volume and (ii) $\ln(p)$-$\ln(v)$.

In the absence of one-dimensional consolidation data, Jaky's [32] formula may be used to approximate the stress ratio under K_0 loading

$$\eta_{K_0} = \frac{\sqrt{6}\sin(\phi)}{3 - 2\sin(\phi)}, \tag{5.51}$$

where ϕ is the effective friction angle. Figure 5.15 (i) compares the experimental data collated by Federico *et al.* [22] with (5.51). Jaky's formula provides an adequate approximation to the experimental data, capturing the general trend. The values of α to achieve the K_0 consolidation stress ratio η_{K_0} for $\gamma = 0.8$, 0.9 and 1.0 are given in Figure 5.15 (ii) for both experimental data [22] and Jaky's formula. For example, with a friction angle of 25°, Jaky's formula predicts a stress ratio of $\eta_{K_0} = 0.480$, which is achievable with $\alpha = 0.336$, 0.246, 0.175 for $\gamma = 1.0$, 0.9 and 0.8 respectively.

Figure 5.13 (i) compares K_0 consolidation data on LCT [23] with predictions from the MCC and two-parameter models. The experimental data suggests a stress ratio of $\eta_{K_0} = 0.6$. From Figure 5.13 (ii) $\gamma \approx 0.9$ and $M = 0.964$ ($\phi = 29.5°$). Using (5.47) and (5.48), we obtain $\alpha = 0.3$. The two-parameter model with $\alpha = 0.3$ and $\gamma = 0.9$ provides an excellent fit to the K_0 experimental data. For MCC, once the gradient of the CSL has been specified, the stress path predicted for one-dimensional consolidation is fixed (that is, K_0 is directly dependent upon M). In Figure 5.13 (i) we see that the MCC model is unable to provide a good simulation of the K_0 consolidation stress path. Figure 5.13 (ii) compares the UTC experimental data from Gens [23] with the response from the MCC and two-parameter models ($\alpha = 0.3$, $\gamma = 0.9$) for OCR = 2.

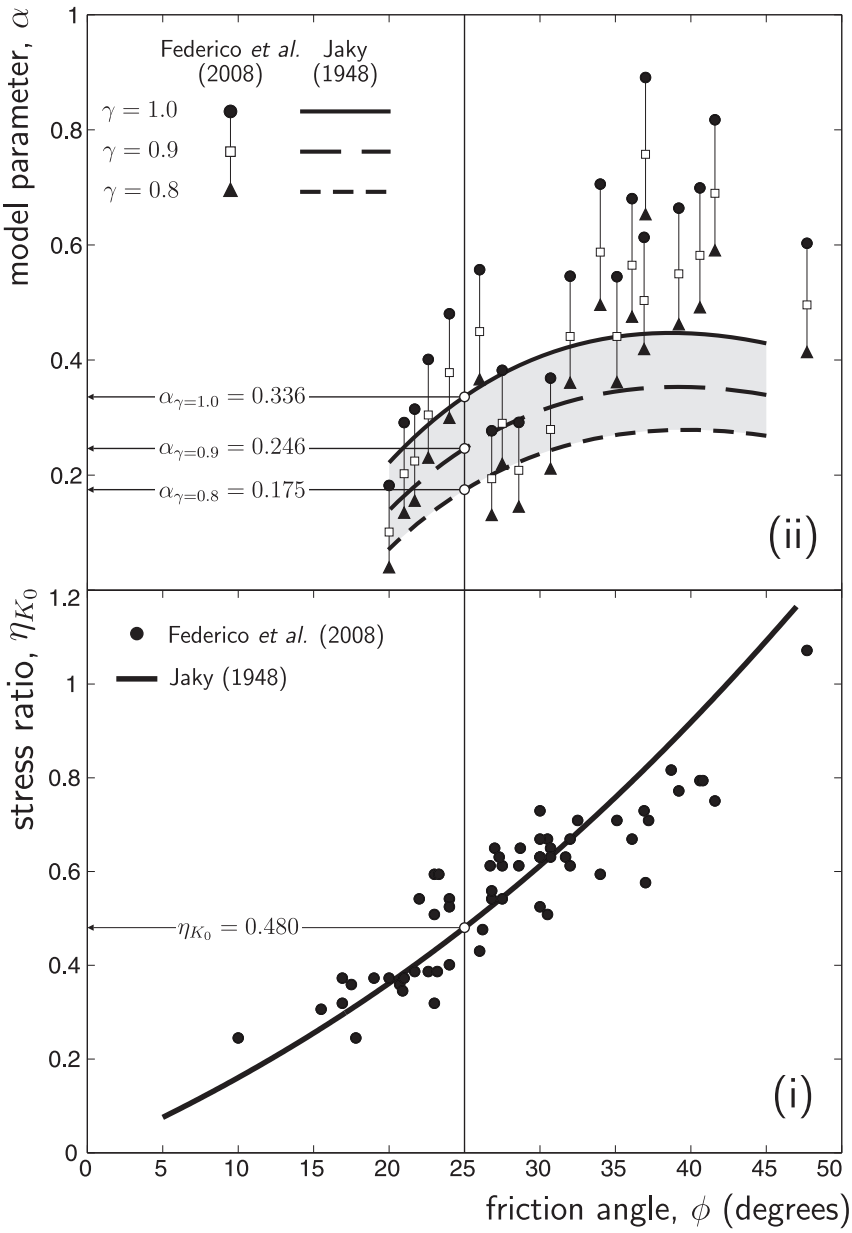

Figure 5.15: Calibration of material constant α: (i) one-dimensional consolidation stress ratio against friction angle, comparing experimental data (discrete points) [22] against Jaky's equation [32] and (ii) α ranges for $\gamma = 0.8$, 0.9 and 1.0, corresponding to the data obtained from [22]. Graph (ii) also shows the α versus friciton angle relationships for $\gamma = 0.8$, 0.9 and 1.0 using Jaky's [32] relationship.

5.4.3 Shear modulus: G

The two-parameter model developed here makes use of a hyperelastic relationship with a variable bulk but constant shear modulus, G. The value of the shear modulus can be obtained through examination of the swelling response of a K_0 consolidated material. Figure 5.16 shows the one-dimensional loading (consolidation) and unloading to an OCR of 10 of the two-parameter model (with $\alpha = 0.3$ and $\gamma = 0.9$), along with swelling data from Gens [23] (shown by discrete points) on LCT . The size of the yield surface at the end of one-dimensional swelling is also shown.

The model starts at A, with a reference pressure of 80kPa. Subjected to one-dimensional compressive straining, the stress response initially moves around the hardening yield surface to B. From B the stress

path moves along a near-constant η_{K_0} line to C, at which point the strain path is then reversed. The initial swelling stress direction response is governed by the ratio of the shear modulus, to that of the bulk modulus ($K = p/\kappa$). Here, a value of $G = 18$MPa provides good agreement with the initial swelling behaviour of LCT. Increasing or decreasing G causes a stiffening or softening of this return path, respectively. As the hydrostatic pressure reduces (and the OCR increases), the ratio of the shear to bulk modulus increases, causing a stiffening of the stress response (larger change in deviatoric stress for a given hydrostatic increment). In order to attain the required OCR, the constitutive model intersects the yield surface (at D) and moves along the softening yield surface until the required OCR is realised at E, as seen in Figure 5.16.

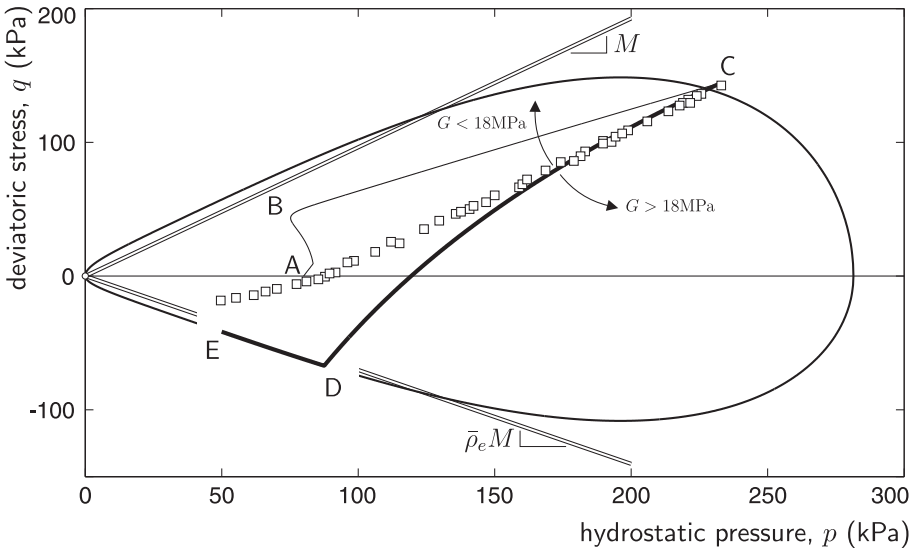

Figure 5.16: One-dimensional K_0 consolidation followed by swelling comparison with swelling experimental data on LCT (shown by discrete points) from Gens [23].

Dafalias *et al.* [20] showed that it is possible to obtain an equivalent stress response to that shown in Figure 5.16 with a constant Poisson's ratio. This results in a variable bulk and shear modulus; however as mentioned in Section 5.1.1, such an elasticity law can result in non-conservative material behaviour [4, 29, 51]. An alternative would be to use a hyperelastic material law, such as that introduced by Houlsby [29], with a variable shear modulus of the form

$$G = G_0 + \alpha^{\mathrm{e}} p, \tag{5.52}$$

where G_0 is the constant component of the shear modulus and the constant, α^{e}, controls the variability of the shear modulus with pressure. However, this coupling between the shear modulus and pressure introduces anisotropy (in the form of transverse-isotropy) into the elastic constitutive equations. As discussed in Chapter 3, this significantly complicates matters when undertaking finite deformation analyses.

5.5 Experimental comparisons

In this section comparisons are made with 31 experimental tests on LCT [23] using variants of from the two-parameter family of CS hyperplastic models. A reference pressure of 80kPa, compressibility index of $\kappa = 0.0073$, initial elastic volumetric strain $\varepsilon^{\mathrm{e}}_{v0} = 0$ and a shear modulus of $G = 18$MPa were used for the material's elastic properties. $p_c = 80$kPa, $M = 0.964$, $\lambda = 0.0447$ and $\bar{\rho}_e = 0.729$ define the yield surface.

5.5.1 Isotropic simulations

Figure 5.17 illustrates the material responses given $\alpha = \gamma = 1$ (MCC, dashed line) and $\alpha = 0.3$, $\gamma = 0.9$ (continuous line) under drained triaxial compression (DTC) for the following six OCRs: 1, 1.25, 1.5, 2, 4 and 10. The results are compared against experimental data from Gens [23]. In these tests, the material was initially under a hydrostatic stress state with $p = 233.3$, 186.7, 155.6, 166.7, 58.3 or 23.3kPa, corresponding to the six OCRs. The material was subsequently compressed axially whilst maintaining constant lateral pressure.

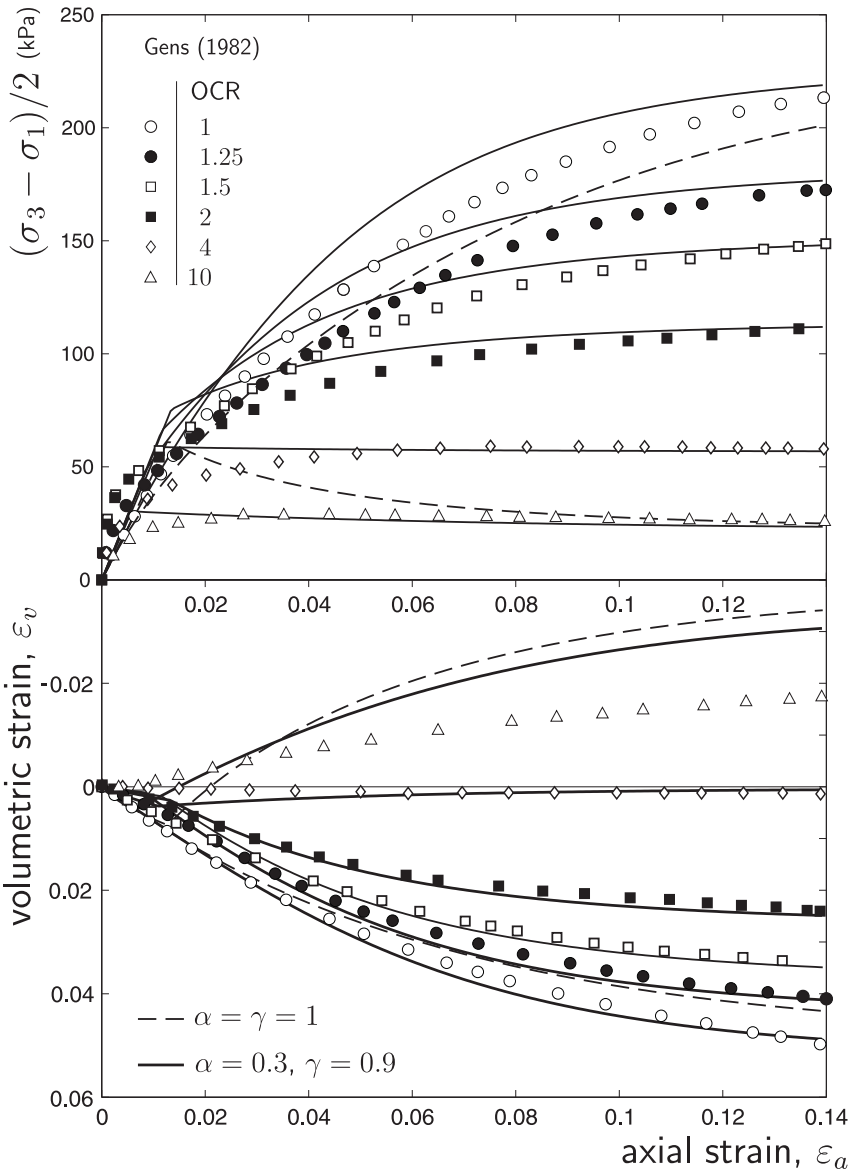

Figure 5.17: DTC test simulations compared with experimental data (shown by discrete points) [23]. Above: axial strain (ε_a) against deviatoric stress ($(\sigma_3 - \sigma_1)/2$). Below: axial strain (ε_a) versus volumetric strain (ε_v).

Figure 5.18 compares the stress paths for (i) $\alpha = \gamma = 1$ and (ii) $\alpha = 0.3$, $\gamma = 0.9$ under UTC and UTE for five overconsolidation ratios. Similarly to the drained tests, the material was initially under hydrostatic stress states of $p = 233.3$, 155.6, 116.7, 58.3 or 23.3kPa, corresponding to the five OCRs of 1, 1.5 2, 4 and 10. An isochoric strain path of $\{\Delta\varepsilon\} = \pm\{\Delta\varepsilon_1 \quad -\Delta\varepsilon_1/2 \quad -\Delta\varepsilon_1/2\}^T$, corresponding to

UTC and UTE, was then applied until the CS was reached.

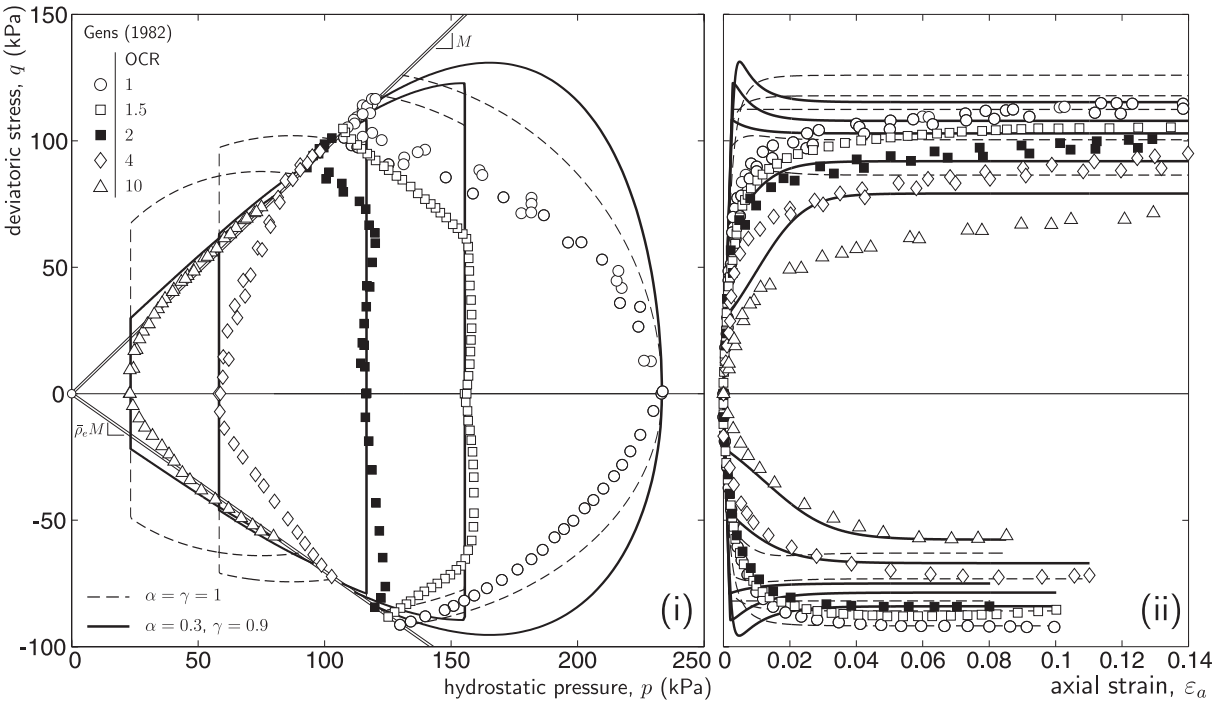

Figure 5.18: UTC and UTE following isotropic compression and swelling, comparisons with experimental data (shown by discrete points) from Gens [23]: (i) stress space response (ii) axial strain-deviatoric stress response.

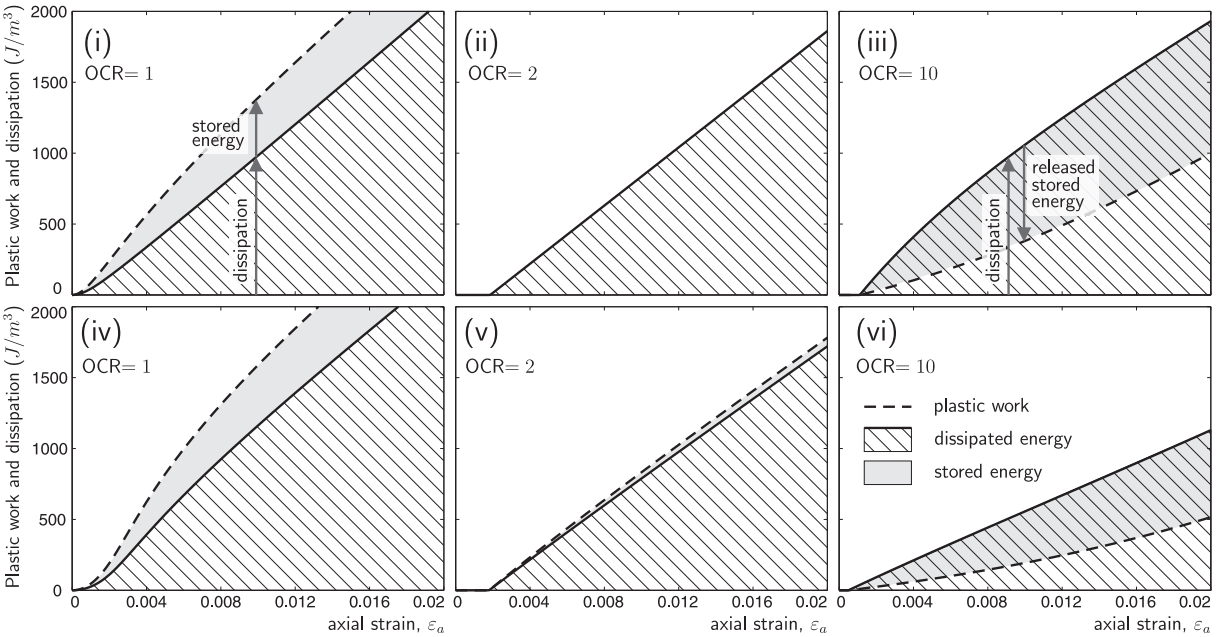

Figure 5.19: UTC stored/dissipated energy and plastic work for the MCC model with OCRs of (i) 1, (ii) 2 and (iii) 10 and for the two-parameter model with $\alpha = 0.3$, $\gamma = 0.9$ for OCRs of (iv) 1, (v) 2 and (vi) 10.

The material point stress paths for the MCC ($\alpha = \gamma = 1$) simulations significantly overestimate the stress ratio $\eta = q/p$ prior to arrival at the CS under high OCRs. The results for the two-parameter family

of models with $\alpha = 0.3$ and $\gamma = 0.9$ impressively improve the quality of the prediction in the high OCR range. However, the initial response for normally consolidated soil (OCR= 1) is worse than that given by the MCC model. This observation is important. It indicates that Collins and Hilder's dissipation function [9] is not entirely satisfactory for both normally consolidated and heavily over-consolidated soils without using different material parameters. Figure 5.19 shows the cumulative dissipated/stored energy and total plastic work under triaxial compression (for axial strains up to 2%) for (i-iii) MCC ($\alpha = \gamma = 1$) and (iv-vi) a two-parameter model with $\alpha = 0.3$ and $\gamma = 0.9$. For OCRs less than $2/\gamma$, the plastic work is greater than the dissipated energy (energy is stored), whereas for OCRs greater than $2/\gamma$, the opposite is true (previously locked-in energy is released). The rate of plastic work and plastic dissipation are given by (2.34) and (2.30) respectively, where $\chi_{ij} = (\gamma p_c/2)\delta_{ij}$ and $\varphi_{ij} = \sigma_{ij} - \chi_{ij}$. When the hydrostatic pressure, p, drops below $\gamma p_c/2$, the product of the shift stress with the plastic strain rate becomes negative due to the dilative plastic strains resulting in total plastic work less than dissipation. This is seen in Figures 5.19 (iii) and (vi) for the heavily over-consolidated simulations. For the MCC model at an OCR of 2, the dissipative energy and the plastic work are equal (as shown in Figure 5.19), with zero stored energy.

5.5.2 Anisotropic simulations

The response of the two-parameter model with $\alpha = 0.3$ and $\gamma = 0.9$ was further investigated for drained and undrained triaxial tests following K_0 consolidation (and swelling to various OCRs). The simulations were again compared with experimental data on LCT [23]. Figures 5.13 (i) and 5.16 show the K_0 consolidation and swelling response of the two-parameter model. Although the initial swelling behaviour provides a good fit to the experimental data, at higher OCRs the constitutive model's response is a poor representation of the material behaviour. Nevertheless, this response, once swelled to the appropriate OCR, is taken as the initial starting conditions for the anisotropic material point simulations (points C to H for the two-parameter model and points C' and G' for the MCC in Figure 5.21 (i) for the undrained tests).

Figure 5.20 presents the DTC simulations for the K_0 consolidated material at OCRs of 1, 1.5, 2, 4 and 7. They are compared against LCT data from Gens [23], shown by discrete points. The two-parameter CS model provides a good fit to the experimental data for low OCRs (OCR$<$ 2); offering a significant improvement over the MCC model, as shown by the dashed line in Figure 5.20. However, for high OCRs the two-parameter model significantly overestimates both the peak deviatoric stress and the dilative volumetric strain (although there is still an improvement over the MCC model).

The UTC and UTE simulations are shown in Figure 5.21 and compared with experimental data from Gens [23] (as shown by discrete points) for six OCRs. Figures 5.21 (i) and (ii) give the hydrostatic-deviatoric stress and the axial strain-deviatoric stress responses respectively. Remarkably, for an isotropic model, the two-parameter CS model provides a reasonable fit to the experimentally observed response for all OCRs under triaxial compression. The response under triaxial extension is, however, far from satisfactory, with the peak deviatoric stress significantly overestimated for all OCRs. This is due to purely elastic behaviour until the yield surface is reached, as shown by the constant pressure response in Figure 5.21 (i) for UTE with OCR = 1 until a deviatoric stress of ≈ -105kPa is obtained. The stress path then moves round the hardening yield surface until it reaches the CS. The experimental stress-strain response (Figure 5.21 (ii)) shows significantly more non-linearity over this deviatoric stress range, gradually moving towards a CS.

The axial strain versus stress ratio, $\eta = q/p$, response of the MCC and two-parameter models under UTC and UTE following one-dimensional loading and unloading is shown in Figures 5.22 (i) and (ii) respectively. Although both models converge to the same CS stress ratios, the MCC model significantly

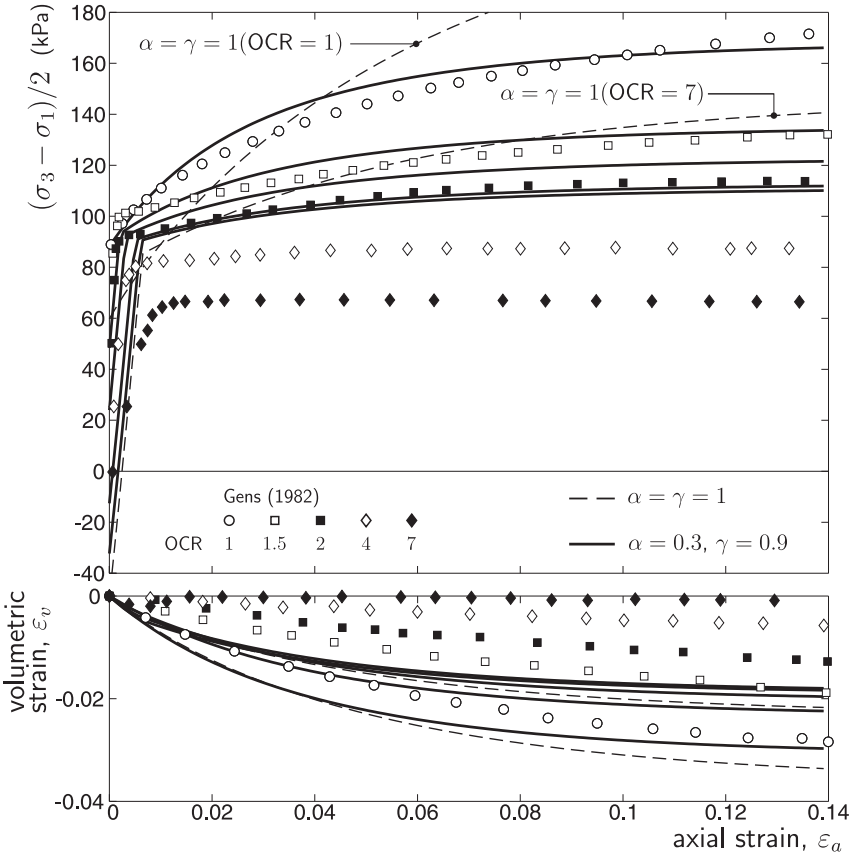

Figure 5.20: DTC following K_0 consolidation and swelling comparisons with experimental data (shown by discrete points) from Gens [23]. Above: axial strain (ε_a) against deviatoric stress ($(\sigma_3 - \sigma_1)/2$). Below: axial strain (ε_a) against volumetric strain (ε_v).

overestimates the peak stress ratio for the over-consolidated tests. This inadequacy is partially addressed by the two-parameter model, although their is still considerable room for improvement.

Figure 5.23 shows the UTC and UTE stress paths following one-dimensional loading and unloading for the two-parameter model in dissipative stress space. Due to the zero deviatoric shift stress component, the dissipative and true deviatoric stresses are equal, the dissipative pressure is given by (5.11) where the shift stress is given by (5.10). The dissipative yield surfaces are shown at key points along the stress paths. The one-dimensional loading behaviour is shown in Figure 5.23 (i) along with the dissipative yield surfaces at the initial state, A, and at the end of the K_0 consolidation stage, C. Note that both the ellipsoidal yield surfaces are centred on the dissipative stress origin, with their axis ratios controlled by A and B in (5.13). Upon unloading at C, as shown in Figure 5.23 (ii), the stress path returns inside the dissipative yield surface. In dissipative stress space, the unloading stress path lies above the loading path, whereas in true stress space (as shown in Figure 5.21) the converse is true. It is also important to note that the model yields prior to re-intersecting with f^{φ}_{C} as A and B are continuously changing along the unloading stress path, even when the model is behaving elastically[7]. It is re-emphasised that dissipative stress space is an instantaneous space and f^{φ} an instantaneous yield surface applicable at the particular stress state under consideration. The undrained triaxial stress paths are shown in Figure 5.23 (iii) and the dissipative yield surface shown at the CS for the UTC path at an OCR of one (point I). As expected, all of the stress paths arrive at the CS with zero dissipative pressure.

[7]Note, for the special case of the MCC model ($\alpha = \gamma = 1$) A and B are independent of the hydrostatic pressure and the dissipative yield surface remains fixed during elastic behaviour.

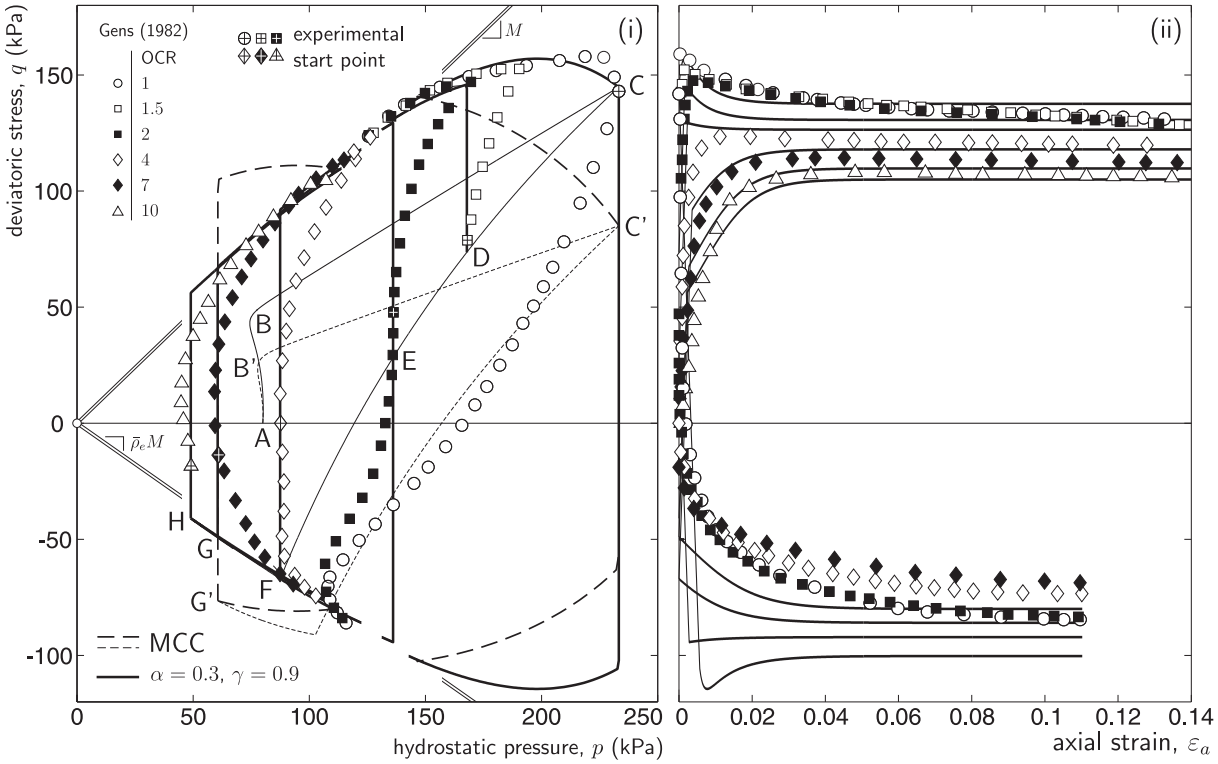

Figure 5.21: UTC and UTE following K_0 consolidation and swelling comparisons with experimental data (shown by discrete points) from Gens [23]: (i) stress space response (ii) axial strain versus deviatoric stress response.

5.6 Observations

The final section in this chapter has compared the two-parameter CS hyperplastic model response with experimental data on LCT from Gens [23]. This model provides a useful improvement over the classical MCC model, especially in the heavily over-consolidated region (a condition at which most natural geotechnical materials exist). The MCC model is unable to reproduce one of the most fundamental particulate material stress paths; that of K_0 consolidation. Once the gradient of the CSL, M, has been specified, the asymptotic stress ratio under K_0 consolidation is fixed. The two-parameter hyperplastic model allows the new parameters to be directly selected, so that the correct asymptotic state is achieved. However, a good fit to the swelling response following one-dimensional consolidation requires a relatively high shear modulus. This high shear modulus causes the constitutive model's response under DTC to be over-stiff (see Figures 5.17, 5.18 and 5.20). The two-parameter model was originally compared with experimental data on LCT by Coombs and Crouch [18]. There a shear modulus of 4MPa led to an improved fit to the DTC data. However, if this shear modulus was used under K_0 swelling, then the stress response would be over-soft. The use of a high shear modulus also causes a progressive stiffening of the K_0 swelling response, as seen in Figure 5.16, which is at odds with observed experimental results.

An alternative to using a lower shear modulus would be to allow plastic behaviour within the conventional yield surface. This would allow for a high elastic shear modulus (governing the initial loading/unloading behaviour) and a progressive softening of the stress response with increasing inelasticity. The presence of this inelastic material behaviour is supported by the stress response under UTE following both hydrostatic and K_0 consolidation, as shown in Figures 5.21 (i) and 5.18 (i), where significant non-linearity is seen in the experimental data. The non-symmetry (about the hydrostatic axis) in Fig-

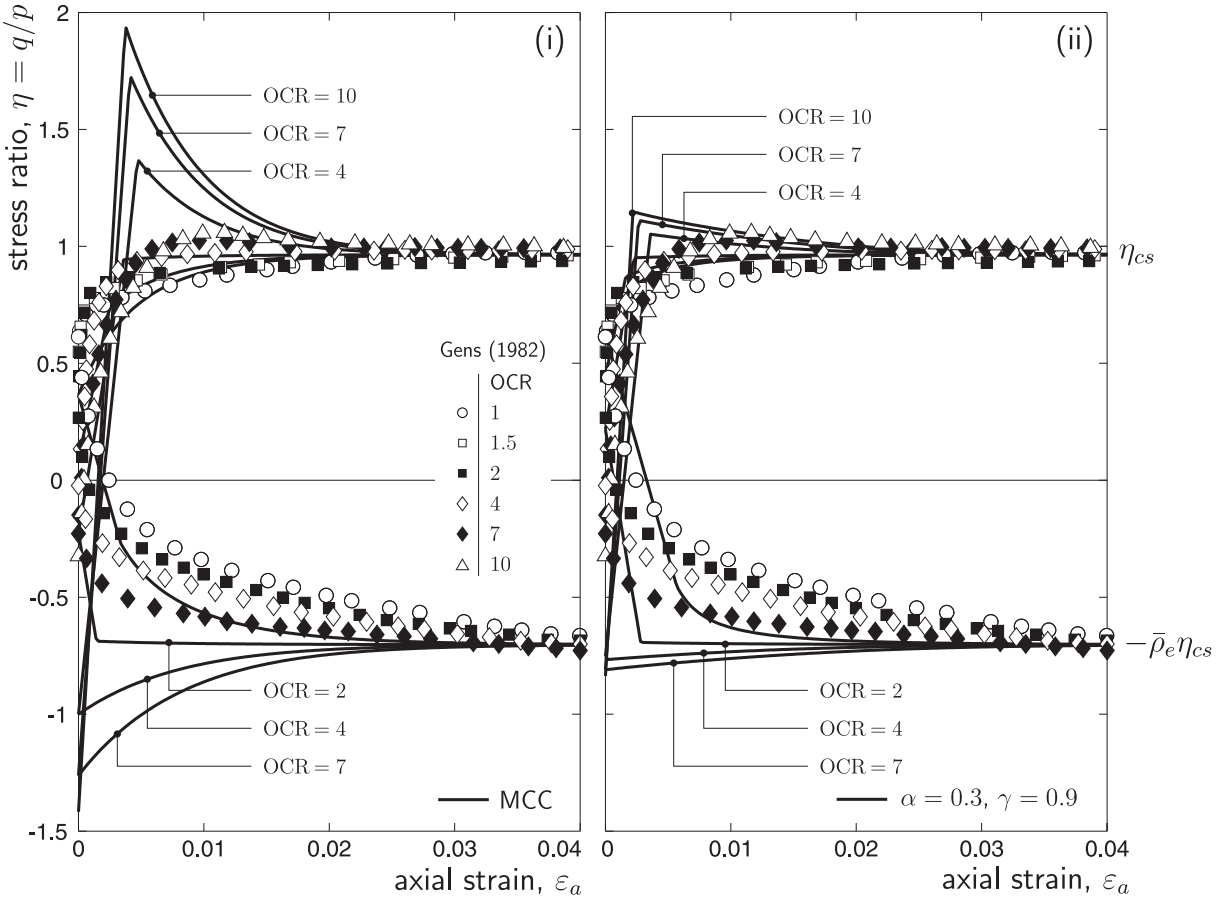

Figure 5.22: UTC and UTE following K_0 consolidation and swelling comparisons with experimental data (shown by discrete points) from Gens [23]: axial strain versus stress ratio response for (i) MCC and (ii) the two-parameter model with $\alpha = 0.3$ and $\gamma = 0.9$.

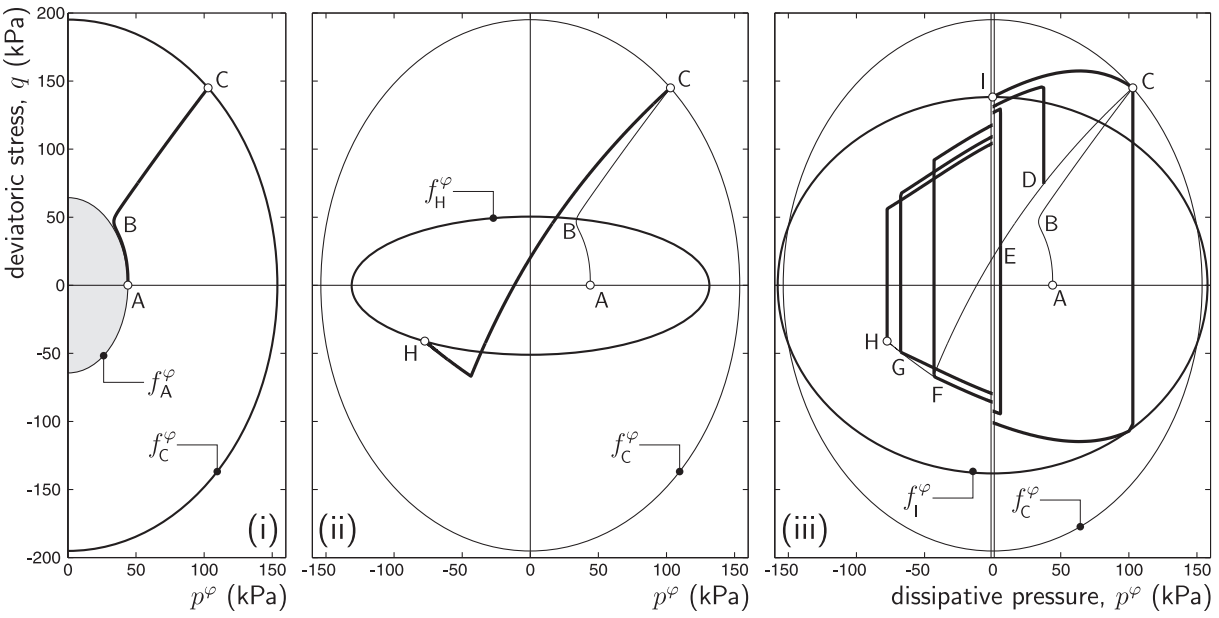

Figure 5.23: Stress paths in dissipative stress space: (i) one-dimensional loading, (ii) one-dimensional unloading and (iii) UTC and UTE.

ure 5.21 (i), would also suggest that the yield surface has some directional dependance.

The following conclusions can be drawn from this chapter:

(i) non-associated flow is a natural consequence of the particular form of the dissipation function in the family of hyperplasticity models examined;

(ii) a Lode angle dependency can be incorporated within hyperplasticity models using (5.20), which avoids the difficulties caused by redefining q [11];

(iii) the particular form of yield function, f, can significantly influence the efficiency of the iterative bE stress integration procedure;

(iv) α and γ can be determined from one-dimensional consolidation and UTC with an OCR equal to 2, respectively;

(v) the two-parameter model provides the following advantages over the classical MCC model:

  (a) control over the shape of the yield surface independent of the gradient of the CSL;

  (b) ability to reproduce the one-dimensional consolidation stress path; and

  (c) significantly improved agreement with experimental data for high OCRs.

(vi) on the other hand, the isotropic two-parameter CS model is unable to:

  (a) give improved fits (to undrained triaxial tests) over the MCC model for normally consolidated soils;

  (b) reproduce the one-dimensional swelling response to high OCRs;

  (c) provide an adequate fit to UTE following K_0 consolidation at low OCRs; and

  (d) provide a measure of the anisotropy inherent in the soil fabric.

Chapter 5 references

[1] P Anantanasakul, *Three-dimensional experiments and modelling of anisotropic clay*, PhD. Thesis, Oregon State University (2010).

[2] JP Bardet, *Lode dependences for isotropic pressure-sensitive elastoplastic materials*, J. Appl. Mech.-T. ASME 57 (1990), 498–506.

[3] SK Bhowmik & JH Long, *A general formulation for the cross sections of yield surfaces in octahedral planes*. In: GN Pande and J Middleton (eds.) NUMENTA 90 (1990), 795–803.

[4] RI Borja & C Tamagnini, *Cam-Clay plasticity Part III: Extension of the infinitesimal model to include finite strains*, Comput. Meth. Appl. Mech. Engrg 155 (1998), 73–95.

[5] RM Brannon & S Leelavanichkul, *A multi-stage return algorithm for solving the classical damage component of constitutive models for rocks, ceramics, and other rock-like media*, Int. J. Fract. 163 (2010), 133–149.

[6] R Butterfield, *A natural compression law for soils (an advance on e-log p′)*, Géotechnique 29 (1979), 469–480.

[7] A Casagrande, *Characteristics of cohesionless soils affecting the stability of slopes and earth fills*, Contributions to soil mechanics, Boston Socitey of Civil Engineers (1936), 257–276.

[8] IF Collins & GT Houlsby, *Application of thermomechanical principles to the modelling of geoetchnical materials*, Proc. R. Soc. Lond. A. 453 (1997), 1975–2001.

[9] IF Collins & T Hilder, *A theorectical framework for constructing elastic/plastic constitutive models of triaxial tests*, Int. J. Numer. Meth. Geomech. 26 (2002), 1313–1347.

[10] IF Collins & PA Kelly, *A thermomechanical analysis of a family of soil models*, Géotechnique 52 (2002), 507–518.

[11] IF Collins, *A systematic procedure for constructing critical state models in three dimensions*, Int. J. Solids Struct. 40 (2003), 4379–4397.

[12] IF Collins & B Muhunthan, *On the relationship between stress–dilatancy, anisotropy, and plastic dissipation for granular materials*, Géotechnique 53 (2003), 611–618.

[13] IF Collins, *Elastic/plastic models for soils and sands*, Int. J. Mech. Sci. 47 (2005), 493–508.

[14] IF Collins, *The concept of stored plastic work or frozen elastic energy in soil mechanics*, Géotechnique 55 (2005), 373–382.

[15] IF Collins, B Muhunthan, ATT Tai & MJ Pender, *The concept of a 'ReynoldsTaylor state' and the mechanics of sands*, Géotechnique 57 (2007), 437–447.

[16] IF Collins, B Muhunthan & B Qu, *Thermomechanical state parameter models for sands*, Géotechnique 60 (2010), 611–622.

[17] WM Coombs, RS Crouch & CE Augarde, *Reuleaux plasticity: Analytical backward Euler stress integration and consistent tangent*, Comput. Methods Appl. Mech. Engrg. 199 (2010), 1733–1743.

[18] WM Coombs & RS Crouch, *Algorithmic issues for three-invariant hyperplastic Critical State models*, Comput. Methods Appl. Mech. Engrg. 200 (2011), 2297–2318.

[19] WM Coombs & RS Crouch, *Non-associated Reuleaux plasticity: Analytical stress integration and consistent tangent for finite deformation mechanics*, Comput. Methods Appl. Mech. Engrg. 200 (2011), 1021–1037.

[20] YF Dafalias, MT Manzari & AG Padadimitriou, *SANICLAY: simple anisotropic clay plasticity model*, Int. J. Numer. Anal. Meth. Geomech. 30 (2006), 1231–1257.

[21] DC Drucker, RE Gibson & DJ Henkel, *Soil mechanics and work-hardening theories of plasticity*, Trans. ASCE 103 (1957), 338–346.

[22] A Federico, G Elia & V Germano, *A short note on the earth pressure and mobilized angle of internal friction in one-dimensional compression of soils*, J. GeoEngineering 3 (2008), 41–46.

[23] A Gens, *Stress-strain characteristics of a low plasticity clay*, PhD. Thesis, Imperial College of Science and Technology, University of London (1982).

[24] A Gens & DM Potts, *Critical state models in computational geomechanics*, Eng. Comput. 178 (1988), 178–197.

[25] KM Górski, E Hivon, AJ Banday, BD Wandelt, FK Hansen, M Reinecke & M Bartelmann, *HEALPix: a framework for high-resolution discretization and fast analysis of data distributed on the sphere*, Astrophys. J. 622 (2005), 759–771.

[26] G Gudehus, *Comparison of some constitutive laws for soils under radially symmetric loading and unloading*. In: Proceedings of the 3rd International Conference on Numerical Methods in Geomechanics, Aachen, 1979, 1309–1323.

[27] K Hashiguchi, *Verification of compatibility of isotropic consolidation characteristics of soils to multiplicative decomposition of deformation gradient*, Soils Found. 48 (2008), 597–602.

[28] GT Houlsby, *A Study of Plasticity Theories and Their Applicability to Soils*, PhD. Thesis, University of Cambridge, 1981.

[29] GT Houlsby, *The use of a variable shear modulus in elastic-plastic models for clays*, Comput. Geotech. 1 (1985), 3–13.

[30] GT Houlsby & AM Puzrin, *A thermomechanical framework for constitutive models for rate-independent dissipative materials*, Int. J. Plasticity 16 (2000), 1017–1047.

[31] GT Houlsby & AM Puzrin, *Principles of Hyperplasticity*, Springer-Verlag London Limited, 2006.

[32] J Jaky, *Pressure in silos*, Proc 2nd Int. Conf. on Soil Mechanics and Foundation Engineering, Rotterdam, Nederland, 1 (1948), 103–107.

[33] PV Lade & JM Duncan, *Cubical triaxial tests on conhesionless soil*, J. Soil Mech. Found. Div. ASCE 99 (1973), 793–812.

[34] PV Lade & MM Kirkgard, *Effects of stress rotation and changes of b-values on cross-anisotropic behavior of natural K_0-consolidated soft clay*, Soils Found. 40 (2000), 93–105.

[35] PV Lade, *Instability, shear banding and failure in granular materials*, Int. J. Solids Struct. 39 (2002), 3337–3357.

[36] H Matsuoka & T Nakai, *Stress-deformation and strength characteristics of soil under three different principal stresses*, Proc. JSCE 232 (1974), 59–70.

[37] PHG Parry, Corresspondence on *On yielding of soils*, Géotechnique 8 (1958), 183–186.

[38] DM Potts, *Numerical analysis: a virtual dream or peactical reality?*, Géotechnique 53 (2003), 535–573.

[39] DM Potts & L Zdravkoić, *Finite element analysis in geotechnical engineering: Application*, Thomas Telford Publishing, London, 2001.

[40] AM Puzrin & GT Houlsby, *A thermomechanical framework for rate-independent dissipative materials with internal functions*, Int. J. Plasticity 17 (2001), 1147–1165.

[41] AM Puzrin & GT Houlsby, *Fundamentals of kinematic hardening hyperplasticity*, Int. J. Solids Struct. 38 (2001), 3771–3794.

[42] KH Roscoe, AN Schofield & CP Wroth, *On the yielding of soils*, Géotechnique 8 (1958), 22–53.

[43] KH Roscoe & JB Burland, *On the generalised stress-strain behaviour of 'wet' clay*. In: J Heyman & FA Leckie (eds.), Engineering Plasticity (1968), Cambridge University Press, 535–609.

[44] AN Schofield & CP Wroth, *Critical State Soil Mechanics*, McGraw-Hill Publishing Company Limited, 1968.

[45] RT Shield, *On Coulomb's law of failure in soils*, J. Mech. Phys. Solids 4 (1955), 10–16.

[46] KJ Willam & EP Warnke, *Constitutive model for the triaxial behaviour of concrete*, Proceedings of the May 17-19 1974, International Association of Bridge and Structural Engineers Seminar on Concrete Structures Subjected to Triaxial Stresses, held at Bergamo Italy, 1974.

[47] DM Wood, *Geotechnical modelling*, Spon Press, 2004.

[48] Y Yamakawa, K Hashiguchi & K Ikeda, *Implicit stress-update algorithm for isotropic Cam-clay model based on the subloading surface concept at finite strains*, Int. J. Plasticity 26 (2010), 634–658.

[49] HS Yu, *Plasticity and Geotechnics*, Springer Press, 2006.

[50] H Ziegler, *An introduction to thermomechanics*, 2nd edn. North Holland Pub. Co, Amsterdam, 1983.

[51] M Zytynski, MF Randolph, R Nova & CP Wroth, *On modeling the unloading-reloading behaviour of soils*, Int. J. Numer. Anal. Meth. Geomech. 2 (1978), 87–93.

Chapter 6

Anisotropic hyperplasticity

Several limitations were identified with the two-parameter family of Critical State (CS) hyperplasticity models developed in the preceding chapter. They are unable to:

(a) give improved fits (to undrained triaxial tests) over the Modified Cam-clay (MCC) model for normally consolidated soils;

(b) reproduce the one-dimensional drained unloading (K_0 swelling) response to high over-consolidation ratios (OCRs);

(c) provide an adequate fit to undrained triaxial extension (UTE) following one-dimensional drained loading (K_0 consolidation) at low OCRs; and

(d) capture the anisotropy of the soil fabric.

Over the last 30 years there have been several extensions in the classical MCC constitutive model in order to overcome these (and other) limitations. The catalogue of constitutive models is continuously increasing in such a way that it is not possible to provide a comprehensive review of each modification. The majority of the extensions can be classified into those that rotate the yield surface off the hydrostatic axis and those that include plasticity within the conventional yield surface. A brief overview of these modifications is now provided.

Rotational extensions to the MCC model introduce anisotropy by allowing the yield surface's major axis to rotate away from the hydrostatic axis [11–13, 33–35, 46, 58, 60] (while pinned at the stress origin). One of the earliest of these is the model proposed by Dafalias in 1986 [13]. In triaxial stress space, this rotated and distorted elliptic yield function[1] (as shown in Figure 6.1 (i)) can be written as

$$f = (N^2 - \beta^2)p(p - p_c) + (q_{\text{txl}} - p\beta)^2 = 0, \tag{6.1}$$

where q_{txl} is the difference between the major and minor principal stresses, $q_{\text{txl}} = \sigma_3 - \sigma_1$, and N is the Critical State line (CSL) gradient consistent with this deviatoric stress measure (that is, $N = (q_{\text{txl}}/p)_{cs}$). β provides a measures of the rotation of the yield surface off the hydrostatic axis in triaxial stress space. This particular form of f, when combined with an associated flow rule, maintains a unique Critical State surface (CSS) for any degree of anisotropy. That is, the isochoric normal to the yield surface remains on the locus $q_{\text{txl}} = pN$. However, when $\beta = N$ the yield function collapses to a line coincident with the CSL

$$f_{(\beta=N)} = (q_{\text{txl}} - pN)^2 = 0.$$

[1] Note, that this yield function is not merely a sheared/rotated isotropic MCC yield function. Although the original (isotropic) elliptic yield function may be thought of as heaving undergone shearing and rotation, it remains an ellipse (albeit with a new aspect ratio and size).

Therefore in Dafalias' model, the level of anisotropy must be $\beta \leq N$ [11]. The form of the yield function (6.1) also causes significant problems when trying to implement a Lode angle dependency (LAD), as a consequence of incurring deviatoric concavity as β increases [8–10]. Recognising this limitation, Dafalias-type anisotropic models have been proposed that include a LAD on the plastic potential surface whilst maintaining a circular deviatoric yield surface [11]. Despite this advancement, these single surface models are unable to capture the behaviour of heavily over-consolidated clays. Thus their use is best limited to normally or lightly over-consolidated soils [11, 34]. A further shortcoming of these models is that they abruptly change from elastic to inelastic material behaviour, whereas real geomaterials show a progressive growth in plasticity.

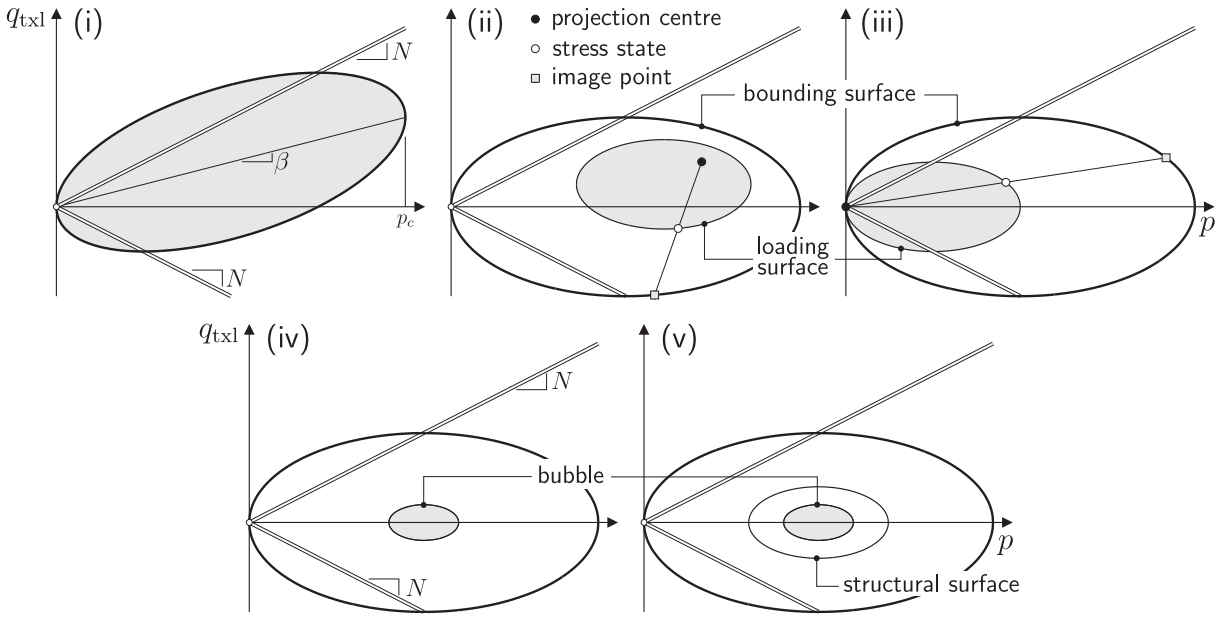

Figure 6.1: Extensions to the classical MCC constitutive model, where the elastic regions are shaded grey: (i) Dafalias' [13] elliptic yield function, (ii) anisotropic bounding surface plasticity, (iii) isotropic bounding surface plasticity, (iv) single inner surface (*bubble*) plasticity and (v) structural surface plasticity.

Non-elliptical plasticity models [46] have been developed, motivated by the recognition that elliptic yield surfaces provide a poor approximation to the response of moderately to heavily overconsolidated clays (on the *dry* side of the CSL), where they significantly over-predict the peak deviatoric stress. Pestana and Whittle's MIT-S1 model [46] used a single distorted lemniscate-shaped yield surface (with non-associated plastic flow) which was allowed to rotate away from the hydrostatic axis. Those authors also included the void ratio as a state variable in the constitutive formulation, as proposed by Been and Jefferies [2], in order to provide a model able to predict the behaviour of both clays and sands. However, unlike the family of constitutive models (that become non-elliptical through specifying α and γ not equal to unity) presented in the previous chapter, the MIT models have not been constructed from a strong thermodynamic basis, but rather from an empirical approach.

Bounding surface plasticity (also known as *subloading surface plasticity* [25]) was initially proposed by Dafalias in his PhD thesis of 1975 [16]. Such models [3, 14–16, 31, 61, 63, 64] can introduce anisotropy[2] into the constitutive equations and plasticity within the conventional yield surface through the use of a projection (or similarity) centre and an image point on the outer *bounding surface* (as shown in Fig-

[2]Not that some bounding surface plasticity models maintain isotropy, such as the recent subloading surface model proposed by Yamakawa *et al.* [61], by fixing the projection centre at the stress origin such that the inner yield surface remains aligned with (and pinned on) the hydrostatic axis (as shown in Figure 6.1 (iii)).

ure 6.1 (ii)). These models allow a smooth transition from elastic to inelastic material behaviour as the inner yield surface (which grows from the similarity centre) increases in size under continued loading. Upon unloading[3] the inner surface can collapse to a point and the projection centre may shift to the unloading stress state, erasing any past material history[4]. This *jump* anisotropy destroys the uniqueness of the CSS, as the CS becomes path dependent for any stress path that involves unloading [9]. Bounding surface models also exhibit spurious *ratcheting* for small cycles of unloading and reloading. Furthermore, they do not satisfy the consistency condition explicitly on the inner loading surface. Consistency is enforced on the bounding surface and the size of the plastic strain increment is determined through a simple proximity rule [61].

Inner surface (bubble) plasticity models [41, 47–49, 51–53] offer plasticity within the conventional yield surface by including an inner, additional, yield surface (the bubble). In these models the elastic region is now confined to the interior of this bubble which can translate within the outer surface (as shown in Figure 6.1 (iv)). The translation is controlled by the particular form of the hardening law. These models have their roots in the multi-surface plasticity models initially proposed by Mroz [42] and Iwan [32]. The two surface approach was motivated by trying to capture hysteretic cyclic behaviour. Unlike bounding surface models, these formulations can maintain a unique asymptotic CSS for stress paths that involve unloading, provided that an appropriate translational hardening law is used [9]. *Structural surface plasticity* models [1, 53] contain three (or more) surfaces; the conventional yield surface, a bubble surface and a structural (or history) surface lying within the conventional yield surface an enclosing the bubble (as shown in Figure 6.1 (v)). This additional surface serves to provide information about the previous stress history of the material (that is, the relative directions of the current and previous loading paths [53]). However, these models still give rise to an abrupt change from elastic to elasto-plastic behaviour, albeit with a smaller purely elastic region than that of a single surface plasticity model.

Infinite surface (or continuous) hyperplasticity models [30, 50] use internal functionals to describe the progressive inelastic behaviour under loading. The free energy and dissipation functions become functionals generating an infinite number of yield surfaces providing smooth stress-strain curves. The past history of the material is maintained within an internal variable function [30]. However the practical implementation of these models is not straightforward. Indeed Puzrin and Burland [50] mentioned the following:

> "*A well-known disadvantage of the infinite number of surfaces hardening rule is that for cyclic loading with decreasing amplitude, it may require virtually infinite computer memory.*"

The mathematical formulation based on functionals results in constitutive model "*calculations* [that] *are less straightforward than in conventional models*" [50], requiring a large number of material parameters.

Recently there has been interest in introducing a measure of the material fabric into the MCC model, with so-called *structured Cam-clay* models [29, 39, 54, 55]. These models try to account for the phenomenon of *in-situ* soils behaving stiffer than laboratory experiments on reconstituted soil samples suggest. They have also be used to predict the behaviour of cemented clays. These models include a *destructuring index* which describes the changes in the internal fabric under deformation (similar to the approach used in damage plasticity). The formulations introduce additional complications in the form of trying to calibrate and link, though empirical equations, this destructuring index to the soil's material properties [29]. However, there is no clear link between re-arrangement of the material fabric and these

[3]The term unloading is used here to denote strain increments that cause the following $\{f_{,\sigma}\}^T\{\Delta\sigma_t\} < 0$. That is, the direction of the stress increment $\{\Delta\sigma_t\}$ is on the opposite side of the yield surface tangent plane to that of the normal to the yield surface $\{f_{,\sigma}\}$; it is inwardly directed.

[4]For isotropic bounding surface models with the projection centre fixed at the stress origin, this jumping does not occur. In these models the unloading response is purely elastic.

empirical destructuring equations.

There have been models proposed that combine rotation of the yield surface off the hydrostatic axis with one or more more inner yield surfaces within the conventional yield surface [23, 24, 52, 59, 60]. The MIT-E3 is one such model, developed by Whittle and co-workers [59, 60] to simulate the behaviour of normally to moderately over-consolidated clays (OCR significantly less than 8). However, as their yield surfaces are based on a rotated (and distorted) ellipsoid, they can dramatically overestimate the peak deviatoric stress of heavily over-consolidated soils. As a number of soils of significant engineering importance (such as London Clay) are heavily over-consolidated (OCRs greater than 10), this inability to simulate their response is a real limitation.

The majority of the models described above have their roots in classical plasticity theory. *Incrementally non-linear* constitutive equations [4, 17] (or *hypoplastic* models [36–38, 40, 56], as discussed in Section 2.2) offer an alternative approach championed (mainly) by the French schools of constitutive modelling. It appears that some of these models are able to provide convincing reproductions of the experimental behaviour of soil. However, the constitutive equations are arguably unnecessarily complex, the models are difficult to validate and the formulations can contain internal contradictions [4]. Recently Nader [44] showed that traditional hypoplastic models are unable to convincingly reproduce the reloading behaviour of soils. Nader proposed an extension to the classical theory to overcome this omission. However, the model presented appeared to be unable to reproduce experimentally observed hysteretic behaviour (following the same curve on under unloading an reloading).

This chapter extends the isotropic α-γ family of models presented in the previous chapter by (i) allowing the yield surface to *shear* off the hydrostatic axis and (ii) by including plasticity within the conventional yield surface. The model was motivated by the need to overcome the limitations discussed in Section 5.6, with the knowledge that the α-γ yield surface offers promise in predicting of both normally and heavily over-consolidated soils within a single, consistent framework. The model described here was first presented by Coombs (with the associated paper by Coombs *et al.* [6]) at the UK Association for Computational Mechanics in Engineering conference in 2011.

Section 6.1 formulates the two-surface anisotropic hyperplasticity model, by describing the elasticity relationship, yield function and direction of plastic flow. The hardening/softening relationships controlling the yield surface growth, anisotropic shearing and translation of the inner yield surface are all described in Section 6.2. The calibration procedure for the new constitutive model is presented in Section 6.3. Section 6.4 describes the algorithmic implementation of the model, including (i) stress integration, (ii) influence of the yield function, (iii) stress return paths, (iv) errors associated with the stress integration procedure, (v) robustness and (vi) linearisation of the constitutive equations for finite deformation analysis. The model is compared with experimental data on Lower Cromer till (LCT) in Section 6.5. Finally, observations on these findings are made in Section 6.6.

In line with geotechnical convention, as with the previous chapter, compressive stresses are positively valued (σ_1 is the least compressive, minor, principal stress and σ_3 the most compressive, major, principal stress). All stresses are treated as being effective stresses (that is, total stress minus the pore pressure) although the prime notation is omitted. The anisotropic constitutive model developed in this chapter must be described using the full nine-dimensional stress space. Due to symmetry, the nine components can be reduced to six. However, care must be taken to ensure that the shear components are correctly accounted for when, for example, calculating the $L2$ norm of a vector.

6.1 Constitutive formulation

The family of constitutive models developed in this chapter adopt the same isotropic non-linear hyperelastic relationship as described in Section 5.1.1.

6.1.1 Shear anisotropy

The procedure for developing plasticity relations from the principles of hyperplasticity was presented in Section 2.2.2. Examination of the behaviour of the isotropic two-parameter family of models suggested that there was merit in investigating the consequences of using a dissipation rate function similar to that presented in Chapter 5, but with the addition of a term linking the volumetric and deviatoric dissipation components

$$\dot{\Phi} = \sqrt{(\dot{\varepsilon}_v^{\mathrm{p}} + \beta_{ij}\dot{\gamma}_{ij}^{\mathrm{p}})^2 A^2 + (\dot{\varepsilon}_\gamma^{\mathrm{p}} B)^2}, \tag{6.2}$$

where β_{ij} accounts for this coupling and A and B are the same stress-like quantities used in the preceding chapter, given by $(5.6)_2$ and (5.20). It seems physically plausible that there should be some coupling between the dissipation arising from volumetric and deviatoric straining. The shearing of particulate media results in volumetric change in the material as a result of clusters (or grains) sliding over one another causing dilation or compaction. (6.2) was first introduced (in triaxial stress space) by Collins and Hilder [5] as an extension to the isotropic family of CS models. However, the model was only presented conceptually, and limited to the axi-symmetric triaxial case (that is, it was not formulated in six-dimensional stress state or integrated for use in boundary value simulations). (6.2) is similar to that proposed by Muhunthan *et al.* [43] who introduced a cross-coupling in the dissipation equation for the MCC model[5]. Following the standard procedure (as given in Section 2.2.2), we obtain the dissipative stresses as

$$p^\varphi = \frac{\partial\dot{\Phi}}{\partial\dot{\varepsilon}_v^{\mathrm{p}}} = \frac{A^2(\dot{\varepsilon}_v^{\mathrm{p}} + \beta_{ij}\dot{\gamma}_{ij}^{\mathrm{p}})}{\dot{\Phi}} \qquad \text{and} \qquad s_{ij}^\varphi = \frac{\partial\dot{\Phi}}{\partial\dot{\gamma}_{ij}^{\mathrm{p}}} = \frac{B^2\dot{\gamma}_{ij}^{\mathrm{p}} + A^2(\dot{\varepsilon}_v^{\mathrm{p}} + \beta_{kl}\dot{\gamma}_{kl}^{\mathrm{p}})\beta_{ij}}{\dot{\Phi}}. \tag{6.3}$$

Rearranging (6.3), the plastic strain rates are

$$\dot{\varepsilon}_v^{\mathrm{p}} = \frac{p^\varphi\dot{\Phi}}{A^2} - \beta_{ij}\dot{\gamma^{\mathrm{p}}}_{ij} \qquad \text{and} \qquad \dot{\gamma^{\mathrm{p}}}_{ij} = \frac{\dot{\Phi}}{B^2}\big(s_{ij}^\varphi - p^\varphi\beta_{ij}\big). \tag{6.4}$$

Substituting (6.4) into (6.2), to eliminate the plastic strain rates, and rearranging, we obtain the instantaneous anisotropic dissipative yield function as

$$F^\varphi = (p^\varphi)^2B^2 + \Big\{\{s^\varphi\} - p^\varphi\{\beta\}\Big\}^T\Big\{\{s^\varphi\} - p^\varphi\{\beta\}\Big\}A^2 - A^2B^2 = 0. \tag{6.5}$$

From (6.5) it is apparent that introducing a cross-coupling in the rate of dissipation function results in the dissipative yield surface being sheared off the hydrostatic axis, where $\{\beta\}$ is a six-component, traceless (deviatoric), measure of this inclination. If $\{\beta\} = \{0\}$ we recover the isotropic dissipative yield surface presented in the previous chapter, with the ellipsoid's major axis coincident with the hydrostatic axis.

When $\{s^\varphi\} = p^\varphi\{\beta\}$, the dissipative pressure is equal to $p^\varphi = \pm A$. Here the stress state is located at the compressive and tensile limits of the yield surface in dissipative stress space. From $(6.4)_2$, at these limits, the plastic shear strain rate is zero, defining the normal consolidation line (NCL) in dissipative stress space. For the tensile apex of the anisotropic yield surface to be at the origin in true stress space,

[5] If $\alpha = \gamma = 1$ then (6.2) and the rate of dissipation function used by Muhunthan *et al.* [43] are equivalent.

the shift stress components must be linked through

$$\{s^\chi\} = p^\chi\{\beta\}. \tag{6.6}$$

Assuming that the hydrostatic component of the shift stress $\{\chi\}$ is given by the same hydrostatic measure used in the preceding chapter (5.10), then the shift stress components become

$$p^\chi = \gamma p_c/2 \qquad \text{and} \qquad \{s^\chi\} = \gamma p_c/2\{\beta\}, \qquad \text{that is} \qquad \{\sigma^\chi\} = \frac{\gamma p_c}{2}\big\{\{1\} + \{\beta\}\big\}. \tag{6.7}$$

The deviatoric component of the shift stress moves the *centre* of the yield surface off the hydrostatic axis. Substituting (6.7) into (6.5), the anisotropic yield surface in true stress space follows as

$$F = (p - \gamma p_c/2)^2 B^2 + \big\{\{s\} - p\{\beta\}\big\}^T \big\{\{s\} - p\{\beta\}\big\} A^2 - A^2 B^2 = 0. \tag{6.8}$$

The true stress space yield surface with a Willam-Warnke (W-W) [57] LAD is shown in Figure 6.2. Papadimitriou *et al.* [45] recently compared Collins and Hilder's [5] anisotropic yield surface (6.8) with that of Dafalias and co-workers' SANICLAY model [11] using experimental data from LCT [20]. They concluded that (6.8) offered improved realism over that of SANICLAY's yield function but at the cost of an additional parameter. However, Papadimitriou *et al.* [45] (i) used an arbitrarily chosen plastic flow rule (eliminating one of the main benefits of the hyperplastic formulation) defined by the same plastic potential surface used in [11] and (ii) placed a LAD only on this plastic potential, not on the yield surface.

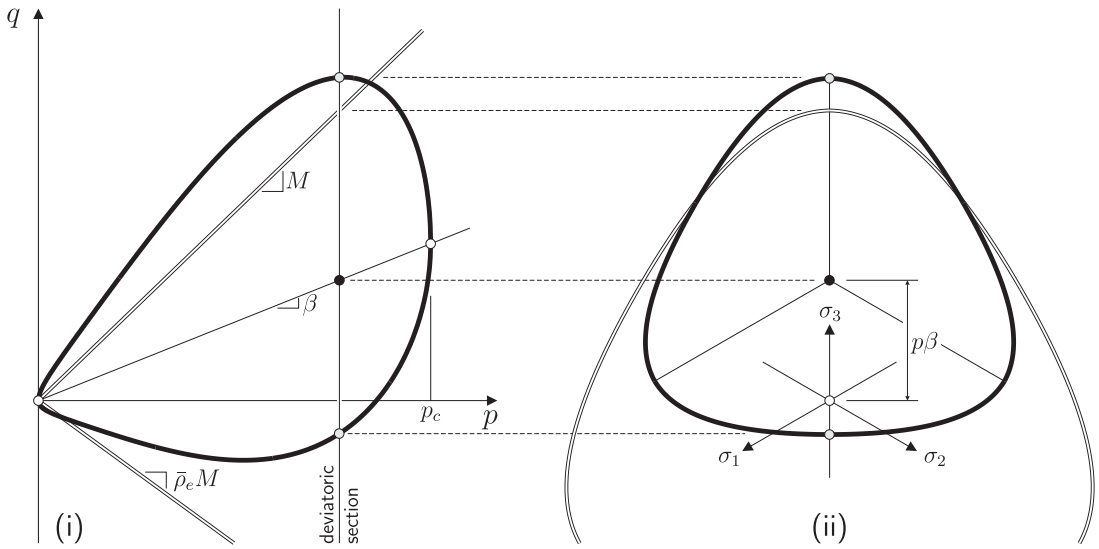

Figure 6.2: Anisotropic yield surface with $\alpha = 0.3$, $\gamma = 0.9$ and $M = 1$ with a W-W LAD ($\bar{\rho}_e = 0.73$): (i) p-q stress space and (ii) a deviatoric section through the yield and CS surfaces.

Figure 6.2 (ii) shows a deviatoric section through the anisotropic yield surface (6.8). The W-W LAD [57], as used in the preceding chapter for the isotropic family of CS models, is now based on a local measure of the Lode angle, θ, from the $\{\beta\}$ axis. The second and third deviatoric stress invariants (denoted J_2 and J_3 in $(2.9)_3$) are measured using the deviatoric distance from the axis of anisotropy, $\{s\} - p\{\beta\}$, rather than the standard deviatoric measure $\{s\}$. Note that $\{\beta\}$ corresponds to a shearing of the yield surface in the deviatoric direction, rather than a rotation away from the hydrostatic axis. This distinction is important, as an initially convex yield surface will remain convex for any degree of shearing, demonstrated by the following.

From (6.8), the deviatoric stress invariant (in the p versus q plane), q, on the yield surface is

$$q = p\beta \pm \underbrace{\frac{B}{A}\sqrt{\gamma p(2-\gamma)(p-p_c)}}_{\text{isotropic component}}. \tag{6.9}$$

The first term in (6.9) represents an anisotropic deviatoric shearing of the isotropic yield surface. The second term describes the isotropic surface presented from the preceding chapter in (5.16). The ratio of the distance between the axis of anisotropy and the yield surface *above* and *below* this axis is constant for any deviatoric plane, that is

$$\frac{|q_{\min} - p\beta|}{|q_{\max} - p\beta|} = \bar{\rho}_e. \tag{6.10}$$

This constant ratio allows the introduction of a local LAD where the deviatoric shape is maintained for any degree of anisotropy. Thereby avoiding the difficulties seen in rotational formulations where the yield surface deviatoric section distorts and can lose convexity as anisotropy increases [8–10].

6.1.2 Inner surface inelasticity

Single surface plasticity models fail to capture the progressive irrecoverable deformations of particulate media which occur within the conventional yield surface. Prompted by this limitation, the following modification is made to the anisotropic rate of dissipation (6.2) to

$$\dot{\Phi} = \dot{\Phi}_1 + \dot{\Phi}_2 = \underbrace{\sqrt{(\dot{\varepsilon}^{\mathrm{p}}_{v_1} + \beta_{ij}\dot{\gamma}^{\mathrm{p}}_{ij_1})^2 A^2 + (\dot{\varepsilon}^{\mathrm{p}}_{\gamma_1} B)^2}}_{\dot{\Phi}_1} + \underbrace{\sqrt{(\dot{\varepsilon}^{\mathrm{p}}_{v_2} + \beta_{ij}\dot{\gamma}^{\mathrm{p}}_{ij_2})^2 A_f^2 + (\dot{\varepsilon}^{\mathrm{p}}_{\gamma_2} B_f)^2}}_{\dot{\Phi}_2}, \tag{6.11}$$

where $\dot{\Phi}_1$ is as given in (6.2) and $\dot{\Phi}_2$ is the new additive rate associated with the inelastic material behaviour within the outer surface F (which maybe thought of as similar to, but clearly not the same as the conventional yield surface). The dissipation attributed to $\dot{\Phi}_1$ can be considered as a measure of the material's long-term past history, marking the threshold for new dissipation, new distortion and re-arrangement of the material fabric, whereas $\dot{\Phi}_2$ provides the small strain dissipative behaviour and recent stress history of the material.

Taking the plastic strain rate derivatives of $\dot{\Phi}_2$ (where the subscripted 2 has been omitted from the stress and strain quantities for compactness), we obtain the inner-surface dissipative stresses as

$$p^{\varphi} = \frac{\partial \dot{\Phi}_2}{\partial \dot{\varepsilon}^{\mathrm{p}}_v} = \frac{A_f^2(\dot{\varepsilon}^{\mathrm{p}}_v + \beta_{ij}\dot{\gamma}^{\mathrm{p}}_{ij})}{\dot{\Phi}_2}, \qquad s^{\varphi}_{ij} = \frac{\partial \dot{\Phi}_2}{\partial \dot{\gamma}^{\mathrm{p}}_{ij}} = \frac{B_f^2\dot{\gamma}^{\mathrm{p}}_{ij} + A_f^2(\dot{\varepsilon}^{\mathrm{p}}_v + \beta_{kl}\dot{\gamma}^{\mathrm{p}}_{kl})\beta_{ij}}{\dot{\Phi}_2}. \tag{6.12}$$

Rearranging, we obtain

$$\dot{\varepsilon}^{\mathrm{p}}_v = \frac{p^{\varphi}\dot{\Phi}_2}{A_f^2} - \beta_{ij}\dot{\gamma}^{\mathrm{p}}{}_{ij} \qquad \text{and} \qquad \dot{\gamma}^{\mathrm{p}}_{ij} = \frac{\dot{\Phi}_2}{B_f^2}\big(s^{\varphi}_{ij} - p^{\varphi}\beta_{ij}\big). \tag{6.13}$$

Substituting these into $\dot{\Phi}_2$ (to eliminate the plastic strain rates) and rearranging, we obtain the instantaneous dissipative inner-surface yield function as

$$f^{\varphi} = (p^{\varphi})^2 B_f^2 + \Big\{\{s^{\varphi}_{\}} - p^{\varphi}\{\beta\}\Big\}^T \Big\{\{s^{\varphi}\} - p^{\varphi}\{\beta\}\Big\} A_f^2 - A_f^2 B_f^2 = 0. \tag{6.14}$$

As before, the dissipative stress is defined as the true stress, $\{\sigma\}$ less the shift stress, $\{\chi\}$. Here we allow the inner surface (in true stress space) to translate away from the stress origin and off the hydrostatic axis through a shift stress with both volumetric, p^{χ}, and deviatoric, $\{s^{\chi}\}$ components. The yield function

in true stress space becomes

$$f = (p - p^\chi)^2 B_f^2 + \{s^\beta\}^T \{s^\beta\} A_f^2 - A_f^2 B_f^2 = 0, \tag{6.15}$$

where the local deviatoric stress $\{s^\beta\}$ is defined as

$$\{s^\beta\} = \{s\} - \{s^\chi\} - (p - p^\chi)\{\beta\}. \tag{6.16}$$

This deviatoric stress is a measure of the distance between the current stress state and the inclined inner yield surface's major axis. This axis, as with $\{\beta\}$ for (6.8), passes through the points of purely compactive and purely dilative plastic flow on the inner yield surface (points (i) and (ii) in Figure 6.3).

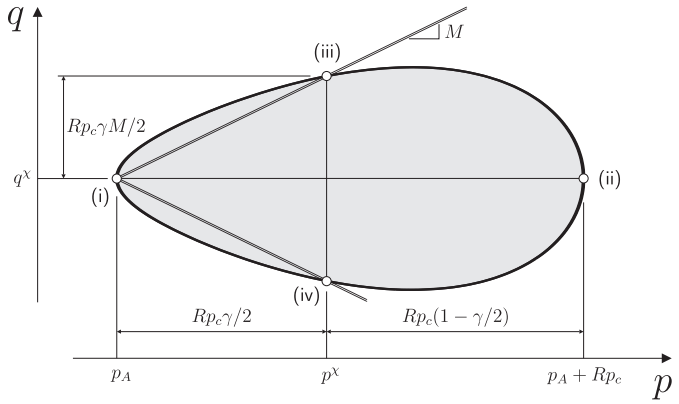

Figure 6.3: Inner surface identifying quantities which control A_f and B_f.

The stress-like parameters A_f and B_f, that define the size and the axis ratio of the surface in dissipative stress space, are determined by assuming that the inner yield (6.15) and outer (6.5) surfaces are geometrically similar[6]. Figure 6.3 shows the inner yield surface, as defined by (6.15), for the case of zero anisotropy. In the special case of triaxial conditions and with $\beta = \mathrm{tr}\Big([\beta][\beta]\Big) = 0$, (6.15) becomes

$$f = \big(p - p^\chi\big)^2 B_f^2 + \big(q - q^\chi\big)^2 A_f^2 - A_f^2 B_f^2 = 0. \tag{6.17}$$

Considering points (i) and (ii) in Figure 6.3

$$p = p^\chi \pm A_f \qquad \text{and} \qquad q = q^\chi : \qquad \begin{array}{ll} \text{(i)} & p = p_A, \\ \text{(ii)} & p = p_A + Rp_c, \end{array} \tag{6.18}$$

where $R \in [0, 1]$ is the constant ratio of the size of the inner surface to that of the outer surface and $p_A = p^\chi - Rp_c\gamma/2$ is the least compressive extremity (or apex) of this bubble. Assuming that A_f has the form

$$A_f = A_{f_1}(p - p_A) + A_{f_2} Rp_c, \tag{6.19}$$

where A_{f_1} and A_{f_2} are determined by considering stress states (i) and (ii), we arrive at

$$A_f = (1 - \gamma)(p - p_A) + \frac{\gamma R p_c}{2}. \tag{6.20}$$

[6]That is, congruent, by a unform scaling from a similarity centre.

For points (iii) and (iv) in Figure 6.3

$$p = p^{\chi} \qquad \text{and} \qquad q = q^{\chi} \pm B_f : \qquad \begin{array}{ll} \text{(iii)} & q = q^{\chi} + MRp_c\gamma/2, \\ \text{(iv)} & q = q^{\chi} - \bar{\rho}_e MRp_c\gamma/2. \end{array} \tag{6.21}$$

Assuming that B_f has an equivalent form to A_f, we obtain

$$B_f = \bar{\rho}(\theta)M\Big((1-\alpha)(p-p_A) + \alpha\gamma Rp_c/2\Big). \tag{6.22}$$

Substituting $p_A = p^{\chi} - Rp_c\gamma/2$ into (6.20) and (6.22), allows A_f and B_f to be written as

$$A_f = (1-\gamma)(p-p^{\chi}) + (2-\gamma)\gamma Rp_c/2 \qquad \text{and} \qquad B_f = \bar{\rho}(\theta)M\Big((1-\alpha)(p-p^{\chi}) + \gamma Rp_c/2\Big). \tag{6.23}$$

Shearing the inner yield surface (that is, when $\{\beta\}$ is non-zero) has no consequence on A_f and B_f as these parameters depend only on the size of the yield surface (Rp_c) and the distance between the current hydrostatic pressure and the *centre* of the inner surface ($p - p^{\chi}$).

Figure 6.4 shows the two-surface anisotropic hyperplasticity model in (i) p-q stress space and (ii) at a deviatoric section through the *centre* of the inner yield surface (that is where $p = p^{\chi}$)[7]. The projection (or similarity) centre $\{\sigma_0\}$ is the point about which the inner and outer surfaces are geometrically similar, such that a ray extending from the projection centre passes through points on the inner yield and outer surfaces with common normals (and plastic flow directions). The distance between these intersections are controlled by R, such that we have the following expression linking a stress state on the inner yield surface, $\{\sigma\}$, and its image point, $\{\breve{\sigma}\}$, on the outer surface

$$\{\breve{\sigma}\} = \{\sigma\} + \Big((1-R)/R\Big)\Big\{\{\sigma\} - \{\sigma_0\}\Big\}. \tag{6.24}$$

The projection centre can then be defined by considering the intersection of two lines: (i) passing through the stress origin and the apex of the inner yield surface and (ii) passing through the *centres* of the inner yield and outer surfaces

$$\{\sigma_0\} = \frac{1}{(1-R)}\Big\{\{\sigma^{\chi}\} - Rp_c\gamma\big\{\{1\} + \{\beta\}\big\}/2\Big\}. \tag{6.25}$$

Vanishing bubble

In the limiting case where $R \to 0$, A_f and B_f become

$$A_f = (1-\gamma)(p-p^{\chi}) \qquad \text{and} \qquad B_f = \bar{\rho}(\theta)M(1-\alpha)(p-p^{\chi}). \tag{6.26}$$

Substituting (6.26) into (6.15), the inner surface yield function becomes

$$f = \Big(\bar{\rho}(\theta)M(1-\alpha)\Big)^2(p-p^{\chi})^2\Big(1-(1-\gamma)^2\Big) + \{s^{\beta}\}^T\{s^{\beta}\}(1-\gamma)^2 = 0, \tag{6.27}$$

which is satisfied when $p = p^{\chi}$ and $\{s\} = \{s^{\chi}\}$, that is when the stress state and the centre of the (zero-sized) inner surface coincide[8]. This allows the inner surface yield function to be written as

$$f = \big(p-p^{\chi}\big)^2 + \big\{\{s\} - \{s^{\chi}\}\big\}^T\big\{\{s\} - \{s^{\chi}\}\big\} = 0. \tag{6.28}$$

[7] In this figure, the centre of the inner surface happens to lie in the plane of the compression meridian. In general this need not be the case.

[8] In addition to the trivial case of $\alpha = \gamma = 1$.

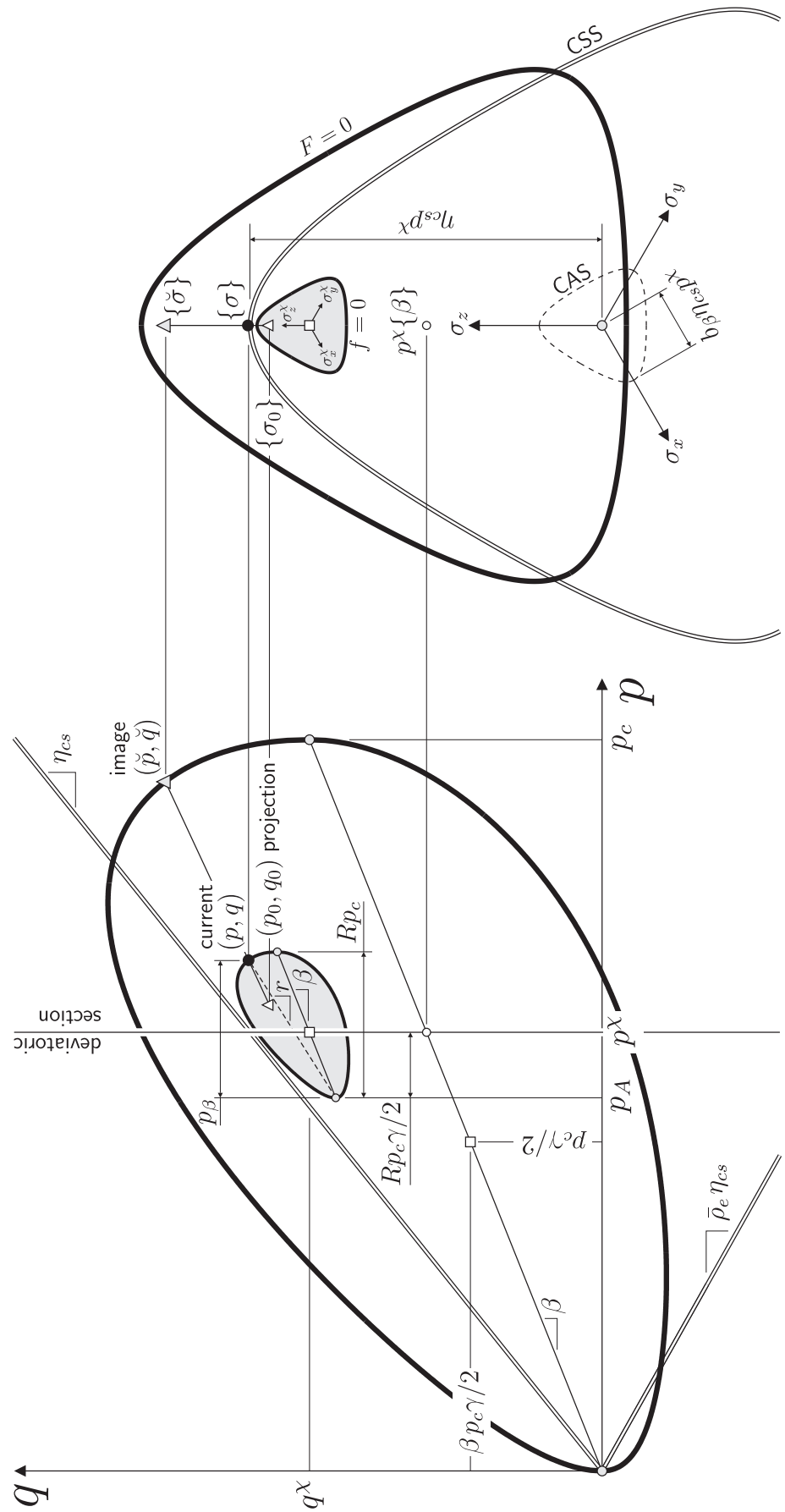

Figure 6.4: Two surface anisotropic model with $\eta_{cs} = 0.8$, $\alpha = 0.6$, $\gamma = 0.9$ and $\bar{\rho}_e = 0.7$: (i) in p-q stress space and (ii) deviatoric section through $p = p^\chi$. The LAD Critical State surface (CSS) and critical anisotropy surface (CAS, see Section 6.2.2) are identified in the deviatoric section. The black circle, white square and white triangle identify the current stress state (on the inner yield surface), image point (on the outer surface) and projection centre (within the inner surface) respectively.

However, the case where $R = 0$ causes a difficulty in that the image point is undefined as (6.24) becomes singular (in addition to other problems with the plastic flow direction). Application of the two-surface model in this thesis is restricted to a finite positive R.

6.1.3 Plastic flow

The direction of plastic flow in dissipative stress space for the inner-surface is obtained from the derivative of (6.14) with respect to the dissipative stresses as

$$\{f^{\varphi}{}_{,\varphi}\} = \frac{2}{3}B_f^2\Big(p^{\varphi} + A_f^2\{p^{\varphi}\{\beta\} - \{s^{\varphi}\}\}^T\{\beta\}\Big)\{1\} + 2A_f^2\big\{\{s^{\varphi}\} - p^{\varphi}\{\beta\}\big\}. \tag{6.29}$$

Substituting for the dissipative stresses, $\{\sigma^{\varphi}\} = \{\sigma\} - \{\sigma^{\chi}\}$, we obtain the direction of plastic flow in true stress space as

$$\{g_{,\sigma}\} = \frac{2}{3}\Big(B_f^2(p - p^{\chi}) - A_f^2\{s^{\beta}\}^T\{\beta\}\Big)\{1\} + 2A_f^2\{s^{\beta}\}. \tag{6.30}$$

The direction of this plastic flow and the normal to the yield surface *above* the axis of anisotropy (that is, when $\eta \geq \beta$), in terms of the dilation angle, are shown in Figure 6.5 (i) for $\beta = 0$, $M/2$ and M when the inner and outer surfaces coincide ($R = 1$, $A_f = A$ and $B_f = B$). As with the isotropic models discussed in the preceding chapter, when α and γ are not equal to 1, the direction of plastic flow and the normal to the yield surface do not coincide. The departure between the direction of plastic flow and the normal to the yield surface, when $R = 1$, *above* the axis of anisotropy, is

$$\{f_{,\sigma}\} - \{g_{,\sigma}\} = \frac{2}{3}\Big(A(1-\gamma)\big(B^2 + (q - p\beta)^2\big) + MB(1-\alpha)\big(\gamma p(2-\gamma)(p - p_c)\big)\Big)\{1\}. \tag{6.31}$$

The normal to the yield surface is given in Appendix E. The disparity between these directions arises from the volumetric components. Perhaps surprisingly, the difference in the directions is also independent of the level of anisotropy. On the yield surface, with $R = 1$, q is given by (6.9). Substituting for q in (6.31) eliminates β from the equation. If we were to measure the friction angle from the axis of anisotropy, rather than the hydrostatic axis, we would recover the isotropic plastic flow properties (as shown in Figure 5.5).

When $\{\beta\} = \{0\}$, the positions of purely deviatoric plastic flow are located at a friction angle of $\arctan(M)$, on the CSS. As the surface anisotropy increases, the stress ratios corresponding to these isochoric plastic flow states change. Setting $\{g_{,\sigma}\}^T\{1\} = 0$ (the isochoric plastic flow condition) and enforcing $F = 0$, we obtain the following quartic in p/p_c for the position of zero volumetric plastic strains (for a given M, α and γ) on the outer surface as

$$\begin{aligned}
(p/p_c)^4\Big(M^2(1-\alpha)^2 + \beta^2\gamma(2-\gamma)(1-\gamma)^2\Big) &+ \dots \\
(p/p_c)^3\gamma\Big(M^2\big(\alpha(1-\alpha) - (1-\alpha)^2\big) + \beta^2(2-\gamma)\big(\gamma(1-\gamma) - (1-\gamma)^2\big)\Big) &+ \dots \\
(p/p_c)^2\gamma^2\Big(M^2\big((1-\alpha)^2/4 + \alpha^2/4 - \alpha(1-\alpha)\big) + \beta^2(2-\gamma)\big(\gamma/4 - (1-\gamma)\big)\Big) &+ \dots \\
(p/p_c)\gamma^3\Big(M^2\big(\alpha(1-\alpha)/4 - \alpha^2/4\big) - \beta^2(2-\gamma)/4\Big) &+ \dots \\
M^2\alpha^2\gamma^4/16 &= 0.
\end{aligned} \tag{6.32}$$

The normalised stress ratio of the point on the yield surface with isochoric plastic flow ($\eta_{\dot{\varepsilon}_v^p=0}$) for β between 0 and M is shown in Figure 6.6 (ii). Figure 6.6 (i) shows the location of these points in normalised p-q stress space. As β increases, so $\eta_{\dot{\varepsilon}_v^p=0}$ under triaxial compression increases. However, $\eta_{\dot{\varepsilon}_v^p=0}$ under triaxial extension initially reduces but then increases to a stress ratio above that of the original CS. Introducing $\{\beta\}$ into the constitutive equations results in the loss of uniqueness of the isochoric cone as that flow state is clearly dependent on the degree of anisotropy. However, as will be shown in Section 6.2.2,

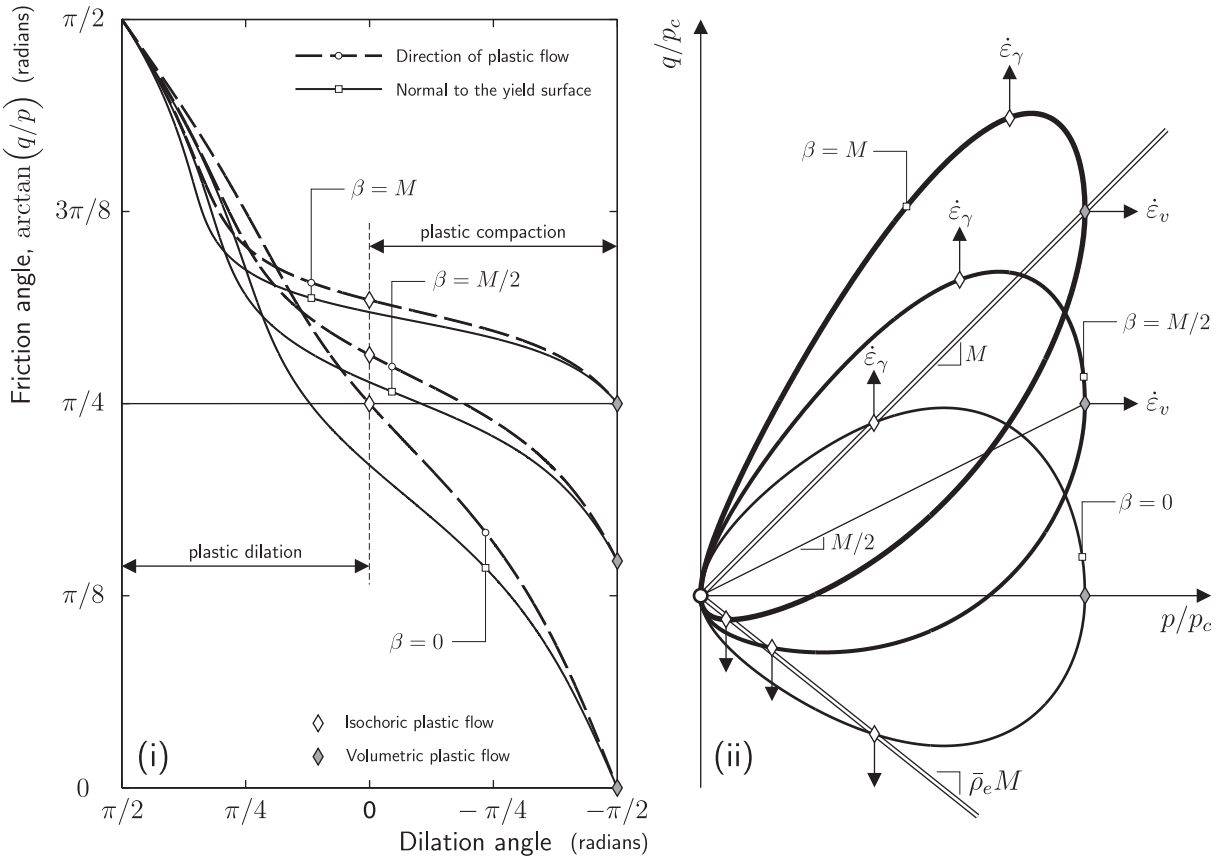

Figure 6.5: Anisotropic yield surface with $\alpha = 0.6$, $\gamma = 0.9$, $R = 1$, $M = 1$ and $\bar{\rho}_e = 0.8$: (i) direction of plastic flow and the normal to the yield surface for $\beta = 0$, $M/2$ and M and (ii) yield surfaces in normalised triaxial p-q stress space.

the model proposed in this thesis still offers a unique (final) CSS which is independent of the degree of anisotropy.

The position of purely hydrostatic compressive plastic flow remains at the *nose* (the most compressive extremity) of the yield surface on the NCL, coinciding with the axis of anisotropy $\{\beta\}$, as shown in Figure 6.5 (ii). This can also be seen by the grey shaded diamond symbol in Figure 6.5 (i) where the position of plastic flow with pure compaction (that is, with a dilation angle of $-\pi/2$) lies at a friction angle of $\arctan(\beta)$.

6.1.4 Lode angle dependency

As shown in Figure 6.4, the anisotropic two-surface model includes a dependence on the Lode angle, θ, through B (5.20) and B_f (6.23) in a manner analogous to that used in the isotropic model of Chapter 5. To ensure convexity, the Lode angle is a local measure based on the local deviatoric stress measured from the anisotropic axes of the outer and inner yield surfaces respectively. The Lode angle, for the inner surface, is calculated from $(2.11)_3$ with J_2 and J_3 replaced by

$$J_2^\beta = \frac{1}{2}\mathrm{tr}\Big([s^\beta][s^\beta]\Big) \qquad \text{and} \qquad J_3^\beta = \frac{1}{3}\mathrm{tr}\Big([s^\beta][s^\beta][s^\beta]\Big), \tag{6.33}$$

respectively, where $[s^\beta]$ is the three by three matrix equivalent of $\{s^\beta\}$, given by (6.16).

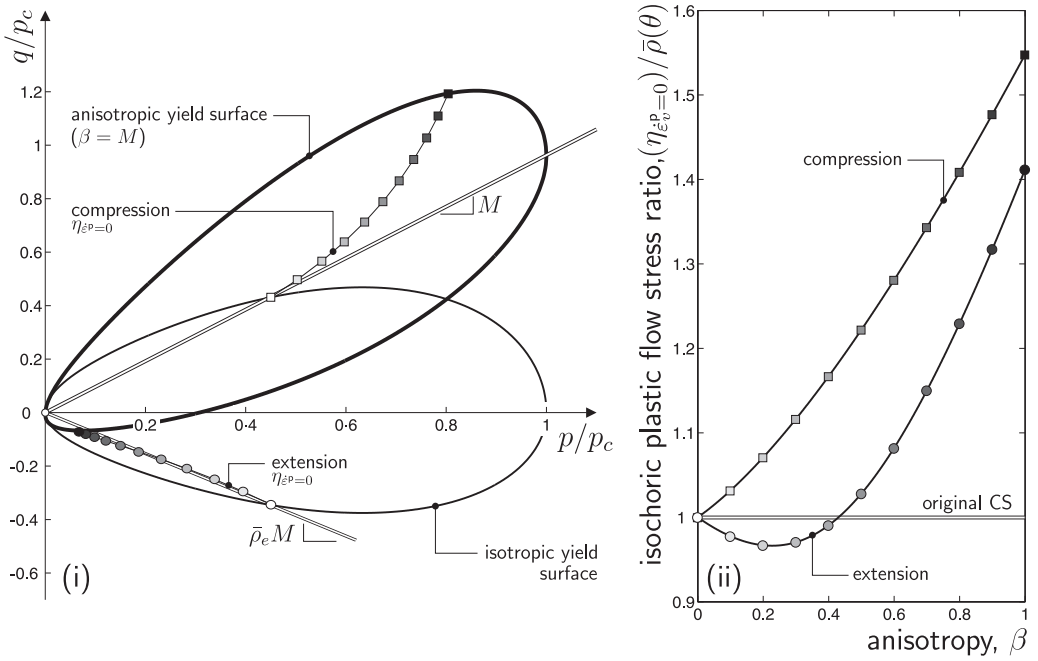

Figure 6.6: Development of the position of isochoric plastic flow for the anisotropic model with $\alpha = 0.6$, $\gamma = 0.9$, $M = 1$, $R = 1$ and $\bar{\rho}_e = 0.8$: (i) p-q stress space and (ii) stress ratio versus anisotropy.

6.1.5 β-α-γ family of models

Figure 6.7 shows the potential family of models which the two-surface, two-parameter anisotropic hyperplasticity model offers. The left of the figure presents models with no LAD, whereas the models on the right have a W-W LAD with $\bar{\rho}_e = 0.7$. The first row, Figure 6.7 (i), contains the classical MCC constitutive model ($\alpha = \gamma = 1$, $\bar{\rho}_e = 1$, $R = 1$ and $\{\beta\} = \{0\}$), which provides the basis for all of the models in the figure. Figure 6.7 (ii) extends the MCC model by shearing the ellipsoid's major axis off the hydrostatic axis. This shearing was proposed by Collins *et al.* [5] through introducing a coupling term in the dissipation equation (6.2). That formulation [5] did not include a LAD or an inner surface. The centre of the third row of Figure 6.7 (iii) shows one member of the two-parameter single surface isotropic family of CS models (with $\alpha = 0.4$ and $\gamma = 0.9$) proposed by Collins and Hilder [5] (with no LAD, left) and Coombs and Crouch [7] (with a W-W LAD, right, as described in Chapter 5). Figure 6.7 (iv) shows the β, α, γ model (for $\alpha = 0.4$, $\gamma = 0.9$ and $\beta = 0.4$), with and without a LAD together with an inner surface, as described in this chapter.

The two-surface LAD anisotropic two-parameter CS model (lower right, Figure 6.7) is the most sophisticated member of this family of hyperplastic constitutive models. The model reduces back to the classical MCC constitutive model by allowing inner yield and outer surfaces to coincide, fixing the yield surface's major axis on the space diagonal ($\{\beta\} = \{0\}$) and setting $\alpha = \gamma = 1$. The complexity of adding an inner surface, shear anisotropy and changing the shape (thereby non-associated plastic flow) can be introduced or removed as analyses dictate (the computational cost of the extra features are discussed in Section 7.2.2).

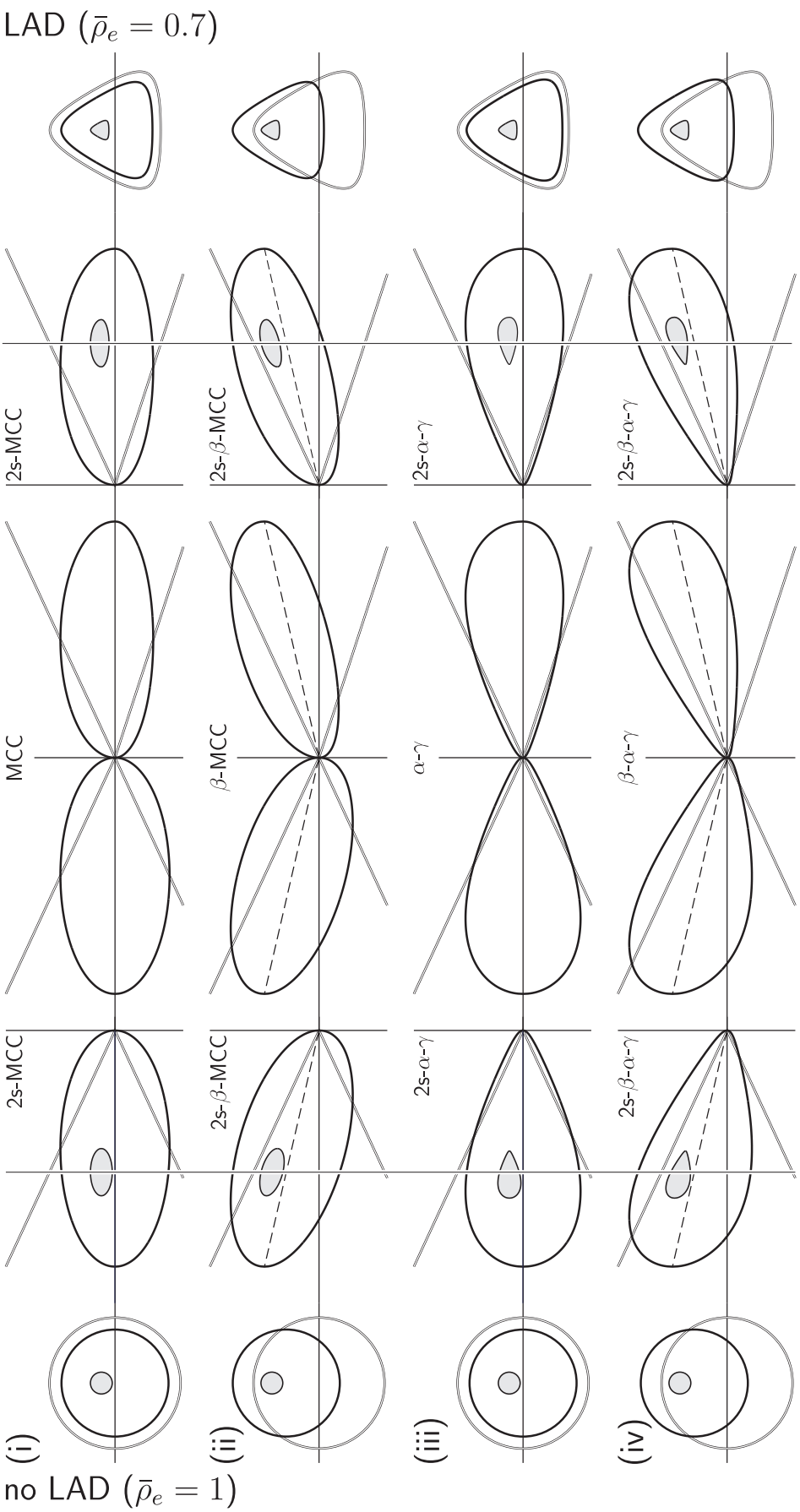

Figure 6.7: Family of yield surfaces from the anisotropic two-surface two-parameter model with $M = 0.8$: (i) $\alpha = \gamma = 1$ with $\beta = 0$, (ii) $\alpha = \gamma = 1$ with $\beta = 0.4$, (iii) $\alpha = 0.4$, $\gamma = 0.9$ with $\beta = 0$ and (iv) $\alpha = 0.4$, $\gamma = 0.9$ with $\beta = 0.4$.

6.2 Hardening/softening relationships

6.2.1 Isotropic expansion/contraction

The hardening relationship for p_c, controlling both the size of the outer (and, through R) the inner yield surfaces, is assumed to be the same as that used in Chapter 5 for the isotropic family of plasticity models (5.25).

6.2.2 Anisotropic Critical State

The anisotropic two-surface model allows the axes of both the inner yield and outer surfaces to shear away from the hydrostatic axis via a shared but non-zero $\{\beta\}$. With the yield surface and direction of plastic flow suggested above, unless the level of anisotropy reduces to zero ($\{\beta\} \rightarrow \{0\}$) when approaching the CS, the original isotropic CSS will be lost and the stress ratio at that *final* CS dependent on the stress path taken to reach that state. To overcome this loss of uniqueness, we make use of the following anisotropic hardening relationship, initially proposed by Wheeler *et al.* [58][9]

$$\{\dot{\beta}\} = C_\beta \left(\Big\{ a_\beta \{r\} - \{\beta\} \Big\} \langle \dot{\varepsilon}_v^{\mathrm{p}} \rangle + x_\beta \Big\{ b_\beta \{r\} - \{\beta\} \Big\} \dot{\varepsilon}_\gamma^{\mathrm{p}} \right), \tag{6.34}$$

where $\langle (\cdot) \rangle$ is the ramp function of $(\cdot)$

$$\langle \dot{\varepsilon}_v^{\mathrm{p}} \rangle = \dot{\varepsilon}_v^{\mathrm{p}} \quad \text{if} \quad \dot{\varepsilon}_v^{\mathrm{p}} > 0 \qquad \text{and} \qquad \langle \dot{\varepsilon}_v^{\mathrm{p}} \rangle = 0 \quad \text{if} \quad \dot{\varepsilon}_v^{\mathrm{p}} \leq 0. \tag{6.35}$$

The use of a ramp function results in the evolution of anisotropy being invariant to dilative (negative) plastic strains[10]. Compressive plastic volumetric strains in (6.34) drag the current level of anisotropy towards the target value of $a_\beta\{r\}$, where $\{r\}$ is given below and a_β is a material constant. The motivation for this change in $\{\beta\}$ follows the same argument as that given by Wheeler *et al.* [58]:

> "*...plastic volumetric strains, involving slippage at inter-particle or inter-ped contacts, result in a gradual rearrangement of the soil fabric towards a configuration that has a degree of anisotropy that is controlled by the anisotropy of the stress state under which this plastic straining is occurring.*"

Deviatoric plastic strains[11], $\dot{\varepsilon}_\gamma^{\mathrm{p}}$, drag the current level of anisotropy towards a different target value of anisotropy given by $b_\beta\{r\}$. The local stress ratio, $\{r\}$, provides the direction of evolution of anisotropy (see Figure 6.4 (i)). It is defined as the deviatoric to volumetric stress ratio measured from the *apex* of the inner yield surface, given by

$$\{r\} = \frac{\{s^r\}}{p_\beta} = \frac{\{s\} - \{s^\chi\} + R p_c \gamma \{\beta\}/2}{p - p^\chi + R p_c \gamma / 2} \tag{6.36}$$

When examining (6.34) we see that the material constant x_β controls the relative contribution from the volumetric and deviatoric plastic strains and C_β scales the absolute rate of evolution. If $x_\beta = 0$ then the anisotropic hardening is only dependent on the compressive plastic volumetric strains and under a constant load path the level of anisotropy will asymptotically approach $a_\beta\{r\}$. However, setting $x_\beta = 0$

[9] Note, that this form of hardening law has been used in several models since being proposed by Wheeler *et al.* [58], namely the S-CLAY1 and S-CLAY1S [34, 35], BSCLAY [52], amongst others.

[10] Note, that Pestana and Whittle [46] also made use of a ramp function on the plastic volumetric strain increment in their proposed rotational hardening law.

[11] Note, that unlike Wheeler *et al.*'s [58] hardening law, constructed in triaxial *p-q* stress space, the modulus sign is not required on the deviatoric plastic strain rate as $\dot{\varepsilon}_\gamma^{\mathrm{p}}$ is the L2 norm of the deviatoric plastic strain rate $\{\dot{\gamma}^{\mathrm{p}}\}$.

would result in a non-unique level of anisotropy at the CS, with $\{\beta\}$ being dependent on the accumulated compressive volumetric plastic strains along the stress path to the CSS. As $x_\beta \to \infty$ then the hardening law will be dominated by the deviatoric plastic strains. Unlike some anisotropic hardening laws, which depend purely on plastic volumetric strains [13, 60], the expression adopted here, (6.34), gives rise to a unique level of anisotropy at the CS[12]. This degree of anisotropy is referred to here as the Critical Anisotropy State (CAS). When approaching the CS the plastic volumetric strain disappears while the level of anisotropy tends towards the deviatoric target value $b_\beta\{r\}$. The anisotropy of the yield surface at the CS is independent of both (i) the initial anisotropy and (ii) the stress path taken to the reach this state. It is only dependent on the final CS stress state. This unique level of *fabric* anisotropy also results in a unique CSL in the bi-logarithmic void ratio versus hydrostatic pressure plane. The majority of previous formulations that include anisotropic shearing of the yield surface do not predict a unique CAS. One exception is Wheeler *et al.*'s S-CLAY1 model [58] (and subsequent extensions).

The ramp function on the plastic volumetric strains ensures that the level of anisotropy does not diverge from the target value when experiencing plastic dilation. This function means that under dilative plastic straining, it is only the isochoric component of the rate that influences $\{\beta\}$. Unlike other anisotropic CS formulations [11–13, 33, 34, 46, 58, 60], hyperplastic anisotropy is introduced by shearing the inner and outer yield surfaces without any additional geometric constraints on the surfaces. This allows the degree of anisotropy to equal, or even exceed, M without the deviatoric radii of the surfaces disappearing (as shown in Figure 6.6 (i)). The yield surface used by Wheeler *et al.* [58] (as originally introduced by Dafalias in 1986 [13], given by (6.1)) collapses to a line when the level of anisotropy equals the gradient of the CSL.

Substituting (6.36) into (6.34) and re-arranging, we obtain

$$\{\dot{\beta}\} = C_\beta \left(d_\beta \frac{\{s\} - \{s^\chi\}}{p_\beta} + \{\beta\} \left(\frac{d_\beta R p_c \gamma}{2 p_\beta} - \left(\langle \dot{\varepsilon}_v^{\mathrm{p}} \rangle + x_\beta \dot{\varepsilon}_\gamma^{\mathrm{p}} \right) \right) \right), \tag{6.37}$$

where

$$d_\beta = \left(a_\beta \langle \dot{\varepsilon}_v^{\mathrm{p}} \rangle + x_\beta b_\beta \dot{\varepsilon}_\gamma^{\mathrm{p}} \right) \qquad \text{and} \qquad p_\beta = p - p^\chi + R p_c \gamma / 2. \tag{6.38}$$

p_β (as shown in Figure 6.4 (i)) is a hydrostatic measure of the position of the current stress state from that of the apex of the inner yield surface. When $R = 1$ the inner yield and outer surfaces coincide and $p_\beta = p$, as $p^\chi = p_c \gamma / 2$.

When approaching the CS, the volumetric component of plastic flow reduces and the evolution of $\{\beta\}$ is controlled by the deviatoric plastic strains. In the limiting case, where $\dot{\varepsilon}_v^{\mathrm{p}} = 0$, $\{\dot{\beta}\}$ becomes

$$\{\dot{\beta}\}_{\dot{\varepsilon}_v^{\mathrm{p}}=0} = C_\beta x_\beta \Big\{ b_\beta \{r\} - \{\beta\} \Big\} \dot{\varepsilon}_\gamma^{\mathrm{p}}. \tag{6.39}$$

Under continued plastic shearing with no change in state, $\{\dot{\beta}\} \to \{0\}$ and

$$\{\beta\}_{cs} = b_\beta \{r\}_{cs}, \tag{6.40}$$

where $(\cdot)_{cs}$ denotes a quantity at the CS. If $b_\beta = 0$, anisotropy disappears when approaching the CS and $(p/p_c) = \gamma/2$ at a stress ratio $\eta = q/p = M$. When $b_\beta \neq 0$, the value of M to maintain the original required p-q stress ratio at the CS is obtained from η_{cs}, γ, α and b_β. At the CS the inner yield and outer surfaces coincide at a stress state on the CS cone where $\{\sigma\} = \{\breve{\sigma}\} = \{\sigma_0\}$, i.e. the stress, image and

[12] That is, if $x_\beta \neq 0$.

similarity centre states are coincident[13]. The value of M required to maintain the unique η_{cs}, can be obtained by the procedure given below.

(i) First, by recognising that $\{g_{,\sigma}\}^T\{1\} = 0$ at η_{cs}, from (6.30) we have

$$B^2 = \frac{A^2(\eta_{cs})^2 b_\beta(1-b_\beta)}{1-\gamma(p_a)_{cs}/2}, \qquad \text{where} \qquad (p_a)_{cs} = \left(\frac{p_c}{p}\right)_{cs}. \tag{6.41}$$

(ii) From the outer surface yield function (6.8), B^2 may be expressed as

$$B^2 = \frac{A^2(\eta_{cs})^2(1-b_\beta)^2}{\gamma(2-\gamma)((p_a)_{cs}-1)}. \tag{6.42}$$

(iii) Eliminating B^2 between (6.41) and (6.42) provides $(p_a)_{cs}$ as

$$(p_a)_{cs} = \frac{1-b_\beta+b_\beta\gamma(2-\gamma)}{b_\beta\gamma(2-\gamma)+\gamma(1-b_\beta)/2}. \tag{6.43}$$

Therefore the relative position of the CS on the outer surface is solely a function of b_β and γ.

(iv) Rearranging (6.42) and substituting for A and B, we obtain M as

$$M = \eta_{cs}\left(\frac{\big(1-\gamma+\gamma(p_a)_{cs}/2\big)(1-b_\beta)}{\big(1-\alpha+\alpha\gamma(p_a)_{cs}/2\big)\sqrt{\gamma(2-\gamma)\Big((p_a)_{cs}-1\Big)}}\right), \tag{6.44}$$

where η_{cs} is the experimentally determined stress ratio at the CS.

By obtaining the stress ratio, η_{cs}, and defining the level of anisotropy, b_β, at the CS, through (6.44) it is possible to obtain the appropriate M to maintain the unique asymptotic η_{cs} (for a given α and γ). Figure 6.8 (i) gives the relative position of the CS on the outer surface[14] normalised by the isotropic position ($\gamma/2$) for $b_\beta \in [0, 0.9]$ with $\gamma = 0.7$ to 1 in 0.1 increments (identified by the grey shaded region). The value of M required to maintain a specific unique η_{cs} is shown for $\alpha = 0.6$ in Figure 6.8 (i) and for $\alpha = 1$ and 0.3 in Figure 6.8 (ii). As α decreases, so does the range of M values required to maintain a given η_{cs}. The value of M/η_{cs} and the relative position of the intersection of the CSL with the outer surface $2p/\gamma p_c$ have been identified for $b_\beta = 0.6$ and $\gamma = 0.9$ in Figure 6.8. Classical normalised CS gradients of $M/\eta_{cs} = 0.685$, 0.885 and 0.585 maintain the original gradient of the CSS, η_{cs}, for $\alpha = 0.6$, 0.3 and 1 respectively (as shown in Figures 6.8).

In 1965 Horne [27, 28] investigated the behaviour of rotund, rigid, cohesionless particles[15]. The work offered the following conclusion regarding the response of granular material within a triaxial test cell [28]

> *"... the complete behaviour in the triaxial test may be explained in terms of an induced degree of anisotropy which increases to a maximum close to the peak stress ratio, subsequently decreasing until the condition of no further volume change causes the degree of anisotropy to become stabilized."*

[13] Therefore, the procedure for determining M can be conducted by only considering the outer yield surface.

[14] Note, that as in the isotropic case, α has no influence on the relative position of the intersection between f and the CSS.

[15] Horne's [27, 28] work ignored the effect of elastic/plastic deformation, crushing and cracking, assuming that the deformation occurs as a result of the relative motion between groups of particles.

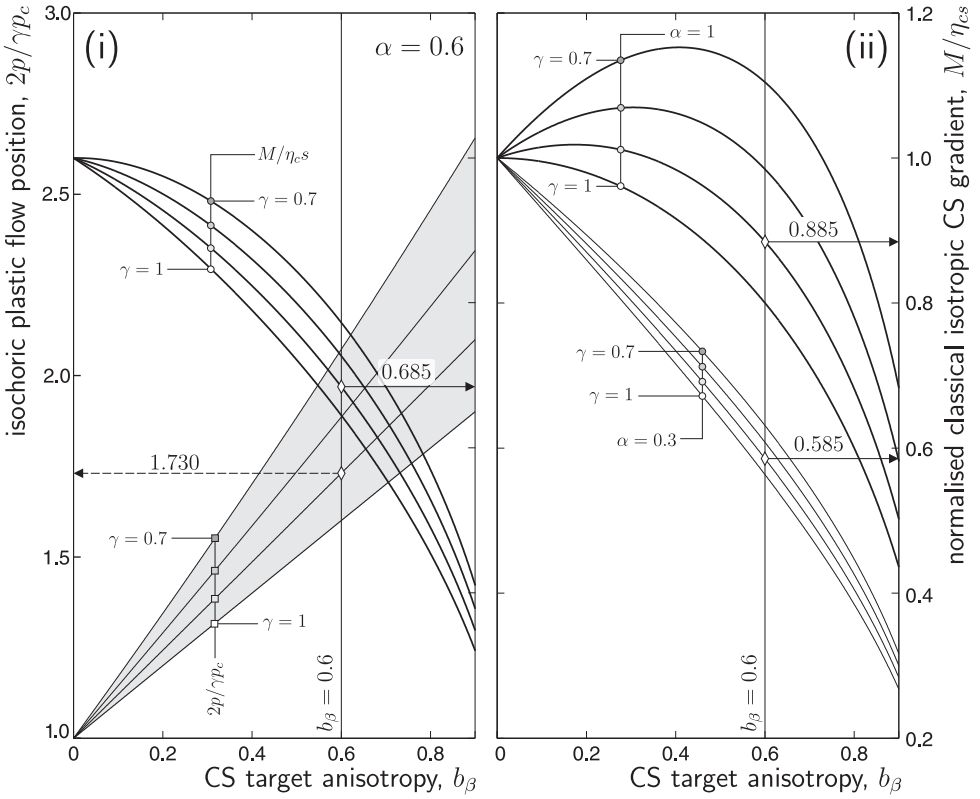

Figure 6.8: Influence of anisotropy on the CS: (i) normalised position of the CS on the outer surface ($2p/\gamma p_c$) and normalised classical isotropic gradient of the CSL M/η_{cs} for $\alpha = 0.6$ with $\gamma = 0.7$ to 1 in 0.1 increments (ii) normalised classical isotropic gradient of the CSL M/η_{cs} for $\alpha = 1$ and $\alpha = 0.3$.

That is, particulate material may exhibit anisotropy which reaches a stabilised asymptotic value, just as the stress state approaches the CS. However, Horne's work was based on spherical particles and the extension to elongated clay platelets has not been made.

The argument for a unique CS for initially anisotropic materials, regardless of their stress history, has been strengthened by recent two-dimensional discrete element analysis on elongated particles by Fu and Dafalias [18, 19]. In [18], the authors concluded that:

> *"...a common ultimate state in terms of fabric characteristics is reached at large strains regardless of the initial fabrics prior to shear deformation. ...A direct implication of this conclusion is the uniqueness of the critical state line in the e-p* [void ratio versus pressure] *space..."*

They also found that the anisotropy orientation at the CS did not coincide with the shear band direction, but instead it was at some inclination *"...between the shear band direction and the minor principal stress direction"* [18]. That work used a measure of *fabric anisotropy intensity* (with 0 being isotropic and 1 perfect alignment in one preferential direction) together with a direction measure to quantify the orientations of the elongated particles. This fabric anisotropy intensity was defined as the difference between the principal components of the *particle orientation-based fabric tensor*, defined as

$$[F_p] = \frac{1}{2n_p} \sum_{k=1}^{2n_p} \{n^k\}\{n^k\}^T,$$

where $\{n^k\}$ is a unit vector representing the k^{th} particle's major axis orientation and n_p is the total number of particles. The overall fabric intensity (approximately 0.6 in their analysis) was found to be

independent of the initial fabric for direct shear and bi-axial compression investigations [18].

Volumetric target: a_β

a_β controls the instantaneous target level of anisotropy under compressive volumetric plastic straining. Although rather difficult to measure, b_β has a clear interpretation as the relative level of anisotropy at the CS. However, the interpretation of a_β is less straightforward. To assist in this understanding we consider the stress path in Figure 6.9.

(i) Starting at the *nose* of the yield surface ($\{\dot{\gamma}^{\mathrm{p}}\} = \{0\}$) on the anisotropic axis ($\eta = \beta$);

(ii) move along a path such that the stress point remains on the *nose* of the yield surface while the level of anisotropy increases (by virtue of (6.37)); in order to

(iii) reach a steady state of anisotropy for the expanding (hardening) yield surface.

The irrecoverable volumetric compaction leads to a re-arrangement of the soil particles, causing an increase in the anisotropy until (iii) is reached. At this steady state $\{\beta\} \rightarrow a_\beta\{r\}$ (or in triaxial conditions $\beta \rightarrow a_\beta\eta$) and the deviatoric plastic flow[16] becomes

$$\{\dot{\gamma}^{\mathrm{p}}\} = \dot{\gamma} \times 2A^2\big(1 - a_\beta\big)\{s\}, \tag{6.45}$$

where $\dot{\gamma}$ is the plastic multiplier. A steady state, with the first condition[17] of the above stress path $\{\dot{\gamma}^{\mathrm{p}}\} = \{0\}$, can only be obtained if $a_\beta = 1$. If $a_\beta \neq 1$ then we have a discrepancy between the condition of pure plastic volumetric compaction, on the axis of anisotropy (NCL, $\eta = \beta$), and attaining a steady state. The conclusion is that, to provide consistency within the model, a_β should be fixed at a value of unity. It should not be considered as a material constant.

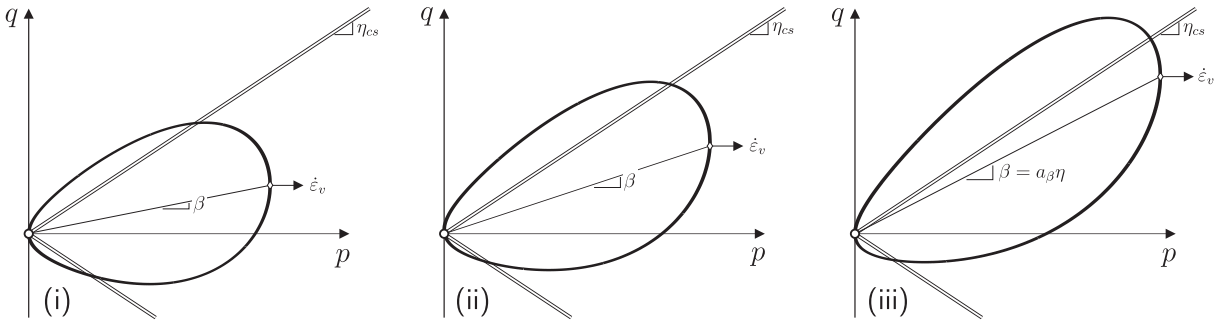

Figure 6.9: Stress path showing continuous elasto-plastic compaction with increasing anisotropy leading to a steady state at (iii).

6.2.3 Inner surface translation

The concept of a projection (or similarity) centre, $\{\sigma_0\}$, was formalised by Hashiguchi [25] for the subloading surface plasticity model to ensure that the inner surface remains geometrically similar to its outer surface. This projection centre is defined as the intersection point between rays linking common normals on the inner and outer surfaces. This construction maintains a constant ratio between the distances from the similarity centre to the inner yield surface and the inner to the outer surface along any ray emanating from the projection centre [25] (see Figure 6.4).

[16] Under the condition of coincident inner and outer surfaces: $R = 1$, $A_f = A$ and $B_f = B$.
[17] Excluding the trivial case of non-dissipative stress paths where the plastic multiplier $\dot{\gamma} = 0$.

Using geometric considerations (that is, by considering the intersection of two rays; one through the *apices*[18] of the surface and one through the *centres* of the surfaces), the *centre* of the inner yield surface is related to the projection centre through

$$\{\sigma^{\chi}\} = \frac{p_c\gamma}{2}\{1\} + (1-R)\Big\{\{\sigma_0\} - p_c\gamma\big\{\{1\} + \{\beta\}\big\}/2\Big\}, \tag{6.46}$$

which simplifies to

$$\{\sigma^{\chi}\} = (1-R)\{\sigma_0\} + \frac{Rp_c\gamma}{2}\big\{\{1\} + \{\beta\}\big\}, \tag{6.47}$$

where $p_c\gamma\{1\}/2$ is the centre of the outer surface. Taking the rate of (6.47), we obtain

$$\{\dot{\sigma}^{\chi}\} = (1-R)\{\dot{\sigma}_0\} + \frac{R\dot{p}_c\gamma}{2}\big\{\{1\} + \{\beta\}\big\} + \frac{Rp_c\gamma}{2}\{\dot{\beta}\}, \tag{6.48}$$

where the rate of evolution of p_c and $\{\beta\}$ are given by (5.24) and (6.37), respectively. The evolution of $\{\sigma_0\}$ is obtained by considering the cases shown in Figure 6.10. Starting from the state in Figure 6.10 (i), with the current stress state, image point and projection centre all located at $p_{c_n}\{1\}$, the model is then subjected to a compressive volumetric strain increment, resulting in the state in Figure 6.10 (ii). Throughout this loading the stress state, image point and projection centre remain coincident. By considering the hydrostatic growth of the yield surfaces, from (5.24), the projection centre must translate as

$$\{\dot{\sigma}_0\} = \frac{\dot{\varepsilon}_v^{\mathrm{p}}}{(\lambda-\kappa)}\{\sigma_0\}. \tag{6.49}$$

If the model is then subjected to a purely isochoric strain increment, again with the stress state, image point and projection centre coincident, as shown in Figure 6.10 (iii) with $p = p_{c_{n+1}} = p_0$ (where p_0 is the projection centre hydrostatic pressure) throughout the load path, the projection centre will evolve as

$$\{\dot{\sigma}_0\} = \dot{p}_0\{\beta\}. \tag{6.50}$$

Finally, if the inner yield surface is located within the outer surface, under plastic straining it will translate towards the image point on the outer surface through

$$\{\dot{\sigma}_0\} = C_{\chi}||\{\dot{\varepsilon}^{\mathrm{p}}\}||\Big\{\{\sigma\} - \{\sigma_0\}\Big\}. \tag{6.51}$$

Combining (6.49)-(6.51), the evolution of the projection centre is obtained as

$$\{\dot{\sigma}_0\} = C_{\chi}||\{\dot{\varepsilon}^{\mathrm{p}}\}||\Big\{\{\sigma\} - \{\sigma_0\}\Big\} + \frac{\dot{\varepsilon}_v^{\mathrm{p}}}{(\lambda-\kappa)}\{\sigma_0\} + \dot{p}_0\{\beta\}. \tag{6.52}$$

The first term translates the inner surface towards the image point, $\{\breve{\sigma}\}$, on the outer surface at a rate controlled by C_{χ}. This translation rule means that the inner surface can touch the outer surface but never overlap with it[19]. The second and third terms in (6.52) ensure that the projection centre remains consistent with the hydrostatic growth and anisotropic shearing of the outer surface. The first two terms in (6.52) are equivalent to those used by Mróz *et al.* [41], although here we assume a constant ratio between the sizes of the inner and outer surfaces.

[18] Strictly, there are no apices for these surfaces; the meridians are C_1 continuous at the points where they meet. Here, the least compressive hydrostatic limits of the surfaces are referred to as apices.

[19] That is, as $\{\sigma\} \to \{\breve{\sigma}\}$, $\{\{\sigma\} - \{\sigma_0\}\} \to \{0\}$ and the rate of translation diminishes.

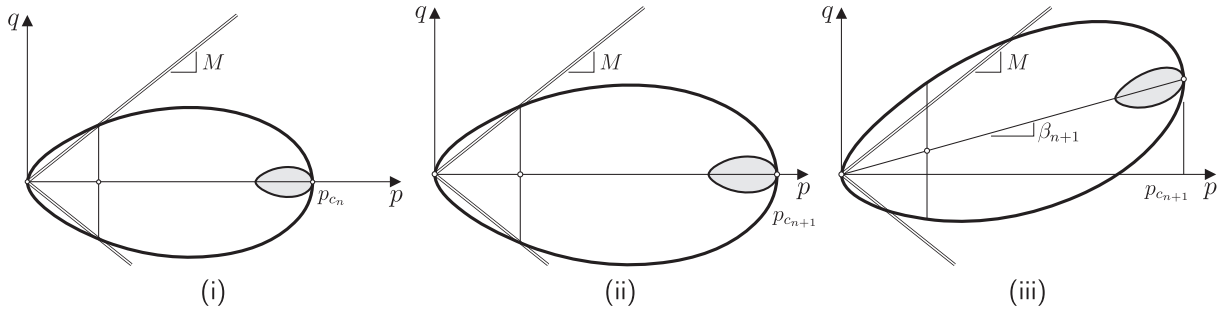

Figure 6.10: Translational hardening law for the inner yield surface: (i) initial condition, (ii) hydrostatic compaction and (iii) isochoric shearing.

Substituting (6.52) into (6.48) we obtain the evolution of the inner surface *centre* as

$$\{\dot{\sigma}^\chi\} = (1-R)\Big\{C_\chi||\{\dot{\varepsilon}^{\mathrm{p}}\}||\Big\{\{\sigma\}-\{\sigma_0\}\Big\}+\frac{\dot{p}_c}{p_c}\{\sigma_0\}+p_0\{\dot{\beta}\}\Big\}+\frac{R\dot{p}_c\gamma}{2}\Big\{\{1\}+\{\beta\}\Big\}+\frac{Rp_c\gamma}{2}\{\dot{\beta}\}, \quad (6.53)$$

where $\dot{p}_c$ is given by (5.24), $\{\dot{\beta}\}$ by (6.34) and the projection centre is given by (6.25) with a hydrostatic component of

$$p_0 = \frac{p^\chi - Rp_c\gamma/2}{(1-R)}. \quad (6.54)$$

Substituting (5.24), (6.25) and (6.54) into (6.53), re-arranging and simplifying, we obtain the evolution of the centre of the inner surface as

$$\begin{aligned}\{\dot{\sigma}^\chi\} &= C_\chi||\{\dot{\varepsilon}^{\mathrm{p}}\}||\Big\{(1-R)\{\sigma\}+Rp_c\gamma\big\{\{1\}+\{\beta\}\big\}/2\Big\}\\ &\quad+\Big(\dot{\varepsilon}_v^{\mathrm{p}}/(\lambda-\kappa)-C_\chi||\{\dot{\varepsilon}^{\mathrm{p}}\}||\Big)\{\sigma^\chi\}+p^\chi\{\dot{\beta}\}. \end{aligned} \quad (6.55)$$

Combining the elasticity law (from the free energy function (5.1)), yield function and direction of plastic flow (from the dissipation function (6.11)) and the hardening laws for (i) the surface growth (5.24), (ii) the shear anisotropy (6.34) and (iii) the translation of the inner surface (6.55), we obtain the full set of constitutive relations for the two-surface anisotropic hyperplasticity model. These are summarised below.

6.2.4 Complete model formulation

In this subsection, to provide clarity, the essential constitutive equations are drawn together out of the preceding subsections and Chapter 5. The below equations summarise the elasticity, inelasticity and hardening relationships for the two-surface anisotropic hyperplasticity model (a total of six equations) along with the required 12 material constants. Four of these constants (κ, G, M and λ) are inherited from the classical MCC constitutive model. The Lode angle dependent single-surface isotropic model presented in Chapter 5 added α, γ and $\bar{\rho}_e$. The remaining five (R, b_β, x_β, C_β and C_χ) are additional material constants required for the two-surface anisotropic model. The two-surface anisotropic constitutive model can be summarised to the below six equations.

(i) The elastic stress relationship (5.2)

$$\{\sigma\} = p_r \exp\left(\frac{\varepsilon_v^{\mathrm{e}} - \varepsilon_{v0}^{\mathrm{e}}}{\kappa}\right)\{1\} + 2G\{\gamma^{\mathrm{e}}\};$$

(ii) yield function (6.15), direction of plastic flow (6.30)

$$f = (p - p^{\chi})^2 B_f^2 + \{s^{\beta}\}^T\{s^{\beta}\}A_f^2 - A_f^2 B_f^2 = 0,$$

$$\{g_{,\sigma}\} = \frac{2}{3}\Big(B_f^2(p - p^{\chi}) - A_f^2\{s^{\beta}\}^T\{\beta\}\Big)\{1\} + 2A_f^2\{s^{\beta}\}; \qquad \text{and}$$

(iii) the hardening rules from (5.24), (6.34) and (6.55) are given by

$$\dot{p}_c = \left(\frac{p_c}{\lambda - \kappa}\right)\dot{\varepsilon}_v^{\mathrm{p}}, \qquad \{\dot{\beta}\} = C_{\beta}\left(\Big\{\{r\} - \{\beta\}\Big\}\langle\dot{\varepsilon}_v^{\mathrm{p}}\rangle + x_{\beta}\Big\{b_{\beta}\{r\} - \{\beta\}\Big\}\dot{\varepsilon}_{\gamma}^{\mathrm{p}}\right) \qquad \text{and}$$
$$\{\dot{\sigma}^{\chi}\} = C_{\chi}||\{\dot{\varepsilon}^{\mathrm{p}}\}||\Big\{(1 - R)\{\sigma\} + Rp_c\gamma\big\{\{1\} + \{\beta\}\big\}/2\Big\} + \{\sigma^{\chi}\}\Big(\dot{\varepsilon}_v^{\mathrm{p}}/(\lambda - \kappa) - C_{\chi}||\{\dot{\varepsilon}^{\mathrm{p}}\}||\Big) + p^{\chi}\{\dot{\beta}\}.$$

Infinitesimal elasto-plastic tangent

The infinitesimal elasto-plastic tangent $[D^{\mathrm{ep}}]$ can be determined from (2.23) where the direction of plastic flow and the derivative of the yield function with respect to stress are given by (6.30) and (E.1), respectively. The scalar measure of the plastic tangent stiffness is given by

$$H = -\{f_{,\beta}\}^T\{H_{\beta}\} - \{f_{,\sigma^{\chi}}\}^T\{H_{\sigma^{\chi}}\} - f_{,p_c}H_{p_c}, \tag{6.56}$$

where the yield function derivatives are given in Appendix E. The instantaneous directions of plastic hardening, $H_{(.)}$, are obtained from the hardening laws of p_c (5.24), $\{\beta\}$ (6.34) and $\{\sigma^{\chi}\}$ (6.55) divided by the plastic multiplier rate, $\dot{\gamma}$

$$\begin{aligned}
H_{p_c} &= \left(\frac{p_c}{\lambda - \kappa}\right)\{g_{,\sigma}\}^T\{1\}, \\
\{H_{\beta}\} &= C_{\beta}\left\{\big(\{r\} - \{\beta\}\big)\langle\{g_{,\sigma}\}^T\{1\}\rangle + x_{\beta}\big(b_{\beta}\{r\} - \{\beta\}\big)\frac{\dot{\varepsilon}_{\gamma}^{\mathrm{p}}}{\dot{\gamma}}\right\} \qquad \text{and} \\
\{H_{\sigma^{\chi}}\} &= C_{\chi}||\{g_{,\sigma}\}||\Big\{(1 - R)\{\sigma\} + Rp_c\gamma\big\{\{1\} + \{\beta\}\big\}\Big\} + \\
&\quad \{\sigma^{\chi}\}\left(\frac{\{g_{,\sigma}\}^T\{1\}}{\lambda - \kappa} - C_{\chi}||\{g_{,\sigma}\}||\right) + p^{\chi}\{H_{\beta}\}.
\end{aligned} \tag{6.57}$$

Combining these directions of instantaneous hardening with the direction of plastic flow (6.30), the derivative of the yield function with respect to stress (E.1) and the elastic tangent stiffness matrix $(5.4)_1$, we obtain the equations necessary to form the infinitesimal elasto-plastic tangent for the two-surface anisotropic model.

6.3 Calibration

In this section the calibration procedure for the two-surface anisotropic model is presented. The model is calibrated using data from LCT [20], which was examined in the preceding chapter for the simpler two-parameter single-surface isotropic CS model.

6.3.1 Hydrostatic loading/swelling: λ, κ, C_{χ} and R

Compressibility indices: λ and κ

The elastic and plastic compressibility indices are obtained from one-dimensional (or preferably hydrostatic) consolidation (drain compression) tests with unloading/loading cycles. κ and λ are determined by plotting the void ratio (or specific volume $v = (1 + e)$) against pressure on a bi-logarithmic scale. The gradient of a linear fit to the virgin loading behaviour provides the plastic compressibility index, λ,

whereas the unloading (swelling) behaviour provides κ, as shown for LCT data [20] in Figure 5.12. It should be noted that, κ now gives the initial elastic unloading/loading stiffness, that is, the gradient of the initial part of the unloading and elastic reloading curves (as identified in Figure 6.11).

Inner surface size and rate of translation: R and C_χ

C_χ controls the rate at which inelasticity develops inside the outer surface (or rather the rate of translation of the inner surface). It can be determined through examination of the hydrostatic consolidation unloading and re-loading response. For large C_χ the material response (when $F < 0$) is dominated by the elasticity law. As C_χ reduces, the degree of plasticity inside the outer surface increases as the inner surface is dragged through stress space. Hydrostatic consolidation starting from an initial hydrostatic stress (and isotropic material) state allows the influence of C_χ to be decoupled from the other material constants (once λ, κ and R have been independently determined). Examining the hydrostatic response for an initially isotropic material, allows the effects of shearing to be excluded such that the influence of C_χ may be isolated from the material constants controlling the evolution of anisotropy.

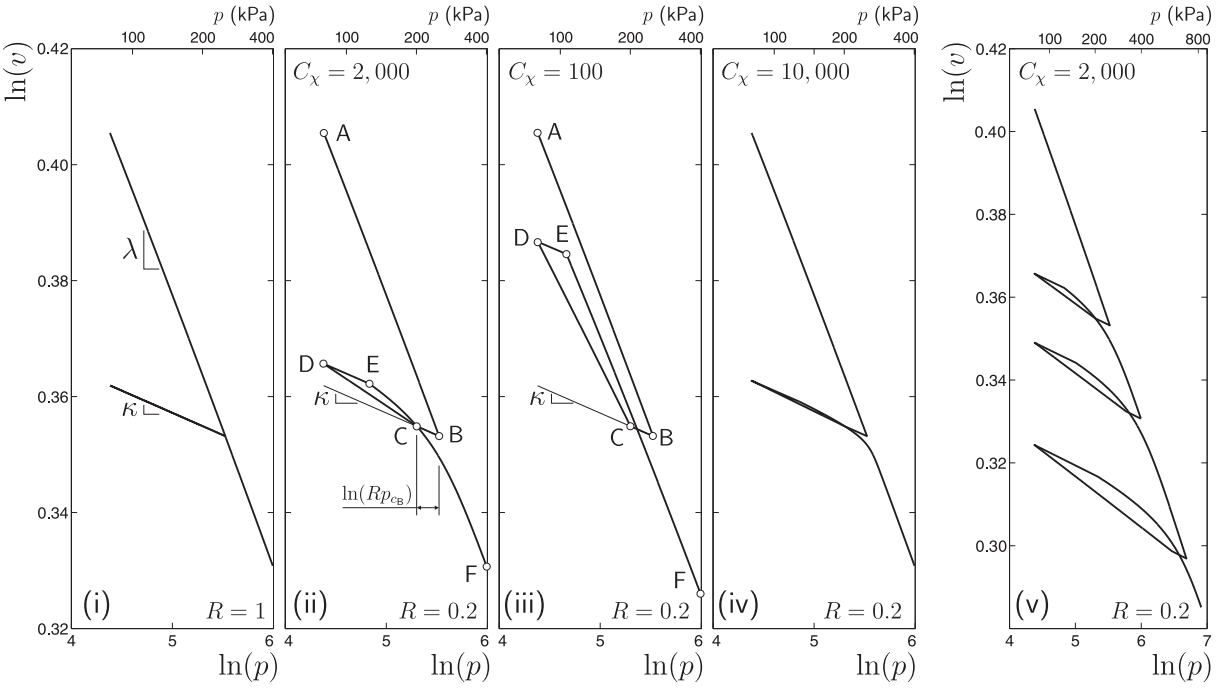

Figure 6.11: Hydrostatic consolidation $\ln(p)$ versus $\ln(v)$ response from an hydrostatic stress state and isotropic material state for (i) single surface model ($R = 1$) and the two-surface model with $R = 0.2$ and (ii) $C_\chi = 2,000$, (iii) $C_\chi = 100$, (iv) $C_\chi = 10,000$ and (v) multiple load-unload-reload cycles for $C_\chi = 2,000$.

Figure 6.11 ((i) to (iv)) shows the hydrostatic consolidation $\ln(p)$ versus $\ln(v)$ response for compression to a pressure of 250kPa (starting from a reference pressure of 80kPa), swelling to 80kPa and then compression to 400kPa. The response under these conditions is independent of the values of α and γ as the stress state (when undergoing elasto-plastic behaviour) is located at the *nose* (or *apex*) of the yield surface[20]. The single surface response ($R = 1$) is shown in Figure 6.11 (i), where the gradients of the virgin consolidation and elastic unlaoding/re-loading paths are given by λ and κ respectively[21]. Figures 6.11 (ii)-(iv) show the response for different values of C_χ with $R = 0.2$. The following points describe the path (where the points are labeled in Figures 6.11 (ii) and (iii)):

[20]The behaviour is also independent of M, $\bar{\rho}_e$, G and the anisotropic shear hardening parameters b_β, x_β and C_β.
[21]This is the classical MCC response when using a bi-logarithmic hardening relationship.

A : hydrostatic pressure of 80kPa at an initial specific volume of 1.5 with an isotropic material state and a stress state located at the *nose* both the inner yield and outer surfaces;

A to B : drained hydrostatic loading (consolidation) to a pressure of 250kPa;

B to C : elastic hydrostatic unloading with $\Delta \ln(v) = \kappa(\Delta \ln(p))$ within the inner yield surface until $f = 0$;

C to D : elasto-plastic hydrostatic unloading to a pressure of 80kPa with the $\ln(p)$ versus $\ln(v)$ response predominately controlled by C_χ;

D to E : elastic hydrostatic re-loading with $\Delta \ln(v) = \kappa(\Delta \ln(p))$ within the inner yield surface until $f = 0$ at E; and

E to F : elasto-plastic hydrostatic loading to a pressure of 400kPa with the material response asymptotically approaching the virgin consolidation response of $\Delta \ln(v) = \lambda(\Delta \ln(p))$.

Including an inner surface within the conventional outer surface introduces a hysteric response. As C_χ increases, so the area of this hysteric loop reduces, as shown by Figures 6.11 (ii) to (iv). For low values of C_χ the hydrostatic unloading and re-loading response is dominated by C_χ, clearly seen in Figure 6.11 (iii) where the gradient of the elasto-plastic unloading-reloading response is closer to the virgin consolidation line than the purely elastic response. For large values of C_χ, the response under swelling is largely governed by the elastic compressibility index κ, as shown in Figure 6.11 (iv) for $C_\chi = 10,000$. The response under multiple load-unload cycles is shown in Figure 6.11 (v) for $C_\chi = 2,000$. As expected, increasing the pressure change after further consolidation increases the magnitude of the hysteresis.

C_χ should preferably be calibrated from hydrostatic consolidation load-unload-reload experimental data. However, if such cyclic data is not available, then the model could be calibrated from a single unloading response following hydrostatic consolidation. The initial response provides κ and the deviation from this linear relationship in $\ln(p)$-$\ln(v)$ space provides C_χ. The size of the inner surface can also be estimated from this hydrostatic data as the point where the experimental response deviates from the κ line.

Lower Cromer till

Figure 6.12 compares predictions using the two-surface anisotropic hyperplastic model with hydrostatic consolidation and swelling LCT experimental data [20]. The initial virgin consolidation behaviour is described by λ, set here to the same value as used in the preceding chapter, 0.0447. κ is now the initial slope of the swelling response. The first three data points provide a value of $\kappa = 0.005$. The isotropic family of CS models analysed in the previous chapter used a softer value of 0.0073 to provide a best-fit to the full unloading response. The remainder of the unloading response suggests use of a C_χ value of $3,700$, with the inner surface size ratio set to 0.2. With these material constants, the model is able to provide good agreement with the laboratory findings.

6.3.2 Anisotropic Critical State position: b_β and γ

As described in Section 6.2.2, the location of the CSL is influence by both γ and b_β. Rearranging, (6.43) we obtain

$$\left(\frac{p}{p_c}\right)_{cs} = \frac{\gamma\Big(1 + b_\beta\big(3 - 2\gamma\big)\Big)}{2\Big(1 - b_\beta\big(\gamma^2 - 2\gamma + 1\big)\Big)}, \tag{6.58}$$

that is, the relative position of the CSL (at p) in terms of the size of the yield surface p_c. If $b_\beta = 0$ then the model looses plastic anisotropy at the CS and γ alone determines the position of the intersection of the CSL with the outer surface (at $p = \gamma p_c/2$). Decreasing γ causes the CSL to move towards the stress

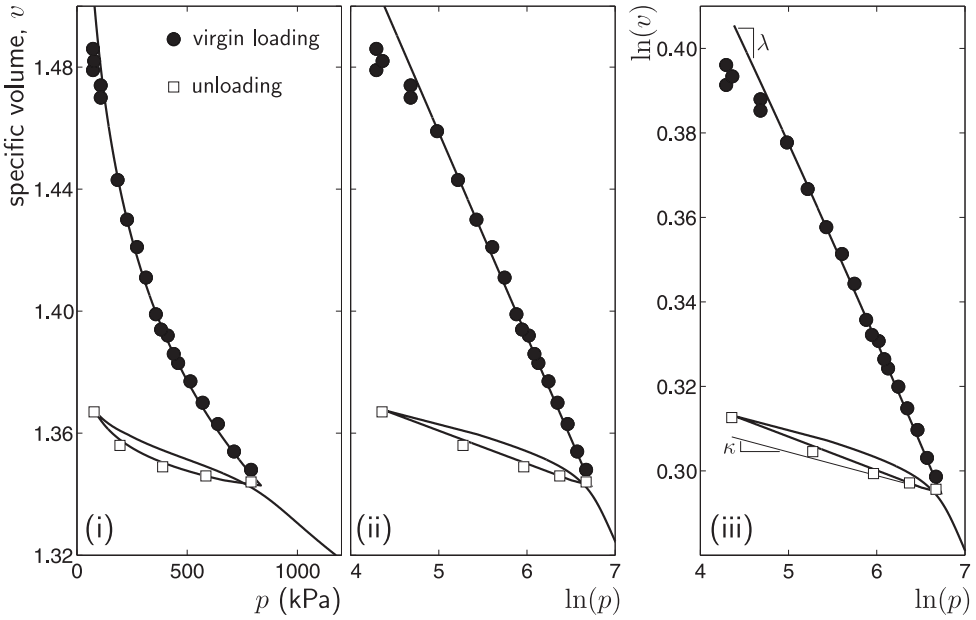

Figure 6.12: Hydrostatic consolidation and swelling behaviour of LCT [20] (shown by discrete points) and the two-surface anisotropic model in terms of (i) hydrostatic pressure versus specific volume, (ii) $\ln(p)$ versus specific volume and (iii) $\ln(p)$ versus $\ln(v)$.

origin, at a lower pressure for a given specific volume. If $\gamma = 1$ then the intersection of the CSL with the outer surface is given by

$$\left(\frac{p}{p_c}\right)_{cs} = \frac{1 + b_\beta}{2} \,. \tag{6.59}$$

Increasing b_β moves the CSL away from the stress origin (closer to the hydrostatic consolidation line, HCL)

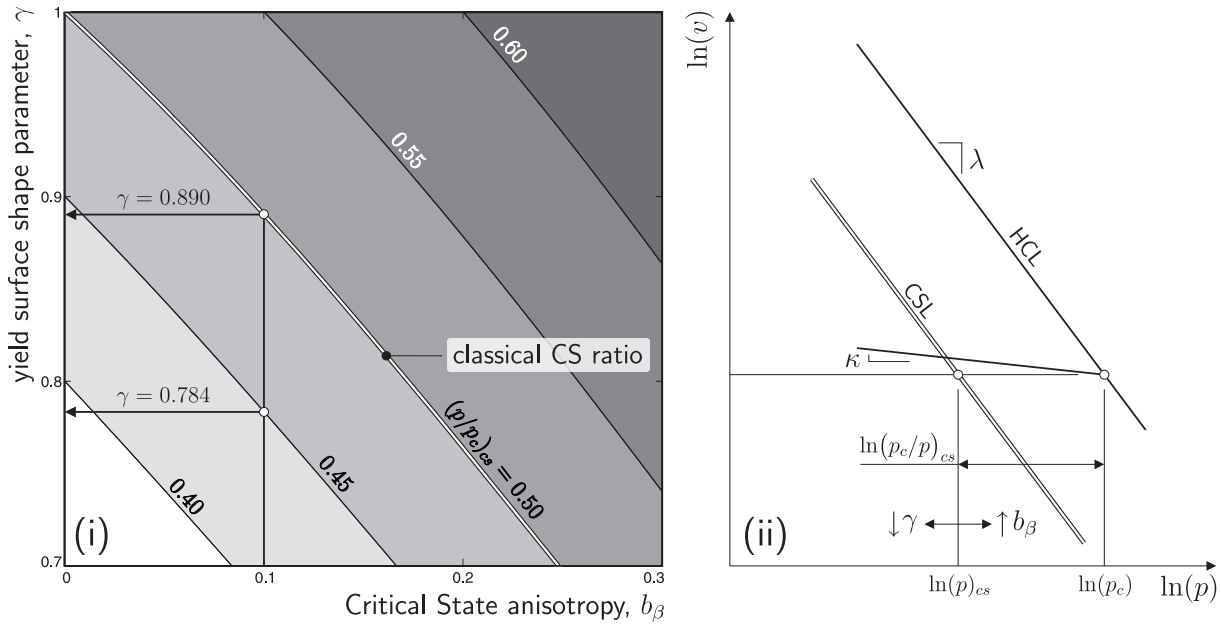

Figure 6.13: Influence of γ and b_β on the position of the intersection of the yield surface with the CSL: (i) contours of $(p/p_c)_{cs}$ with $\gamma \in [0.7, 1]$ and $b_\beta \in [0, 0.3]$ and (ii) $\ln(p)$ versus $\ln(v)$ schematic of the position of the CSL relative to the HCL.

Figure 6.13 demonstrates the influence of changing the values of γ and b_β on the position of the intersection of the CSL with the yield surface. The values of $(p/p_c)_{cs}$ from (6.58) are contoured in Figure 6.13 (i) and the effect of γ and b_β shown schematically in Figure 6.13 (ii) (for the case where $R = 1$). For a given b_β and a required $(p/p_c)_{cs}$, γ can be determined by solving the quadratic

$$\gamma^2\Big(2b_\beta\big(1-(p/p_c)_{cs}\big)\Big)+\gamma\Big(4b_\beta(p/p_c)_{cs}-3b_\beta-1\Big)+2(p/p_c)_{cs}\big(1-b_\beta\big)=0. \tag{6.60}$$

The values of γ to achieve $(p/p_c)_{cs}$ equal to 0.45 and 0.50 with $b_\beta = 0.1$ are 0.784 and 0.890 respectively, as shown in Figure 6.13 (i). Figure 6.14 shows the yield surfaces at the CS for the combinations of $\gamma = 0.9$, 0.8 and 0.7 with $b_\beta = 0$, 0.1, 0.2 and 0.3. The gradient of the classical CSL, M, was calculated from (6.44) with $\eta_{cs} = 1$, $\alpha = 0.4$ and $\bar{\rho}_e = 0.8$. The positions of isochoric plastic flow, at η_{cs} on the compression meridian, are identified by the white diamonds. The relative position of the intersection of the CSL with the outer surface is given above each of the sub-plots.

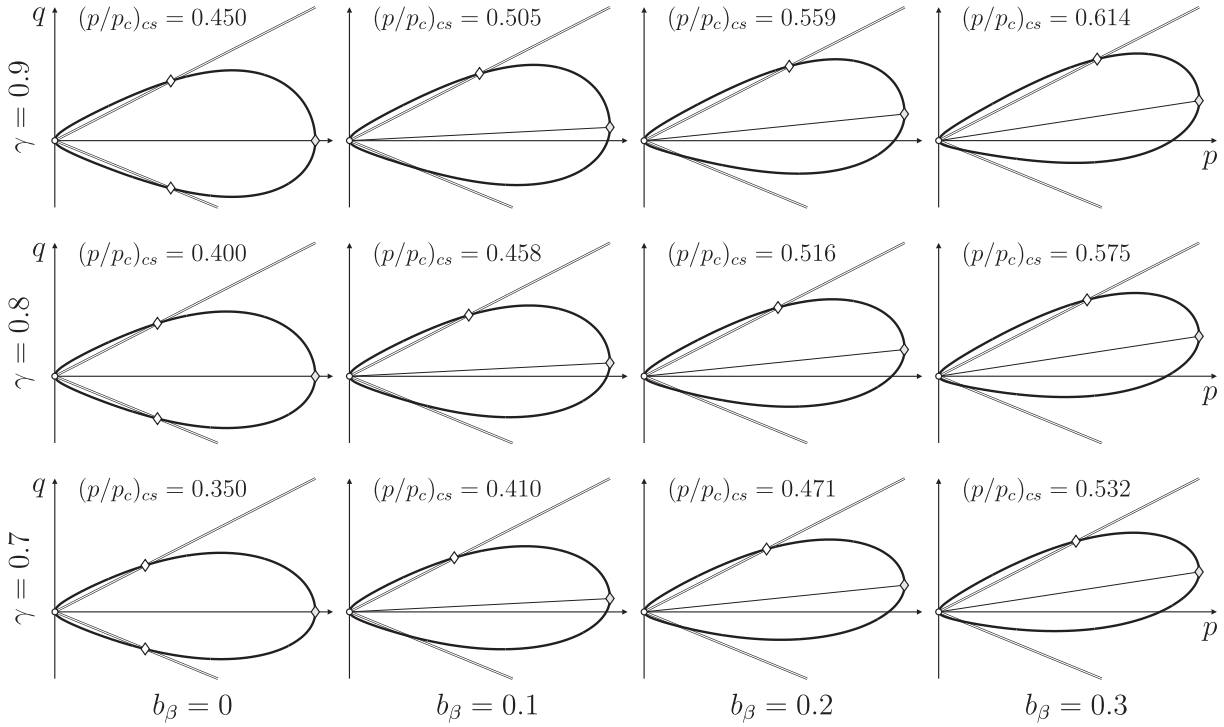

Figure 6.14: Yield surfaces at the CS for $\alpha = 0.4$ and $\bar{\rho}_e = 0.8$ with $\gamma = 0.9$, 0.8 and 0.7 and $b_\beta = 0$, 0.1, 0.2 and 0.3. The positions of isochoric plastic flow at η_{cs} on the compression meridian (and on the extension meridian for $b_\beta = 0$) are identified by the white diamonds, where M is obtained from (6.44).

Although b_β controls the intensity of the anisotropy at the CS, it also influences the model stress strain response in a rather complex way, particularly as the CSL is approached. Figure 6.15 (i) demonstrates the effect of b_β varying between 0 and 0.5 in 0.1 intervals for undrained triaxial compression (UTC) and extension following K_0 consolidation from a normally consolidated state (OCR = 1)[22]. Increasing b_β causes a change in the UTC response of the model from a softer response (low values of b_β) to a *hooking* stiffening stress response. This *hooking* can only occur when the anisotropy developed under one-dimensional consolidation, β_{K_0} given by (6.62), is less than b_β.

Except for large values of C_β, where the yield surface will rotate swiftly to the CAS, the model's

[22]Note that, the simulations do not start from a common state following K_0 consolidation as varying b_β (without re-calculating x_β) changes the one-dimensional loading response of the model. Only the K_0 response when $b_\beta = 0$ is shown in Figure 6.15 (i).

response under UTE (as shown in Figure 6.15 (i)) demonstrates hardening near the CSL. As b_β increases, the length of this *hooking* stress path under UTE also increases. This is a consequence of the yield surface being required to shear to a larger extent in order to arrive at the specified CAS.

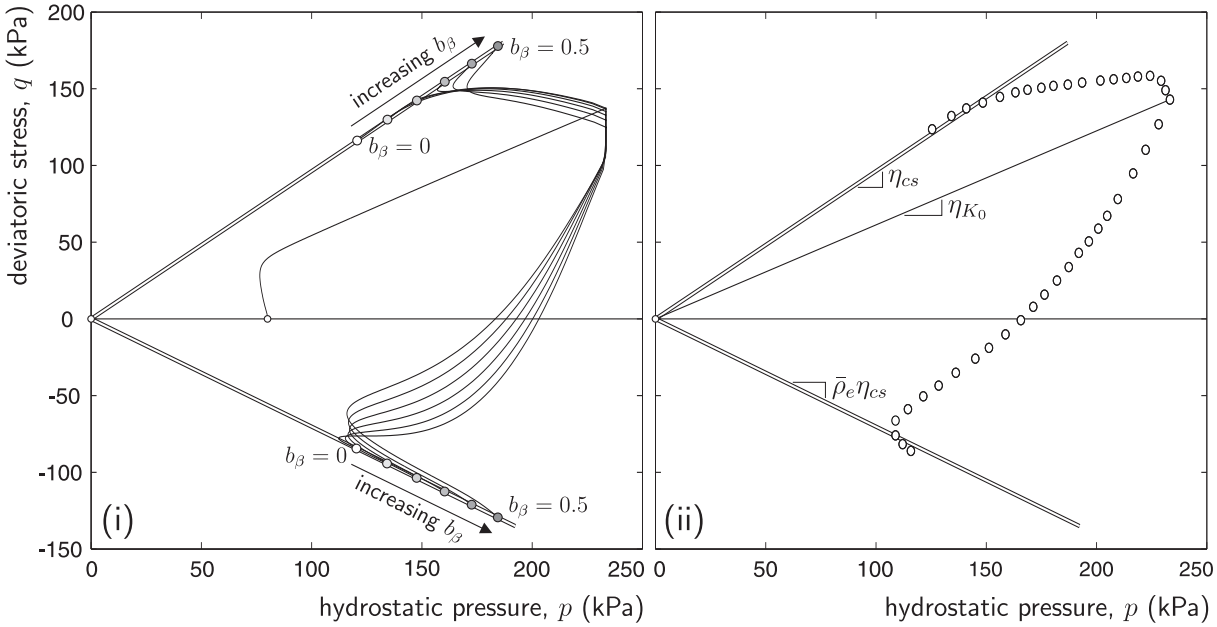

Figure 6.15: UTC and UTE following normal K_0 consolidation (OCR= 1): (i) influence of b_β on the stress path with $\gamma = 0.9$ and (ii) experimental data on LCT from Gens [20].

The following steps can be used to obtain b_β and γ:

(i) obtain $(p/p_c)_{cs}$ from experimental data (as shown in Section 5.4.2, Figure 5.14);

(ii) set $\gamma = 2(p/p_c)_{cs}$ and vary b_β while comparing the simulated output against experimental data on UTC and UTE at an OCR of 1 following K_0 consolidation;

(iii) fix b_β based on the best fit to the experimental data and then re-calculate γ using (6.60).

Lower Cromer till

Figure 6.15 (ii) reproduces the experimental data on LCT [20] under UTC and UTE following K_0 consolidation at an OCR of one. Comparing the model's response with the LCT experimental data, it is apparent that values of $b_\beta > 0.2$ are not appropriate. A value of $b_\beta = 0.1$ provides a reasonable approximation to the experimental data behaviour near the CSL.[23]

In the previous chapter it was suggested that γ be specified on the basis of determining the ratio of the pressures at the initial to that at the final state (at the CS) from UTC data at an OCR of two. Once b_β is specified, the position of the CSL can be fixed by the appropriate selection of γ. In Chapter 5, Figure 5.14 showed experimental data on LCT [20] for hydrostatic consolidation and swelling following by UTC for OCRs of 1, 1.5, 2, 4 and 10 in (i) specific volume versus hydrostatic pressure and (ii) $\ln(p)$-$\ln(v)$ space. The distance between the HCL and CSL provides the ratio of the size of the yield surface to the pressure at the CS. From Figure 5.14 (ii), $(p/p_c)_{cs} = 0.45$, therefore if $b_\beta = 0.1$ we obtain $\gamma \simeq 0.78$ from (6.60) (see Figure 6.13).

[23]Note that, the anisotropy under one-dimensional consolidation for $b_\beta = 0.1$, $a_\beta = 1$, $\gamma = 0.8$ and $\alpha = 0.5$ is $\beta_{K_0} = 0.21$ for $\eta_{K_0} = 0.6$.

6.3.3 Triaxial response of highly over-consolidated soils: α

As shown in the preceding chapter, α makes the yield surface more *tear drop* shaped (with the taper nearest the stress origin), thereby reducing the significant over-estimation seen in the MCC model of the deviatoric stresses, under UTC (or UTE) at high OCRs. Setting $\alpha < 1$ allows the two-surface model to be used for both normally and highly over-consolidated geomaterials by making the yield surface more cone-like on the *dry* side of the CSL. With sufficient stress path data being available, it would be possible to determine α from the experimentally observed yield points. However, the point at which yielding first occurs is not so easily detected and full stress path data are often not available.

The previous chapter calibrated α for the isotropic two-parameter family of CS models using one-dimensional consolidation (K_0 loading) experimental data. Once γ had been specified (in addition to the gradient of the CSL, η_{cs} which was equal to M for the family of isotropic single-surface models), α was determined analytically such that under K_0 loading the constitutive model reproduced the experimentally recorded asymptotic stress ratio $\eta_{K_0} = q/p$. However, using the same value of α as determined for the isotropic model would lead to the non-physical result of no anisotropy being developed under K_0 loading. Thus α should be determined in a different manner.

The response of the single surface isotropic CS model for $\alpha = 0.3$ was compared in Chapter 5 with experimental data on LCT. The material's response under drained triaxial compression (DTC) from a hydrostatic stress state at an OCR of 10 (Figure 5.17) significantly overestimated the dilative behaviour. This is due to α's influence on the direction of plastic flow. As shown in Figure 6.5, when α decreases the dilative component of the plastic flow increases, resulting in good agreement in terms of the stress deviator for heavily OCR soils but not in terms of the volumetric strain response.

Anisotropic shearing of the yield surface partially decouples α from the K_0 consolidation response, allowing for greater flexibility when specifying α. Furthermore, the presence of an inner surface allows the value of α to be increased, potentially improving the volumetric response under drained triaxial tests at high OCRs whilst maintaining good agreement with the deviatoric stress.

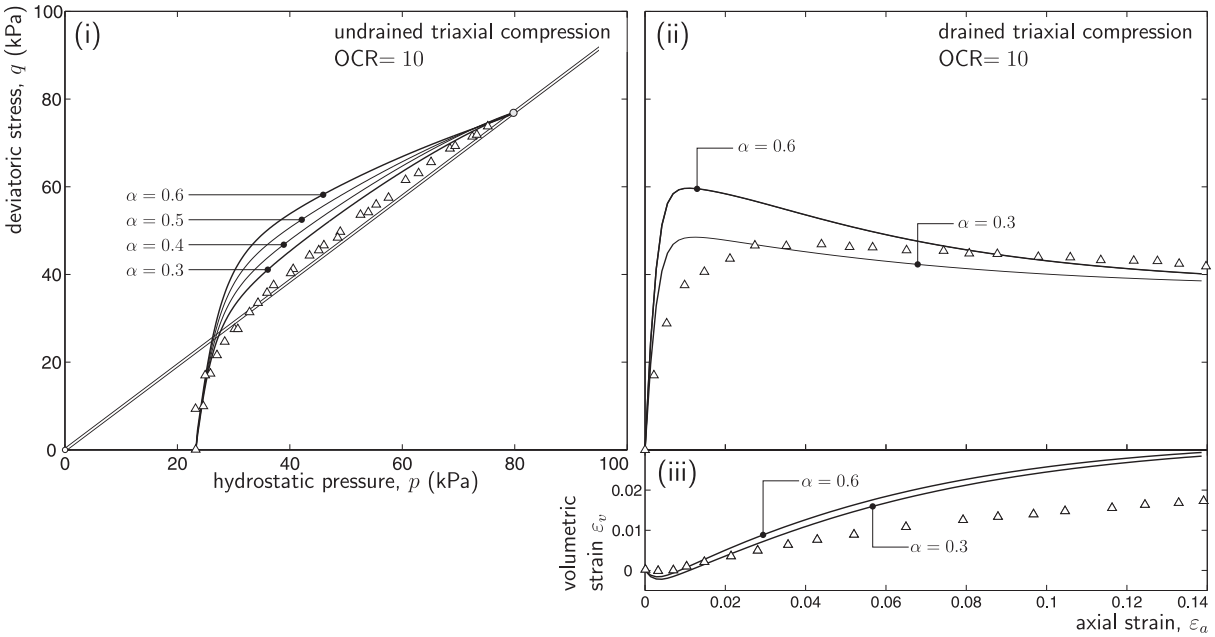

Figure 6.16: Influence of α on the (i) UTC, (ii) DTC deviatoric stress and (iii) DTC volumetric strain response. The model predictions are compared with data from LCT (shown by discrete points, [20]) at an OCR of 10.

Lower Cromer till

Figure 6.16 compares the model's triaxial compression response under both drained and undrained conditions with experimental data on LCT at an OCR of 10. The volumetric response under DTC (Figure 6.16 (iii)) is an improvement on that seen in Figure 5.17 for the isotropic model. However, the influence of α on the volumetric behaviour is rather minor[24]. Improving the model's volumetric strain response further would require reducing γ. Yet, as discussed in the preceding section, γ also controls the position of the CSL. It is not possible to obtain a perfect fit to all of the experimental data for all OCRs. Studies conducted by the author have shown that a value of $\alpha = 0.4$ generally provides good agreement with the material response for both UTC and DTC, in terms of the deviatoric stress.

6.3.4 Isotropic Critical State cone: M and $\bar{\rho}_e$

UTC test data allows the stress ratio at the CS, η_{cs}, to be determined. M can then be calculated using the equations presented in Section 6.2.2 once α, γ and b_β have been specified.

The stress ratio at the CS under extension, when compared to that under compression, provides the normalised extension deviatoric radius $\bar{\rho}_e$. This necessitates capture of triaxial compression and extension test data (from either an isotropic or anisotropic initial state) to a sufficiently large axial strain such that the CS is attained. Data from a single OCR is sufficient to determine $\bar{\rho}_e$, however results at more than one OCR are preferential. In the absence of information from triaxial extension experiments, $\bar{\rho}_e$ could be estimated from the triaxial compression friction angle (ϕ) through (4.3), such that $\bar{\rho}_e$ coincides with that predicted by the Mohr-Coulomb criterion.

Lower Cromer till

The stress ratio at the CS for LCT and the normalised deviatoric radius under triaxial extension were found (in the preceding chapter) to be equal to $\eta_{cs} = 0.964$ and $\bar{\rho}_e = 0.729$ respectively. Using the constants given in Table 6.1 and (6.44), M is 0.921.

6.3.5 Development of plastic anisotropy: C^β and x_β

Relative influence of volumetric/deviatoric plastic strains: x_β

Once α, γ, a_β and b_β have been determined, x_β, controlling the relative contribution from volumetric and deviatoric plastic straining on the evolution of $\{\beta\}$, can be obtained from one-dimensional consolidation data. For this calibration procedure we assume that the elastic strains are negligible under sufficiently large straining during K_0 consolidation. In this case the ratio of the deviatoric to volumetric plastic strains (on the outer surface under triaxial conditions) is

$$\frac{\dot{\varepsilon}^{\mathrm{p}}_{\gamma}}{\dot{\varepsilon}^{\mathrm{p}}_{v}} = \frac{A^2(\eta_{K_0} - \beta)}{B^2(1 - \gamma p_a/2) - A^2(\eta_{K_0} - \beta)\beta} = n_p, \tag{6.61}$$

where η_{K_0} is the experimentally determined stress ratio (q/p) under one-dimensional K_0 loading, $p_a = p_c/p$, β is the L2 norm of $\{\beta\}$ and $n_p = \sqrt{2/3}$ (as given in Section 5.4.2). From (6.9), assuming triaxial stress conditions, β can be obtained as

$$\beta = \eta - \frac{B}{A}\sqrt{\gamma(2-\gamma)\Big(p_a - 1\Big)}. \tag{6.62}$$

[24]Note, that the DTC results for $\alpha = 0.4$ and 0.5 are not shown in Figure 6.16 (ii) and (iii) due to congestion, the results span between those of $\alpha = 0.3$ and 0.6.

Rearranging (6.61) and substituting for β from (6.62), we obtain a quartic in $(p_a)_{K_0}$

$$\begin{aligned}
(p_a)^4_{K_0}\Big(-n_p^2M^2\alpha^2\gamma^2a_1/4\Big) &+ \dots \\
(p_a)^3_{K_0}\Big(b\gamma^2/4 - n_p^2M^2\big[\alpha^2\gamma^2a_2/4 + \alpha\gamma(1-\alpha)a_1\big]\Big) &+ \dots \\
(p_a)^2_{K_0}\Big(b\big[\gamma(1-\gamma) - \gamma^2/4\big] - n_p^2M^2\big[a_1(1-\alpha)^2 + \alpha^2\gamma^2a_3 + \alpha\gamma(1-\alpha)a_2\big]\Big) &+ \dots \\
(p_a)_{K_0}\Big(b\big[(1-\gamma)^2 - \gamma(1-\gamma)\big] - n_p^2M^2\big[a_2(1-\alpha)^2 + \alpha\gamma(1-\alpha)a_3\big]\Big) &+ \dots \\
\Big(-b(1-\gamma)^2 - n_p^2M^2a_3(1-\alpha)^2\Big) &= 0, \qquad (6.63)
\end{aligned}$$

where

$$\begin{aligned}
b &= \gamma(2-\gamma)\Big(1+n_p(\eta_{K_0})\Big)^2, & a_1 &= \gamma^2\Big(1/4 - 2 + \gamma + (2-\gamma)^2\Big), \\
a_2 &= \gamma\Big(-1 + 2(2-\gamma) + \gamma(2-\gamma) - 2\gamma(2-\gamma)^2\Big), & a_3 &= 1 - 2\gamma(2-\gamma) + \gamma^2(2-\gamma)^2
\end{aligned}$$

and $(p_a)_{K_0} = p_c/p$ is the position on the yield surface where, under constant K_0 loading, (6.61) is satisfied. Once solved for $(p_a)_{K_0}$, the asymptotic level of anisotropy under constant K_0 loading can be obtained from (6.62). At this state, $\dot{\beta} \to 0$, which allows us to obtain x_β by setting (6.34) equal to zero, as

$$x_\beta = \frac{a_\beta(\eta_{K_0}) - \beta_{K_0}}{n_p\Big(\beta_{K_0} - b_\beta(\eta_{K_0})\Big)}. \qquad (6.64)$$

Here β_{K_0} is the asymptotic anisotropy under constant K_0 consolidation, determined from (6.62) with $\eta = \eta_{K_0}$ and $(p_a)_{K_0}$ from (6.63).

Rate of development of anisotropy: C_β

The value of C_β, typically between 10 and 30, controls the anisotropic shearing rate. Once b_β has been specified, C_β controls the model's behaviour when approaching the CSL. For low values of C_β (where the level of anisotropy is less than that at the CS state) the model will predict a *hooking* stress path response; the stress path moves up the CSL until the level anisotropy reaches the CAS. When the level of anisotropy is greater than the CS value (again for low values of C_β) a softening response will be observed in the vicinity of the CSL, as the degree of anisotropic shearing of the yield surface reduces to the CAS. For sufficiently large values of C_β the paths to the CS do not exhibit this *hooking* or *softening* response.

The K_0 normally consolidated undrained triaxial behaviour can provide the information required to determine C_β. The experimental responses under compression (where the initial anisotropy is typically greater than the CAS) and extension (where the initial anisotropy is typically less than the CAS) allows a range for C_β to be identified. The one-dimensional consolidation, by the virtue of the rate at which η_{K_0} is approached, and the unloading path at high OCRs can also suggest a suitable value for C_β.

Lower Cromer till

The asymptotic stress ratio of LCT under one-dimensional consolidation is equal to $\eta_{K_0} = 0.6$, as shown in Figure 6.17. To attain this stress ratio under K_0 consolidation, x_β was determined analytically (using (6.64)) as $x_\beta = 4.8$. The rate of development of anisotropy, C_β, was then set to 14.

Figure 6.17 shows the K_0 consolidation and swelling experimental data from LCT (discrete points) and the response of the two-surface anisotropic hyperplasticity model (A→D). The response during consolidation is shown in Figure 6.17 (i). The material point starts at A, with the inner and outer surfaces shown by the dashed lines. After one-dimensional straining to a pressure of 233kPa the material point

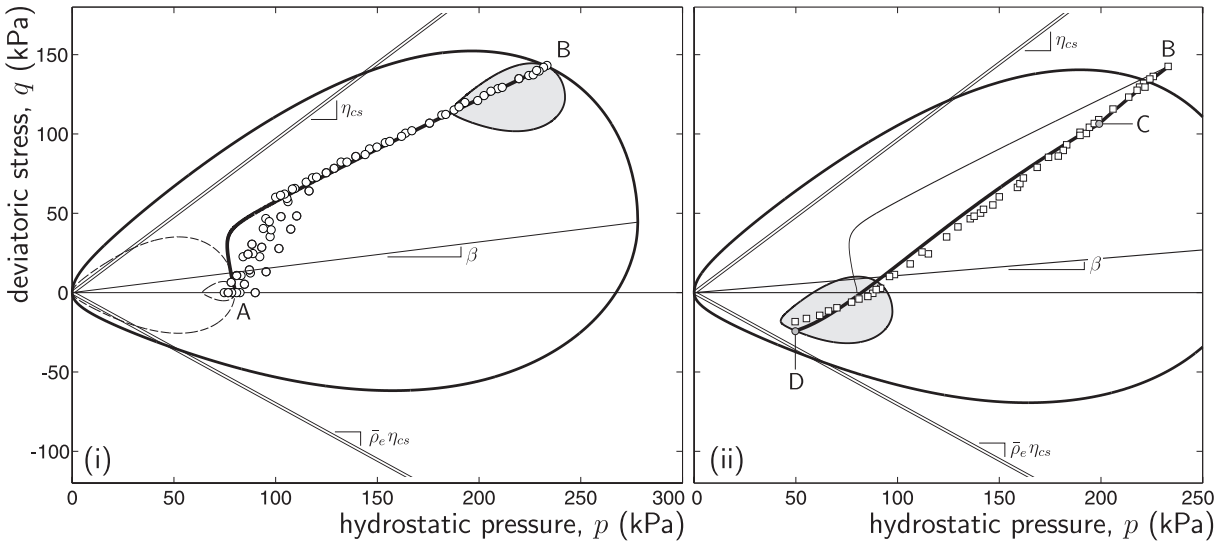

Figure 6.17: K_0 consolidation and swelling comparison with experimental data (shown by discrete points) on LCT from Gens [20].

is located at B. The inner yield and outer surfaces are shown (together with the axis of anisotropy, $\beta = 0.160$) at B. Excellent agreement is seen between the model and the experimental data on LCT.

6.3.6 Shear stiffness: G

The final material parameter to be calibrated is the shear stiffness, G. As in the previous chapter, use is made of the initial unloading response under K_0 consolidation to predict G. Typically, G for the two-surface anisotropic model will be significantly larger than that used in the single-surface isotropic model presented in the previous chapter due to κ now representing the initial loading/unloading elastic compressibility index. It is the ratio of the bulk modulus to shear modulus that governs the initial K_0 consolidation unloading behaviour. The presence of the inner yield surface allows a higher small strain shear modulus to be used.

Lower Cromer till

The K_0 swelling behaviour of LCT is shown in Figure 6.17 (ii), together with the model response. The following phases of unloading are noted:

B to C : elastic swelling inside the yield surface with the stress response controlled solely by the elastic material constants;

C : onset of elasto-plastic behaviour; and

C to D : elasto-plastic swelling response controlled chiefly by the translation and shear hardening laws (in addition to the elastic material constants).

To obtain good agreement with the data on LCT between B and C, the value of the shear modulus was set at $G = 28$MPa. During unloading softening of the two surfaces occurs between C and D. In addition, there is a reduction in the degree of anisotropy during this path (from $\beta = 0.160$ at B to $\beta = 0.108$ at D). Again good agreement is observed between the experimental data and the response predicted by the constitutive model, overcoming one of the main inadequacies seen in the single-surface isotropic family of models presented in the preceding chapter.

6.3.7 Complete set of material constants

The full set of two-surface anisotropic model constants for LCT and London Clay are given in Table 6.1. The calibration procedure suggested in this section offers the preferred approach for determining the material constants for the model as test paths which isolated the effects of some of the constants have been identified. The follow sub-section describes the minimum set of just six material constants that can be determined from only three experimental tests.

	Constant	Description	Section/Figure	Default	LCT	LC
elastic	κ	initial bi-logarithmic elastic compressibility index	Section 6.3.1 (Figure 6.11)	-	0.005	0.019
	G	constant elastic shear modulus	Section 6.3.6	-	28 MPa	18 MPa
yield surface	λ	bi-logarithmic plastic compressibility index	Section 6.3.1 (Figure 6.11)	-	0.0447	0.073
	M	classical isotropic gradient of the CSL (determined analytically from the gradient of the CS line η_{cs} once α, γ and b_β have been determined)	Section 6.3.4 (Figure 6.8)	(6.44)	0.921	0.666
	$\bar{\rho}_e$	normalised deviatoric radius under triaxial extension to that under triaxial compression	Section 6.3.4	(4.3)	0.729	0.903
	α	yield surface shape and plastic flow direction parameter	Section 6.3.3	0.6	0.4	0.6
	γ	yield surface shape and plastic flow direction parameter	Section 6.3.2 (Figures 6.13 & 6.14)	0.89	0.78	0.9
	R	ratio of the size of the inner yield surface to that of the outer surface	Section 6.3.1 (Figure 6.11)	0.2	0.2	0.2
shear & translation	b_β	isochoric plastic flow target of $\{\beta\}$ controlling the level of anisotropy at the CS as $\beta_{cs} = b_\beta \eta_{cs}$	Section 6.3.2 (Figures 6.13, 6.14 & 6.15)	0.1	0.1	0.1
	x_β	relative contributions of volumetric and deviatoric plastic strains on the evolution of $\{\beta\}$ (determined analytically from one-dimensional consolidation data, η_{K_0})	Section 6.3.5	(6.64)	4.8	1.8
	C_β	rate of evolution of $\{\beta\}$	Section 6.3.5	-	14	16
	C_χ	rate of translation of the inner surface towards the image point on the outer surface	Section 6.3.1 (Figure 6.11)	-	3700	1000

Table 6.1: Material constants for the two-surface anisotropic model with values for (i) Lower Cromer till (LCT) according to the data from Gens [20] and (ii) London Clay (LC) according to the data from Hight *et al.* [26], in addition to suggested default values.

Minimum set of material constants

The complete set of material constants for the two-surface anisotropic model numbers 12. However, it is possible to reduce this to a minimum set of six core constants, the others assume default values (as given in Table 6.1). The classical MCC model requires four constants (namely, κ, G, λ and M), only two additional constants controlling the rate of translation of the inner yield surface, C_χ, and the rate of development of anisotropy, C_β, are required to utilise the two-surface model. Two of the default constants require calculation by the user, these are:

$\bar{\rho}_e$: the normalised deviatoric radius under triaxial extension obtained from η_{cs} (via the equivalent friction angle, ϕ) using (4.3); and

x_β : the relative contributions of volumetric and deviatoric plastic straining on the development of anisotropy, $\{\beta\}$, obtained from η_{K_0} using (6.64).

The other four default constants are fixed at:

α : equal to 0.6; to reduce the over-prediction of the peak deviatoric stress at high OCRs of the MCC model;

b_β : equal to 0.1;

γ : equal to 0.89; so that position of the CSL relative to the size of the yield surface is the same as for the MCC model (that is, $(p/p_c)_{cs} = 0.5$); and

R : equal to 0.2.

The values of b_β and R have been set at 0.1 and 0.2 respectively as they appear reasonable for both the experimental data on LCT and that of London clay (presented in Chapter 7). Fixing six of the two-surface anisotropic model's constants leaves six non-default constants which are specified through:

κ : initial hydrostatic drained unloading or re-loading;

G : initial K_0 unloading stiffness;

λ : virgin drained hydrostatic loading;

M : UTC to obtain η_{cs} which is then used to calculate M through (6.44);

C_χ : drained hydrostatic unloading or re-loading (deviation from κ line); and

C_β : elasto-plastic K_0 unloading behaviour.

Therefore, data from the following three experimental tests is required to calibrate the reduced material constant two-surface anisotropic model:

(i) drained hydrostatic loading, to provide λ, and unloading to provide κ and C_χ;

(ii) a single UTC test to provide the stress ratio at the CS η_{cs} (for M); and

(iii) drained one-dimensional loading, to provide η_{K_0} (for x_β), and unloading to provide G and C_β.

These three tests can be easily conducted using standard geotechnical laboratory (triaxial) apparatus.

Attempts have been made to link the classical material constants κ, λ and M to soil classification indices, such as the liquid and plastic limits (see Yan *et al.* [62] and the references contained within). Such studies provide useful connections between simple test methods used by geotechnical engineers and the stiffness and strength parameters which define the CS family of constitutive models.

6.4 Algorithmic treatment

This section describes the algorithmic aspects associated with incorporating the two-surface anisotropic constitutive model into a finite-element (FE) code. The backward Euler (bE) stress integration procedure operates with the residuals and unknowns used in the previous chapter with a further two terms added. One of these new terms describes the orientation of the yield surfaces, while the other identifies the centre of the inner yield surface. A pseudo-code for the constitutive algorithm is given in Figure 6.25. The influence of the form of the yield function is investigated and the paths corresponding to compressive, deviatoric and dilative stress returns are illustrated in principal stress space. Errors associated with the bE integration procedure are then quantified and the robustness of the stress integration algorithm examined. Finally, the constitutive equations are linearisied for small strain and finite deformation analysis, thereby providing the algorithmic consistent tangent.

6.4.1 Integration

As in the previous two chapters, an implicit bE stress integration algorithm (first introduced in Section 2.3), is used again to arrive at an incremental form for the constitutive equations. Using the following twenty residuals

$$\{b\} = \left\{ \begin{array}{c} \{\varepsilon^{\mathrm{e}}\} - \{\varepsilon^{\mathrm{e}}_t\} + \Delta\gamma\{g_{,\sigma}\} \\ p_c - \tilde{p}_c \\ \{\sigma^{\chi}\} - \{\tilde{\sigma}^{\chi}\} \\ \{\beta\} - \{\tilde{\beta}\} \\ f \end{array} \right\}, \tag{6.65}$$

where $\tilde{p}_c$, $\{\tilde{\sigma}^{\chi}\}$ and $\{\tilde{\beta}\}$ are obtained from implicit integration of the instantaneous hardening laws. Taking the derivative of the residuals (6.65) respect to the following set of unknowns

$$\{x\} = \Big\{ \{\varepsilon^{\mathrm{e}}\} \quad p_c \quad \{\sigma^{\chi}\} \quad \{\beta\} \quad \Delta\gamma \Big\}^T, \tag{6.66}$$

the (20×20) Hessian matrix is obtained as

$$[A] = \left[\begin{array}{rrrrr} [I] + \Delta\gamma[g_{,\sigma\sigma}][D^{\mathrm{e}}] & \Delta\gamma\{g_{,\sigma p_c}\} & \Delta\gamma[g_{,\sigma\sigma^{\chi}}] & \Delta\gamma[g_{,\sigma\beta}] & \{g_{,\sigma}\} \\ -\{\tilde{p}_{c,\sigma}\}^T[D^{\mathrm{e}}] & 1 - (\tilde{p}_{c,p_c}) & -\{\tilde{p}_{c,\sigma^{\chi}}\}^T & -\{\tilde{p}_{c,\beta}\}^T & -(\tilde{p}_{c,\Delta\gamma}) \\ -[\tilde{\sigma}^{\chi}{}_{,\sigma}][D^{\mathrm{e}}] & -\{\tilde{\sigma}^{\chi}{}_{,p_c}\} & [I] - [\tilde{\sigma}^{\chi}{}_{,\sigma^{\chi}}] & -[\tilde{\sigma}^{\chi}{}_{,\beta}] & -\{\tilde{\sigma}^{\chi}{}_{,\Delta\gamma}\} \\ -[\tilde{\beta}_{,\sigma}][D^{\mathrm{e}}] & -\{\tilde{\beta}_{,p_c}\} & -[\tilde{\beta}_{,\sigma^{\chi}}] & [I] - [\tilde{\beta}_{,\beta}] & -\{\tilde{\beta}_{,\Delta\gamma}\} \\ \{f_{,\sigma}\}^T[D^{\mathrm{e}}] & f_{,p_c} & \{f_{,\sigma^{\chi}}\}^T & \{f_{,\beta}\}^T & 0 \end{array} \right]. \tag{6.67}$$

The implicit hardening law for the evolution of the size of the outer surface was given by (5.25). Through implicit integration of (6.55), we obtain the incremental evolution law for the centre of the inner surface as

$$\{\tilde{\sigma}^{\chi}_{n+1}\} = \Big[\tilde{\sigma}^{\chi}_{denom}\Big]^{-1} \underbrace{\Big\{ \{\sigma^{\chi}_n\} + C_{\chi}||\{\Delta\varepsilon^{\mathrm{p}}\}||\Big\{(1-R)\{\sigma\} + \frac{Rp_c\gamma}{2}\big\{\{1\} + \{\beta\}\big\}\Big\}\Big\}}_{\{\tilde{\sigma}^{\chi}_{num}\}}, \tag{6.68}$$

where

$$\Big[\tilde{\sigma}^{\chi}_{denom}\Big] = \left[\left(1 - \frac{\Delta\varepsilon^{\mathrm{p}}_v}{(\lambda-\kappa)} + C_{\chi}||\{\Delta\varepsilon^{\mathrm{p}}\}||\right)[I] - \frac{\{\Delta\beta\}\{1\}^T}{3}\right], \tag{6.69}$$

and $\{\Delta\beta\} = \{\beta_{n+1}\} - \{\beta_n\}$. $\{\beta_n\}$ and $\{\sigma^{\chi}_n\}$ respectively identify the orientation and the centre of the inner surface at the previous state. Implicit integration of (6.34), provides the evolution law for the

shearing of the yield surfaces as

$$\{\tilde{\beta}_{n+1}\} = \frac{\{\tilde{\beta}_{num}\}}{(\tilde{\beta}_{denom})} = \frac{p_\beta\{\beta_n\} + C_\beta\Big(d_\beta\big\{\{s\} - \{s^\chi\}\big\}\Big)}{p_\beta + C_\beta\Big(p_\beta\big(\langle\Delta\varepsilon_v^{\mathrm{p}}\rangle + x_\beta\Delta\varepsilon_\gamma^{\mathrm{p}}\big) - Rp_c\gamma d_\beta/2\Big)}. \tag{6.70}$$

d_β and p_β are given in (6.38) and (6.36) respectively. The derivatives required for the Hessian matrix (6.67) are listed in Appendix E (except the direction of plastic flow, which is given in (6.30)).

6.4.2 Yield function

Chapter 5 revealed that the form of the yield function, f, can have a significant influence on the stability and efficiency of the stress integration procedure using the bE method. Figure 6.18 shows contours of the inner surface yield function (6.15) for the two-surface anisotropic model (i) in p-q stress space and (ii) in the deviatoric plane for five hydrostatic stress states (where the deviatoric sections are identified in Figure 6.18 (i)). The yield surface examined has the following properties: $\alpha = 0.6$, $\gamma = 0.9$, $R = 0.2$, $M = 0.9$, $\beta = 0.5$ and $\bar{\rho}_e = 0.8$. A discontinuity is seen in Figure 6.18 (i), and Figure 6.18 (ii) $p/p_c = 0.90$, along the axis of anisotropy passing through the inner yield surface when viewed in p-q stress space. This discontinuity is a consequence of f having a LAD. When $\{\beta\} = \{0\}$ or $\bar{\rho}_e = 1$ this discontinuity disappears.

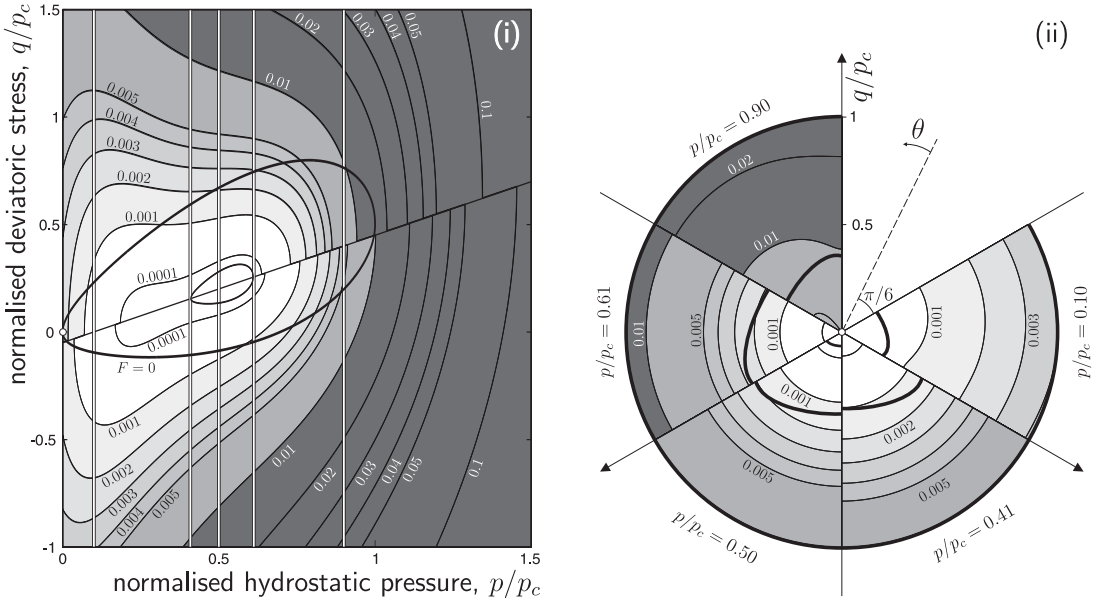

Figure 6.18: Inner yield surface contours of the yield function f in (i) normalised p-q stress space and (ii) five deviatoric planes centred on the inner surface axis of anisotropy with six-fold symmetry.

Figure 6.19 shows contours of the following yield function

$$f = \frac{(p - p^\chi)^2}{A_f^2} + \frac{\{s^\beta\}^T\{s^\beta\}}{B_f^2} - 1 = 0, \tag{6.71}$$

which is the natural extension of the isotropic yield function introduced by Collins and Hilder [5]. Using (6.71), a discontinuity appears near the *apex* of the inner surface where a high gradient in the contours of the yield function is evident. The presence of this region (with an example point highlighted in Figure 6.19 (i)) presents serious problems for a stress return algorithm based on the bE method. The descent direction associated with these contours is inappropriate. The consequence of this is that a stress state could potentially be *trapped* outside of the yield surface, unable to converge.

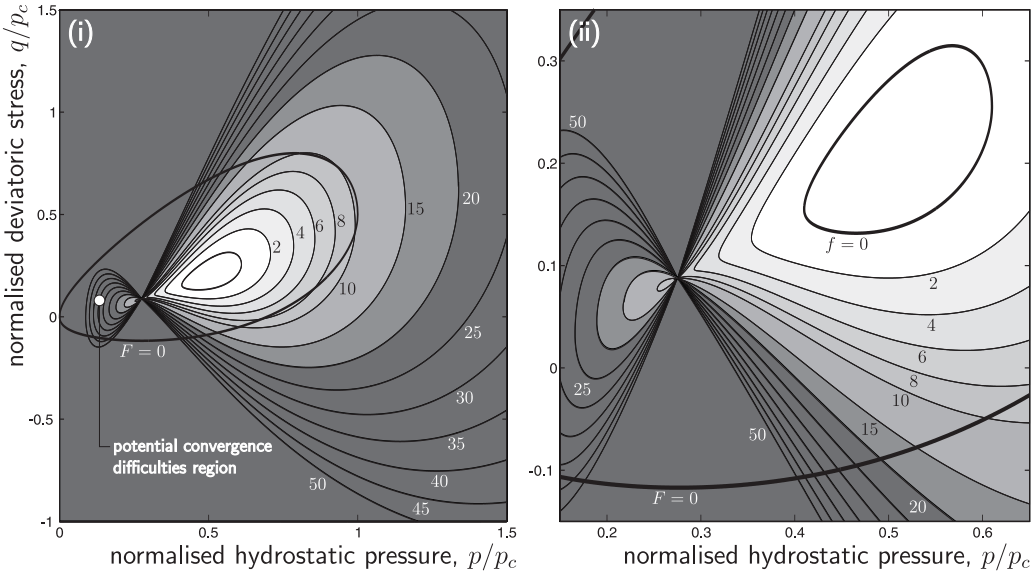

Figure 6.19: Inner yield surface contours of the yield function (6.71) using the natural extension of the isotropic single surface yield function proposed by Collins *et al.* [5].

6.4.3 Stress return

The stress return paths are demonstrated in Figure 6.20 for (i) general compressive, (ii) purely deviatoric and (iii) general tensile trial stresses. The two-surface anisotropic model (with the material constants for LCT, as given in Table 6.1) was used with a reference pressure of 100kPa and an initial outer surface of size $p_c = 200$kPa. Starting from a hydrostatic stress state of $\{\sigma_n\} = 100\ \{1\}$kPa and an isotropic material state (with $\{\beta\} = \{0\}$ and $\{\sigma^\chi\} = \{\sigma_n\}$) the model was subjected to the different trial strain states given in Table 6.2. Each of the trial strain states have a length of $2,000\mu$ (that is, 2×10^{-3}). The resulting stress return path is shown in Figure 6.20 in both three-dimensional principal stress space and a deviatoric stress space view. The final inner yield and outer surfaces are also shown. The principal stress state and material parameters at the final converged state are given in Table 6.2.

	compressive (i)	deviatoric (ii)	tensile (iii)
$\{\varepsilon_t^e\} \times 10^{-3}$	$\{1.00 \quad 0.50 \quad 1.66\}$	$\{1.25 \quad -1.54 \quad 0.29\}$	$\{-0.46 \quad -0.92 \quad -1.72\}$
$\{\sigma\}$ (kPa)	$\{145.0 \quad 137.3 \quad 166.9\}$	$\{120.7 \quad 69.6 \quad 103.1\}$	$\{63.0 \quad 59.2 \quad 52.4\}$
$\{\beta\} \times 10^{-3}$	$\{-0.3 \quad -2.5 \quad 2.8\}$	$\{4.0 \quad -4.9 \quad 0.9\}$	$\{4.2 \quad 0.8 \quad -5.0\}$
$\{\sigma^\chi\}$ (kPa)	$\{127.5 \quad 119.9 \quad 137.8\}$	$\{110.3 \quad 76.0 \quad 98.5\}$	$\{74.4 \quad 72.0 \quad 67.9\}$
p_c (kPa)	205.6	200.6	198.1
iterations	9	8	9

Table 6.2: Stress return principal values (with zero shear components) corresponding to the stress return paths in Figure 6.20 (i) compressive, (ii) isochoric and (iii) tensile trial strain states.

Figure 6.20 demonstrates that the direction of the stress return path is radial to the inner yield surface. Note that the stress returns all occur in different sextants of stress space. Despite the discontinuity in the yield function contours (Figure 6.18) the stress return algorithm satisfactorily and rapidly returns onto the correct yield surface.

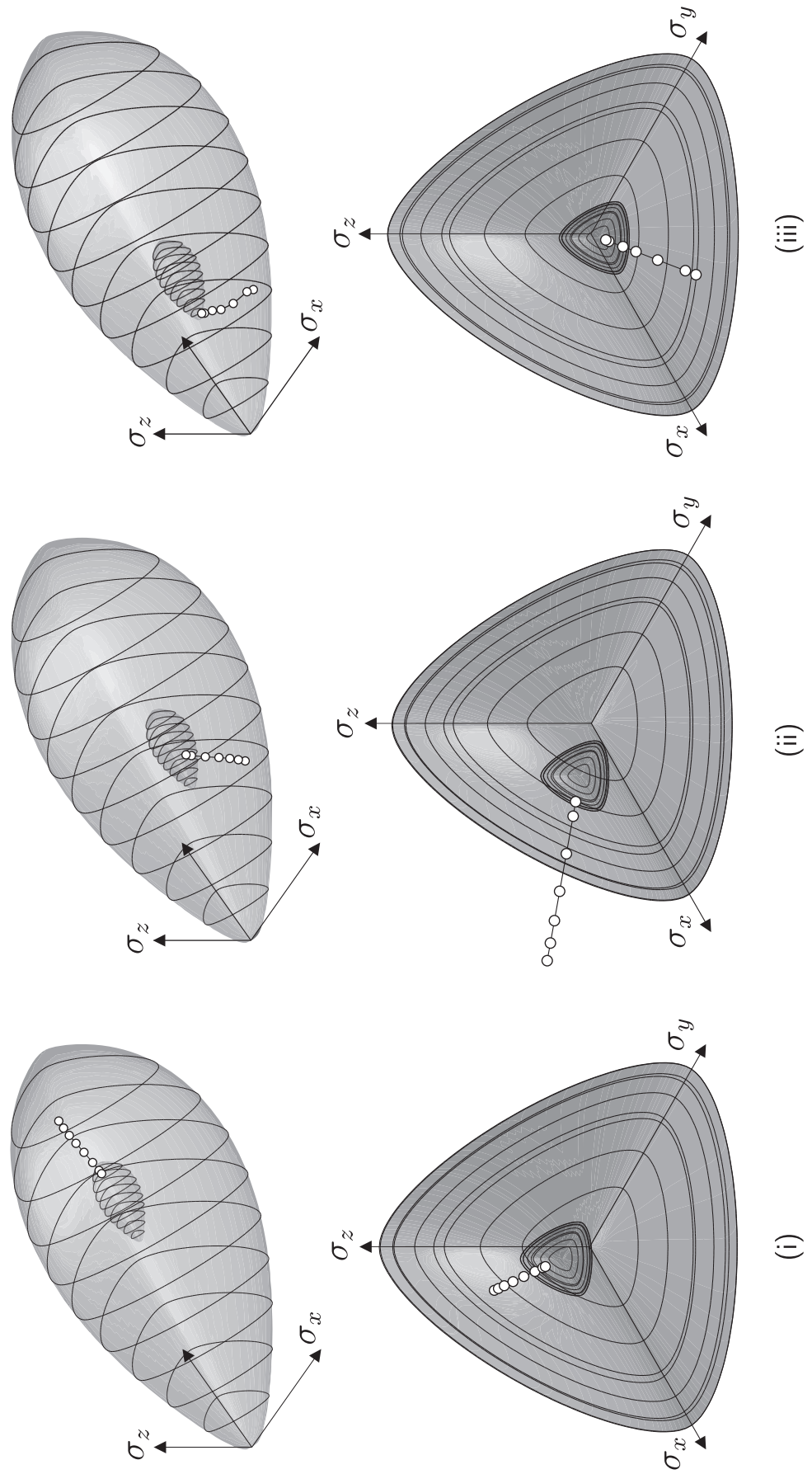

Figure 6.20: Stress return path for the anisotropic two surface plasticity model subjected to the following normal trial strain components (i) $\{\varepsilon_t^e\} = \{1.00 \quad 0.50 \quad 1.66\}^T \times 10^{-3}$, (ii) $\{\varepsilon_t^e\} = \{1.25 \quad -1.54 \quad 0.29\}^T \times 10^{-3}$ and (iii) $\{\varepsilon_t^e\} = \{-0.46 \quad -0.92 \quad -1.72\}^T \times 10^{-3}$ with zero shear strain components.

Even for these the relatively large strain increments, the constitutive model converges in 8 or 9 iterations. The hardening response of the model is dominated by the translation of the inner yield surface, with very minor changes in the size of the outer surface, p_c, and the degree of anisotropy, $\{\beta\}$. This is particularly evident in the deviatoric strain increment return path (seen in Figure 6.20 (ii)), where the inner surface translates deviatorically 24.6kPa away from the hydrostatic axis.

6.4.4 Error analysis

The errors resulting from the approximate stress integration procedure are now quantified using the same error measure as used in the preceding chapters. The constitutive model used the material constants for LCT, as given in Table 6.1, with the size of the outer surface set at 200kPa and a reference pressure of 100kPa. From an initial hydrostatic stress state $\{\sigma_n\} = 100 \times \{1\}$kPa, an anisotropic material state $\{\beta_n\} = \{-0.1 \quad -0.1 \quad 0.2 \quad 0 \quad 0 \quad 0\}^T$ and $\{\sigma_n^\chi\} = \{\sigma_n\}$, the model was subjected to an elastic strain increment of $\Delta\varepsilon_\gamma \in [0, 4] \times 10^{-3}$ and $\theta \in [-\pi/6, \pi/6]$ within three of the sextants of stress space. The volumetric strain increment was set to (i) 0, (ii) 1×10^{-3} or (iii) $\Delta\varepsilon_v = -0.5 \times 10^{-3}$. These gave rise to a trial hydrostatic pressure of $p_t = 100$, 122.1 or 90.5kPa respectively.

The single increment return was compared with the solution obtained by splitting the strain increment into 1,000 sub-increments[25] and the error maps (using the error measure given in Chapter 4, (4.32)) plotted in Figure 6.21. The error analysis procedure is illustrated graphically on the right of Figure 6.21 (i) at a deviatoric section through $p = p_c/2$ (that is, at 100kPa). The inner yield and outer surfaces are drawn to scale, showing the (relatively large) magnitude of the trial deviatoric stress increment at over 20 times the size of the inner yield surface (at a hydrostatic pressure of 100kPa). Due to the symmetry, only three of the six stress sextants are investigated (sextants (A), (B) and (C)). The maximum errors within each of the sextants are given in Table 6.3.

	sextant	(i)	(ii)	$\Delta\varepsilon_v$	(iii)	$\Delta\varepsilon_v$
(A)	$\sigma_x > \sigma_y > \sigma_z$	9.729%	11.738%	1×10^{-3}	9.216%	-0.5×10^{-3}
(B)	$\sigma_x > \sigma_z > \sigma_y$	9.739%	11.781%	1×10^{-3}	9.219%	-0.5×10^{-3}
(C)	$\sigma_z > \sigma_x > \sigma_y$	7.078%	8.947%	1×10^{-3}	6.743%	-0.5×10^{-3}
(D)	$\sigma_z > \sigma_x > \sigma_y$	–	8.810%	1×10^{-3}	6.812%	-1×10^{-3}
(E)	$\sigma_x > \sigma_y > \sigma_z$	–	14.962%	2×10^{-3}	6.836%	-0.5×10^{-3}

Table 6.3: Maximum stress return errors for the two-surface anisotropic model in each stress sextant for (i) deviatoric trial strains, (ii) compressive trial strains and (iii) tensile trial strains.

The larger errors were found in the regions which return near the compression meridians as a consequence of the high deviatoric curvature near the yield surface. Conversely, the lowest errors were located in the regions returning near the extension meridians. The maximum errors remain fairly constant when moving from a deviatoric (Figure 6.21 (i)) to a dilative Figure 6.21 (iii) strain increment, partly due to the anisotropic hardening law (6.37) being invariant to dilative volumetric plastic strains. Doubling the size of the dilative volumetric strain increment (with a trial pressure of 81.9kPa) only increases the error by 0.1%. The influence of the rate of hardening of the inner yield surface is explored via sextant (E) in Figure 6.21 (iii) where C_χ has been halved to a value of $1,850$. Halving C_χ decreases the maximum error in the sextant by 2.4%. The effect of reducing C_β to 7, with a compressive volumetric strain increment, is shown in sextant (D) of Figure 6.21 (ii) where the error reduced by only 0.1%. Doubling the volumetric

[25] Note, that the error analysis was conducted using the Fortran90 implementation of the two-surface anisotropic model.

compressive strain increment (to $\Delta\varepsilon_v = 2 \times 10^{-3}$ with a trial pressure of 149.2kPa) increases the maximum error within sextant (E) of Figure 6.21 (ii), from that of sextant (A), by 3.2%. These errors are not unexpected for an advanced constitutive model with relatively large strain increments. By comparison, recall from the preceding chapter that the errors for the MCC model peaked at 24.1% (see Table 5.3, Chapter 5).

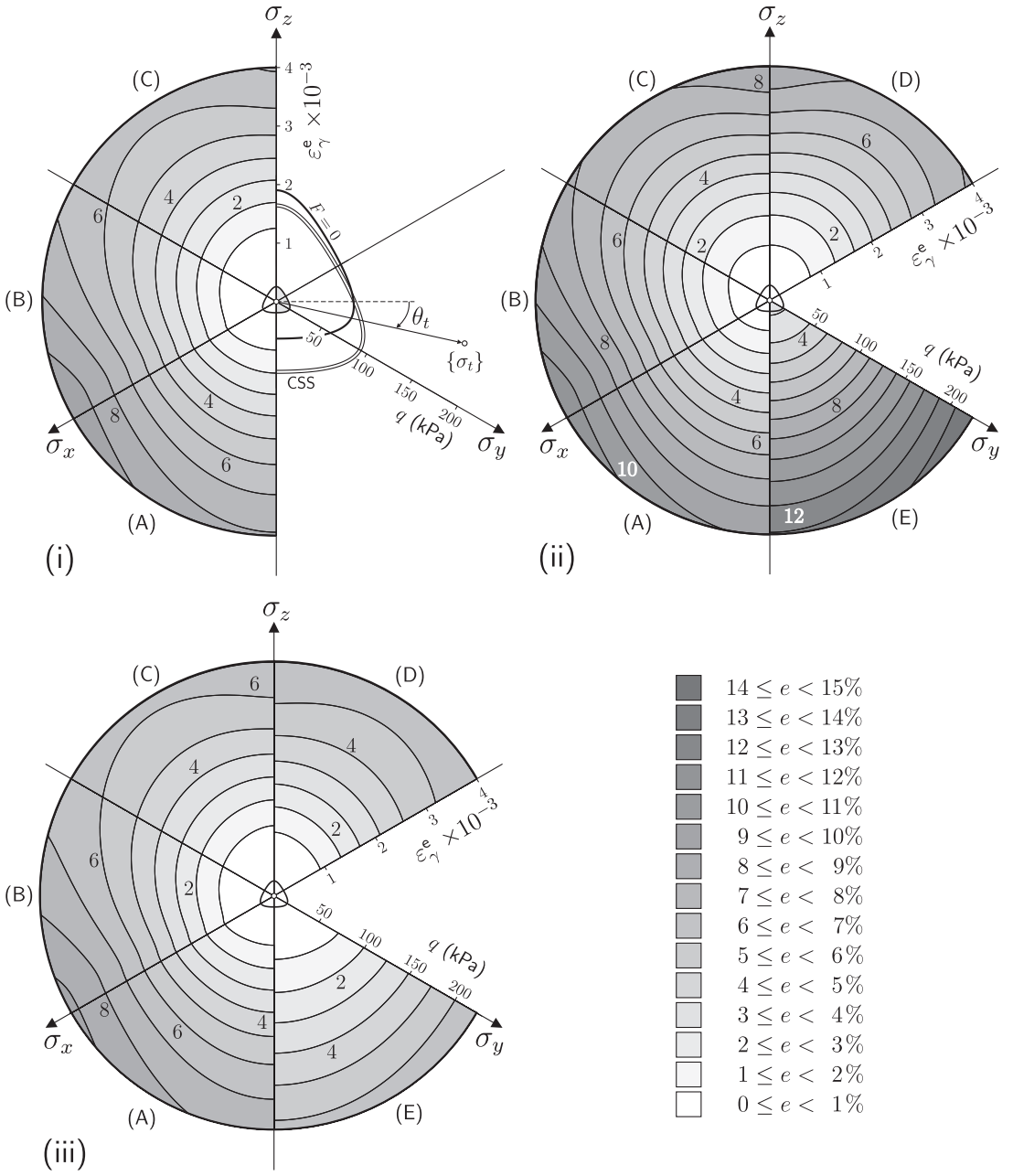

Figure 6.21: Errors in the return stress associated with the iterative bE integration scheme for $\Delta\varepsilon_\gamma \in [0, 4] \times 10^{-3}$ and $\theta_t \in [-\pi/6, \pi/6]$ within three quadrants of stress space: (i) deviatoric trial strains, (ii) compressive trial strains and (iii) tensile trial strains.

6.4.5 Robustness

Algorithmic issues: $p = p^{\chi}$

At a stress state where the hydrostatic stress is equal to the inner surface *apex* pressure p_A, it is evident that $p_\beta = 0$ and the stress ratio $\{r\}$ is undefined (see Figure 6.4 (i)). Using Hopital's rule, as $p_\beta \to 0$ the stress ratio $\{r\} \to \{0\}$. When returning onto the *apex* of the inner yield surface, the direction of plastic flow is purely dilative. Therefore, d_β is equal to zero as $\langle \Delta\varepsilon_v^{\mathrm{p}} \rangle = 0$ and the linearised evolution law for $\{\beta\}$, from (6.70), is undefined, with both the numerator and denominator equal to zero. In this case, the incremental evolution law for the inclination of the yield surface becomes $\{\tilde{\beta}\} = \{\beta_n\}$.

Gudehus plots

Similar to the examples presented in Chapters 4 and 5, Gudehus [22] plots for the two-surface anisotropic model provide a useful indication of the stability and robustness of the stress integration algorithm. Figures 6.22 and 6.23 show Gudehus stress surfaces for initially isotropic ($\{\beta\} = \{0\}$) and anisotropic ($\{\beta\} = \{-0.1 \quad -0.1 \quad 0.2 \quad 0 \quad 0 \quad 0\}^T$) states. The material constants for LCT (Table 6.1) were used in this analysis, with a reference pressure of 100kPa and an initial outer surface size of $p_c = 300$kPa. The *centre* of the inner yield surface was initially located on the hydrostatic axis at $p^{\chi} = 100$kPa.

The model was then subjected to 832 strain probes in 64 *spheres* starting at different locations on the inner yield surface. Each *sphere* has a strain radius of $150\mu\varepsilon$ (that is, 1.5×10^{-4})[26]. The directions of both the individual strain probes and the initial positions on the yield surface were obtained using the HEALPix software [21]. A stress surface was then plotted using the return stress states, shaded according to the distance between the starting and final stress state (black and white being the longest and shortest stress paths respectively).

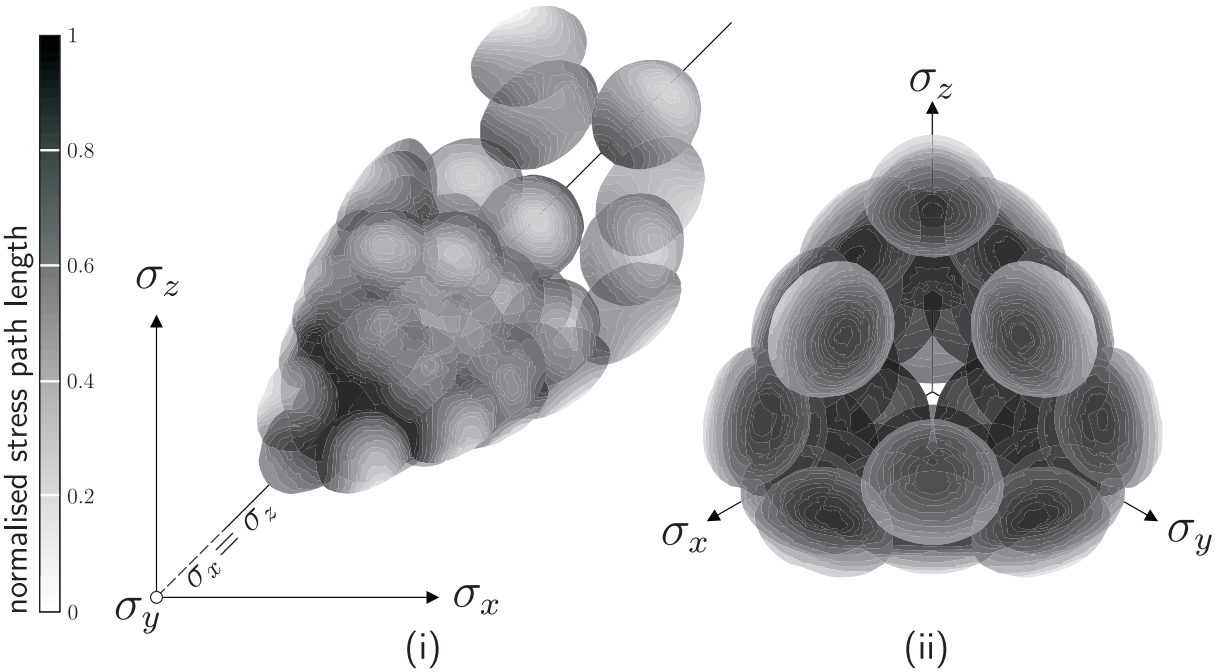

Figure 6.22: Gudehus stress plots for an initially isotropic state of the two-surface anisotropic model (using material constants for LCT).

[26]Note, that this level of strain was selected as it allows the individual surfaces to be visulised. If the strain radius is set too large then it is difficult to identify the boundaries between the Gudehus stress surfaces.

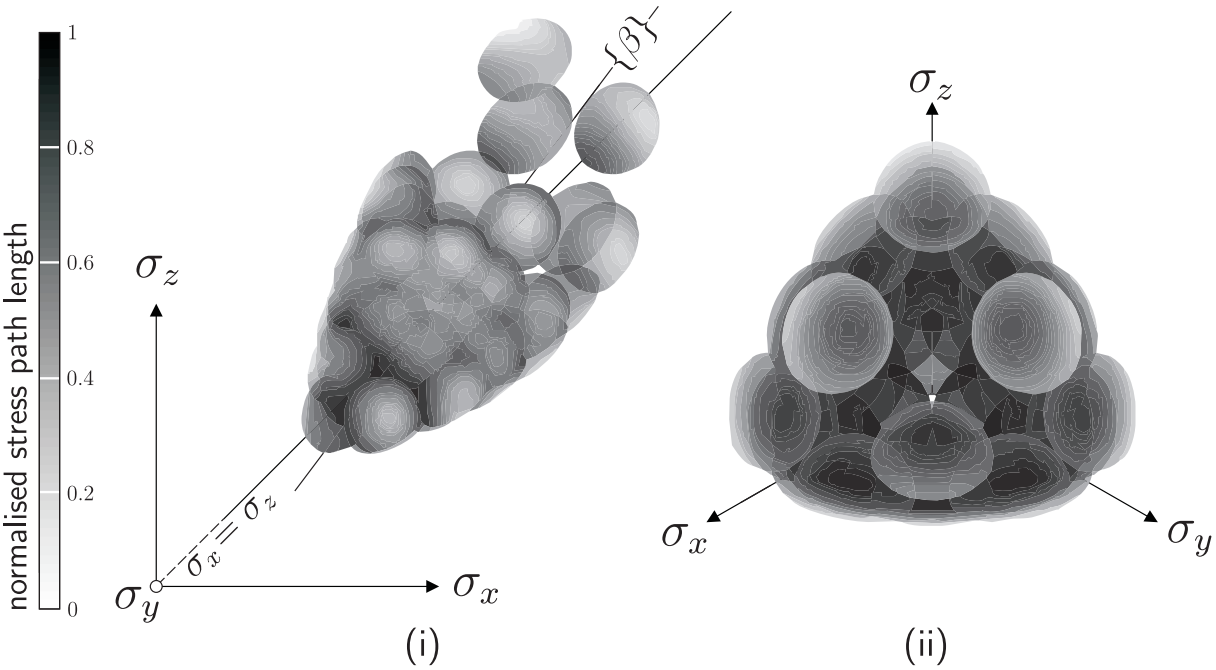

Figure 6.23: Gudehus stress plots for an initially anisotropic state of the two-surface anisotropic model with $\{\beta\} = \{0.2 \quad -0.1 \quad -0.1 \quad 0 \quad 0 \quad 0\}^T$ (using material constants for LCT).

Random strain path

Within a complex three-dimensional boundary value simulation, the strain paths that a constitutive model could be subjected to may be far removed from simple axi-symmetric triaxial compression or extensions paths used for the calibration procedure. The following investigation serves as a challenging test for any constitutive model and integration scheme. It is suggested that this type of exercise should always be undertaken if the model is to be used in FE analyses in order to check the robustness of the complete algorithm. Figure 6.24 shows a sequence of Gudehus plots for the two-surface anisotropic model with the same material parameters as used previously, starting from an hydrostatic stress state ($\{\beta\} = \{0\}$) with $p^\chi = 100$kPa. The analysis had the following sequence:

(i) hydrostatic straining to 200kPa;

(ii) the model was then subjected to 832 strain probes of magnitude $500\mu\varepsilon$, with their directions determined from the HEALpix software [21];

(iii) one of the 832 return states was randomly selected to be the starting state for the next *strain sphere*; then

(iv) repeat steps (ii) and (iii) for 200 *strain spheres*.

Five of the 200 stress responses are plotted for probes 1, 50, 100, 150 and 200, where the surfaces are shaded according to the distance from the starting stress state to the return stress state. The starting state is identified by a black square. The stress path between the starting points for the strain spheres is also plotted on the projections in (i) a deviatoric plane and (ii) the σ_x-σ_z plane.

The stress responses, when inside the yield surface, have a circular deviatoric section due to the elastic isotropy. The Gudehus plots are flattened in the direction of the yield surface as a portion of the strain increment is taken up by the plastic response, leaving a reduced elastic strain (and hence

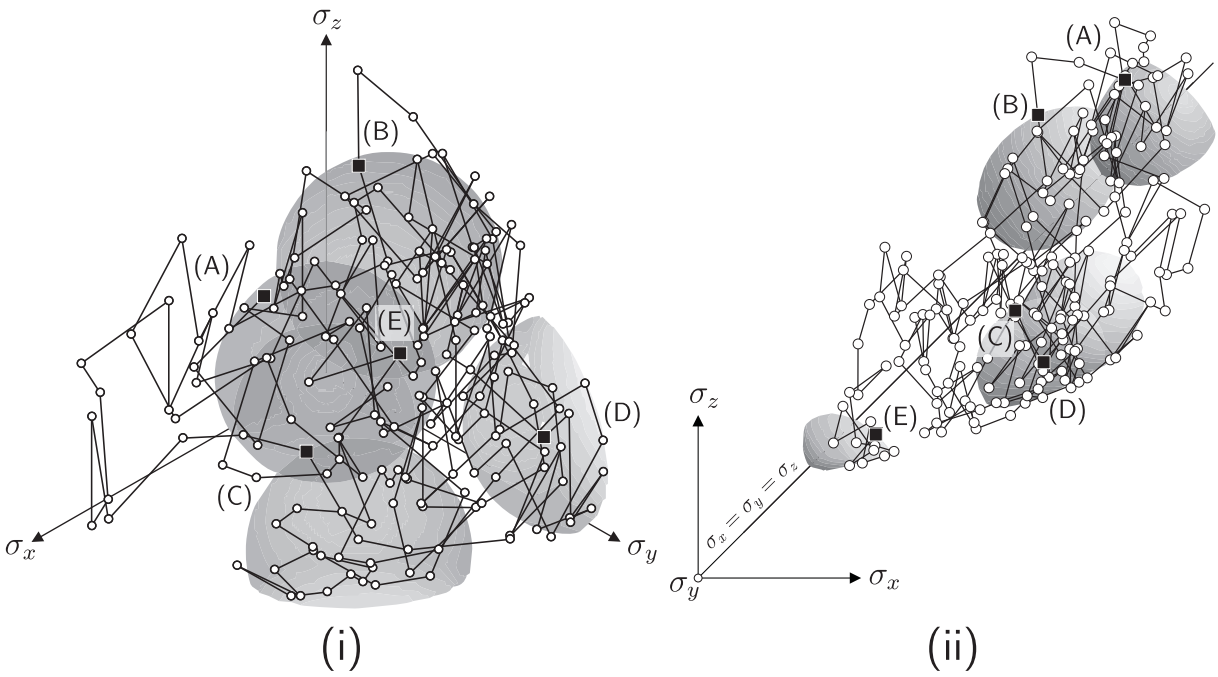

Figure 6.24: Sequence of Gudehus stress plots for the two-surface anisotropic model with LCT material constants. Five of the 200 Gudehus plots are presented for steps 1 (A), 50 (B), 100 (C), 150 (D) and 200 (E) in (i) deviatoric view and (ii) σ_y–σ_z plane.

stress) response. This effects can be seen in Figure 6.24 where the flattening reveals the shape of the yield surface. The smoothness of the surfaces in Figures 6.22-6.24 demonstrates the robustness of the implemented constitutive model and algorithm.

6.4.6 Linearisation

Small strain

As presented in Section 2.4, the tangent consistent with the implicit backward Euler stress integration scheme is obtained from inverting $[A^{alg}]^{-1}$

$$\Big\{\{d\sigma\} \quad dp_c \quad \{d\sigma^\chi\} \quad \{d\beta\} \quad d\Delta\gamma\Big\}^T = \Big[A^{alg}\Big]\Big\{\{d\varepsilon_t^{\mathrm{e}}\} \quad 0 \quad \{0\} \quad \{0\} \quad 0\Big\}^T \tag{6.72}$$

where $[A^{alg}]^{-1}$ is obtained by minimising the residuals with respect to $\{\varepsilon_t^{\mathrm{e}}\}$ (with the other internal variable frozen) as

$$\Big[A^{alg}\Big]^{-1} = \begin{bmatrix} [C^{\mathrm{e}}] + \Delta\gamma[g_{,\sigma\sigma}] & \Delta\gamma\{g_{,\sigma p_c}\} & \Delta\gamma[g_{,\sigma\sigma^\chi}] & \Delta\gamma[g_{,\sigma\beta}] & \{g_{,\sigma}\} \\ -\{\tilde{p}_{c,\sigma}\}^T & 1-(\tilde{p}_{c,p_c}) & -\{\tilde{p}_{c,\sigma^\chi}\}^T & -\{\tilde{p}_{c,\beta}\}^T & -(\tilde{p}_{c,\Delta\gamma}) \\ -[\tilde{\sigma}^\chi{}_{,\sigma}] & -\{\tilde{\sigma}^\chi{}_{,p_c}\} & [I]-[\tilde{\sigma}^\chi{}_{,\sigma^\chi}] & -[\tilde{\sigma}^\chi{}_{,\beta}] & -\{\tilde{\sigma}^\chi{}_{,\Delta\gamma}\} \\ -[\tilde{\beta}_{,\sigma}] & -\{\tilde{\beta}_{,p_c}\} & -[\tilde{\beta}_{,\sigma^\chi}] & [I]-[\tilde{\beta}_{,\beta}] & -\{\tilde{\beta}_{,\Delta\gamma}\} \\ \{f_{,\sigma}\}^T & f_{,p_c} & \{f_{,\sigma^\chi}\}^T & \{f_{,\beta}\}^T & 0 \end{bmatrix}. \tag{6.73}$$

$[D^{alg}]$ is obtained from the first six rows and columns of $[A^{alg}]$, requiring the inversion of the 20 by 20 matrix containing the derivatives calculated at the return state.

Finite deformation

For infinitesimal analysis, $[D^{alg}]$ derived in the preceding section provides the appropriate material tangent for the Newton-Raphson solver within a FE code. For the finite deformation framework described in

1. INPUT: $\{\varepsilon_t^{\mathrm{e}}\}$, p_{c_n}, $\{\beta_t\}$, $\{\sigma_t^{\chi}\}$ and p_r.
2. CONSTANTS: κ, λ, G, M, $\bar{\rho}_e$, γ, α, C_χ, C_β, b_β, x_β and R.
   (a) Calculate the trial elastic stress $\{\sigma_t\}$ from (5.2)
   (b) Determine the trial yield function f (6.15)
   (c) IF $f <$ `tol`
   - Elastic response, $\{\sigma\} = \{\sigma_t\}$, $\{\varepsilon^{\mathrm{e}}\} = \{\varepsilon_t^{\mathrm{e}}\}$, $\{\beta\} = \{\beta_t\}$ and $\{\sigma^{\chi}\} = \{\sigma_t^{\chi}\}$
   - $[D^{alg}] = [D^{\mathrm{e}}]$ from (5.4) and $[D^{\beta}] = [D^{\chi}] = [0]$

   (d) ELSE
   - Elastoplastic response, set the initial conditions for the bE stress integration (2.48)
   - Calculate the derivatives required for the Hessian matrix $[A]$ (6.67)
   - WHILE $|\{b\}| >$ `tol` AND `itnum` $<$ `maxIt`
     - `itnum` = `itnum` + 1
     - Form the Hessian matrix $[A]$ (6.67) and calculate the increment in the unknowns (2.47)
     - Update unknowns $\{\varepsilon^{\mathrm{e}}\}$, p_c, $\{\beta\}$, $\{\sigma^{\chi}\}$ and $\Delta\gamma$
     - Update $\{\sigma\}$ and $[D^{\mathrm{e}}]$ from $\{\varepsilon^{\mathrm{e}}\}$ using (5.2) and (5.4)
     - Calculate the derivatives required for the Hessian matrix $[A]$ (6.67)
     - Calculate the residuals $\{b\}$ (6.66)
   - Form the derivatives required for $[A^{alg}]^{-1}$ (6.73)
   - Invert $[A^{alg}]^{-1}$ to obtain the consistent tangent $[D^{alg}]$
   - Calculate the small strain consistent backstress tangents $[D^{\beta}]$ from (6.76) and $[D^{\chi}]$ from (6.78)
3. OUTPUT: $\{\varepsilon^{\mathrm{e}}\}$, $\{\sigma\}$, p_c , $\{\beta\}$, $\{\sigma^{\chi}\}$, $[D^{alg}]$, $[D^{\beta}]$ and $[D^{\chi}]$.

Figure 6.25: Pseudo-code for the anisotropic two-surface two-parameter family of CS models. The tolerance (`tol`) was typically set to 1×10^{-12}, with a maximum of 25 iterations (`maxIt`) to find convergence.

Chapter 3, the required tangent is given by (3.67). Within this, the derivative of the updated Kirchhoff stress with respect to the deformation gradient is given by

$$\left[\tau,_F\right] = \underbrace{\left[\tau,_{\varepsilon_t^{\mathrm{e}}}\right]\left[\varepsilon_t^{\mathrm{e}},_{b_t^{\mathrm{e}}}\right]\left[b_t^{\mathrm{e}},_{F_{n+1}}\right]}_{\text{isotropic}} + \underbrace{\left[\tau,_{\beta_t}\right]\left[\beta_t,_{F_t^{\mathrm{e}}}\right]\left[F_t^{\mathrm{e}},_{F_{n+1}}\right]}_{\text{shear anisotropy}} + \underbrace{\left[\tau,_{\sigma_t^{\chi}}\right]\left[\sigma_t^{\chi},_{F_t^{\mathrm{e}}}\right]\left[F_t^{\mathrm{e}},_{F_{n+1}}\right]}_{\text{inner surface anisotropy}}, \tag{6.74}$$

where the first component of the right, $\left[\tau,_{\varepsilon_t^{\mathrm{e}}}\right]$, is the small strain algorithmic tangent $\left[D^{alg}\right]$. The first product term in (6.74) is the isotropic contribution to the spatial tangent whereas the second the third terms are associated with the plastic anisotropic response of the model. $\left[\tau,_{\beta_t}\right] = \left[D^{\beta}\right]$ and $\left[\tau,_{\sigma_t^{\chi}}\right] = \left[D^{\chi}\right]$ (referred to here as the small strain consistent backstress tangents) describe how the updated Kirchhoff stress changes as a function of the trial anisotropic shearing and centre of the yield surface respectively, assuming fixed internal variables and $\{\varepsilon_t^{\mathrm{e}}\}$. During elastic behaviour these tangents are null as an infinitesimal change in the trial backstress measures have no influence on the return stress. If the model is undergoing elasto-plastic behaviour then these matrices are obtained in a manner analogous to the formulation of the small strain consistent tangent.

The consistent linearisation of the residuals with respect to the trial anisotropic shearing of the yield

surface $\{\beta_t\}$ provides the following

$$\begin{Bmatrix} \{d\sigma\} \\ dp_c \\ \{d\sigma^\chi\} \\ \{d\beta\} \\ d\Delta\gamma \end{Bmatrix} = \begin{bmatrix} [D^{alg}] & \{A^{alg}_{12}\} & [A^{alg}_{13}] & [A^{alg}_{14}] & \{A^{alg}_{15}\} \\ \{A^{alg}_{21}\} & A^{alg}_{22} & \{A^{alg}_{23}\} & \{A^{alg}_{24}\} & A^{alg}_{25} \\ [A^{alg}_{31}] & \{A^{alg}_{32}\} & [A^{alg}_{33}] & [A^{alg}_{34}] & \{A^{alg}_{35}\} \\ [A^{alg}_{41}] & \{A^{alg}_{42}\} & [A^{alg}_{43}] & [A^{alg}_{44}] & \{A^{alg}_{45}\} \\ \{A^{alg}_{51}\} & A^{alg}_{52} & \{A^{alg}_{53}\} & \{A^{alg}_{54}\} & A^{alg}_{55} \end{bmatrix} \begin{Bmatrix} \{0\} \\ 0 \\ [\tilde{\sigma}^\chi{}_{,\beta_t}]\{d\beta_t\} \\ [\tilde{\beta}_{,\beta_t}]\{d\beta_t\} \\ 0 \end{Bmatrix} \tag{6.75}$$

From (6.75), we obtain the following relationship between an increment in the updated stress and the trial anisotropic shearing of the yield surface

$$\{d\sigma\} = \underbrace{\left[[A^{alg}_{13}][\tilde{\sigma}^\chi{}_{,\beta_t}] + [A^{alg}_{14}][\tilde{\beta}_{,\beta_t}] \right]}_{[D^\beta]} \{d\beta_t\}, \tag{6.76}$$

where $[D^\beta] = [\sigma_{n+1,\beta_t}]$ describes how the return stress evolves with respect to changes in the trial anisotropic shearing of the yield surface when the other input variables (and the trial elastic strain) are frozen.

The evolution of the return stress with respect to changes to the trial centre of the inner surface $\{\sigma^\chi_t\}$ is obtained in a manor analogous to that preformed for $\{\beta_t\}$

$$\begin{Bmatrix} \{d\sigma\} \\ dp_c \\ \{d\sigma^\chi\} \\ \{d\beta\} \\ d\Delta\gamma \end{Bmatrix} = \left[A^{alg}\right] \begin{Bmatrix} \{0\} \\ 0 \\ [\tilde{\sigma}^\chi{}_{,\sigma^\chi_t}]\{d\sigma^\chi_t\} \\ \{0\} \\ 0 \end{Bmatrix} \tag{6.77}$$

The relationship between an increment in the updated stress and the trial centre of the inner yield surface is then given by

$$\{d\sigma\} = \underbrace{\left[[A^{alg}_{13}][\tilde{\sigma}^\chi{}_{,\sigma^\chi_t}] \right]}_{[D^\chi]} \{d\sigma^\chi_t\}. \tag{6.78}$$

Similar to $[D^\beta]$, $[D^\chi] = [\sigma_{n+1,\sigma^\chi_t}]$ describes how the return stress changes with changes with respect to the trial centre of the inner yield surface. Note that the procedure for obtaining the backstress tangents requires the inversion of the same 20 by 20 matrix $[A^{alg}]^{-1}$ as that used for the small strain algorithmic tangent, at little extra computational effort compared with the small strain constitutive model.

6.5 Experimental comparisons

In this section experimental data from LCT [20] are re-examined and simulations using the two-surface anisotropic hyperplasticity model are compared with the laboratory results. Chapter 7 goes on to compare the two-surface anisotropic model with experimental data on London clay from a hollow cylinder apparatus. Those comparisons appear in the following chapter as the majority of the simulations require analysis using a three-dimensional FE program.

6.5.1 Lower Cromer till

Experimental tests on LCT [20] (first presented in Section 5.5) are now simulated using the two-surface anisotropic model, using the material constants given in Table 6.1. All of the simulations started from a reference pressure of 80kPa on the hydrostatic axis and assumed a zero initial volumetric elastic reference

strain.

Isotropic investigations

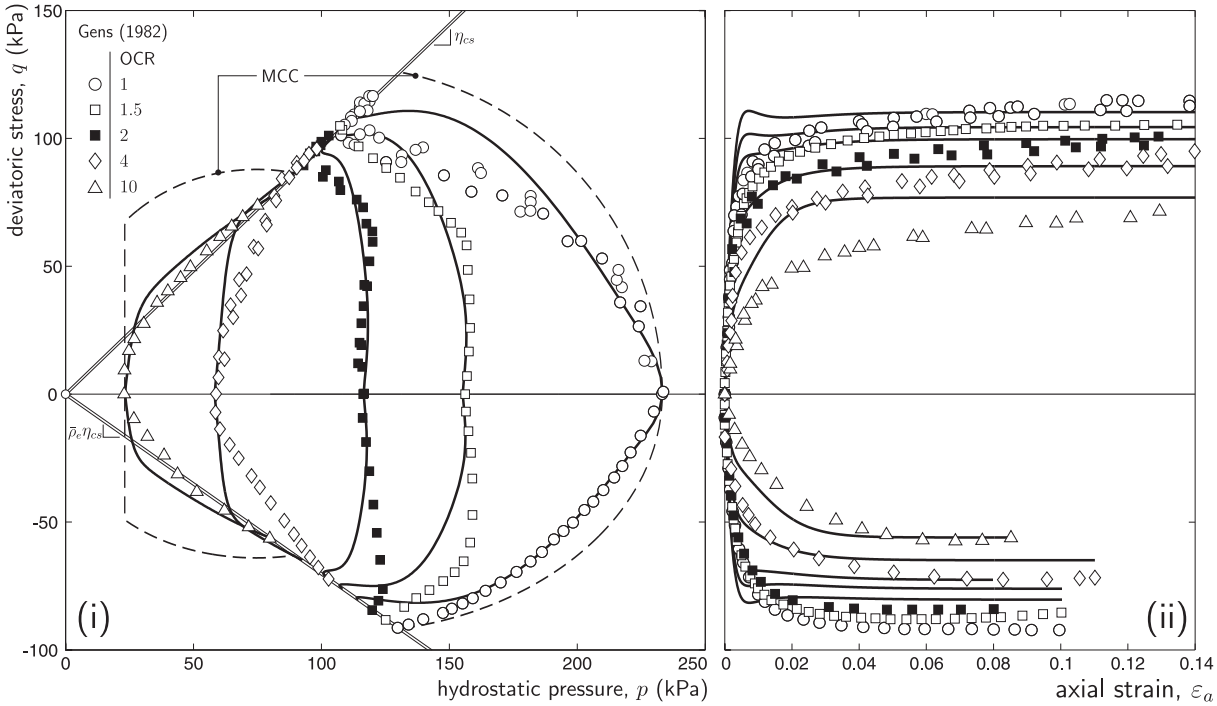

Figure 6.26: UTC and UTE tests following hydrostatic compression and swelling comparison with experimental data (shown by discrete points) on LCT from Gens [20]: (i) stress path in p-q space (dashed lines show the MCC model predictions) and (ii) axial strain versus deviatoric stress response.

Figure 6.26 shows the two-surface anisotropic model's response and experimental data under UTC and UTE for five OCRs. The simulations started with drained hydrostatic compression to 233.3kPa followed by drained hydrostatic unloading to a given OCR (of 1, 1.5, 2, 4 or 10). The model was then subjected to UTC or UTE to an axial strain of $\varepsilon_a = 0.14$ (the extension tests were simulated to the end of the experimental data, at axial strains of between $\varepsilon_a = 0.08$ and 0.11). The undrained stress paths for the MCC model are also shown (dashed line) for OCRs 1 and 10 in Figure 6.26 (i). The two-surface anisotropic model shows good agreement with the experimental data and is able to capture satisfactorily the non-linear material behaviour within the outer surface. This model shows a significant improvement over the single-surface two-parameter model response (shown in Figure 5.18) for the lightly over-consolidated specimens.

The model responses under DTC from a hydrostatic stress state (and isotropic initial state) at six OCRs, are shown in Figure 6.27. The simulations were undertaken using a single displacement-controlled, small strain, eight-noded hexahedral FE with a uniform stress (and strain) field through the element. The simulations started with drained hydrostatic compression to 233.3kPa, followed by drained hydrostatic unloading to a given OCR (of 1, 1.25, 1.5, 2, 4 or 10) and DTC to an axial strain of $\varepsilon_a = 0.14$. The principal stress *deviation* $(\sigma_3 - \sigma_1)/2$ (where the major principal stress is in the axial direction) and volumetric strain response versus axial strain are shown for the DTC stage, in Figure 6.27. In this figure the experimental data are shown by discrete points; each symbol representing a different OCR. The constitutive model gives a reasonable agreement with the experimental data, particularly in the case of the high OCRs (OCR$\geq$ 2). For the lower OCRs, an over-stiff principal stress deviation is observed, although the stress deviation at higher axial strains is in good agreement with the experimental data.

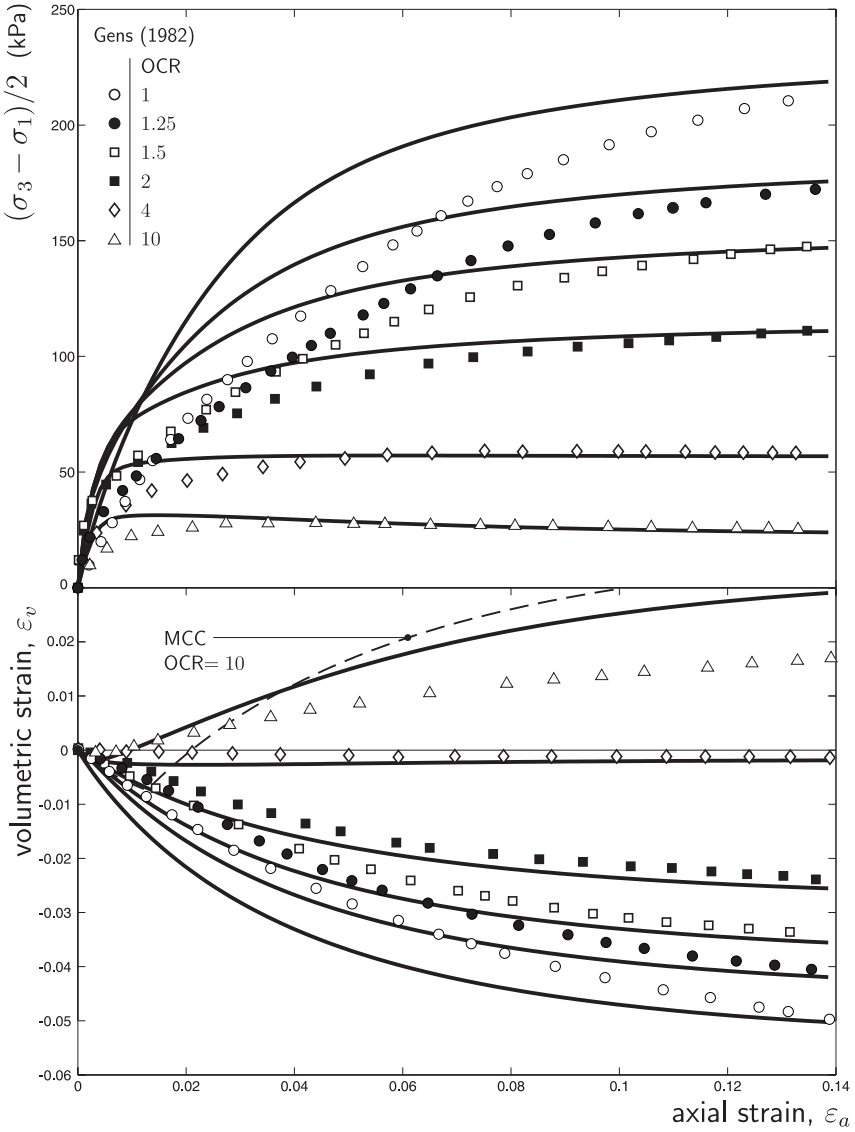

Figure 6.27: DTC tests following hydrostatic compression and swelling, comparison with experimental data (shown by discrete points) on LCT from Gens [20].

Anisotropic investigations

The anisotropic simulations started with drained one-dimensional (K_0) compression to a pressure of 233.3kPa, followed by drained K_0 unloading (swelling) to a given OCR. The one-dimensional consolidation and swelling response of the two-surface anisotropic model was shown in Figure 6.17.

Figure 6.28 shows the experimental results from LCT [20] under UTC and UTE following one-dimensional loading and unloading to different OCRs. The stress path response for the MCC and the two-surface anisotropic models are shown in Figures 6.28 (i) and (iii), respectively, for all OCRs. The axial strain versus deviatoric stress responses are shown in Figures 6.28 (ii) and (iv). For all of the tests, the full stress path is simulated using a single set of material constants. That is, the same constants are used for the complete response, including one-dimensional consolidation, swelling and UTC or UTE (A-G). The two-surface model shows a reasonable agreement with the experimental data for all OCRs. The only significant deviation is under UTE at an OCR of 1, where an over-stiff response is observed. The new model provides a significant improvement over the MCC formulation, particularly for the high

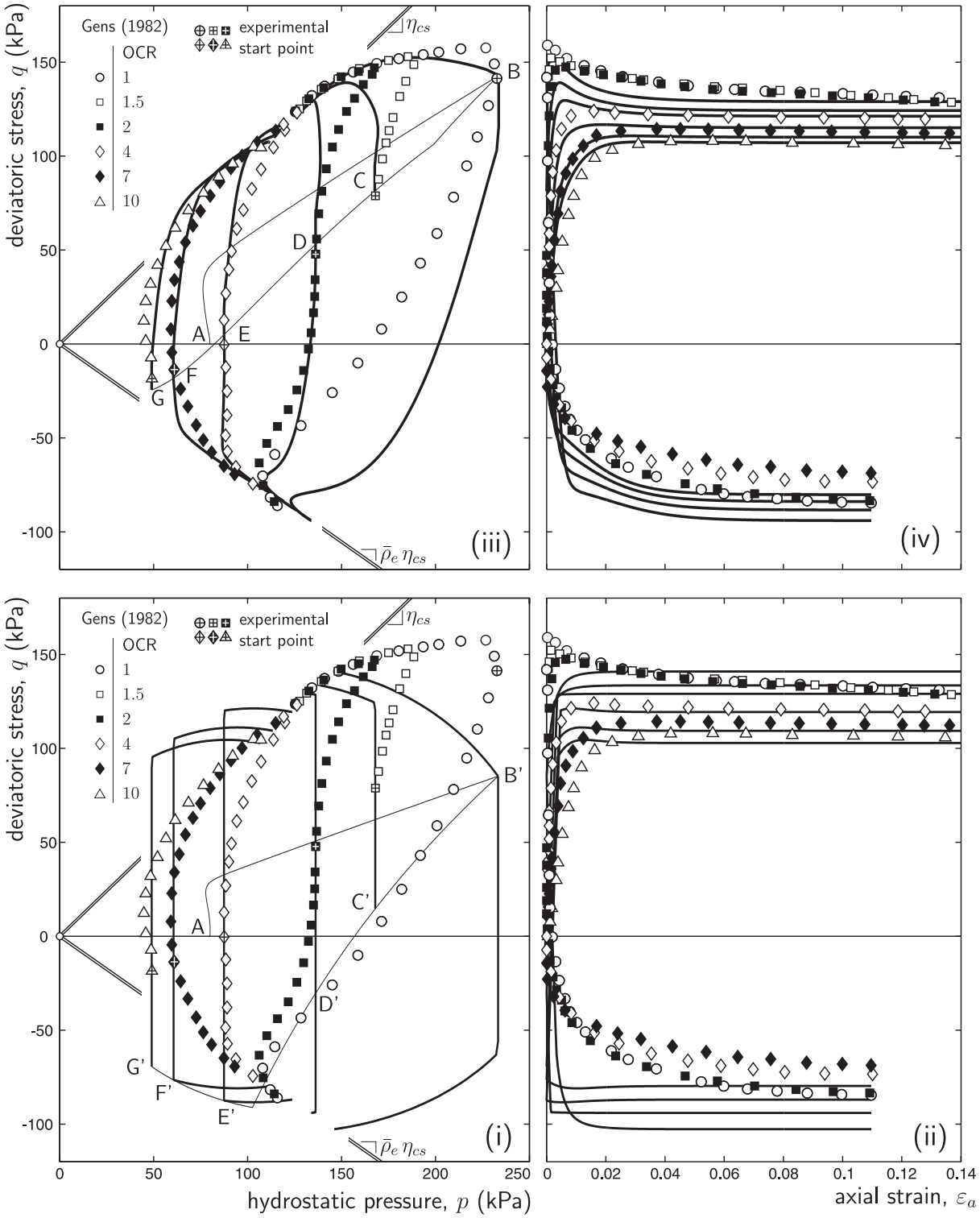

Figure 6.28: UTC and UTE tests following K_0 consolidation and swelling comparison with experimental data (shown by discrete points) on LCT from Gens [20]: (i), (iii) stress path in p-q space and (ii), (iv) axial strain-deviatoric stress response for (i), (ii) the MCC model and (iii), (iv) the two-surface anisotropic model.

OCRs (> 2) where MCC produces an unrealistically high deviatoric stress response prior to yielding. Also the MCC model is unable to convincingly reproduce the full stress stress path of one-dimensional

consolidation, swelling (AB'G') and UTC or UTE.

The model responses under DTC following K_0 loading and unloading to five OCRs are shown in Figure 6.29. The simulations were undertaken using a single displacement-controlled (small strain) eight-noded hexahedral FE with a uniform stress (and strain) state through the element. The two-surface model shows a good agreement with the experimental data for all OCRs, in terms of both the principal stress deviation and the volumetric strain response. The model provides a significant improvement over the two-parameter family of models, and the simpler classical MCC model (see Figure 5.20 in the previous chapter).

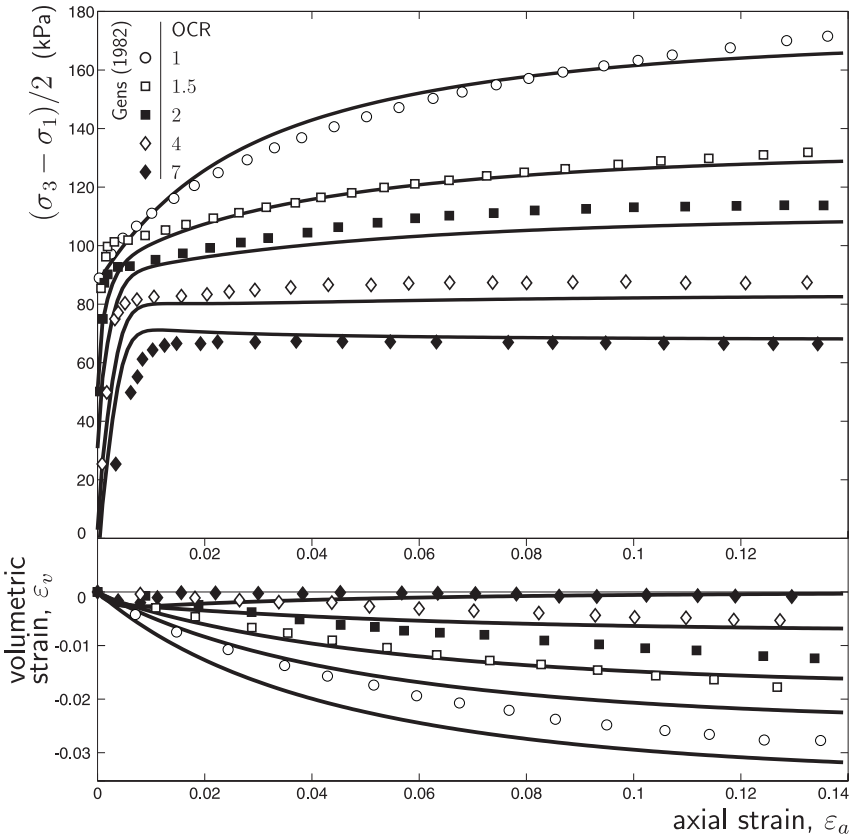

Figure 6.29: DTC following K_0 consolidation and swelling, comparison with experimental data (shown by discrete points) on LCT from Gens [20].

6.6 Observations

This chapter has presented a two-surface anisotropic extension to the single surface isotropic α-γ CS model [7]. The following conclusions can be drawn.

(i) The newly developed two-surface anisotropic model has the following key properties:

(a) the non-linear elasticity law, yield function and direction of plastic flow are all obtained from just two scalar functions;

(b) a unique CSS exists, regardless of the stress path followed;

(c) a measure of the inherent anisotropy is provided by the second-order tensor β_{ij} which can be interpreted as the degree of shearing of the yield surface (expressed in terms of the dissipation rate);

(d) a unique asymptotic level of anisotropy is reached at the CS (as suggested by recent DEM findings [18, 19]);

(e) convexity of the LAD yield and CSSs hold for any degree of anisotropy (see Section 6.1.1); and

(f) the model is part of a family of constitutive models (see Figure 6.7) which reduce down to the classical MCC constitutive model.

(ii) The stress integration procedure for the two-surface anisotropic model:

(a) is robust, as shown by the Gudehus and random strain path experiments;

(b) is well behaved, as shown by the error analysis in sub-section 6.4.4; and

(c) linearisable in order to form the algorithmic consistent tangent for both small strain and finite deformation numerical analysis.

(iii) The model is able to qualitatively and quantitatively capture the observed experimental behaviour of LCT. The following points are worth highlighting:

(a) the full stress path is able to be followed for all of the material point simulations using a single set of material parameters;

(b) good agreement is seen with experimental data for the K_0 loading and unloading behaviour (overcoming one of the limitations of the isotropic family of models presented in Chapter 5);

(c) the new model significantly improves the predictive capabilities of the MCC model, for both normally consolidated and heavily overconsolidated soils, as shown in Figure 6.26 (overcoming another limitation of the isotropic family of models);

(d) good agreement is seen under UTE following K_0 loading and unloading for OCRs>1. The simulation of normally consolidated states qualitatively captures the experimental response although it overestimates the deviatoric stresses;

(e) a good agreement is seen with experimental DTC and UTC following K_0 loading and unloading for all OCRs.

Chapter 7 offers results from several numerical boundary value simulations using the new two-surface anisotropic model (and the simpler formulations presented in the two preceding chapters). The model performance is also compared with recent experimental data from London clay using a hollow cylinder apparatus.

Chapter 6 references

[1] B Baudet & S Stallebrass, *A constitutive model for structured clays*, Géotechnique (54) 2004, 269–278.

[2] K Been & MG Jefferies, *A state paramter for sands*, Géotechnique 35 (1985), 99–112.

[3] RI Borja, C-H lin & FJ Montáns, *Cam-Clay plasticity, part IV: Implicit integration of anisotropic bouding surface model with nonlinear hyperelasticity and ellipsoidal loading function*, Comput. Methods Appl. Mech. Engrg. 190 (2001), 3293–3323.

[4] R Chambon, J Desrues & W Hammad, *CLoE, a new rate-type constitutive model for geomaterials theoretical basis and implementation*, Int. J. Numer. Anal. Meth. Geomech. 18 (1994), 253–278.

[5] IF Collins & T Hilder, *A theorectical framework for constructing elastic/plastic constitutive models of triaxial tests*, Int. J. Numer. Meth. Geomech. 26 (2002), 1313–1347.

[6] WM Coombs, RS Crouch & CE Augarde, *Unique Critical State hyperplasticity*, 19th UK Conference on Computational Mechanics (ACME-UK), 2011, 49–52.

[7] WM Coombs & RS Crouch, *Algorithmic issues for three-invariant hyperplastic Critical State models*, Comput. Meth. Appl. Mech. Engrg. 200 (2011), 2297–2318.

[8] WM Coombs, RS Crouch & CE Augarde, *Influence of lode angle dependency on the critical state for rotational plasticity*, X International Conference on Computational Plasticity (COMPLAS X), Barcelona, 2009.

[9] WM Coombs, RS Crouch & CE Augarde, *On the necessity for rotational yielding in anisotropic plasticity*, 17th UK Conference on Computational Mechanics (ACME-UK), 2009, 345–348.

[10] RS Crouch & JP Wolf, *On a three-dimensional anisotropic plasticity model for soil*, Géotechnique 45 (1995), 301–305.

[11] YF Dafalias, MT Manzari & AG Papadimitriou, *SANICLAY: simple anisotropic clay plasticity model*, Int. J. Numer. Anal. Meth. Geomech. 30 (2006), 1231–1257.

[12] YF Dafalias, *A simple anisotropic clay plasticity model*, Mech. Res. Commun. 29 (2002), 241–245.

[13] YF Dafalias, *An anisotropic critical state clay plasticity model*, Mech. Res. Commun. 13 (1986), 341–347.

[14] YF Dafalias, *Bounding surface plasticity. I: mathematical foundation and hypoplasticity*, J. Eng. Mech. ASCE 112 (1986), 966–987.

[15] YF Dafalias & EP Popov, *Cyclic, loading for materials with a vanishing elastic region*, Nuclear Engineering and Design 41 (1977), 293–302.

[16] YF Dafalias, *On cyclic and anisotropic plasticity*, Ph.D. thesis, Department of Civil Engineering, University of California, Berkeley (1975).

[17] F Darve, E Flavigny & E Rojas, *A class of incrementally non-linear constitutive relations and applications to clays*, Comput. Geotech. 2 (1986), 43–66.

[18] P Fu & YF Dafalias, *Fabric evolution within shear bands of granular materials and its relation to critical state theory*, Int. J. Numer. Anal. Meth. Geomech. (2010).

[19] P Fu & YF Dafalias,*Study of anisotropic shear strength of granular materials using DEM simulation*, Int. J. Numer. Anal. Meth. Geomech. 35 (2011), 1098–1126.

[20] A Gens, *Stress-strain characteristics of a low plasticity clay*, PhD. Thesis, Imperial College of Science and Technology, University of London, 1982.

[21] KM Górski, E Hivon, AJ Banday, BD Wandelt, FK Hansen, M Reinecke & M Bartelmann, *HEALPix: a framework for high-resolution discretization and fast analysis of data distributed on the sphere*, Astrophys. J. 622 (2005), 759–771.

[22] G Gudehus, *Comparison of some constitutive laws for soils under radially symmetric loading and unloading*, in Proceedings of the 3rd International Conference on Numerical Methods in Geomechanics, Aachen, 1979, 1309–1323.

[23] K Hashiguchi & T Mase, *Extended yield condition of soils with tensile yield strength and rotational hardening* Int. J. Plasticity 23 (2007), 1939–1956.

[24] K Hashiguchi & Z-P Chen, *Elastoplastic constitutive equation of soils with the subloading surface and the rotational hardening*, Int. J. Numer. Anal. Meth. Geomech. 22 (1998), 197–227.

[25] K Hashiguchi, *Mathematically consistent formulation of elastoplastic constitutive equations*, in Numerical Methods in Geomechanics, Innsbruck, Swoboda (ed.), 1988, 467–472.

[26] DW Hight, F McMillan, JJM Powell, RJ Jardine & CP Allenou, *Some characteristics of London Clay*, Characterisation of Engineering Properties of Natural Soils, Tan *et al.* (eds.), 2003.

[27] MR Horne, *The behaviour of an assembly of rotund, rigid, cohesionless particles I.* Proc. R. Soc. London. Ser. A. 286 (1965), 62–78.

[28] MR Horne, *The behaviour of an assembly of rotund, rigid, cohesionless particles II.* Proc. R. Soc. London. Ser. A. 286 (1965), 79–97.

[29] S Horpibulsuk, MD Liu, DS Liyanapathirana & J Suebsuk, *Behaviour of cemented clay simulated via the theoretical framework of the Structured Cam Clay model*, Comput. Geotech. 37 (2010), 1–9.

[30] G Houlsby & A Puzrin, *Principles of Hyperplasticity*, Springer-Verlag London Limited, 2006.

[31] M Huang, Y Liu & D Sheng, *Simulation of yielding and stress-stain behaviour of shanghai soft clay*, Comput. Geotech. 38 (2011), 431–353.

[32] WD Iwan, *On a class of models for the yielding behavior of continuous and composite systems* J. App. Mech. 34 (1967), 612–617.

[33] J Jiang & HI Ling, *A framework of an anisotropic elastoplastic model for clays*, Mech. Res. Commun. 37 (2010), 394–398.

[34] M Karstunen & M Koskinen, *Plastic anisotropy of soft reconstituted clays*, Can. Geotech. J. 45 (2008), 314–328.

[35] M Karstunen, H Krenn, SJ Wheeler, M Koskinen & R Zentar, *Effect of anisotropy and destructuration on the behavior of murro test embankment*, Int. J. Geomech.-ASCE 5 (2005), 87–97.

[36] D Kolymbas & I Herle, *Hypoplasticity for soils with low friction angles*, Comput. Geotech. 31 (2004), 365–373.

[37] D Kolymbas, *An outline of hypoplasticity*, Arch. appl. mech. 61 (1991), 143–151.

[38] D Kolymbas, *A rate-dependent constitutive equation for soils* Mech. Res. Comm. 4 (1977), 367–372.

[39] MD Liu & JP Carter, *A structured Cam Clay model* Can. Geotech. J. 39 (2002), 1313–1332.

[40] D Mašín & I Herle, *State boundary surface of a hypoplastic model for clays*, Comput. Geotech. 32 (2005), 400–410.

[41] Z Mróz, VA Norris & OC Zienkewicz, *Application of an anisotropic hardening model in the analysis of elasto-plastic deformation of soils* Géotechnique 29 (1979), 1–34.

[42] Z Mróz, *On the description of anisotropic workhardening*, J. Mech. Phys. Solids 15 (1967), 163–175.

[43] B Muhunthan, JL Chameau & E Masad, *Fabric effects on the yield behaviour of soils* Soils Found. 36 (1996), 85–97.

[44] JJ Nader, *A new constitutive theory extending hypoplasticity*, Mech. Res. Commun. 30 (2010), 505–509.

[45] AG Papadimitriou, AD Vranna, YF Dafalias & MT Manzari, *Effect of yield surface shape on the simulated elasto-plastic response of cohesive soils*, 7th European Conference on Numerical Methods in Geoetchnical Engineering (NUMGE), 2010, 63–68.

[46] JM Pestana & AJ Whittle, *Formulation of a unified constitutive model for clays and sands*, Int. J. Numer. Anal. Meth. Geomech. 23 (1999), 1215–1243.

[47] JH Prévost, *Anisotropic undrained stress-strain behavior of clays*, J. Geotech. Eng.-ASCE 104 (1978), 1075–1090.

[48] JH Prévost, *Plasticity theory for soil stress-strain behavior*, J. Eng. Mech.-ASCE 104 (1978), 1177–1194.

[49] JH Prévost, *Mathematical modelling of monotonic and cyclic undrained clay behaviour*, Int. J. Numer. Anal. Meth. Geomech. 1 (1977), 195–216.

[50] AM Puzrin & JB Burland, *Kinematic hardening plasticity formulation of small strain behaviour of soils*, Int. J. Numer. Anal. Meth. Geomech. 24 (2000), 753–781.

[51] M Rouainia & DM Wood, *Implicit numerical integration for a kinematic hardening soil plasticity model*, Int. J. Numer. Anal. Meth. Geomech. 25 (2001), 1305–1325.

[52] N Sivasithamparam, D Kamrat-Pietrasewska & M Karstunen, *An anisotropic bubble model for soft clays*, 7th European Conference on Numerical Methods in Geoetchnical Engineering (NUMGE), 2010, 21–26.

[53] SE Stallebrass & RN Taylor, *The development and evaluation of a constitutive model for the prediction of ground movements in overconsolidated clay*, Géotechnique 47 (1997), 235–253.

[54] J Suebsuk, S Horpibulsuk & MD Liu, *Modified Structured Cam Clay: A generalised critical state model for destructured, naturally structured and artificially structured clays*, Comput. Geotech. 37 (2010), 956–968.

[55] M Taiebat, YF Dafalias & R Peek, *A destructuration theory and its application to SANICLAY model*, Int. J. Numer. Anal. Meth. Geomech. 34 (2010), 1009–1040.

[56] T Weifner & D Kolymbas, *Review of two hypoplastic equations for clay considering axisymmetric element deformations* Comput. Geotech. 35 (2008), 760–774.

[57] KJ Willam & EP Warnke, *Constitutive model for the triaxial behaviour of concrete*, Proceedings of the May 17-19 1974, International Association of Bridge and Structural Engineers Seminar on Concrete Structures Subjected to Triaxial Stresses, held at Bergamo Italy, 1974.

[58] SJ Wheeler, A Näätänen, M Karstunen & M Lojander, *An anisotropic elastoplastic model for soft clays*, Can. Geotech. J. 40 (2003), 403–418.

[59] AJ Whittle, *Evaluation of a constitutive model for overconsolidated clays*, Géotechnique 43 (1993), 289–313.

[60] AJ Whittle & MJ Kavvadas, *Formulation of MIT-E3 Constitutive Model for Overconsolidated Clays*, J. Geotech. Eng.-ASCE 120 (1994), 173–198.

[61] Y Yamakawa, K Hashiguchi, & K Ikeda, *Implicit stress-update algorithm for isotropic Cam-clay model based on the subloading surface concept at finite strains*, International Journal of Plasticity, 26 (2010), 634–658.

[62] WM Tan, K-V Yuen & GL Yoon, *Bayesian probabilistic approach for the correlations of compression index for marine clays*, J. Geotech. Geoenviron. 135 (2009), 1932–1940.

[63] Y-P Yao, W Hou & A-N Zhou, *UH model: three-dimensional unified hardening model for overconsolidated clays*, Géotechnique 59 (2009), 451–469.

[64] H-S Yu, C Khong, & J Wang, *A unified plasticity model for cyclic behaviour of clay and sand*, Mech. Res. Commun. 34 (2007), 97–114.

Chapter 7

Numerical analyses

Chapters 4, 5 and 6 have developed three constitutive models: (Chapter 4) a simple modified Reuleaux (mR) frictional plasticity model, (Chapter 5) a family of isotropic hyperplastic Critical State (CS) models and (Chapter 6) a family of anisotropic two-surface hyperplastic CS models. In each case the models were compared with experimental data after the model definitions and algorithmic aspects had been described. This chapter presents 58 finite-element (FE) simulations to verify the models' stability and performance in a general purpose finite deformation FE code developed by the author.

Section 7.1 describes the key findings of previous FE analyses using the simple non-associated frictional perfect plasticity mR model. Simulations using several versions from the two-surface anisotropic CS family appear in Section 7.2. The frictional cone models are compared with the CS models using a plane strain rigid footing analysis in Section 7.3. Experimental data from Nishimura [28] on London Clay (LC) using a hollow cylinder apparatus (HCA) are simulated in Section 7.4. The analyses are undertaken using the modified Cam-clay (MCC) model and the two-surface anisotropic CS model at (i) a material point level and (ii) using a FE discretisation of the HCA. This section also considers the stability of the two-surface constitutive model in order to identify the threshold when discontinuities are predicted to first appear in the material. Closing observations are drawn in Section 7.5.

7.1 Frictional inelasticity

Chapter 4 compared the mR deviatoric function with that of Mohr-Coulomb (M-C) and Drucker-Prager (D-P) [15]. It was shown that the mR Lode angle dependency (LAD) overcame the inadequacies in both the M-C (being invariant to the intermediate principal stress) and D-P (being independent of the Lode angle, θ).

Verification of the mR constitutive model algorithm has been given in the papers by Coombs and co-workers [9, 11–13] for two-dimensional (plane strain) and three-dimensional small strain and finite deformation FE simulations. For all of these analyses, the mR model showed asymptotic quadratic convergence of the global Newton-Raphson (N-R) procedure, confirming the correctness of the algorithmic consistent tangent (Section 4.5). In particular it was noted that although the mR model provides significantly increased realism over the M-C and D-P models (Figure 4.4, Chapter 4), the analysis time for a finite deformation cavity expansion simulation only increased by 5.3% [9]. The Willam-Warnke (W-W) [38] model provides a similar level of realism to that of mR, but the analysis time increases by 41.9% due to the multiple iterations required for each integration point stress return. The use of the mR model in the small strain rigid footing analysis presented by Coombs *et al.* [12] only required a 2.2% run-time increase compared to the M-C model, whereas the W-W model increased the run-time by over 30%. Coombs and Crouch [11] demonstrated the use of the mR model for finite deformation cylindrical

expansion, cavity expansion and rigid footing analyses, including the use of the mR model with a tension cut-off (as discussed in Section 4.3.5, Chapter 4). The simulations are not reproduced here for the sake of brevity.

7.2 Critical State hyperplasticity

The CS models introduced in Chapters 5 and 6 are now analysed using 26 small strain and 19 finite deformation FE simulations (in addition to seven material point simulations). A sensitivity analysis of the two-surface anisotropic CS model is presented using 25 small strain undrained triaxial compression (UTC) simulations. Section 7.2.2 compares five members of the full family of two-parameter anisotropic hyperplasticity models using (i) a single three-dimensional finite-element, finite deformation, unit cube and (ii) one and two-dimensional finite deformation cavity expansion simulations.

Coombs and Crouch [10] compared the classical MCC constitutive model (as presented in Chapter 5) against a published small strain and finite-deformation undrained plane strain flexible footing solution [7]. Their analysis verified both the constitutive model (when reduced down to MCC) and the finite deformation framework (as presented in Chapter 3).

7.2.1 Undrained triaxial compression sensitivity analysis

This sub-section presents a sensitivity analysis for the two-surface anisotropic model using 25 small strain axi-symmetric UTC simulations conducted using the Fortran90 implementation of the FE program[1]. Each of the Lower Cromer till (LCT) material constants given in Table 6.1 was subjected to perturbation of $\pm 10\%$, apart from x_β and M, which instead received a $\pm 10\%$ perturbation on η_{K_0} and η_{cs}. In the cases where α, γ, b_β, η_{cs} or η_{K_0} were changed, both M and x_β were re-calculated using (6.44) and (6.64) respectively.

The material had a reference pressure of 80kPa and started from an isotropic state and hydrostatic stress condition, as follows

$$\{\sigma\} = 80\{1\} \text{ kPa} \qquad \text{with} \qquad \{\sigma^\chi\} = p_c\Big(1 - R(1-\gamma/2)\Big)\{1\}, \qquad \{\beta\} = \{0\} \qquad \text{and} \qquad p_c = 80 \text{ kPa}.$$

With these initial conditions, the stress state lies on the compressive *nose* of both the inner and outer surfaces. The analysis comprised two steps:

(i) drained hydrostatic compression to 233.3kPa; and

(ii) UTC[2] using 100 displacement-controlled loadsteps to an axial strain of $\varepsilon_a = -0.14$ (that is, the top surface of the FE discretisation was displaced by 5.32mm corresponding to a 14% reduction in its original height).

The first stage was conducted at a material point level. This stress and material state was then applied to the integration points in a FE discretisation of a cylindrical triaxial specimen using 200 eight-noded axi-symmetric quadrilateral elements with reduced four point Gaussian quadrature (as shown in Figure 7.1 (i)). Due to symmetry (both axial and vertical), only one quarter of the specimen was modelled. The cylinder had a radius and height of $r = 19$mm and $H = 76$mm respectively. The 25 simulations each consumed a total of between 224 and 232 N-R iterations, with a maximum within any one loadstep of

[1] In the literature, undrained analyses (particularly in the case of rigid footing simulations) have been conducted with constitutive models that are insensitive to the first invariant of stress (such as the Prandtl-Reuss and Tresca models). These models exhibit isochoric plastic flow and (if the appropriate elastic parameters are utilised) can been used to represent the zero volume change condition of weightless undrained analysis without introducing a fluid bulk modulus (as described in Appendix B.1.4). However, if the self weight of a soil is to be considered then the size of the yield surface should be dependent on the depth (or rather the overburden at that particular material point).

[2] In all of the UTC simulations the fluid bulk modulus was set to 10GPa.

4 or 5 iterations. Therefore, all 25 simulations had a similar run-time, controlled primarily by the total number of N-R iterations[3].

The solution based on the LCT calibrated material constants (Table 6.1) was taken as the reference solution for comparison with the perturbed material constant results. The deviatoric stress at an axial strain of $\varepsilon_a = -0.14$ for the reference solution was $q = 110.145$kPa, having an error of only 0.24% compared to the solution obtained from the material point simulation in Chapter 6 (Section 6.5). The maximum deviatoric stress, deviatoric and hydrostatic stresses at an axial strain of $\varepsilon_a = -0.14$ and radial strain, ε_r, are given in Table 7.1 for each of the 25 simulations (in addition to the material point result from Chapter 6). The radial strain was calculated using

$$\varepsilon_r = \frac{\Delta r}{r_0}, \tag{7.1}$$

where Δr was the radial displacement of the outer, mid-height node and r_0 was the original cylinder radius (19mm). For the material point simulation, the constitutive model was subjected to an isochoric strain increment, thereby enforcing the undrained condition. Therefore, for a given axial strain, the radial strain in the material point simulation was

$$(\varepsilon_r)_{mp} = \big(1 + (\varepsilon_a)_{mp}\big)^{-1/2} - 1, \tag{7.2}$$

where $(\cdot)_{mp}$ denotes a material point quantity. For an axial strain of $(\varepsilon_a)_{mp} = -0.14$, the radial strain is $(\varepsilon_r)_{mp} = 0.0783$ (for a displaced radius of 20.49mm). This radial strain is significantly smaller than that seen in the FE simulations due to the non-uniform strain field in the FE analysis as a consequence of an assumed platen constraint at the ends of the cylindrical specimen which leads to barrelling at the mid-height.

The axial strain versus deviatoric stress is shown in Figure 7.1 (ii) for all 25 simulations. The reference (calibrated) solution is identified by the thick black line. Figure 7.1 (iii) gives the initial ($\varepsilon_a \in [0, 0.02]$) axial strain versus deviatoric stress response. The majority of the 25 simulations are clustered around the reference solution; only the perturbed solutions for γ and η_{cs} show significant deviation. This can also be seen in terms of the peak, final deviatoric stress and hydrostatic pressure at $\varepsilon_a = -0.14$ in Table 7.1. The insensitivity of the model's response to small perturbations in the material constants relates back to Gudehus' [19] requirement of *well-posed* constitutive algorithms (discussed in Section 1.2), in that a model should be stable, when appropriate, to small changes in its constants.

Figure 7.2 shows the response at all of the Gauss points in the calibrated simulation for (i) axial strain versus deviatoric stress and (ii) hydrostatic pressure versus deviatoric stress. The global FE solution is identified by the thick black line and the experimental data (from Gens [17]) are shown by discrete points. The original and deformed FE meshes are shown in Figure 7.2 (iii). Although the majority of the integration point responses almost match the global FE response, there is still a significant variation in both axial strain and deviatoric stress at the end of the analysis. It is important to note, that most of the Gauss point stress states are not located on the compression meridian ($\theta = \pi/6$). This can be seen in Figure 7.2 (ii) where although the Gauss points arrive at the CS, the stress ratio, $\eta = q/p$, is not equal to η_{cs}.

In Figure 7.3 (ii) the hydrostatic pressure versus deviatoric stress response is shown, whereas in Figure 7.3 (iii), the axial strain versus stress ratio responses are compared for the *central* Gauss point of

[3]In general the material parameters also influence the run-time by changing the number of local iterations required to obtain convergence with the bE stress integration algorithm. Due to the relatively small perturbation on the material constants in the sensitivity analysis, this effect was negligible here.

constant		M	x_β	$q_{\max}$	$q_{\varepsilon_a=0.14}$	$p_{\varepsilon_a=0.14}$	$\eta_{\varepsilon_a=0.14}$	ε_r
		(6.44)	(6.62)	(kPa)	(kPa)	(kPa)		
material point (Section 6.5.1)		0.921	4.8	110.560	110.282	114.465	0.9635	0.0783
calibrated (Table 6.1)	LCT	0.921	4.8	110.297	110.145	114.926	0.9597	0.1082
κ	0.0045	0.921	4.8	109.304	109.025	113.482	0.9632	0.1078
	0.0055			111.428	111.013	115.373	0.9647	0.1087
G (MPa)	25.2	0.921	4.8	110.296	110.132	113.925	0.9681	0.1082
	31.8			110.299	110.161	113.926	0.9682	0.1083
λ	0.0402	0.921	4.8	110.453	110.169	113.995	0.9689	0.1082
	0.0492			110.248	109.965	113.904	0.9678	0.1083
η_{cs}	0.868	0.830	2.3	99.394	99.084	114.417	0.8687	0.1040
	1.060	1.014	30.3	131.569	126.617	114.463	1.1090	0.1128
$\bar{\rho}_e$	0.656	0.921	4.8	110.291	109.217	114.209	0.9657	0.0884
	0.802			110.390	110.324	115.285	0.9568	0.1174
α	0.36	0.916	6.1	111.293	110.019	113.947	0.9680	0.1096
	0.44	0.926	3.9	110.287	110.001	113.872	0.9685	0.1070
γ	0.702	0.928	3.6	102.687	101.800	106.111	0.9619	0.1075
	0.858	0.915	7.2	118.320	118.019	122.585	0.9652	0.1093
R	0.18	0.921	4.8	110.296	110.013	114.927	0.9597	0.1083
	0.22			110.299	110.016	114.924	0.9598	0.1082
b_β	0.09	0.926	4.8	110.054	108.798	112.370	0.9707	0.1092
	0.11	0.917	4.9	111.642	113.563	116.540	0.9580	0.1075
η_{K_0}	0.54	0.921	12.7	112.905	110.012	114.948	0.9595	0.1118
	0.66		2.9	110.298	109.991	114.656	0.9620	0.1054
C_β	12.6	0.921	4.8	110.298	110.013	113.901	0.9684	0.1074
	15.4			110.550	110.015	114.939	0.9596	0.1090
C_χ	3330	0.921	4.8	110.296	110.013	113.927	0.9681	0.1083
	4070			110.299	110.016	114.924	0.9598	0.1082

Table 7.1: Undrained triaxial compression sensitivity analysis: comparison of results from the 25 simulations in addition to the material point simulation in Section 6.5.

the 25 analyses (shown by the thin grey lines) with the material point simulation from Chapter 6. The *central* element is identified in Figure 7.3 (i) and the *central* Gauss point is the integration point closest to the centre of the triaxial cell. This point was selected as the stress (and strain) state most closely resembles that of the material point simulation presented in Section 6.5. Apart from the two analyses using the perturbed stress ratio at the CS (η_{cs}), all of the simulations tend to the same unique CSL.

The effect of each of the material constants can be summarised as follows:

κ, G : changing $\pm 10\%$ had little influence on the model's response for UTC at an OCR of one, as the elastic deformation was masked by the plastic deformation.

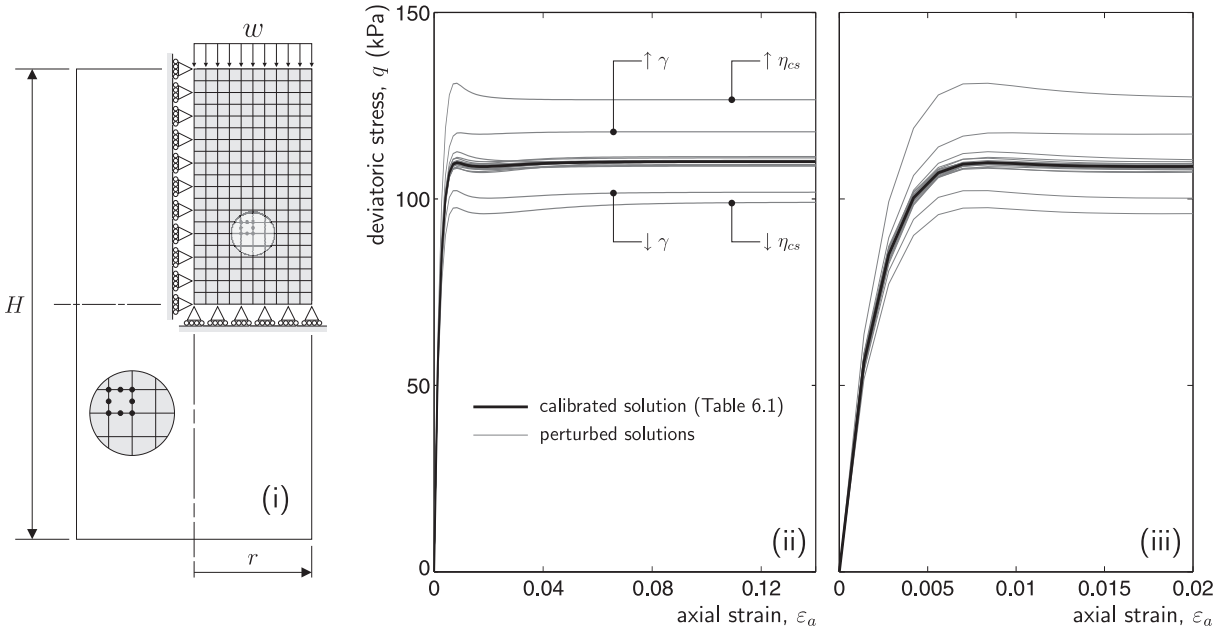

Figure 7.1: Undrained triaxial compression sensitivity analysis: (i) axi-symmetric triaxial cell discretisation and geometry, (ii) and (iii) axial strain versus deviatoric stress response for the 25 simulations.

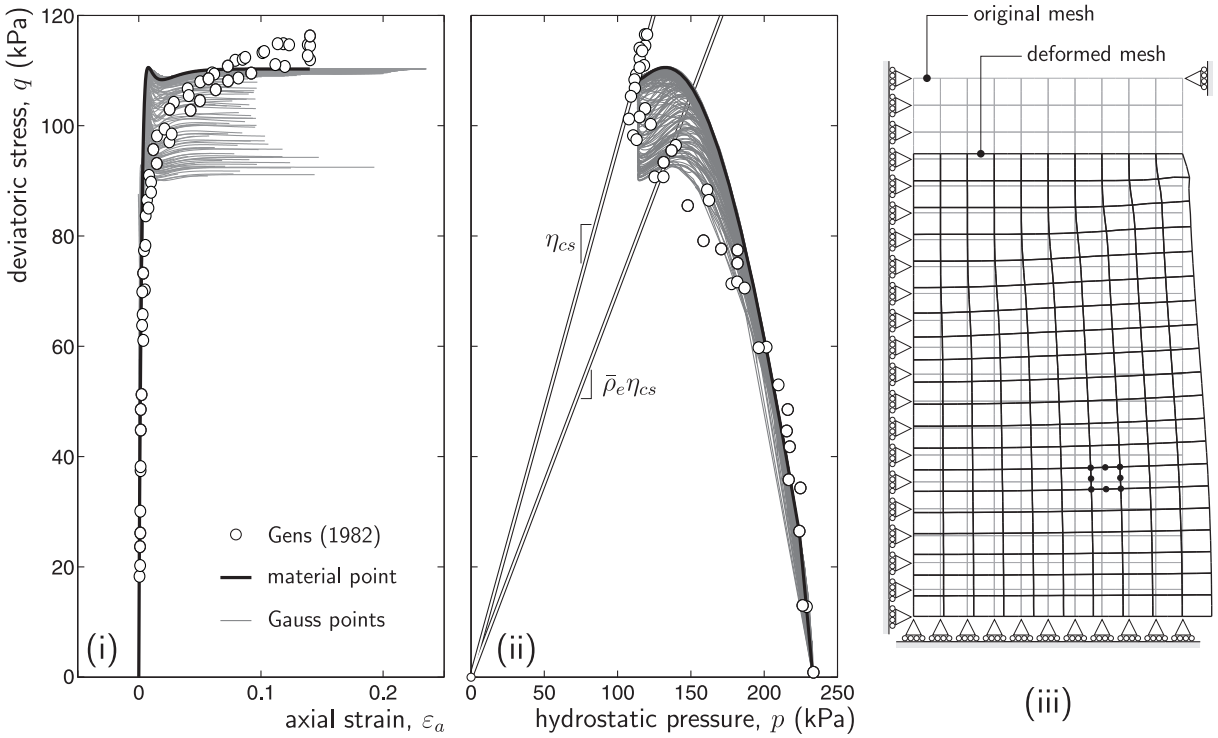

Figure 7.2: Undrained triaxial compression Gauss point (for the calibrated solution), material point and experimental data [17] comparison: (i) axial strain versus deviatoric stress response, (ii) hydrostatic pressure versus deviatoric stress response and (iii) axi-symmetric triaxial cell; original and deformed meshes.

λ : changing $\pm 10\%$ had little influence on the model's response for UTC at an OCR of one.

η_{cs} : changes the stress ratio at the CS and significantly influences the model's response. As expected the hydrostatic pressure at the CS remains unchanged (being controlled by only γ and b_β). However,

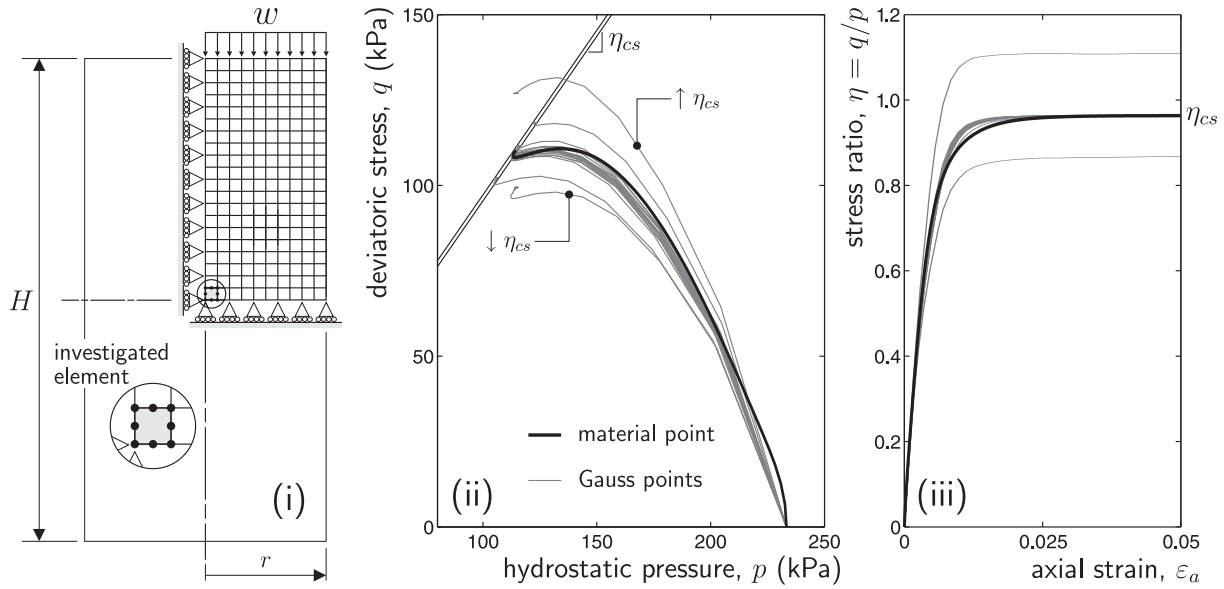

Figure 7.3: Undrained triaxial compression Gauss point and material point comparison: (i) axi-symmetric triaxial cell discretisation and geometry, (ii) hydrostatic pressure versus deviatoric stress response and (iii) axial strain versus stress ratio response.

the deviatoric stress at the CS is proportional to η_{cs}. Thus, increasing η_{cs} causes an increase in $q_{\max}$ relative to q at the CS due to η_{cs} having a strong influence on x_β (discussed further below).

$\bar{\rho}_e$: if this sensitivity analysis were conducted at a material point level, changing $\bar{\rho}_e$ would have no influence on the simulation behaviour. However, due to the non-uniform stress distribution through the triaxial specimen in the FE analysis, few Gauss points were located on the compression meridian (as shown in Figure 7.2). Therefore, changing $\bar{\rho}_e$ does influence the simulation's response. Most notably, changing $\bar{\rho}_e$ influences the outer radial displacement at the mid-height of the cylinder. Increasing and decreasing $\bar{\rho}_e$ increases and decreases ε_r respectively.

α : changing α influences the peak deviatoric stress; increasing α increases $q_{\max}$. This was due to α changing the shape of the yield surface (as shown in Figure 5.1). As α increases, the deviatoric radius near the compressive nose of the yield surface also increases.

γ : changes the position of the intersection between the Critical State line (CSL) and the outer surface. Increasing γ moves the final stress state towards the compressive nose of the outer surface (decreasing γ had the opposite effect).

R, C_χ : changing $\pm 10\%$ had little influence on the model's response for UTC, at an OCR of one.

b_β : changes the position of the intersection between the CSL and the outer surface. Increasing b_β moves the final stress state towards the compressive nose of the outer surface (decreasing b_β had the opposite effect).

η_{K_0} : changing the stress ratio under K_0 consolidation changes x_β. Decreasing η_{K_0} increases x_β which causes the anisotropic surfaces to *shear* by a greater amount for a given deviatoric plastic strain increment. This increase in x_β results in a higher peak deviatoric stress, $q_{\max}$, as $\{\beta\}$ exceeds $\{\beta_{cs}\}$ prior to arrival at the CS. The *hooking* behaviour (as discussed in Chapter 6, Section 6.3.5) was suppressed when approaching the CSL with $x_\beta = 12.7$. This was again due to $\{\beta\}$ exceeding $\{\beta_{cs}\}$ prior to arrival at the CS.

C_β : changing C_β alters the rate of *shearing* of the surfaces. Increasing C_β increases $q_{\max}$ whereas decreasing C_β had the opposite effect. The value of C_β also influences the model's behaviour when approaching the CSL; with higher values reducing the *hooking* behaviour.

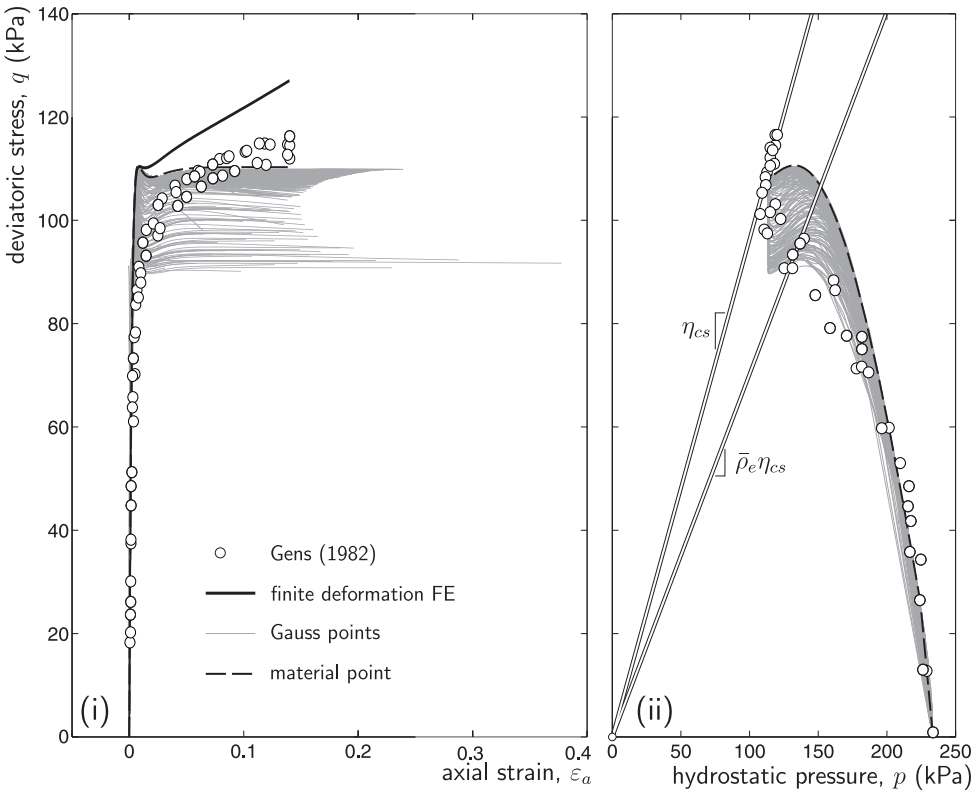

Figure 7.4: Finite deformation undrained triaxial compression FE simulation: (i) axial strain versus deviatoric stress and (ii) hydrostatic stress versus deviatoric stress for all of the Gauss points, the global FE response and the small strain material point simulation from Chapter 6.

With a global axial strain of -0.14 and integration point strains $\varepsilon_a > 0.2$ (as seen in Figure 7.2), the small strain assumption is no longer appropriate. The triaxial compression test (using the calibrated constants[4]) was therefore analysed using the finite deformation framework presented in Chapter 3.

Borja and Tamagnini [7] derived the following relationship between the small strain (Cauchy) and finite deformation (Kirchhoff) compressibility indices

$$\kappa_{\text{fd}} = \frac{\kappa}{1-\kappa} \qquad \text{and} \qquad \lambda_{\text{fd}} = \frac{\lambda}{1-\lambda}, \tag{7.3}$$

where $(\cdot)_{\text{fd}}$ identify the finite deformation parameters. These relationships should be used to obtain the compressibility indices appropriate for finite deformation analysis based on a logarithmic strain-Kirchhoff stress formulation, as used in the recent paper by Yamakawa *et al.* [41].

The results are shown in Figure 7.4 for (i) axial strain versus deviatoric stress and (ii) hydrostatic stress versus deviatoric stress for all of the Gauss points, the global FE response and the small strain material point simulation (first seen in Chapter 6). The peak equivalent deviatoric stress was 127kPa (at an axial strain of -0.14), 15.2% higher than that seen in the material point simulation. The radial strain at the mid-height, calculated from (7.1), was 0.0977. The finite deformation analysis took the greatest

[4]The finite deformation elastic and plastic compressibility indices were calculated from (7.3) using κ and λ given in Table 6.1.

number of global N-R iterations (313), with a maximum number of iterations within any one loadstep of 4.

The response from the materials point in the finite deformation analysis (see Figure 7.4) were similar to those from the small strain analyses (see Figure 7.2), albeit with larger axial strains. However, the global FE response, shown by the thick solid line in Figure 7.4 (i), shows a progressive stiffening following a local minimum at an axial strain of approximately $\varepsilon_a = -0.013$. This stiffening behaviour is a consequence of the finite deformation analysis accounting for the simulation's evolving geometry. Therefore, the stress paths of the material points do not demonstrate any stiffening behaviour (in terms of their deviatoric stress) once they have arrived at the CS. The stiffening behaviour of the global finite deformation FE response perhaps explains why the material point simulation (first presented in Figure 6.26 from Chapter 6) is unable to capture the experimentally observed behaviour in the 90 to 110 kPa deviatoric stress range. If the stress ratio at the CS, η_{cs}, was reduced then it would be possible to obtain an improved fit to the experimental data from the finite deformation simulation. However, it is not clear from the experimental data what this *finite deformation CS stress ratio* should be or if a peak deviatoric stress was reached (without taking the experimental test to a higher axial strain).

7.2.2 Critical State model comparisons

This sub-section compares five members from the family of two-parameter anisotropic hyperplasticity models, as introduced in Section 6.1.5 and shown in Figure 6.7. Table 7.2 lists the LCT material constants for the following five models: (i) the MCC model, (ii) the two-parameter CS model ($\alpha\gamma$), (iii) the two-surface two-parameter model ($2\mathsf{s}\alpha\gamma$), (iv) the anisotropic single surface two-parameter model ($\beta\alpha\gamma$) and (v) the two-surface anisotropic two-parameter model ($2\mathsf{s}\beta\alpha\gamma$). The number of constants for each model (n_{mc}) is given, together with the number of constants (in parenthesis) comprising the reduced set[5]. The number of unknowns and residuals in the backward Euler (bE) stress integration procedure (n_u) is also given. Note that the isotropic MCC and isotropic single-surface two-parameter models were formulated in principal stress space, reducing the number of elastic strain unknowns from six (general stress space) to three (principal stress space). The remaining models must be formulated in generalised six-dimensional stress (strain) space[6].

Three types of analyses were undertaken. First a single element unit cube was investigated to verify the derived spatial consistent tangents and to compare the models' responses for a simple three-dimensional analysis. This was followed by a finite deformation cavity expansion simulation in (i) one-dimension and (ii) two-dimensions, where only part of the cavity was pressurised.

Unit cube, single element investigations

Here the finite deformation analysis of a unit cube is described. A single eight-noded hexahedral element with eight-point Gaussian quadrature was used. The cube was restrained against normal displacement on its lower horizontal face and two of its adjacent vertical faces (see the right of Figure 7.5). The free corner was subjected to a compressive vertical load of 45kN applied in 20 loadsteps. The free vertical faces of the cube were subjected to a constant normal pressure of 100kPa throughout the analysis. Five instances of the two-parameter two-surface anisotropic CS model were used to model the material behaviour. All of the models started from an isotropic state under a hydrostatic stress. A reference pressure, p_r, of 100kPa

[5]The reduced set of six *core* material constants for the two-surface anisotropic model was discussed in Section 6.3.7.

[6]Note that anisotropic models (that is, the $2\mathsf{s}\alpha\gamma$, $\beta\alpha\gamma$ and $2\mathsf{s}\beta\alpha\gamma$ models) must be formulated in generalised six component stress space because, in general, the principal directions of stress (and strain) of the trial and the updated state do not coincide.

model	MCC	$\alpha\gamma$	2s$\alpha\gamma$	$\beta\alpha\gamma$	2s$\beta\alpha\gamma$
n_{mc}	5(4)	7	9	10	12(6)
n_u	5	5	14	14	20
κ	0.0073	0.0073	0.005	0.0073	0.005
G (MPa)	18	18	28	18	28
λ	0.0447	0.0447	0.0447	0.0447	0.0447
M	0.964	0.964	0.964	0.921	0.921
$\bar{\rho}_e$	0.729	0.729	0.729	0.729	0.729
α	–	0.3	0.3	0.4	0.4
γ	–	0.9	0.9	0.78	0.78
R	–	–	0.2	–	0.2
C_χ	–	–	3,700	–	3,700
b_β	–	–	–	0.1	0.1
x_β	–	–	–	4.8	4.8
C_β	–	–	–	14	14

Table 7.2: LCT material constants for the family of hyperplastic CS models: modified Cam-Clay (MCC), two-parameter single-surface model ($\alpha\gamma$), two-parameter two-surface model (2s$\alpha\gamma$), anisotropic two-parameter single-surface model ($\beta\alpha\gamma$) and anisotropic two-parameter two-surface model (2s$\beta\alpha\gamma$).

was adopted. Other state parameters were as follows:

$$p_c = 200\text{kPa}, \qquad \{\beta\} = \{0\} \qquad \text{and} \qquad \{\sigma_\chi\} = p_r\{1\}.$$

The external load versus vertical compressive displacement response of the five models is given in Figure 7.5. A similar response was observed for all models. The MCC model gives the softest response and the two-surface anisotropic model has the least vertical corner displacement for the applied external load. The two-surface models (2s$\alpha\gamma$ and 2s$\beta\alpha\gamma$) have a smoother response due to the progressive development of plasticity within the conventional yield surface. At the end of the analysis all of the Gauss points for the two-surface models experienced some inelastic behaviour whereas, for the single surface models, the Gauss point near the fully restrained corner remained elastic.

model	$\sum$(NRit)	max(NRit)	n_{pgp}	t/t_{MCC}	w (m)
MCC	79	6	7	1	0.0607
$\alpha\gamma$	78	5	7	0.949	0.0535
2s$\alpha\gamma$	92	6	8	2.908	0.0520
$\beta\alpha\gamma$	82	5	7	1.691	0.0593
2s$\beta\alpha\gamma$	93	5	8	3.184	0.0506

Table 7.3: Unit cube single element finite deformation results.

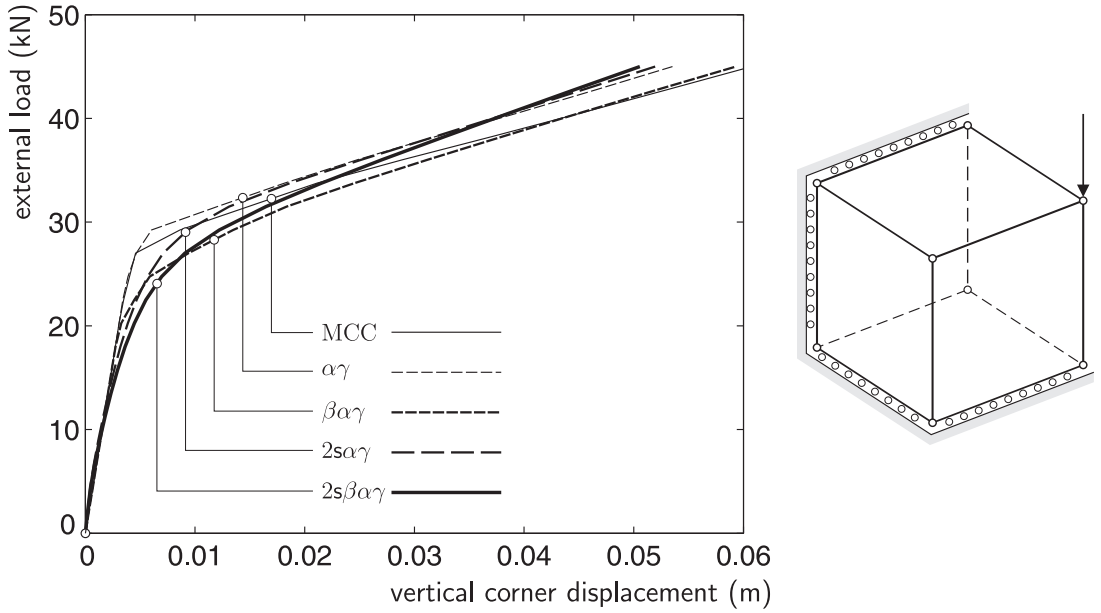

Figure 7.5: Unit cube single element finite deformation CS model comparison: vertical corner displacement versus external force.

The total and maximum number of N-R iterations needed to obtain convergence (to within a tolerance of 1×10^{-9}) for any loadstep are given in Table 7.3. The number of plastic Gauss points at the end of the analysis, the time taken for each of the analysis normalised with respect to the time taken for the MCC model (t/t_{MCC}) and the vertical corner displacement (w) are also listed. The two-surface models increase the total number of N-R iterations as elasto-plastic behaviour occurs earlier than for the single-surface models. Interestingly, the single-surface isotropic two-parameter model ($\alpha\gamma$) requires one less N-R iteration compared to that of the MCC model, resulting in a marginally lower run-time. Including anisotropy ($\beta\alpha\gamma$), or an additional surface (2s$\alpha\gamma$), increases the run-time by 69% and 191% respectively. The run-time increase is significantly higher when including an additional surface because of the earlier onset of elasto-plastic behaviour within an analysis. Including both an additional surface and anisotropy increases the run-time by 218%. The percentage run-time increase is considerable because the single-element analysis is dominated by the time spent in the constitutive algorithm. For larger analyses, the proportion of the time spent in the constitutive algorithm diminishes as the main computational overhead is associated with the solution of the global linear system (3.38).

The convergence results (normalised out-of-balance force versus N-R iteration) for the two-surface anisotropic two-parameter constitutive model are given in Figure 7.6 (i) for all 20 loadsteps. The rate of convergence for the final loadstep is plotted on a bi-logarithmic scale in Figure 7.6 (ii), where the slope of the line gives the rate of convergence between N-R iterations. From this figure it is seen that the 2s$\beta\alpha\gamma$ asymptotically achieves the desired quadratic rate of convergence. This convergence rate can also be seen for loadsteps 16 to 20 in Table 7.4, where the exponent of the residual out-of-balance force norm reduced by two between each iteration. This confirms the derivation of the spatial algorithmic consistent tangent (Section 6.4.6) for the two-surface anisotropic model.

Throughout this thesis emphasis has been placed on the importance of the derivation of the tangent which is consistent with both the constitutive model's stress integration procedure and the finite deformation procedure. Table 7.5 compares the total and maximum number of N-R iterations within any loadstep and the number of constitutive model calls (n_{cmc}) using different tangents for the single-element analysis using the two-surface anisotropic model. The run-time for the analysis, normalised with respect to the

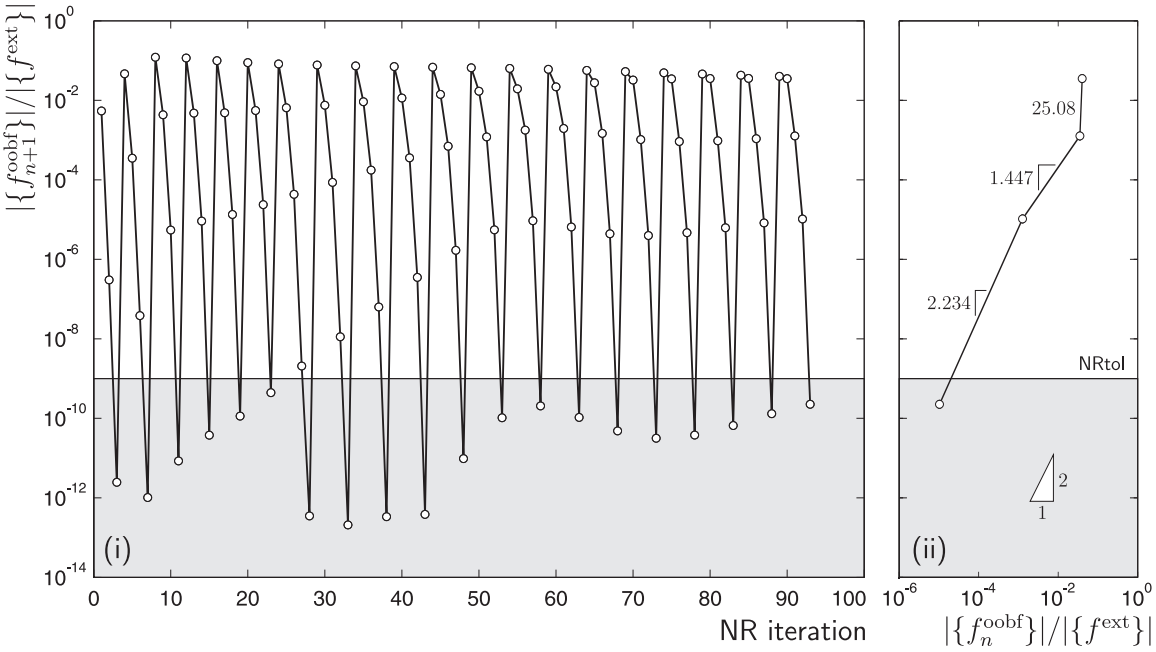

Figure 7.6: Unit cube single element finite deformation convergence results for the two-surface anisotropic hyperplasticity model: (i) N-R iteration versus normalised out-of-balance force and (ii) bi-logarithmic normalised out-of-balance force plot for the final loadstep.

Normalised residual out-of-balance force

N-R iteration	loadstep				
	16	17	18	19	20
1	5.268×10^{-02}	4.911×10^{-02}	4.585×10^{-02}	4.286×10^{-02}	4.012×10^{-02}
2	3.235×10^{-02}	3.463×10^{-02}	3.540×10^{-02}	3.549×10^{-02}	3.516×10^{-02}
3	1.034×10^{-03}	9.194×10^{-04}	9.634×10^{-04}	1.086×10^{-03}	1.270×10^{-03}
4	3.969×10^{-06}	4.678×10^{-06}	6.234×10^{-06}	8.218×10^{-06}	1.037×10^{-05}
5	3.157×10^{-11}	3.807×10^{-11}	6.604×10^{-11}	1.304×10^{-10}	2.259×10^{-10}

Table 7.4: Unit cube single element finite deformation convergence results for the two-surface anisotropic hyperplasticity model for the final five loadsteps.

time taken with the anisotropic spatial consistent tangent ($t/t_{[D^{cst}]}$), is also given. Each of the tangents lead to the same solution, as given in Figure 7.5, but the speed at which they do so varies considerably. Table 7.5 is split into two parts: those that take into account to finite deformation contributions to the material tangent and those that do not (small strain)[7]. The table also compares the results when using the isotropic (3.45) and anisotropic[8] (3.67) spatial tangents with the three different material tangents ($[D^{\text{e}}]$, $[D^{\text{ep}}]$ and $[D^{alg}]$).

When using the anisotropic spatial algorithmic consistent tangent, the analysis consumed a total of 93 N-R iterations, with a maximum of 5 iterations required within any loadstep. When the isotropic

[7]Note that all of the simulations are finite deformation analyses. Here the term finite deformation and small strain are used to distinguish between those analyses that calculate the element stiffness matrix, $[k^e]$, (3.44) based on $[D^{cst}]$ from (3.67) or $[D^{(\cdot)}]$ from the constitutive model respectively.

[8]Recall that the anisotropic tangent accounts for the influence of the deformation gradient on the deviatoric component of the centre of the inner yield surface, $\{s^{\chi}\}$, and the inclination of the surfaces, $\{\beta\}$.

consistent spatial tangent was used (that is, the tangent did not account for the dependency of $\{\beta\}$ and $\{\sigma_\chi\}$ on the deformation gradient), the total number of iterations increased to 105, with a 16% increase in the run-time. However, if the small strain consistent tangent was used to form the element stiffness matrices, then the run-time increased by 38%, requiring 122 iterations for the entire analysis. Using the elasto-plastic infinitesimal tangent ($[D^{\text{ep}}]$) or the elastic tangent ($[D^{\text{e}}]$) in the calculation of the spatial tangent increased the analysis run-time by 683% and 7,129% respectively. This increased the number of calls to the constitutive model by 6.5 and 56.3 times, compared to using the true consistent tangent. Using the isotropic spatial tangent[9] with $[D^{\text{ep}}]$ and $[D^{\text{e}}]$ had little effect compared to the results with the anisotropic spatial tangent using $[D^{\text{ep}}]$ and $[D^{\text{e}}]$. This is because the material tangent dominates the spatial tangent, with the contributions from $[D^\beta]$ and $[D^\chi]$ being relatively minor.

If the initial stiffness tangent (that is, the tangent calculated prior to any deformation) is used throughout the analysis, then the simulation takes 5,024 N-R iterations with a run-time increase of 6,821% and a maximum of 600 iterations to find convergence within any loadstep. As the deformation increases, the difference in the spatial and material consistent tangents also increases. Even for the relatively minor deformation of the single-element in this analysis, the difference in run-time and number of iterations is significant.

	tangent	$[D^\beta]$	$[D^\chi]$	$\sum$NRit	max(NRit)	n_{cmc}	$t/t_{[D^{cst}]}$
finite deformation	$[D^{alg}]$	✓	✓	93	5	744	1
		–	–	105	6	840	1.160
	$[D^{\text{ep}}]$	✓	✓	603	57	4824	7.825
		–	–	604	57	4832	7.840
	$[D^{\text{e}}]$	✓	✓	5235	626	41880	72.192
		–	–				
small strain	$[K_0]$	initial stiffness		5024	600	40192	69.205
	$[D^{alg}]$	–	–	122	8	976	1.383
	$[D^{\text{ep}}]$	–	–	605	57	4840	7.861
	$[D^{\text{e}}]$	–	–	5211	621	41688	71.797

Table 7.5: Unit cube single-element finite deformation tangent comparison.

Axial symmetric cavity expansion

This sub-section reports on the expansion of a drained cylindrical cavity using the five constitutive models (in addition to the MCC model with no Lode angle dependency (LAD)) identified in Table 7.2. The initial state for the cavity expansion simulations was obtained through material point analysis (with a reference pressure of 80kPa) of:

(i) one-dimensional drained loading (*consolidation*) to a pressure of 233.3kPa; then

(ii) one-dimensional unloading (*swelling*) to an OCR of two, corresponding to a pressure of 136kPa.

The material point triaxial p-q stress space response for the $\beta\alpha\gamma$ and 2s$\alpha\gamma$ models are shown in Figure 7.7. The response of the MCC and $\alpha\gamma$ models were given in Figures 5.13 (i) and 5.16 of Chapter 5 and the two-surface anisotropic model response was given in Figure 6.17 of Chapter 6. The material point simulations are compared with experimental data (shown by discrete points) from a test on LCT by Gens [17]. Apart

[9] That is setting $[D^{cst}_\beta] = [0]$ in (3.67).

from the MCC model, all of the models are able to match the full loading and initial unloading behaviour of LCT, although at the start of loading the models predict a reduction in hydrostatic stress not seen in the experiments. However, only the two-surface models are able to provide a good agreement with the unloading behaviour to an OCR of 2. The material parameters and stress state after the one-dimensional procedure are given in Table 7.6. Note that the LAD has no influence on the behaviour of the single surface models for this material point simulation. Therefore the stress state and material parameters for the MCC model with and without a LAD will be identical at the start of the FE cavity expansion simulation.

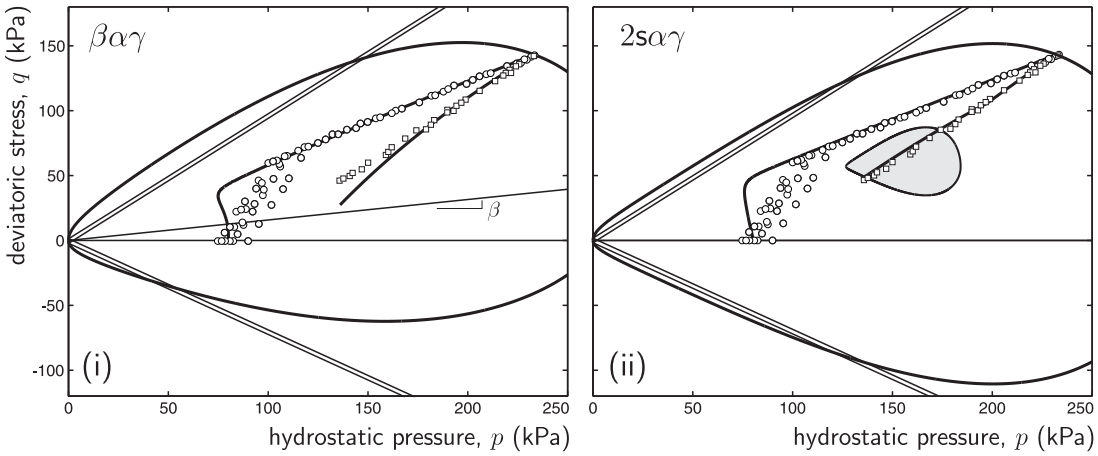

Figure 7.7: One-dimensional compression and unloading to an OCR of 2 comparison with experimental data (shown by discrete points) on LCT from Gens [17] with (i) the single-surface anisotropic two-parameter model and (ii) the two-surface two-parameter model. The final yield surfaces are shown for both models.

model	$\{\hat{\sigma}\}$ (kPa)	p_c (kPa)	$\{\hat{\sigma}_\chi\}$ (kPa)	$\{\hat{\beta}\}$
MCC	$\{148.5 \quad 148.5 \quad 111.0\}^T$	266.8	–	–
$\alpha\gamma$	$\{124.1 \quad 124.1 \quad 159.9\}^T$	289.9	–	–
2s$\alpha\gamma$	$\{116.0 \quad 116.0 \quad 176.0\}^T$	287.3	$\{129.3 \quad 129.3 \quad 199.0\}^T$	–
$\beta\alpha\gamma$	$\{124.8 \quad 124.8 \quad 158.4\}^T$	279.1	–	$\{-0.064 \quad -0.064 \quad 0.129\}^T$
2s$\beta\alpha\gamma$	$\{114.6 \quad 114.6 \quad 179.5\}^T$	277.5	$\{124.2 \quad 124.2 \quad 200.7\}^T$	$\{-0.061 \quad -0.061 \quad 0.122\}^T$

Table 7.6: Finite deformation cavity expansion analysis: constitutive model initial material parameters after one-dimensional loading and unloading to an OCR of two.

A uniform infinite cavity expansion was first analysed. This required a one-dimensional axi-symmetric analysis. However, the two-dimensional axi-symmetric finite deformation FE code was used here to model the problem. The cavity was discredited using 50 axi-symmetric eight-noded quadrilateral elements with reduced four-point quadrature (as shown towards the bottom of Figure 7.8). The size of the elements was progressively increased by a factor of 1.1 from the internal cavity face to the fixed outer boundary at 84m. In the analysis, the internal radius was expanded from an initial size of $a_0 = 0.042$m to $a = 0.21$m (that is, five $\times$ its original size) using 200 equal displacement-controlled loadsteps.

The normalised displaced internal radius (a/a_0) versus internal pressure response for the six models is given in Figure 7.8 and the results summarised in Table 7.7. Throughout all of the analyses, the load required to expand the cavity increased, tending towards a limit pressure in each case. With one

model	$\sum$(NRit)	max(NRit)	n_{pgp}	t/t_{MCC}	$p_{\max}$ (kPa)
MCC	555	5	50	1	713.9
MCC (no LAD)	532	5	50	0.944	878.2
$\alpha\gamma$	582	5	56	1.068	785.2
2s$\alpha\gamma$	561	5	162	2.155	761.3
$\beta\alpha\gamma$	577	5	56	1.362	738.0
2s$\beta\alpha\gamma$	549	5	144	2.115	709.2

Table 7.7: One-dimensional finite deformation cavity expansion analysis.

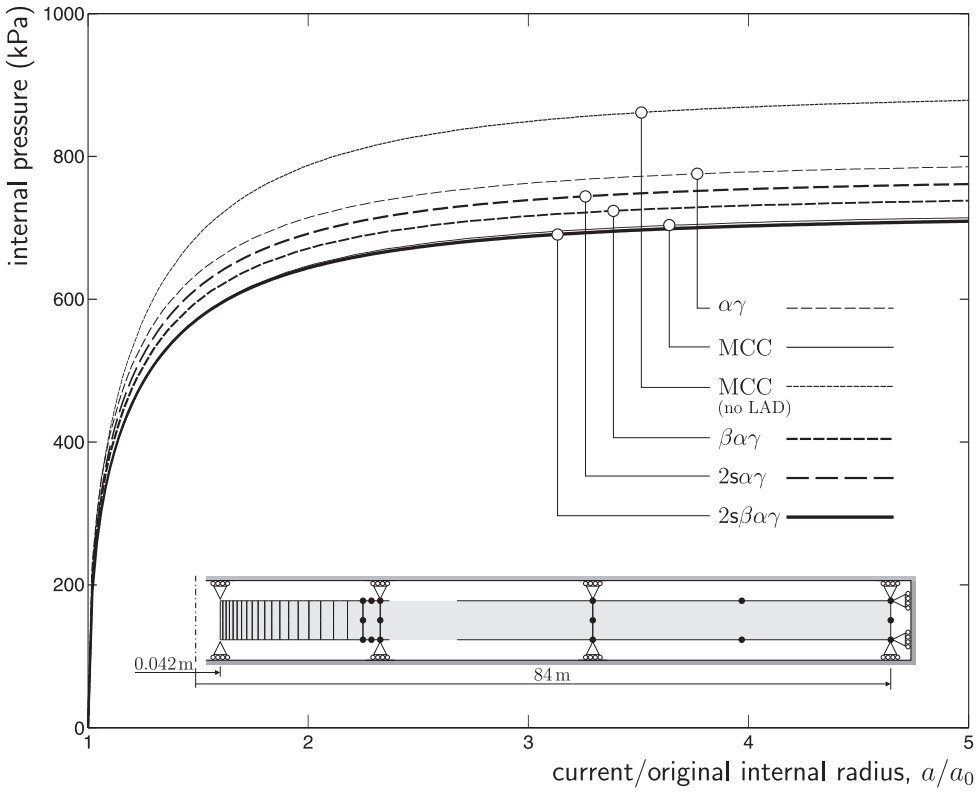

Figure 7.8: One-dimensional finite deformation cavity expansion analysis ratio of the current to original internal radius versus internal pressure response.

exception; the six models gave rise to different limit pressures. The MCC model with no LAD gave the highest internal pressure, whereas the two-surface anisotropic model (2s$\beta\alpha\gamma$) provided the lowest, with a difference of 169kPa (24%) between the results. Surprisingly, the sophisticated two-surface anisotropic model and the simple MCC model (with a LAD) exhibited very similar limit pressures. Although the two models started from quite different deviatoric stress levels, they arrived at a similar pressure limit. Not including a LAD on the MCC model increases the maximum pressure by a considerable amount (23%), demonstrating the consequence of ignoring a model's dependency on the Lode angle.

The total number of N-R iterations, the maximum number of iterations within any one loadstep, the run-times proportional to that of the MCC model and the number of elasto-plastic Gauss points at the end of the analysis for the six models are given in Table 7.7. As commented previously, in larger analyses (simulations with a greater number of finite-elements) the run-time is generally less dominated by the

constitutive model. This can be seen in the differences in the normalised run-times for the two-surface anisotropic model between Table 7.3 and Table 7.7. For the one-dimensional cavity expansion analysis, the two-surface anisotropic model took 112% longer than the MCC model, compared to 218% for the single-element unit cube analysis. This additional run-time was partially due to the fact that by the end of the analysis 144, of the 200 Gauss points were undergoing elasto-plastic behaviour in the 2s$\beta\alpha\gamma$ model, compared to only 50 in the MCC model[10]. This explains why the 2s$\alpha\gamma$ model, although less sophisticated than the 2s$\beta\alpha\gamma$ model, had a longer run-time, as more integration points were experiencing elasto-plastic behaviour. The run-time for the $\alpha\gamma$ model was marginally longer than that of the MCC model (with LAD) mainly due to the increased total number of N-R iterations, up by 27 on MCC and again also due to the increased number of elasto-plastic Gauss points (up 6 on MCC at the end of the analysis).

To explore the differences in the models in more depth, the analysis of a partially pressurised cavity is now presented. A five metre square domain was discretised using 135 eight-noded axi-symmetric finite-elements with reduced four point Gaussian quadrature (as shown in Figure 7.9). One metre of the internal cylindrical cavity was pressurised and only half of the domain was modelled due to the assumed symmetry. Again the cavity had an internal initial radius (a_0) of 0.042m and the constitutive models started from the same initial conditions as for the infinite cavity expansions analysis (as given in Table 7.6). The following cyclic loading procedure was applied over 400 loadsteps:

1.	internal load uniformly distributed over the pressurised section of 5kN in 80 loadsteps (loadsteps 1 to 80);	A to B
2.	unload to 2.5kN in 40 loadsteps (loadsteps 81 to 120);	B to C
3.	re-load to 7.5kN in 80 loadsteps (loadsteps 121 to 200);	C to D
4.	unload to 3.5kN in 40 loadsteps (loadsteps 201 to 240);	D to E
5.	re-load to 12kN in 80 loadsteps (loadsteps 241 to 320);	E to F
6.	unload to 10kN in 40 loadsteps (loadsteps 321 to 360); and	F to G
7.	finally reload to 20kN in 40 loadsteps (loadsteps 361 to 400);	G to H

These seven loading stages are identified in Figure 7.10 for the two-surface anisotropic model using the letters given above. This figure shows the internal pressure versus cavity expansion response of the five models (the MCC model (without a LAD) was not included due to congestion and to aid clarity of the other simulations). Results given in Table 7.8 summarise the following key features from the analysis: total number of N-R iterations, maximum number of iterations within any one loadstep, number of elasto-plastic Gauss points at the end of the analysis, run-times proportional to that of the MCC model, maximum relative expansion of the cavity (a/a_0) and the pressure at the end of the analysis ($p_{\max}$).

The run-time for the 2s$\beta\alpha\gamma$ model is now only 49.6% longer than that of the MCC model, again due to the larger analysis altering the relative time spent in the constitutive model sub-routines. Although the total number of N-R iterations between the two models is similar, the number of elasto-plastic Gauss points for the 2s$\beta\alpha\gamma$ model is over double that of the MCC model at the end of the analysis. Also, throughout all of the unloading stages, the MCC model predicted purely elastic behaviour whereas some of the Gauss points, when using 2s$\beta\alpha\gamma$ model, experienced an elasto-plastic response. These facts (in addition to the added sophistication of the constitutive formulation) contribute to explaining the increase

[10]It should be noted that when undergoing elastic behaviour the material point run-time for the anisotropic models (the $\beta\alpha\gamma$, 2s$\alpha\gamma$ and 2s$\beta\alpha\gamma$ models) is less than that of the isotropic models (the *MCC* and single surface $\alpha\gamma$ models). This is due to the computational overhead associated with finding the eigenvalues and vectors of the trial elastic strain in the isotropic models that is not required in the anisotropic models working in six-dimensional stress space.

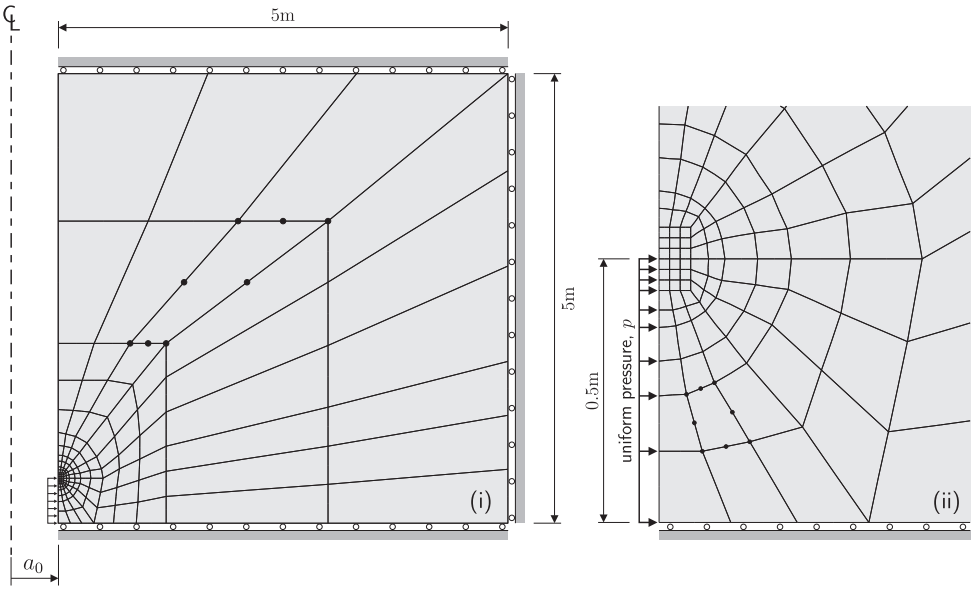

Figure 7.9: Two-dimensional axi-symmetric finite deformation cavity expansion analysis discretisation: (i) entire 5m by 5m domain and (ii) detail around the pressurised section.

in run-time for the two-surface models.

As shown in Figure 7.10 (ii), the two-surface models demonstrate a hysteretic response during unloading and re-loading whereas the single surface models, for this analysis, follow the same purely elastic path during unloading and re-loading[11]. Due to the high value of the constant controlling the rate of translation of the inner yield surface, C_χ, the degree of hysteresis seen in these loops is rather small. Lowering the value of C_χ will increase the area enclosed by the unloading and re-loading paths, as demonstrated for hydrostatic loading and unloading in Figure 6.11 of Chapter 6.

model	$\sum$(NRit)	max(NRit)	n_{pgp}	t/t_{MCC}	a/a_0	$p_{\max}$ (kPa)
MCC	925	5	225	1	1.550	307.2
MCC (no LAD)	916	4	208	0.974	1.410	337.8
$\alpha\gamma$	896	5	249	0.971	1.438	331.2
2s$\alpha\gamma$	925	5	482	1.441	1.443	330.0
$\beta\alpha\gamma$	917	5	251	1.104	1.493	318.9
2s$\beta\alpha\gamma$	931	5	476	1.496	1.485	320.7

Table 7.8: Two-dimensional finite deformation cavity expansion analysis.

The pressure versus expansion response of the models in Figure 7.10 is dominated by the shape of the yield surfaces. This is evident by examining results from the single and two-surface models which share the same value of α and γ; the analyses lead to very similar responses. Increasing α results in a softer response, with the MCC model ($\alpha = 1$) appearing softer than the $\beta\alpha\gamma$ and 2s$\beta\alpha\gamma$ models ($\alpha = 0.4$), which are softer than the $\alpha\gamma$ and 2s$\alpha\gamma$ models ($\alpha = 0.3$). This finding is a consequence of the high value of C_χ, which gives rise to the model responses being controlled mainly by the geometry of the outer surface.

[11]Note, that this is not the case in general for single-surface plasticity models. Such models can (and do) exhibit elasto-plasticity upon unloading due to stress transfer within the analysis.

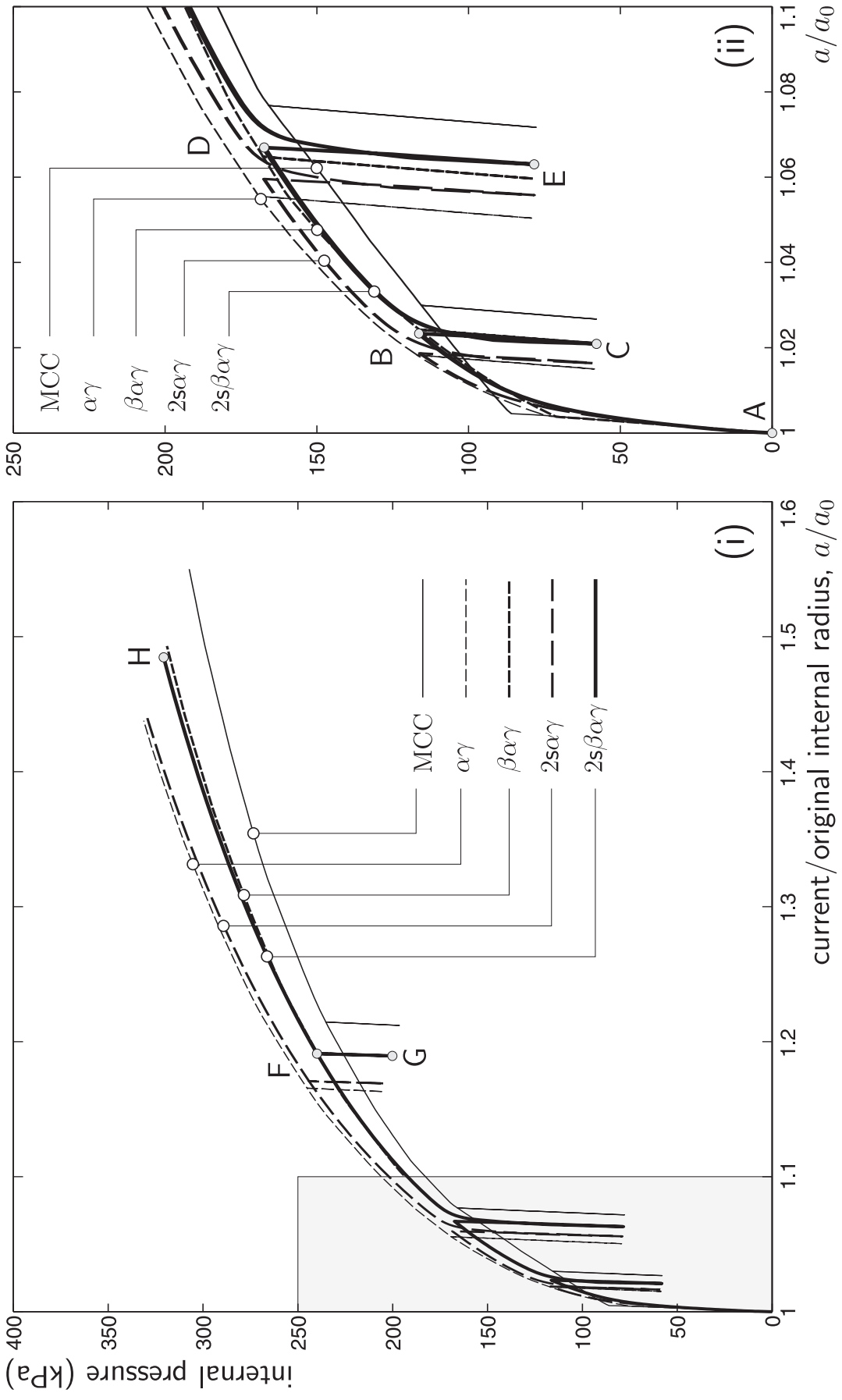

Figure 7.10: Two-dimensional finite deformation cavity expansion analysis ratio of the current to original internal radius (a/a_0) versus internal pressure response for (i) $a/a_0 \in [1, 1.6]$ and (ii) $a/a_0 \in [1, 1.1]$.

7.3 Two-dimensional plane strain rigid footing

Models of varying complexity have been presented in this thesis, from the simple non-associated frictional mR cone (first seen in Chapter 4) to the two-parameter single surface CS model (Chapter 5) and finally the two-surface anisotropic family of CS models (Chapter 6). This section poses the question

> *"How do the sophisticated hyperplastic Critical State constitutive models compare with the simple frictional cone models in a standard footing analysis? Is the extra complexity justified?"*

To answer this question, the analysis of a plane strain rigid footing bearing onto a weightless half-space is now presented. Here the M-C, D-P and mR models are compared with the MCC and the 2s$\beta\alpha\gamma$ models, with their respective material constants listed in Table 7.2. The one metre wide smooth rigid strip footing was subjected to a vertical downwards displacement of 0.5m in 500 equal displacement-controlled loadsteps. Due to symmetry, only half of the 40m by 20m domain was discretised using 171 eight-noded plane strain quadrilateral elements, integrated using reduce four point Gaussian quadrature (as shown in Figure 7.11)[12].

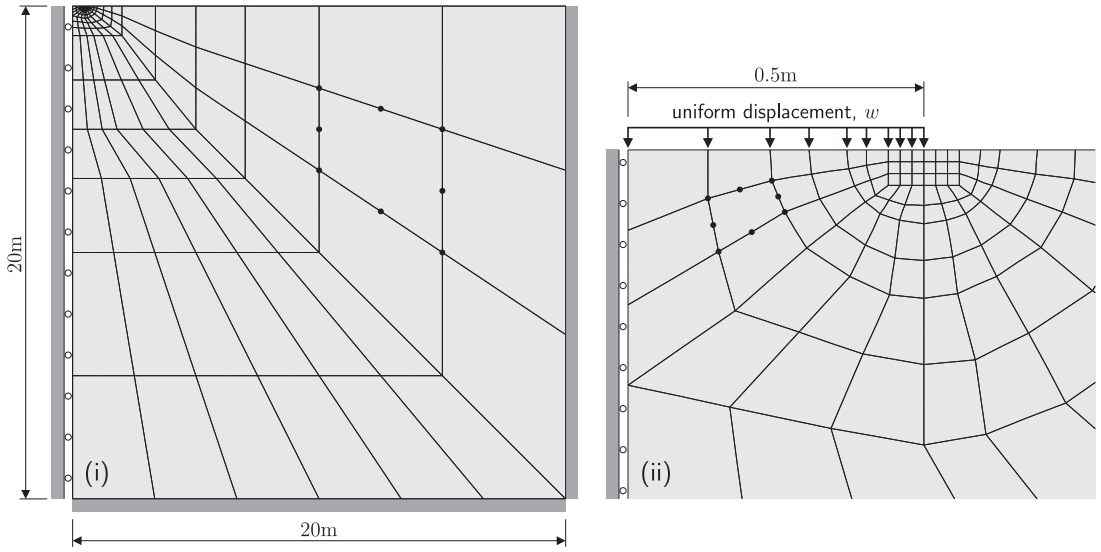

Figure 7.11: Model comparison plane strain rigid footing analysis discretisation: (i) entire 20m by 20m domain and (ii) detail around the rigid footing.

The initial state of the CS constitutive models was obtained through:

(i) one-dimensional drained loading (*consolidation*) to a pressure of 233.3kPa; then

(ii) one-dimensional unloading (*swelling*) to an OCR of four, corresponding to a pressure of 87.5kPa.

The material parameters and stress state following these two steps for the MCC and the 2s$\beta\alpha\gamma$ models are given in Table 7.9.

The M-C, D-P and mR constitutive models require specification of the effective friction angle, apparent cohesion and dilation angle. The effective friction angle, ϕ, of the soil can be obtained from the gradient

[12]Note, that the upper left hand side 5m square block of this discretisation is the same mesh as initially presented by de Souza Neto *et al.* [36] and later used by Coombs *et al.* [12] for the small strain analysis of frictional cone models. The mesh is highly refined near the corner of the rigid footing and was shown to give excellent agreement with the analytical Prandtl solution for the M-C constitutive model [12, 36].

model	$\{\hat{\sigma}\}$ (kPa)	p_c (kPa)	$\{\hat{\sigma}_\chi\}$ (kPa)	$\{\hat{\beta}\}$
MCC	$\{123.1 \quad 123.1 \quad 16.0\}^T$	264.9	–	–
2s$\beta\alpha\gamma$	$\{\ 85.4 \quad 85.4 \quad 91.3\}^T$	276.7	$\{\ 93.8 \quad 93.8 \quad 111.6\}^T$	$\{0.055 \quad 0.055 \quad 0.110\}^T$

Table 7.9: Small strain footing analysis: constitutive model initial material parameters after one-dimensional loading and unloading to an OCR of four.

of the CSL, by rearranging (5.22) from Chapter 5, as

$$\phi = \arcsin\left(\frac{3M}{2\sqrt{6}+M}\right). \tag{7.4}$$

For LCT, the gradient of the CSL was determined from experimental data (see Figure 5.18 from Chapter 5), given by $M = 0.964$, resulting in an effective friction angle of $\phi = 29.6°$. For this friction angle, the normalised deviatoric radius under triaxial extension for the M-C model (from (4.3) in Chapter 4) is $\bar{\rho}_e = 0.718$. However, as the mR model allows flexibility in specifying $\bar{\rho}_e$ independent of the friction angle, the normalised radius was set equal to that of the CS models at $\bar{\rho}_e = 0.729$. Therefore, the mR model's yield surface lies outside that of the M-C and D-P ($\bar{\rho} = \bar{\rho}_e = 0.729$) models, but is enclosed by the D-P ($\bar{\rho} = 1$) yield surface, as shown to the left of Figure 7.12. The apparent cohesion was set to 0, so that the compression meridian of the frictional cone models coincided with the CSS compression meridian and the dilation angle set at ϕ.

The elastic properties for the frictional cone models were set so that they agreed with the average bulk modulus and constant shear modulus of the single surface CS models during the K_0 loading and unloading material history. That is, the bulk modulus was determined at a pressure of $p = 160.4$kPa. This resulted in an initial bulk modulus of 22.0MPa ($\kappa = 0.0073$ using (5.3) from Chapter 5 with $\varepsilon^{\mathrm{e}}_{v0} = 0$), giving a Young's modulus of 42.4MPa and a Poisson's ratio of 0.18. The frictional cone models started from a hydrostatic stress state with a mean pressure of $p = 87.5$kPa[13].

The theoretical limit pressure for the M-C model, as given by the Prandtl (and Reissner) solution (see Yu [42] p. 316, amongst others), is

$$\text{limit pressure} = \Big(\cot(\phi)\tan^2\big(\pi/4+\phi/2\big)\exp^{\pi\tan(\phi)} - \cot(\phi)\Big) \times c. \tag{7.5}$$

This equation gives the limit pressure for a rigid footing bearing onto a weightless soil for the case of zero surface surcharge. (7.5) was obtained by combining a slip failure mechanism beneath an infinite rigid footing (under plastic equilibrium with the imposed footing pressure) with classical plasticity theory (see Craig [14] pp. 281–283 for more information). Using an equivalent apparent cohesion, c, consistent with the initial state of 49.6kPa and a friction angle of 29.56° (0.5159 radians), the Prandtl limit pressure is 1.44MPa (with (limit pressure)$/c = 29.11$). The normalised limit pressue obtained from the FE analysis with the M-C model was 29.48, having an error of only 1.3% when compared with the analytical solution.

The pressure versus displacement response for the five models (two CS and three frictional cone models) is shown in Figure 7.12 and the results summarised in Table 7.10. The D-P model (with $\bar{\rho} = 1$) is significantly stiffer than the M-C and mR constitutive models. Despite the not insignificant 0.5m displacement, the D-P ($\bar{\rho} = 1$) model did not reach a limit load[14]. However, after this displacement, the

[13]Note, that this is equivalent to setting an apparent cohesion of 49.6kPa. Both result in a hydrostatic pressure difference of 87.5kPa between the yield surface apex and the initial starting stress state.

[14]Even when the displacement is increased to 1m the D-P model still does not attain a limit load. This is due to setting the D-P yield surface such that it intersects with the M-C criterion at the compression meridians; resulting in a peak

model	$\sum$(NRit)	max(NRit)	n_{pgp}	t/t_{MCC}	$p_{\max}$ (kPa)	$u_{p=1\text{MPa}}$ (mm)
MCC	1378	4	662	1	1,187	350
2s$\beta\alpha\gamma$	1337	4	681	1.866	1,264	287
M-C	1281	8	536	0.761	1,463	79
D-P ($\bar{\rho}=1$)	1247	4	562	0.737	6,483	59
mR	1366	5	546	0.833	2,302	69

Table 7.10: Small strain footing analysis results.

D-P ($\bar{\rho}=1$) footing pressure was over 4.4 times that of the M-C model. As expected, the pressure versus displacement response of the mR model lies between that of the M-C and D-P ($\bar{\rho}=1$) models, with a limit load 57% higher than that of the M-C model. The D-P ($\bar{\rho}=\bar{\rho}_e$) model attains a limit pressure of 1.96MPa, lying between the M-C model mR models. The variation in the pressure-displacement response of the two D-P simulations (as shown in Figure 7.12) highlights the importance of the appropriate $\bar{\rho}$ specification. The initial elastic responses of the three models (D-P, M-C and mR) are identical up to a displacement of 4mm. Following this, their behaviours remain similar until a displacement of approximately 30mm is attained, whereafter the solutions begin to diverge.

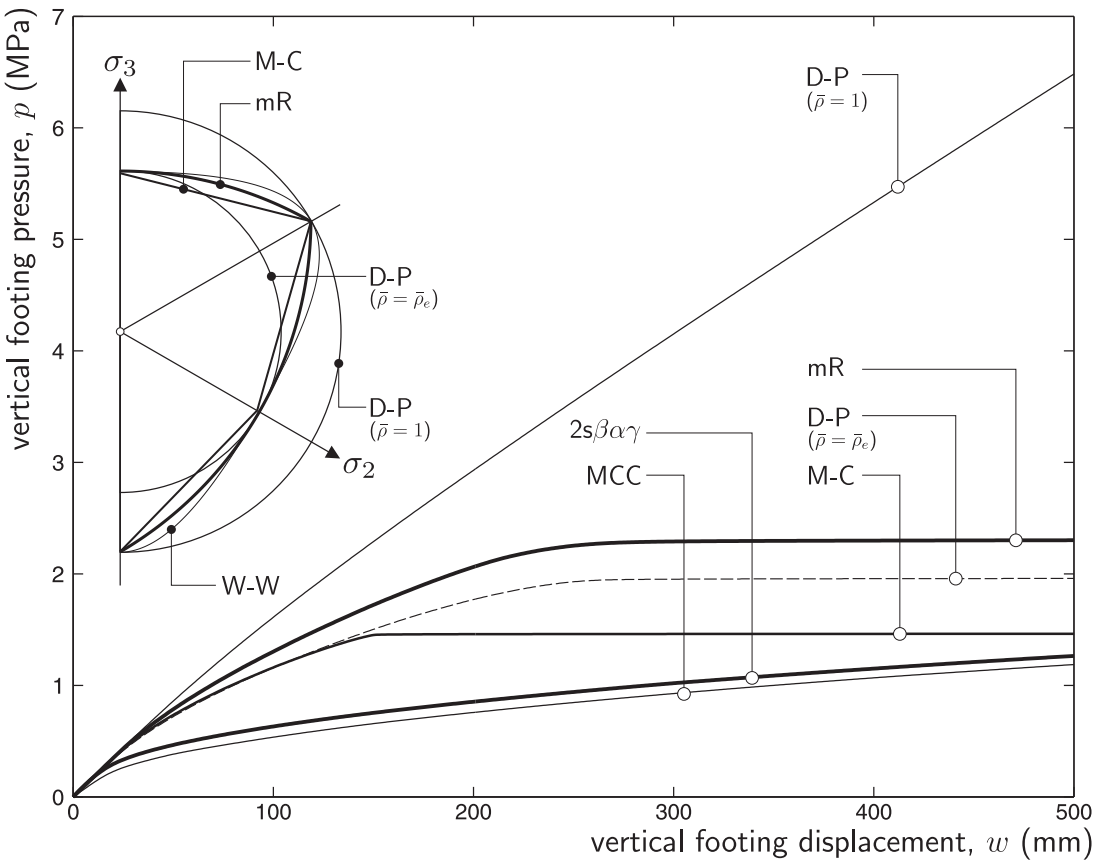

Figure 7.12: Small strain footing analysis: pressure versus displacement response for two of the five CS models (MCC and 2s$\beta\alpha\gamma$) and the three frictional cone models (M-C, D-P and mR).

effective friction angle of 47.7° at a Lode angle of 23.1°.

The run-time of the two surface anisotropic model is only 87% longer than that of the MCC model. The frictional cone models have run-times 24%, 26% and 17% lower than that of MCC for the M-C, D-P ($\bar{\rho} = 1$) and mR models respectively. The reason for this reduction in the run-times for the simple frictional cone models is that they all allow closed-form analytical stress integration based on the bE method. Also, the three cone models exhibit no hardening or softening. The CS models require multiple iterations when undergoing elasto-plastic material behaviour to reach convergence at each Gauss point in the FE analysis. The run-time for the mR model is only marginally longer than that of the M-C and D-P ($\bar{\rho} = 1$) models, despite its considerable advantages over these classical material models in terms of reproducing experimentally observed multi-axial deviatoric yielding (Figure 4.4, Chapter 4).

The CS models give rise to significantly softer results than the frictional cone models. This is due to the Gauss points experiencing elasto-plastic behaviour from the initial loadstep. The approximate displacement for a pressure of 1MPa is given in Table 7.10. The two-surface anisotropic model gives a displacement of 287mm, whereas the MCC model gives a 22% softer displacement of 350mm. The frictional cone models have displacements of 56, 69 and 79mm for the D-P ($\bar{\rho} = 1$), mR and M-C models respectively. That is, 5.9, 5.0 and 4.4 times less displacement than the more sophisticated 2s$\beta\alpha\gamma$ model. Without field data to compare these results to, it is not possible to establish which model gives the most realistic solution. However, it seems likely that the simple frictional cone models produce over-stiff solutions prior to arrival at their limit loads.

Figure 7.13 shows the nodal displacement vectors, $\{\Delta u\}$, for the final loadstep for the M-C and 2s$\beta\alpha\gamma$ models where there lengths have been increased one-hundred fold. The M-C model (which has reached its limit load) displays the characteristic wedge rigid body motion with significant heave in the vicinity of the footing. The two-surface anisotropic model has a more uniform, lower magnitude displacement field with quite different directions compared to the M-C model. Note that all of the displacement vectors for the 2s$\beta\alpha\gamma$ move vertically downwards (in addition to some horizontal displacement) and the nodal displacements on the centreline displace by a greater amount compared to the M-C model.

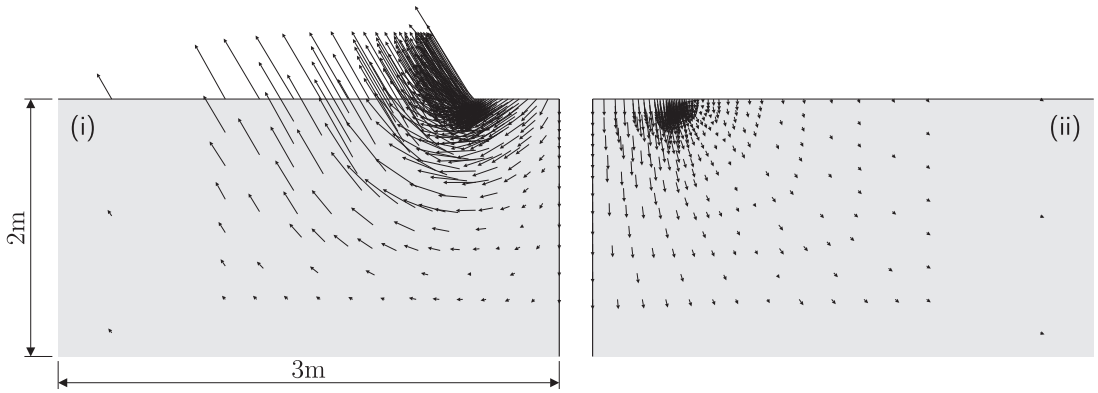

Figure 7.13: Nodal displacement vectors for the final loadstep (with a scaling factor of 100) of the small strain rigid footing analysis for (i) the M-C model and (ii) the 2s$\beta\alpha\gamma$ model.

The displaced surface profiles for the M-C, mR and 2s$\beta\alpha\gamma$ models are shown in Figure 7.14, together with the deformed mesh from the M-C simulation. The associated flow frictional cone models demonstrate significant local heave around the footing which is not seen in the two-surface anisotropic model. There is also considerable horizontal displacement of the nodes beneath the footing. This leads to mesh entanglement in the region of peak heave near the corner of the rigid footing (as shown by the inset distorted mesh in Figure 7.14). This entanglement does not influence the small strain simulation as the analysis is based on the original nodal coordinates. The two-surface anisotropic surface profile is

smoother than the frictional cone models and does not demonstrate any heave, with the adjacent surface lower than the original ground level.

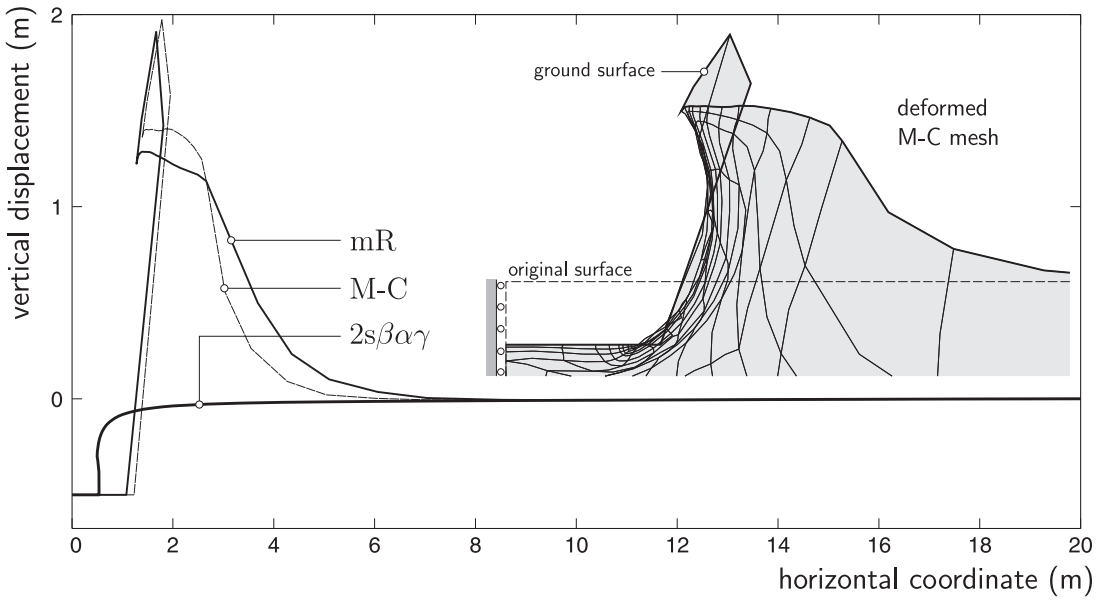

Figure 7.14: Displaced surface profile of the M-C, mR and 2s$\beta\alpha\gamma$ models in the small strain rigid footing analysis.

The frictional cone models investigated in Chapter 4 offer valuable, simple idealisations, capturing the basic behaviour of soil and are computationally fast. However, this analysis has shown that they can lead to over-stiff responses which can significantly overestimate the heave. These elementary models are very sensitive to the choice of the normalised deviatoric radius under triaxial extension, $\bar{\rho}_e$, far more so than the CS models.

7.4 Hollow cylinder apparatus

The penultimate section in this chapter presents the analysis of a series of hollow cylinder experimental investigations by Nishimura [28] on LC. The two-surface anisotropic model is first calibrated using triaxial experimental data. The hollow cylinder apparatus (HCA) tests are then simulated using (i) a single three-dimensional FE and (ii) a full three-dimensional discretisation of the HCA.

7.4.1 London Clay

LC is categorised as a stiff, fissured, heavily overconsolidated clay of high plasticity[15]. This material has undergone significant experimental investigation and computational analysis since the 1950s [27, 28] (see Nishimura [28] p. 12 for details) as a consequence of its engineering importance with regard to deep foundation design and underground excavations in the UK's capital city. LC was deposited within a marine environment during the Eocene epoch (56–34 million years ago) [20]. It is mainly composed of Illite and Montmorillonite minerals, with smaller fractions of Kaolinite. The clay fraction of LC is typically between 40% and 60% with a plasticity index of between 40 and 70 (depending on location) [28]. Due to its *brittle* nature, LC poses a challenge for models based on the concept of the CS. Indeed, it was commented by Nishimura [28] that:

> *"It has been well recognised, however, that the behaviour of the natural London Clay observed in laboratory is one of the exceptions that do not conform, under most conditions,* [to] *the*

[15] That is, the combination of a high plasticity index ($> 30\%$) with a high liquid limit ($> 50\%$).

> [Critical State] *framework. The natural London Clay generally exhibits brittle behaviour and shearing involves bifurcation at an early stage."*

That is, the clay tends to rupture, due to pre-existing fissures prior to arrival at the CS. Following rupture, the material can no longer be modelled using standard continuum methods as the behaviour is governed by the sliding/friction between discontinuity planes. This behaviour results in the loss of one of the key concepts in Critical State soil mechanics; a unique void ratio - ultimate shear strength relationship, as observed by Bishop *et al.* [5].

In this section a series of anisotropic undrained triaxial tests is presented which provides a means to calibrate the two-surface anisotropic model. These simulations are followed by model comparison against recent stress path tests performed in a HCA by Nishimura [28]. Thereby testing an important requirement of constitutive models, as suggested by Prévost and Wolf [31], that:

> *"a material model may only be deemed to be satisfactory when with its aid, it is possible first to determine the stress-strain-strength behaviour of the material at hand in one piece of tests equipment... , and then to predict the observed behaviour of the same material in some other type of testing equipment..."*

The 2s$\beta\alpha\gamma$ model's material constants (Table 6.1) were obtained by following the calibration procedure outlined in Section 6.3. λ, κ, R and C^{χ} where obtained from hydrostatic consolidation data (starting from a specific volume of 2.35) on reconstituted samples tested by Gasparre [16]. The hydrostatic consolidation experimental data is shown (using discrete points) in Figure 7.15 (i) together with the two-surface anisotropic model's specific volume versus hydrostatic pressure response. The simulation started from an isotropic material at a hydrostatic stress state (on the compressive nose of the inner yield and outer bounding surfaces) with a reference pressure of 30kPa. The model was subjected to a hydrostatic strain path to a pressure of 640kPa, followed by unloading back to the original reference pressure. Good agreement is observed between the experimental data for both hydrostatic virgin consolidation (A to B) and swelling (B to C). The model's reloading response is also shown (by the finer line from C to D) to a specific volume of 1.8.

Anisotropic calibration investigations

The remaining LC material parameters in Table 6.1 were calibrated from UTC and undrained triaxial extension (UTE) test results following one-dimensional loading and unloading, as presented by Hight *et al.* [20] (original data from Jardine [25]). The stress ratio at the CS for LC was determined to be $\eta_{cs} = 0.688$ and the stress ratio under one-dimensional consolidation is $\eta_{K_0} = 0.443$ (as seen in Figure 7.15 (ii)). The material test data for OCRs of 1, 1.5, 4 and 7 (discrete points), and the two-surface anisotropic constitutive model simulation, are shown in Figure 7.15 (ii) in hydrostatic versus deviatoric (p-q) stress space. In Figure 7.15 (iii) the axial strain versus deviatoric stress response is given.

The two-surface anisotropic model is able to capture the observed material response in a convincing way. Not all of the experimental tests attained the CS (in particular, triaxial extension at an OCR of 4). Also, the number of data points for all of the tests is quite limited. However, these triaxial results are useful for calibrating the two-surface anisotropic model prior to simulating the, more interesting, multi-axial HCA experiments.

7.4.2 Material point HCA investigations

The torsional HCA allows for independent control of four stress components through the application of axial load (W), torque (M_T) and internal (p_i) and external (p_o) pressures (as seen in Figure 7.16 (i)). However, interpretation of the results from the HCA is not so simple; indeed Wood [39] commented that:

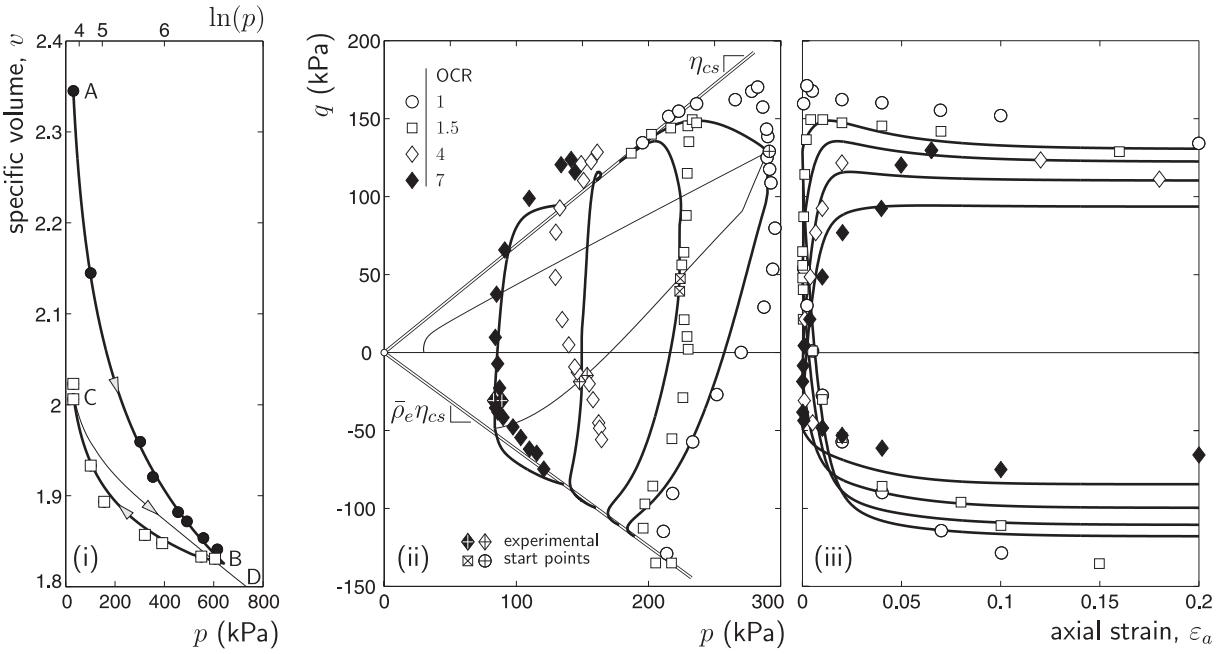

Figure 7.15: London Clay calibration experimental data: (i) isotropic consolidation and swelling comparison with data (shown by discrete points) from Gasparre [16]. UTC and UTE following K_0 consolidation and swelling comparison with experimental data from Hight *et al.* [20] (original data from Jardine [25]): (ii) stress path in *p*-*q* space and (iii) axial strain-deviatoric stress response.

> *"Interpretation of the results of hollow cylinder tests is something of an exercise in deconvolution... Four degrees of freedom seem to be the maximum that we can achieve in laboratory element testing and we are always going to have to extrapolate using our constitutive model in order to describe the final two degrees of freedom..."*

The additional flexibility of the apparatus (in terms of controlling different stress components) is at the expense of stress variations through the wall of the cylinder. These variations are caused by (i) different internal and external pressures and (ii) application of an axial torque. The average normal stresses (see Hight *et al.* [21], amongst others), as shown in Figure 7.16 (ii), can be assumed to be

$$\sigma_z = \frac{W}{\pi(r_o^2 - r_i^2)} + \frac{p_o r_o^2 - p_i r_i^2}{r_o^2 - r_i^2}, \qquad \sigma_r = \frac{p_o r_o + p_i r_i}{r_o + r_i} \qquad \text{and} \qquad \sigma_\theta = \frac{p_o r_o - p_i r_i}{r_o - r_i}, \tag{7.6}$$

while the average shear stress is given by

$$\sigma_{z\theta} = \frac{3M_T}{2\pi(r_o^3 - r_i^3)}. \tag{7.7}$$

σ_z and σ_θ are obtained by considering equilibrium whereas σ_r and $\sigma_{z\theta}$ assume a linear elastic stress distribution through the specimen [21]. The non-uniformity of the stresses through the cylinder can be reduced by decreasing the wall thickness to inner radius ratio, with large thin-walled cylinders being preferred [39].

Nishimura and co-workers [27, 28] presented a series of undrained HCA tests on LC from undisturbed block samples. The tests were conducted with an aim to achieve the following conditions:

(i) constant total pressure, p_t (that is, the sum of the effective pressure, p, and the pore water pressure, u);

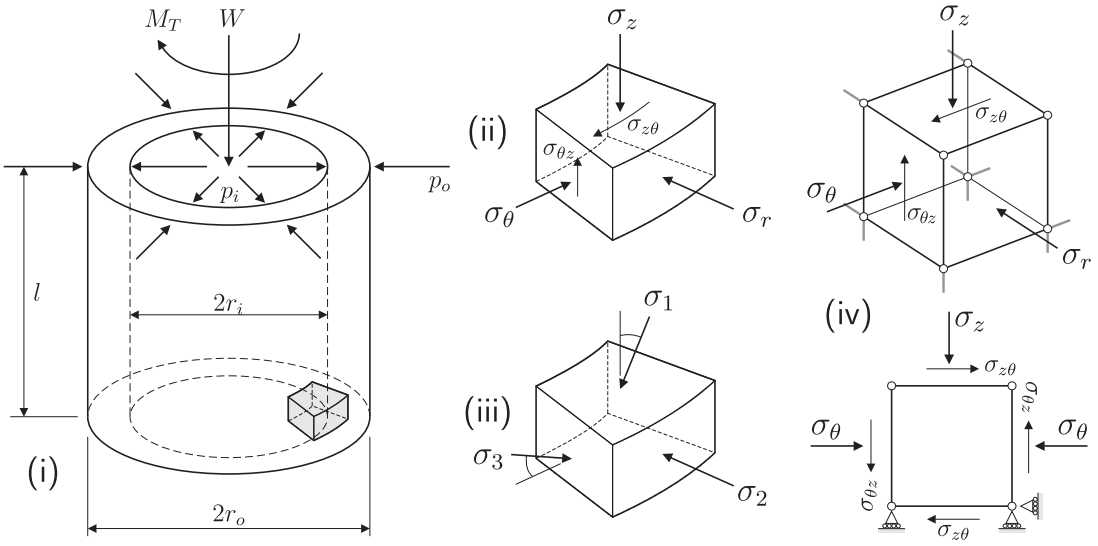

Figure 7.16: Hollow cylinder apparatus (i) applied loads and pressures, (ii) average internal stresses, (i) principal stresses and (iv) single eight-noded hexahedral finite-element: loading and boundary conditions.

(ii) constant ratio of the intermediate principal stress

$$b = \frac{\sigma_2 - \sigma_3}{\sigma_1 - \sigma_3}; \tag{7.8}$$

(iii) constant stress path with

$$\frac{\sigma_z - \sigma_\theta}{2} = \frac{\sigma_{z\theta}}{\tan(2\alpha_{d\sigma})}, \tag{7.9}$$

where $\alpha_{d\sigma}$ is the incremental stress path direction.

These three conditions (together with the starting stress condition) allow determination of the idealised, uniform, stress state for the undrained HCA experiments. Assuming that the radial stress is the intermediate principal stress (as shown in Figure 7.16 (iii)), we obtain the major and minor principal stresses as

$$\sigma_{1,3} = \frac{\sigma_z + \sigma_\theta}{2} \pm \sqrt{\left(\frac{\sigma_z - \sigma_\theta}{2}\right)^2 + (\sigma_{z\theta})^2}. \tag{7.10}$$

Substituting (7.10) for the major and minor principal stresses in (7.8), and using the condition of constant pressure, with $\sigma_z + \sigma_\theta = 3p_t - \sigma_r$, we obtain

$$b = \frac{1}{2} + \frac{3(\sigma_r - p_t)}{4\sqrt{\left((\sigma_z - \sigma_\theta)/2\right)^2 + (\sigma_{z\theta})^2}}. \tag{7.11}$$

Finally substituting for $(\sigma_z - \sigma_\theta)/2$ from (7.9), gives the radial stress as

$$\sigma_r = p_t + \frac{4(b - 1/2)\sigma_{z\theta}\sqrt{\tan\left(2\alpha_{d\sigma}\right)^{-2} + 1}}{3}. \tag{7.12}$$

From the total mean stress, p_t, and (7.9), the axial and circumferential stresses follow as

$$\sigma_\theta = \frac{3p_t - \sigma_r}{2} - \frac{\sigma_{z\theta}}{\tan(2\alpha_{d\sigma})} \qquad \text{and} \qquad \sigma_z = 3p_t - \sigma_r - \sigma_\theta. \tag{7.13}$$

These constant stress path tests can be driven by the applied shear stress, $\sigma_{z\theta}$, with the other normal stresses subsequently calculated from (7.12) and (7.13), once the total mean stress (p_t), intermediate principal stress ratio (b) and stress path direction ($\alpha_{d\sigma}$) have be specified.

Analysis of the HCA tests, as performed experimentally by Nishimura [28], can be split into four stages, as given below.

(i) *In-situ* stress path (assuming an initial depth burial depth of 16.3m[16]) following three geological events [28]:

  (a) deposition of 175m of LC with a bulk unit weight of 19.8kN/m^3 simulated by the drained one-dimensional loading to a vertical stress of 3.673MPa;

  (b) erosion of the 175m over-burden simulated by the drained one-dimensional unloading to a vertical stress of 208kPa; and

  (c) deposition of terrace gravel of bulk unit weight 19.1kN/m^3 to a depth of 5.8m simulated by the drained one-dimensional re-loading to a vertical stress of 319kPa.

(ii) Shift the current stress state to the assumed *in-situ* stress conditions of an effective pressure $p =$ 323kPa and

  (a) *isotropic* tests series (IC) starting from a hydrostatic stress state with $\sigma_z = \sigma_\theta = \sigma_r$;

  (b) *anisotropic* test series (AC) starting from a stress state off the hydrostatic axis with $(\sigma_z - \sigma_\theta) = -165$kPa and $\sigma_\theta = \sigma_r$.

  Note, that although the test series were identified by Nishimura [28] as *isotropic* and *anisotropic*, both test series were performed on anisotropic samples of LC. A more appropriate description would be *hydrostatic* and *in-situ* as these terms describe the initial stress conditions of the samples, rather than implying some difference in the state of the material.

(iii) For the AC tests, follow an undrained change in the intermediate principal stress ratio, from an initial value of 1, to the required b value along the stress path

$$\{\Delta\sigma_r \quad \Delta\sigma_\theta \qquad \Delta\sigma_z\} = \Delta\sigma\{-2 \quad 1 \quad 1\},$$

  following a Tresca meridian in principal stress space, such that total pressure (set at 573kPa with a pore pressure of 250kPa) and $(\sigma_z - \sigma_\theta)$ remain constant. Changing b from 1 to 0.5 requires $\Delta\sigma = 27.5$kPa.

(iv) Undrained shear with a constant total pressure and constant b along a fixed $\alpha_{d\sigma}$ stress path, with the normal stress components (driven by the shear stress $\sigma_{z\theta}$) obtained from (7.12) and (7.13).

Stages (i) and (ii) were conducted at a material point whereas the subsequent undrained stress paths were conducted using a single small strain eight-noded hexahedral element with the boundary conditions and loading as shown in Figure 7.16 (iv). These boundary conditions result in a uniform stress (and strain) distribution through the element. The average stresses (σ_z, σ_r and σ_θ), total mean stress (p_t), pore-water pressure (u), internal (p_i) and external (p_e) pressures and axial load (W) for stages one to three for the anisotropic (AC) test series (with $b = 0.5$) are given in Table 7.11[17].

[16] The experimental tests were conducted on samples taken from a current *in-situ* depth of 16.3m.

[17] Note, that the shear stress $\sigma_{z\theta}$ is zero for the first three stages of the HCA investigations.

stage	σ_z	σ_r	σ_θ	p_t	u	W	p_i	p_o
	(kPa)	(kPa)	(kPa)	(kPa)	(kPa)	(N)	(kPa)	(kPa)
I.	213.0	378.0	378.0	323.0	0	602	378.0	378.0
II.	463.0	628.0	628.0	573.0	250	1,308	628.0	628.0
III.	490.5	573.0	655.5	573.0	250	1,386	537.2	592.2

Table 7.11: Average stresses and external loads for the HCA AC test series ($b = 0.5$) pre-shear stages.

The LC material constants (as given in Table 6.1) were used throughout the anaylsis with a reference pressure of 80kPa. The constitutive model's normal components of stress, the centre of the inner surface and the anisotropy inherent in the surfaces at the end of stage (i) were

$$\{\hat{\sigma}\} = \left\{ \begin{array}{r} 389.8 \\ 389.8 \\ 318.8 \end{array} \right\} \text{kPa}, \qquad \{\hat{\sigma}^\chi\} = \left\{ \begin{array}{r} 529.0 \\ 529.0 \\ 450.7 \end{array} \right\} \text{kPa} \qquad \text{and} \qquad \{\hat{\beta}_n\} = \left\{ \begin{array}{r} -0.0435 \\ -0.0435 \\ 0.0870 \end{array} \right\}, \tag{7.14}$$

with the size of the outer surface $p_c = 2.50$MPa. The material point experienced a hydrostatic pressure of 378kPa and stress deviator $(\sigma_z - \sigma_\theta) = -86$kPa. In stage (ii), both the stress state and the position of the inner yield surface were translated (with all of the other parameters, such as p_c and $\{\beta\}$, frozen) so that the starting stress state for stage (iii) was in agreement with that experienced in the experimental test. The initial state for the AC test series was

$$\{\hat{\sigma}_n\} = \left\{ \begin{array}{c} \sigma_r \\ \sigma_\theta \\ \sigma_z \end{array} \right\} = \left\{ \begin{array}{c} 378 \\ 378 \\ 213 \end{array} \right\} \text{kPa}, \qquad \{\hat{\varepsilon}^{\text{e}}_n\} = \left\{ \begin{array}{c} 0.01037 \\ 0.01037 \\ 0.00578 \end{array} \right\}, \qquad \text{and} \qquad \{\hat{\sigma}^\chi_n\} = \left\{ \begin{array}{c} 517.2 \\ 517.2 \\ 344.8 \end{array} \right\} \text{kPa}.$$

The IC test series started on the hydrostatic axis with an initial state given by

$$\{\hat{\sigma}_n\} = \left\{ \begin{array}{c} \sigma_r \\ \sigma_\theta \\ \sigma_z \end{array} \right\} = \left\{ \begin{array}{c} 323 \\ 323 \\ 323 \end{array} \right\} \text{kPa}, \qquad \{\hat{\varepsilon}^{\text{e}}_n\} = \left\{ \begin{array}{c} 0.00884 \\ 0.00884 \\ 0.00884 \end{array} \right\}, \qquad \text{and} \qquad \{\hat{\sigma}^\chi_n\} = \left\{ \begin{array}{c} 462.2 \\ 462.2 \\ 454.8 \end{array} \right\} \text{kPa}.$$

In both test series the initial inclination of the yield surfaces was set to that given in $(7.14)_3$ and the initial outer surface size set to $p_c = 2.50$MPa. Throughout the undrained analysis the fluid bulk modulus was fixed at 10GPa. Stage (iv) followed a constant $\alpha_{d\sigma}$ stress path, with the directions given in Table 7.12. The relative increments in the stresses for the two isotropic and five anisotropic paths are given, normalised with respect to the magnitude of the *driving* stress increment ($\Delta\sigma_z$ for the zero-torsion tests and $\Delta\sigma_{z\theta}$ for the non-zero torsion tests). The load-controlled test path was followed, using both the two-surface anisotropic model and the MCC model, until the experimentally identified rupture point was attained (that is, to the same difference between the major and minor principal strains at which rupture was first recorded).

The uniform material point simulation results from the isotropic test series are shown and compared with the experimental data in Figure 7.17. The $(\sigma_1 - \sigma_3)$ versus $\Delta(\varepsilon_1 - \varepsilon_3)$ response and effective stress ratio versus $\Delta(\varepsilon_1 - \varepsilon_3)$ response are given in Figure 7.17 (i) and (ii) respectively. The initial MCC model[18] response (shown by the dashed line) is identical (and elastic) for both of the test simulations.

[18]The MCC model constants were set as follows: $\kappa = 0.023$, $\lambda = 0.073$, $G = 18$MPa, $M = 0.688$ and $\bar{\rho}_e = 0.903$

test series	AC0005	AC2305	AC4505	AC6705	AC9005	IC0005	IC9005
$\alpha_{d\sigma}$	0°	15°	30°	55°	90°	0°	90°
$\Delta\sigma_r$	0	0	0	0	0	0	0
$\Delta\sigma_\theta$	+1	+1.732	+0.577	-0.364	-1	+1	-1
$\Delta\sigma_z$	-1	-1.732	-0.577	+0.364	+1	-1	+1
$\Delta\sigma_{z\theta}$	0	+1	+1	+1	0	0	0

Table 7.12: HCA test series stress path directions (-ve indicates compression and +ve tension).

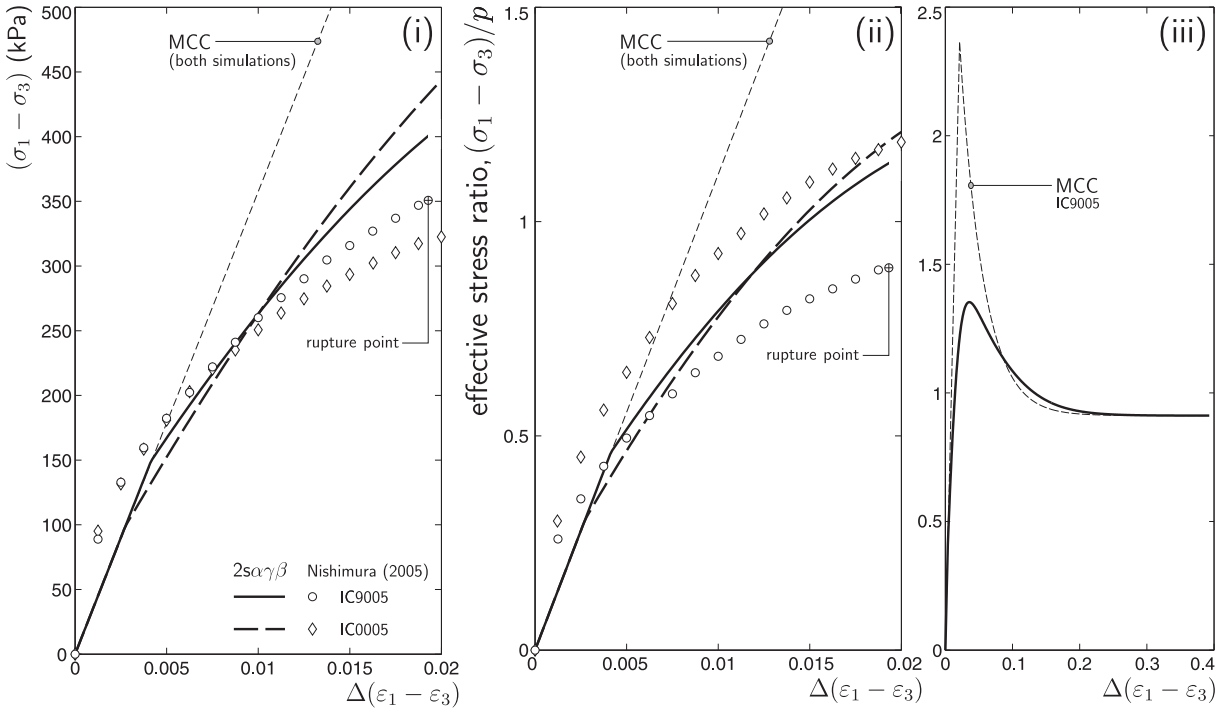

Figure 7.17: Hollow cylinder isotropic test simulations for the two-surface anisotropic model (2s$\beta\alpha\gamma$) and the MCC model with $b = 0.5$: (i) $(\sigma_1 - \sigma_3)$ versus $\Delta(\varepsilon_1 - \varepsilon_3)$ response, (ii) effective stress ratio versus $\Delta(\varepsilon_1 - \varepsilon_3)$ response and (ii) effective stress ratio versus $\Delta(\varepsilon_1 - \varepsilon_3)$ displacement-controlled response for IC9005. Experimental data by Nishimura [28] shown as discrete points.

The two-surface model produces a different response depending on the stress path direction[19] and is able to qualitatively capture the non-linearity seen in the experimentally recorded behaviour.

In order to extend the single-element FE simulations by shearing to a CS, the isotropic tests were further examined by undertaking a (single-element) displacement-controlled simulation. The following procedure was used within each loadstep to ensure that the appropriate stress path was captured:

(i) displace the top face by a given displacement increment;

(ii) use the standard FE procedure to arrive at nodal forces and displacements;

(iii) calculate the axial stress σ_z based on the nodal reactions on the top face;

(iv) calculate the appropriate circumferential stress and modify the external force vector $\{f^{\text{ext}}\}$; and

[19]Note, that the IC0005 test corresponds to axial compression whereas the IC9005 test corresponds to axial extension, with the circumferential stress maintaining a constant mean stress.

(v) repeat steps (ii)-(iv) until the normalised residual out-of-balance force, given by (3.42), converges to within the specified tolerance (in this case 1×10^{-9}).

The top face was displaced by 20% of the height of the element, in 500 equal loadsteps. Due to the external force vector continuously changing, the number of iterations required to reach convergence typically exceeded 50.

The effective stress ratio versus $\Delta(\varepsilon_1 - \varepsilon_3)$ IC9005 simulation response for the anisotropic two-surface model and the MCC model are given in Figure 7.17 (iii). As seen in the over-consolidated triaxial test simulations (for example Figure 6.28, Chapter 6), the MCC model predicts a significantly higher peak effective stress ratio than the two-surface anisotropic model. This is due to the stress paths being initially heavily over-consolidated on the *dry-side* of the CSL[20]. Both the MCC and the 2s$\beta\alpha\gamma$ model converge to the same effective stress ratio on the CSL but their paths to arrive at this state are quite different.

Experimental data on LC from Nishimura [28] for the anisotropic (AC) test series are shown in Figure 7.18. The responses of the MCC model and the two-surface anisotropic model are shown by the dashed and solid thick lines respectively. The MCC model significantly overestimates both the stress deviator $(\sigma_1 - \sigma_3)$ and the effective stress ratio $((\sigma_1 - \sigma_3)/p)$ for all of the simulations. Again, the two-surface anisotropic model qualitatively captures the main features of the non-linear experimental behaviour and provides a significant improvement over the MCC model.

Figure 7.19 shows the response of the two-surface anisotropic model in terms of the difference between the principal stresses and the axial and circumferential stresses (where compressive stresses are positively valued) versus the effective hydrostatic pressure for the undrained shear stage of the five AC tests. Although the total pressure remains constant, the effective pressure increases as the stress moves towards the CS. Those tests undergoing compressive ($\alpha_{d\sigma} = 0°$, 15° and 30°) and tensile ($\alpha_{d\sigma} = 55°$ and 90°) shear can now be clearly identified[21].

It should be emphasised that the same material constants have been used to simulate the entire stress history of the material, from deposition and consolidation through to erosion and re-loading with overburden, followed by the undrained HCA simulations. A constitutive model's ability to reproduce a soil's complete load history is an essential requirement of a material model (Gudehus [19]). The two-surface anisotropic model was calibrated using the triaxial test data and then the other tests simulated without adjusting the material constants (or initial parameters). However, the stress (and strain) distribution through the wall of the hollow cylinder is not uniform. When initially performing these analyses, it was not immediately clear whether this might explain some of the differences between the single-element simulations and the experimental data. This is further explored in the next sub-section.

7.4.3 Structural HCA simulations

Here, the AC0005 and AC9005 tests are analysed using a multi-element model of the HCA specimen, rather than a single element model (which assumes uniform stress and strain fields within the hollow cylinder). The stresses are applied by controlling the internal (p_i) and external (p_o) pressures, axial load (W) and applied torque (M_T). Rearranging the average stress equations provided by Hight *et al.* [21], we obtain the external forces as

$$M_T = \frac{2\pi(r_o^3 - r_i^3)\sigma_{z\theta}}{3} \qquad \text{and} \qquad W = \pi(r_o^2 - r_i^2)\Big(\sigma_z - \sigma_r/2 - \sigma_\theta/2\Big), \tag{7.15}$$

where r_i and r_o are the internal and external cylinder radii.

[20] Similar behaviour was observed in Chapter 5, Section 5.5, where the MCC model overestimated the peak deviatoric stress compared with experimental data on LCT from Gens [17].

[21] Here, the terms *compressive* and *tensile shear* are associated with those tests that cause an increase and decrease in the axial stress, σ_z.

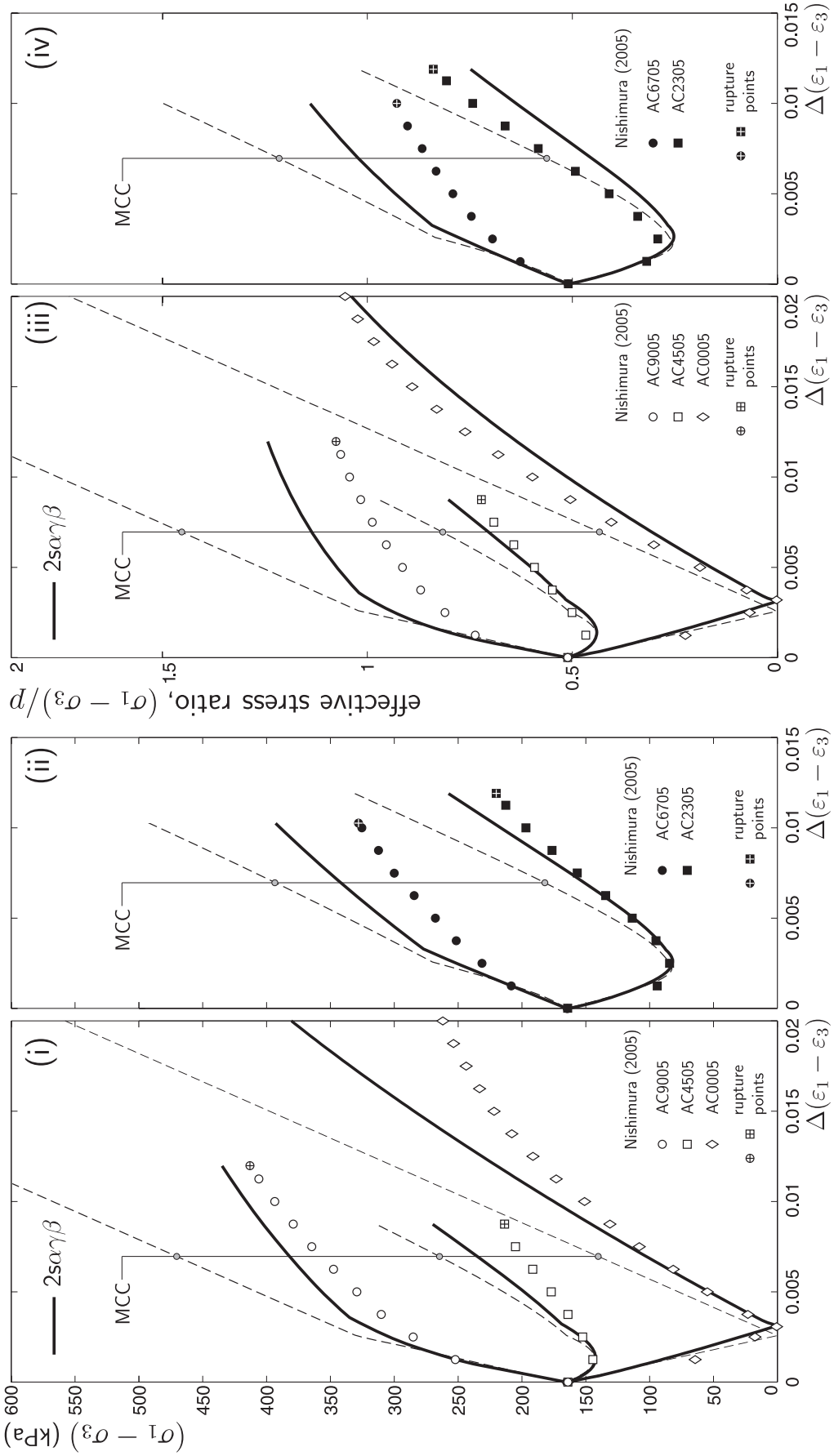

Figure 7.18: HCA AC test simulations: (i) and (ii) $(\sigma_1 - \sigma_3)$ versus $\Delta(\varepsilon_1 - \varepsilon_3)$ response, (iii) and (iv) effective stress ratio versus $\Delta(\varepsilon_1 - \varepsilon_3)$ response.

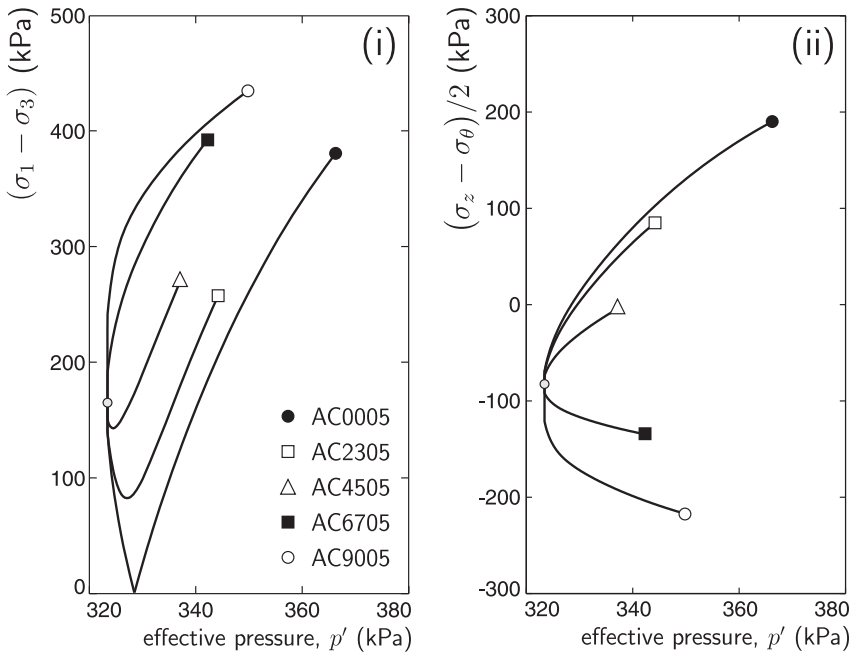

Figure 7.19: Hollow cylinder anisotropic test simulations for the two-surface anisotropic model (2s$\beta\alpha\gamma$) with $b = 0.5$: (i) $(\sigma_1 - \sigma_3)$ versus effective pressure response and (ii) $(\sigma_z - \sigma_\theta)$ versus effective pressure response.

The pressures are

$$p_i = \frac{\sigma_r(r_o + r_i) - \sigma_\theta(r_o - r_i)}{2r_i} \qquad \text{and} \qquad p_o = \frac{\sigma_r(r_o + r_i) + \sigma_\theta(r_o - r_i)}{2r_o} \,. \tag{7.16}$$

The average normal strain measures, also provided by Hight *et al.* [21], are given by

$$\varepsilon_z = \frac{w}{l} \,, \qquad \varepsilon_r = \frac{u_o - u_i}{r_o - r_i} \qquad \text{and} \qquad \varepsilon_\theta = \frac{u_o + u_i}{r_o + r_i} \,, \tag{7.17}$$

where u_i and u_o are the internal and external radial displacements at the centre of the hollow cylinder respectively and w is the vertical displacement of the top of the HCA. The average shear strain is

$$\varepsilon_{\theta z} = \frac{2\theta_c(r_o^3 - r_i^3)}{3l(r_o^2 - r_i^2)} \,, \tag{7.18}$$

where θ_c identifies the the angular circumferential displacement.

The model state, following stages (i) and (ii) of the full material history path (as given in Section 7.4.2), was still determined by means of a single material point analysis. The material condition following these stages became the starting condition for all of the Guass points in the multi-element FE discretisation. The subsequent undrained stages were conducted using an axial symmetric FE discretisation of the HCA implemented in Fortran90. The HCA had an internal radius of $r_i = 19$mm, external radius of $r_o = 35.5$mm and a height of $l = 190$mm (see Nishimura [28], p. 61). The axial load acted as the driving variable for these FE simulations.

The hollow cylinder was discretised using 250 eight-noded quadrilateral elements with reduced four-point Gaussian quadrature, as shown in Figure 7.20 (ii). Due to symmetry (both cylindrical and vertical) only one quarter of a vertical cut through the hollow cylinder was modelled. The end ring of the HCA was modelled using ten isotropic elastic eight-noded quadrilateral elements (again using reduced four-point

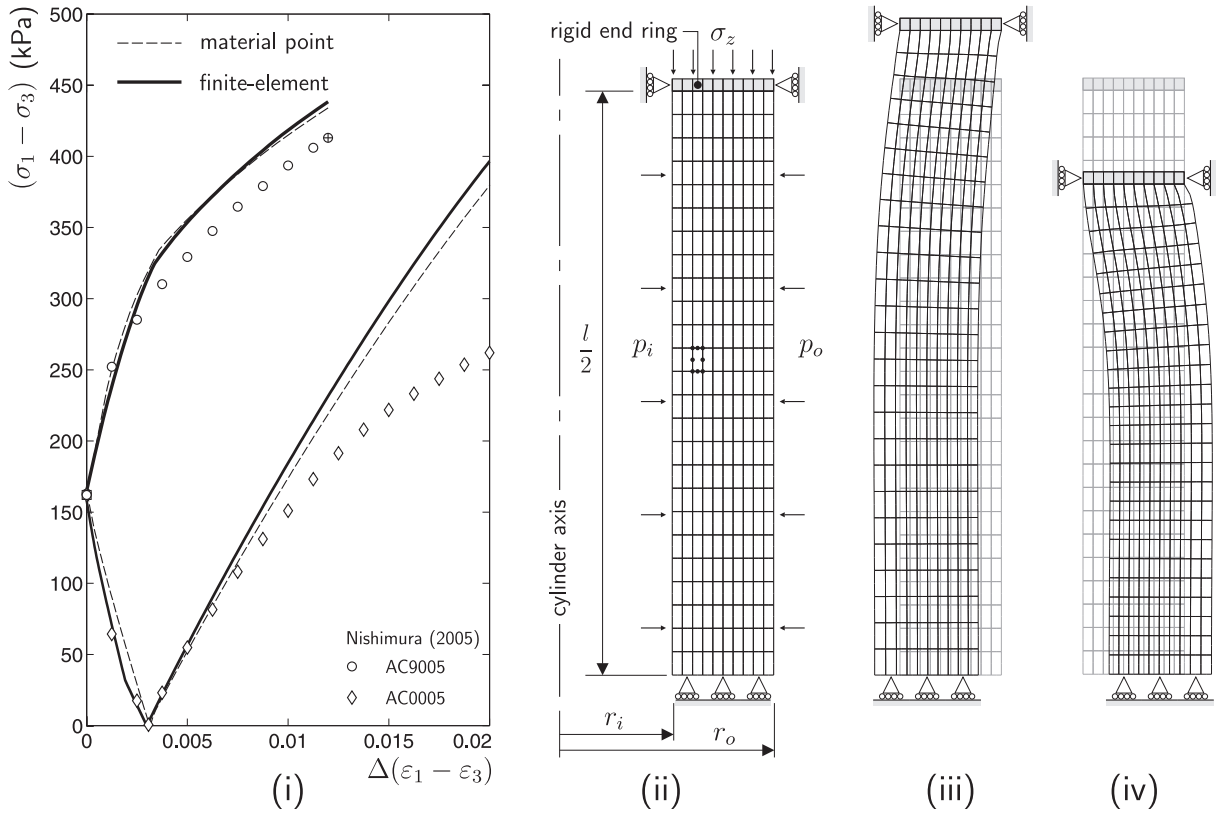

Figure 7.20: Hollow cylinder anisotropic test simulations: (i) $(\sigma_1 - \sigma_3)$ versus $\Delta(\varepsilon_1 - \varepsilon_3)$ response, (ii) FE analysis geometry and discretisation, (iii) AC90005 deformed mesh and (iv) AC0005 deformed mesh (both using a $\times 10$ scaling on the nodal displacements).

Gaussian quadrature) with a Young's modulus of 100GPa and Poisson's ratio of 0.2. This stiff end ring was constrained in the radial direction and had full displacement compatibility at the interface with the clay[22]. An axial load was applied to the top surface of the stiff ring which ensured a uniform displacement at the top of the LC hollow cylinder.

Figure 7.20 (i) shows the $(\sigma_1 - \sigma_3)$ versus $\Delta(\varepsilon_1 - \varepsilon_3)$ response for the multi-element simulation, the material point analysis reported in the preceding section and the experimental data (shown by discrete points) from Nishimura [28]. The multi-element FE results appear very similar to those of the material point analyses. However, the initial response of the multi-element response is marginally stiffer and softer (than the single-element response) for tests AC0005 and AC9005 respectively due to the stress state of the Gauss points following the change in the intermediate principal stress ratio, b (stage (iii) of the tests). The stress response for all 1,000 Gauss points, as b changed from 1 to 0.5, is shown in Figure 7.21 (i) by the grey lines. The global multi-element response, from A to B, is shown by the thick black line. The distribution of the stress deviator, $(\sigma_1 - \sigma_3)$, through the hollow cylinder wall at the end of stage (iii) is shown in Figure 7.21 (ii). There is a variation of more than 35kPa for $(\sigma_1 - \sigma_3)$ from the average value of 165kPa. These differences in the state at the start of the undrained shearing cause the stiffer (under compression) and softer (under extension) responses when compared against the uniform stress state material point simulations (Figure 7.20 (i)).

[22]That is, no relative movement was allowed on the interface between the end ring and the clay cylinder.

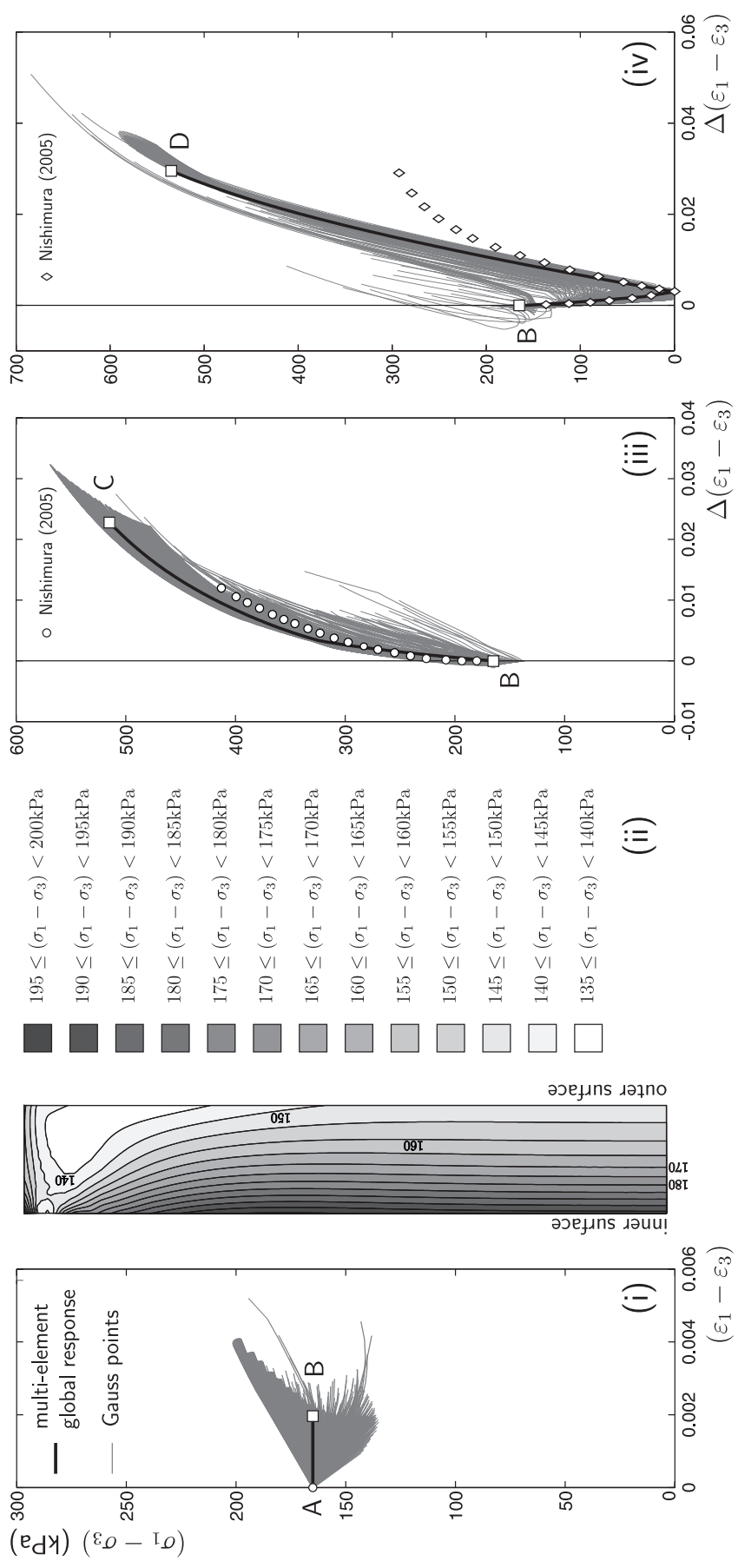

Figure 7.21: Hollow cylinder anisotropic test simulations Gauss point stress paths: (i) FE simulation of stages two and three, (ii) stress deviator $(\sigma_1 - \sigma_3)$ distribution through the cylinder wall, (iii) AC9005 undrained shearing and (iv) AC0005 undrained shearing.

The original and deformed meshes are shown in Figures 7.20 (iii) and (iv) for the AC9005 and AC0005 simulations respectively. The nodal displacements were exaggerated by a factor of 10 to help visualise the deformed shape. Under extension (AC9005), the centre of the cylinder moves inwards, whereas under compression (AC0005) the mid-height of the hollow cylinder expands outwards.

Figures 7.21 (iii) and (iv) show the $(\sigma_1 - \sigma_3)$ versus $\Delta(\varepsilon_1 - \varepsilon_3)$ response for all of the FE Gauss points (thin grey lines) in the axial extension (AC9005) and compression (AC0005) simulations respectively. The global multi-element responses, from B to C and B to D, are shown by the thick black lines. The experimental data from Nishimura [28] are also given. There is a noticeable variation in the stress path through the HCA specimen. However, the majority of the Gauss point responses match the global response well.

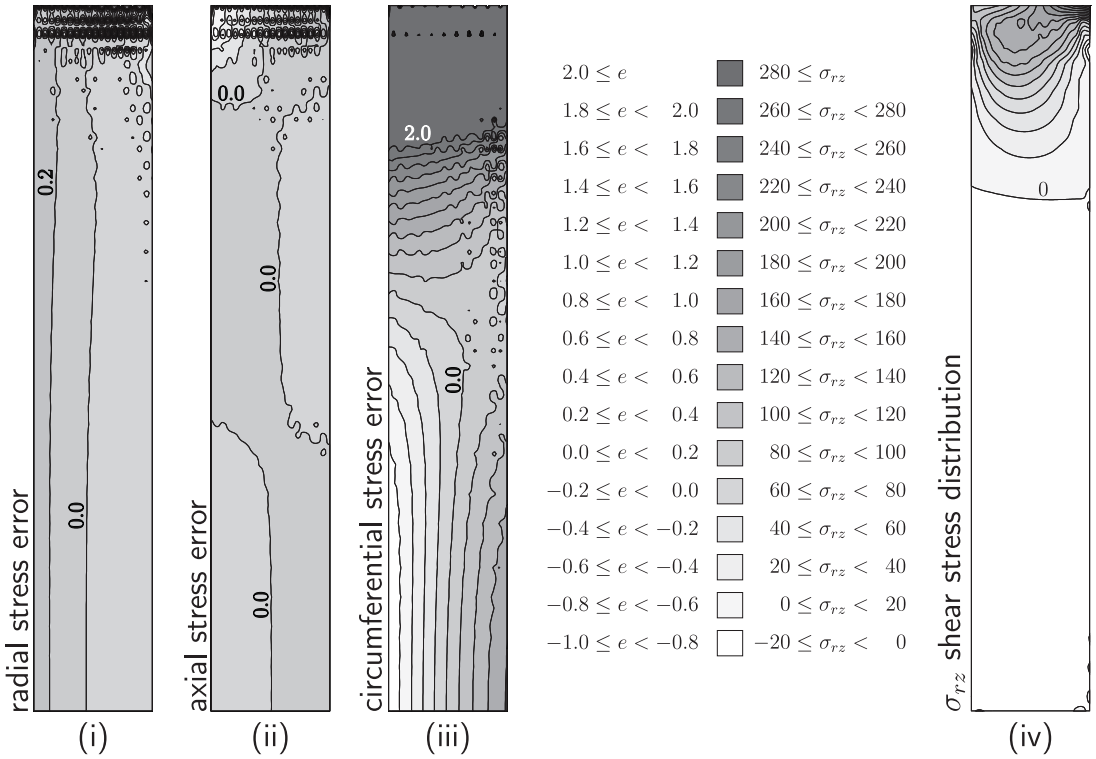

Figure 7.22: Hollow cylinder anisotropic test simulations stress distribution through the hollow cylinder wall for simulation AC0005: (i) radial stress error, (ii) axial stress error, (iii) circumferential stress error and (iv) in-plane shear stress (kPa).

One of the motivations for simulating the HCA tests using the FEM was the non-uniform stress (and strain) distribution acting through the wall of the hollow cylinder. Figure 7.22 shows the (i) radial stress error, (ii) axial stress error, (iii) circumferential stress error and (iv) in-plane shear stress. The errors were calculated from

$$\text{error}_{\sigma_{(\cdot)}} = \frac{\sigma_{(\cdot)_{FE}} - \sigma_{(\cdot)_{mp}}}{\sigma_{(\cdot)_{mp}}}, \tag{7.19}$$

where $\sigma_{(\cdot)_{FE}}$ is the finite-element Gauss point stress and $\sigma_{(\cdot)_{mp}}$ is the assumed average material point stress given by equations (7.6) and (7.7).

The term *error* is not quite appropriate. These measures are indicators of the difference between the Gauss point stresses and the idealised mid-wall, mid height stress state. The multi-element solution offers a more realistic prediction of the true stress state, thus the error lies with the simplified material point stresses. *Stress deviation* might be a better expression but that could lead to confusion with the

deviatoric stress, $\{s\}$, or the stress deviator $(\sigma_1 - \sigma_3)$. The maximum errors are located in the vicinity of the end ring. The lowest errors (that is, the closest agreement with the average material point stresses) are near the middle of the wall at the mid-height of the hollow cylinder. The single-element material point simulation assumes zero shear stress in the radial-axial plane (σ_{rz}). However, the two-dimensional axi-symmetric analysis has non-zero σ_{rz}, with the maximum shear stresses near the top (and bottom) of the hollow cylinder.

The region of lowest error is now examined in more detail. The Gauss point response for the two elements near the mid-height wall centre (Figure 7.23 (ii)) are shown in Figures 7.23 (i) and (iii). The eight Gauss points show good agreement with the initial experimental data behaviour (shown by discrete points) for both the AC0005 and AC9005 tests (similar to that of the global multi-element FE response and the average single-element material point simulation). Figure 7.23 (iii) shows the Gauss points' $(\sigma_1 - \sigma_3)/p$ versus $\Delta(\varepsilon_1 - \varepsilon_3)$ response. Again, similar behaviour to that of the global FE and the average material point simulations was seen.

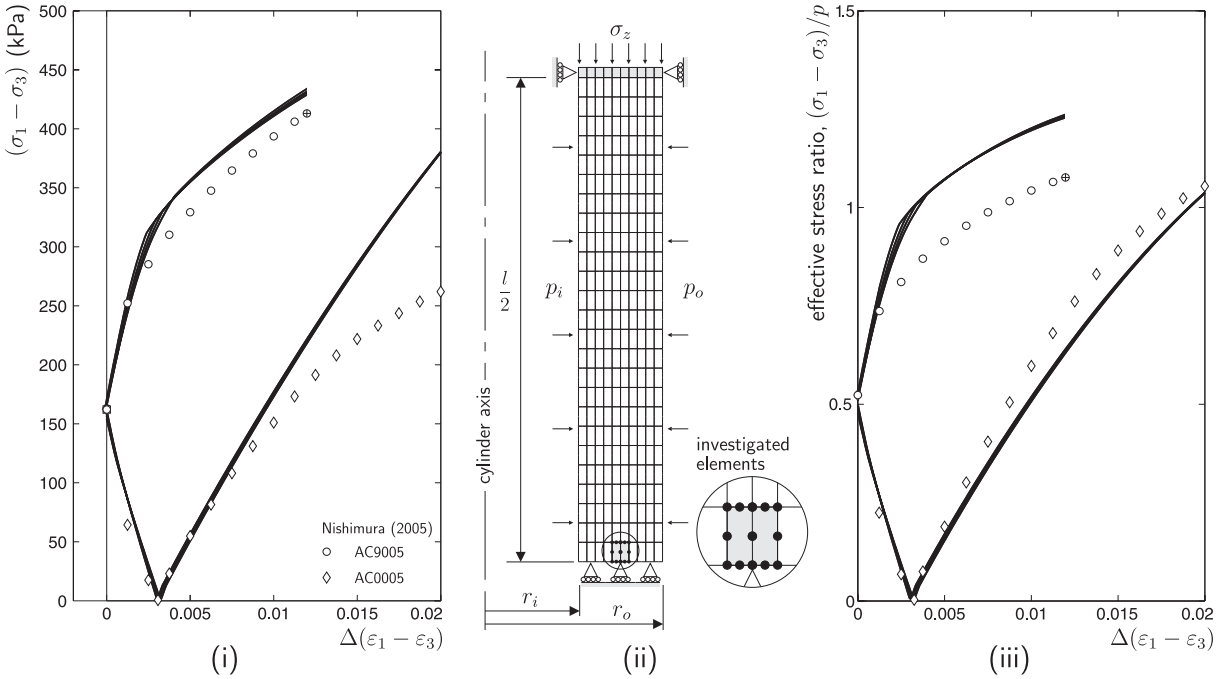

Figure 7.23: Hollow cylinder anisotropic test simulations response for the mid-wall, mid-height element Gauss points: (i) $(\sigma_1 - \sigma_3)$ versus $\Delta(\varepsilon_1 - \varepsilon_3)$ response, (ii) FE analysis investigated elements, (iii) $(\sigma_1 - \sigma_3)/p$ versus $\Delta(\varepsilon_1 - \varepsilon_3)$ response.

7.4.4 Rupture: identifying the continuum to discontinuum transition

In the HCA analysis, the experiments were only simulated up to the point of experimental *rupture*. This *rupture* point was determined visually during the LC experiments by Nishimura [28]. However, the emergence of discontinuities could only be detected on the surface of the specimens. It is probable that not all ruptures, even if on the surface, were identified immediately due to the presence of a latex membrane surrounding the hollow cylinder specimen. This change from continuum to discontinuum behaviour (where the strains localise into a narrow band) could explain the degradation of the constitutive model's predictive capability at higher strains in the HCA.

Since the 1958 and 1962 papers by Hill [22, 23], there has been a strong interest in the mathematical identification of instabilities which can be predicted purely from the characteristics of the constitutive

equations [1–4, 6, 24, 26, 29, 32–34, 38, 40]. Failure[23] indicators in materials can be grouped into two categories: continuous (or loss of stability) and discontinuous (or localisation) [32]. In continuous failure, the homogeneity of strains (and stresses) is preserved, whereas for discontinuous failure a spatial discontinuity is observed in the strain rate field. Continuous failure can be detected through investigating the infinitesimal elasto-plastic tangent, $[D^{\text{ep}}]$. The first indicator occurs when the determinant of the symmetric component of $[D^{\text{ep}}]$ falls to zero

$$\det\left(\frac{1}{2}\Big[[D^{\text{ep}}]+[D^{\text{ep}}]^T\Big]\right)=0. \tag{7.20}$$

We refer to this as a *strong* indicator of the loss of stability. The second indicator occurs when the determinant of $[D^{\text{ep}}]$ falls to zero we refer to this as a *weak* indicator of the loss of stability. These two continuous failure indicators can be expressed as

$$e_{\mathsf{A}}=\underbrace{\min\left(\frac{\det[D^{\text{ep}}_{sym}]}{\det[D^{\text{e}}]}\right)}_{\text{strong instability}}\qquad\text{and}\qquad e_{\mathsf{D}}=\underbrace{\min\left(\frac{\det[D^{\text{ep}}]}{\det[D^{\text{e}}]}\right)}_{\text{weak instability}}, \tag{7.21}$$

where $(\cdot)_{sym}$ denotes the symmetric component of $(\cdot)$. The first of these, e_{A}, is the stricter of the conditions (that is, a material will fail e_{A} before failing e_{D}). This is due to the fact that the eigenvalues of the symmetric component of a positive definite tensor bound those of the full matrix. If $[D^{\text{ep}}]$ is positive definite (that is, $\det\big([D^{\text{ep}}_{sym}]\big)>0$) then the material response is unique under any loading [24].

In a load (or equivalently stress) controlled test, we have the following relation between the rate of change of strain with stress

$$\{\dot{\varepsilon}\}=[D^{\text{ep}}]^{-1}\{\dot{\sigma}\}. \tag{7.22}$$

When the determinant of the infinitesimal elasto-plastic tangent falls to zero, $\{\dot{\varepsilon}\}$ is undefined and a loss of uniqueness of the strain solution occurs [24], as shown in Figure 7.24. Under strain (or displacement) controlled simulations, we have an equivalent relation to that of the stress controlled test, however now

$$\{\dot{\sigma}\}=[C^{\text{ep}}]^{-1}\{\dot{\varepsilon}\}. \tag{7.23}$$

Here $[C^{\text{ep}}]=[D^{\text{ep}}]^{-1}$ is the infinitesimal elasto-plastic compliance matrix. A loss of uniqueness occurs when the determinant of $[C^{\text{ep}}]$ falls to zero [24], that is when

$$\{f_{,\sigma}\}^T\big[D^{\text{e}}\big]\{g_{,\sigma}\}+H=0. \tag{7.24}$$

in a non-associated, hardening elasto-plastic material (see (2.23), Chapter 2 for the format of the infinitesimal elasto-plastic tangent stiffness matrix). This condition corresponds to a *snap-back* in the stress versus strain response of the material, as shown by point E in Figure 7.24.

Discontinuous failure indicators grew out of the work by Hill [23] on acceleration waves. Hill considered planes (with unit normal denoted by n_i or $\{n\}$) across which the acceleration was discontinuous. This jump in acceleration is equivalent to a jump in the strain rate (and consequently the stress rate) in a material's constitutive relations [23]. Using Hill's procedure, a localisation (or acoustic) tensor can be defined as

$$(Q^{(\cdot)}_{at})_{jk}=n_iD^{(\cdot)}_{ijkl}n_l, \tag{7.25}$$

[23]Here, the term failure is used to describe when the material no longer behaves as a continuum, that is, some loss of stability or bifurcation of the material has taken place.

where $D^{(\cdot)}_{ijkl}$ is the fourth-order tangent stiffness tensor under consideration. Alternatively (7.25) can be expressed in matrix form using the following expression

$$\left[Q^{(\cdot)}_{at}\right] = \left[T\right]^T \left[D^{(\cdot)}\right] \left[T\right], \qquad \text{where} \qquad \left[T\right]^T = \begin{bmatrix} n_1 & 0 & 0 & 0 & n_3 & n_2 \\ 0 & n_2 & 0 & n_3 & 0 & n_1 \\ 0 & 0 & n_3 & n_2 & n_1 & 0 \end{bmatrix}, \tag{7.26}$$

and n_i are the components of the normal to the potential discontinuity plane. The acoustic tensor allows us to specify two indicators of localisation

$$e_{\mathsf{B}} = \underbrace{\min\left(\frac{\det[Q^{\mathrm{ep}}_{at_{sym}}]}{\det[Q^{\mathrm{e}}_{at}]}\right)}_{\text{strong localisation}} \qquad \text{and} \qquad e_{\mathsf{C}} = \underbrace{\min\left(\frac{\det[Q^{\mathrm{ep}}_{at}]}{\det[Q^{\mathrm{e}}_{at}]}\right)}_{\text{weak localisation}}. \tag{7.27}$$

$[Q^{\mathrm{ep}}_{at}]$ and $[Q^{\mathrm{e}}_{at}]$ denote the acoustic tensors associated with $[D^{\mathrm{ep}}]$ and $[D^{\mathrm{e}}]$ using the same search direction n_i. For the case of associated plasticity, $[D^{\mathrm{ep}}]$ is symmetric and the localisation indicators e_{B} and e_{C} are identical, as are e_{A} and e_{D}.

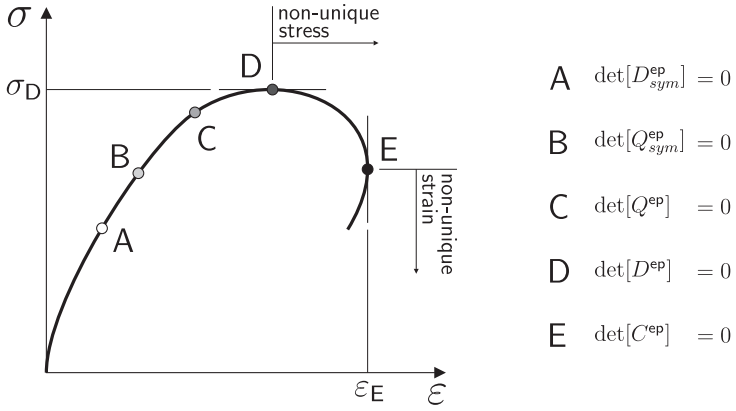

Figure 7.24: Hierarchy of failure indicators.

The Bromwich bounds [8] allows the sequence of failure indicators to be established. e_{A} is the strictest condition, followed by e_{B}, then e_{C} and finally e_{D} [37]; shown schematically in Figure 7.24. The determinant of $[C^{\mathrm{ep}}]$ drops to zero at point E in Figure 7.24 after passing through the non-unique stress point, D.

London Clay one-dimensional stability

The stability indicators were used when examining LC under drained uniaxial straining (K_0 loading) to a pressure of 290kPa, followed by unloading to a pressure of 20kPa in axial strain increments of size 1×10^{-4}. The constitutive model's hydrostatic pressure versus deviatoric stress response (with material constants given in Table 6.1, a reference pressure of 30kPa and an initially isotropic material and normally consolidated hydrostatic stress state) is given in Figure 7.25 (ii). The minimum value of the normalised determinant of the acoustic tensor (as given by e_{C} in $(7.27)_2$) versus axial strain is given in Figure 7.25 (i). The values of the stability indicators at points A to G are given in Table 7.13. The HEALPix software [18], which divides the surface of a sphere into equal area patches, was used to generate the 11,040 search directions for the acoustic tensor analysis. Figure 7.25 (iii) shows the axial strain versus deviatoric stress and hydrostatic pressure paths for the loading (from A to B) and unloading (B to G).

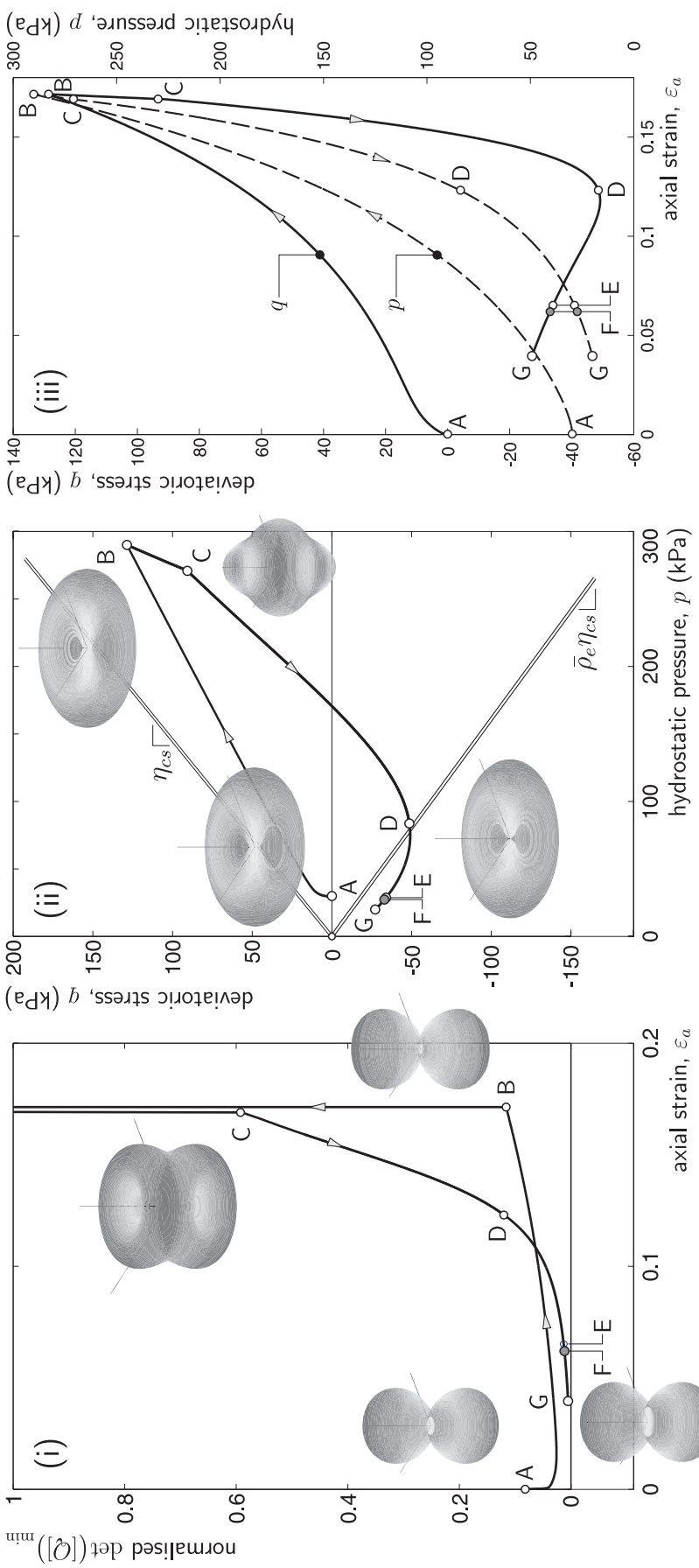

Figure 7.25: Acoustic tensor analysis of the material point behaviour of the two-surface anisotropic model using the material constants for LC under one-dimensional loading and unloading: (i) axial strain versus normalised $\det([Q])_{\min}$, (ii) hydrostatic pressure versus deviatoric stress response and (iii) axial strain versus deviatoric and hydrostatic stress.

The surface plots on Figures 7.25 (i) and (ii) illustrate two ways of visualising the determinant of the acoustic tensor. For each of the 11,040 search directions, the determinant of the acoustic tensor is calculated and a point generated from:

(i) $\{x\} = \Big(1 - e_{\mathsf{C}}\Big)\{n\}$ for Figure 7.25 (i); and

(ii) $\{x\} = e_{\mathsf{C}}\{n\}$ for Figure 7.25 (ii).

A surface is then plotted through these points. If the determinate of the acoustic tensor drops to zero then the $\{x\} = e_{\mathsf{C}}\{n\}$ surface will pass through the origin whereas the $\{x\} = \Big(1 - e_{\mathsf{C}}\Big)\{n\}$ surface will intersect a unit sphere surrounding the surface. The former surface is a more direct indicator of the reduction in e_{C} but the latter surface allows for an easier assessment of the direction of the normal to the plane across which the discontinuity occurs. These surfaces are plotted for points A, B, C and G. For all eight of these surfaces there is an obvious symmetry in about the vertical z axis. Clearly, if the global cartesian co-ordinate axes were orientated such that one of the axes did not coincide with the axis of the cylinder, then the primary symmetry would not be with respect to the z axis.

point	A	B	C	D	E	F	G
e_{A}	0.0644	0.0953	0.4038	0.0629	-0.0000	-0.0004	-0.0018
e_{B}	0.0819	0.1081	0.6481	0.1196	0.0130	0.0116	0.0050
e_{C}	0.0819	0.1081	0.6481	0.1196	0.0130	0.0116	0.0050
e_{D}	0.0650	0.0983	0.4047	0.0642	0.0004	-0.0000	-0.0016

Table 7.13: Instability analysis for the one-dimensional loading and unloading.

For the applied strain increments and selected search directions, the determinant of the symmetric and full acoustic tensor matrix never fell to (or below) zero. However, the determinant of the symmetric component of $[D^{\text{ep}}]$ falls below zero at point E and $e_{\mathsf{D}} < 0$ at point F. One possible reason for the determinant of the acoustic tensor remaining greater than zero could be an insufficient number of search directions, thereby missing the minimum $\det\big([Q^{\text{ep}}_{at}]\big)$. Alternatively, the fact that the material point simulation was followed using finite increments of strain could have meant that the points where $e_{\mathsf{B}} = 0$ and $e_{\mathsf{C}} = 0$ were missed. However, these possibilities seem unlikely due to the large number of search directions, small increments in the axial strain and the fact that all of the failure indicators continue to reduced along the unloading path.

London Clay undrained triaxial stability

An acoustic tensor analysis for UTE and UTC following one-dimensional loading and unloading is presented in Figure 7.26. The material point stress paths and axial strain versus deviatoric stress for these simulations was shown in Figure 7.15. The normalised determinant of the acoustic tensor (that is, stability measure e_{C}) versus axial strain for the UTE tests is shown in Figure 7.26 (i) and the UTC tests in Figure 7.26 (ii) and (iii). Note that the tests with OCRs of one and seven start from points B and D from Figure 7.25. Again, the determinant of the acoustic tensor never falls below zero for the UTE or the UTC tests. The two $\Big(1 - e_{\mathsf{C}}\Big)$ acoustic tensor plots in Figure 7.26 (i) and (ii) correspond to an axial strain of 0.1 for UTE and UTC, respectively, both at an OCR of 1.5. The minimum values of the four stability indicators, for the four OCRs and two loading directions, are given in Table 7.14. The points where the determinant of the symmetric and full infinitesimal elasto-plastic stiffness matrices fall below zero are identified. For all of the simulations, e_{D} falls below zero prior to arrival at the CS. This can

be seen in Figure 7.26 (iv) where the axial strain versus deviatoric stress paths are reproduced with the instability points identified.

For the UTE simulations, as the axial strain increases, so the value of e_{C} decreases and tends towards a stationary value of ≈ 0.11. For the heavily overconsolidated test (OCR= 7) e_{C} reaches a minimum value of 0.0781, at an axial strain of 0.0178, before increasing as the deformation increases. The behaviour of the normally consolidated UTC simulation was quite different from the other UTC tests, as the e_{C} value started at the minimum value along its compression path before increasing towards a stationary value at higher axial strains.

		undrained triaxial extension				undrained triaxial compression			
		$(e_{\mathsf{A}})_{\min}$	$(e_{\mathsf{B}})_{\min}$	$(e_{\mathsf{C}})_{\min}$	$(e_{\mathsf{D}})_{\min}$	$(e_{\mathsf{A}})_{\min}$	$(e_{\mathsf{B}})_{\min}$	$(e_{\mathsf{C}})_{\min}$	$(e_{\mathsf{D}})_{\min}$
OCR	1	-0.0040	0.1219	0.1219	-0.0001	-0.0122	0.1032	0.1032	-0.0067
	1.5	-0.0038	0.1178	0.1178	-0.0002	-0.0104	0.1736	0.1736	-0.0054
	4	-0.0036	0.1091	0.1091	-0.0003	-0.0088	0.1749	0.1749	-0.0045
	7	-0.0035	0.0781	0.0781	-0.0007	-0.0066	0.1648	0.1648	-0.0034

Table 7.14: UTC and UTE instability analysis: minimum stability indicator values.

While these findings are interesting, there is little interpretation which can be given to $\det\big([Q_{at}^{\text{ep}}]\big) > 0$ (however close it might be to zero). The instability analysis only allows a binary interpretation (continuum to discontinuum). However, as complex hardening/softening plasticity models generally are not constructed with specific discontinuity predictions built into the formulation, there is merit in mapping the field of $\det\big([Q_{at}^{\text{ep}}]\big)$ with respect to the stress state and degree of anisotropy such that a greater understanding can be gained on the relationship between the form of the model and its stability. There is no unique stress-space map of $\det\big([Q_{at}^{\text{ep}}]\big)$ for the two-surface plasticity model as $[D^{\text{ep}}]$ depends on both $\{\beta\}$ and $\{\sigma^{\chi}\}$.

Throughout all of this subsection's analyses the infinitesimal elasto-plastic tangent matrix had the following form

$$[D^{\text{ep}}] = \begin{bmatrix} [\hat{D}^{\text{ep}}] & [0] \\ [0] & G[1] \end{bmatrix}, \qquad \text{where} \qquad [\hat{D}^{\text{ep}}] = \begin{bmatrix} a & c & e \\ c & a & e \\ d & d & b \end{bmatrix} \tag{7.28}$$

and G is the shear modulus. The symmetry of the top two by two block of $[\hat{D}^{\text{ep}}]$ is due to the radial and circumferential components of $\{\sigma\}$ and $\{\beta\}$ being equal (that is, $\sigma_2 = \sigma_3$ and $\beta_2 = \beta_3$, with an axial major component). This also explains why we see the equal terms d and e in the third row and column respectively. The axial symmetry of the acoustic tensor plots (see in Figures 7.25 and 7.26) are a direct consequence of the symmetry in the infinitesimal elasto-plastic stiffness matrix.

London Clay HCA stability

The final analysis in this chapter explorers the stability of the anisotropic HCA simulations. In particular, the AC9005 and AC0005 material point tests were assessed.

The $\Delta(\varepsilon_1 - \varepsilon_3)$ versus e_{C} responses for the material point simulations are shown in Figure 7.27. The points at which the four stability indicators fall below zero are identified for the two tests. The strain difference $\Delta(\varepsilon_1 - \varepsilon_3)$ at these points is listed in Table 7.15. For AC0005 (dashed line in Figure 7.27) the failure indicators drop below zero in pairs. In AC9005 the four failure indicators appear in the same order as given in Figure 7.24, that is $e_{\mathsf{A}} \leq 0$ first, then $e_{\mathsf{B}} \leq 0$ followed by $e_{\mathsf{C}} \leq 0$ and finally $e_{\mathsf{D}} \leq 0$. For

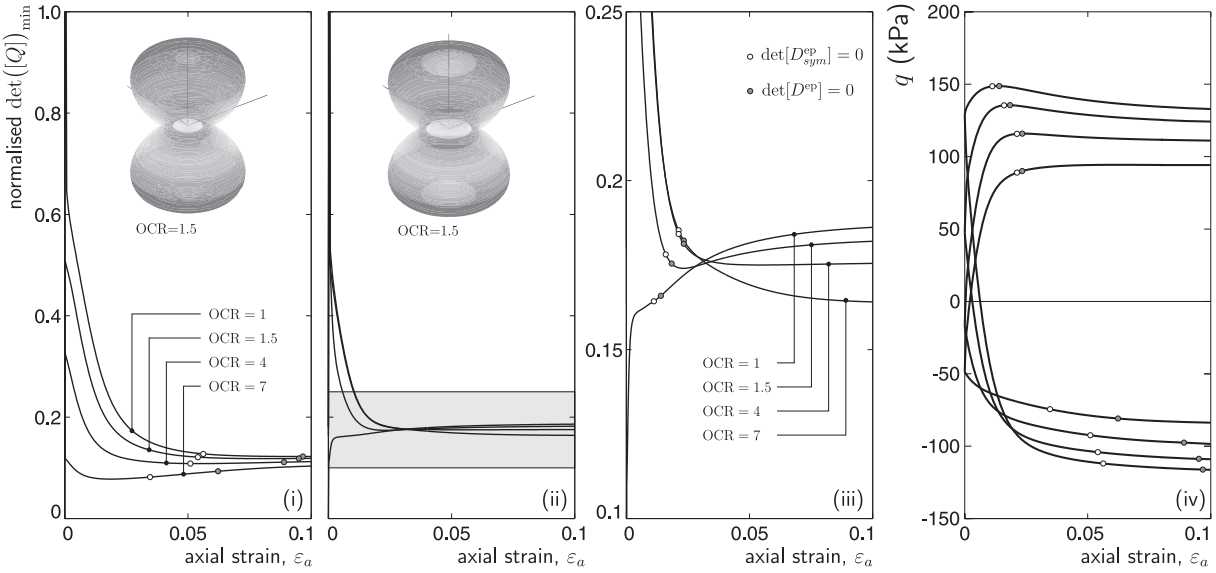

Figure 7.26: Acoustic tensor analysis of the material point behaviour of the two-surface anisotropic model under (i) UTE, (ii) and (iii) UTC. (iv) gives the axial strain versus deviatoric stress response for all of the simulations.

both of the simulations the instabilities develop at a higher strain than the rupture surfaces were first detected experimentally ($\Delta(\varepsilon_1 - \varepsilon_3) = 0.0289$ for AC0005 and $\Delta(\varepsilon_1 - \varepsilon_3) = 0.0120$ for AC9005) [28].

	$e_{\mathsf{A}} < 0$	$e_{\mathsf{B}} < 0$	$e_{\mathsf{C}} < 0$	$e_{\mathsf{D}} < 0$	$\{n\}_{e_{\mathsf{C}}=0}$	$\{m\}_{e_{\mathsf{C}}=0}$	$\{n\}^T\{m\}$
	$\Delta(\varepsilon_1 - \varepsilon_3)$	$\Delta(\varepsilon_1 - \varepsilon_3)$	$\Delta(\varepsilon_1 - \varepsilon_3)$	$\Delta(\varepsilon_1 - \varepsilon_3)$			mode
AC0005	0.0497	0.0497	0.0522	0.0522	$\left\{\begin{matrix} 0.0 \\ \pm 0.8 \\ \pm 0.6 \end{matrix}\right\}$	$\pm\left\{\begin{matrix} \pm 0.0000 \\ 0.7649 \\ \pm 0.6442 \end{matrix}\right\}$	-0.225
AC9005	0.0492	0.0525	0.0689	0.0810	$\left\{\begin{matrix} \pm 0.0202 \\ \pm 0.6170 \\ \pm 0.7867 \end{matrix}\right\}$	$\pm\left\{\begin{matrix} \pm 0.0022 \\ \pm 0.6723 \\ \pm 0.7402 \end{matrix}\right\}$	-0.167

Table 7.15: HCA undrained shear single finite-element instability analysis.

The $\det([Q^{ep}_{at}])$ acoustic tensor surfaces are shown in Figure 7.27 at the point where e_{C} falls below zero. It can be seen in both of the surface plots that in at least direction the determinant falls below zero. However, it is not easy to identify all of the directions where $e_{\mathsf{C}} \leq 0$ on these three-dimensional plots. To clarify this it is helpful to plot the normalised determinant of the acoustic tensor in a different way. Figure 7.28 contours the acoustic tensor surfaces in terms of their latitude and longitude. Using this projection, the search direction is given by

$$\{n\} = \Big\{\cos(\phi_{hp})\sin(\theta_{hp}) \qquad \sin(\phi_{hp})\sin(\theta_{hp}) \qquad \cos(\theta_{hp})\Big\}^T, \tag{7.29}$$

where $\theta_{hp} \in [0, 2\pi]$ and $\phi_{hp} \in [0, 2\pi]$ uniquely define the search direction. Plotting the stability measure, e_{C}, in terms of ϕ_{hp} and $z = \cos(\theta_{hp})$ allows the instability points to be easily identified. From Figure 7.28 we see that the AC0005 and AC9005 material point simulations develop four and eight instability locations (as identified using the crossed-through symbols) where $e_{\mathsf{C}} \leq 0$ respectively.

The search directions where the minimum value of e_{C} was found for the two simulations are given in

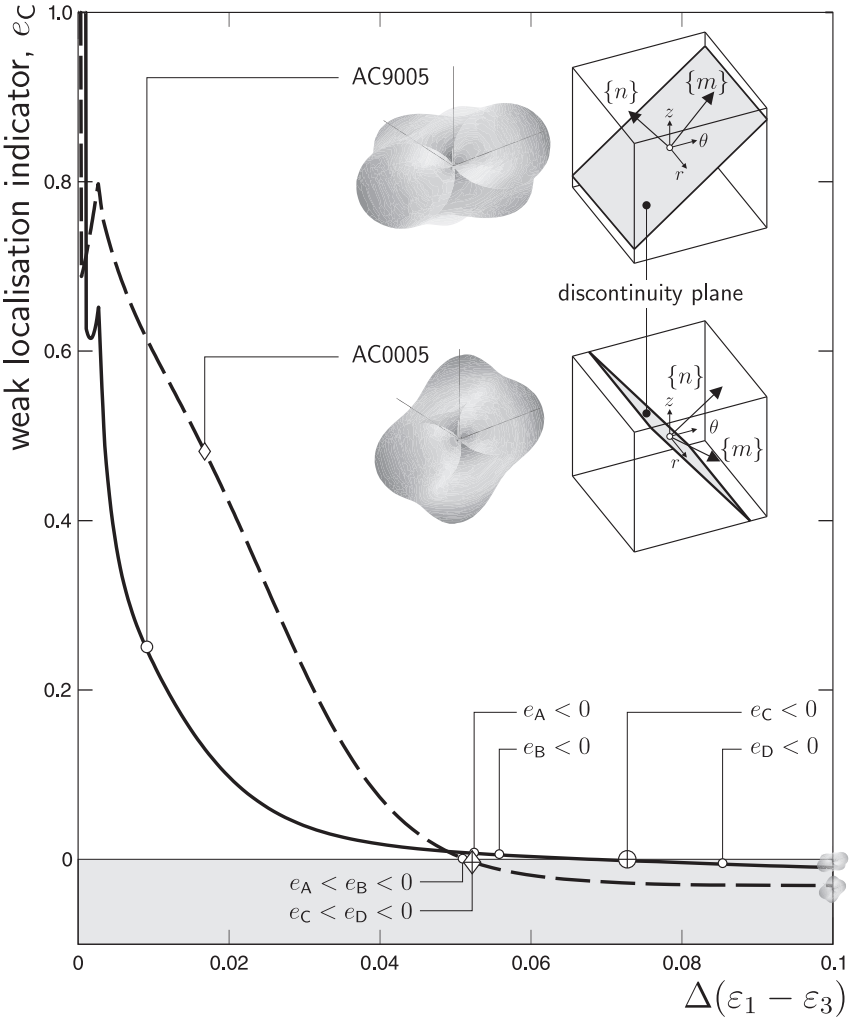

Figure 7.27: Acoustic tensor analysis for the HCA undrained shear single finite-element simulation.

Table 7.15. These directions are normal to the plane of instability (as shown for one of the instability planes on the right hand side of Figure 7.27). Due to symmetry, these four/eight normals correspond to two/four instability planes. The discontinuity planes are shown in Figure 7.29. For the AC0005 simulations the radial coordinate axis lies in the bifurcation plane (that is, $\{n\}^T\{1 \quad 0 \quad 0\} = 0$), whereas the AC9005 normals have a small radial coordinate component. Unexpectedly, the z and θ components in the AC0005 and AC9005 test normals, respectively, have almost equal components, where the slight variation is possibly due to the initial starting conditions.

Following the procedure of Borja and Aydin [6], comparing the search direction, $\{n\}$, with the eigenvector associated with the minimum eigenvalue of $[Q_{at}^{\text{ep}}]$ (denoted here by $\{v_{\min}\}$), we can determine the mode of the discontinuity,as follows

$$\text{mode} = \{n\}^T\{v_{\min}\}: \quad \begin{array}{ll} = -1 & \text{pure compaction band} \\ < 0 & \text{compactive shear band} \\ = 0 & \text{simple shear band} \quad (\equiv \text{fracture mode II or III}) \\ > 0 & \text{dilative shear band} \\ = 1 & \text{pure dilation band} \quad (\equiv \text{fracture mode I: opening}) \end{array} \tag{7.30}$$

The direction of the eigenvector associated with the minimum eigenvalue, $\{v_{\min}\}$, can be positive or

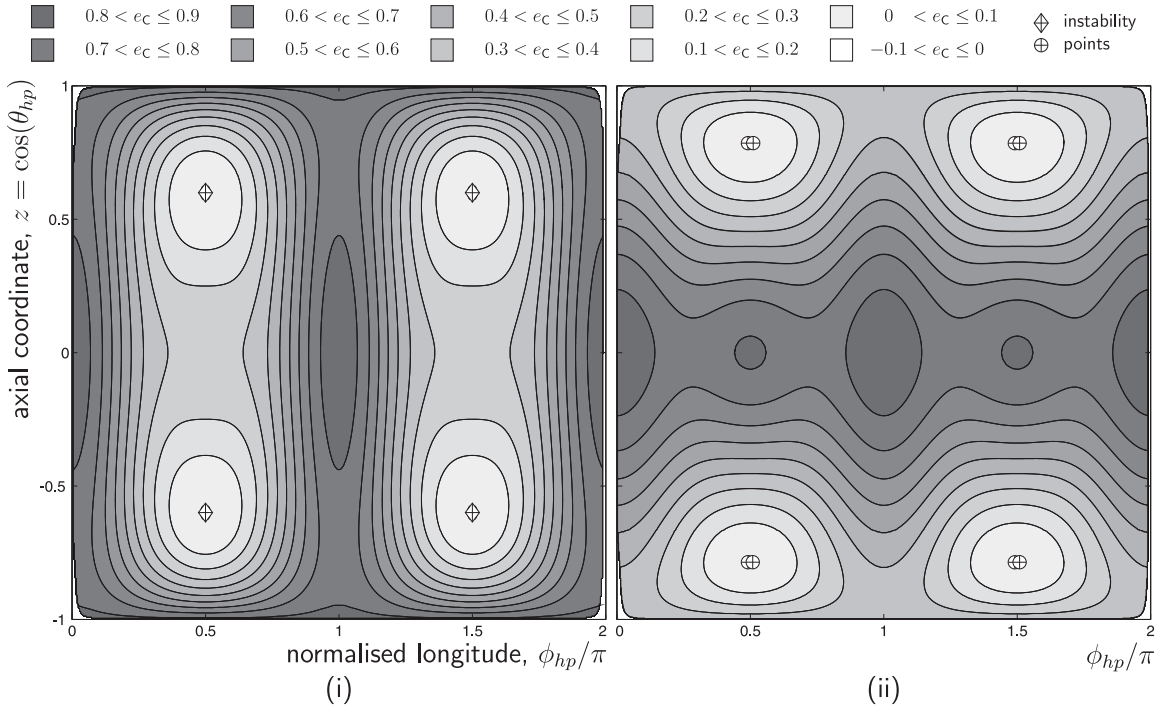

Figure 7.28: Unfolded acoustic tensor surfaces for the HCA simulations (i) AC0005 and (ii) AC9005.

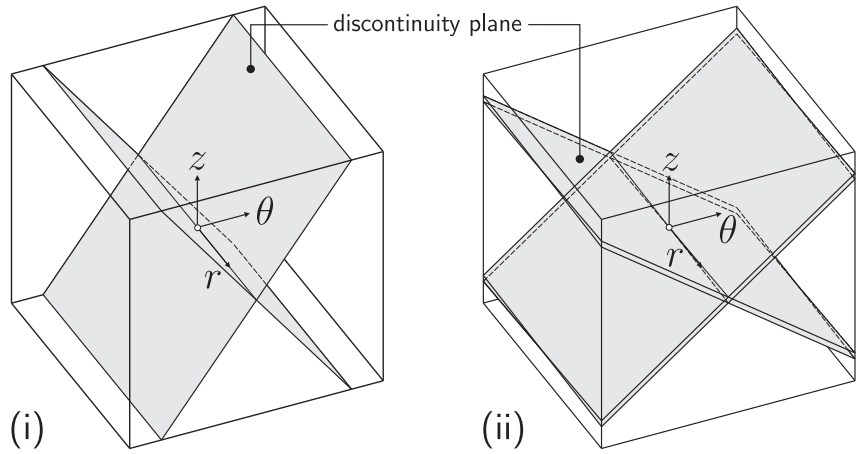

Figure 7.29: Discontinuity planes for the undrained shear HCA simulations (i) AC0005 and (ii) AC9005.

negative. Following the procedure of Borja and Aydin, the direction of $\{v_{\min}\}$ can be determined from the requirement that

$$\{f_{,\sigma}\}^T[D^e]\{\xi\} > 0, \qquad \text{where} \qquad [\xi] = \{v_{\min}\}\{n\}^T. \tag{7.31}$$

$\{\xi\}$ is the instability *characteristic* vector, whose trace is equivalent to the mode defined in (7.30) (that is, $\text{tr}[\xi] = \{v_{\min}\}^T\{n\}$), where $\{\xi\}$ is formed from $[\xi]$ in the same manner as $[\sigma]$ is expressed as $\{\sigma\}$. The inequality in (7.31) stems from the assumption that the material is exhibiting some inelastic behaviour on both sides of the instability plane. Using $(7.31)_1$ the mode of the discontinuities were determined for tests AC0005 and AC9005 as -0.225 and -0.167 respectively. Both simulations exhibit dilative shear bands, with the dilative plastic strains at the point on the yield surface[24], although the bands occur at different orientations through the samples. The stress state and yield surfaces at the computationally

[24]That is, the image point on the outer surface is located on the *dry side* of the Critical State line.

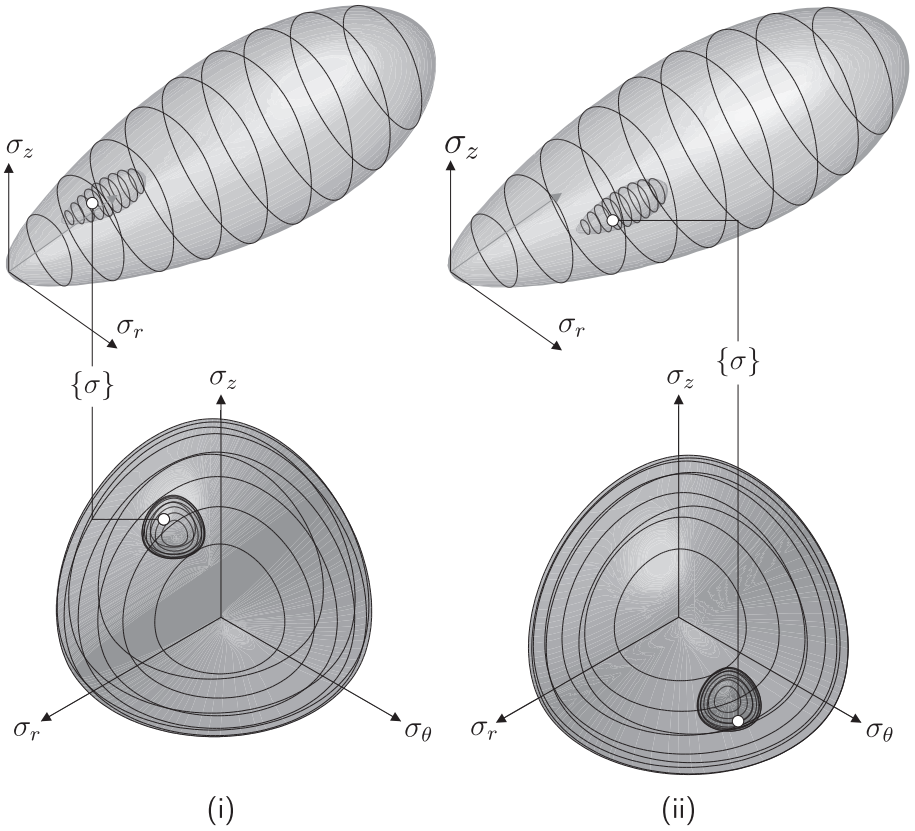

Figure 7.30: Stress state and yield surfaces for the two-surface anisotropic model at point of instability development for the (i) AC0005 ($\Delta(\varepsilon_1 - \varepsilon_3) = 0.0522$) and (ii) AC9005 ($\Delta(\varepsilon_1 - \varepsilon_3) = 0.0689$) HCA analyses.

determined point of rupture ($e_C \leq 0$) are shown in Figure 7.30 for (i) AC0005 ($\Delta(\varepsilon_1 - \varepsilon_3) = 0.0522$ with $\eta = 0.823$) and (ii) AC9005 ($\Delta(\varepsilon_1 - \varepsilon_3) = 0.0689$ with $\eta = 0.824$).

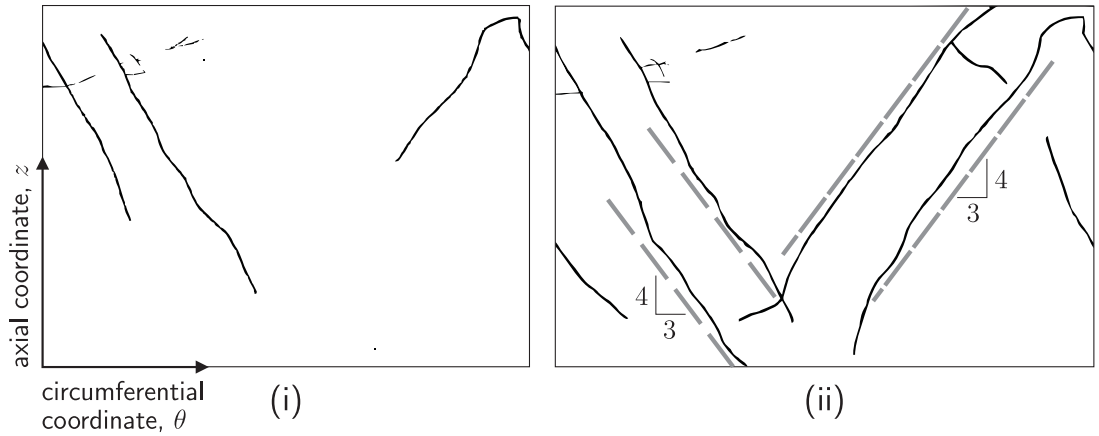

Figure 7.31: Discontinuity planes for the anisotropic undrained shear HCA AC0005 test in the z-θ plane: comparison of experimentally observed bifurcation planes on LC at (i) $\Delta(\varepsilon_1 - \varepsilon_3) = 0.058$ and (ii) $\Delta(\varepsilon_1 - \varepsilon_3) = 0.11$ from Nishimura [28] (reproduced from p. 263). Dashed lines indicate computationally predicted planes at $\Delta(\varepsilon_1 - \varepsilon_3) = 0.0522$ (where e_C first drops below zero).

The orientation of the discontinuities for AC0005 are compared with the experimentally observed rupture planes observed on LC by Nishimura [28] at strains of $\Delta(\varepsilon_1 - \varepsilon_3) = 0.058$ and $\Delta(\varepsilon_1 - \varepsilon_3) = 0.11$

in Figures 7.31 (i) and (ii)[25]. The computationally predicted discontinuity orientations, also shown on Figure 7.31 (ii), show good agreement with the experimentally observed rupture surfaces. The deviation of the experimentally recorded slip bands, near the top and bottom of the plots, is a consequence of the end constraints acting on the specimen.

It is important to note that the hyperplastic two-surface anisotropic model was not constructed from an *a-priori* assumption about the material instabilities. While these HCA instability results are far from comprehensive or conclusive, they do serve as an encouraging indicator of model performance. Further work is required to understand more completely the role of the inner surface and the form of anisotropic hardening/softening on the stability of the model. Additionally, more work is required on the use of advanced experimental imaging techniques to monitor the emergence of rupture surfaces during testing.

7.5 Observations

This chapter has presented a series of numerical simulations using the constitutive models developed in Chapters 4, 5 and 6. The model results have been compared against one another as well as against the classical M-C, D-P and MCC constitutive models. The observations drawn from this chapter are listed below.

(i) In Chapter 4 it was shown that the mR deviatoric section improves on the realism offered by the classical M-C and D-P models. The following additional observations should be made:

  (a) the improved realism of the mR model is achieved at a cost of only 2.2% (small strain rigid footing [12]) to 5.3% (finite deformation cavity expansion [9]) increase in the run-time compared to that of the M-C model;

  (b) similar realism is achieved using a frictional cone based on a W-W [38] deviatoric section, however this comes at the cost of a 31% (small strain rigid footing [12]) and 42% (finite deformation cavity expansion [9]) increase in run-time compared to the M-C model as, unlike the mR model, no closed form backward Euler stress integration solution is currently available for the frictional W-W surface;

  (c) the mR model demonstrated global asymptotic quadratic convergence in all of the small strain and finite deformation FE simulations presented by Coombs and co-workers [9, 11–13], confirming the correct derivation of the algorithmic consistent tangent; and

  (d) it appears that the use of an associated flow rule, with both the mR and M-C models, causes an over-estimation of the local heave in a rigid footing analysis (*in-situ* measurements are required to confirm this hypothesis).

(ii) Chapters 5 and 6 developed isotropic single-surface and anisotropic two-surface families of CS hyperplastic constitutive models respectively. This chapter has demonstrated the use different members of those families of models in FE analyses. The following points are worth highlighting:

  (a) the UTC FE sensitivity analysis revealed the effect of varying the material constants for the two-surface anisotropic model, showing that a $\pm 10\%$ change has only a marginal influence on the simulation. Other test paths could be explored in the future;

  (b) the single element test demonstrated the importance of deriving the algorithmic consistent tangent when implementing the constitutive models within an FE analysis code. In the examples given, relying on the elastic or infinitesimal elasto-plastic stiffness tangents increased the run-time by 72 or 8 times;

[25] Note, that the left and right edges of Figures 7.31 (i) and (ii) are connected, as the figures show the unwrapped outer surface of the cylinder.

(c) the single-surface models were unable to capture the one-dimensional unloading behaviour of LCT (Figure 7.7);

(d) the shape of the yield surface (controlled by both α and γ) has the greatest influence on the cavity expansion response, due to the high C_χ value for LCT;

(e) the two-surface models demonstrated hysteretic behaviour during unloading and re-loading in the cavity expansion simulation, whereas the single-surface models followed the same unload-reload path;

(f) the M-C, D-P and mR models are likely to significantly over-predict the stiffness and limit loads for a drained plane strain footing analysis[26];

(g) the displacement for a footing pressure of 1MPa was 22% higher with the MCC model compared with the two-surface anisotropic model;

(h) as the number of unknowns (nodal degrees of freedom) in a FE analysis increases, it appears that the relative computational cost associated with using the sophisticated two-surface anisotropic model diminishes; and

(i) throughout all of the simulations the two-surface anisotropic model (when using the algorithmic consistent tangent) demonstrated asymptotic quadratic convergence of the global N-R procedure, verifying the both the small strain algorithmic tangent derived in Section 6.4.6 and the anisotropic spatial tangent given in Chapter 3.

(iii) In Section 7.4, the two-surface anisotropic model was calibrated using hydrostatic consolidation and unloading data together with anisotropic UTC and UTE experimental data on LC. The full stress history followed by experimental tests on LC in a HCA were then simulated without altering the calibrated material constants. The following observations can be drawn from those simulations:

(a) the two-surface anisotropic model is able to qualitatively capture the experimentally seen material behaviour, whereas the MCC model gives an over-stiff response;

(b) the MCC model significantly over-estimates the peak stress ratio;

(c) there is considerable variation in the stress components through the wall of the hollow cylinder specimen, however the influence of these non-uniformities is rather small; and

(d) the mid-height (and centre) Gauss points in the anisotropic multi-element FE simulations showed good qualitative agreement with the experimentally observed behaviour.

(iv) The final analysis in this chapter was focused on the instabilities that develop within constitutive models. The following key points should be noted:

(a) in the one-dimensional loading and unloading and the subsequent undrained triaxial simulations, instability of the acoustic tensor was not observed, however the determinant of the infinitesimal elasto-plastic tangent fell to zero; and

(b) in the simulation of the hollow cylinder tests, the development of instabilities were predicted to occur at a higher strain than observed experimentally. However, the direction of these instabilities showed a good agreement with the experimentally observed discontinuity planes.

[26]The two-surface anisotropic model was calibrated from experimental data on LCT. The opening angles of the frictional cone models were set such that their yield surface compression meridians coincided with the CS compression meridians and their elastic properties chosen to roughly agree with those from the CS models. The sophisticated two-surface model (which is able to better capture the experimental response than the frictional cone models) predicted a significantly softer response than the simple single-surface models suggest. This suggests that the frictional cone models over-estimate the stiffness of the footing analysis.

Chapter 7 references

[1] D Bigoni, *Bifurcation and instability of non-associative elastoplastic solids*, Material instabilities in elastic and plastic solids, Springer-Verlag, Wien New York, (2000), 1–52.

[2] D Bigoni & T Hueckel, *Uniqueness and localization-I. Associative and non-associative elastoplasticity*, Int. J. Solids Structures 28 (1991), 197–213.

[3] D Bigoni & T Hueckel, *Uniqueness and localization-II. Coupled elastoplasticity*, Int. J. Solids Structures 28 (1991), 215–224.

[4] D Bigoni & D Zaccaria, *On the eigenvalues of the acoustic tensor in elastoplasticity*, Eur. J. Mech. A/Solids 13 (1994), 621–638.

[5] AW Bishop, DL Webb & PI Lewin, *Undisturbed samples of London Clay from the Ashford Common shaft: strength-effective stress relationships*, Géotechnique 15 (1965), 1–31.

[6] RI Borja & A Aydin, *Computational modeling of deformation bands in granular media. I. Geological and mathematical framework*, Comput. Meth. Appl. Mech. Engrg. 193 (2004), 2667–2698.

[7] RI Borja & C Tamagnini, *Cam-Clay plasticity Part III: Extension of the infinitesimal model to include finite strains*, Comput. Meth. Appl. Mech. Engrg. 155 (1998), 73–95.

[8] TJ Bromwich, *Quadratic forms and their classification by means of invariant factors*, Cambridge Tracts in Mathematics and Mathematical Physics, London, 1906.

[9] WM Coombs, *Reuleaux plasticity: overcoming Mohr-Coulomb and Drucker-Prager limitations*, presented at the BGA 42nd Cooling prize competion, Loughborough, 2011.

[10] WM Coombs & RS Crouch, *Algorithmic issues for three-invariant hyperplastic Critical State models*, Comput. Methods Appl. Mech. Engrg. 200 (2011), 2297–2318.

[11] WM Coombs & RS Crouch, *Non-associated Reuleaux plasticity: Analytical stress integration and consistent tangent for finite deformation mechanics*, Comput. Meth. Appl. Mech. Engrg. 200 (2011), 1021–1037.

[12] WM Coombs, RS Crouch & CE Augarde, *Reuleaux plasticity: Analytical backward Euler stress integration and consistent tangent*, Comput. Meth. Appl. Mech. Engrg. 199 (2010), 1733–1743.

[13] WM Coombs, RS Crouch & CE Augarde, *On the use of Reuleaux plasticity for geometric non-linear analysis*. In: 18th UK Conference on Computational Mechanics (ACME-UK), 2010, 113–116.

[14] RF Craig, *Craig's soil mechanics*, Seventh edition, Spon Press, 2004.

[15] DC Drucker & W Prager, *Soil mechanics and plastic analysis or limit design*, Quart. Appl. Math. 10 (1952), 157–164.

[16] A Gasparre, *Adavnced laboratory characterisation of london clay*, PhD. Thesis, Imperial College London, 2005.

[17] A Gens, *Stress-strain characteristics of a low plasticity clay*, PhD. Thesis, Imperial College of Science and Technology, University of London, 1982.

[18] KM Górski, E Hivon, AJ Banday, BD Wandelt, FK Hansen, M Reinecke & M Bartelmann, *HEALPix: a framework for high-resolution discretization and fast analysis of data distributed on the sphere*, Astrophys. J. 622 (2005), 759–771.

[19] G Gudehus, *Requirements for Constitutive Relations for Soils*. In: Z Bažant (ed.), Mechanics of Geomaterials, 47–63, John Wiley & Sons Ltd., 1985.

[20] DW Hight, F McMillan, JJM Powell, RJ Jardine & CP Allenou, *Some characteristics of London Clay*. In: Tan *et al.* (eds.), Characterisation of Engineering Properties of Natural Soils, 2003.

[21] DW Hight, A Gens & MJ Symes, *The development of a new hollow cylinder appparatus for investigating the effects of principal stress rotation in soils*, Géotechnique 33 (1983), 355–383.

[22] R Hill, *A general theory of uniqueness and stability in elastic-plastic solids*, J. Mech. Phys. Solids 6 (1958), 236–249.

[23] R Hill, *Acceleration waves in solids*, J. Mech. Phys. Solids 10 (1962), 1–16.

[24] S Imposimato & R Nova, *An investigation on the uniqueness of the incremental response of elastoplastic models for virgin sand*, Mech. Cohes.-Frict. Mat. 3 (1998), 65–87.

[25] RJ Jardine, *Investigation of pile-soil behaviour, with special reference to the foundations of offshore structures*, PhD Thesis, Imperial College, University of London, 1985.

[26] J Mosler, *Numerical analyses of discontinuous material bifurcation: strong and weak discontinuities*, Comput. Meth. Appl. Mech. Engrg. 194 (2005), 979–1000.

[27] S Nishimura, NA Minh & RJ Jardine, *Shear strength anisotropy of natural London Clay*, Géotechnique 51 (2007), 49–62.

[28] S Nishimura, *Laboratory study on anisotropy of natural London Clay*, PhD. Thesis, Imperial College London (2005).

[29] J Oliver, AE Huespe, JC Cante & G Díaz, *On the numerical resolution of the discontinuous material bifurcation problem*, Int. J. Numer. Meth. Eng. 83 (2010), 786–804.

[30] D Potts & L Zdravkoić, *Finite element analysis in geotechnical engineering: Application*, Thomas Telford Publishing, London, 2001.

[31] JH Prévost & JP Wolf, *Nonlinear soil mechanics and dynamic soil-structure interaction*, Lausanne, Switzerland, 1987.

[32] E Rizzi, G Maier & K Willam, *On failure indicators in multi-dissipative materials*, Int. J. Solids Struct. 33 (1996), 3187–3214.

[33] JW Rudnicki & JR Rice, *Conditions for the localization of deformation in pressure-sensitive dilatant materials*, J. Mech. Phys. Solids 23 (1975), 371–394.

[34] HL Schreyer & MK Neilsen, *Discontinuous bifurcation states for associated smooth plasticity and damage with isotropic elasticity*, Int. J. Solids Struct. 33 (1996), 3239–3256.

[35] IM Smith, *A general purpose system for finite element analyses in parallel*, Eng. Comput. 17 (2000), 75–91.

[36] EA de Souza Neto, D Perić & DRJ Owen, *Computational methods for plasticity: Theory and applications*, John Wiley & Sons Ltd, 2008.

[37] KJ Willam & M-M Iordache, *On the lack of symmetry in materials*. In: WA Wall, K-U Bietzinger & K Schweizerhof (eds.), Trends in computational structural mechanics, CIMNE, Barcelona, Spain, 2001.

[38] KJ Willam & EP Warnke, *Constitutive model for the triaxial behaviour of concrete*, Proceedings of the May 17-19 1974, International Association of Bridge and Structural Engineers Seminar on Concrete Structures Subjected to Triaxial Stresses, held at Bergamo Italy, 1974.

[39] DM Wood, *Geotechnical modelling*, Spon Press, 2004.

[40] L Xue & T Belytschko, *Fast methods for determining instabilities of elasticplastic damage models through closed-form expressions*, Int. J. Numer. Meth. Eng. 84 (2010), 1490–1518.

[41] Y Yamakawa, K Hashiguchi & K Ikeda, *Implicit stress-update algorithm for isotropic Cam-clay model based on the subloading surface concept at finite strains*, Int. J. Plasticity 26 (2010), 634–658.

[42] HS Yu, *Plasticity and Geotechnics*, Springer, 2006.

[43] HS Yu & GT Houlsby, *Finite cavity expansion in dilatant soils: Loading analysis*, Géotechnique 41, (1991), 173–183.

Chapter 8

Conclusions

"The soil seems to defeat its investigators again and again."

G Gudehus (1985) [6]

"...no one mathematical model can completely describe the complex behaviour of real soils under all conditions."

WF Chen (1985) [3]

Chapters 1, 2 and 3 provided an introduction to this thesis, established some of the basic principles of inelastic continuum analysis and presented a framework for the numerical implementation of constitutive models with anisotropic inelasticity within a finite deformation displacement-based finite-element code. In Section 1.2 of Chapter 1, Chen's *basic criteria for model evaluation* [3] were listed. The first two, those of *theoretical* and *experimental evaluation*, are covered in the following discussion. The third criterion of *numerical and computational evaluation*, that is, the ease of implementation within non-linear multi-element analysis codes, was addressed by explaining the finite deformation framework presented in Chapter 3. With the adopted approach, any existing small strain constitutive algorithm[1] can be incorporated within the finite-element code without modification.

The novel research undertaken in this study is described in Chapters 4 to 7. The original features and key conclusions from those chapters are now summarised. The constitutive models developed and implemented during this research are listed in Table 8.1.

Simple frictional plasticity

Chapter 4 presented a pressure-sensitive (cone-type) frictional plasticity model using a deviatoric section defined by a modified Reuleaux triangle. The modified Reuleaux yield criterion provides a significantly improved fit to the deviatoric yielding of particulate materials over that of the classical Mohr-Coulomb and the widely used Drucker-Prager criteria (Figure 4.4) by containing a dependency on both the Lode angle and the intermediate principal stress. However, unlike other existing deviatoric yield criteria which embrace these two influences, the modified Reuleaux formulation allows for analytical backward Euler stress integration, even for the case of non-associated volumetric plastic flow. This single-step analytical procedure is entirely robust and provides a 2–4 times speed gain over the conventional iterative approach (Figure 4.11).

Requirements of a constitutive model were set out in Section 1.2 of Chapter 1. Reviewing these, it is clear that the modified Reuleaux frictional cone model is *complete* (can be used for all stress and strain paths), *manageable* (requires only four material parameters that can be easily determined), *founded on physical interpretation* (motivated by the desire to include the influence of both the Lode angle and the intermediate principal stress) and can be easily incorporated within non-linear boundary value codes.

[1] exhibiting isotropic elasticity and either isotropic or anisotropic plasticity.

The numerical analysis reviewed in Chapter 7 showed that the modified Reuleaux constitutive model requires a modest increase in computational effort (only 5.8% in the run-time for the finite-deformation cavity expansion and 2.2% for the small strain rigid footing analyses) over that of the Mohr-Coulomb model.

In summary, the modified Reuleaux cone model overcomes the inadequacies inherent in, and provides a suitable replacement for, both the Mohr-Coulomb and Drucker-Prager models, yet requires no additional material constants or significant increase in computation time.

Isotropic hyperplasticity

Chapter 5 developed a single-surface isotropic family of two-parameter Critical State models (based on the original model by Collins and Hilder [4]) using the principles of hyperplasticity. This chapter (i) extended the model to include a Lode angle dependency, (ii) described a robust stress integration procedure and (iii) linearised the model for use within displacement-based boundary value simulations. Volumetric non-associated plastic flow is a natural consequence of the particular form of the dissipation function. A Lode angle dependency can be incorporated in a straightforward manner into this dissipation function, resulting in deviatoric non-associated plastic flow and a Lode angle dependent yield function. This was achieved without the difficulties caused by previous approaches of redefining the deviatoric stress invariant. It was shown that the particular form of the yield function significantly influences the efficiency of the iterative backward Euler stress integration algorithm. An appropriate form of the yield function was proposed that (i) removes any *elastic regions* outside the yield surface and (ii) leads to monotonic convergence of the iterative stress return. Particular attention was paid to the robustness of the integration algorithm so that the model is, as required by Prévost and Wolf (Section 1.2), *"able to make statements about the material behaviour for all stress and strain paths"* [11].

The two-parameter model, as its name suggests, includes two additional material constants compared to the classical modified Cam-clay constitutive model. Recalling the *manageability* requirement of Section 1.2, in addition to providing the pseudo-code for the constitutive algorithm, a detailed calibration procedure was provided that gave a physical insight to the role of the two constants which can be obtained from standard laboratory tests. This calibration procedure allows potential users to determine analytically the additional material constants based on one-dimensional consolidation (drained loading) and undrained triaxial compression experimental data. Comparisons with experimental data showed that the two-parameter model has advantages over the modified Cam-clay model in terms of its ability to reproduce one-dimensional loading and offer an improved fit to heavily overconsolidated soil behaviour.

Numerical analysis in Chapter 7 confirmed the viability of the two-parameter model for use within a general purpose displacement-based finite-element code. All model simulations showed asymptotic quadratic convergence of the global equilibrium equations, confirming the derivation of the algorithmic consistent tangent. The run-times for the two-parameter model were, in general, very close to (and sometimes shorter than) those of the modified Cam-clay constitutive model.

In summary, the two-parameter model provides a valuable (but rather simple) extension to the classical modified Cam-clay model, significantly improving the fit to heavily overconsolidated soils and providing extra richness in terms of a Lode angle dependency with no noticeable computational cost.

Anisotropic hyperplasticity

Chapter 6 extended the single-surface Critical State model by introducing anisotropy, allowing the yield surface to *shear* away from the hydrostatic axis and including dissipative behaviour at low strains within the conventional yield surface. Using the principles of hyperplasticity, the two-surface anisotropic model's non-linear elasticity law, yield function and direction of plastic flow were all obtained from just two scalar

functions. The resulting model (which collapses down to the classical modified Cam-clay model) has the following key features:

(i) a unique convex isotropic Critical State surface, which is independent of any previous material history or stress path followed;

(ii) a measure of the inherent anisotropy interpreted as the degree of shearing of the yield surface (expressed in terms of the dissipation rate as a cross-coupling between the strain rates);

(iii) a unique level of anisotropy reached at the Critical State (as suggested by recent discrete element findings); and

(iv) convexity of the Lode angle dependent surface which holds for any degree of anisotropy.

To the author's knowledge, this is the first time that all of these features have been combined in a two-surface Critical State plasticity model cast within a hyperplastic framework. The *requirements of a constitutive model* [6, 11] (as set out in Section 1.2) have been fulfilled as follows:

(i) *physical interpretation*: modification of the rate of dissipation to include cross-coupling between the volumetric and deviatoric components, along with dissipative behaviour at lower strains was motivated by inability of the single-surface model's dissipation function to reproduce the experimentally observed material behaviour. The coupling accounts for the plastic dilation or compaction resulting from deviatoric loading and plastic shearing under hydrostatic loading.

(ii) *tractability*: full derivation and numerical implementation of the constitutive algorithm has been presented. This allows the model to be followed and implemented.

(iii) *material constants*: physical interpretation was provided and a calibration procedure outlined to encourage suitably experienced practising geotechnical engineers to use this relatively sophisticated model. *Default* values were provided for six of the twelve material constants, resulting in a model that provides enhanced simulation capabilities over the classical modified Cam-clay model, whilst only requiring two additional material constants. The reduced set of material constants could be calibrated using just three standard laboratory tests.

(iv) *well-posed* and *complete*: the full algorithmic and numerical treatment of the model has been provided. The stability and uniqueness of the material model was demonstrated through the smoothness of the Gudehus [7] stress surface plots and random strain test paths, confirming the robustness of the stress integration algorithm. Finally, the sensitivity analysis presented in Chapter 7 showed that the model is stable following small changes to its material constants.

The model is able to capture qualitatively and quantitatively the observed experimental behaviour of Lower Cromer till and London clay. In particular it is able to reproduce a rather complex stress path for all of the material point simulations using a single set of material constants. The new model significantly improves the predictive capabilities of the modified Cam-clay model, for both normally and heavily overconsolidated clays. It also overcomes the limitations of the isotropic family of models presented in Chapter 5. As stated at the beginning of this thesis:

> *"The intention of this thesis was not to develop a new constitutive model from scratch, but rather to identify weaknesses in existing models and then remove those limitations using a consistent framework..."*

This goal has been achieved in the anisotropic two-surface two-parameter hyperplastic Critical State model.

	model	developed	implemented	AF	NAF	LAD	section
perfect plasticity	P-R		✓	✓			3.5.2
frictional	M-C		✓	✓	✓	✓	4.2
	D-P		✓	✓	✓		4.2
	mR	✓	✓	✓	✓	✓	4.1
	W-W		✓	✓	✓	✓	7.1
hardening/softening	KH vM		✓	✓			3.5.4
Critical State	MCC		✓	✓		✓	5.1
	$\alpha\gamma$	✓	✓		✓	✓	5.1
	$\beta\alpha\gamma$	✓	✓		✓	✓	6.1
	2s$\alpha\gamma$	✓	✓		✓	✓	6.1
	2s$\beta\alpha\gamma$	✓	✓		✓	✓	6.1

AF: associated plastic flow NAF: non-associated plastic flow LAD: Lode angle dependency

Table 8.1: Developed and implemented constitutive models.

Numerical analyses

The numerical analyses in Chapter 7 confirmed the viability of the anisotropic two-surface model for use within a general purpose displacement-based finite-element code. All of the model simulations showed asymptotic quadratic convergence of the global equilibrium equations, thereby confirming the derivation of the models' algorithmic consistent tangents and the anisotropic finite deformation framework. A single-element simulation demonstrated the importance of deriving the algorithmic consistent tangent. Using the elastic or infinitesimal elasto-plastic stiffness tangents (instead of the algorithmic tangent) increased the run-time by 72 and 8 times respectively. Increasing the size of the simulations (in terms of the number of elements) reduced the relative run-time penalty arising from using the more sophisticated constitutive models. This was due to a greater proportion of the run-time being spent in the solution of the global equilibrium equation in the larger analyses. It was also observed that in certain situations, the simpler single-surface models arrived at very similar solutions to that of the sophisticated two-surface model.

The final section of Chapter 7 presented for the first time (as far as the author is aware) detailed single and multi-element analyses of a series of undrained hollow cylinder experiments using the anisotropic two-surface model. The model was calibrated using anisotropic undrained triaxial compression and extension experimental data prior to simulating the hollow cylinder tests. The same material constants were used to predict the entire stress history of the London clay specimen. This gave confidence that the model was able to satisfy an important requirement for constitutive models [11], namely:

> *"a material model may only be deemed to be satisfactory when with its aid, it is possible first to determine the stress-strain-strength behaviour of the material at hand in one piece of tests equipment... and then to predict the observed behaviour of the same material in some other type of testing equipment..."*

The two-surface anisotropic model was able to capture qualitatively the experimentally observed material behaviour, whereas the modified Cam-clay model gave an over-stiff response, significantly over-estimating the peak stress ratio. The bifurcation instabilities predicted by the constitutive model using an acoustic tensor analysis showed good agreement (in terms of the instability direction) compared to those observed in the experimental tests.

8.1 Recommendations and future work

Considerable effort has been made throughout this thesis to provide constitutive algorithms that are clear, easy to implement and use. When developing material models it is imperative that the resulting algorithms are accessible to academics, potential developers and practising engineers. Neglecting this clarity and *manageability* requirement will only serve to widen the *"gulf* [that] *has arisen between research and practice in geotechnical engineering"* [1].

An obvious limitation of the Critical State hyperplasticity models (presented in Chapters 5 and 6) is the use of an elasticity law with a fixed shear modulus. Real soils appear to exhibit a pressure-dependent shear modulus. This effect can easily be incorporated into the existing constitutive models using a different free-energy function, such as that proposed by Houlsby [9]. The use of such a hyperelasticity relationship would allow the single-surface plasticity models to give a reasonable fit to the experimentally observed one-dimensional unloading behaviour of soils. However, the cross-coupling between the volumetric and deviatoric strains required in the free-energy function to give such a relationship results in an anisotropic relation between stress and elastic strain. Such a model cannot be incorporated within the finite-deformation framework presented in Chapter 3. However, the recent 2011 paper by Caminero *et al.* [2] detailed a finite deformation formulation that allows the implementation of models containing both anisotropic elasticity and plasticity, whilst maintaining the infinitesimal format of the stress integration scheme. As with the framework presented in Chapter 3, the proposed formulation treats the effects of geometric non-linearity in the form of pre- and post-processors operating on the conventional constitutive algorithm. Modifying the existing finite deformation framework, based on the paper by Caminero *et al.* [2], to allow for anisotropic elasticity, would be a valuable extension to this work.

The anisotropic two-surface two-parameter model used recent findings from discrete element modelling to guide the choice of hardening laws, especially in relation to the character of particulate media at the Critical State. This idea is not new; Cundall and Strack developed the discrete element method as a tool for *"fundamental research into the behaviour of granular assemblies"* [5]. In the author's view, there is real potential for the use of discrete element studies to guide the development of conventional continuum constitutive models.

As identified in the introduction; *"unlike models developed for other engineering materials, a direct link has yet to be made between (i) the degree of anisotropy in these models and (ii) the evolving material fabric"*. Perhaps in future it will be possible to use imaging techniques to identify and track constituent platelets and grains throughout a loading process. This information could help guide the development of continuum constitutive models based, not on an abstract representation of the material behaviour, but on micro-mechanical fabric interaction. Thereby providing stronger links between soil classification tools (such as plastic and liquid limits) and numerical models of macroscopic soil behaviour.

Throughout this thesis it has been shown that the efficiency of the implicit backward Euler stress integration method is dependent on the adopted form for the yield function. Although the stress integration routines of the isotropic single-surface and anisotropic two-surface models were shown to be robust, it is highly likely that the efficiency of these algorithms could be improved by finding a more appropriate form of the yield function. In the author's opinion, concepts from convex analysis[2], such as identifying the canonical form[3] of the yield function function, could prove to be highly fruitful. Similarly, there is considerable promise in investigating the potential use of instantaneous dissipative stress space to recast the backward Euler stress integration algorithm.

[2]Convex analysis has seen little use in plasticity theory. Han and Reddy [8] (and Houlsby and Puzrin [10] for the particular case of hyperplasticity) provide some information on re-casting plasticity theory in convex analysis terms.

[3]A canonical function is defined as a positively homogeneous function of degree one (a gauge or Minkowski function, see Tiel [12], amongst others), minus unity.

Chapter 8 references

[1] MD Bolton & YP Chen, *Micro-geomechanics*. In: International Workshop on Constitutive and Centrifuge Modelling: Two Extremes, Monte Verita, Switzerland, 2001.

[2] MÁ Caminero, FJ Montáns & KJ Bathe, *Modeling large strain anisotropic elasto-plasticity with logarithmic strain and stress measures*, Comput. Struct. 89 (2011), 826–843.

[3] WF Chen, *Constitutive Relations for Concrete Rock and Soils: Discusser's Report*. In: Z Baẑant (ed.), Mechanics of Geomaterials, 65–86, John Wiley & Sons Ltd., 1985.

[4] IF Collins & T Hilder, *A theorectical framework for constructing elastic/plastic constitutive models of triaxial tests*, Int. J. Numer. Meth. Geomech. 26 (2002), 1313–1347.

[5] PA Cundall & ODL Strack, *A discrete numerical model for granular assemblies*, Géotechnique 29 (1979), 47–65.

[6] G Gudehus, *Requirements for Constitutive Relations for Soils*. In: Z Baẑant (ed.), Mechanics of Geomaterials, 47–63, John Wiley & Sons Ltd., 1985.

[7] G Gudehus, *Comparison of some constitutive laws for soils under radially symmetric loading and unloading*, in Proceedings of the 3rd International Conference on Numerical Methods in Geomechanics, Aachen, 1979, 1309–1323.

[8] W Han & BD Reddy, *Plasticity: mathematical theory and numerical analysis*, Springer, 1999.

[9] GT Houlsby, *The use of a variable shear modulus in elastic-plastic models for clays*, Comput. Geotech. 1 (1985), 3–13.

[10] GT Houlsby & AM Puzrin, *Principles of hyperplasticity*, Springer-Verlag London Limited, 2006.

[11] JH Prévost & JP Wolf, *Nonlinear soil mechanics and dynamic soil-structure interaction*, Lausanne, Switzerland, 1987.

[12] J van Tiel, *Convex analysis: an introductory text*, John Wiley & Sons, 1984.

Appendix A

Spatial consistent tangent

In this appendix the derivation of the consistent spatial tangent stiffness matrices are presented for the case of isotropic and anisotropic plasticity. δ_{ij} denotes the Kronecker delta tensor with the following properties

$$\delta_{ij} = 1 \quad \text{if} \quad i = j, \qquad \delta_{ij} = 0 \quad \text{if} \quad i \neq j, \qquad \delta_{ij}(\cdot)_i = (\cdot)_j \qquad \text{and} \qquad \delta_{ij}\delta_{jk} = \delta_{ik}.$$

A.1 Isotropic elasto-plasticity

The spatial tangent stiffness matrix for finite deformation isotropic elasto–plasticity is given by

$$\left(D_{\sigma}^{cst}\right)_{ijkl} = \frac{1}{J}\frac{\partial \tau_{ij}}{\partial F_{kq}} F_{lq} - \delta_{ik}\sigma_{jl}. \tag{A.1}$$

Turning our focus to the formulation of the derivative of the Kirchhoff stress with respect to the deformation gradient, using the chain rule, we obtain

$$\frac{\partial \tau_{ij}}{\partial F_{kl}} = \frac{\partial \tau_{ij}}{\partial (\varepsilon_t^{\mathrm{e}})_{mq}} \frac{\partial (\varepsilon_t^{\mathrm{e}})_{mq}}{\partial (b_t^{\mathrm{e}})_{rs}} \frac{\partial (b_t^{\mathrm{e}})_{rs}}{\partial F_{kl}}. \tag{A.2}$$

Using the elastic logarithmic strain definition from $(3.14)_1$, we obtain

$$\frac{\partial \tau_{ij}}{\partial F_{kl}} = \frac{1}{2}\frac{\partial \tau_{ij}}{\partial (\varepsilon_t^{\mathrm{e}})_{mq}} \frac{\partial \ln\left(b_t^{\mathrm{e}}\right)_{mq}}{\partial (b_t^{\mathrm{e}})_{rs}} \frac{\partial (b_t^{\mathrm{e}})_{rs}}{\partial F_{kl}}, \tag{A.3}$$

where $\partial \tau_{ij}/\partial (\varepsilon_t^{\mathrm{e}})_{mq}$ is the small strain algorithmic tangent, $(D^{alg})_{ijmq}$. The derivative $\partial \ln\left(b_t^{\mathrm{e}}\right)_{mq}/\partial (b_t^{\mathrm{e}})_{rs}$ can be calculated as a particular case of the derivative of an isotropic tensor function with respect to its argument. Post multiplying the final product term on the right of (A.3) by F_{lq} and substituting for the trial elastic left Cauchy-Green strain tensor, $(b_t^{\mathrm{e}})_{ij}$, we obtain

$$\frac{\partial (b_t^{\mathrm{e}})_{rs}}{\partial F_{kl}} F_{lq} = \frac{\partial \left(\Delta F_{rw} (b_n^{\mathrm{e}})_{wv} \Delta F_{sv}\right)}{\partial F_{kl}} F_{lq}. \tag{A.4}$$

Substituting for the increment in the deformation gradient ΔF

$$\frac{\partial (b_t^{\mathrm{e}})_{rs}}{\partial F_{kl}} F_{lq} = \frac{\partial \left(F_{rx} (F_n)^{-1}_{xw} (b_n^{\mathrm{e}})_{wv} F_{sy} (F_n)^{-1}_{yv}\right)}{\partial F_{kl}} F_{lq}. \tag{A.5}$$

Using the product rule

$$\begin{aligned}\frac{\partial(b_t^{\mathrm{e}})_{rs}}{\partial F_{kl}}F_{lq} &= \frac{\partial F_{rx}}{\partial F_{kl}}\big((F_n)^{-1}_{xw}(b_n^{\mathrm{e}})_{wv}F_{sy}(F_n)^{-1}_{yv}\big)F_{lq} + \frac{\partial F_{sy}}{\partial F_{kl}}\big(F_{rx}(F_n)^{-1}_{xw}(b_n^{\mathrm{e}})_{wv}(F_n)^{-1}_{yv}\big)F_{lq},\\ &= \delta_{rk}\delta_{xl}\big((F_n)^{-1}_{xw}(b_n^{\mathrm{e}})_{wv}F_{sy}(F_n)^{-1}_{yv}\big)F_{lq} + \delta_{sk}\delta_{yl}\big(F_{rx}(F_n)^{-1}_{xw}(b_n^{\mathrm{e}})_{wv}(F_n)^{-1}_{yv}\big)F_{lq},\\ &= \delta_{rk}\big((F_n)^{-1}_{lw}(b_n^{\mathrm{e}})_{wv}F_{sy}(F_n)^{-1}_{yv}\big)F_{lq} + \delta_{sk}\big(F_{rx}(F_n)^{-1}_{xw}(b_n^{\mathrm{e}})_{wv}(F_n)^{-1}_{lv}\big)F_{lq}. \end{aligned} \tag{A.6}$$

Through rearrangement, we obtain

$$\begin{aligned}\frac{\partial(b_t^{\mathrm{e}})_{rs}}{\partial F_{kl}}F_{lq} &= \delta_{rk}\Delta F_{qw}(b_n^{\mathrm{e}})_{wv}\Delta F_{sv} + \delta_{sk}\Delta F_{rw}(b_n^{\mathrm{e}})_{wv}\Delta F_{qv},\\ &= \delta_{rk}(b_t^{\mathrm{e}})_{qs} + \delta_{sk}(b_t^{\mathrm{e}})_{rq}. \end{aligned} \tag{A.7}$$

Combining (A.1), (A.3) and (A.7), we obtain the follow equation for the elasto-plastic spatial tangent operator

$$\big(D_\sigma^{cst}\big)_{ijkl} = \frac{1}{J}D^{alg}_{ijmq}\frac{\partial \ln\big(b_t^{\mathrm{e}}\big)_{mq}}{\partial(b_t^{\mathrm{e}})_{rs}}\Big(\delta_{rk}(b_t^{\mathrm{e}})_{qs} + \delta_{sk}(b_t^{\mathrm{e}})_{rq}\Big) - \delta_{ik}\sigma_{jl}. \tag{A.8}$$

A.2 Anisotropic elasto-plasticity

For anisotropic elasto-plasticity the spatial tangent operator is defined by (3.67), where $\big[D_\beta^{cst}\big]_{ijkl}$ is given by

$$\big(D_\beta^{cst}\big)_{ijkl} = \frac{1}{J}\frac{\partial\tau_{ij}}{\partial(\beta_t)_{ab}}\frac{\partial(\beta_t)_{ab}}{\partial F_{kq}}F_{lq}. \tag{A.9}$$

$\partial\tau_{ij}/\partial(\beta_t)_{ab} = D^{\beta}_{ijab}$ is the measure of the change in the return stress with respect to a change in the trial backstress whilst freezing the other input variables[1]. Using the chain rule we obtain

$$\big(D_\beta^{cst}\big)_{ijkl} = \frac{1}{J}D^{\beta}_{ijab}\frac{\partial(\beta_t)_{ab}}{\partial(R_t^{\mathrm{e}})_{cd}}\frac{\partial(R_t^{\mathrm{e}})_{cd}}{\partial F_{kq}}F_{lq}, \tag{A.10}$$

where

$$(\beta_t)_{ab} = (\Delta\Lambda^{\mathrm{e}})_{ac}(\beta_n)_{cd}(\Delta\Lambda^{\mathrm{e}})_{ad}, \qquad (\Delta\Lambda^{\mathrm{e}})_{ac} = (R_t^{\mathrm{e}})_{ae}(R_n^{\mathrm{e}})_{ce}. \tag{A.11}$$

Taking the derivative of the trial backstress with respect to the trial elastic spatial rotation, we obtain

$$\begin{aligned}\frac{\partial(\beta_t)_{ij}}{\partial(R_t^{\mathrm{e}})_{kl}} &= \frac{\partial(R_t^{\mathrm{e}})_{ia}}{\partial(R_t^{\mathrm{e}})_{kl}}R^{\mathrm{e}}_{ba}(\beta_n)_{bc}(R_n^{\mathrm{e}})_{cd}(R_t^{\mathrm{e}})_{jd} + (R_t^{\mathrm{e}})_{ia}R^{\mathrm{e}}_{ba}(\beta_n)_{bc}(R_n^{\mathrm{e}})_{cd}\frac{\partial(R_t^{\mathrm{e}})_{jd}}{\partial(R_t^{\mathrm{e}})_{kl}},\\ &= \delta_{ik}\delta_{al}R^{\mathrm{e}}_{ba}(\beta_n)_{bc}(R_n^{\mathrm{e}})_{cd}(R_t^{\mathrm{e}})_{jd} + (R_t^{\mathrm{e}})_{ia}R^{\mathrm{e}}_{ba}(\beta_n)_{bc}(R_n^{\mathrm{e}})_{cd}\delta_{jk}\delta_{dl},\\ &= \delta_{ik}R^{\mathrm{e}}_{bl}(\beta_n)_{bc}(R_n^{\mathrm{e}})_{cd}(R_t^{\mathrm{e}})_{jd} + (R_t^{\mathrm{e}})_{ia}R^{\mathrm{e}}_{ba}(\beta_n)_{bc}(R_n^{\mathrm{e}})_{cl}\delta_{jk}. \end{aligned} \tag{A.12}$$

Substituting $(A.11)_2$ into (A.12)

$$\frac{\partial(\beta_t)_{ij}}{\partial(R_t^{\mathrm{e}})_{kl}} = \delta_{ik}R^{\mathrm{e}}_{bl}(\beta_n)_{bc}(\Delta\Lambda^{\mathrm{e}})_{jc} + \delta_{jk}(\Delta\Lambda^{\mathrm{e}})_{ib}(\beta_n)_{bc}(R_n^{\mathrm{e}})_{cl}. \tag{A.13}$$

Using the following definition of the trial elastic rotation tensor

$$(R_t^{\mathrm{e}})_{ij} = (v_t^{\mathrm{e}})^{-1}_{ia}(F_t^{\mathrm{e}})_{aj} = (v_t^{\mathrm{e}})^{-1}_{ia}F_{ab}(F_n^{\mathrm{p}})^{-1}_{bj}, \tag{A.14}$$

[1] Note, that D^{β}_{ijab} is the only term in (A.10) that depends on the particular constitutive model used.

the derivative of $(R_t^{\mathrm{e}})_{cd}$ with respect to F_{kq} in (A.10) becomes

$$\begin{aligned}\frac{\partial (R_t^{\mathrm{e}})_{ij}}{\partial F_{kl}} &= \frac{\partial (v_t^{\mathrm{e}})_{ia}^{-1}}{\partial F_{kl}} F_{ab} (F_n^{\mathrm{p}})_{bj}^{-1} + (v_t^{\mathrm{e}})_{ia}^{-1} \frac{\partial F_{ab}}{\partial F_{kl}} (F_n^{\mathrm{p}})_{bj}^{-1}, \\ &= \frac{\partial (v_t^{\mathrm{e}})_{ia}^{-1}}{\partial (b_t^{\mathrm{e}})_{cd}} \frac{\partial (b_t^{\mathrm{e}})_{cd}}{\partial F_{kl}} F_{ab} (F_n^{\mathrm{p}})_{bj}^{-1} + (v_t^{\mathrm{e}})_{ia}^{-1} \delta_{ak} \delta_{bl} (F_n^{\mathrm{p}})_{bj}^{-1}, \\ &= (L_\beta)_{iacd} \frac{\partial (b_t^{\mathrm{e}})_{cd}}{\partial F_{kl}} (F_t^{\mathrm{e}})_{aj} + (v_t^{\mathrm{e}})_{ik}^{-1} (F_n^{\mathrm{p}})_{lj}^{-1}, \end{aligned} \tag{A.15}$$

where $(L_\beta)_{ijkl}$ is the partial derivative of the inverse square root of the symmetric b_{ij}^{e} tensor with respect to its argument

$$(L_\beta)_{ijkl} = \left. \frac{\partial (b_t^{\mathrm{e}})^{-1/2}}{\partial (b_t^{\mathrm{e}})} \right|_{ijkl}. \tag{A.16}$$

$(L_\beta)_{ijkl}$ is calculated as a particular case of the derivative of a symmetric tensor function with respect to its argument, analogous to the calculation of L_{ijkl} required for the calculation of the isotropic spatial tangent modulus. The trial left Cauchy-Green elastic strain tensor $(b_t^{\mathrm{e}})_{ij}$ is defined as

$$(b_t^{\mathrm{e}})_{ij} = (F_t^{\mathrm{e}})_{ia} (F_t^{\mathrm{e}})_{ja} = F_{ib} (F_n^{\mathrm{p}})_{ba}^{-1} (F_n^{\mathrm{p}})_{ca}^{-1} F_{jc}, \tag{A.17}$$

taking the derivative of $(b_t^{\mathrm{e}})_{ij}$ with respect to the deformation gradient F_{kl}

$$\begin{aligned}\frac{\partial (b_t^{\mathrm{e}})_{ij}}{\partial F_{kl}} &= \frac{\partial F_{ib}}{\partial F_{kl}} (F_n^{\mathrm{p}})_{ba}^{-1} (F_n^{\mathrm{p}})_{ca}^{-1} F_{jc} + F_{ib} (F_n^{\mathrm{p}})_{ba}^{-1} (F_n^{\mathrm{p}})_{ca}^{-1} \frac{\partial F_{jc}}{\partial F_{kl}}, \\ &= \delta_{ik} \delta_{bl} (F_n^{\mathrm{p}})_{ba}^{-1} (F_n^{\mathrm{p}})_{ca}^{-1} F_{jc} + F_{ib} (F_n^{\mathrm{p}})_{ba}^{-1} (F_n^{\mathrm{p}})_{ca}^{-1} \delta_{jk} \delta_{cl}, \\ &= \delta_{ik} (F_n^{\mathrm{p}})_{la}^{-1} (F_n^{\mathrm{p}})_{ca}^{-1} F_{jc} + F_{ib} (F_n^{\mathrm{p}})_{ba}^{-1} (F_n^{\mathrm{p}})_{la}^{-1} \delta_{jk}, \\ &= \delta_{ik} (F_n^{\mathrm{p}})_{la}^{-1} (F_t^{\mathrm{e}})_{ja} + (F_t^{\mathrm{e}})_{ia} (F_n^{\mathrm{p}})_{la}^{-1} \delta_{jk}. \end{aligned} \tag{A.18}$$

Multiplying (A.15) by the updated deformation gradient F_{lq} we obtain

$$\frac{\partial (R_t^{\mathrm{e}})_{ij}}{\partial F_{kq}} F_{lq} = (L_\beta)_{iacd} \frac{\partial (b_t^{\mathrm{e}})_{cd}}{\partial F_{kq}} F_{lq} (F_t^{\mathrm{e}})_{aj} + (v_t^{\mathrm{e}})_{ik}^{-1} (F_t^{\mathrm{e}})_{lj}, \tag{A.19}$$

where the derivative of the trial left Cauchy-Green elastic strain tensor with respect to the deformation gradient is given by

$$\begin{aligned}\frac{\partial (b_t^{\mathrm{e}})_{cd}}{\partial F_{kq}} F_{lq} &= \delta_{ck} (F_n^{\mathrm{p}})_{qa}^{-1} F_{lq} (F_t^{\mathrm{e}})_{da} + \delta_{dk} (F_t^{\mathrm{e}})_{ca} (F_n^{\mathrm{p}})_{qa}^{-1} F_{lq}, \\ &= \delta_{ck} (F_t^{\mathrm{e}})_{la} (F_t^{\mathrm{e}})_{da} + \delta_{dk} (F_t^{\mathrm{e}})_{ca} (F_t^{\mathrm{e}})_{la}, \\ &= \delta_{ck} (b_t^{\mathrm{e}})_{ld} + \delta_{dk} (b_t^{\mathrm{e}})_{cl}. \end{aligned} \tag{A.20}$$

Substituting (A.20) into (A.19), we obtain

$$\begin{aligned}\frac{\partial (R_t^{\mathrm{e}})_{ij}}{\partial F_{kq}} F_{lq} &= (L_\beta)_{iacd} \left[\delta_{ck} (b_t^{\mathrm{e}})_{ld} + \delta_{dk} (b_t^{\mathrm{e}})_{cl} \right] (F_t^{\mathrm{e}})_{aj} + (v_t^{\mathrm{e}})_{ik}^{-1} (F_t^{\mathrm{e}})_{lj}, \\ &= (L_\beta)_{iakd} (b_t^{\mathrm{e}})_{ld} (F_t^{\mathrm{e}})_{aj} + (L_\beta)_{iack} (b_t^{\mathrm{e}})_{cl} (F_t^{\mathrm{e}})_{aj} + (v_t^{\mathrm{e}})_{ik}^{-1} (F_t^{\mathrm{e}})_{lj}. \end{aligned} \tag{A.21}$$

Using the definition of the trial elastic deformation gradient, $(F_t^{\mathrm{e}})_{ij} = (v_t^{\mathrm{e}})_{ie} (R_t^{\mathrm{e}})_{ej}$, (A.21) becomes

$$\frac{\partial (R_t^{\mathrm{e}})_{ij}}{\partial F_{kq}} F_{lq} = \Big((L_\beta)_{iakd} (b_t^{\mathrm{e}})_{ld} (v_t^{\mathrm{e}})_{ae} + (L_\beta)_{iack} (b_t^{\mathrm{e}})_{cl} (v_t^{\mathrm{e}})_{ae} + (v_t^{\mathrm{e}})_{ik}^{-1} (v_t^{\mathrm{e}})_{le} \Big) (R_t^{\mathrm{e}})_{ej}, \tag{A.22}$$

Combining (A.22) and (A.13)

$$\begin{aligned}\frac{\partial(\beta_t)_{ij}}{\partial(R_t^{\mathrm{e}})_{mn}}\frac{\partial(R_t^{\mathrm{e}})_{mn}}{\partial F_{kq}}F_{lq} &= \Big(\delta_{ia}R^{\mathrm{e}}_{cb}(\beta_n)_{cd}(\Delta\Lambda^{\mathrm{e}})_{jd}+\delta_{ja}(\Delta\Lambda^{\mathrm{e}})_{ic}(\beta_n)_{cd}(R^{\mathrm{e}}_n)_{db}\Big)\Big((L_\beta)_{afkd}(b_t^{\mathrm{e}})_{ld}(v_t^{\mathrm{e}})_{fe}+\dots\\ &\quad (L_\beta)_{afck}(b_t^{\mathrm{e}})_{cl}(v_t^{\mathrm{e}})_{fe}+(v_t^{\mathrm{e}})^{-1}_{ak}(v_t^{\mathrm{e}})_{le}\Big)(R_t^{\mathrm{e}})_{eb},\\ &= \Big(\delta_{ia}(\Delta\Lambda^{\mathrm{e}})_{ec}(\beta_n)_{cd}(\Delta\Lambda^{\mathrm{e}})_{jd}+\delta_{ja}(\Delta\Lambda^{\mathrm{e}})_{ic}(\beta_n)_{cd}(\Delta\Lambda^{\mathrm{e}})_{ed}\Big)\dots\\ &\quad \Big((L_\beta)_{afkd}(b_t^{\mathrm{e}})_{ld}(v_t^{\mathrm{e}})_{fe}+(L_\beta)_{afck}(b_t^{\mathrm{e}})_{cl}(v_t^{\mathrm{e}})_{fe}+(v_t^{\mathrm{e}})^{-1}_{ak}(v_t^{\mathrm{e}})_{le}\Big),\\ &= \Big(\delta_{ia}(\beta_t)_{ej}+\delta_{ja}(\beta_t)_{ie}\Big)\Big((L_\beta)_{afkd}(b_t^{\mathrm{e}})_{ld}(v_t^{\mathrm{e}})_{fe}+(L_\beta)_{afck}(b_t^{\mathrm{e}})_{cl}(v_t^{\mathrm{e}})_{fe}+(v_t^{\mathrm{e}})^{-1}_{ak}(v_t^{\mathrm{e}})_{le}\Big).\end{aligned} \tag{A.23}$$

Substituting (A.23) into (A.10), we obtain the anisotropic component of the spatial stiffness tangent as

$$\begin{aligned}\big(D^{cst}_{\beta}\big)_{ijkl} &= \frac{1}{J}D^{\beta}_{ijmn}\Big(\delta_{ma}(\beta_t)_{en}+\delta_{na}(\beta_t)_{me}\Big)V_{aekl},\\ &= \frac{1}{J}\Big(D^{\beta}_{ijan}(\beta_t)_{en}+D^{\beta}_{ijma}(\beta_t)_{me}\Big)V_{aekl},\end{aligned} \tag{A.24}$$

where V_{aekl} is given by

$$V_{aekl}=(L_\beta)_{afkd}(b_t^{\mathrm{e}})_{ld}(v_t^{\mathrm{e}})_{fe}+(L_\beta)_{afck}(b_t^{\mathrm{e}})_{cl}(v_t^{\mathrm{e}})_{fe}+(v_t^{\mathrm{e}})^{-1}_{ak}(v_t^{\mathrm{e}})_{le}. \tag{A.25}$$

Using the symmetries $D^{\beta}_{ijan}=D^{\beta}_{ijna}$ and $(\beta_t)_{en}=(\beta_t)_{ne}$, (A.24) becomes

$$\big(D^{cst}_{\beta}\big)_{ijkl}=\frac{2}{J}D^{\beta}_{ijan}(\beta_t)_{en}V_{aekl}. \tag{A.26}$$

Using the symmetries of $(L_\beta)_{afck}$ and $(b_t^{\mathrm{e}})_{ld}$, V_{aekl} reduces to

$$V_{aekl}=2(L_\beta)_{afkd}(b_t^{\mathrm{e}})_{ld}(v_t^{\mathrm{e}})_{fe}+(v_t^{\mathrm{e}})^{-1}_{ak}(v_t^{\mathrm{e}})_{le}. \tag{A.27}$$

Finally we can write $\big(D^{cst}_{\beta}\big)_{ijkl}$ as

$$\big(D^{cst}_{\beta}\big)_{ijkl}=\frac{2}{J}D^{\beta}_{ijan}(\beta_t)_{en}\Big(2(L_\beta)_{afkd}(b_t^{\mathrm{e}})_{ld}(v_t^{\mathrm{e}})_{fe}+(v_t^{\mathrm{e}})^{-1}_{ak}(v_t^{\mathrm{e}})_{le}\Big). \tag{A.28}$$

Appendix B

Finite-element implementation

This appendix presents the matrix equations for the finite-element implementation of the finite-deformation elasto-plastic framework described in Chapter 3. The general three-dimensional case is presented first followed by the special cases of two-dimensional plane-strain and axi-symmetric analysis.

B.1 Three-dimensional implementation

The six-component stress and strain vectors were ordered according to (2.6). The nine-component measures used the following ordering

$$\{\sigma\} \quad = \quad \{\sigma_{xx} \quad \sigma_{yy} \quad \sigma_{zz} \quad \sigma_{xy} \quad \sigma_{yx} \quad \sigma_{yz} \quad \sigma_{zy} \quad \sigma_{zx} \quad \sigma_{xz}\}^T. \tag{B.1}$$

B.1.1 Deformation gradient

The increment in the deformation gradient is calculated through

$$\big[\Delta F\big] = \Big[[1] - [\delta F]\Big]^{-1}, \tag{B.2}$$

where the nine-component vector form of $[\delta F]$ is obtained through

$$\{\delta F\} = [G]\{\Delta u\}, \qquad \text{and} \qquad \big[\delta F\big] = \begin{bmatrix} \{\delta F_1\} & \{\delta F_4\} & \{\delta F_9\} \\ \{\delta F_5\} & \{\delta F_2\} & \{\delta F_6\} \\ \{\delta F_8\} & \{\delta F_7\} & \{\delta F_3\} \end{bmatrix}, \tag{B.3}$$

where $\{\delta F_1\}$ refers to the first entry of the nine component vector obtained from $(\text{B.3})_1$. The incremental nodal displacements $\{\Delta u\}$ have the following format

$$\{u\} = \{\Delta u_{x_1} \quad \Delta u_{y_1} \quad \Delta u_{z_1} \qquad \ldots \qquad \Delta u_{x_n} \quad \Delta u_{y_n} \quad \Delta u_{z_n}\}^T, \tag{B.4}$$

and n is the number of nodes per element. The spatial non-linear nine-component strain displacement matrix, $[G]$, for three-dimensional analysis is given by

$$\big[G\big] = \begin{bmatrix} N_{1,x} & 0 & 0 & \dots & N_{n,x} & 0 & 0 \\ 0 & N_{1,y} & 0 & \dots & 0 & N_{n,y} & 0 \\ 0 & 0 & N_{1,l}\, z & \dots & 0 & 0 & N_{n,z} \\ N_{1,y} & 0 & 0 & \dots & N_{n,y} & 0 & 0 \\ 0 & N_{1,x} & 0 & \dots & 0 & N_{n,x} & 0 \\ 0 & N_{1,z} & 0 & \dots & 0 & N_{n,z} & 0 \\ 0 & 0 & N_{1,y} & \dots & 0 & 0 & N_{n,y} \\ 0 & 0 & N_{1,x} & \dots & 0 & 0 & N_{n,x} \\ N_{1,z} & 0 & 0 & \dots & N_{n,z} & 0 & 0 \end{bmatrix}. \tag{B.5}$$

B.1.2 Jacobian matrix

The Jacobian matrix provides the link between the local element and the global finite-element co-ordinate systems. The three by three matrix can be calculated through

$$[J] = \begin{bmatrix} x_{,\xi} & y_{,\xi} & z_{,\xi} \\ x_{,\eta} & y_{,\eta} & z_{,\eta} \\ x_{,\zeta} & y_{,\zeta} & z_{,\zeta} \end{bmatrix} = \begin{bmatrix} N_{1,\xi} & N_{2,\xi} & \dots & N_{n,\xi} \\ N_{1,\eta} & N_{2,\eta} & \dots & N_{n,\eta} \\ N_{1,\zeta} & N_{2,\zeta} & \dots & N_{n,\zeta} \end{bmatrix} \begin{bmatrix} x_1 & y_1 & z_1 \\ x_2 & y_2 & z_2 \\ \vdots & \vdots & \vdots \\ x_n & y_n & z_n \end{bmatrix} \tag{B.6}$$

where x_i, y_i and z_i are the current global nodal co-ordinates, n is the number of nodes associated with an element and $N_{i,(\cdot)}$ are the derivatives of the element shape functions with respect to the element local co-ordinates ξ, η and ζ.

B.1.3 Inclined boundary conditions

Inclined boundary conditions were implemented using the *transformation approach* which applies the inclined conditions exactly through rotation of components of the stiffness matrix and force vectors. The global stiffness equation becomes

$$\begin{bmatrix} [T][K_{1,1}][T]^T & [T][K_{1,2}] & \dots & [T][K_{1,n}] \\ [K_{2,1}][T]^T & [K_{2,2}] & \dots & [K_{2,n}] \\ \vdots & \vdots & \ddots & \vdots \\ [K_{n,1}][T]^T & [K_{n,2}] & \dots & [K_{n,n}] \end{bmatrix} \begin{Bmatrix} \{\bar{\delta u}_1\} \\ \{\delta u_2\} \\ \vdots \\ \{\delta u_n\} \end{Bmatrix} = \begin{Bmatrix} \{\bar{f}_1^{\text{oobf}}\} \\ \{f_2^{\text{oobf}}\} \\ \vdots \\ \{f_n^{\text{oobf}}\} \end{Bmatrix}, \tag{B.7}$$

where $\bar{(\cdot)}$ denote quantities associated with the rotated configuration and $[T] = [T_x][T_y][T_z]$ is the transformation matrix, obtained from

$$[T_x] = \begin{bmatrix} 1 & 0 & 0 \\ 0 & \cos(\theta_x) & \cos(\pi/2-\theta_x) \\ 0 & \cos(\pi/2+\theta_x) & \cos(\theta_x) \end{bmatrix}, \quad [T_y] = \begin{bmatrix} \cos(\theta_y) & 0 & \cos(\pi/2-\theta_y) \\ 0 & 1 & 0 \\ \cos(\pi/2+\theta_y) & 0 & \cos(\theta_y) \end{bmatrix},$$
$$[T_z] = \begin{bmatrix} \cos(\theta_z) & \cos(\pi/2-\theta_z) & 0 \\ \cos(\pi/2+\theta_z) & \cos(\theta_z) & 0 \\ 0 & 0 & 1 \end{bmatrix}. \tag{B.8}$$

The solution procedure is given by:

(i) transform the stiffness matrix and the out-of-balance force vector for the nodes with inclined boundary conditions though

$$[\bar{K}(i,:)] = [T][K(i,:)], \qquad [\bar{K}(:,i)] = [\bar{K}(:,i)][T]^T \qquad \text{and} \qquad \{\bar{f}(i)\} = [T]\{f(i)\},$$

where i denotes the nodal degrees of freedom;

(ii) solve the reduced transformed stiffness equation for the unknown displacements $\{\bar{\delta u}(j)\}$ and reaction forces $\{\bar{f}^r(k)\}$

$$\{\delta\bar{u}(j)\}[\bar{K}(j,j)] = \Big\{\{\bar{f}^{\text{oobf}}(j)\} - [\bar{K}(j,k)]\{\delta u(k)\}\Big\} \qquad \text{and} \qquad \{\bar{f}^r\} = [\bar{K}]\{\delta\bar{u}\} - \{\bar{f}^{\text{oobf}}\},$$

where j and k denote the free (unknown) and fixed (known) degrees of freedom respectively; and

(iii) transform the displacements and reaction forces back into the original configuration

$$\{f^r(i)\} = [T]^T\{\bar{f}^r(i)\} \qquad \text{and} \qquad \{\delta u(i)\} = [T]^T\{\bar{\delta u}(i)\}.$$

B.1.4 Undrained analysis

Undrained incompressible finite-element analysis can be implemented via the addition of the pore-water pressure to the Gauss point stresses

$$\{\sigma\} = \{\sigma'\} + \{\sigma_u\}, \tag{B.9}$$

where $\{\sigma'\}$ are the effective stresses (the stress in a conventional drained analysis) and $\{\sigma_u\}$ is the pore-water pressure, given by

$$\{\sigma_u\} = K_f(\varepsilon_v)\{1\}. \tag{B.10}$$

K_f is the fluid bulk modulus, $\varepsilon_v = (\varepsilon_{xx}+\varepsilon_{yy}+\varepsilon_{zz})$ is the volumetric strain and $\{1\} = \{1 \quad 1 \quad 1 \quad 0 \quad 0 \quad 0\}^T$. The material point stiffness matrix becomes

$$[D^{cst}] = [D^{cst'}] + [D_f], \qquad \text{where} \qquad [D_f] = K_f\Big[\{1\}\{1\}^T\Big]. \tag{B.11}$$

Smith and Griffiths [1] recommended that the fluid bulk modulus be $K_f \geq 60K$, where $K = E/\big(3(1-2v)\big)$ is the bulk modulus of the material.

B.2 Two-dimensional implementation

B.2.1 Stress format

The implemented finite-element program used the following ordering of four-component stress and strain vectors

$$\{\sigma\} = \{\sigma_{xx} \quad \sigma_{yy} \quad \sigma_{zz} \quad \sigma_{xy}\}^T \qquad \text{and} \qquad \{\varepsilon\} = \{\varepsilon_{xx} \quad \varepsilon_{yy} \quad \varepsilon_{zz} \quad \varepsilon_{xy}\}^T. \tag{B.12}$$

B.2.2 Plane-strain

For plane-strain analysis the out-of-plane strain, ε_{zz}, is zero. However, for inelastic analysis the elastic and plastic strains, in general are non-zero satisfying the condition that $\varepsilon^{\text{e}}_{zz} = -\varepsilon^{\text{p}}_{zz}$. The spatial non-linear

four-component strain displacement matrix, $[G]$, for two-dimensional plane-strain analysis is

$$\big[G\big] = \begin{bmatrix} N_{1,x} & 0 & \dots & N_{n,x} & 0 \\ 0 & N_{1,y} & \dots & 0 & N_{n,y} \\ N_{1,y} & 0 & \dots & N_{n,y} & 0 \\ 0 & N_{1,x} & \dots & 0 & N_{n,x} \end{bmatrix}. \tag{B.13}$$

The increment in the deformation gradient can be calculated through (B.3) with $[G]$ given by (B.13).

B.2.3 Axi-symmetry

Axi-symmetric analysis is conveniently formulated in polar co-ordinates and accounts for the out-of-plane circumferential strain, obtained through the ratio of the current to the original radial co-ordinate. The spatial non-linear five-component strain displacement matrix, $[G]$, for two-dimensional plane-strain analysis is given by

$$\big[G\big] = \begin{bmatrix} N_{1,x} & 0 & \dots & N_{n,x} & 0 \\ 0 & N_{1,y} & \dots & 0 & N_{n,y} \\ N_1/r & 0 & \dots & N_n/r & 0 \\ N_{1,y} & 0 & \dots & N_{n,y} & 0 \\ 0 & N_{1,x} & \dots & 0 & N_{n,x} \end{bmatrix}, \tag{B.14}$$

where r is the updated radial co-ordinate of the Gauss point. Again, the increment in the deformation gradient can be calculated through (B.3) with $[G]$ given by (B.14). The element internal force vector is obtained as [1]

$$\{f^e\} = \sum_{i=1}^{n_{gp}} \big[B_{n+1}\big]_i \{\sigma_{n+1}\}_i \det\Big(\big[J\big]_i\Big) w_i r_i, \tag{B.15}$$

where n_{gp} is the number of Gauss point associated with the element, $[J]$ is the Jacobian matrix and w is the weight function. The element stiffness matrix is calculated from

$$\big[k^e\big] = \sum_{i=1}^{n_{gp}} \big[G_{n+1}\big]_i \big[D_\sigma^{cst}\big]_i \big[G_{n+1}\big]_i^T \det\Big(\big[J\big]_i\Big) w_i r_i, \tag{B.16}$$

where $\big[D_\sigma^{cst}\big]$ is the spatial consistent tangent stiffness matrix. Note the addition of the current radial co-ordinate, r, in the calculation of both the element stiffness matrix and force vector.

References

[1] IM Smith & DV Griffiths, *Programming the Finite Element Method*, John Wiley & Sons Ltd., 2004.

[2] E Hinton & DRJ Owen, *Finite element programming*, Academic Press Inc. Ltd., 1977.

Appendix C

Principal constitutive equations

C.1 Stress derivatives

The isotropic models in Chapters 4 and 5 were developed using principal stresses and strains. Their implementation requires the following derivatives that were not included in the main body of the thesis for the sake of brevity. The first derivative of $\xi = \mathrm{tr}[\sigma]/\sqrt{3}$ with respect to stress is given by

$$\{\xi_{,\hat{\sigma}}\} = \frac{1}{\sqrt{3}}\{\hat{1}\}, \qquad \text{where} \qquad \{\hat{1}\} = \{1 \quad 1 \quad 1\}^T. \tag{C.1}$$

The derivative of $\rho = \sqrt{2J_2}$, where $J_2 = \big(\{\hat{s}\}^T\{\hat{s}\}\big)/2$, $\{\hat{s}\} = \{\hat{\sigma}\} - \xi\{\hat{1}\}/\sqrt{3}$, with respect to $\{\hat{\sigma}\}$ is

$$\{\rho_{,\hat{\sigma}}\} = \{\rho_{,\hat{s}}\}\{\hat{s}_{,\hat{\sigma}}\} = \{\hat{s}\}/\rho \tag{C.2}$$

and the second derivative is obtained as

$$\big[\rho_{,\hat{\sigma}\hat{\sigma}}\big] = \frac{\rho\big[J_{2,\hat{\sigma}\hat{\sigma}}\big] - \{\rho_{,\hat{\sigma}}\}\{\hat{s}\}^T}{\rho^2}. \tag{C.3}$$

The derivatives of J_2 and $J_3 = (s_1^3 + s_2^3 + s_3^3)/3$ are given by

$$\{J_{2,\hat{\sigma}}\} = \{\hat{s}\}/\rho \qquad \text{and} \qquad \{J_{3,\hat{\sigma}}\} = \{s_2 s_3 \quad s_1 s_3 \quad s_1 s_2\}^T + J_2\{\hat{1}\}/3. \tag{C.4}$$

The second derivatives are

$$\big[J_{3,\hat{\sigma}\hat{\sigma}}\big] = \frac{2}{3}\begin{bmatrix} s_1 & s_3 & s_2 \\ s_3 & s_2 & s_1 \\ s_2 & s_1 & s_3 \end{bmatrix} \qquad \text{and} \qquad \big[J_{2,\hat{\sigma}\hat{\sigma}}\big] = \frac{1}{3}\Big(3[I] - \{\hat{1}\}\{\hat{1}\}^T\Big). \tag{C.5}$$

Taking the partial derivative of the Lode angle $(2.9)_3$, we obtain

$$\{\theta_{,\hat{\sigma}}\} = \frac{-\sqrt{3}}{2\cos 3\theta}\underbrace{\left(J_2^{-3/2}\{J_{3,\hat{\sigma}}\} - \frac{3}{2}J_3 J_2^{-5/2}\{\hat{s}\}\right)}_{\{\vartheta\}}. \tag{C.6}$$

When on the extension meridian ($\theta = -\pi/6$) and when on the compression meridian ($\theta = \pi/6$), (C.6) is indeterminate. Here l'Hôpital's rule is used to construct the derivatives

$$\{\theta_{,\hat{\sigma}}\}_{\theta=-\pi/6} = \frac{\rho}{2\sqrt{6}}\left[\vartheta_{,\hat{\sigma}}\right]\{-1 \quad 1 \quad 0\}^T \qquad \text{and} \qquad \{\theta_{,\hat{\sigma}}\}_{\theta=\pi/6} = \frac{\rho}{2\sqrt{6}}\left[\vartheta_{,\hat{\sigma}}\right]\{0 \quad 1 \quad -1\}^T, \tag{C.7}$$

where the derivative of $\{\vartheta\}$, see (C.6), with respect to $\{\sigma\}$ is given by

$$\left[\vartheta_{,\hat{\sigma}}\right] = -\frac{3}{2}J_2^{-5/2}\left(\{\hat{s}\}\{J_{3,\hat{\sigma}}\}^T + \{J_{3,\hat{\sigma}}\}\{\hat{s}\}^T + J_3\left[J_{2,\hat{\sigma}\hat{\sigma}}\right]\right) + J_2^{-3/2}\left[J_{3,\hat{\sigma}\hat{\sigma}}\right] + \frac{15}{4}J_3J_2^{-7/2}\{\hat{s}\}\{\hat{s}\}^T. \tag{C.8}$$

The second derivative of Lode angle with respect to $\{\hat{\sigma}\}$ is obtained as

$$[\theta_{,\hat{\sigma}\hat{\sigma}}] = 3\tan(3\theta)\{\theta_{,\hat{\sigma}}\}\{\theta_{,\hat{\sigma}}\}^T - \frac{\sqrt{3}}{2\cos(3\theta)}[\vartheta_{,\hat{\sigma}}]. \tag{C.9}$$

C.2 Lode angle dependency $\bar{\rho}(\theta)$

This section provides the derivatives of the modified Reuleaux (mR) [1] and Willam-Warnke (W-W) [2] deviatoric functions with respect to the principal stresses. When using anisotropic constitutive models the stress return and consistent tangent must be formed in true, six-component, stress space. However, due to the θ singularities at $\pm\pi/6$, it is advantageous when working in six-component space to convert to principal stress space find the derivatives of the Lode angle dependency (LAD) and convert back to true stress space using the procedure given in Section C.3.

C.2.1 Modified Reuleaux

The derivative of the mR LAD (4.1) with respect to $\{\sigma\}$ is given by

$$\{\bar{\rho}_{,\hat{\sigma}}\} = \bar{\rho}_{,\bar{\rho}\bar{\rho}}\ \bar{\rho}^2_{,\varphi}\ \varphi_{,\theta}\{\theta_{,\hat{\sigma}}\}, \qquad \text{where} \tag{C.10}$$

$$\bar{\rho}_{,\bar{\rho}\bar{\rho}} = \frac{1}{2\bar{\rho}}, \qquad \bar{\rho}^2_{,\varphi} = 2\bar{a}\,\bar{r}\sin\varphi \qquad \text{and} \qquad \varphi_{,\theta} = 1 + \frac{\bar{a}\cos(5\pi/6-\theta)}{\bar{r}\sqrt{1-(\bar{a}\sin(5\pi/6-\theta)/\bar{r})^2}}. \tag{C.11}$$

Second derivatives of $\bar{\rho}$ and φ follow as

$$\left[\bar{\rho}_{,\sigma\sigma}\right] = \{\bar{\rho}_{,\sigma\bar{\rho}}\}\{\bar{\rho}_{,\sigma}\}^T + \{\bar{\rho}_{,\sigma\varphi}\}\{\varphi_{,\sigma}\}^T + \bar{\rho}_{,\sigma\varphi,\sigma}\left[\varphi_{,\sigma\sigma}\right], \tag{C.12}$$

$$\{\bar{\rho}_{,\sigma\bar{\rho}}\} = -\frac{\bar{a}\bar{r}\sin\varphi}{\bar{\rho}^2}\{\varphi_{,\sigma}\}, \qquad \{\bar{\rho}_{,\sigma\varphi}\} = \frac{\bar{a}\bar{r}\cos\varphi}{\bar{\rho}}\{\varphi_{,\sigma}\}, \qquad \bar{\rho}_{,\sigma\varphi,\sigma} = \frac{\bar{a}\bar{r}\sin\varphi}{\bar{\rho}} \qquad \text{and} \tag{C.13}$$

$$\left[\varphi_{,\hat{\sigma}\hat{\sigma}}\right] = \{\varphi_{,\hat{\sigma}\theta}\}\{\theta_{,\hat{\sigma}}\}^T + \varphi_{,\theta}\left[\theta_{,\hat{\sigma}\hat{\sigma}}\right], \tag{C.14}$$

where

$$\{\varphi_{,\hat{\sigma}\theta}\} = \frac{\bar{a}}{\bar{r}}\left(\frac{S\bar{r}^2\left(1-(S\bar{a}/\bar{r})^2\right)^2 - \bar{a}^2SC^2}{\bar{r}^2(1-(S\bar{a}/\bar{r})^2)\sqrt{1-(S\bar{a}/\bar{r})^2}}\right)\{\theta_{,\hat{\sigma}}\}. \tag{C.15}$$

Here $C = \cos(5\pi/6-\theta)$ and $S = \sin(5\pi/6-\theta)$.

C.2.2 Willam-Warnke

The W-W [2] LAD was used in Chapters 5 and 6 as the deviatoric yield criterion for the isotropic and anisotropic Critical State constitutive models. The derivative of that LAD, as given by (5.21), with

respect to θ is

$$\bar{\rho}_{,\theta} = \frac{a_1 S\Big(b_1(1+2C/b_2) - 4C(a_1 C + b_2)\Big)}{b_1^2}, \qquad \text{where} \qquad b_1 = 2a_1C^2{+}1 \qquad \text{and} \qquad b_2 = \Big(2a_1C^2{+}a_2\Big)^{1/2}. \tag{C.16}$$

Here $C = \cos(\pi/6 - \theta)$ and $S = \sin(\pi/6 - \theta)$.

C.3 Stress transformation

The following relations can be used to transform between six-component and principal stress and strain space

$$\{\sigma\} = [Q]^T \left\{ \begin{array}{c} \{\hat{\sigma}\} \\ \{0\} \end{array} \right\}, \qquad \{\varepsilon\} = [Q]^{-1} \left\{ \begin{array}{c} \{\hat{\varepsilon}\} \\ \{0\} \end{array} \right\} \qquad \text{and} \qquad [D] = [Q]^T [\hat{D}][Q], \tag{C.17}$$

where $(\hat{\cdot})$ denotes the principal stress and strain quantities. The transformation matrix is given by

$$[Q] = \begin{bmatrix} (t_1)^2 & (t_2)^2 & (t_3)^2 & t_1t_2 & t_2t_3 & t_3t_1 \\ (t_4)^2 & (t_5)^2 & (t_6)^2 & t_4t_5 & t_5t_6 & t_6t_4 \\ (t_7)^2 & (t_8)^2 & (t_9)^2 & t_7t_8 & t_8t_9 & t_9t_7 \\ 2t_1t_4 & 2t_2t_5 & 2t_3t_6 & t_1t_5 + t_4t_2 & t_2t_6 + t_5t_3 & t_3t_4 + t_6t_1 \\ 2t_4t_7 & 2t_5t_8 & 2t_6t_9 & t_4t_8 + t_7t_5 & t_5t_9 + t_8t_6 & t_6t_7 + t_9t_4 \\ 2t_7t_1 & 2t_8t_2 & 2t_9t_3 & t_7t_2 + t_1t_8 & t_8t_3 + t_2t_9 & t_9t_1 + t_3t_7 \end{bmatrix}, \tag{C.18}$$

where the components t_i are associated with the trial elastic strain eigenvectors

$$[t] = \begin{bmatrix} t_1 & t_4 & t_7 \\ t_2 & t_5 & t_8 \\ t_3 & t_6 & t_9 \end{bmatrix}. \tag{C.19}$$

References

[1] WM Coombs, RS Crouch & CE Augarde, *Reuleaux plasticity: analytical backward Euler stress integration and consistent tangent*, Comput. Meth. Appl. Mech. Engrg. 199 (2010), 1733–1743.

[2] KJ Willam & EP Warnke, *Constitutive model for the triaxial behaviour of concrete*, Proceedings of the May 17-19 1974, International Association of Bridge and Structural Engineers Seminar on Concrete Structures Subjected to Triaxial Stresses, held at Bergamo Italy, 1974.

Appendix D

General constitutive equations

D.1 Stress derivatives

The first derivative of $\xi = \mathrm{tr}[\sigma]/\sqrt{3}$ with respect to stress is given by

$$\{\xi_{,\sigma}\} = \frac{1}{\sqrt{3}}\{1\}, \qquad \text{where} \qquad \{1\} = \{1 \quad 1 \quad 1 \quad 0 \quad 0 \quad 0\}^T. \tag{D.1}$$

The derivative of $\rho = \sqrt{2J_2}$, where $J_2 = \mathrm{tr}\big([s]^2\big)/2$, $[s] = [\sigma] - \xi[1]/\sqrt{3}$ and $[1]$ is the third order identity matrix, with respect to $\{\sigma\}$ is

$$\{\rho_{,\sigma}\} = \{\rho_{,s}\}\{s_{,\sigma}\} = \frac{\{s\}}{\rho}[\delta] \tag{D.2}$$

where $[\delta] = [I] - \{1\}\{1\}^T/3$. The derivatives of J_2 and $J_3 = \mathrm{tr}\big([s]^3\big)/3$ with respect to $\{\sigma\}$ are given by

$$\{J_{2,\sigma}\} = \frac{1}{3}\begin{Bmatrix} 2\sigma_{xx} - \sigma_{yy} - \sigma_{zz} \\ 2\sigma_{yy} - \sigma_{xx} - \sigma_{zz} \\ 2\sigma_{zz} - \sigma_{xx} - \sigma_{yy} \\ 6\sigma_{xy} \\ 6\sigma_{yz} \\ 6\sigma_{zx} \end{Bmatrix}, \qquad \{J_{3,\sigma}\} = \frac{1}{9}\begin{Bmatrix} (2\sigma_{yy} - \sigma_{xx} - \sigma_{zz})(2\sigma_{zz} - \sigma_{xx} - \sigma_{yy}) - 9\sigma_{yz}^2 + 3J_2 \\ (2\sigma_{xx} - \sigma_{yy} - \sigma_{zz})(2\sigma_{zz} - \sigma_{xx} - \sigma_{yy}) - 9\sigma_{xz}^2 + 3J_2 \\ (2\sigma_{xx} - \sigma_{yy} - \sigma_{zz})(2\sigma_{yy} - \sigma_{xx} - \sigma_{zz}) - 9\sigma_{xy}^2 + 3J_2 \\ 18\sigma_{yz}\sigma_{xz} - 6(2\sigma_{zz} - \sigma_{xx} - \sigma_{yy})\sigma_{xy} \\ 18\sigma_{xz}\sigma_{xy} - 6(2\sigma_{xx} - \sigma_{yy} - \sigma_{zz})\sigma_{yz} \\ 18\sigma_{xy}\sigma_{yz} - 6(2\sigma_{yy} - \sigma_{xx} - \sigma_{zz})\sigma_{xz} \end{Bmatrix}. \tag{D.3}$$

The second derivative of ρ with respect to stress is given by (C.3) but with the stress invariant derivatives as follows. The symmetric second derivatives of J_2 and J_3 with respect to $\{\sigma\}$ are

$$[J_{2,\sigma\sigma}] = \frac{1}{3}\begin{bmatrix} 2 & & & & & \\ -1 & 2 & & & & \\ -1 & -1 & 2 & & & \\ 0 & 0 & 0 & 6 & & \\ 0 & 0 & 0 & 0 & 6 & \\ 0 & 0 & 0 & 0 & 0 & 6 \end{bmatrix}, \qquad [J_{3,\sigma\sigma}] = \frac{2}{3}\begin{bmatrix} s_{xx} & & & & & \\ s_{zz} & s_{yy} & & & & \\ s_{yy} & s_{xx} & s_{zz} & & & \\ \sigma_{xy} & \sigma_{xy} & -2\sigma_{xy} & -3s_{zz} & & \\ -2\sigma_{yz} & \sigma_{yz} & \sigma_{yz} & 3\sigma_{xz} & -3s_{xx} & \\ \sigma_{xz} & 2\sigma_{xz} & \sigma_{xz} & 3\sigma_{yz} & 3\sigma_{xy} & -2s_{yy} \end{bmatrix}. \tag{D.4}$$

Appendix E

Anisotropic model derivatives

This appendix provides the derivatives necessary for the backward Euler stress integration and consistent linearisation of the anisotropic two-surface two-parameter Critical State hyperplasticity model presented in Chapter 6. The derivatives are formed in true stress space with a compression positive convention. The derivatives of the Lode angle with respect to stress will depend on the implemented Lode angle dependency, the derivatives for the Willam-Warnke and modified Reuleaux deviatoric functions are given in Appendix C.2.

Yield function

The derivative of the yield function (6.15) with respect to stress is given by

$$\begin{aligned}
\{f_{,\sigma}\} &= \frac{f_{,p}}{3}\{1\} + 2A_f^2[\delta]\{s^\beta\} + f_{,\bar{\rho}}\{\bar{\rho}_{,\sigma}\}, \qquad \text{where} \\
f_{,p} &= 2\Big(B_f^2\Big(p - p^\chi - A_f(1-\gamma)\Big) + B_f\bar{\rho}M(1-\alpha)\Big((p-p^\chi)^2 - A_f^2\Big) \ldots \\
&\quad + A_f\Big\{(1-\gamma)\{s^\beta\} - A_f\{\beta\}\Big\}^T\{s^\beta\}\Big), \\
f_{,\bar{\rho}} &= 2B_f b_M\Big((p-p^\chi)^2 - A_f^2\Big) \qquad \text{and} \qquad b_M = M\Big((1-\alpha)(p-p^\chi) + Rp_c\gamma/2\Big).
\end{aligned} \tag{E.1}$$

The derivatives of the yield function with respect to p_c, $\{\sigma^\chi\}$ and $\{\beta\}$ are given by

$$\begin{aligned}
f_{,p_c} &= R\gamma\left[B_f\bar{\rho}M\Big([p-p^\chi]^2 - A_f^2\Big) + A_f(2-\gamma)\Big(\{s^\beta\}^T\{s^\beta\} - B_f^2\Big)\right], \\
\{f_{,\sigma^\chi}\} &= -\{f_{,\sigma}\} \qquad \text{and} \qquad \{f_{,\beta}\} = -2A_f^2(p-p^\chi)\{s^\beta\} - f_{,\bar{\rho}}\,(p-p^\chi)\{\bar{\rho}_{,s^\beta}\}.
\end{aligned} \tag{E.2}$$

Plastic flow

The derivative of the direction of plastic flow (6.30) with respect to stress is obtained as

$$\begin{aligned}
[g_{,\sigma\sigma}] &= \frac{\{g_{,\sigma p}\}\{1\}^T}{3} + 2A_f^2\Big[[\delta] - \{\beta\}\{1\}/3\Big][\delta] + \{g_{,\sigma\bar{\rho}}\}\{\bar{\rho}_{,\sigma}\}^T, \qquad \text{where} \\
\{g_{,\sigma p}\} &= \frac{2}{3}\left[B_f^2 + 2M\bar{\rho}B_f(1-\alpha)(p-p^\chi) + A_f\Big\{A_f\{\beta\} - 2(1-\gamma)\{s^\beta\}\Big\}^T\{\beta\}\right]\{1\} \ldots \\
&\quad + 2A_f[\delta]\Big\{2(1-\gamma)\{s^\beta\} - A_f\{\beta\}\Big\}, \\
\{g_{,\sigma\bar{\rho}}\} &= \frac{4}{3}\Big(B_f d_M(p-p^\chi)\Big)\{1\} \qquad \text{and} \qquad [\delta] = [I] - \{1\}\{1\}^T/3.
\end{aligned} \tag{E.3}$$

The derivatives of the plastic flow direction with respect to p_c, $\{\sigma^\chi\}$ and $\{\beta\}$ are given by

$$\begin{aligned}
\{g_{,\sigma p_c}\} &= 2R\gamma\left\{\left(B_f\bar{\rho}M(p-p^\chi) - A_f(2-\gamma)\{s^\beta\}^T\{\beta\}\right)\{1\}/3 + A_f(2-\gamma)[\delta]\{s^\beta\}\right\},\\
[g_{,\sigma\sigma^\chi}] &= -[g_{,\sigma\sigma}] \qquad \text{and}\\
[g_{,\sigma\beta}] &= 2A_f^2\left[\left\{(p-p^\chi)\{\beta\} - \{s^\beta\}\right\}\{1\}^T/3 - (p-p^\chi)[\delta]\right] - (p-p^\chi)\{g_{,\sigma\bar{\rho}}\}\{\bar{\rho}_{,s^\beta}\}^T. \qquad \text{(E.4)}
\end{aligned}$$

Hardening law: $\tilde{p}_c$

The derivatives of $\tilde{p}_c$ (5.25) are given by

$$\{\tilde{p}_{c,\sigma}\}^T = \Delta\gamma p_n\{1\}^T[g_{,\sigma\sigma}], \qquad (\tilde{p}_{c,p_c}) = \Delta\gamma p_n\{g_{,\sigma p_c}\}^T\{1\}, \qquad (\tilde{p}_{c,\Delta\gamma}) = p_n\{g_{,\sigma}\}^T\{1\},$$

$$\{\tilde{p}_{c,\sigma^\chi}\} = -\{\tilde{p}_{c,\sigma}\} \qquad \text{and} \qquad \{\tilde{p}_{c,\beta}\}^T = \Delta\gamma p_n\{1\}^T[g_{,\sigma\beta}], \qquad \text{where}$$

$$p_n = \frac{\partial\tilde{p}_c}{\partial(\Delta\varepsilon_v^{\mathrm{p}})} = \frac{p_{c_n}}{(\lambda-\kappa)(1-\Delta\varepsilon_v^{\mathrm{p}}/(\lambda-\kappa))^2}. \qquad \text{(E.5)}$$

The derivative of (6.68) with respect to the plastic strain increment is given by

$$\begin{aligned}
\left[\tilde{\sigma}^\chi_{,\Delta\varepsilon^{\mathrm{p}}}\right] &= \frac{\{\tilde{\sigma}^\chi_{,||\Delta\varepsilon^{\mathrm{p}}||}\}\{g_{,\sigma}\}^T}{||\{g_{,\sigma}\}||} + \{\tilde{\sigma}^\chi_{,\Delta\varepsilon_v^{\mathrm{p}}}\}\{1\}^T, \qquad \text{where}\\
\{\tilde{\sigma}^\chi_{,||\Delta\varepsilon^{\mathrm{p}}||}\} &= C^\chi[\tilde{\sigma}^\chi_{denom}]^{-2}\Big\{\{(1-R)\{\sigma\} + Rp_c\gamma\{1+\beta\}/2\}(\tilde{\sigma}^\chi_{denom}) - \{\tilde{\sigma}^\chi_{num}\}\Big\} \qquad \text{and}\\
\{\tilde{\sigma}^\chi_{,\Delta\varepsilon_v^{\mathrm{p}}}\} &= \frac{[\tilde{\sigma}^\chi_{denom}]^{-2}\{\tilde{\sigma}^\chi_{num}\}}{(\lambda-\kappa)}. \qquad \text{(E.6)}
\end{aligned}$$

Hardening law: $\{\tilde{\sigma}^\chi\}$

The derivative of $\{\tilde{\sigma}^\chi\}$ (6.68) with respect to stress is given by

$$[\tilde{\sigma}^\chi_{,\sigma}] = \Delta\gamma[\tilde{\sigma}^\chi_{,\Delta\varepsilon^{\mathrm{p}}}][g_{,\sigma\sigma}] + C^\chi||\{\Delta\varepsilon^{\mathrm{p}}\}||(1-R)\left[\tilde{\sigma}^\chi_{denom}\right]^{-1}, \qquad \text{(E.7)}$$

and with respect to the size of the outer surface

$$\{\tilde{\sigma}^\chi_{,p_c}\} = \Delta\gamma[\tilde{\sigma}^\chi_{,\Delta\varepsilon^{\mathrm{p}}}]\{g_{,\sigma p_c}\} + \frac{C^\chi||\{\Delta\varepsilon^{\mathrm{p}}\}||R\gamma}{2}\left[\tilde{\sigma}^\chi_{denom}\right]^{-1}\Big\{\{1\} + \{\beta\}\Big\}. \qquad \text{(E.8)}$$

The derivative of the evolution of the centre of the subloading surface with respect to the inclination of the yield surfaces is

$$[\tilde{\sigma}^\chi_{,\beta}] = \Delta\gamma[\tilde{\sigma}^\chi_{,\Delta\varepsilon^{\mathrm{p}}}][g_{,\sigma\beta}] + \left[\tilde{\sigma}^\chi_{denom}\right]^{-2}\left[\frac{C^\chi||\{\Delta\varepsilon^{\mathrm{p}}\}||Rp_c\gamma}{2}\left[\tilde{\sigma}^\chi_{denom}\right] + \left(\frac{\{1\}^T\{\tilde{\sigma}^\chi_{num}\}}{3}\right)[I]\right],$$

and with respect to the centre of the subloading surface and the plastic multiplier

$$[\tilde{\sigma}^\chi_{,\sigma^\chi}] = \Delta\gamma[\tilde{\sigma}^\chi_{,\Delta\varepsilon^{\mathrm{p}}}][g_{,\sigma\sigma^\chi}], \qquad \text{and} \qquad \{\tilde{\sigma}^\chi_{,\Delta\gamma}\} = [\tilde{\sigma}^\chi_{,\Delta\varepsilon^{\mathrm{p}}}]\{g_{,\sigma}\}. \qquad \text{(E.9)}$$

Hardening law: $\{\tilde{\beta}\}$

The derivative of $\{\tilde{\beta}\}$ (6.70) with respect to the incremental plastic strain is given by

$$[\tilde{\beta}_{,\Delta\varepsilon^{\mathrm{p}}}] = \{\tilde{\beta}_{,\langle\Delta\varepsilon_v^{\mathrm{p}}\rangle}\}(\langle\Delta\varepsilon_v^{\mathrm{p}}\rangle_{,\Delta\varepsilon_v^{\mathrm{p}}})\{1\}^T + \left[\{\tilde{\beta}_{,\Delta\varepsilon_\gamma^{\mathrm{p}}}\}\frac{\{g_{,\sigma_{dev}}\}^T}{||\{g_{,\sigma_{dev}}\}||}\right][\delta], \qquad \text{(E.10)}$$

where $\{g_{,\sigma_{dev}}\} = \{g_{,\sigma}\} - (\{g_{,\sigma}\}^T\{1\}/3)\{1\}$ is the deviatoric direction of plastic strains. The derivatives of the ramp function are

$$(\langle\Delta\varepsilon_v^{\mathrm{p}}\rangle_{,\Delta\varepsilon_v^{\mathrm{p}}}) = 1 \quad \text{for} \quad \Delta\varepsilon_v^{\mathrm{p}} > 0 \qquad \text{and} \qquad (\langle\Delta\varepsilon_v^{\mathrm{p}}\rangle_{,\Delta\varepsilon_v^{\mathrm{p}}}) = 0 \quad \text{for} \quad \Delta\varepsilon_v^{\mathrm{p}} \leq 0. \tag{E.11}$$

The derivative of (6.70) with respect to $\langle\Delta\varepsilon_v^{\mathrm{p}}\rangle$ is given by

$$\{\tilde{\beta}_{,\langle\Delta\varepsilon_v^{\mathrm{p}}\rangle}\} = \frac{C_\beta}{(\tilde{\beta}_{denom})^2}\Big\{a_\beta(\tilde{\beta}_{denom})\{s - s^\chi\} - (p_\beta - Rp_c a_\beta/2)\{\tilde{\beta}_{num}\}\Big\} \tag{E.12}$$

and with respect to $\Delta\varepsilon_\gamma^{\mathrm{p}}$

$$\{\tilde{\beta}_{,\Delta\varepsilon_\gamma^{\mathrm{p}}}\} = \frac{C_\beta x_\beta}{(\tilde{\beta}_{denom})^2}\Big\{b_\beta(\tilde{\beta}_{denom})\{s - s^\chi\} - (p_\beta - Rp_c b_\beta/2)\{\tilde{\beta}_{num}\}\Big\}. \tag{E.13}$$

The derivative of $\{\tilde{\beta}\}$ with respect to stress is given by

$$[\tilde{\beta}_{,\sigma}] = \Delta\gamma[\tilde{\beta}_{,\Delta\varepsilon^{\mathrm{p}}}][g_{,\sigma\sigma}] + \frac{1}{3}\{\tilde{\beta}_{,p}\}\{1\}^T + [\tilde{\beta}_{,s}][\delta], \qquad \text{where} \tag{E.14}$$

$$\{\tilde{\beta}_{,p}\} = \frac{\{\beta_n\}(\tilde{\beta}_{denom}) - \Big(1 + C_\beta(\langle\Delta\varepsilon_v^{\mathrm{p}}\rangle + x_\beta\Delta\varepsilon_\gamma^{\mathrm{p}})\Big)\{\tilde{\beta}_{num}\}}{(\tilde{\beta}_{denom})^2} \qquad \text{and} \qquad [\tilde{\beta}_{,s}] = \frac{C_\beta d_\beta [I]}{(\tilde{\beta}_{denom})}. \tag{E.15}$$

The derivatives of $\{\tilde{\beta}\}$ with respect to $\{\beta\}$ and $\{\sigma^\chi\}$ are simply given by

$$[\tilde{\beta}_{,\beta}] = \Delta\gamma[\tilde{\beta}_{,\Delta\varepsilon^{\mathrm{p}}}][g_{,\sigma\beta}] \qquad \text{and} \qquad [\tilde{\beta}_{,\sigma^\chi}] = -[\tilde{\beta}_{,\sigma}]. \tag{E.16}$$

The derivative of $\{\tilde{\beta}\}$ with respect to the size of the outer surface is given by

$$\begin{aligned}\{\tilde{\beta}_{,p_c}\} \quad = \quad & \Delta\gamma[\tilde{\beta}_{,\Delta\varepsilon^{\mathrm{p}}}]\{g_{,\sigma p_c}\} + \frac{R\gamma}{2(\tilde{\beta}_{denom})^2}\Big\{(\tilde{\beta}_{denom})\{\beta_n\}\ldots \\ & -\Big(1 + C_\beta(\langle\Delta\varepsilon_v^{\mathrm{p}}\rangle + x_\beta\Delta\varepsilon_\gamma^{\mathrm{p}} - d_\beta)\Big)\{\tilde{\beta}_{num}\}\Big\}\end{aligned} \tag{E.17}$$

and finally with respect to the plastic multiplier

$$\{\tilde{\beta}_{,\Delta\gamma}\} = [\tilde{\beta}_{,\Delta\varepsilon^{\mathrm{p}}}]\{g_{,\sigma}\}. \tag{E.18}$$

Bibliography

AJ Abbo & SW Sloan, *A smooth hyperbolic approximation to the MohrCoulomb yield criterion*, Comput. Struct. 54 (1995), 427-441.

A Anandarajah, *Discrete element method for simulating behavior of cohesive soils*, J. Geotech. Eng.-ASCE 120 (1994), 1593–1615.

A Anandarajah, *On the influence of fabric anisotropy on the stress-strain behaviour of clays*, Comput. Geotech. 27 (2000), 1–17.

A Anandarajah, *Computational Methods in Elasticity and Plasticity: Solids and Porous Media*, Springer, 2010.

P Anantanasakul, *Three-dimensional experiments and modelling of anisotropic clay*, PhD. Thesis, Oregon State University (2010).

PA Baran & PM Sweezy, *Monopoly capital: an essay on the American economic and social order*, Penguin Books, 1968.

JP Bardet, *Lode dependences for isotropic pressure-sensitive elastoplastic materials*, ASME J. Appl. Mech. 57 (1990), 498–506.

KJ Bathe, *Finite Element Procedures*, Praentice-Hall, New Jersey, 1996.

KJ Bathe, E Ramm & EL Wilson, *Finite element formulations for large deformation dynamic analysis*, Int. J. Numer. Meth. Eng. 9 (1975), 353–386.

B Baudet & S Stallebrass, *A constitutive model for structured clays*, Géotechnique (54) 2004, 269–278.

R Becker, *An alternative approach to integrating plasticity relations*, Int. J. Plasticity 27 (2011), 1224–1238.

K Been & MG Jefferies, *A state paramter for sands*, Géotechnique 35 (1985), 99–112.

T Benz, M Wehnert & PA Vermeer, *A Lode angle dependent formulation of the Hardening Soil model*, 12th IACMAG (2008), 653–660.

SK Bhowmik & JH Long, *A general formulation for the cross sections of yield surfaces in octahedral planes*. In: GN Pande and J Middleton (eds.) NUMENTA 90 (1990), 795–803.

D Bigoni, *Bifurcation and instability of non-associative elastoplastic solids*, Material instabilities in elastic and plastic solids, Springer-Verlag, Wien New York, (2000), 1–52.

D Bigoni & T Hueckel, *Uniqueness and localization-I. Associative and non-associative elastoplasticity*, Int. J. Solids Structures 28 (1991), 197–213.

D Bigoni & T Hueckel, *Uniqueness and localization-II. Coupled elastoplasticity*, Int. J. Solids Structures 28 (1991), 215–224.

D Bigoni & D Zaccaria, *On the eigenvalues of the acoustic tensor in elastoplasticity*, Eur. J. Mech. A/Solids 13 (1994), 621–638.

AW Bishop, DL Webb & PI Lewin, *Undisturbed samples of London Clay from the Ashford Common shaft: strength-effective stress relationships*, Géotechnique 15 (1965), 1–31.

MD Bolton & YP Chen, *Micro-geomechanics*. In: S Springman (ed.), International Workshop on Constitutive and Centrifuge Modelling: Two Extremes, Monte Verita, Switzerland, 2001.

RI Borja & A Aydin, *Computational modeling of deformation bands in granular media. I. Geological and mathematical framework*, Comput. Meth. Appl. Mech. Engrg. 193 (2004), 2667–2698.

RI Borja, C-H lin & FJ Montáns, *Cam-Clay plasticity, part IV: Implicit integration of anisotropic bouding surface model with nonlinear hyperelasticity and ellipsoidal loading function*, Comput. Methods Appl. Mech. Engrg. 190 (2001), 3293–3323.

RI Borja & C Tamagnini, *Cam-Clay plasticity Part III: Extension of the infinitesimal model to include finite strains*, Comput. Meth. Appl. Mech. Engrg 155 (1998), 73–95.

RM Brannon & S Leelavanichkul, *A multi-stage return algorithm for solving the classical damage component of constitutive models for rocks, ceramics, and other rock-like media*, Int. J. Fract. 163 (2010), 133–149.

TJ Bromwich, *Quadratic forms and their classification by means of invariant factors*, Cambridge Tracts in Mathematics and Mathematical Physics, London, 1906.

R Butterfield, *A natural compression law for soils (an advance on e-log p′)*, Géotechnique 29 (1979), 469–480.

M Cai, *Influence of intermediate principal stress on rock fracturing and strength near excavation boundaries-Insight from numerical modeling*, Int. J. of Rock Mech. Min. 45 (2008), 763–772.

MÁ Caminero, FJ Montáns & KJ Bathe, *Modeling large strain anisotropic elasto-plasticity with logarithmic strain and stress measures*, Comput. Struct. 89 (2011), 826–843.

DE Carlson & A Hoger, *The derivative of a tensor-valued function of a tensor*, Quart. Appl. Math 44 (1986), 409–423.

A Casagrande, *Characteristics of cohesionless soils affecting the stability of slopes and earth fills*, Contributions to soil mechanics, Boston Socitey of Civil Engineers (1936), 257–276.

JL Chaboche & G Cailletaud, *Integration methods for complex plastic constitutive equations*, Comput. Meth. Appl. Mech. Engrg. 133 (1996), 125–155.

R Chambon, J Desrues & W Hammad, *CLoE, a new rate-type constitutive model for geomaterials theoretical basis and implementation*, Int. J. Numer. Anal. Meth. Geomech. 18 (1994), 253–278.

WF Chen, *Constitutive Relations for Concrete Rock and Soils: Discusser's Report*. In: Z Baẑant (ed.), Mechanics of Geomaterials, 65–86, John Wiley & Sons Ltd., 1985.

WF Chen & E Mizuno, *Nonlinear analysis in soil mechanics: theory and implementation*, Elsevier, 1990.

J Clausen, L Damkilde & L Andersen, *Efficient return algorithms for associated plasticity with multiple yield planes*, Int. J. Numer. Meth. Eng. 66 (2006), 1036–1059.

J Clausen, L Damkilde & L Andersen, *An efficient return algorithm for non-associated plasticity with linear yield criteria in principal stress space*, Comput. Struct. 85 (2007), 1795–1807.

IF Collins, *A systematic procedure for constructing critical state models in three dimensions*, Int. J. Solids Struct. 40 (2003), 4379–4397.

IF Collins, *The concept of stored plastic work or frozen elastic energy in soil mechanics*, Géotechnique 55 (2005), 373–382.

IF Collins, *Elastic/plastic models for soils and sands*, Int. J. Mech. Sci. 47 (2005), 493–508.

IF Collins & T Hilder, *A theorectical framework for constructing elastic/plastic constitutive models of triaxial tests*, Int. J. Numer. Meth. Geomech. 26 (2002), 1313–1347.

IF Collins & GT Houlsby, *Application of thermomechanical principles to the modelling of geoetchnical materials*, Proc. R. Soc. Lond. A. 453 (1997), 1975–2001.

IF Collins & PA Kelly, *A thermomechanical analysis of a family of soil models*, Géotechnique 52 (2002), 507–518.

IF Collins & B Muhunthan, *On the relationship between stress–dilatancy, anisotropy, and plastic dissipation for granular materials*, Géotechnique 53 (2003), 611–618.

IF Collins, B Muhunthan & B Qu, *Thermomechanical state parameter models for sands*, Géotechnique 60 (2010), 611–622.

IF Collins, B Muhunthan, ATT Tai & MJ Pender, *The concept of a 'ReynoldsTaylor state' and the mechanics of sands*, Géotechnique 57 (2007), 437–447.

WM Coombs, *Reuleaux plasticity: overcoming Mohr-Coulomb and Drucker-Prager limitations*,

presented at the BGA 42nd Cooling prize competition, Loughborough, 2011.

WM Coombs & RS Crouch, *Non-associated Reuleaux plasticity: Analytical stress integration and consistent tangent for finite deformation mechanics*, Comput. Meth. Appl. Mech. Engrg. 200 (2011), 1021–1037.

WM Coombs & RS Crouch, *Algorithmic issues for three-invariant hyperplastic Critical State models*, Comput. Methods Appl. Mech. Engrg. 200 (2011), 2297–2318.

WM Coombs, RS Crouch & CE Augarde, *Influence of lode angle dependency on the critical state for rotational plasticity*, X International Conference on Computational Plasticity (COMPLAS X), Barcelona, 2009.

WM Coombs, RS Crouch & CE Augarde, *On the necessity for rotational yielding in anisotropic plasticity*, 17th UK Conference on Computational Mechanics (ACME-UK), 2009, 345–348.

WM Coombs, RS Crouch & CE Augarde, *Reuleaux plasticity: Analytical backward Euler stress integration and consistent tangent*, Comput. Meth. Appl. Mech. Engrg. 199 (2010), 1733–1743.

WM Coombs, RS Crouch & CE Augarde, *70-line 3D finite deformation elastoplastic finite-element code*. In: T Benz and S Nordal (eds.), 7th European Conference on Numerical Methods in Geoetchnical Engineering (2010), 151–156.

WM Coombs, RS Crouch & CE Augarde, *On the use of Reuleaux plasticity for geometric non-linear analysis*. In: 18th UK Conference on Computational Mechanics (ACME-UK), 2010, 113–116.

WM Coombs, RS Crouch & CE Augarde, *Unique Critical State hyperplasticity*, 19th UK Conference on Computational Mechanics (ACME-UK), 2011, 49–52.

RF Craig, *Craig's soil mechanics*, Seventh edition, Spon Press, 2004.

MA Crisfield, *Non-linear Finite Element Analysis of Solids and Structures. Volume 1: Essentials*, John Wiley & Sons Ltd, 1991.

MA Crisfield & GF Moita, *A unified co-rotational framework for solids, shells and beams*, Int. J. Solids Struct. 33 (1996), 2969–2992.

RS Crouch, H Askes & T Li, *Analytical CPP in energy-mapped stress space: application to a modified Drucker-Prager yield surface*, Comput. Meth. Appl. Mech. Engrg. 198 (2009), 853–859.

RS Crouch & JP Wolf, *On a three-dimensional anisotropic plasticity model for soil*, Géotechnique 45 (1995), 301–305.

PA Cundall & ODL Strack, *A discrete numerical model for granular assemblies*, Géotechnique 29 (1979), 47–65.

YF Dafalias, *On cyclic and anisotropic plasticity*, Ph.D. thesis, Department of Civil Engineering, University of California, Berkeley (1975).

YF Dafalias, *An anisotropic critical state clay plasticity model*, Mech. Res. Commun. 13 (1986), 341–347.

YF Dafalias, *Bounding surface plasticity. I: mathematical foundation and hypoplasticity*, J. Eng. Mech. ASCE 112 (1986), 966–987.

YF Dafalias, *Plastic spin: necessity or redundancy?*, Int. J. Plas. 14 (1998), 909–931.

YF Dafalias, *A simple anisotropic clay plasticity model*, Mech. Res. Commun. 29 (2002), 241–245.

YF Dafalias, MT Manzari & AG Padadimitriou, *SANICLAY: simple anisotropic clay plasticity model*, Int. J. Numer. Anal. Meth. Geomech. 30 (2006), 1231–1257.

YF Dafalias & EP Popov, *Cyclic, loading for materials with a vanishing elastic region*, Nuclear Engineering and Design 41 (1977), 293–302.

F Darve, E Flavigny & E Rojas, *A class of incrementally non-linear constitutive relations and applications to clays*, Comput. Geotech. 2 (1986), 43–66.

J Donea, A Huerta, J-Ph Ponthot & A Rodríguez-Ferran, *Arbitrary Lagrangian-Eulerian Methods*. In: Encyclopedia of Computational Mechanics 14 (2004), 413–437.

DC Drucker, RE Gibson & DJ Henkel, *Soil mechanics and work-hardening theories of plasticity*, Trans. ASCE 103 (1957), 338–346.

DC Drucker & W Prager, *Soil mechanics and plastic analysis or limit design*, Quart. Appl. Math.

10 (1952), 157–164.

AL Eterovic & KJ Bathe, *A hyperplastic-based large strain elasto-plastic constitutive formulation with combined isotropic-kinematic hardening using the logarithmic stress and strain measures*, Int. J. Numer. Meth. Engng. 30 (1990), 1099–1114.

A Federico, G Elia & V Germano, *A short note on the earth pressure and mobilized angle of internal friction in one-dimensional compression of soils*, J. GeoEngineering 3 (2008), 41–46.

E Fjær & H Ruistuen, *Impact of the intermediate principal stress on the strength of heterogeneous rock*, J. Geophys. Res. 107 (2002).

P Fu & YF Dafalias, *Fabric evolution within shear bands of granular materials and its relation to critical state theory*, Int. J. Numer. Anal. Meth. Geomech. (2010).

P Fu & YF Dafalias, *Study of anisotropic shear strength of granular materials using DEM simulation*, Int. J. Numer. Anal. Meth. Geomech. 35 (2011), 1098–1126.

YC Fung, *Foundations of solid mechanics*, Prentice-Hall Inc., 1965.

G Garbiel & KJ Bathe, *Some computational issues in large strain elasto-plastic analysis*, Comput. Struct. 56 (1995), 249–267.

A Gasparre, *Adavnced laboratory characterisation of london clay*, PhD. Thesis, Imperial College London, 2005.

A Gens, *Stress-strain characteristics of a low plasticity clay*, PhD. Thesis, Imperial College of Science and Technology, University of London (1982).

A Gens & DM Potts, *Critical state models in computational geomechanics*, Eng. Comput. 178 (1988), 178–197.

JS Goldsworthy, MB Jaksa, WS Kaggwa, GA Fenton, DV Griffiths & HG Poulos, *Cost of foundation failures due to limited site investigations*, International conference on Structural and Foundation Failures, 2004.

KM Górski, E Hivon, AJ Banday, BD Wandelt, FK Hansen, M Reinecke & M Bartelmann, *HEALPix: a framework for high-resolution discretization and fast analysis of data distributed on the sphere*, Astrophys. J. 622 (2005), 759–771.

AE Green & PM Naghdi, *A general theory of of an elastic-plastic continuum*, Arch. Ration. Mech. An. 18 (1965), 251–281.

DV Griffiths, *Failure criteria interpretation based on Mohr-Coulomb friction*, ASCE J. Geotech. Eng. 116 (1990), 986–999.

G Gudehus, *Comparison of some constitutive laws for soils under radially symmetric loading and unloading*. In: Proceedings of the 3rd International Conference on Numerical Methods in Geomechanics, Aachen, 1979, 1309–1323.

G Gudehus, *Requirements for Constitutive Relations for Soils*. In: Z Baẑant (ed.), Mechanics of Geomaterials, 47–63, John Wiley & Sons Ltd., 1985.

W Han & BD Reddy, *Plasticity: mathematical theory and numerical analysis*, Springer, 1999.

K Hashiguchi, *Mathematically consistent formulation of elastoplastic constitutive equations*, in Numerical Methods in Geomechanics, Innsbruck, Swoboda (ed.), 1988, 467–472.

K Hashiguchi, *Verification of compatibility of isotropic consolidation characteristics of soils to multiplicative decomposition of deformation gradient*, Soils Found. 48 (2008), 597–602.

K Hashiguchi & Z-P Chen, *Elastoplastic constitutive equation of soils with the subloading surface and the rotational hardening*, Int. J. Numer. Anal. Meth. Geomech. 22 (1998), 197–227.

K Hashiguchi & T Mase, *Extended yield condition of soils with tensile yield strength and rotational hardening* Int. J. Plasticity 23 (2007), 1939–1956.

JE Hellings, *Geotechnical failure: the cause is not always obvious and may be complex*, http://reliability.geoengineer.org/TC40/13ARC_Hellings.pdf, 2007, accessed 6th June 2009.

DW Hight, A Gens & MJ Symes, *The development of a new hollow cylinder appparatus for investigating the effects of principal stress rotation in soils*, Géotechnique 33 (1983), 355–383.

DW Hight, F McMillan, JJM Powell, RJ Jardine & CP Allenou, *Some characteristics of London*

Clay, Characterisation of Engineering Properties of Natural Soils, Tan *et al.* (eds.), 2003.

R Hill, *The mathematical theory of plasticity*, Oxford University Press, London, 1950.

R Hill, *A general theory of uniqueness and stability in elastic-plastic solids*, J. Mech. Phys. Solids 6 (1958), 236–249.

R Hill, *Acceleration waves in solids*, J. Mech. Phys. Solids 10 (1962), 1–16.

E Hinton, *NAFEMS introduction to nonlinear finite element analysis*, NAFEMS, 1992.

GA Holzapfel, *Nonlinear solid mechanics*, John Wiley & Sons Ltd. 2000.

H-K Hong & C-S Liu, *Internal symmetry in bilinear elastoplasticity* Int. J. Nonlin. Mech. 34 (1999), 279–288.

MR Horne, *The behaviour of an assembly of rotund, rigid, cohesionless particles I.* Proc. R. Soc. London. Ser. A. 286 (1965), 62–78.

MR Horne, *The behaviour of an assembly of rotund, rigid, cohesionless particles II.* Proc. R. Soc. London. Ser. A. 286 (1965), 79–97.

S Horpibulsuk, MD Liu, DS Liyanapathirana & J Suebsuk, *Behaviour of cemented clay simulated via the theoretical framework of the Structured Cam Clay model*, Comput. Geotech. 37 (2010), 1–9.

GT Houlsby, *A study of plasticity theories and their applicability to soils*, PhD. Thesis, University of Cambridge, 1981.

GT Houlsby, *The use of a variable shear modulus in elastic-plastic models for clays*, Comput. Geotech. 1 (1985), 3–13.

GT Houlsby & AM Puzrin, *A thermomechanical framework for constitutive models for rate-independent dissipative materials*, Int. J. Plasticity 16 (2000), 1017–1047.

GT Houlsby & AM Puzrin, *Principles of hyperplasticity*, Springer-Verlag London Limited, 2006.

M Huang, Y Liu & D Sheng, *Simulation of yielding and stress-stain behaviour of shanghai soft clay*, Comput. Geotech. 38 (2011), 431–353.

TJR Hughes & J Winget, *Finite rotation effects in numerical integration of rate constitutive equations arising in large-deformation analysis*, Int. J. Numer. Meth. Eng. 15 (1980), 1862–1867.

AA Ilyushin, *Some problems in the theory of plastic deformation*, Prikl. Mat. Mekh. 7 (1943), 245–272.

S Imposimato & R Nova, *An investigation on the uniqueness of the incremental response of elastoplastic models for virgin sand*, Mech. Cohes.-Frict. Mat. 3 (1998), 65–87.

Inadequate site investigation, Institution of Civil Engineers, 1991.

K Issen & V Challa, *Influence of the Intermediate Principal Stress on Compaction Localization Conditions*, The 41st U.S. Symposium on Rock Mechanics (USRMS), June 17–21, 2006.

M Itskov, *On the application of the additive decomposition of generalised strain measures in large strain plasticity*, Mech. Res. Commun. 31 (2004), 507–517.

WD Iwan, *On a class of models for the yielding behavior of continuous and composite systems* J. App. Mech. 34 (1967), 612–617.

J Jaky, *Pressure in silos*, Proc 2nd Int. Conf. on Soil Mechanics and Foundation Engineering, Rotterdam, Nederland, 1 (1948), 103–107.

RJ Jardine, *Investigation of pile-soil behaviour, with special reference to the foundations of offshore structures*, PhD Thesis, Imperial College, University of London, 1985.

J Jiang & HI Ling, *A framework of an anisotropic elastoplastic model for clays*, Mech. Res. Commun. 37 (2010), 394–398.

M Jirásek, *Nonlocal theories in continuum mechanics*, Acta Polytech. 44 (2004), 16–34.

M Karstunen & M Koskinen, *Plastic anisotropy of soft reconstituted clays*, Can. Geotech. J. 45 (2008), 314–328.

M Karstunen, H Krenn, SJ Wheeler, M Koskinen & R Zentar, *Effect of anisotropy and destructuration on the behavior of murro test embankment*, Int. J. Geomech.-ASCE 5 (2005), 87–97.

D-N Kim, FJ Montáns, and K-J Bathe, *Insight into a model for large strain anisotropic elasto-plasticity*, Comput. Mech. 44 (2009), 651–668.

M Kojić, *The Governing Parameter Method for implicit integration of viscoplastic constitutive relations for isotropic and orthotropic metals*, Compt. Mech. 19 (1996), 49–57.

M Kojić, *Stress integration procedures for inelastic material models within the Finite Element Method*, Appl. Mech. Rev. 55 (2002), 389–414.

M Kojić & KJ Bathe, *Inelastic analysis of solids and structures*, Springer, 2005.

D Kolymbas, *A rate-dependent constitutive equation for soils* Mech. Res. Comm. 4 (1977), 367–372.

D Kolymbas, *An outline of hypoplasticity*, Arch. Appl. Mech. 61 (1991), 143–151.

D Kolymbas & I Herle, *Hypoplasticity for soils with low friction angles*, Comput. Geotech. 31 (2004), 365–373.

A Kossa & L Szabó, *Exact integration of the von Mises elastoplasticity model with combined linear isotropic-kinematic hardening*, Int. J. Plasticity 25 (2009), 1083–1106.

A Kossa & L Szabó, *Numerical implementation of a novel accurate stress integration scheme of the von Mises elastoplasticity model with combined linear hardening*, Finite Elem. Anal. Des. 46 (2010), 391–400.

E Kreyszig, *Advanced engineering mathematics*, John Wiley & Sons, 1999.

RD Krieg & SM Key, *Implementation of a time dependent plasticity theory and structural computer programs*. In: JA Stricklin & KJ Saczalski (eds.), Constituive Equations in Viscoplasticity: Computational and Engineering Aspects, ASME, New York, 20 (1976), 125–137.

RD Krieg & DB Krieg, *Accuracies of numerical solution methods for the elastic-perfactly plastic model*, J. Press. Vess.-T. ASME 99 (1977), 510–515.

GT-C Kung, C-Y, Ou & CH Juang, *Modeling small-strain behavior of Taipei clays for finite element analysis of braced excavations*, Comput. Geotech. 36 (2009), 304–319.

PV Lade, *Instability, shear banding and failure in granular materials*, Int. J. Solids Struct. 39 (2002), 3337–3357.

PV Lade & JM Duncan, *Cubical triaxial tests on conhesionless soil*, J. Soil Mech. Found. Div. ASCE 99 (1973), 793–812.

PV Lade & MM Kirkgard, *Effects of stress rotation and changes of b-values on cross-anisotropic behavior of natural K_0-consolidated soft clay*, Soils Found. 40 (2000), 93–105.

EH Lee, *Elastic-plastic deformation at finite strains*, J. App. Mech. 36 (1969), 1–6.

EH Lee and DT Lu, *Finite-strain elastic-plastic theory with application to plane-wave analysis*, J. App. Phys. 38 (1967), 19–27.

MD Liu & JP Carter, *A structured Cam Clay model* Can. Geotech. J. 39 (2002), 1313–1332.

B Loret & JH Prévost, *Accurate numerical solutions for drucker-prager elastic-plastic models*, Comput. Meth. Appl. Mech. Engrg. 54 (1986), 259–277.

N Lu & WJ Likos, *Unsaturated soil mechanics*, John Wiley & Sons, 2004.

D Mašín & I Herle, *State boundary surface of a hypoplastic model for clays*, Comput. Geotech. 32 (2005), 400–410.

H Matsuoka & T Nakai, *Stress-deformation and strength characteristics of soil under three different principal stresses*, Proc. JSCE 232 (1974), 59–70.

GA Maugin, *A.A. Ilyushin's works: an appraisal from Paris*, J. Eng. Math. (2011), doi: 10.1007/s10665-010-9450-4.

GA Maugin, *The thermomechanics of plasticity and fracture*, Cambridge University Press, 1992.

A Mendelson, *Plasticity: theory and application*, The Macmillan Co., NY, 1968.

C Miehe, *Comparison of two algorithms for the computation of fourth-order isotropic tensor functions*, Comput. Struct. 66 (1998), 37–43.

C Miehe, M Apel, & M Lambrecht, *Anisotropic additive plasticity in the logarithmic strain space: modular kinematic formulation and implementation based on incremental minimization principles*

for standard materials, Comput. Meth. Appl. Mech. Engrg. 191 (2002), 5383–5425.

SC Möller & PA Vermeer, *On numerical simulation of tunnel installation*, Tunn. Undergr. Sp. Tech., 23 (2008), 461–475.

TK Molstad, *Finite deformation analysis using the finite element method*, PhD. Thesis, Univeristy of British Columbia, 1977.

FJ Montáns & KJ Bathe, *Towards a model for large strain anisotropic elasto-plasticity*. In: Oate E, Owen R (eds.) Computational plasticity. Springer, Berlin, 2007, 13-36.

FC Moon, *Franz Reuleaux: Contributions to 19th C. kinematics and theory of machines*, Tech. report, Cornell Library Technical Reports and Papers, 2002.

AP Morris & DA Ferrill, *The importance of the effective intermediate principal stress (σ_2') to fault slip patterns*, J. Struct. Geol. 31 (2009), 950–959.

J Mosler, *Numerical analyses of discontinuous material bifurcation: strong and weak discontinuities*, Comput. Meth. Appl. Mech. Engrg. 194 (2005), 979–1000.

Z Mróz, VA Norris & OC Zienkewicz, *Application of an anisotropic hardening model in the analysis of elasto-plastic deformation of soils* Géotechnique 29 (1979), 1–34.

Z Mróz, *On the description of anisotropic workhardening*, J. Mech. Phys. Solids 15 (1967), 163–175.

B Muhunthan, JL Chameau & E Masad, *Fabric effects on the yield behaviour of soils* Soils Found. 36 (1996), 85–97.

JJ Nader, *A new constitutive theory extending hypoplasticity*, Mech. Res. Commun. 30 (2010), 505–509.

JC Nagtegaal, DM Parks & JR Rice, *On numerically accurate finite element solutions in the fully plastic range*, Comput. Meth. Appl. Mech. Engrg. 4 (1974), 153–177.

JC Nagtegaal, *On the implementation of inelastic constitutive equations with special reference to large deformation problems*, Comput. Meth. Appl. Mech. Engrg. 33 (1982), 469–484.

GC Nayak & OC Zienkiewicz, *Elasto-plastic stress analysis. A generalization for various constiutive relations including strain softening*, Int. J. Numer. Meth. Eng. 5 (1972), 113–135.

M Nazem, D Sheng, JP Carter & SW Sloan, *Arbitrary Lagrangian-Eulerian method for large-strain consolidation problems* Int. J. Numer. Anal. Meth. Geomech. 32 (2008), 1023–1050.

S Nishimura, *Laboratory study on anisotropy of natural London Clay*, PhD. Thesis, Imperial College London (2005).

S Nishimura, NA Minh & RJ Jardine, *Shear strength anisotropy of natural London Clay*, Géotechnique 51 (2007), 49–62.

J Oliver, AE Huespe, JC Cante & G Díaz, *On the numerical resolution of the discontinuous material bifurcation problem*, Int. J. Numer. Meth. Eng. 83 (2010), 786–804.

M Ortiz & JB Martin, *Symmetry-preserving return ampping algorithms and incrementally extremal paths: a unification of concepts*, Int. J. Numer. Meth. Eng. 28 (1989), 1839–1853.

M Ortiz & EP Popov, *Accuracy and stability of integration algorithms for elastoplastic constitutive relations*, Int. J. Numer. Meth. Eng. 21 (1985), 1561–1576.

M Ortiz & JC Simo, *An analysis of a new class of integration algorithms for elastoplastic constitutive relations*, Int. J. Numer. Meth. Eng. 23 (1986), 353–366.

AG Papadimitriou, AD Vranna, YF Dafalias & MT Manzari, *Effect of yield surface shape on the simulated elasto-plastic response of cohesive soils*, 7th European Conference on Numerical Methods in Geoetchnical Engineering (NUMGE), 2010, 63–68.

PHG Parry, Corresspondence on *On yielding of soils*, Géotechnique 8 (1958), 183–186.

JM Pestana & AJ Whittle, *Formulation of a unified constitutive model for clays and sands*, Int. J. Numer. Anal. Meth. Geomech. 23 (1999), 1215–1243.

PM Pinsky, M Ortiz & KS Pister, *Numerical integration of rate constitutive equations in finite deformation analysis*, Comput. Meth. Appl. Mech. Engrg. 40 (1983), 137–158.

DM Potts, *Numerical analysis: a virtual dream or peactical reality?*, Géotechnique 53 (2003), 535–573.

DM Potts & L Zdravković, *Finite element analysis in geotechnical engineering: application*, Thomas Telford Publishing, London, 2001.

JH Prévost, *Mathematical modelling of monotonic and cyclic undrained clay behaviour*, Int. J. Numer. Anal. Meth. Geomech. 1 (1977), 195–216.

JH Prévost, *Anisotropic undrained stress-strain behavior of clays*, J. Geotech. Eng.-ASCE 104 (1978), 1075–1090.

JH Prévost, *Plasticity theory for soil stress-strain behavior*, J. Eng. Mech.-ASCE 104 (1978), 1177–1194.

JH Prévost, *A Simple Plasticity Theory for Cohesionless Frictional Soils*, Soil Dyn. Earthq. Eng. 4 (1985), 9–17.

JH Prévost & JP Wolf, *Nonlinear soil mechanics and dynamic soil-structure interaction*, Lausanne, Switzerland, 1987.

AM Puzrin & JB Burland, *Kinematic hardening plasticity formulation of small strain behaviour of soils*, Int. J. Numer. Anal. Meth. Geomech. 24 (2000), 753–781.

AM Puzrin & GT Houlsby, *A thermomechanical framework for rate-independent dissipative materials with internal functions*, Int. J. Plasticity 17 (2001), 1147–1165.

AM Puzrin & GT Houlsby, *Fundamentals of kinematic hardening hyperplasticity*, Int. J. Solids Struct. 38 (2001), 3771–3794.

CA Radeke, BJ Glasser & JG Kinast, *Large-scale powder mixer simulations using massively parallel GPU architectures*, Chem. Eng. Sci. 65 (2010), 6435–6442.

F Reuleaux, *The kinematics of machinery: Outlines of a theory of machines*, Macmillan and Co., London, 1876.

M Rezaiee-Pajand, M Sharifian & M Sharifian, *Accurate and approximate integrations of Drucker-Prager plasticity with linear isotropic and kinematic hardening*, Eur. J. Mech. A-Solid 30 (2011), 345–361.

E Rizzi, G Maier & K Willam, *On failure indicators in multi-dissipative materials*, Int. J. Solids Struct. 33 (1996), 3187–3214.

KH Roscoe, AN Schofield & CP Wroth, *On the yielding of soils*, Géotechnique 8 (1958), 22–53.

KH Roscoe & JB Burland, *On the generalised stress-strain behaviour of 'wet' clay*. In: J Heyman & FA Leckie (eds.), Engineering Plasticity (1968), Cambridge University Press, 535–609.

M Rouainia & DM Wood, *Implicit numerical integration for a kinematic hardening soil plasticity model*, Int. J. Numer. Anal. Meth. Geomech. 25 (2001), 1305–1325.

JW Rudnicki & JR Rice, *Conditions for the localization of deformation in pressure-sensitive dilatant materials*, J. Mech. Phys. Solids 23 (1975), 371–394.

SL Salas, E Hille & G Etgen, *Calculus*, 9th ed., John Wiley & Sons Inc., 2003.

A Säyao & YP Vaid, *Effect of intermediate principal stress on the deformation response of sand*, Can. Geotech. J. 33 (1996), 822–828.

AN Schofield & CP Wroth, *Critical State Soil Mechanics*, McGraw-Hill Publishing Company Limited, 1968.

HL Schreyer & MK Neilsen, *Discontinuous bifurcation states for associated smooth plasticity and damage with isotropic elasticity*, Int. J. Solids Struct. 33 (1996), 3239–3256.

RT Shield, *On Coulomb's law of failure in soils*, J. Mech. Phys. Solids 4 (1955), 10–16.

JC Simo, *A framework for finite strain elastoplasticity based on maximum plastic dissipation and the multiplicative decomposition. Part II: computational aspects*, Comput. Meth. Appl. Mech. Engrg. 68 (1988), 1–31.

JC Simo & F Armero, *Geometrically non-linear enhanced strain mixed methods and the method of incompatible modes*, Int. J. Numer. Meth. Eng. 33 (1992), 1413–1449.

JC Simo & TJR Hughes, *General return mapping algorithims for rate-independent plasticity*, Constitutive Laws for Engineering Materials: Theory and Applications, Cambridge University Press, 1987.

JC Simo & TJR Hughes, *Computational inelasticity*, Springer, New York, 1998.

JC Simo & M Ortiz, *A unified approach to finite deformation elastoplastic analysis based on the use of hyperelastic constitutive equations*, Comput. Meth. Appl. Mech. Engrg. 49 (1985), 221–245.

JC Simo & MS Rifai, *A class of mixed assumed strain methods and the method of incompatible modes*, Int. J. Numer. Meth. Eng. 29 (1990), 1595–1638.

JC Simo & RL Taylor, *Consistent tangent operators for rate-independent elastoplasticity*, Comput. Meth. Appl. Mech. Engrg. 48 (1985), 101–118.

JC Simo, RL Taylor & KS Pister, *Variational and projection methods for the volume constraint in finite deformation elasto-plasticity*, Comput. Meth. Appl. Mech. Engrg. 51 (1985), 177–208.

Site Investigation & Engineering Practice, Allied Exploration & Geotechnics Limited, 2007.

N Sivasithamparam, D Kamrat-Pietrasewska & M Karstunen, *An anisotropic bubble model for soft clays*, 7th European Conference on Numerical Methods in Geoetchnical Engineering (NUMGE), 2010, 21–26.

IM Smith, *A general purpose system for finite element analyses in parallel*, Eng. Comput. 17 (2000), 75–91.

EA de Souza Neto & D Perić, *A computational framework for a class of fully coupled models for elastoplastic damage at finite strains with reference to the linearization aspects*, Comput. Meth. Appl. Mech. Eng. 130 (1996), 179–193.

EA de Souza Neto, D Perić, M Dutko & DRJ Owen, *Design of simple low order finite elements for large strain analysis of nearly incompressible solids*, Int. J. Solids Structs 33 (1996), 3277–3296.

EA de Souza Neto, D Perić & DRJ Owen, *A model for elastoplastic damage at finite strains: algorithmic issues and applications*, Eng. Comput. 11 (1994), 257–281.

EA de Souza Neto, D Perić & DRJ Owen, *Computational methods for plasticity: Theory and applications*, John Wiley & Sons Ltd, 2008.

A Spencer, *Continuum Mechanics*, Dover Publications, 1980.

SE Stallebrass, & RN Taylor, *The development and evaluation of a constitutive model for the prediction of ground movements in overconsolidated clay*, Géotechnique 47 (1997), 235–253.

P Stephenson & M Skinner, *Application of numerical analysis to the Kings Place Project*, Workshop on numerical modelling in geomechanics, Newcastle-upon-Tyne, April 2009.

J Suebsuk, S Horpibulsuk & MD Liu, *Modified Structured Cam Clay: A generalised critical state model for destructured, naturally structured and artificially structured clays*, Comput. Geotech. 37 (2010), 956–968.

L Szabó, *A semi-analytical integration method for J2 flow theory of plasticity with linear isotropic hardening*, Comput. Meth. Appl. Mech. Engrg. 198 (2009), 2151-2166.

M Taiebat, YF Dafalias & R Peek, *A destructuration theory and its application to SANICLAY model*, Int. J. Numer. Anal. Meth. Geomech. 34 (2010), 1009–1040.

SP Timoshenko & S Woinowsky-Krieger, *Theory of Plates and Shells*, McGraw-Hill, 1959.

LN Trefethen, *Ten digit algorithms*, Conference on Numerical Analysis, Dundee, 2005.

C Truesdell & W Noll, *The non-linear field theories of mechanics*, Springer-Verlag, 1965. C Turnbull, *The exact stress integration of elasto-plasticity models*, MEng. Final Year Research Report, Durham Univeristy, 2010.

J van Tiel, *Convex analysis: an introductory text*, John Wiley & Sons, 1984.

M Vrh, M Halilovič & B Štok, *Improved explicit integration in plasticity*, Int. J. Numer. Meth. Eng. 81 (2010), 910–938.

G Weber & L Anand, *Finite deformation constitutive equations and a time integration procedure for isotropic, hyperelastic-viscoplastic solids*, Comput. Meth. Appl. Mech. Engrg. 79 (1990), 173–202.

Z Wei, D Perić & DRJ Owen, *Consistent linearization for the exact stress update of Prandtl-Reuss non-hardening elastoplastic models*, Int. J. Num. Meth. Eng. 39 (1996), 1219–1235.

T Weifner & D Kolymbas, *Review of two hypoplastic equations for clay considering axisymmetric element deformations* Comput. Geotech. 35 (2008), 760–774.

AJ Whittle & YMA Hashash, *Soil modeling and prediction of deep excavation behavior*, in Shibuya, Mitachi & Miura (ed.), Pre-faliure deformation of geomaterials (1994), 589–594.

M Wilkins, *Calculation of elastic-plastic flow*, in S Fernback & M Rotenberg (eds.), Methods of Computational Physics, Vol 3, Academic Press, N.Y., 1964.

KJ Willam & M-M Iordache, *On the lack of symmetry in materials*. In: WA Wall, K-U Bietzinger & K Schweizerhof (eds.), Trends in computational structural mechanics, CIMNE, Barcelona, Spain, 2001.

KJ Willam & EP Warnke, *Constitutive model for the triaxial behaviour of concrete*, Proceedings of the May 17-19 1974, International Association of Bridge and Structural Engineers Seminar on Concrete Structures Subjected to Triaxial Stresses, held at Bergamo Italy, 1974.

SJ Wheeler, A Näätänen, M Karstunen & M Lojander, *An anisotropic elastoplastic model for soft clays*, Can. Geotech. J. 40 (2003), 403–418.

AJ Whittle, *Evaluation of a constitutive model for overconsolidated clays*, Géotechnique 43 (1993), 289–313.

AJ Whittle & MJ Kavvadas, *Formulation of MIT-E3 Constitutive Model for Overconsolidated Clays*, J. Geotech. Eng.-ASCE 120 (1994), 173–198.

DM Wood, *Soil Behaviour and Critical State Soil Mechanics*, Cambridge Univeristy Press, 1990.

DM Wood, *Geotechnical modelling*, Spon Press, 2004.

CP Wroth & A Palmer, *Preface to the Proceedings of the symposium on Plasticity and Soil Mechanics*, Cambridge, (1973), 13–15.

A Wynne, *Getting to the core*, http://www.nce.co.uk/getting-to-the-core/1949566.article, 2008, accessed 7th June 2009.

L Xue & T Belytschko, *Fast methods for determining instabilities of elasticplastic damage models through closed-form expressions*, Int. J. Numer. Meth. Eng. 84 (2010), 1490–1518.

Y Yamakawa, K Hashiguchi & K Ikeda, *Implicit stress-update algorithm for isotropic Cam-clay model based on the subloading surface concept at finite strains*, Int. J. Plasticity 26 (2010), 634–658.

WM Tan, K-V Yuen & GL Yoon, *Bayesian probabilistic approach for the correlations of compression index for marine clays*, J. Geotech. Geoenviron. 135 (2009), 1932–1940.

Y-P Yao, W Hou & A-N Zhou, *UH model: three-dimensional unified hardening model for overconsolidated clays*, Géotechnique 59 (2009), 451–469.

M-H Yu, *Advances in strength theories for materials under complex stress state in the 20th Century*, Appl. Mech. Rev. 55 (2002), 169–218.

H-S Yu, *Plasticity and geotechnics*, Springer, 2006.

HS Yu & GT Houlsby, *Finite cavity expansion in dilatant soils: Loading analysis*, Géotechnique 41, (1991), 173–183.

H-S Yu, C Khong, & J Wang, *A unified plasticity model for cyclic behaviour of clay and sand*, Mech. Res. Commun. 34 (2007), 97–114.

L Zdravkoić, DM Potts & DW Hight, *The effect of strength anisotropy on the behaviour of embankments on soft ground*, Géotechnique 52 (2002), 447–457.

H Ziegler, *An introduction to thermomechanics*, 2nd edn. North Holland Pub. Co, Amsterdam, 1983.

M Zytynski, MF Randolph, R Nova & CP Wroth, *On modeling the unloading-reloading behaviour of soils*, Int. J. Numer. Anal. Meth. Geomech. 2 (1978), 87–93.